

**FACULTY
OF MATHEMATICS
AND PHYSICS**
Charles University

HABILITATION THESIS

**Nuclear magnetic resonance
and density functional theory
in solid state physics**

Vojtěch Chlan

Prague 2020

I would like to thank to all my collaborators and colleagues as the presented results could hardly be accomplished without their contributions, samples, and discussions in the past years.

My greatest thanks belong to my wife and family for their support.

Contents

Introduction	1
1 Nuclear Magnetic Resonance in Solids	3
1.1 Hyperfine magnetic interaction	3
1.2 Hyperfine electric quadrupole interaction	4
1.3 NMR shifts	5
2 Calculation of NMR parameters	7
2.1 Calculation of hyperfine magnetic fields	8
2.2 Calculation of electric field gradients	10
2.3 Calculation of chemical and Knight shieldings	10
2.4 Role of anisotropic interactions	11
3 NMR & DFT: Applications to magnetic and non-magnetic solids	15
3.1 Hexagonal ferrites	15
3.2 Magnetite and other ferrites	24
3.3 Non-magnetic systems	30
Concluding remarks	37
References	43
List of commented papers	46
Reprints of commented papers	47
P. Novák and V. Chlan, Phys. Rev. B 81, 174412 (2010).	48
V. Chlan, H. Štěpánková, R. Řezníček, and P. Novák, Solid State Nucl. Magn. Reson. 40, 27–30 (2011).	55
J. Toepfer, D. Seifert, J.-M. Le Breton, F. Langenhorst, V. Chlan, K. Kouřil, and H. Štěpánková, J. Solid State Chem. 226, 133–141 (2015).	59
V. Chlan, K. Kouřil, K. Uličná, H. Štěpánková, J. Toepfer, and D. Seifert, Phys. Rev. B 92, 125125 (2015).	68
V. Chlan, K. Kouřil, and H. Štěpánková, Acta Phys. Pol. A 127, 594–596 (2015).	78
K. Kouřil, V. Chlan, H. Štěpánková, P. Novák, K. Knížek, J. Hybler, T. Kimura, Y. Hiraoka, and J. Buršík, J. Magn. Magn. Mater 322, 1243–1245 (2010).	81

K. Kouřil, V. Chlan, H. Štěpánková, A. Telfah, P. Novák, K. Knížek, Y. Hiraoka, and T. Kimura, <i>Acta Phys. Pol. A</i> 118, 732–733 (2010).	84
V. Chlan, K. Kouřil, H. Štěpánková, R. Řezníček, and J. Englich, <i>Acta Phys. Pol. A</i> 126, 42–43 (2014).	86
R. Řezníček, V. Chlan, H. Štěpánková, and P. Novák, <i>Phys. Rev. B</i> 91, 125134 (2015).	88
↔ supplementary material	98
R. Řezníček, V. Chlan, H. Štěpánková, P. Novák, J. Zukrowski, A. Kozłowski, Z. Kakol, Z. Tarnawski, and J. M. Honig, <i>Phys. Rev. B</i> 96, 195124 (2017).	108
R. Řezníček, V. Chlan, H. Štěpánková, P. Novák, and M. Maryško, <i>J. Phys. Condens. Matter</i> 24, 055501 (2012).	115
↔ supplementary material	125
V. Chlan, P. Novák, H. Štěpánková, J. Englich, J. Kuriplach, and D. Nižňanský, <i>J. Appl. Phys.</i> 99, 08M903 (2006).	128
V. Procházka, H. Štěpánková, V. Chlan, J. Tuček, J. Čuda, K. Kouřil, J. Filip, and R. Zbořil, <i>J. Phys. Condens. Matter</i> 23, 205503 (2011).	131
R. Řezníček, V. Chlan, and J. Haase, <i>Phys. Rev. B</i> 99, 125121 (2019).	136
↔ supplementary material	145
V. Chlan, P. Doležal, R. Sgallová, M. Klicpera, C. Franz, and P. Ja- vorský, <i>J. Phys. Condens. Matter</i> 31, 385601 (2019).	149
↔ supplementary material	158
R. Gühne, V. Chlan, G. V. M. Williams, S. V. Chong, K. Kadowaki, A. Poepl, and J. Haase, <i>J. Magn. Reson.</i> 302, 34–42 (2019).	160
Y. O. Zagorodniy, V. Chlan, H. Štěpánková, Y. Fomichov, J. Pejchal, V. V. Laguta, and M. Nikl, <i>J. Phys. Chem. Solids</i> 126, 93–104 (2019).	169

Introduction

Nuclear magnetic resonance (NMR) is a unique spectroscopic method for studying condensed matter: it gains information about the structure and important properties at atomic level, from the point of view of atomic nuclei. At the same time the measurement itself does not significantly perturb its point of interest, the electronic system. Namely, the resonant frequencies of nuclei are usually several orders of magnitude lower than analogous frequencies for electrons, phonons, or other species, which are thus affected by weak quasi-static fields only.

While NMR spectroscopy is a robust and irreplaceable method for studying structure and dynamics of liquids, where subtle electron-nuclear and inter-nuclear interactions can be captured in high-resolution spectra, the use of NMR in solid-state physics is much more limited. It is partly because of higher experimental demands in the solid-state NMR measurements, but to a great extent also due to the fact that analysis and interpretation of solid-state NMR spectra is more difficult. Ironically, the uniqueness of the method then becomes a curse: often there are no other experimental methods with adequate resolution to which the NMR results could be compared. The interpretation of NMR spectra of complex solids and magnetic materials may thus become extremely challenging.

The lack of other complementary experimental methods, fortunately, does not apply to methods for calculation of electronic structure. In this regard, the situation is in fact quite appropriate: the local character of NMR is exactly what supports such connection, since relatively small models in the electronic structure calculation are sufficient to describe the experimental spectra. Combination of the two methods, one experimental and one computational, but both focused on atomic scale, brings two main benefits:

- The calculations of spectroscopic parameters greatly simplify understanding of experimental NMR spectra, or even allow the interpretation in cases where it would be unfeasible otherwise.
- On the other hand, confronting the *ab initio* calculation with NMR experiment via the spectroscopic parameters supports the credibility of the calculated model. This applies not only to the properties being directly compared, but justifies the model as a whole, and thus also increases the reliability of other calculated physical properties – even those which cannot be obtained experimentally.

We have been applying and developing this comparative approach in the last decade. At the beginning we were concerned mostly with the local magnetic fields and gradients of electric fields in magnetically ordered materials, hence magnetic, multiferroic, and related materials were the subject of majority of the presented papers. More recently with advancement of computational possibilities our focus has been widened also to non-magnetic solids.

The thesis is structured in the following way: first chapter briefly introduces the nuclear magnetic resonance method, especially describes interactions of nuclear moments with local magnetic and electric fields – hyperfine magnetic field, electric field gradient, and chemical and Knight shift – and how they manifest in the NMR spectroscopy. Second chapter presents the methods of density functional

theory (DFT) calculations, which were used in our studies, with focus on local magnetic and electric fields: how the related quantities can be determined and how accurately, and also where the usual practice fails and other solutions need to be searched for. The way, how the approach of comparing NMR experiments and DFT calculations was applied in practice, is then presented in the last chapter in a form of commenting on the main results of the published papers.

1. Nuclear Magnetic Resonance in Solids

The nuclear magnetic resonance phenomenon is based on the interaction of nuclear moments with local magnetic and electric fields. The key prerequisite is the presence of nuclei with suitable nuclear spin I : nuclei with $I \geq \frac{1}{2}$ possess magnetic dipole moment and those with $I \geq 1$ possess electric quadrupole moment. The energy level of the ground state for such nuclei is then split by Zeeman interaction with magnetic field and/or by electric quadrupole interaction, and by exciting the transitions between the split levels it is possible to induce the NMR. The acquired NMR spectrum corresponds to the values of these local fields and thus carries essential spectroscopic information about the structure and other properties of the studied system.

The local magnetic and electric fields originate mostly by interaction of nucleus with electronic system, as is the case of magnetically ordered solids where the values of the local fields are directly reflected in the NMR spectrum. For non-magnetic solids the magnetic field is supplied as a very homogeneous static external magnetic field \mathbf{B}_0 and the resonance then probes subtle deviations from the value of \mathbf{B}_0 . Regardless of the origin of the local fields, the key property of NMR (as for most spectroscopies) is the fact that, in general, nuclei in two different environments (e.g., nonequivalent crystal sites) have different values of the local fields, and therefore, different resonance frequencies in the NMR spectrum.

Besides the Coulomb interaction between the positive charge of the atomic nucleus and the surrounding electronic charge density, the nucleus interacts with electrons also via its nuclear moments: magnetic dipole moment and electric quadrupole moment. These interactions are usually termed the hyperfine interactions and are briefly described in the following paragraphs, accompanied by description of NMR shifts. Some of these quantities are, as well, of interest for Mössbauer spectroscopy, which was also utilized as an experimental method (together with or instead of NMR) in several of the presented works.

1.1 Hyperfine magnetic interaction

A nucleus with non-zero spin possesses nuclear dipole magnetic moment which can be – in analogy with electrons – expressed by units of nuclear magneton μ_N , a quantity about three orders of magnitude smaller than the Bohr magneton μ_B :

$$\mu_N = \frac{e\hbar}{2m_p} \sim \frac{1}{1836} \mu_B. \quad (1.1)$$

The interaction of nuclear spin with electrons in the atom results in a local magnetic field at the nucleus. This hyperfine field can be expressed as a sum of contributions of individual electrons [1]:

$$\mathbf{B}_{\text{hf}} = -\frac{\mu_0 \mu_B}{2\pi} \sum_i \left(\frac{\mathbf{l}_i}{r^3} + \frac{\mathbf{s}_i}{r^3} - \frac{3\mathbf{r}(\mathbf{s}_i \cdot \mathbf{r})}{r^5} + \frac{8\pi}{3} \mathbf{s}_i \delta(\mathbf{r}) \right), \quad (1.2)$$

where the first term describes the field induced by electron orbital moment \mathbf{l} , while the remaining terms describe the field arising due to interaction with electron spin \mathbf{s} . The terms for dipole field adequately describe interaction with spin of electron within the dipole limit, whereas the last term gives the Fermi contact interaction. The contact field arises in cases when electron is present in a very close proximity to the nucleus (or inside the volume of nucleus), so that the dipole approximation breaks down, and additionally, relativistic effects have to be considered [1, 2]. Typically, the contact term is significant for atoms where the core s states are spin-polarized by d - s or f - s exchange with unpaired electrons in $3d$ or $4f$ shells; in case of $3d$ atoms, such as Fe, the contact field is usually the dominant contribution to the hyperfine field \mathbf{B}_{hf} .

In non-magnetic systems, where all electrons are effectively paired in the atomic orbitals as well as within the chemical bonds, the hyperfine magnetic field is zero with a high precision (the non-zero effects, such as indirect nuclear spin-spin interaction, appear as terms in the second-order perturbation theory [2]). On the other hand, in magnetic systems the contributions of unpaired electrons are not compensated, yielding high value of magnetic hyperfine field at the nuclei. Then the very presence of such a hyperfine magnetic field is the key aspect for application of NMR spectroscopy to studying the magnetic materials [3]. The time-averaged value of hyperfine field for nuclei of paramagnetic atoms can be from several units of Tesla up to hundreds of Tesla, and additionally, transferred hyperfine field of lower magnitude can appear also at nuclei of neighboring non-magnetic atoms.

1.2 Hyperfine electric quadrupole interaction

For nuclei with spin $I > \frac{1}{2}$ the distribution of charge inside the nucleus deviates from the spherical one and is connected with presence of nuclear quadrupole (or higher order) electric moment, described as tensor \mathbf{Q} . The electric quadrupole moment \mathbf{Q} interacts with gradient of electric field \mathbf{E} , which is generated by the surrounding electronic density and neighboring nuclei [1, 2]:

$$H_Q = \frac{e}{6} \mathbf{Q} \nabla \mathbf{E}. \quad (1.3)$$

Rotational symmetry and parity of the nucleus in the ground state dictate a special form of tensor \mathbf{Q} , allowing defining it with just one scalar component, Q [1]. The tensor of electric field gradient can then be considered as traceless,

$$\mathbf{V} = \nabla \mathbf{E} - \frac{1}{3} \text{Tr}(\nabla \mathbf{E}), \quad (1.4)$$

and described by two parameters: the largest component V_{zz} and the asymmetry $\eta = \frac{V_{yy} - V_{xx}}{V_{zz}}$, with such a choice of coordinate system that $|V_{zz}| \geq |V_{yy}| \geq |V_{xx}|$. The electric quadrupole interaction is strongly influenced by the local symmetry: presence of 3-fold axis or higher symmetry causes η to be zero; moreover, for nucleus in cubic symmetry the electric quadrupole interaction does not influence the NMR spectrum.

1.3 NMR shifts

For non-magnetic materials in zero magnetic field, the hyperfine magnetic field effectively cancels out, and thus does not cause splitting of nuclear energy levels. Application of homogeneous magnetic field is then required to observe NMR, and the role of observable spectroscopic quantity is taken by subtle effects that change – locally – the value of the applied external field. When the external magnetic field is present, much weaker local magnetic fields are induced within the electron system and manifest as small changes of frequency in the NMR spectrum: the electronic response to the static field acts essentially as a "shielding", slightly shifting the resonance frequency from the value of bare, unshielded nucleus [1, 2],

$$\omega = \gamma \mathbf{B} = \gamma(1 - \sigma) \mathbf{B}_0. \quad (1.5)$$

In diamagnetic liquids and solids the effect is termed chemical shielding and when confronted with a shielding of the reference compound, the difference gives rise to so called chemical shift δ , usually expressed in ppm:

$$\delta = 10^6(\sigma_{\text{ref}} - \sigma). \quad (1.6)$$

Analogous terms in metals are called Knight shielding and Knight shift (K) and arise predominantly due to Fermi contact interaction with conduction electrons which are slightly polarized by the external magnetic field. The values of K are usually positive ("paramagnetic") and a few orders of magnitude larger than δ , thus often expressed as a percentage:

$$\omega = \gamma \mathbf{B} = \gamma(1 + K) \mathbf{B}_0. \quad (1.7)$$

In general, both quantities δ , K are tensors, so that the resonance frequency depends also on direction of the external magnetic field with respect the tensors' principal axes – such anisotropic properties correspond to the local symmetry of the crystal site with resonating nucleus.

2. Calculation of NMR parameters

Density Functional Theory (DFT) [4] belongs to the most important methods available for computations in condensed-matter physics, especially for many-body problems that are encountered when obtaining the electronic structures of solids. As in other self-consistent field (SCF) approaches, in DFT the many-body Schrodinger equation is rephrased as one-electron Kohn-Sham equations [5], which are then iteratively solved. Usually a reasonable set of approximations is applied to the original exact Hamiltonian, such as Born-Oppenheimer approximation and approximate potentials for the exchange and correlation (e.g., Local Density Approximation [4] or some variant of Generalized Gradient Approximation [6–8]). This self-consistent process yields, at its end, the electron density uniquely corresponding to the ground state for the studied many-body problem.

There exists a plethora of different DFT codes encompassing various approaches, parametrizations, and further approximations to tackle the solution to the SCF problem. In order to reach the hyperfine and related parameters, which are localized at or very close to the nucleus, it is natural to employ approaches that include description of the core electrons for all involved atoms, i.e., all-electron methods, also termed full-potential methods [9, 10]. This approach contrasts with pseudo-potential methods, where the core states of each atom are replaced by pre-calculated potentials [11, 12], which leads to notable increase in computational speed with almost no decrease of accuracy. Despite slower than the pseudopotential methods, the Full-Potential Linearized Augmented Plane Wave (FP LAPW) approach [13] is widely considered as one of the most precise electronic structure methods in solid state physics. In the FP LAPW scheme the volume of the crystal unit cell is divided into non-overlapping atomic spheres and an interstitial region, which differ by wave-functions used for description. Inside the atomic spheres the basis consists of “atomic-like” functions, while in the interstitial plane waves are used, and the solutions to the Kohn-Sham equations are expanded in such a combined basis set.

The DFT code that was used in all presented works is WIEN2k [14], which is based on FP LAPW, while employs additionally APW+lo (Augmented Plane Waves + local orbitals [15]) approach to be mixed with LAPW, allows additional local orbitals for better description of semi-core states [16], and various other features [17, 18]. Some of the spectroscopic parameters relevant for NMR can be evaluated from the calculated electron density and are often readily available, such as the hyperfine fields and electric field gradients, while obtaining other properties like NMR shifts requires additional and costly procedures.

In magnetically ordered materials the shape of experimental NMR spectrum is determined by the hyperfine magnetic fields at nuclei, while in non-magnetic materials the key parameter is NMR shift and (nuclear) magnetic dipole-dipole interaction. In both cases, if an appreciable electric quadrupole interaction is present, also the electric field gradients have to be considered, because strong electric quadrupole interaction can be decisive for the character and shape of the spectrum. In the following text we briefly describe how all these quantities are

calculated in the WIEN2k, what is their accuracy, and how various shortcomings can be overcome or circumvented.

2.1 Calculation of hyperfine magnetic fields

With electron density of the ground state available from a successfully converged SCF problem, it is relatively simple to calculate – for any specified nuclear site – the contribution due to the dipolar fields of electron spins or due to the orbital motion of the electrons. Since also the population matrices are calculated (and defined in the $|l, m, \sigma\rangle$ space, where l , m , and σ are orbital, magnetic, and spin quantum numbers) it is only a matter of obtaining mean value of a single particle operator \hat{X} with Kohn-Sham eigenfunctions ϕ_i :

$$\langle\psi|\hat{X}|\psi\rangle = \sum_{E_i \leq E_F} \langle\phi_i|\hat{X}|\phi_i\rangle, \quad (2.1)$$

with the form of \hat{X} according to orbital or spin-dipolar part in Eq. (1.2). Several approximations are applied [19]: first, the operator \hat{X} is considered non-zero within the given atomic sphere only, second, the terms non-diagonal in l are neglected, and third, the relativistic mass enhancement is only approximately accounted for. All three approximations are relatively mild and perform well for localized magnetic moments of $3d$ and $4f$ compounds; on the other hand they would be less appropriate for, e.g., hyperfine field due to orbital moments in metals. The calculation of orbital and spin-dipolar hyperfine fields requires spin-orbit interaction to be included, but otherwise the time cost for such step is comparable to a single SCF iteration in a standard calculation.

For the Fermi contact term the process is even less demanding in terms of computational effort, however, it is less straightforward since the contact term expression (1.2) contains delta function, which diverges at point-like nucleus. Most DFT codes (including WIEN2k) do not consider finite size nuclei, but represent each nucleus with a point-like Coulomb potential. Since it can be shown [19] that the consideration of finite size of the nucleus is in fact not important for the hyperfine field, the situation is solved in the following way: the calculated electron (spin) density is averaged over a sphere with Thomson radius $r_T = \frac{Ze^2}{mc^2}$, which is typically an order of magnitude larger than the actual radius of the nucleus. The contact field is then integrated for such averaged spin density. A good agreement with experiments is reached for cases of nonmagnetic impurities in magnetic matrices [20–23], because the contact field at the impurity atom is dominated by spin-polarization of valence s states due to interactions with neighboring atoms. This approach works as well when evaluating isomer shifts for Mössbauer spectroscopy, where one also needs to calculate the electron charge density due to s -electrons within the nucleus [24].

Unfortunately, for magnetic atoms with unpaired $3d$ or $4f$ electrons, the contributions of core s states turn out to be significantly underestimated in comparison with experiments [25, 26]. This mismatch is, however, not caused by the applied mechanism with density smearing in the Thomson sphere, but it is clearly a failure of local density approximation to correctly describe the non-local d - s exchange interaction for the core states [19, 26]. To correct this shortcoming and make the calculated results applicable for comparison with experiments, we developed

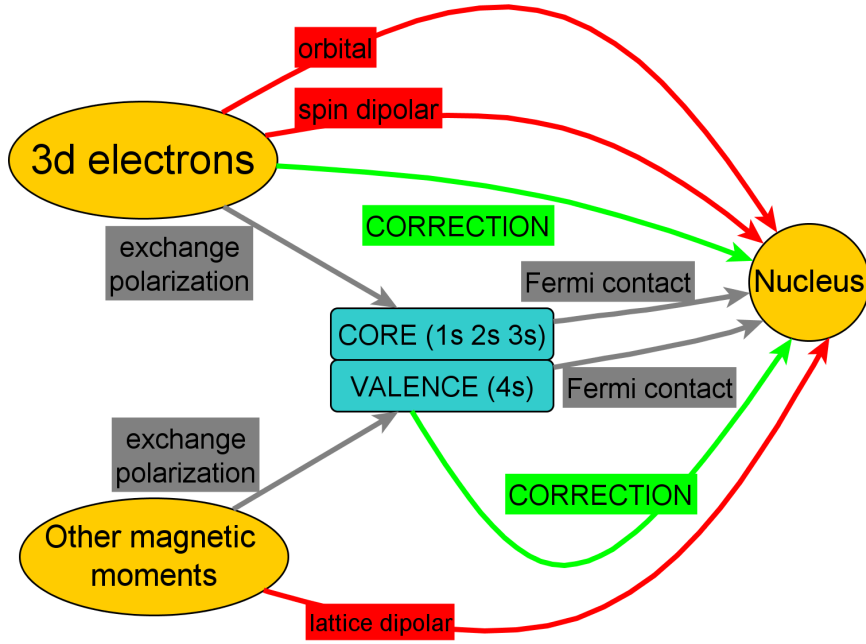


Figure 2.1: The scheme of sources of hyperfine magnetic field. The calculation of Fermi contact field (grey pathways) is circumvented by determining the core and valence contributions directly from magnetic moments (green pathways); the problematic exchange polarization is thus completely avoided.

an approach [VC1] that circumvents the problematic d - s exchange entirely (see Fig. 2.1) – for a specific atomic species, in our case Fe atoms.

The approach makes use of the fact that calculated atomic magnetic moments are in much better agreement with the experiments (e.g., neutron diffraction or magnetic measurements), in contrast to the underestimated hyperfine fields. Our analysis [VC1] for Fe in various magnetic compounds showed that the core contribution to the contact field scaled linearly with the magnetic moment of $3d$ electrons. Likewise, the valence contribution, which arises mostly due to transferred hyperfine field from neighboring atoms, scaled linearly with magnetic moment of valence $4s$ states of a given Fe atom. Therefore, our *ansatz* for reconstruction of the contact field was:

$$B_c = a_{3d}m_{3d} + a_{4s}m_{4s} , \quad (2.2)$$

where constants a_{3d} and a_{4s} were determined from fits to experimental ^{57}Fe NMR data. This correction to the Fermi contact term provided a suitable tool to explain and predict the values of the hyperfine fields on the Fe nuclei in various iron compounds containing ferric (and to some extent also ferrous) ions in the high spin configuration. Although the set of constants a_{3d} and a_{4s} relates to a specific type of atom only (in our case Fe, and for another species the process would have to be done separately), the application does not cost any extra computational resources and allows to obtain reliable contact hyperfine magnetic fields with precision better than 1 T (cf. 50 T, the typical value of contact field at ^{57}Fe).

2.2 Calculation of electric field gradients

The electric field gradient (EFG) tensor can be directly evaluated from the electron density of the ground state, again at no extra computational costs, since the EFG components are connected with charge density by integrals of the charge density $\rho(\mathbf{r})$ over the unit cell [27], e.g., for V_{zz} as:

$$V_{zz} = \int \rho(\mathbf{r}) \frac{2P_2(\cos \vartheta)}{r^3} d\mathbf{r}, \quad (2.3)$$

where P_2 is the second-order Legendre polynomial. The $\rho(\mathbf{r})$ is represented by lattice harmonics $Y_{LM}(\mathbf{r})$, and in the LAPW method the integral is in practice a summation over occupied states [28]:

$$V_{zz} = \sum_{E < E_F} \sum_{lm} \sum_{l'm'} R_{lm} R_{l'm'} G_{ll'}^{Mmm'} \frac{2P_2(\cos \vartheta)}{r^3}. \quad (2.4)$$

where R_{lm} are LAPW radial functions with angular momentum l or l' , and G are the Gaunt coefficients [29]. For example when obtaining the component V_{zz} , we are interested in V_{20} component in the spherical representation of the EFG tensor, i.e., $L = 2$ and $M = 0$, and the number of non-zero contributions is then limited by G to combinations p - p , d - d , s - d , and p - f . This ability of the calculation to resolve EFG contributions according to particular l value is very important when interpreting the (dominant) sources of the EFG value in many practical cases [30, 31].

2.3 Calculation of chemical and Knight shieldings

While chemical shifts of molecules have been accessible for calculations for decades [32, 33], the implementation for solids has been delayed – among other complications – by the fact that the magnetic field breaks translational symmetry of the problem (leading to issues with gauge). For solids, within the projector augmented-wave (PAW) method [34], the gauge-including projector augmented-wave (GIPAW) approach [35] became successful for practical applications, especially when improved to be usable with nowadays ultrasoft-pseudopotentials in the pseudopotential DFT methods [36]. But for the family of APW/LAPW methods, and WIEN2k code in particular, the calculation of chemical shielding has been implemented only relatively recently [37–39]. The calculation involves enhancement of the basis set by local orbitals positioned at higher energies (unoccupied states), and then solving the eigenproblem for the original and six additional reciprocal k-point meshes (shifted along all six directions), for which the induced current as well as the magnetic susceptibility is obtained. The full chemical shielding tensor is then constructed straightforwardly from these seven calculations by integrating the current according to Biot-Savart law.

Compared to standard LAPW calculations, the chemical shielding calculations are significantly more demanding in terms of computational efforts. The difficulty further increases when the studied compound is a metal, which usually requires exceedingly dense sampling of the reciprocal space by the k-points. Additionally

for metals, the shielding due to polarization of conduction electrons, i.e., the Knight shielding K , has to be considered, as in metals it is the dominant source of shielding relevant for NMR spectroscopy. In order to determine K , explicit external magnetic field has to be applied in the calculation framework to obtain the induced contact hyperfine field due to electron spins, and likewise one has to calculate the spin-dipolar term. Again, the computational requirements are very high and make the application affordable for rather small or medium-size systems.

In NMR experiments the observed quantity, however, is the chemical (or Knight) shift, i.e., the difference in shielding between the measured and the reference compound. Therefore, in order to allow for comparison with experiment, one should – in principle – calculate also such NMR reference compound. This is usually not a well suited approach, since it increases the uncertainty of the final figures, and additionally, the reference compounds are quite often liquids, or solids with peculiar structures (e.g., nitrates with large unit cells and containing crystal water molecules) exceeding in complexity the studied compound. Much more convenient and reliable approach [40–42] involves matching the calculated shieldings with experimental shifts of several compounds using a linear regression (with slope usually very close to 1).

2.4 Role of anisotropic interactions

When attempting to model the experimental NMR spectrum, one now has all relevant spectroscopic parameters available for calculation with reasonable precision:

- the total magnetic field – in form of hyperfine magnetic field for magnetic systems, or external magnetic field modified by the NMR shielding for non-magnetic systems,
- and the electric field gradient for electric quadrupole interaction (if present).

Nevertheless, in very complex cases with many non-equivalent atomic positions the experimental spectra may consist of a high number of spectral lines, which may be overlapping or insufficiently resolved. The spectroscopic parameters of different lines in the experimental spectrum then can be simply too similar – compared to the precision of the calculated parameters – to allow for unambiguous assignment of the spectrum, i.e., to match each individual spectral line to its respective atomic position using the calculated parameters. In such cases there is a need for additional parameters to be compared, which can be for instance the anisotropies of the relevant quantities, namely the anisotropy of hyperfine magnetic field and the anisotropy of chemical or Knight shielding.

We developed such an approach employing the anisotropy of hyperfine interaction in Ref. [VC2] and tested it for the ordered spinel structure of lithium ferrite. In spite of lithium ferrite being a relatively simple compound with only two crystallographically non-equivalent Fe sites (tetrahedral and octahedral), two of the five lines in the zero-field experimental ^{57}Fe NMR spectrum cannot be unambiguously interpreted solely from the experiment: the lines have the same integral intensity and the corresponding Fe sites differ only by the orientation of the local axes with respect to the vector of magnetization. In other words, the two sites are crystallographically equivalent but magnetically non-equivalent,

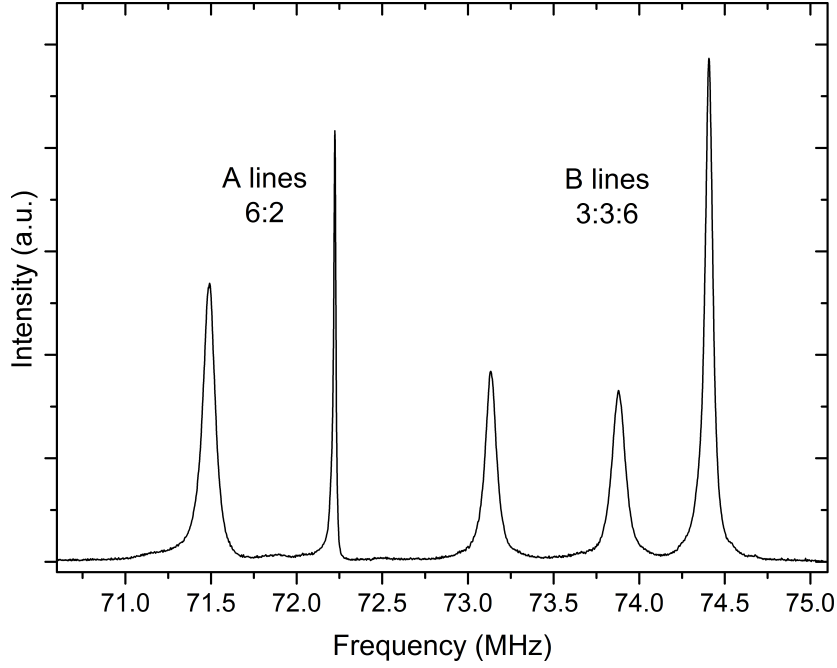


Figure 2.2: NMR spectrum of ordered lithium ferrite measured at 4.2 K in zero magnetic field. In the octahedral sub-spectrum (B lines) the two lines at 73.134 and 73.879 MHz are impossible to assign solely from the NMR experiment.

and thus can be distinguished only by the anisotropic part of hyperfine magnetic interaction, which is briefly described below.

The total local magnetic field at ^{57}Fe nucleus is mainly given by the hyperfine field with the Fermi contact, the orbital, and the spin-dipolar contributions, from which only the Fermi contact term is purely isotropic, i.e., its absolute value does not depend on direction of electronic magnetization. Additionally, atomic moments in the surrounding lattice also contribute to the local field by their (classical) dipolar fields; this contribution to the local field is purely anisotropic and can be straightforwardly determined by summation within a sufficiently large Lorentz sphere. The total local field then consists of isotropic and anisotropic part,

$$\mathbf{B}_{\text{loc}}(\mathbf{n}) = \mathbf{B}_{\text{iso}} + \mathbf{B}_{\text{aniso}}(\mathbf{n}), \quad (2.5)$$

and for a given direction of magnetization \mathbf{n} a single crystallographic site – depending on its local symmetry – may give rise to one or more lines in the spectrum.

Experimentally, one can observe situations for values of \mathbf{n} different from the easy direction by recording NMR spectra of a single crystal under application of external magnetic field, sufficient to rotate the vector of magnetization from the easy direction into the desired direction \mathbf{n} [43]. In the calculations, the direction of magnetization can be arbitrarily specified as a hkl vector in the unit cell, whenever the spin-orbit interaction is considered for a spin-polarized case. Thus, confronting the behavior of experimental and calculated spectra for varying \mathbf{n} yields extra information: the sites can be additionally distinguished according to anisotropy of their hyperfine magnetic fields.

The ^{57}Fe spectrum of tetrahedral A sites in Li ferrite is clearly understood [43] from the NMR experiment by simple symmetry considerations, in fact already without the application of external magnetic field. All eight tetrahedral Fe sites

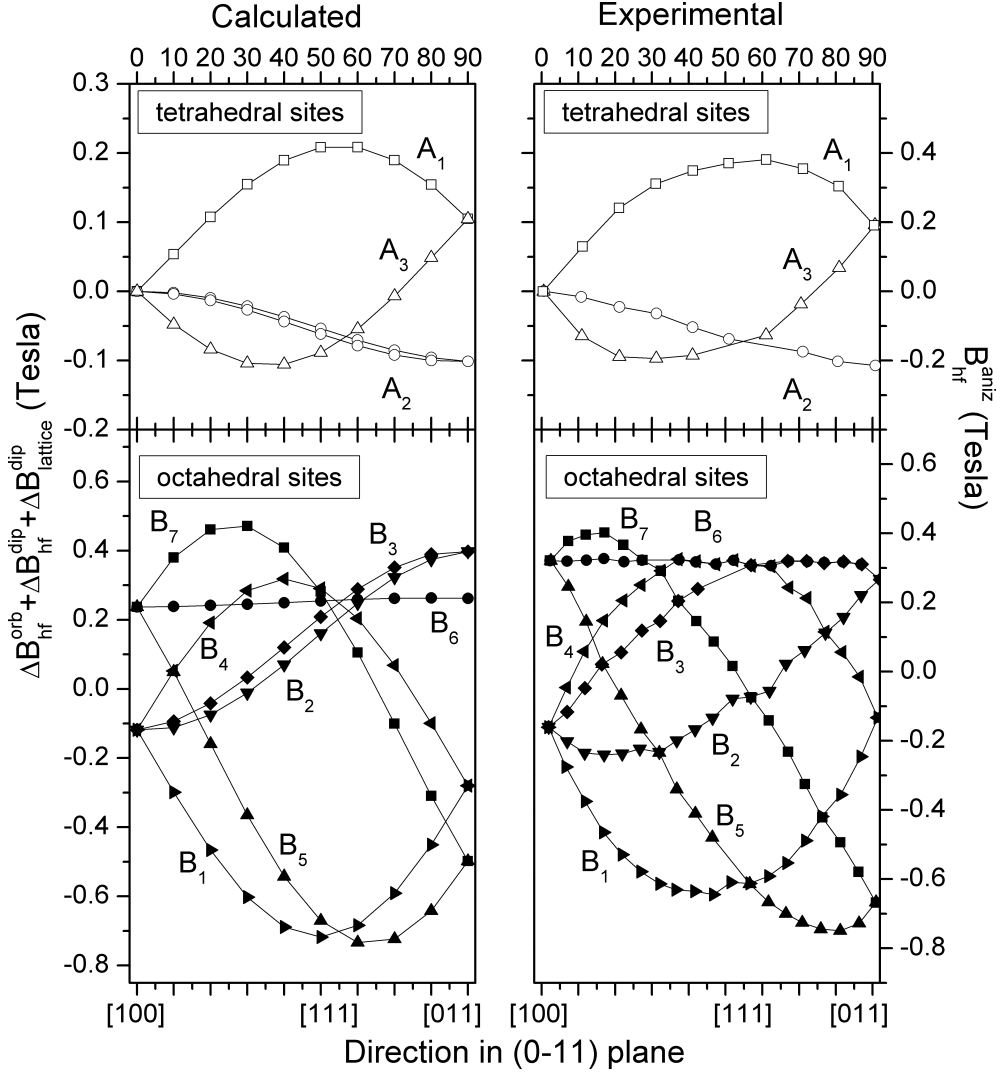


Figure 2.3: The comparison of calculated and experimental ^{57}Fe hyperfine field anisotropies in ordered lithium ferrite. The experimental fields were derived from angular dependences of ^{57}Fe NMR spectra measured at 4.2 K in external magnetic field 0.266 T [43]; our calculations modeled the experiment for directions of magnetization within (011) plane. Both experimental and calculated fields were adjusted by subtracting their isotropic parts. Adapted from Ref. [VC2]

possess trigonal symmetry with axis oriented along $\langle 111 \rangle$, i.e., there are four groups – each containing two tetrahedral sites – with local axes along either the $[111]$, $[\bar{1}11]$, $[1\bar{1}1]$, or $[11\bar{1}]$ direction. Concurrently, the easy axis of magnetization in lithium ferrite lies in one of these directions. Therefore, one of the four groups of tetrahedral sites has the local axis parallel with the easy direction of magnetization, while for the other three groups they are not parallel: the vectors of these directions are intersecting (forming an angle of ~ 70.5 degrees). This leads to a fundamental difference in how the resonance frequencies in tetrahedral subspectrum depend on the direction of magnetization, and consequently causes these two types of tetrahedral sites to be easily distinguishable, yielding the 2:6 line ratio in zero-field ^{57}Fe spectrum in Fig. 2.2.

Such simple situation is not found for the octahedral spectrum, which is split

into three lines 3:3:6 for the easy direction of magnetization and remains ambiguous even when the direction of magnetization is changed by the external field. Specifically, the spectral lines at 73.134 and 73.879 MHz in Fig. 2.2 cannot be unambiguously identified with the corresponding six crystal sites (3:3). Again as in the tetrahedral case, the frequencies of octahedral sites change according to the behavior of their hyperfine field anisotropy, however, this time the differences are more subtle: there is no distinguishing symmetry element present and the sites differ only by the numerical value of the anisotropy. This leads to a deadlock: if the hyperfine tensor was known, the values of hyperfine field anisotropy could be directly calculated and lines assigned to sites. However, the tensor cannot be determined uniquely (ambiguity in sign of one of the parameters) from the experiment because of the lines not being unambiguously assigned. In Ref. [VC2] the situation for octahedral sites was remedied by calculating the anisotropy tensor from DFT, which allowed to match the calculated and experimental data [43], and finally assign also the octahedral lines to their corresponding Fe sites (Fig. 2.3).

The approach employing the anisotropy of hyperfine interaction thus opens another path to assign and interpret the experimental spectra, although this benefit comes at a cost of much more demanding experiments. In order to measure the angular dependences of NMR spectra, naturally one should use a single crystal sample, as well as appropriate NMR experimental setup. And likewise, the calculations and the following analysis may also become quite extensive.

3. NMR & DFT: Applications to magnetic and non-magnetic solids

This chapter presents several publications where we applied the approach of comparing the NMR spectroscopy experiments (in three of the cases also the Mössbauer spectroscopy experiments) with results obtained from calculated DFT models. The topic of the studied systems concerns mainly magnetic solids, namely iron oxides, for which the key parts of the NMR-DFT comparison have been developed [VC1, VC2].

First we present two studies related to valence states of Fe atoms in hexaferrites, where both benefits of the NMR-DFT comparative approach, mentioned in the introduction, are demonstrated: the calculations serve as a helpful tool for interpretation of experiments and conversely the experiment is used to justify the calculated results. Other hexaferrite studies follow, as well as works concerned with magnetite and various magnetic ferrites, and the chapter is completed by application of the comparative approach to several non-magnetic solid-state systems.

3.1 Hexagonal ferrites

Hexagonal ferrites (hexaferrites) are magnetic oxides of iron and atoms of alkali earth metals (Ba, Sr, Pb) or lanthanides (sometimes termed large cations), often accompanied by substitutions of various elements (Co, Al, ...). The industrial and technological importance of hexaferrites as permanent magnets, in magnetic recording, and wide range of high-frequency and electrical devices perhaps overshadows their other interesting properties discovered recently, such as promising multiferroic behavior [44, 45] or outstanding microwave absorption in form of various composites [46, 47].

The hexagonal ferrites consist of stacked structural blocks along the hexagonal axis; there are three possible structural blocks, T, R, and S. According to the type of block used, the compounds can be organized into two main families: first, containing R and S blocks only, where the simplest R-S stacking yields the M-type structure, and second, built with T and S blocks, with Y-type hexaferrite (T-S stacking) being the simplest representative. More complex structures then can be derived (and more importantly also synthesized) by altering the sequence of the building blocks or combining the two families together [48].

The magnetic structure of hexaferrites is ferrimagnetic, with moments of neighboring Fe atoms along the hexagonal axis being mutually antiparallel. Hexaferrites display high magnetic anisotropy of either easy axis character (mostly M-type and related structures) or planar/conical type (usually Y-type and derived structures) [48]. Their magnetic properties, especially the magnetocrystalline anisotropy, are sensitive to magnetic and valence states of Fe atoms [49], and can be also influenced by various cationic substitutions (e.g., Co^{2+}). The determination of Fe valence states in hexaferrites was also one of the main topics in the next two presented papers.

The structure of hexagonal ferrites contains five or more crystallographically

non-equivalent Fe sites, which are also magnetically equivalent when the magnetization is along the hexagonal axis, but may become split for other cases, e.g., for planar hexaferrites. Since the nuclear spin of ^{57}Fe isotope is $1/2$, the electric quadrupole interaction does not apply in NMR, and each non-equivalent Fe site then usually gives rise to one spectral line in the ^{57}Fe NMR spectrum. The experimental NMR spectra of hexaferrites may become difficult to interpret: the complexity of their spectra steeply rises with increasing number of non-equivalent sites in the structure, as well as for ferrites with planar magnetic anisotropy where the anisotropy of hyperfine interaction may affect the shapes of spectral lines or cause splitting. With exception of the simplest and well-studied M-type hexaferrite, the assignment of all NMR spectral lines is often incomplete [50, 51]. For other related hyperfine methods, such as Mössbauer spectroscopy, already the M-type structure with five iron sublattices implies five overlapping sextets, whose analysis can be a complicated problem, and more complex structures are usually beyond the method’s resolution [52, 53].

Localization of valence electron in hexaferrites with mixed valence

Good examples of such more complex structures are strontium W-type and X-type hexagonal ferrites, on which we focused in the study by ^{57}Fe NMR and Mössbauer spectroscopies and DFT calculations in Ref. [VC3]. Both ferrites are composed of the same set of building blocks – R and S – as the simplest M-type structure (“SrM”, $\text{SrFe}_{12}\text{O}_{19}$, space group $P6_3/mmc$), which has the stacking sequence R-S. The stacking sequence of the W-type structure (“SrW”, $\text{SrFe}_{18}\text{O}_{27}$, space group $P6_3/mmc$) is R-S-S and the X-type structure can be considered as a sum of M- and W-type, yielding R-S-R-S-S stacking (“SrX”, $\text{Sr}_2\text{Fe}_{30}\text{O}_{46}$, space group $R\bar{3}m$).

Both SrW and SrX are mixed-valence ferrites, i.e., contain both (nominally) ferric and ferrous ions, and thus our aim was to study the specifics of the valence charge: whether the valence charge is localized in the form of Fe^{2+} and which Fe crystal sites are involved. The applied spectroscopic methods are sensitive to the valence state of Fe atoms: value of isomer shift, which is obtained from Mössbauer spectra, can be attributed to the given valence state, whereas NMR detects Fe^{2+} indirectly as a missing intensity in the ^{57}Fe spectrum from Fe^{3+} atoms. However, first the NMR and Mössbauer spectra had to be interpreted (their lines assigned to crystallographic Fe positions), for which the DFT calculations were utilized. Moreover, the valence states of iron atoms were also determined from the ground state obtained in the electronic structure calculations, and thus the calculated valences were used together with the experimental results to identify the Fe^{2+} sites [VC3].

The five Fe sublattices in the M-type structure are occupied by nominally ferric ions and are labeled as $12k_{\text{VI}}$, $4f_{\text{IV}}$, $4f_{\text{VI}}$, $2b_{\text{V}}$, and $2a_{\text{VI}}$, where the labels indicate the multiplicity, Wyckoff symbol, and oxygen coordination (“IV” and “VI” are tetrahedral and octahedral, respectively, while “V” denotes hexahedral site, usually termed bipyramidal). Accordingly, the ^{57}Fe NMR spectrum of SrM consisted of five narrow and well separated resonance lines, and since its interpretation is well known [54], the lines could be assigned to the respective sublattices, as depicted in Fig. 3.1. The hyperfine magnetic fields, measured by NMR as well as Mössbauer, were in a very good agreement with the calculated values (using corrected contact fields via the method described in [VC1]). Likewise, the calculated values of EFG

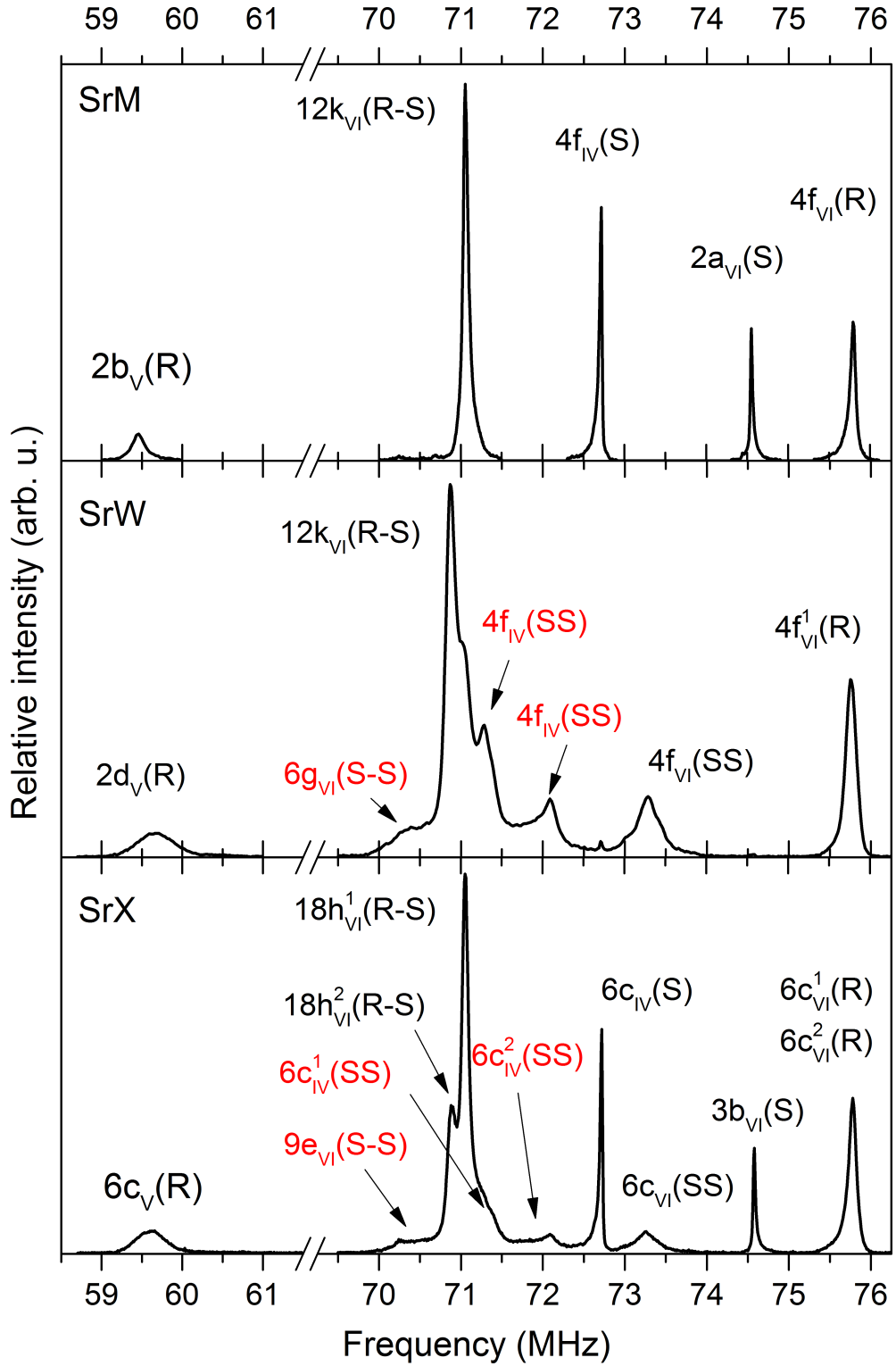


Figure 3.1: Experimental ^{57}Fe NMR spectra of M-type $\text{SrFe}_{12}\text{O}_{19}$, W-type $\text{SrFe}_{18}\text{O}_{27}$, and X-type $\text{Sr}_2\text{Fe}_{30}\text{O}_{46}$ with spectral line assignment indicated. The lines labeled in red were only assigned by employing the DFT calculations. Partially adopted from Ref. [VC3].

on Fe nuclei basically matched the experimental quadrupole splittings – for ^{57}Fe these are observed in Mössbauer only. As expected, the valence states of Fe atoms (obtained by Atoms in Molecules method [55]) were essentially Fe^{3+} , which was also confirmed by the measured isomer shifts.

For SrW hexaferrite with seven Fe sublattices, the interpretation of the ^{57}Fe NMR experiment is already incomplete and only four of the seven lines in the ^{57}Fe NMR spectrum can be directly assigned to sites upon their resemblance with SrM ^{57}Fe NMR spectrum, integral intensities, and response to external magnetic field [56]. The Mössbauer spectra and DFT calculations helped to resolve the issue: the connection of three sites in the S-block part of the structure, $6g_{\text{VI}}$, $4f_{\text{IV}}$, $4e_{\text{IV}}$, with three unassigned lines in the NMR spectrum became possible by comparison with hyperfine fields from NMR and also by comparing EFGs from Mössbauer spectra with those calculated by DFT.

Similar obstacles with interpretation were encountered for SrX structure with its eleven Fe sublattices. While again some of the lines could be assigned – by literally matching these with analogous sites and spectral lines of SrM and SrW hexaferrites – remaining three lines were once more assigned using the calculated hyperfine fields.

All Fe atoms in SrM are in high-spin ferric state Fe^{3+} , but both SrW and SrX contain also some ferrous atoms Fe^{2+} , formally being $\text{SrFe}_2^{2+}\text{Fe}_{16}\text{O}_{27}$ and $\text{Sr}_2\text{Fe}_2^{2+}\text{Fe}_{28}\text{O}_{46}$, respectively. The question of localization of Fe^{2+} in one or more crystallographic positions was thus mainly addressed in the Ref. [VC3]. From the analysis of NMR line intensities, isomer shift in the Mössbauer spectra, and calculated valence in the DFT we concluded that the minority electron tends to be localized in $6g_{\text{VI}}$ and $4f_{\text{VI}}$ of the SrW structure, and in $9e_{\text{VI}}$ and $6c_{\text{VI}}$ of the SrX structure. All these sites are located in between the two neighboring S blocks. Such behavior can be understood given the fact that the S block possesses spinel-like structure, $2\text{Fe}_3\text{O}_4$, and is thus more inclined to incorporate the extra valence electron, compared to R block, $\text{SrFe}_6\text{O}_{11}$.

Related issue of valence charge compensation was the subject of another hexaferrite study [VC4], concerning substituted SrM. There are only ferric Fe present in the SrM, however, when the divalent strontium is replaced by a trivalent cation, the charged substitution is compensated by change of valence of some of the Fe atoms. It has been shown [57–59] that in lanthanum M-type hexaferrite (LaM), where La is formally trivalent, at low temperatures the compensation occurs via localization of minority electron at octahedral 2a sites, forming $\text{Fe}^{2+}(2a)$. Such process is accompanied by a notable increase of magnetocrystalline anisotropy, compared to LaM at room temperature or to anisotropy of SrM (Fig. 3.3 left).

The charge localization in LaM (and also in Nd- and Pr-substituted cases) and its influence on magnetocrystalline anisotropy were studied by combining DFT calculations and ^{57}Fe NMR spectroscopy [VC4]. This time the DFT calculations were not employed to mainly provide help with interpretation of NMR spectra, but we utilized the second "branch" of the relationship between the experiment and calculations: the experiments justified the correctness of our DFT model in describing the localized state. The credibility of the ground state obtained by DFT was important because of employing DFT+U approach [60, 61] and because of dealing with calculation of magnetocrystalline anisotropy energy; both issues

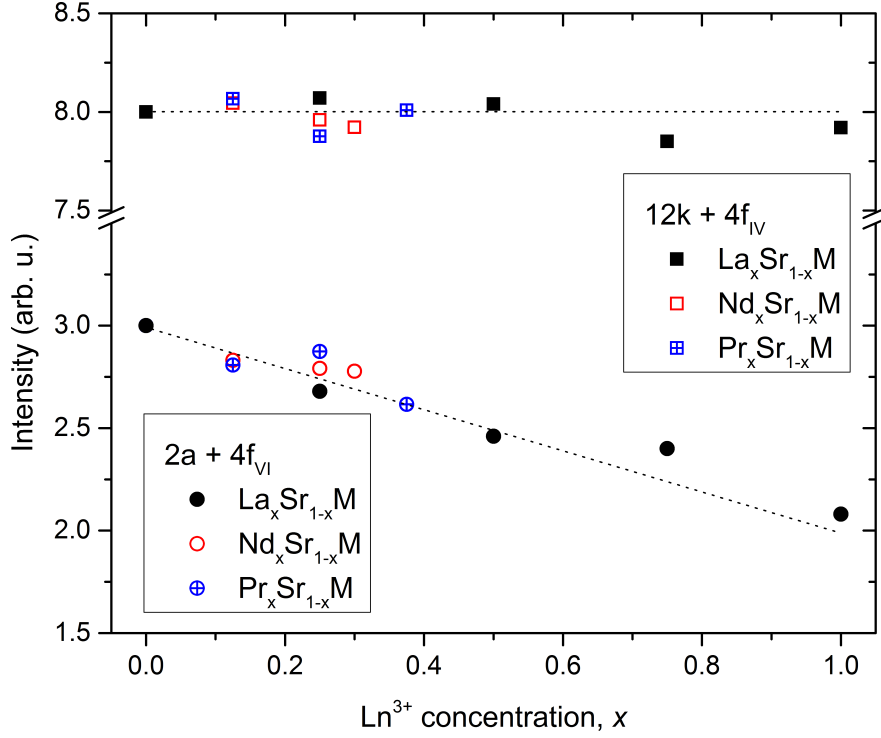


Figure 3.2: Integral intensities of parts of ^{57}Fe NMR spectra in pure and doped SrM and LaM. The dependence of intensities on the concentration of trivalent large cation supported the conclusion that Fe^{2+} localized in octahedral $2a$ sites. Adopted from Ref. [VC4].

are described below in a bit more detail.

When calculating magnetic ferrites, the proper description of Fe $3d$ states is essential and one of the successful, albeit simple approaches is the DFT+U method [60]. The idea is to treat the strong on-site Coulomb interaction of localized $3d$ states, which are not correctly described by the generalized gradient approximation (GGA), with an additional Hubbard-like potential – its strength being parametrized by on-site Coulomb interaction U and site exchange J . For instance, without application of a reasonable U the calculated ground state of some hexaferrites is incorrectly metallic [62], and thus the application of such potential, usually in a form [61] of $U_{\text{eff}} = U - J$ and strength of several eV (4.5 eV in our calculations), is a routine procedure to remedy the shortcoming of GGA exchange-correlation potential.

On the other hand, application of the DFT+U approach may produce additional local energy minima for the SCF process [63–65] and in case of complex structures there is a danger that the calculation converges into a stable state which is not the real ground state. When more than one such stable self-consistent solution is obtained in DFT+U, the proper one has to be chosen – usually according to the lowest total energy, or the justification can also be provided by comparison with suitable experiments; both apply to our case.

In La-, Nd-, and Pr-doped Sr hexaferrites at low temperatures the intensity of ^{57}Fe NMR line corresponding to octahedral $2a$ sites diminishes proportionally to the concentration of the trivalent cation (see Fig. 3.2). The presence of La^{3+} (as well as Nd^{3+} or Pr^{3+}) induces Fe^{2+} in the $2a$ sites, which is accompanied by a

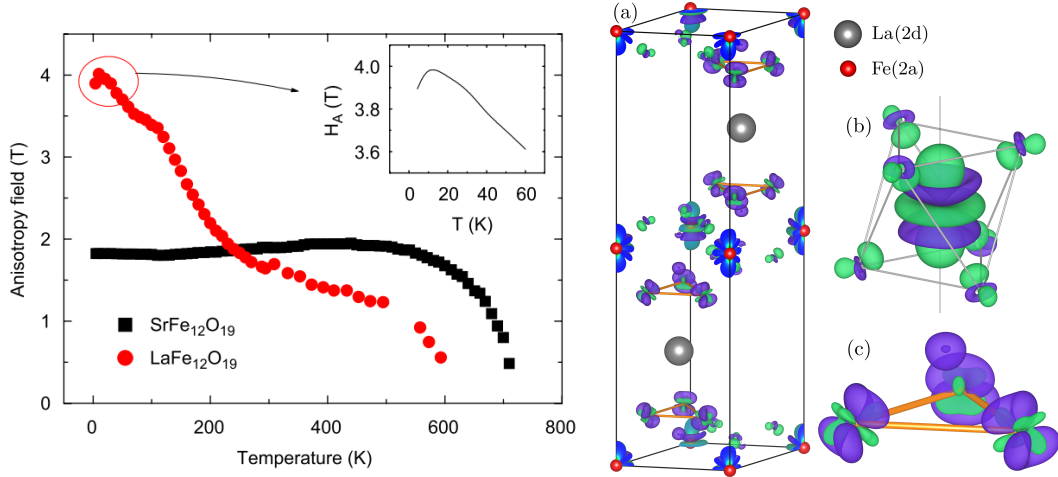


Figure 3.3: The experimentally observed temperature dependence of anisotropic fields [58] (left panel) was modeled and satisfactorily explained by the calculated magnetocrystalline energy. In LaM at low temperatures the Fe²⁺ localizes in 2a sites, as documented by differences in charge density in a 3D plot (right panel, b) and strongly contributes to the anisotropy; with increasing temperature the minority charge delocalizes, mainly within 12k and 2a sites and leads to reduced anisotropy. On the other hand, there is no such process present in SrM as documented by the constant temperature dependence of its anisotropy. Adopted from Refs. [58] and [VC4].

significant reduction of the hyperfine field at ⁵⁷Fe nuclei. The NMR line intensity is thus effectively reduced by the amount of Fe²⁺ and can be utilized to monitor Fe²⁺ concentrations. The linear decrease of Fe(2a) NMR intensity indicates that the distribution of Fe²⁺ in the 2a sublattice is rather static at low temperatures without significant fast electron hopping. Therefore, within the 2a sublattice there are well defined ferric and ferrous ions and their arrangement at low temperatures does not change significantly.

Such a scenario observed in ⁵⁷Fe NMR experiment was searched for by the DFT+U calculations. Our aim was to obtain the “localized” solution, i.e., Fe²⁺ in 2a, as well as the “delocalized” solution – with different (and at the time unknown) way of compensating the extra valence charge – and to use these electronic structures to evaluate magnetocrystalline anisotropy and compare it with experiment (see Fig. 3.3 left).

In order to calculate the magnetocrystalline anisotropy energy E_{MA} , it is useful to utilize so called force theorem approach [66] and evaluate E_{MA} as the difference between the total energies of calculations with different directions of magnetization. In the M-type hexaferrites with uniaxial character of anisotropy, such suitable directions are the hexagonal axis (001), which is the easy axis of magnetization, and any direction in the hexagonal plane, e.g., (100). For these hexaferrites the anisotropy is dominated by single-ion contributions of Fe atoms due to spin-orbit interaction and yields anisotropy constant $K_1 = 0.36$ and 0.09 MJ.m⁻³ for localized and delocalized LaM, respectively, and 0.18 MJ.m⁻³ for SrM. Although these values are about half of the experimental values [67], they are in excellent agreement with the temperature behavior of anisotropy field of LaM and SrM in experiments [58].

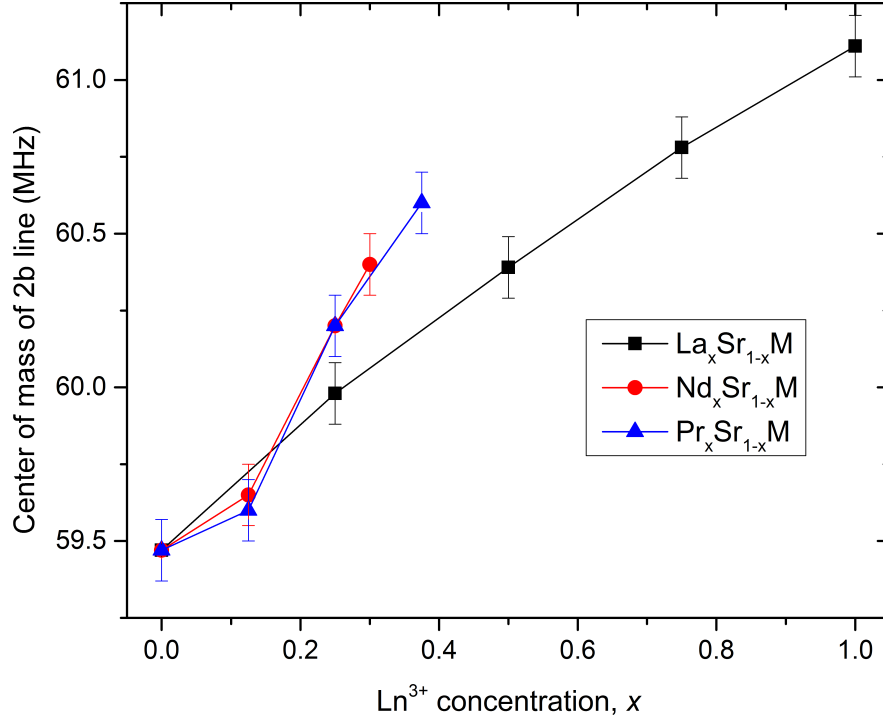


Figure 3.4: Frequency shift of the 2b line resonance in dependence on the concentration of trivalent large cation. Adopted from Ref. [VC4].

Moreover, the spin-orbit interaction can be arbitrarily enabled or disabled for any atomic species in the structure, which allows to evaluate the contributions of individual Fe sublattices to E_{MA} . We thus confirmed that the bipyramidal $\text{Fe}^{3+}(2b)$ causes large anisotropy, nevertheless, its single-ion contribution is constant in both LaM solutions, as well as in SrM. Whereas the key role for the increase of E_{MA} at low temperatures is played by $\text{Fe}^{2+}(2a)$ and to some extent by $\text{Fe}^{3+}(12k)$, see Fig. 3.3 right. When the localization into octahedral 2a sites in LaM takes place, the contribution of $\text{Fe}^{2+}(2a)$ is responsible for about 70 % of the total E_{MA} . On the other hand, at higher temperatures, the delocalized scenario is realized and the minority electron is smeared over multiple Fe sites, partly again 2a, but mostly 12k, negative contribution of which effectively reduces the total magnetocrystalline anisotropy.

The selection of large cation affects strongly not only the magnetic and other physical properties of hexagonal ferrites, but manifests also through relatively subtle effects in the ^{57}Fe NMR spectrum. One could expect that the nearest Fe neighbor to the large cation site, the bipyramidal $\text{Fe}(2b)$ site, should be the most affected site by the substitution of large cation. This is manifested by the hyperfine field of $\text{Fe}(2b)$ visibly increasing with increasing concentration of large cation that substitutes Sr, as observed from frequency shift in NMR spectra (Fig. 3.4). But surprisingly, the changes are not due to extra valence charge brought by substitution of La^{3+} for Sr^{2+} , but rather due to changes of geometry, to which the hyperfine field of bipyramidal site is particularly sensitive. The perturbation of local structure can be most probably caused by the different atomic size of the large cations: the calculated atomic volume of La^{3+} is about 13 % larger than that of Sr^{2+} .

The effect of large cation size on neighboring Fe can be well observed in the ^{57}Fe NMR spectra of Ba and Sr M-type hexaferrites, where the hyperfine field of Fe(2b) differs by about 0.9 T. The remaining four Fe sublattices have essentially the same positions in ^{57}Fe NMR spectra, hence their hyperfine fields are almost unchanged by the type of large cation. The explanation of this difference in BaM and SrM, and its connection to local and lattice geometry, unexpectedly followed from our analysis of lattice deformations on calculated hyperfine magnetic fields [VC5]. Due to larger ionic size of barium, the neighboring bipyramidal site is more expanded compared to SrM, which leads to weaker effect of Fe-O covalency and lower hyperfine field.

Originally, the analysis [VC5] of how the lattice deformations influence the hyperfine fields was motivated by non-uniform shifts found out in ^{57}Fe NMR spectra of SrM oriented thin films [68]. In principle, for samples with reduced dimensions such as nanoparticles or thin films, the values local fields at ^{57}Fe nuclei may differ from those in a bulk single crystal due to presence of demagnetizing field. As a consequence, the spectral lines should be uniformly shifted: those with magnetization parallel to the total magnetization to higher frequencies and vice versa. Our analysis brought a deeper insight into the connection of lattice deformations and observed hyperfine fields and by studying dependences of calculated hyperfine fields on changes of volume and c/a ratio of the lattice parameters, we rejected the conjecture that the observed shifts can be simply explained by lattice mismatch with the substrate. Some other structural defect in the SrM thin film has to be affecting the hyperfine field of each iron site differently.

Atomic arrangement in planar multiferroic hexaferrites

The NMR spectroscopy and DFT calculations were employed to study the local structures of other hexagonal ferrites – in the family of Y-type, planar hexaferrites. Mixed Ba/Sr Zn_2Y -type was one of the first hexaferrites where magnetoelectric properties were discovered, notably with transition temperatures above the room temperature [44].

The structure of Y-hexaferrite consists of T-S block stacking and besides four octahedral sites the structure contains two tetrahedral sites: one in the T block and the other in the S block. Since Zn atoms strongly prefer tetrahedral environment, the octahedral sites are fully occupied by Fe, while the tetrahedrons contain both Fe and Zn. The Zn/Fe distribution between blocks can be described by parameter γ : the S block contains Zn_γ and the T block contains $\text{Zn}_{1-\gamma}$. The distribution of zinc atoms is a one of the key parameters for the ferroelectricity and many other properties [44, 69, 70], with $\gamma = 0.5$ expected to be the most suitable for magnetoelectricity. Therefore, our aim was to study experimentally the Zn distribution in Ba- and Sr- Zn_2Y hexaferrites by means of ^{57}Fe and ^{67}Zn NMR. The role of DFT calculations was mainly to interpret the measured NMR spectra. The viability of such approach was shown in Ref. [VC6], where already a rough DFT model allowed us to assign the two components in ^{67}Zn NMR spectrum to the two respective Zn sites in the T and S block of the Y hexaferrite structure. In the ^{67}Zn spectra, simulated from calculated electric field gradients and hyperfine magnetic fields, the line originating from Zn in S block and T block could be clearly distinguished.

Further improving on the DFT model in Ref. [VC7] provided finer resolution of

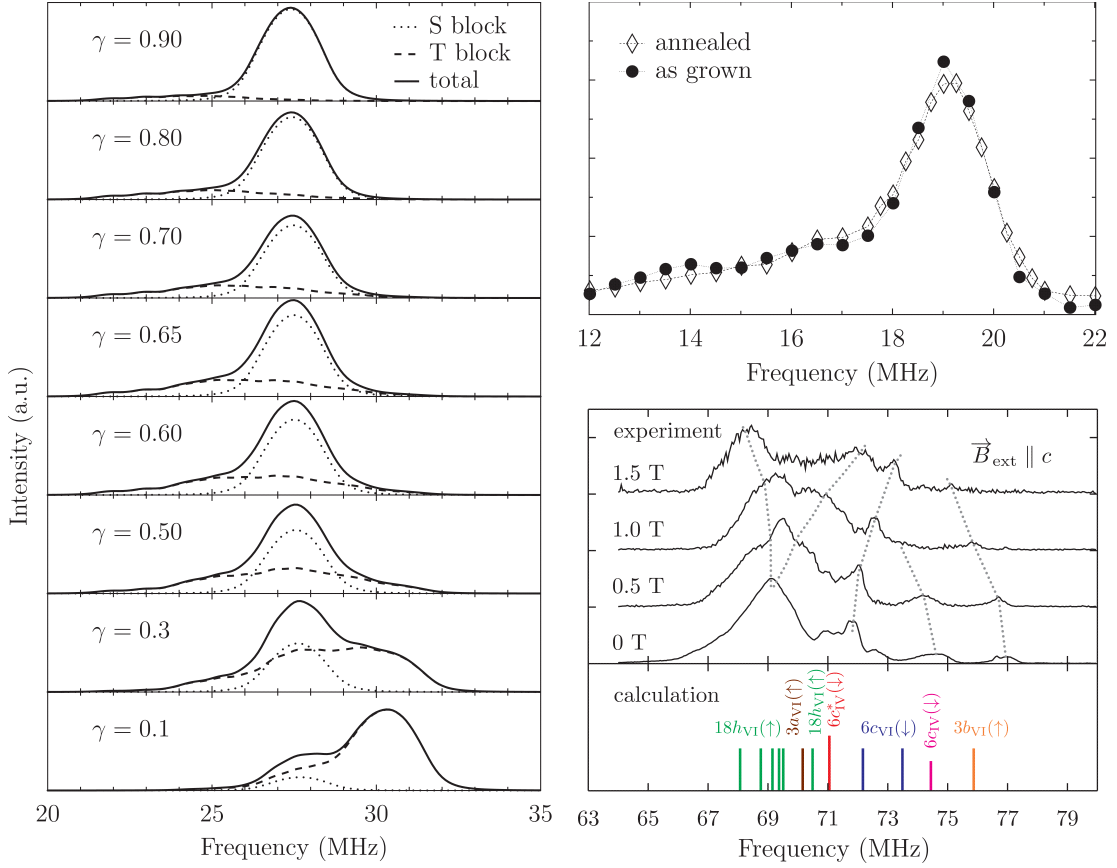


Figure 3.5: The ^{67}Zn NMR spectra simulated for various values of parameter γ (left) allowed determining the Zn distribution in the experimental NMR spectra (top right). Bottom right: the application of external magnetic field and calculations of hyperfine magnetic fields lead to assignment of ^{57}Fe NMR spectra in barium Zn_2Y -ferrite and to evaluation of parameter γ . Adopted from Refs. [VC6–VC8].

the parameter γ (Fig. 3.5 left) and its more reliable determination. Interestingly, the hyperfine field for Zn in the S-block was relatively unaffected by value of γ and the frequency of the corresponding ^{67}Zn resonance line kept constant, while the T-block Zn resonance shifted significantly when γ was changed. The shape of the simulated spectrum thus related to the distribution of Zn in the structure and could be used to determine the value of $\gamma \sim 0.65$ for the experimental spectrum – by a simple comparison. The heat treatment lead to only a minuscule differences in the measured spectra (Fig. 3.5 top right).

In contrast to zinc, the ^{57}Fe spectra are much more complex, containing signals from six different Fe sublattices, some of which are further split due to Zn/Fe disorder within both tetrahedral sites. Reasonable interpretation of ^{57}Fe NMR spectrum was reached in pure Ba- Zn_2Y hexaferrite [VC8], where complications from the Ba/Sr disorder were avoided. Application of external magnetic field in the NMR experiments allowed to separate the Fe crystal sites according to the orientation of their magnetic moments: for atoms with moments parallel to the total magnetization their nuclear resonance shifts to lower frequencies and vice versa. Together with calculation of hyperfine fields on ^{57}Fe nuclei we were eventually able to assign the experimental ^{57}Fe NMR spectrum (Fig. 3.5 bottom

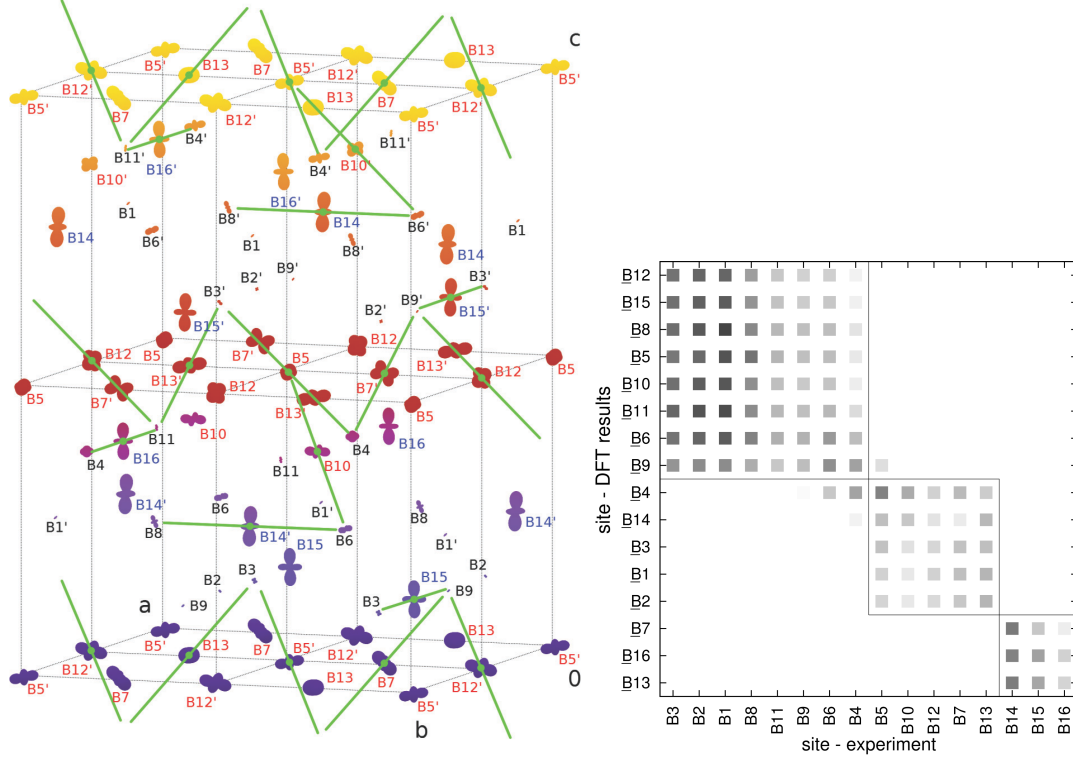


Figure 3.6: Left: graphically represented anisotropy of calculated hyperfine magnetic fields of octahedral Fe sites in the magnetite Cc unit cell. Green lines denote the trimeron structures, where central Fe^{2+} -like atoms display increased anisotropy, compared to relatively isotropic Fe^{3+} -like atoms situated at the end of trimers. Right: assignment of the ^{57}Fe NMR spectral lines to octahedral Fe sites. Intensity of the squares corresponds to mean square deviation between the DFT and NMR results. Adopted from Ref. [VC9].

right), which allowed to determine the $\gamma \sim 0.62$ from ^{57}Fe , in a good agreement with the value from ^{67}Zn NMR results. Our approach thus also demonstrated that NMR is suitable tool to study the atomic arrangement, even in such relatively disordered systems.

3.2 Magnetite and other ferrites

The concept of combining experimental local probe (such as NMR) with electronic structure calculations has been successfully applied – besides the hexaferrites – also to various other magnetic iron oxides. In this section the papers concerning structure of magnetite are presented, followed by presentation of two works where electric quadrupole interaction played a significant role in the analysis of NMR spectra of ferrites for isotopes other than ^{57}Fe .

Low temperature phase of magnetite

One of the most intricate iron oxide structures is that of magnetite which occurs below the Verwey phase transition $T_V \sim 120$ K [71]. The complications with studying such structure are due to large size of the monoclinic unit cell with 8

unique tetrahedral and 16 octahedral Fe positions, while in addition the structure differs only very slightly from the high temperature cubic structure – by monoclinic angle ~ 90.24 degrees and orthorhombic deformation of about 0.3 % [72]. But more importantly, the peculiarity of magnetite at low temperature arises from the rich possibilities of charge and orbital order, allowed by the fact that magnetite is a mixed valence compound: in the cubic phase the octahedral Fe are all equivalent, whereas in the low temperature phase a delicate and unique charge and orbital structure of octahedral Fe is established. Consequently, the charge and orbital ordering, the value of T_V and the presence of the Verwey transition (or lack of it) is very sensitive to exact stoichiometry [73] and the number of defects [74], even the history of the particular magnetite sample can be important [75, 76].

Current understanding is that below T_V the octahedral Fe atoms form a network of linear objects, nicknamed “trimerons”, each consisting of three neighboring Fe atoms. In a trimeron the central Fe donates part of its minority-spin electron density to the remaining two atoms, which in turn are slightly shifted toward the center [77].

From the point of view of NMR, the situation with magnetite is quite ironic: ^{57}Fe NMR is the only spectroscopy that can resolve all the 24 nonequivalent Fe sites, and thus during the history of magnetite research the method significantly contributed to determination of the Cc structure [78], yet the full assignment of the individual spectral lines is not available to this day. In Ref. [VC9] we attempted to tackle this problem by utilizing both presented approaches [VC1, VC2] for comparison of hyperfine fields obtained by NMR and DFT, i.e., DFT calculations were employed to obtain the hyperfine fields including their anisotropic parts for all Fe sites (see Fig. 3.6 left panel). These results were then compared with available NMR experiments, which were the sophisticated measurements of ^{57}Fe NMR dependences on direction of external magnetic field by Moriji Mizoguchi [79]. In order to allow the comparison, the direction of the magnetization was calculated (using the magnetic anisotropy of magnetite [80]) for a given direction of applied external magnetic field in the experiment. Then the anisotropy tensors for all 16 octahedral Fe sites were obtained by fitting the experimental dependences.

The DFT calculations were designed to mimic the experiment and analogous set of anisotropy tensor was derived from the calculated hyperfine fields. By minimizing the mean square deviation of the calculated and experimental fields (or NMR frequencies) we were able to correlate the NMR and DFT data. Although making most of the method (using both the zero-field frequencies and the anisotropic contributions responsible for the angular dependences), our approach yielded only a partial assignment: the 16 octahedral Fe sites in the unit cell can be sorted into three groups 8:5:3, however, inside these groups, as well as inside the group of 8 tetrahedral sites, the lines cannot be identified any further (Fig. 3.6 right panel). The values of spectroscopic parameters within each of the groups are unfortunately too similar to allow for further refinement. These results supported the idea of trimeron structure against other proposed arrangements, e.g., [72, 81]. We proved that character of the ^{57}Fe NMR spectrum, particularly the segregation into 8:5:3, and the trimeron structure are mutually compatible, and it is a topic for future studies, whether this relationship is exclusive.

Another approach of tackling the low temperature phase was undertaken in Ref. [VC10], this time, however, for the Mössbauer spectroscopy, which is a frequent

experimental method for studying magnetite and other iron oxides. Although this method lacks the high resolution in hyperfine magnetic fields compared to NMR, for ^{57}Fe isotope Mössbauer makes up for it by availability of two extra spectroscopic quantities: the quadrupole interaction and the isomer shift. As already mentioned, the quadrupole interaction is not present in NMR for ^{57}Fe isotope with spin $1/2$, but appears in Mössbauer spectroscopy due to spin value of the excited nuclear state of ^{57}Fe being $3/2$. Similarly, the isomer shift is observable thanks to the difference in nuclear radii of excited and ground state of the ^{57}Fe nucleus.

Unlike ^{57}Fe NMR, where generally each non-equivalent Fe site contributes by a single line, in Mössbauer spectroscopy the higher number of possible nuclear transitions between excited and ground state of ^{57}Fe induces up to eight, but typically six spectral lines per Fe site in magnetic materials. Detailed and reliable analysis of Mössbauer spectra with higher number of non-equivalent sites then becomes a difficult procedure of resolving numerous overlapping sextets. To describe the experiment, one then has to adopt a strategy of decomposing to lower number of sextets, usually using some phenomenological assumptions.

Since the overall analysis is limited by such assumptions, which makes a comparison of different Mössbauer studies complicated, we aimed to propose a universal decomposition to four sextets [VC10]. Utilizing our experience with such grouping for the lines in ^{57}Fe NMR spectrum, we suggested decomposing the Mössbauer spectrum of low-temperature magnetite phase into one sextet for tetrahedral Fe and three sextets (with intensities 8:5:3) for the octahedral Fe. To demonstrate that such approximation is adequate, the complete set of parameters for the four sextets was calculated by DFT, i.e., the hyperfine magnetic field, the electric field gradient, and the isomer shift. Then, the Mössbauer spectrum of high-quality single crystal of magnetite was acquired and the approximation by four sextets applied to fit the measured spectrum – successfully, as no feature of the experimental Mössbauer spectrum was left unexplained by the model. We thus proposed a simple tool for analysis of Mössbauer experiments not only in physics, but also in other fields such as chemistry or geology, where often the goal is to determine the changes of magnetite amount in a measured sample or even only check for its presence.

High temperature phase of magnetite

The low temperature phase is both interesting and challenging for its complex crystallographic and domain structure, orbital and charge ordering, and many related physical properties or phenomena, such as the nature of the Verwey transition itself, axis switching induced by external magnetic field [82, 83], or anisotropy [80]. In contrast to these features, the high temperature cubic phase appears to be rather dull. However, recent experiments [84–86] reveal high temperature magnetite phase as a rather dynamic state, especially in the vicinity of the Verwey transition where some form of short-range order resembles ordering of the low-temperature phase.

Besides, there is another interesting magnetic property of magnetite: the behavior of its magnetocrystalline anisotropy and especially the reorientation transition at temperature $T_{\text{SR}} \sim 130$ K, which has long time been disputed to be connected with the Verwey transition [87–89]. The reorientation transition is well visible in the ^{57}Fe NMR experiments: for direction of magnetization along $\langle 100 \rangle$ direction

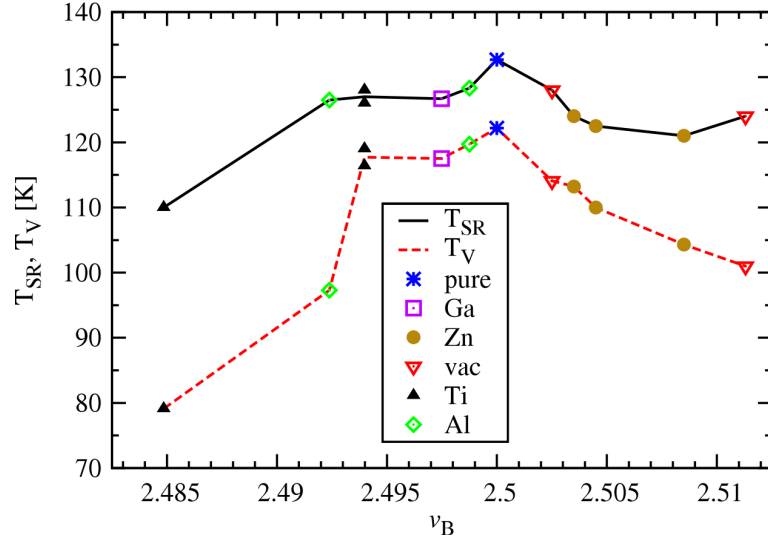


Figure 3.7: Spin reorientation temperature T_{SR} and Verwey transition temperature T_V in dependence on the average valency ν_B of octahedral Fe atoms. Adopted from Ref. [VC11].

(below T_{SR}) all ^{57}Fe nuclei in octahedral Fe sites resonate in a single spectral line, while above T_{SR} with magnetization direction $\langle 111 \rangle$ the line splits 1:3 due to anisotropy of hyperfine interaction.

Studying the influence of Ti, Zn, Al, and Ga doping or low amount of vacancies small on the Verwey transition and the spin reorientation transition [VC11] by means of ^{57}Fe NMR and ac susceptibility measurements, we found a correlation between their temperatures, T_{SR} and T_V (Fig. 3.7). The study was accompanied by calculations of electronic structure to evaluate the valence states in pure and substituted magnetites. Using the calculated valence we showed that the charge density due to defect/substitution spreads over a large distance, and thus the magnetocrystalline anisotropy is not induced by localized anisotropic ions. As a consequence, T_{SR} is only slightly modified by the charged defects.

Additionally, the anisotropy constants in pure cubic magnetite were calculated and confronted with experiments [80] and thermodynamic models [88], which allowed us to propose the following explanation of the anomalous temperature dependence of the magnetocrystalline anisotropy in the cubic phase of magnetite. At temperatures above T_V magnetite displays small magnetocrystalline anisotropy with K_1 anisotropy constant negative. Excited state is degenerate, with large anisotropy and positive K_1 . The gap between this excited state and the ground-state is sensitive to temperature: it is wide at high temperatures but closes with decreasing temperature and eventually, at T_{SR} , leads to change of sign of K_1 constant, and further at T_V the degeneracy of the excited state is lifted entirely and its contribution to K_1 disappears.

Magnetic systems with electric quadrupole interaction

As was shown for the ^{57}Fe isotope, the structural information stemming from the quadrupole interaction can be extracted by the Mössbauer spectroscopy but not by NMR (spin $1/2$ in the ground state of ^{57}Fe), nevertheless, this is not the case for

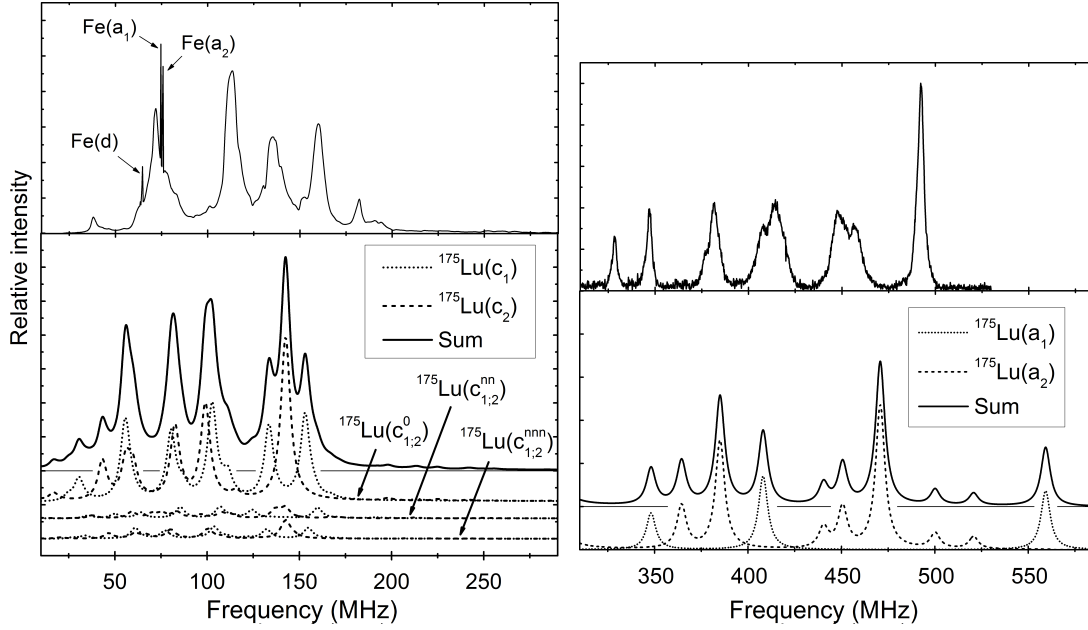


Figure 3.8: Comparison of experimental ^{175}Lu NMR spectrum and the one simulated from *ab initio* calculated EFG and hyperfine fields in lutetium iron garnet. Left panel: contributions from lutetium atoms neighboring to antisite Lu(a) defect, or being next-nearest neighbors, as well as more distant Lu atoms are denoted with indices nn, nnn, and 0. Right panel: contribution directly from ^{175}Lu forming the Lu(a) defect. Adopted from Ref. [VC12].

many other isotopes with higher spins, which are available to NMR spectroscopy. Then, in presence of electric quadrupole interaction, the calculation of electric field gradients is the key part to understand, assign, or even predict the experimental NMR spectra, as will be shown in the remaining presented papers.

In lutetium iron garnet (LuIG) the NMR spectrum consists, besides the ^{57}Fe isotope resonance, also from intensive and exceptionally broad lines of ^{175}Lu isotope (spin $7/2$). The combination of strong electric quadrupole interaction and non-zero transferred hyperfine magnetic field on ^{175}Lu yields a general case where none of the ^{175}Lu nuclear transitions can be considered as “forbidden” and thus up to 28 lines for each of the two (magnetically) non-equivalent Lu sites can be expected. The measured NMR spectrum reflects such scenario and contains a pile of overlapping resonance lines in a broad range of about 20–300 MHz. Additionally, there is another, weaker resonance detectable at higher frequencies, about 300–550 MHz. The lower frequency spectrum must clearly originate from the ^{175}Lu in the dodecahedral sites, nominal for lutetium atoms. This was confirmed by the calculations of LuIG electronic structure [VC12], where simulated ^{175}Lu NMR spectrum from the calculated parameters matched well with the experiment at low frequencies (Fig. 3.8 left panel).

Different situation, however, occurs for the weaker resonance at higher frequencies where two equivalent explanations can be proposed. First, lutetium has another, less abundant stable isotope ^{176}Lu with spin 7 and slightly higher nuclear moments μ and Q compared to ^{175}Lu , and so the resonance at higher frequencies could correspond to ^{176}Lu in dodecahedral sites. Or second, the garnet contains small amount of anti-site defect, consisting of a Lu atom entering an octahedral

site which nominally belongs to Fe, and thus the resonance of ^{175}Lu in such octahedral sites could alternatively give rise to the spectrum at higher frequencies. Both scenarios would produce quite similar intensity of the higher frequency spectrum, about 50 times lower than the intensity of the main ^{175}Lu NMR spectrum at low frequencies, because the abundance of ^{176}Lu is 2.6 % and the concentration of anti-site defect is ~ 1 %, as can be determined from ^{57}Fe spectra.

The issue was resolved by calculating the hyperfine parameters for both scenarios [VC12], i.e., the hyperfine fields as well as electric field gradients at lutetium nuclei were to be obtained. Unlike in case ^{57}Fe where a correction to calculated magnetic fields is required, for lutetium the situation is more favorable and no correction needs to be developed. This is because lutetium atom in the garnet does not possess any appreciable magnetic moment, therefore, the problematic core contribution to the contact hyperfine magnetic field is not encountered at all. The contact field on Lu nucleus is produced predominately due to transferred field from neighboring Fe atoms, via oxygen ligands and valence Lu 6s electrons. In such cases, the calculated fields do not suffer from systematic underestimation [20, 22]. Likewise, the calculated electric field gradients are usually in a good agreement with the experiments [90, 91].

Hyperfine parameters calculated for the ^{175}Lu occupying octahedral sites yielded NMR spectrum well corresponding to the experimentally observed weaker resonance at higher frequencies (Fig. 3.8 right panel). Our calculations thus explained the observed frequency shift for the octahedral (anti-site) Lu resonance, which is caused by a considerable transferred magnetic field ~ 21.7 T, about 4 times larger than the values 5.9 and 3.9 T for dodecahedral Lu (the nominal Lu sites). Presence of such increased transferred field is understandable, as the anti-site Lu, being located within the magnetic Fe sublattice, is exposed to stronger exchange interactions in comparison to the dodecahedral sites. The alternative scenario with ^{176}Lu in dodecahedral sites yielded resonance lines in a similar range as dodecahedral ^{175}Lu , i.e., in a broad range of frequencies below 150 MHz, and thus ^{176}Lu resonance is most probably overlapped by much more intensive ^{175}Lu spectrum. Therefore this alternative could be rejected.

Another example concerning the electric quadrupole interaction and determination of EFG parameters was NMR, Mössbauer, and DFT study of ilmenite FeTiO_3 [VC13]. The local structure of titanium was investigated at various temperatures by $^{47,49}\text{Ti}$ NMR in magnetic field 9.4 T and analogously for ^{57}Fe by Mössbauer spectroscopy in zero field. Both experimental methods were then compared via the spectroscopic parameters to the results of calculations of electronic structure. The ilmenite structure is relatively simple, since nominally the Fe and Ti cations occupy one octahedral site each, however, the NMR spectroscopy of titanium brings issues on its own. The two stable titanium isotopes, ^{47}Ti and ^{49}Ti , have unusually close values of gyromagnetic ratios, and both also possess considerable electric quadrupole moments, which leads to an unavoidable overlap of the their NMR spectra.

Ilmenite is paramagnetic at room temperature and its titanium NMR spectrum is relatively well resolved, allowing to extract the EFG parameters directly by fitting the whole powder-pattern of the quadrupole spectrum including satellite transitions. EFG parameters, $V_{zz} = 2.58(4) \times 10^{21} \text{ Vm}^{-2}$, $\eta = 0.029(3)$, obtained in such way are much more trustworthy, compared to more usual procedure when only

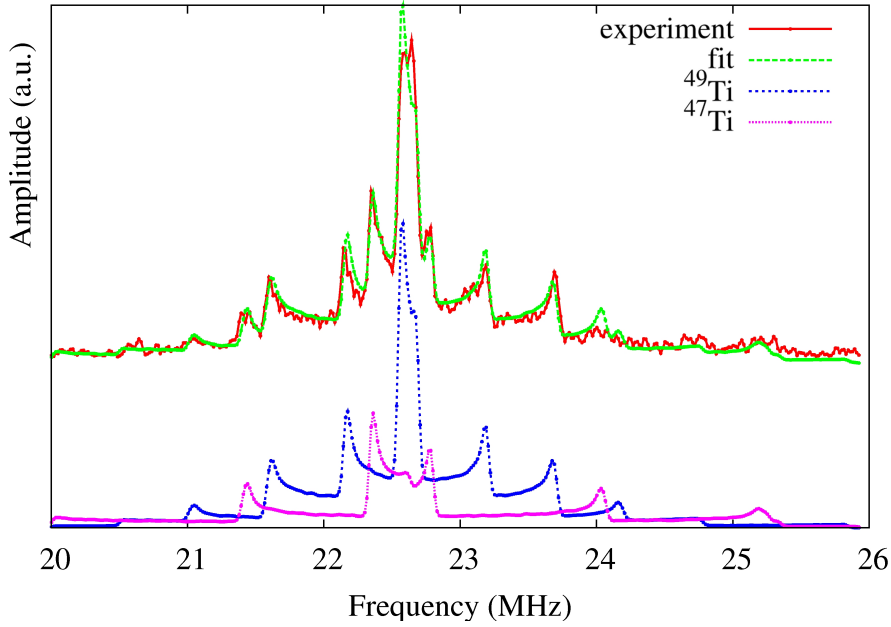


Figure 3.9: ^{47}Ti and ^{49}Ti NMR spectrum of FeTiO_3 at 300 K, fitted and decomposed to contributions of titanium isotopes. Adopted from Ref. [VC13].

the central transition is measured and analyzed [92] and yields $V_{zz} = 2.1(2) \times 10^{21} \text{ Vm}^{-2}$, and higher value of $\eta = 0.35(10)$. For ^{57}Fe the parameter $V_{zz} = 8.6(2) \times 10^{21} \text{ Vm}^{-2}$ was acquired by the Mössbauer experiment at 5 K. Our DFT calculations of electronic structure provided EFG values in a relatively good agreement with both spectroscopic methods, $V_{zz} = 2.24(10)$ for Ti and $V_{zz} = 6.95(10) \times 10^{21} \text{ Vm}^{-2}$ for Fe. The parameter η was zero due to symmetry constraints – presence of 3-fold symmetry axis of Fe and Ti sites.

In further analysis we broke the local symmetry of Ti sites in order to study a possible deviation from the trigonal symmetry and to estimate its influence on EFG parameters. Optimizing the structure with lowered symmetry yielded $\eta \sim 0.17(5)$ in the calculations, which corresponds to the small non-zero value of asymmetry η being indeed found in the $^{47,49}\text{Ti}$ NMR experiments. However, such slight deviation of η from zero could also be interpreted as an effect of distribution of EFG around some mean value, e.g., due to defects or other perturbations of the structure.

3.3 Non-magnetic systems

In contrast to magnetically ordered materials where large values of hyperfine magnetic field can give rise to measurable NMR even without application of external magnetic field, in a non-magnetic system the contributions to hyperfine magnetic field for electrons with opposing spins effectively cancel out. As a consequence, the time-averaged mean value is zero and the main part of the magnetic field is usually supplied by a well-defined homogeneous external field. The spectroscopic information – analogous to hyperfine fields – is then contained in the chemical or Knight shifts. The approach of comparing NMR experiments with DFT calculations can

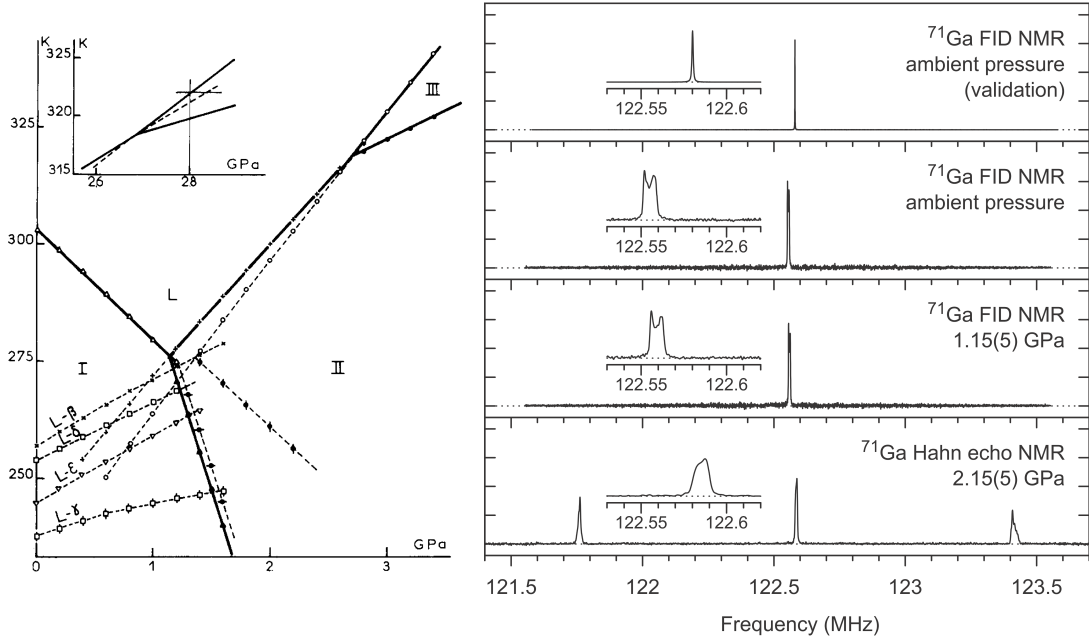


Figure 3.10: Equilibrium phase diagram of gallium, depicting the triple point as well as several metastable equilibrium phase boundaries, taken from [93]. Example of ^{71}Ga NMR spectra of gallium at room temperature for several different pressures, taken from [VC14].

thus be used in the same way, since both shifts can be reasonably calculated, and of course the electric quadrupole interaction is again considered if present in the studied system. In the following text we present four such works where the NMR-DFT comparison was successfully applied in studying non-magnetic solid-state systems.

Local structure of metals

Unlike most of other pure elements, which tend to crystallize as high-symmetry structures under ambient conditions, elemental gallium forms a rather complex structure with orthorhombic unit cell. Gallium displays a rich polymorphism [93–95] and besides the Ga-I phase (orthorhombic, also denoted as α -Ga) or Ga-II (bcc) the phase diagram contains a plethora of stable and metastable crystal phases (Fig. 3.10). Moreover, the liquid phase as well as several solid phases may be significantly supercooled [96], and thus the structure of gallium at a given temperature and pressure depends also on how this state was reached. The NMR spectroscopy has been successfully applied for studying the liquid [97, 98] as well as some of the most common solid phases of gallium [99–101]. The phases emerging above the liquid–Ga-I–Ga-II triple point that require higher pressure have rarely been measured by NMR [102] though, and thus we studied the structure of gallium metal under pressure up to 2.2 GPa by means of ^{71}Ga NMR in combination with DFT calculations [VC14].

At room temperature and ambient pressure the gallium was liquid at room temperature, but under applied pressure of ~ 2 GPa transformed into a crystal phase as manifested by quadrupole splitting in the ^{71}Ga NMR spectrum (Fig. 3.10). The isotope ^{71}Ga has nuclear spin $3/2$ and so the electric quadrupole splitting

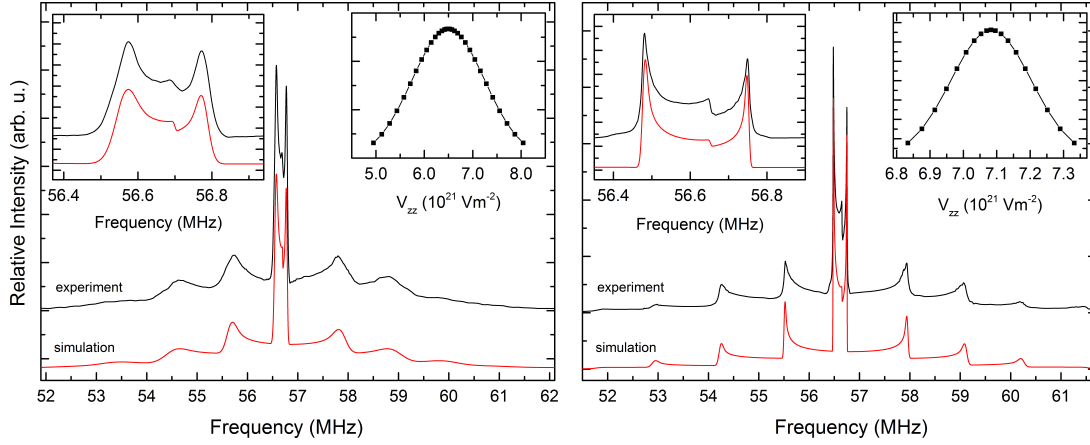


Figure 3.11: ^{139}La NMR spectra of LaCuAl_3 (left) and LaAuAl_3 (right) with their simulations using distribution of V_{zz} parameter. Adopted from Ref. [VC15].

can be expected if the local symmetry of gallium site differs from cubic. Indeed, the experimentally observed spectrum was quadrupolarly split and corresponded to a single crystal site with axial symmetry ($\eta = 0$) and $V_{zz} \sim 1.58 \times 10^{21} \text{ Vm}^{-2}$.

For room temperature and pressure 2.2 GPa, several crystal structures of gallium can be expected: cubic Ga-II, tetragonal Ga-III, and monoclinic β -Ga phase. However, for each of these three structures all Ga atoms in the unit cell are equivalent, hence any of these three phases could give rise to the observed spectrum. Therefore, in order to attribute the ^{71}Ga NMR spectrum to one particular structure, we confronted the experimental EFG parameters with those obtained from calculations of electronic structure.

Since the electric field gradients are readily available in the WIEN2k calculations in each SCF iteration, the only missing aspect in the DFT model was the applied pressure. Pressure dependences were obtained by changing the unit cell volume, while maintaining equilibrium, i.e., the remaining structural degrees of freedom (ratios of lattice parameter and internal atomic positions) were properly optimized. The value of pressure corresponding to a given volume was then extracted from fit to Birch-Murnaghan equation of state [103]. This process allowed direct comparison of the calculated EFG parameters with those derived from the experiment at 2.15 GPa. Our calculations yielded $V_{zz} = 1.64 \times 10^{21} \text{ Vm}^{-2}$ and $V_{zz} = -0.96 \times 10^{21} \text{ Vm}^{-2}$ for Ga-III and Ga-II (both with $\eta = 0$), and $V_{zz} = 2.67 \times 10^{21} \text{ Vm}^{-2}$, $\eta = 0.37$ for β -Ga phase. The obvious assignment of the phase observed in experiment to Ga-III was further supported by calculation of Knight shift $K = 0.45 \%$, which also matched well with the value in experiment $K = 0.47 \%$, whereas the calculated K for Ga-II and β -Ga phase was $K = 0.42 \%$ and $K = 0.49 \%$, respectively. Such agreement of NMR parameters lead us to interpret unambiguously the experimental ^{71}Ga NMR spectrum as the tetragonal Ga-III phase.

Another non-magnetic metallic system where investigation of the crystal structure was addressed by NMR spectroscopy and DFT calculations was LaCuAl_3 [VC15]. Our aim was to show whether the local environment of lanthanum in LaCuAl_3 is uniform or rather there are more non-equivalent La sites due to Cu/Al disorder, as this information was essential for understanding the structure of the

compound's phonon-analogue CeCuAl_3 . Inelastic neutron scattering experiments [104] revealed that the neutron energy spectra of the cerium compound contain an extra peak in addition to the two peaks expected from crystal electric field theory. In order to interpret such results the magnetoelastic interaction between the crystal electric field excitations and the lattice vibrations (so called "vibron") had to be incorporated. On the other hand, alternative explanation could consist simply in presence of multiple non-equivalent Ce sites with different crystal field parameters. NMR spectroscopy was chosen as a suitable method to resolve whether such scenario is possible. Because cerium lacks suitable NMR isotope, only an indirect investigation via NMR of Al and Cu nuclei would be possible. Therefore the study was performed with phonon-analogue compound containing La instead of Ce. This brings additional benefit, as the La compounds are nonmagnetic and thus not affected (broadened) by hyperfine magnetic fields.

A comparative approach was undertaken with LaCuAl_3 , as a compound presumably having more than one La site, and LaAuAl_3 , as a compound known to be well ordered, i.e., having a single type of La surroundings. The NMR spectra of ^{139}La , ^{27}Al , and ^{65}Cu were recorded for LaCuAl_3 in 9.4 T at room temperature, and all displayed well visible features of electric quadrupole interaction. When confronted with results on the ordered LaAuAl_3 system, the ^{139}La spectra of LaCuAl_3 were significantly more broadened in comparison with those of LaAuAl_3 (see Fig. 3.11).

In order to determine the source of such broadening, DFT models of LaCuAl_3 and LaAuAl_3 with various cationic configurations and stoichiometries were calculated and for each such model the EFG parameters were evaluated. The ^{139}La spectrum in LaAuAl_3 could be interpreted by a single spectral component and corresponded well to the (ordered) $I4mm$ structure, and at the same time, the EFG parameters calculated for other possible Au/Al arrangements were significantly different and could not contribute to the spectrum. Whereas in case of LaCuAl_3 the ^{139}La spectra displayed a wide distribution of spectral parameters, which could not be explained by a single La environment – at least one additional structure with different Cu/Al arrangement was needed to interpret the observed spectra. Similar observations were made for ^{27}Al NMR spectra, and in case of LaCuAl_3 also for ^{65}Cu NMR spectrum. Therefore, we concluded that multiple non-equivalent La positions must be present in the crystal structure of LaCuAl_3 . This finding was further elaborated and justified by analysis of calculated configurational energies, where we showed that LaCuAl_3 has a stronger tendency to atomic Cu/Al mixing compared to Au/Al case in LaAuAl_3 .

EFG and band-inversion in topological insulator

The ^{209}Bi NMR accompanied by DFT calculations was used to study Bi_2Se_3 topological insulator [VC16], which is a system where spin-orbit interaction makes the electronic states in bulk different from those near the surface. Strong spin-orbit coupling in the bulk Bi_2Se_3 induces so called "band inversion", i.e., the position of Bi p_z states in energy is decreased and the energy of Se p_z states increased. This leads to charge transfer from Se to Bi and such transfer is manifested as relatively small quadrupole splitting observed in ^{209}Bi NMR spectrum. The splitting further decreases with increasing concentration of charge carriers.

The corresponding ^{209}Bi EFG parameters were obtained from DFT calculations

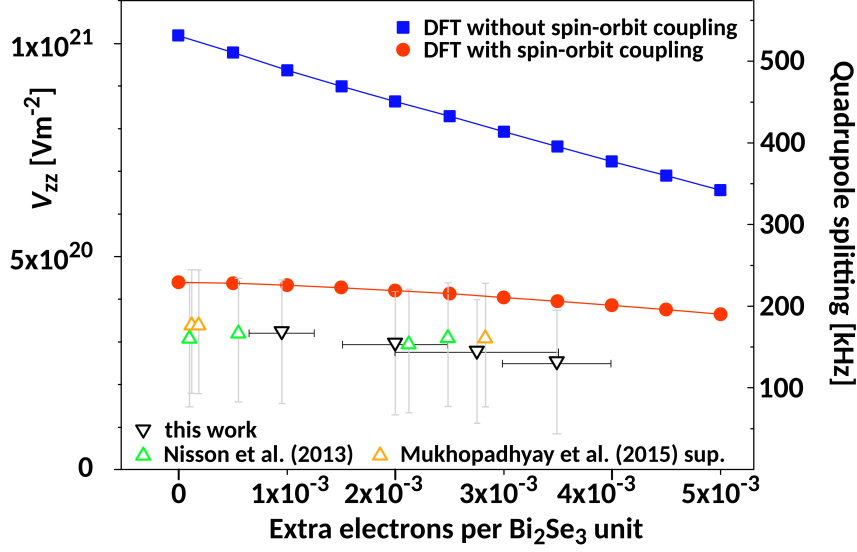


Figure 3.12: Calculated V_{zz} with (red) and without (blue) spin-orbit coupling in dependence on the carrier concentration are compared with experimental quadrupole splittings measured in Ref. [VC16] (black triangles), [105] (green triangles), and [106] (orange triangles). Horizontal error bars indicate the expected variation of the carrier concentration among the samples, vertical error bars indicate the variation of V_{zz} due to uncertainty of ^{209}Bi quadrupole momentum. Adopted from Ref. [VC16].

of Bi_2Se_3 with extra charge added into the unit cell in order to model realistic carrier concentrations (see Fig. 3.12). We showed that the EFG on Bi appears due to anisotropy of its $6p$ states: $6p_z$ states are less occupied than the $6p_x$ and $6p_y$ states. And since the extra charge enters the $6p_z$ states predominantly, the increase of carrier concentration reduces the EFG on ^{209}Bi .

When the spin-orbit interaction is enabled in the calculation, band inversion occurs, which is accompanied by additional transfer of electronic density from Se to Bi p states. The calculations thus allowed us to explain the abrupt decrease of the EFG on bismuth when the strong spin-orbit interaction is present.

Investigation of cationic preference

Not only interpretation of NMR spectra but an additional insight was brought by employing the DFT calculations of $\text{Lu}_3\text{Al}_{5-x}\text{Ga}_x\text{O}_{12}$ garnets [VC17], where the atomic arrangement of Al and Ga was studied. The occupation of tetrahedral and octahedral positions of the garnet lattice by Al and Ga atoms – important for scintillating properties of the material [107] – was independently determined from spectral intensities of ^{27}Al and ^{71}Ga NMR. The NMR results were then confronted with appropriate DFT models and both methods indicated a strong preference of Ga to occupy tetrahedral sites, regardless of Ga concentration x .

Such result appears as a paradox, since gallium has larger ionic radius than aluminium and the tetrahedron in the garnet structure has significantly smaller volume than the octahedron. Besides, there is no apparent difference in the electronic structure, since both Al and Ga atoms possess ns^2np^1 valence electrons that

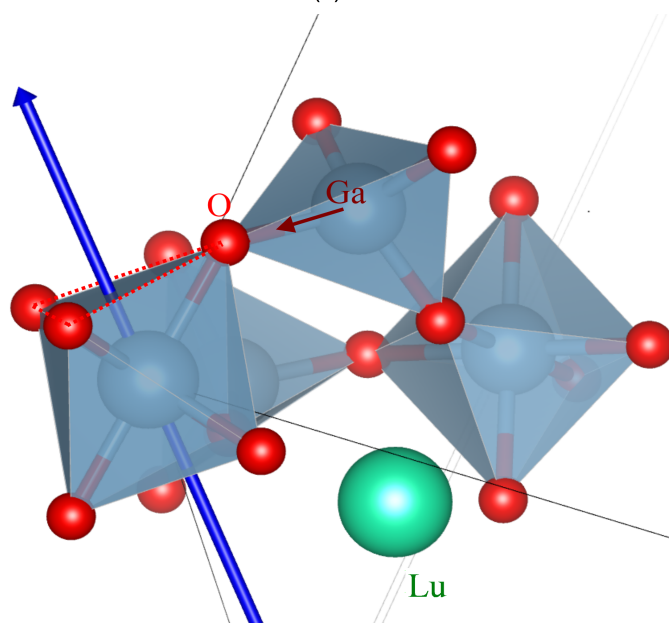
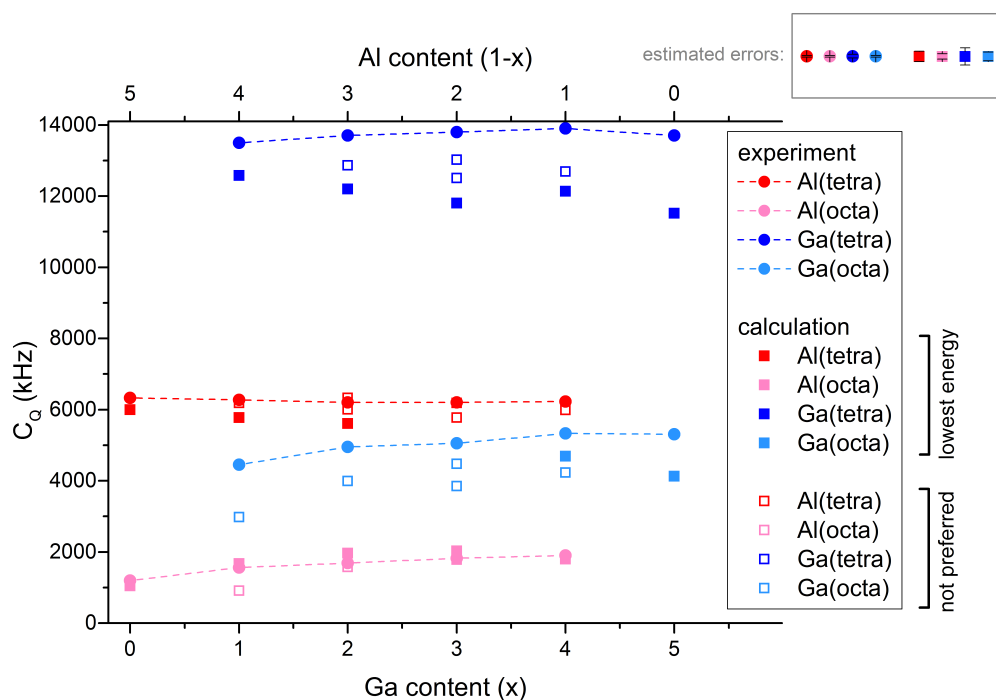


Figure 3.13: Top: Aluminium and gallium quadrupole constants as determined from NMR experiments and from DFT calculations for the mixed $\text{Lu}_3\text{Al}_{5-x}\text{Ga}_x\text{O}_{12}$ garnets. Bottom: Local structure of the garnet with indicated changes upon Ga substitution. Inflation of Ga tetrahedron further increases the trigonal distortion of the oxygen octahedron, while the tetrahedron is rotated to accommodate the shift of the shared oxygen. Partially adopted from Ref. [VC17].

favor the formation of hybridized sp^3 orbitals in the oxygen tetrahedron. However, from our DFT calculations we were able to show that, despite being fully occupied, the semi-core Ga $3d$ electrons are slightly involved in the interactions, and thus become the essential factor making Ga less compatible for octahedral environment. Together with higher electronegativity of Ga, this explained the observed tendencies of atomic distribution in the garnet structure.

Besides the atomic arrangement, the quadrupole coupling constants and chemical shift parameters for Al and Ga nuclei were calculated in a good agreement with the NMR experiments. This allowed us to understand why for octahedral Al and Ga the measured EFG parameters increase with increasing Ga content, while the tetrahedral EFGs keep constant. The DFT modelling showed that the structural relaxation after substitution of Al by larger Ga proceeds via deformation of the octahedrons while the tetrahedrons are rotated in the process, but otherwise left relatively intact.

Concluding remarks

The presented thesis described – as a common theme – the connection of two methods for studying solids: nuclear magnetic resonance experiments and density functional theory calculations. These methods were briefly introduced in the first chapters, and then their mutually beneficial combination was demonstrated in a set of papers concerning magnetic, but also several non-magnetic solid-state systems. The original pathway of this interaction – lying in calculations providing help with the interpretation of experiments – became more and more often completed with the support flowing in the opposite direction, as the precise experiments provided an anchor to reality for the calculations. We tried to show both the difficulties and the advantages of such approach and the deeper understanding it provides.

There are many directions for future developments of this combined method, mostly consisting of improvements on the side of calculations. For example in magnetic materials, the electronic correlations should be better addressed by utilizing beyond-DFT methods. Nowadays, such solution has become feasible in form of incorporating many-body methods (e.g., dynamical mean field theory) selectively within the DFT framework. For nonmagnetic materials, potentials for considering dispersion forces have been recently developed and implemented in all-electron DFT methods, which allows better descriptions of systems we would like to study, such as crystals containing water molecules with hydrogen bonds or layered structures with inter-layer van der Waals forces.

References

- [1] C. P. Slichter, *Principles of magnetic resonance*, Vol. 1 (Springer-Verlag, Berlin Heidelberg, 1990).
- [2] A. Abragam, *The principles of nuclear magnetism* (Clarendon Press, Oxford, 1961).
- [3] E. A. Turov and M. P. Petrov, *Nuclear magnetic resonance in ferro- and antiferromagnets* (Halsted Press, New York, 1972).
- [4] P. Hohenberg and W. Kohn, [Phys. Rev. **136**, B864–B871 \(1964\)](#).
- [5] W. Kohn and L. J. Sham, [Phys. Rev. **140**, A1133–A1138 \(1965\)](#).
- [6] J. P. Perdew, K. Burke, and M. Ernzerhof, [Phys. Rev. Lett. **77**, 3865–3868 \(1996\)](#).
- [7] J. P. Perdew and A. Zunger, [Phys. Rev. B **23**, 5048–5079 \(1981\)](#).
- [8] J. P. Perdew, J. A. Chevary, S. H. Vosko, K. A. Jackson, M. R. Pederson, D. J. Singh, and C. Fiolhais, [Phys. Rev. B **46**, 6671–6687 \(1992\)](#).
- [9] E. Wimmer, H. Krakauer, M. Weinert, and A. J. Freeman, [Phys. Rev. B **24**, 864–875 \(1981\)](#).
- [10] M. Weinert, E. Wimmer, and A. J. Freeman, [Phys. Rev. B **26**, 4571–4578 \(1982\)](#).
- [11] D. R. Hamann, M. Schlüter, and C. Chiang, [Phys. Rev. Lett. **43**, 1494–1497 \(1979\)](#).
- [12] D. Vanderbilt, [Phys. Rev. B **41**, 7892–7895 \(1990\)](#).
- [13] O. K. Andersen, [Phys. Rev. B **12**, 3060–3083 \(1975\)](#).
- [14] P. Blaha, K. Schwarz, F. Tran, R. Laskowski, G. K. H. Madsen, and L. D. Marks, “WIEN2k: An APW+lo program for calculating the properties of solids”, [J. Chem. Phys. **152**, 074101 \(2020\)](#).
- [15] E. Sjöstedt, L. Nordström, and D. J. Singh, [Solid State Commun. **114**, 15–20 \(2000\)](#).
- [16] D. Singh, [Phys. Rev. B **43**, 6388–6392 \(1991\)](#).
- [17] D. Singh, [Phys. Rev. B **40**, 5428–5431 \(1989\)](#).
- [18] R. Yu, D. Singh, and H. Krakauer, [Phys. Rev. B **43**, 6411–6422 \(1991\)](#).
- [19] S. Blügel, H. Akai, R. Zeller, and P. H. Dederichs, [Phys. Rev. B **35**, 3271 \(1986\)](#).
- [20] H. Katayama, K. Terakura, and J. Kanamori, [Solid State Commun. **29**, 431–434 \(1979\)](#).
- [21] M. S. R. Laskar, S. Saha, R. Palit, S. N. Mishra, F. S. Babra, S. Biswas, P. Singh, and S. K. Mohanta, [Hyperfine Interact. **240**, 96 \(2019\)](#).
- [22] S. Cottenier and H. Haas, [Phys. Rev. B **62**, 461–467 \(2000\)](#).
- [23] A. de Oliveira, M. V. Tovar Costa, N. A. de Oliveira, and A. Troper, [J. Magn. Magn. Mater. **320**, e446–e449 \(2008\)](#).

- [24] M. Filatov, *Coord. Chem. Rev.* **253**, 594–605 (2009).
- [25] H. Ebert, P. Strange, and B. L. Gyorffy, *J. Phys. F* **18**, L135–L139 (1988).
- [26] P. Novák, J. Kuneš, W. E. Pickett, W. Ku, and F. R. Wagner, *Phys. Rev. B* **67**, 140403 (2003).
- [27] E. N. Kaufmann and R. J. Vianden, *Rev. Mod. Phys.* **51**, 161–214 (1979).
- [28] K. Schwarz and P. Blaha, *Z. Naturforsch.* **47**, 197–202 (1992).
- [29] A. R. Edmonds, *Angular momentum in quantum mechanics* (Princeton University Press, Princeton NJ, 1974).
- [30] F. Haarmann, K. Koch, D. Grüner, W. Schnelle, O. Pecher, R. Cardoso-Gil, H. Borrmann, H. Rosner, and Y. Grin, *Chem. Eur. J.* **15**, 1673–1684 (2009).
- [31] F. Haarmann, K. Koch, P. Jeglič, O. Pecher, H. Rosner, and Y. Grin, *Chem. Eur. J.* **17**, 7560–7568 (2011).
- [32] W. Lipscomb, “The chemical shift and other second-order magnetic and electric properties of small molecules”, *Adv. Magn. Opt. Reson.* **2**, 137–176 (1966).
- [33] R. Ditchfield, *Mol. Phys.* **27**, 789–807 (1974).
- [34] P. E. Blöchl, *Phys. Rev. B* **50**, 17953–17979 (1994).
- [35] C. J. Pickard and F. Mauri, *Phys. Rev. B* **63**, 245101 (2001).
- [36] J. R. Yates, C. J. Pickard, and F. Mauri, *Phys. Rev. B* **76**, 024401 (2007).
- [37] R. Laskowski and P. Blaha, *Phys. Rev. B* **85**, 035132 (2012).
- [38] R. Laskowski and P. Blaha, *Phys. Rev. B* **85**, 245117 (2012).
- [39] R. Laskowski and P. Blaha, *Phys. Rev. B* **89**, 014402 (2014).
- [40] F. Blanc, J.-M. Basset, C. Copéret, A. Sinha, Z. J. Tonzetich, R. R. Schrock, X. Solans-Monfort, E. Clot, O. Eisenstein, A. Lesage, and L. Emsley, *J. Am. Chem. Soc.* **130**, 5886–5900 (2008).
- [41] T. Charpentier, S. Ispas, M. Profeta, F. Mauri, and C. J. Pickard, *J. Phys. Chem. B* **108**, 4147–4161 (2004).
- [42] R. K. Harris, S. A. Joyce, C. J. Pickard, S. Cadars, and L. Emsley, *Phys. Chem. Chem. Phys.* **8**, 137–143 (2006).
- [43] V. D. Doroshev, V. A. Klochan, N. M. Kovtun, and V. N. Seleznev, *Phys. Status Solidi (a)* **9**, 679–689 (1972).
- [44] T. Kimura, G. Lawes, and A. P. Ramirez, *Phys. Rev. Lett.* **94**, 137201 (2005).
- [45] Y. S. Chai, S. H. Chun, J. Z. Cong, and K. H. Kim, *Phys. Rev. B* **98**, 104416 (2018).
- [46] T. Tsutaoka, *J. Appl. Phys.* **93**, 2789–2796 (2003).
- [47] S. Kim, S. Jang, S. Byun, J. Lee, J. Joo, S. Jeong, and M.-J. Park, *J. Appl. Polym. Sci.* **87**, 1969–1974 (2003).
- [48] R. C. Pullar, *Prog. Mater. Sci.* **57**, 1191–1334 (2012).

- [49] H. Kojima, *Handbook of Ferromagnetic Materials* **3**, 305–391 (1982).
- [50] J. Hankiewicz, Z. Pajak, and A. Murakhowski, *J. Magn. Magn. Mater.* **101**, 134–136 (1991).
- [51] H. Štěpánková, J. Englich, J. Kohout, and H. Lütgemeier, *J. Magn. Magn. Mater.* **140–144**, 2099–2100 (1995).
- [52] G. Albanese, E. Calabrese, A. Deriu, and F. Licci, *Hyperfine Interact.* **28**, 487–489 (1986).
- [53] X. Z. Zhou, I. Horio, A. H. Morrish, Z. W. Li, and K. Hanawa, *IEEE Trans. Magn.* **27**, 4651–4653 (1991).
- [54] R. L. Streever, *Phys. Rev.* **186**, 285–290 (1969).
- [55] R. F. W. Bader, *Atoms in molecules – a quantum theory* (University of Oxford Press, Oxford, 1990).
- [56] H. Štěpánková, J. Englich, J. Kohout, and H. Lütgemeier, *J. Magn. Magn. Mater.* **140–144**, 2099–2100 (1995).
- [57] F. K. Lotgering, *J. Phys. Chem. Solids* **35**, 1663–1669 (1974).
- [58] R. Grössinger, M. Küpferling, M. Haas, H. Müller, G. Wiesinger, and C. Ritter, *J. Magn. Magn. Mater* **310**, 2587–2589 (2007).
- [59] H. Štěpánková, J. Englich, P. Novák, and H. Lütgemeier, *J. Magn. Magn. Mater* **104–107**, 409–410 (1992).
- [60] A. I. Liechtenstein, V. I. Anisimov, and J. Zaanen, *Phys. Rev. B* **52**, R5467–R5470 (1995).
- [61] S. L. Dudarev, G. A. Botton, S. Y. Savrasov, C. J. Humphreys, and A. P. Sutton, *Phys. Rev. B* **57**, 1505–1509 (1998).
- [62] P. Novák, K. Knížek, M. Küpferling, R. Grössinger, and M. W. Pieper, *Eur. Phys. J. B* **43**, 509–515 (2005).
- [63] W. Zhang, K. Koepernik, M. Richter, and H. Eschrig, *Phys. Rev. B* **79**, 155123 (2009).
- [64] B. Dorado, B. Amadon, M. Freyss, and M. Bertolus, *Phys. Rev. B* **79**, 235125 (2009).
- [65] G. Jomard, B. Amadon, F. Bottin, and M. Torrent, *Phys. Rev. B* **78**, 075125 (2008).
- [66] S. Abdelouahed and M. Alouani, *Phys. Rev. B* **79**, 054406 (2009).
- [67] B. T. Shirk and W. R. Buessem, *J. Appl. Phys.* **40**, 1294–1296 (1969).
- [68] J. Buršík, I. Drbohlav, Z. Frait, K. Knížek, R. Kužel, and K. Kouřil, *J. Solid State Chem.* **184**, 3085–3094 (2011).
- [69] P. Novák, K. Knížek, and J. Ruzs, *Phys. Rev. B* **76**, 024432 (2007).
- [70] K. Knížek, P. Novák, and M. Küpferling, *Phys. Rev. B* **73**, 153103 (2006).
- [71] F. Walz, *J. Phys. Condens. Matter* **14**, R285–R340 (2002).
- [72] Y. Joly, J. E. Lorenzo, E. Nazarenko, J.-L. Hodeau, D. Mannix, and C. Marin, *Phys. Rev. B* **78**, 134110 (2008).

- [73] Z. Kakol and J. M. Honig, *Phys. Rev. B* **40**, 9090–9097 (1989).
- [74] Z. Kakol, J. Sabol, J. Stickler, and J. M. Honig, *Phys. Rev. B* **46**, 1975–1978 (1992).
- [75] I. Bialo, A. Kozłowski, M. Wack, A. Włodek, L. Gondek, Z. Kakol, R. Hochleitner, A. Zywczyak, V. Chlan, and S. A. Gilder, *Geophys. J. Int.* **219**, 148–158 (2019).
- [76] L. Carporzen and S. A. Gilder, *J. Geophys. Res.* **115** (2010).
- [77] M. Senn, J. Wright, and J. Attfield, *Nature* **481**, 173–176 (2012).
- [78] P. Novák, H. Štěpánková, J. Englich, and J. Kohout, *Phys. Rev. B* **61**, 1256–1260 (2000).
- [79] M. Mizoguchi, *J. Phys. Soc. Jpn.* **70**, 2333–2344 (2001).
- [80] K. Abe, Y. Miyamoto, and S. Chikazumi, *J. Phys. Soc. Jpn.* **41**, 1894–1902 (1976).
- [81] C. Patterson, *Phys. Rev. B* **90** (2014).
- [82] B. A. Calhoun, *Phys. Rev.* **94**, 1577–1585 (1954).
- [83] V. Chlan, K. Kouřil, H. Štěpánková, J. Řezníček R. and Štěpánek, W. Tabis, G. Krol, Z. Tarnawski, and A. Kakol Z. and Kozłowski, *J. Appl. Phys.* **108**, 083914 (2010).
- [84] J. E. Lorenzo, C. Mazzoli, N. Jaouen, C. Detlefs, D. Mannix, S. Grenier, Y. Joly, and C. Marin, *Phys. Rev. Lett.* **101**, 226401 (2008).
- [85] A. Bosak, D. Chernyshov, M. Hoesch, P. Piekarz, M. Le Tacon, M. Krisch, A. Kozłowski, A. M. Oleś, and K. Parlinski, *Phys. Rev. X* **4**, 011040 (2014).
- [86] V. Chlan, J. Zukrowski, A. Bosak, Z. Kakol, Z. Kozłowski A. and Tarnawski, R. Řezníček, H. Štěpánková, I. Novák P. and Bialo, and J. M. Honig, *Phys. Rev. B* **98**, 125138 (2018).
- [87] J. C. Slonczewski, *Phys. Rev.* **110**, 1341–1348 (1958).
- [88] R. Aragón, *Phys. Rev. B* **46**, 5334–5338 (1992).
- [89] V. Skumryev, H. J. Blythe, J. Cullen, and J. M. D. Coey, *J. Magn. Magn. Mater.* **196–197**, 515–517 (1999).
- [90] D. Torumba, K. Parlinski, M. Rots, and S. Cottenier, *Phys. Rev. B* **74**, 144304 (2006).
- [91] R. Laskowski, G. K. H. Madsen, P. Blaha, and K. Schwarz, *Phys. Rev. B* **69**, 140408 (2004).
- [92] D. Padro, V. Jennings, M. E. Smith, R. Hoppe, P. A. Thomas, and R. Dupree, *J. Phys. Chem. B* **106**, 13176–13185 (2002).
- [93] L. Bosio, *J. Chem. Phys.* **68**, 1221–1223 (1978).
- [94] O. Degtyareva, M. I. McMahon, D. R. Allan, and R. J. Nelmes, *Phys. Rev. Lett.* **93**, 205502 (2004).
- [95] T. Kenichi, K. Kazuaki, and A. Masao, *Phys. Rev. B* **58**, 2482–2486 (1998).

- [96] G. B. Parravicini, A. Stella, P. Ghigna, G. Spinolo, A. Migliori, F. d’Acapito, and R. Kofman, [Appl. Phys. Lett.](#) **89**, 033123 (2006).
- [97] D. Hechtfisher, R. Karcher, and K. Luders, [J. Phys. F](#) **3**, 2021–2022 (1973).
- [98] N. C. Halder, [J. Magn. Reson.](#) **15**, 339–343 (1974).
- [99] M. Huebner, T. Wagner, S. Götz, and G. Eska, [Physica B](#) **210**, 484–495 (1995).
- [100] M. I. Valic and D. L. Williams, [J. Phys. Chem. Solids](#) **33**, 1583–1602 (1972).
- [101] J. D. Stroud and S. L. Segel, [J. Phys. F](#) **5**, 1981–1985 (1975).
- [102] T. Meier, [Annu. Rep. NMR Spectrosc.](#) **93**, 1–74 (2018).
- [103] F. Birch, [Phys. Rev.](#) **71**, 809–824 (1947).
- [104] D. T. Adroja, A. del Moral, C. de la Fuente, A. Fraile, E. A. Goremychkin, J. W. Taylor, A. D. Hillier, and F. Fernandez-Alonso, [Phys. Rev. Lett.](#) **108**, 216402 (2012).
- [105] D. M. Nisson, A. P. Dioguardi, P. Klavinsand, C. H. Lin, K. Shirer, A. C. Shockley, J. Crocker, and N. J. Curro, [Phys. Rev. B](#) **87**, 195202 (2013).
- [106] S. Mukhopadhyay, S. Krämer, H. Mayaffre, H. F. Legg, M. Orlita, C. Berthier, M. Horvatić, G. Martinez, M. Potemski, B. A. Piot, A. Materna, G. Strzelecka, and A. Hruban, [Phys. Rev. B](#) **91**, 081105 (2015).
- [107] H. Ogino, A. Yoshikawa, M. Nikl, J. A. Mares, J. Shimoyama, and K. Kishio, [J. of Cryst. Growth](#) **311**, 908–911 (2009).

Commented papers

- [VC1] P. Novák and V. Chlan, “Contact hyperfine field at Fe nuclei from density functional calculations”, *Phys. Rev. B* **81**, 174412 (2010) [10.1103/PhysRevB.81.174412](#).
- [VC2] V. Chlan, H. Štěpánková, R. Řezníček, and P. Novák, “Anisotropy of hyperfine interactions as a tool for interpretation of NMR spectra in magnetic materials”, *Solid State Nucl. Magn. Reson.* **40**, 27–30 (2011) [10.1016/j.ssnmr.2011.04.002](#).
- [VC3] J. Toepfer, D. Seifert, J.-M. Le Breton, F. Langenhorst, V. Chlan, K. Kouřil, and H. Štěpánková, “Hexagonal ferrites of X-, W-, and M-type in the system Sr-Fe-O: A comparative study”, *J. Solid State Chem.* **226**, 133–141 (2015) [10.1016/j.jssc.2015.02.007](#).
- [VC4] V. Chlan, K. Kouřil, K. Uličná, H. Štěpánková, J. Toepfer, and D. Seifert, “Charge localization and magnetocrystalline anisotropy in La, Pr, and Nd substituted Sr hexaferrites”, *Phys. Rev. B* **92**, 125125 (2015) [10.1103/PhysRevB.92.125125](#).
- [VC5] V. Chlan, K. Kouřil, and H. Štěpánková, “Hyperfine fields and lattice deformations in Ba and Sr hexaferrites”, *Acta Phys. Pol. A* **127**, 594–596 (2015) [10.12693/APhysPolA.127.594](#).
- [VC6] K. Kouřil, V. Chlan, H. Štěpánková, P. Novák, K. Knížek, J. Hybler, T. Kimura, Y. Hiraoka, and J. Bursik, “Hyperfine interactions in magnetoelectric hexaferrite system”, *J. Magn. Magn. Mater.* **322**, 1243–1245 (2010) [10.1016/j.jmmm.2009.03.011](#).
- [VC7] K. Kouřil, V. Chlan, H. Štěpánková, A. Telfah, P. Novák, K. Knížek, Y. Hiraoka, and T. Kimura, “Distribution of Zn in magnetoelectric Y-Type hexaferrite”, *Acta Phys. Pol. A* **118**, 732–733 (2010) [10.12693/APhysPolA.118.732](#).
- [VC8] V. Chlan, K. Kouřil, H. Štěpánková, R. Řezníček, and J. English, “Study of Y-type hexaferrite by means of Fe-57 NMR and electronic structure calculations”, *Acta Phys. Pol. A* **126**, 42–43 (2014) [10.12693/APhysPolA.126.42](#).
- [VC9] R. Řezníček, V. Chlan, H. Štěpánková, and P. Novák, “Hyperfine field and electronic structure of magnetite below the Verwey transition”, *Phys. Rev. B* **91**, 125134 (2015) [10.1103/PhysRevB.91.125134](#).
- [VC10] R. Řezníček, V. Chlan, H. Štěpánková, P. Novák, J. Zukrowski, A. Kozłowski, Z. Kakol, Z. Tarnawski, and J. M. Honig, “Understanding the Mössbauer spectrum of magnetite below the Verwey transition: Ab initio calculations, simulation, and experiment”, *Phys. Rev. B* **96**, 195124 (2017) [10.1103/PhysRevB.96.195124](#).
- [VC11] R. Řezníček, V. Chlan, H. Štěpánková, P. Novák, and M. Maryško, “Magnetocrystalline anisotropy of magnetite”, *J. Phys. Condens. Matter* **24**, 055501 (2012) [10.1088/0953-8984/24/5/055501](#).

- [VC12] V. Chlan, P. Novák, H. Štěpánková, J. Englich, J. Kuriplach, and D. Nižňanský, “Hyperfine interactions in lutetium iron garnet”, *J. Appl. Phys.* **99**, 08M903 (2006) [10.1063/1.2158687](#).
- [VC13] V. Procházka, H. Štěpánková, V. Chlan, J. Tuček, J. Čuda, K. Kouřil, J. Filip, and R. Zbořil, “Electric field gradient in FeTiO_3 by nuclear magnetic resonance and ab initio calculations”, *J. Phys. Condens. Matter* **23**, 205503 (2011) [10.1088/0953-8984/23/20/205503](#).
- [VC14] R. Řezníček, V. Chlan, and J. Haase, “NMR and ab initio study of gallium metal under pressure”, *Phys. Rev. B* **99**, 125121 (2019) [10.1103/PhysRevB.99.125121](#).
- [VC15] V. Chlan, P. Doležal, R. Sgallová, M. Klicpera, C. Franz, and P. Javorský, “Local atomic arrangement in LaCuAl_3 and LaAuAl_3 by NMR and density functional theory”, *J. Phys. Condens. Matter* **31**, 385601 (2019) [10.1088/1361-648X/ab27ac](#).
- [VC16] R. Gühne, V. Chlan, G. V. M. Williams, V. S. Chong, K. Kadowaki, A. Poepl, and J. Haase, “Unusual Bi-209 NMR quadrupole effects in topological insulator Bi_2Se_3 ”, *J. Magn. Reson.* **302**, 34–42 (2019) [10.1016/j.jmr.2019.03.008](#).
- [VC17] Y. O. Zagorodniy, V. Chlan, H. Štěpánková, Y. Fomichov, J. Pejchal, V. V. Laguta, and M. Nikl, “Gallium preference for the occupation of tetrahedral sites in $\text{Lu}_3(\text{Al}_{5-x}\text{Ga}_x)\text{O}_{12}$ multicomponent garnet scintillators according to solid-state nuclear magnetic resonance and density functional theory calculations”, *J. Phys. Chem. Solids* **126**, 93–104 (2019) [10.1016/j.jpcs.2018.10.027](#).

Reprints of commented papers

Contact hyperfine field at Fe nuclei from density functional calculations

P. Novák*

Institute of Physics of ASCR, Cukrovarnická 10, 162 53 Prague 6, Czech Republic

V. Chlan

Faculty of Mathematics and Physics, Charles University, V Holešovičkách 2, 180 00 Praha 8, Czech Republic

(Received 10 December 2009; revised manuscript received 1 March 2010; published 17 May 2010)

The hyperfine field is an important probe of the magnetism of solids, yet its calculation from the first principles in the compounds of 3d metals proved to be difficult. For iron we circumvent this problem by calculating the spin magnetic moments of the 3d electrons and the valence 4s electrons and express the contact hyperfine field as their linear combination. After adding the contributions of the on-site interaction of the nuclear spin with the orbital and spin moment of the 3d electrons, the coefficients of the linear combination are calculated by comparison with the hyperfine field experimentally determined in a number of iron compounds. The method brings the theoretical contact fields within ~ 1 T of the values deduced from experiment.

DOI: [10.1103/PhysRevB.81.174412](https://doi.org/10.1103/PhysRevB.81.174412)

PACS number(s): 76.60.-k, 71.15.Mb

I. INTRODUCTION

The density functional theory with local spin density approximation (LSDA) or semilocal [generalized gradient approximation (GGA)] approximations for the exchange-correlation potential proved to be immensely valuable for understanding of the magnetic properties of solids. Yet there exist several shortcomings of LSDA and GGA when applied to the magnetic systems. In the present paper we concentrate on one of them—severe underestimation of the contact hyperfine field B_c on the nuclei of 3d metal atoms.^{1,2} Compared to B_c , the magnetic moments of these atoms are in much better agreement with the experiment. For the ^{57}Fe nuclei this circumstance is used in the present paper to obtain in a semiempirical way the correction to contact field calculated by the GGA.

In the past there were several attempts to calculate the contact hyperfine field on the Fe nuclei *ab initio*. In particular for bcc Fe Akai and Kotani³ obtained very good agreement with the experiment using the optimized effective potential method. This method, however, is computationally very expensive and it was never used to calculate the hyperfine field in iron compounds. Novák *et al.*² obtained much improved values of B_c for bcc iron as well as for several iron compounds using computationally inexpensive, DFT based method proposed by Lundin and Eriksson.⁴ It was recognized later, however, that Lundin and Eriksson functional violates important sum rule for the exchange-correlation hole, which is imposed by the density functional theory. This brings several shortcomings, e.g., incorrect energy of the core states and the functional is no longer in use.

Two papers most relevant to our present work are devoted to the hyperfine field on the Fe nuclei in metallic systems. Blügel *et al.*⁵ studied the hyperfine field on the 3d and 4d impurities in nickel, while Ebert *et al.*⁶ calculated the hyperfine fields of Ni and Fe in the $\text{Ni}_x\text{Fe}_{1-x}$ alloys. Their results are compared to ours in Sec. V.

The contact field originates from the nonzero electron spin density in a close vicinity of the nuclei,⁵ and because of it, only the s-type electrons contribute to B_c . For the purpose

of the analysis given below, we treat separately the contribution B_{val} of electrons in the valence ns orbitals ($n \geq 4$) and the contribution B_{core} of the core s orbitals (1s, 2s, and 3s),

$$B_c = B_{\text{core}} + B_{\text{val}}. \quad (1)$$

The core orbitals are fully occupied and corresponding spin density at the nucleus is connected with the different radial part of the wave function for spin-up and spin-down ns states. This difference is close to zero for a nonmagnetic atom in compounds or alloys with other magnetic atoms. For the 3d atoms and in most other cases it increases with increasing on-site electronic spin.^{1,5,6} As the dominant part of the iron atomic spin is due to the unpaired 3d electrons and the occupation of the ns orbitals with $n \geq 5$ is very small, we can assume that

$$B_{\text{core}} = B_{\text{core}}(m_{3d}), \quad B_{\text{val}} = B_{\text{val}}(m_{3d}, m_{4s}), \quad (2)$$

where m_{3d} , m_{4s} are spin magnetic moments of the 3d and 4s electrons, respectively. B_{val} depends on both m_{3d}, m_{4s} as the nonzero density on the nucleus arises on one hand from difference of spin-up and spin-down 4s states population and, on the other hand, analogously as for the core states, from the difference of radial functions of these states. In principle the electrons in the p states polarize the ns electrons too. Our calculations showed that their magnetic moment is by more than two orders of magnitude smaller than m_{3d} , however, and the effect of the p states is not considered in what follows. For similar reasons the polarization of core states by the 4s electrons is also neglected.

It is often assumed that the functional dependences in Eq. (2) are linear^{5,6} and the calculations presented in this paper confirm this assumption. The contact hyperfine field can be thus approximated as

$$B_c = a_{3d}m_{3d} + a_{4s}m_{4s}, \quad (3)$$

where a_{3d}, a_{4s} are parameters to be determined.

The hyperfine field B_{hf} may be written as the sum of the isotropic (i.e., independent of the direction of the spin) and anisotropic components

TABLE I. Compounds considered. In all compounds, but bcc Fe only the absolute value of B_{iso} was determined. The signs follow from the discussion in Sec. VI. FeF_3 is an antiferromagnet and the experimental value refers to total hyperfine field (see discussion in Sec. VI).

Compound	Symmetry	Fe site	Local symmetry	B_{iso} (T)	Ref.
$\text{Y}_3\text{Fe}_5\text{O}_{12}$ (YIG)	Cubic	Octahedral a	Trigonal	55.254	7
		Tetrahedral d	Tetragonal	-47.348	
$\text{Lu}_3\text{Fe}_5\text{O}_{12}$ (LuIG)	Cubic	Octahedral a	Trigonal	54.61	8
		Tetrahedral d	Tetragonal	-46.74	
$\text{Li}_{0.5}\text{Fe}_{2.5}\text{O}_4$ (Li ferrite)	Cubic	Octahedral B	Rhombic	51.074	9
		Tetrahedral A	Trigonal	-51.936	
MnFe_2O_4 (Mn ferrite)	Cubic	Octahedral B	Trigonal	-51.074	10
Fe_3O_4 (magnetite)	Cubic	Octahedral B	Trigonal	-48.29	11 and 12
		Tetrahedral A	Cubic	50.77	
$\text{BaFe}_{12}\text{O}_{19}$	Hexagonal	Octahedral $2a$	Trigonal	-54.68	13
		Bipyramidal $2b$	Trigonal	-42.64	
		Tetrahedral $4f_4$	Trigonal	52.77	
		Octahedral $4f_6$	Trigonal	55.40	
FeF_3	Rhombohedral	Octahedral $12k$	Rhombic	-50.83	14
bcc Fe	Cubic	Octahedral	Rhombic	-61.81	1
			Cubic	-33.9	

$$B_{\text{hf}} = B_{\text{iso}} + B_{\text{aniz}}. \quad (4)$$

The contact field is isotropic and in the compounds considered below it makes a dominating part of B_{iso} , though there are two other terms contributing:

$$B_{\text{iso}} = B_c + B_{\text{orb}}^{\text{iso}} + B_{\text{dip}}^{\text{iso}}, \quad (5)$$

where $B_{\text{orb}}^{\text{iso}}, B_{\text{dip}}^{\text{iso}}$ are isotropic parts of the magnetic dipolar interaction of the nuclear spin with the on-site electron orbital and spin magnetic moments.⁵ Combination of Eqs. (3) and (5) gives

$$B_{\text{iso}} = a_{3d}m_{3d} + a_{4s}m_{4s} + B_{\text{orb}}^{\text{iso}} + B_{\text{dip}}^{\text{iso}}. \quad (6)$$

A number of experimental data on the isotropic component B_{iso} of the hyperfine field on the ^{57}Fe nuclei exist and we collect them in the next section. The *ab initio* calculation of the electronic structure yields both the magnetic moments m_{3d}, m_{4s} and the fields $B_{\text{orb}}^{\text{iso}}$ and $B_{\text{dip}}^{\text{iso}}$. Using the experimental values of B_{iso} the parameters a_{3d}, a_{4s} may be then estimated.

II. COMPOUNDS CONSIDERED

Most of the compounds considered here possess either cubic or axial symmetry, the local symmetry of the Fe site is often lower, however (Table I). To extract B_{iso} from the experimental hyperfine field its anisotropic part B_{aniz} (i.e., dependence of the hyperfine field on the direction of the spin magnetic moment) must be separated first. This dependence reflects the local symmetry of the Fe site. In what follows, we assume that the spin magnetic moment is parallel to the magnetization. Neglecting terms of third and higher order, the hyperfine field B_{hf} may be written as

$$B_{\text{hf}} = B_{\text{iso}} + B_{\vartheta}(\vartheta_z^2 - 1/3) + B_{\varepsilon}(\vartheta_x^2 - \vartheta_y^2), \quad (7)$$

where $\vartheta_x, \vartheta_y, \vartheta_z$ are directional cosines of the magnetization referred to the local coordinate system of the site in question. If the local symmetry of the site is cubic, $B_{\text{hf}} = B_{\text{iso}}$. If the local symmetry is axial $B_{\varepsilon} = 0$.

III. DETERMINATION OF $B_{\text{orb}}^{\text{iso}}, B_{\text{dip}}^{\text{iso}}$

The interaction of the nuclear spin with orbital moment of the electrons localized on the same site is nonzero only if the orbital moment is nonzero⁵ and this in turn requires the presence of the spin-orbit coupling. The anisotropy of B_{orb} reflects the anisotropy of the orbital moment. In the compounds considered the ratio of anisotropic and isotropic parts of the Fe orbital moment is small and the same then holds for B_{orb} . The interaction between the nuclear and electron-spin moments has different character. The low-symmetry crystal field makes the electron-density nonspherical, and providing that the atom is magnetic, the dipolar interaction gives rise to the hyperfine field whether or not the spin-orbit coupling is present. If crystal field is strong compared to the spin-orbit coupling, the spatial distribution of electron density only slightly depends on the direction of magnetization and consequently the isotropic part of B_{dip} is small, in contrast to B_{orb} .

Analogously to B_{hf} [Eq. (7)], orbital moment, as well as B_{orb} and B_{dip} reflect the local symmetry of the $3d$ metal site. This can be used when determining the isotropic components of these quantities either from the calculation or from an experiment. We first define the center of the gravity of a quantity X as

$$X_{cg} = \sum_{i=1}^N n_i X(\vartheta_{ix}, \vartheta_{iy}, \vartheta_{iz}), \quad (8)$$

where the summation is over N crystallographically equivalent sites, n_i is the multiplicity of the site, and $X(\vartheta_{ix}, \vartheta_{iy}, \vartheta_{iz})$ is the value of quantity for given direction of the magnetization relative to the i th local coordinate system. X_{cg} complies with the crystal symmetry and, as a consequence, it is isotropic for the cubic systems, providing that the terms of order higher than two in direction cosines of the magnetic moment may be neglected. The isotropic part X^{iso} of the quantity in question is then

$$X^{\text{iso}} = X_{cg} / \sum_{i=1}^N n_i. \quad (9)$$

For systems with symmetry lower than cubic the situation is more complicated, as X_{cg} , beside the isotropic term, contains also terms quadratic in direction cosines of the magnetic moment. To determine the isotropic part of the quantity the calculation or measurement must be then carried out for two directions if the crystal symmetry is axial or for three directions in the case of rhombohedral symmetry.

We note that the orbital moment in the 3d metals is underestimated by as much as 50% when calculated using LDA or GGA (Ref. 1) and this should lead to similar underestimation of B_{orb} in bcc Fe. In iron compounds the situation is unclear. The experimental data on the orbital moment are controversial for the magnetite^{15,16} and not available for other systems considered. On the computational side the GGA+ U compared to GGA may either increase or decrease the orbital moment depending on the details of the energy band structure.

IV. DETAILS OF CALCULATION

The electronic structure was calculated with the full potential augmented plane waves+local orbitals (APW+lo) method, as implemented in the WIEN2k package.¹⁷ The 1s, 2s, 2p, and 3s states of the 3d metal atoms were treated as the core states, while 3p, 3d, 4s, and 4p were included as the valence states. The sensitivity of the results to the parameters of the APW+lo was checked. For the exchange-correlation potential we adopted the GGA form.¹⁸ The radii of the atomic spheres were 2 a.u. for Fe and Mn, 1.5 a.u. for the oxygen and the fluorine, 2.5 a.u. for Ba, Lu, and Y, and 1.7 a.u. for Li.

The manganese ferrite MnFe_2O_4 was assumed to have normal spinel distribution of the cations, i.e., all octahedral (B) sites were occupied by iron, while tetrahedral (A) sublattice was filled with the manganese. The calculations for the magnetite were carried out in the cubic structure, which this compound possesses above the Verwey transition.

In all cases the experimental spin structure was assumed: ferromagnetic for bcc Fe, antiferromagnetic for FeF_3 , and ferrimagnetic for the ferrites. The unit-cell parameters were taken from the literature, while the internal parameters for garnets, spinels, and the barium hexaferrite were obtained by optimization.

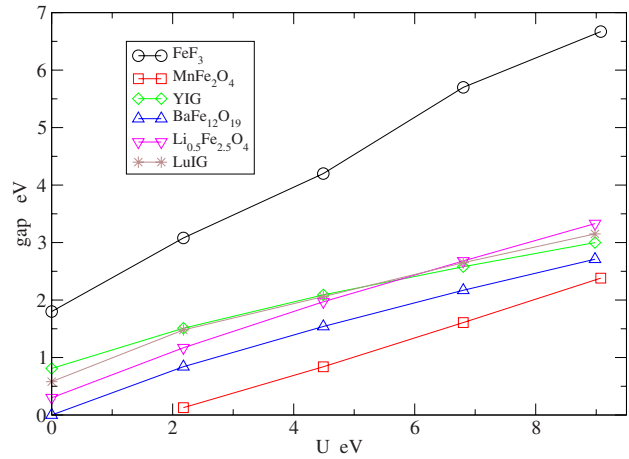


FIG. 1. (Color online) Dependence of the gap on parameter U .

The 3d electrons of the 3d metal ions in oxides and fluorides are strongly correlated and this correlation is not correctly described by either LSDA or GGA. As a consequence the gap is too small and in fact in two ferrites considered here there is no gap at all (Fig. 1). To improve the description of electron correlation we used the rotationally invariant version of the LDA+ U method as described by Liechtenstein *et al.*¹⁹ but with the GGA instead of LSDA exchange-correlation potential and only single parameter $U_{\text{eff}} = U - J$ (hereafter the subscript eff is dropped). The value of the parameter $U = 4.5$ eV was adopted for Fe in oxides and FeF_3 for Mn in MnFe_2O_4 $U = 4$ eV was chosen. The GGA+ U method lowers the energy of the occupied states and increases the energy of the less occupied or empty states. As a consequence the gap E_g increases, its dependence on U being approximately linear (Fig. 1). In FeF_3 , E_g is appreciably larger than in the oxide ferrites, reflecting more ionic state of the fluorides compared to the oxides.

In most of the oxides in question, as well as in FeF_3 , the formal valency of iron is +3, the 3d shell is half filled and the application of GGA+ U does not bring any problem. More complicated is the situation of iron on octahedral sites of Fe_3O_4 . In this case the formal valence of the $\text{Fe}(B)$ ions is +2.5, the system is half-metallic with $\text{Fe}(t_{2g})$, minority-spin bands, crossing the Fermi energy. If the magnetization is along a general direction and the spin-orbit coupling is included, there are four inequivalent $\text{Fe}(B)$ ions in the unit cell. The GGA+ U amplifies the inequivalency and leads to a charge disproportionation. To avoid this physically incorrect situation, we put the magnetization along the $[001]$ direction. For $\vec{M} \parallel [001]$ all $\text{Fe}(B)$ are equivalent and thus no disproportionation can occur.

The calculations of the gap did not include the spin-orbit coupling. Its effect on gaps is small and it would make the calculations time consuming. To find out the orbital moments and B_{orb} , B_{dip} we included the spin-orbit coupling using the second variational treatment.²⁰ By putting the magnetization along several different directions we checked that the angular dependence of the hyperfine field is well described by Eq. (7), i.e., fourth-order terms in direction cosines of the mag-

TABLE II. Results of the calculation. The hyperfine fields are in units of T, magnetic moments are expressed in μ_B . B_c^{calc} is the sum of the contribution of valence (B_{val}) and core (B_{core}) electrons.

Compound	Site	$B_{\text{orb}}^{\text{iso}}$	$B_{\text{dip}}^{\text{iso}}$	m_{3d}	m_{4s}	B_{val}	B_{core}	B_c^{calc}
$\text{Y}_3\text{Fe}_5\text{O}_{12}$	a	-0.672	0.003	-4.0919	-0.0108	-14.42	53.50	39.08
	d	0.747	-0.013	3.9367	0.0144	19.50	-50.67	-31.18
$\text{Lu}_3\text{Fe}_5\text{O}_{12}$	a	-0.495	0.003	-4.1045	-0.0107	-14.1	53.62	36.61
	d	0.613	-0.005	3.9462	0.0111	14.74	-51.70	-36.96
$\text{Li}_{0.5}\text{Fe}_{2.5}\text{O}_4$	B	0.623	-0.002	4.1047	0.0110	16.67	-53.61	-36.93
	A	-0.761	0.002	-3.9824	-0.0271	-14.63	51.70	37.07
MnFe_2O_4	B	0.418	0.235	4.1167	0.0153	20.55	-53.61	-33.06
Fe_3O_4	B	5.188	-3.721	3.8265	0.0118	15.94	-50.15	-34.22
	A	-0.928	-0.048	-3.9414	-0.0100	-13.34	51.17	37.83
$\text{BaFe}_{12}\text{O}_{19}$	$2a$	0.518	-0.001	4.1049	0.0117	15.59	-53.39	-37.80
	$2b$	0.720	0.029	3.9832	0.0175	23.50	-51.50	-27.99
	$4f_4$	-0.774	-0.001	-3.9710	-0.0102	-13.59	51.51	37.93
	$4f_6$	-0.579	0.000	-4.0658	-0.0095	-12.82	52.98	40.16
	$12k$	0.576	0.003	4.0924	0.0149	20.02	-53.13	-33.11
FeF_3		0.310	-0.005	4.2765	0.0090	11.61	-56.13	-44.52
bcc Fe		2.378	-0.175	2.346	-0.0033	-4.49	-28.59	-32.75

netization may be neglected. The results of GGA+ U calculations with the spin-orbit coupling included are collected in Table II.

V. VALENCE AND CORE CONTRIBUTIONS TO CONTACT FIELD

There is hardly a way to separate experimentally the contribution of the valence and core electrons to the hyperfine field, even more difficult would be to find out the dependence of B_c on the valence and core spin. On the other hand to obtain this information using the electron structure calculation is relatively straightforward. In Fig. 2 the dependence of the valence contribution B_{val} on the spin moment of Fe $4s$ electrons is displayed. As seen in Fig. 2 the valence part of B_c is to a very good approximation linear function of m_{4s} . Close correlation between B_{val} and m_{4s} was also found by Ebert *et al.*⁶ for both Fe and Ni in $\text{Ni}_x\text{Fe}_{1-x}$ alloys.

The dependence of the core contribution B_{core} to the contact field on the spin moment of the $3d$ electrons is shown in Fig. 3. The situation is more complex here comparing to B_{val} . The dependence is again approximately linear, but there are only few data for m_{3d} smaller than $3.9\mu_B$ and the dispersion of the data is bigger. As showed in Ref. 6 the linear proportionality between B_{core} and the local Fe moment holds $B_{\text{core}} = a_{\text{Fe}}\mu_{\text{Fe}}$ in $\text{Ni}_x\text{Fe}_{1-x}$ alloys with $a_{\text{Fe}} = -10.4\mu_B/\text{T}$. Similar value $a_{\text{Fe}} = -10.6\mu_B/\text{T}$ was obtained by Blügel *et al.* for the Fe impurity in Ni. These values are not far from the value $a_{3d} = -12.19 \text{ T}/\mu_B$ calculated using the data for bcc Fe in Table II. The linear fit to the data for all compounds considered (dashed line in the inset of Fig. 3) gives slightly higher value $a_{3d} = -12.8\mu_B/\text{T}$.

Inspection of Figs. 2 and 3 reveals that magnitude of B_{val} is smaller than that of B_{core} , though contribution of B_{val} to the contact field is significant.⁷⁻¹⁰

VI. ANALYSIS

There are several remarks to be made in connection with the B_{iso} values collected in Table I. In most cases only the absolute value of the hyperfine field was found experimentally. When attaching the sign to these values, we assumed that (i) the contact field is the dominating part of B_{hf} in the cases considered and (ii) though the calculations underestimate the B_c value, the underestimation is of order of few tens of %, so the signs of experimental B_{iso} and calculated B_c should coincide. Second remark concerns Fe_3O_4 . The value of B_{iso} in Table I refers to the cubic structure that exists

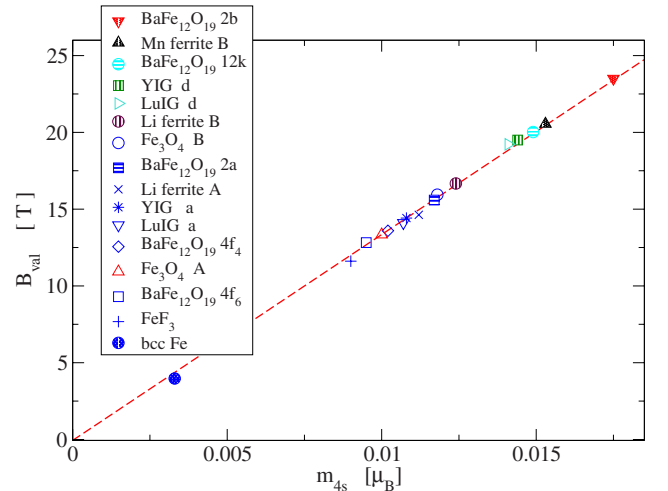


FIG. 2. (Color online) Dependence of the valence electrons contribution to the contact field on the $4s$ spin moment. The dashed line is a linear fit to the results: $B_{\text{val}} \cong a_{4s}m_{4s}$ with $a_{4s} = 1339 \text{ T}/\mu_B$. To increase the resolution of the figure the sign of the data for bcc Fe was inverted.

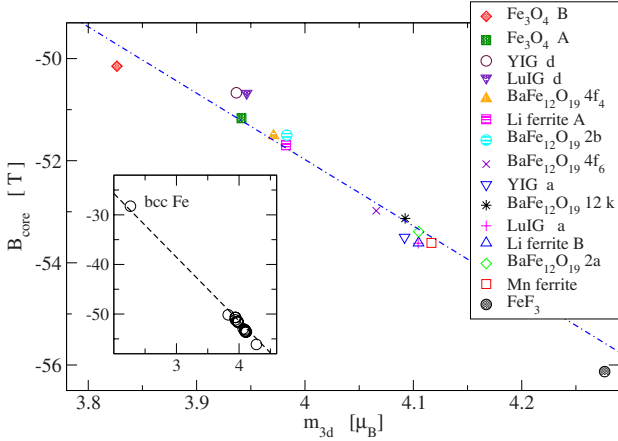


FIG. 3. (Color online) Dependence of the core (1s, 2s, 3s) contribution to B_c on the spin moment of 3d electrons. The inset shows all compounds considered, dashed line is corresponding linear fit to the data. In the main body of the figure the interval $m_{3d} > 3.8\mu_B$ is enlarged, dash and dotted line is linear fit to the data, excluding bcc Fe.

above the Verwey temperature $T_V \cong 122$ K, while the calculations correspond to the absolute zero temperature. Using the experimental data in Refs. 11 and 12 the extrapolation of $B_{\text{iso}}(T \geq T_V)$ to the zero temperature presents little problem, however. Final problem concerns FeF_3 . This compound is antiferromagnetic,¹³ only the total value of B_{hf} was determined experimentally¹⁴ and to our knowledge there is no information on the direction of magnetic moments. For FeF_3 it is thus not possible to determine experimental value of B_{iso} . The GGA+ U calculation showed, however, that the anisotropy of B_{orb} , B_{dip} is negligible (less than 0.001 T) and the classical dipolar field from the spin moments on the other sites of the lattice is rather small $B_{\text{hf}}^{\text{lattice}} \sim -0.03$ T. To a good approximation we may therefore assume that in this case $B_{\text{iso}} \cong B_{\text{hf}}$.

From the results obtained it follows that m_{3d} and m_{4s} are two quantities that should be treated as independent. In the next section we fit the experimental B_{iso} assuming that the dependences in Eq. (2) are linear, though the parameters may differ from the dependences calculated *ab initio*. We note that except for FeF_3 the $B_{\text{hf}}^{\text{lattice}}$ is not needed, as it does not possess the isotropic part.

VII. DISCUSSION

There are several stumbling blocks in the analysis given above. First, in the density functional theory the magnetic spin moments of 3d or 4s electrons are not well defined quantities, even more important is that in the APW+lo method m_{3d} and m_{4s} depend on the radius of the atomic sphere R_{MT} . To see how serious is this dependence, $m_{3d}(R_{\text{MT}})$ is displayed in Fig. 4, while m_{4s} as a function of R_{MT} is shown in Fig. 5. It is seen that 3d moments depend only slightly on the R_{MT} , while for the 4s moments the dependence is an order of magnitude stronger. The strongest effect

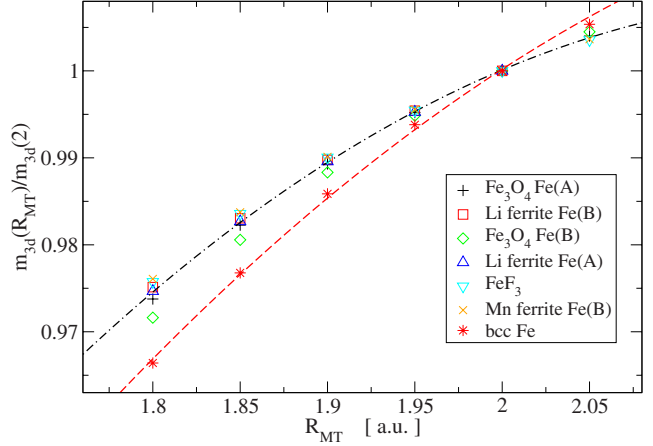


FIG. 4. (Color online) Dependence of the ratio of 3d electron-spin moment $m_{3d}/m_{3d}(R_{\text{MT}}=2 \text{ a.u.})$ on the radius of atomic sphere. Dashed (dashed and dotted) curve serves as a guide for eyes only.

has the radius of atomic sphere for bcc Fe, for which the decrease in R_{MT} from 2 to 1.8 a.u. reduces m_{4s} by $\sim 75\%$.

The second serious problem is that our calculations depend on the parameter U (bcc Fe being an exception as $U=0$ was used in this case). The increase in U makes the majority spin 3d electrons more localized. As a consequence the 3d spin magnetic moment increases monotonically (Fig. 6) and its value saturates for large U , reaching $5\mu_B$ for compounds where nominal valency of iron is 3+. The dependence of the 4s spin magnetic moment on U is displayed in Fig. 7. For both 3d and 4s electrons the dependence is smooth although the data for different compounds span larger interval comparing to their dependence on the atomic sphere radius and the fits showed in Figs. 6 and 7 serve as a guide for eyes only.

The last point to be discussed is the dependence of $B_{\text{orb}}^{\text{iso}}$ on the parameter U . As mentioned in Sec. III, B_{orb} is proportional to the orbital moment. For Fe^{3+} the orbital moment appears thanks to the not fully occupied (fully empty) majority (minority) 3d spin states. As U is increased, energy of the

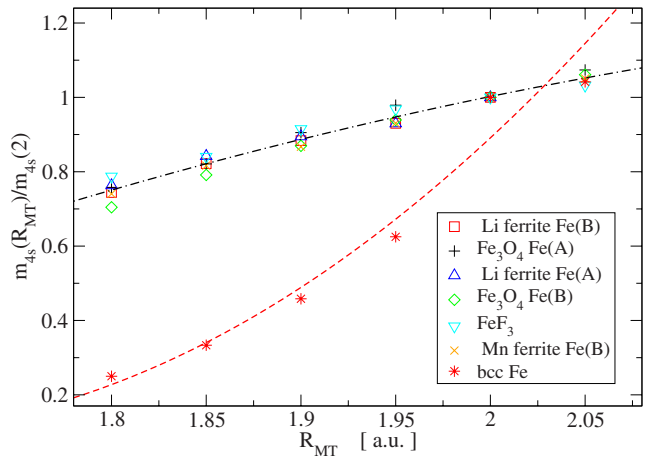


FIG. 5. (Color online) The same as Fig. 4, but for the 4s valence electrons.

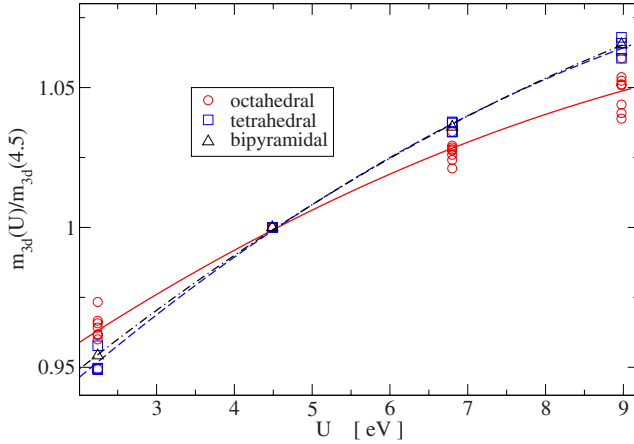


FIG. 6. (Color online) Dependence of the ratio of 3d magnetic moments $m_{3d}(U)/m_{3d}(U=4.5 \text{ eV})$ on the parameter U . The curves correspond to a quadratic fit to data for tetrahedral (dashed), octahedral (full), and bipyramidal (dashed and dotted) coordination.

majority spin states is lowered and their occupation increases, the opposite holds for the minority-spin states. As a consequence the orbital moment and B_{orb} decrease. The calculation for FeF_3 , MnFe_2O_4 , and tetrahedral Fe in magnetite showed that the dependence is approximately linear, magnitude of $B_{\text{orb}}^{\text{iso}}$ decreases by $\sim 50\%$ as U is changed from 2 to 9 eV. Inspection of Table II shows that corresponding uncertainty in $B_{\text{orb}}^{\text{iso}}$ is smaller than 0.5 T. Interestingly, for iron on the octahedral site of magnetite, for which the formal valency is 2.5, $B_{\text{orb}}^{\text{iso}}$ is almost independent of U in this interval.

The comparison between values of B_{iso} obtained from the experiment, values calculated using Eq. (6) and those determined by WIEN2k is given in Table III. It is seen that comparing to WIEN2k the analysis of the preceding section qualitatively improves the agreement with the experiment, reducing the mean deviation $\delta = \langle |B_{\text{iso}}^{\text{exp}} - B_{\text{iso}}^{\text{calc}}| \rangle$ from 15.7 to 1.3 T. The parameters in Eq. (6) have values $a_{3d} = -15.86 \text{ T}/\mu_B$, $a_{4s} = 959.6 \text{ T}/\mu_B$.

Despite the improvement there remains a serious discrepancy for bcc Fe. In this case, because the 3d electrons are

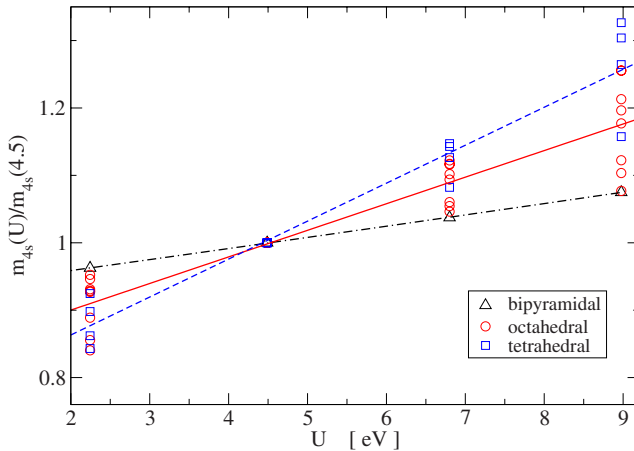


FIG. 7. (Color online) Analogous to Fig. 6, but for the 4s valence electrons and the fits of the data are linear.

TABLE III. Comparison of the isotropic parts of the hyperfine field. The values $B_{\text{iso}}^{\text{exp}}$ deduced from the experiments are confronted with $B_{\text{iso}}^{\text{calc}}$ calculated using Eq. (6) with the parameters a_{3d} and a_{4s} determined using the data for all compounds. $B_{\text{iso}}^{(1)\text{calc}}$ were determined excluding the data bcc Fe. $B_{\text{iso}}^{\text{WIEN2k}}$ refer to isotropic parts of the hyperfine field as calculated by the WIEN2k program.

Compound, site	$B_{\text{iso}}^{\text{exp}}$	$B_{\text{iso}}^{\text{calc}}$	$B_{\text{iso}}^{(1)\text{calc}}$	$B_{\text{iso}}^{\text{WIEN2k}}$
bcc Fe	-33.90	-37.99		-30.65
YIG <i>a</i>	55.25	53.86	54.52	38.41
YIG <i>d</i>	-47.35	-47.88	-47.15	-30.44
LuIG <i>a</i>	54.61	54.34	55.04	39.03
LuIG <i>d</i>	-46.74	-48.45	-47.82	-30.87
Li-ferrite <i>B</i>	-51.07	-52.48	-52.56	-36.19
Li-ferrite <i>A</i>	51.94	51.90	52.37	36.22
Mn-ferrite <i>B</i>	-51.07	-49.96	-49.10	-32.41
BaFe ₁₂ O ₁₉ <i>2a</i>	-54.68	-53.36	-53.72	-37.28
<i>2b</i>	-42.64	-45.63	-43.89	-27.25
<i>4f₄</i>	52.77	52.42	53.14	37.15
<i>4f₆</i>	55.40	54.79	55.85	39.58
<i>12k</i>	-50.83	-50.03	-49.29	-32.53
FeF ₃	-61.81	-58.88	-60.34	-44.22
Fe ₃ O ₄ <i>A</i>	50.77	51.94	52.70	33.46
<i>B</i>	-48.29	-47.90	-47.93	-32.04
bcc Fe	-33.90	-37.00		-30.65

much more delocalized than in the rest of the compounds considered, we used GGA and not GGA+ U . Imperfect treatment of the electron correlations could then cause the discrepancy.

Because of the above uncertainty of GGA calculation for bcc Fe the coefficients a_{3d} and a_{4s} were determined excluding bcc Fe. The results are denoted as $B_{\text{iso}}^{(1)\text{calc}}$ in Table III and it is seen that calculated B_{iso} is in a fair agreement with $B_{\text{iso}}^{\text{exp}}$, the mean deviation δ being smaller than 1 T. The expansion coefficients in units of T/μ_B are

$$a_{3d} = -16.92, \quad a_{4s} = 1229. \quad (10)$$

It is of interest to compare these values with the values obtained by fitting the data calculated using WIEN2k (Figs. 2 and 3): $a_{3d}^{\text{WIEN2k}} = -12.99$, $a_{4s}^{\text{WIEN2k}} = 1339 \text{ T}/\mu_B$. Clearly GGA based calculation underestimate the contribution of the core 1s, 2s, and 3s electron, while giving correctly the valence part of the B_c once bcc Fe is excluded from the fitting procedure. This is in line with the good agreement between measured and calculated hyperfine field in special cases when B_c is dominated by the transferred hyperfine interaction (as for Cu impurities in Fe, Co, and Ni,^{5,21,22} where B_c originates mainly from the spin polarization of Cu 4s valence states via interactions with the magnetic neighbors).

Inspection of Table III reveals that to obtain parameters [Eq. (10)] mostly the compounds containing nominally trivalent iron were used, iron on the *B* site of the magnetite being the only exception. Because Fe^{3+} is an *S*-state ion the orbital moment and consequently also $B_{\text{orb}}^{\text{iso}}$ is rather small. Although

qualitatively orbital moment is given correctly by the GGA (GGA+ U) calculation, its numerical value often differs from the value deduced from the experiment.¹ As the contact hyperfine field depends only on the spin moments and not on the valency, the values [Eq. (10)] should be reliable.

VIII. CONCLUSIONS

We believe that Eq. (6) in conjunction with the parameters given by Eq. (10) provide a suitable tool to explain and predict the values of the contact field on the Fe nuclei in iron compounds containing ferric ions in the high spin d^5 electron configuration, where the orbital moment is small. These systems include ferrites with spinel and garnet structure, W-, Y-, and M-hexaferrites, maghemite, hematite, hydrated ferrites, and possibly others. We also believe that the results can be useful even when orbital moment of Fe is bigger. In these cases the method can provide relatively reliable contact field.

Comparison with the experiment could then shed more light on the discrepancy of local and semilocal approximations to DFT when calculating the orbital moment dependent quantities.

When calculating the electronic structure, we treated the iron in different environments in as homogeneous way as possible, in particular the radius of Fe atomic sphere $R_{MT}=2$ a.u. and the parameter $U=4.5$ eV in the GGA+ U method were used. This seemingly limits applicability of the method. We note, however, that the dependence of the magnetic moments on these parameters is smooth (Figs. 4–6) and the interpolation in case that other values of these parameters are used does not represent problem.

ACKNOWLEDGMENTS

This work was supported by the Grant Agency of the Academy of Sciences of Czech Republic under Project No. IAA100100803 and by the project KONTAKT ME08059.

*novakp@fzu.cz

- ¹R. Coehoorn, *J. Magn. Magn. Mater.* **159**, 55 (1996).
- ²P. Novák, J. Kuneš, W. E. Pickett, W. Ku, and F. R. Wagner, *Phys. Rev. B* **67**, 140403(R) (2003).
- ³H. Akai and T. Kotani, *Hyperfine Interact.* **120-121**, 3 (1999).
- ⁴U. Lundin and O. Eriksson, *Int. J. Quantum Chem.* **81**, 247 (2001).
- ⁵S. Blügel, H. Akai, R. Zeller, and P. H. Dederichs, *Phys. Rev. B* **35**, 3271 (1987).
- ⁶H. Ebert, H. Winter, B. L. Gyorffy, D. D. Johnson, and F. J. Pinski, *J. Phys. F: Met. Phys.* **18**, 719 (1988).
- ⁷P. Novák, J. Englich, H. Štěpánková, J. Kohout, H. Lütgemeier, K. Wagner, and W. Tolksdorf, *Phys. Rev. Lett.* **75**, 545 (1995).
- ⁸V. Chlan, P. Novák, H. Štěpánková, J. Englich, J. Kuriplach, and D. Nižňanský, *J. Appl. Phys.* **99**, 08M903 (2006).
- ⁹V. D. Doroshev, V. A. Klochan, N. M. Kovtun, and V. N. Seleznev, *Phys. Status Solidi A* **9**, 679 (1972).
- ¹⁰H. Štěpánková, B. Sedlák, V. Chlan, P. Novák, and Z. Šimša, *Phys. Rev. B* **77**, 092416 (2008).
- ¹¹P. Novák, H. Štěpánková, J. Englich, J. Kohout, and V. A. M. Brabers, *Phys. Rev. B* **61**, 1256 (2000).
- ¹²Proceedings of the ICF8, Kyoto, Tokyo, Japan, 2000, edited by M. Abe and Y. Yamazaki (The Japan Society of Powder and Powder Metallurgy, Tokyo, 2000).
- ¹³H. Štěpánková, J. Englich, E. G. Caspary, and H. Lütgemeier, *J. Magn. Magn. Mater.* **177-181**, 253 (1998).
- ¹⁴G. K. Wertheim, H. J. Guggenheim, and D. N. E. Buchanan, *Phys. Rev.* **169**, 465 (1968).
- ¹⁵D. J. Huang, H. J. Lin, and C. T. Chen, *Phys. Rev. Lett.* **96**, 039702 (2006).
- ¹⁶E. Goering, M. Lafkioti, and S. Gold, *Phys. Rev. Lett.* **96**, 039701 (2006).
- ¹⁷P. Blaha, K. Schwarz, G. K. H. Madsen, D. Kvasnicka, and J. Luitz, in *WIEN2k, An Augmented Plane Wave+Local Orbitals Program for Calculating Crystal Properties*, edited by K.-H. Schwarz (Technische Universität, Wien, Austria, 2001).
- ¹⁸J. P. Perdew, K. Burke, and M. Ernzerhof, *Phys. Rev. Lett.* **77**, 3865 (1996).
- ¹⁹A. I. Liechtenstein, V. I. Anisimov, and J. Zaanen, *Phys. Rev. B* **52**, R5467 (1995).
- ²⁰D. J. Singh, *Plane Waves, Pseudopotentials, and the LAPW Method* (Kluwer Academic, Dordrecht, 1994).
- ²¹P. H. Dederichs, R. Zeller, H. Akai, and H. Ebert, *J. Magn. Magn. Mater.* **100**, 241 (1991).
- ²²V. S. Stepanyuk, R. Zeller, P. H. Dederichs, and I. Mertig, *Phys. Rev. B* **49**, 5157 (1994).



Anisotropy of hyperfine interactions as a tool for interpretation of NMR spectra in magnetic materials

V. Chlan^{a,*}, H. Štěpánková^a, R. Řezníček^a, P. Novák^b

^a Faculty of Mathematics and Physics, Charles University, V Holešovičkách 2, 180 00 Prague 8, Czech Republic

^b Institute of Physics of ASCR, Cukrovarnická 10, 162 53 Prague 6, Czech Republic

ARTICLE INFO

Article history:

Received 18 January 2011

Received in revised form

29 March 2011

Available online 21 April 2011

Keywords:

Anisotropy

Hyperfine field

Nuclear magnetic resonance

Electronic structure

ABSTRACT

Approach for interpretation of nuclear magnetic resonance (NMR) spectra in magnetic materials is presented, consisting in employing the anisotropy of hyperfine interaction. The anisotropic parts of hyperfine magnetic fields on ⁵⁷Fe nuclei are calculated *ab initio* for a model example of lithium ferrite and utilized to assign the experimental NMR spectral lines to iron sites in the crystal structure.

© 2011 Elsevier Inc. All rights reserved.

1. Introduction

Nuclear magnetic resonance (NMR) is capable to provide accurate and detailed information concerning crystal, electron and magnetic structure of magnetically ordered solids. For spectra measured in zero external magnetic field the frequency of resonating nuclei is proportional to the hyperfine magnetic field, and thus depends strongly on the local structure. It may be difficult, however, to assign unambiguously individual spectral lines to individual crystal lattice sites on which the resonating nuclei are located. In particular this difficulty appears in complex magnetic materials with the same atom (isotope) in different sublattices and/or on inequivalent lattice sites. The knowledge of the symmetry of the system helps, but even then the information gathered from the experiment is often insufficient. Determination of the resonance frequency using the *ab initio*, density functional theory (DFT) based calculation, would resolve the problem, unfortunately another difficulty emerges for the 3d metal compounds. It is well established that the DFT significantly underestimates the Fermi contact term that makes big contribution to the isotropic (i.e. independent of the direction of magnetization) part of the resonance frequency. The comparison of experiment and theory thus remains problematic, despite many attempts to remedy the situation [4,10,1,8,3,6,9].

In the present paper we propose to use the anisotropic part of the resonance frequencies calculated using the DFT to find the correspondence between the NMR lines observed experimentally and the crystal sites. Although such approach has not been attempted yet, we believe that it could serve as an additional and independent clue, moreover, without need of any explicit corrections to the calculated values. In this paper we test this approach on ⁵⁷Fe NMR in ordered lithium ferrite Fe_{2.5}Li_{0.5}O₄, i.e. ferrimagnetic system with two magnetic sublattices (Fe³⁺) and relatively simple structure. We compare the dependence of ⁵⁷Fe NMR spectra on the direction of electron magnetization (the experimental data of Doroshev et al. [5]) with our calculations of hyperfine fields with electron magnetization oriented along corresponding directions.

2. Hyperfine magnetic field

In magnetic materials the Hamiltonian of interaction of nuclear spin $\hat{\mathbf{I}}$ with magnetic field has usual form

$$\hat{H} = -\gamma \hbar \hat{\mathbf{I}} \cdot \mathbf{B}_{\text{loc}}, \quad (1)$$

where γ is the gyromagnetic ratio (for ⁵⁷Fe $I=1/2$ and $\gamma=1.38 \text{ MHz T}^{-1}$). The local magnetic field \mathbf{B}_{loc} consists of several contributions:

$$\mathbf{B}_{\text{loc}} = \mathbf{B}_{\text{hf}} + \mathbf{B}_{\text{latt}}^{\text{dip}} + \mathbf{B}_{\text{ext}}. \quad (2)$$

Term \mathbf{B}_{hf} denotes hyperfine magnetic field, $\mathbf{B}_{\text{latt}}^{\text{dip}}$ stands for dipolar magnetic interaction of the nuclear spin with atomic magnetic moments in the surrounding lattice, and \mathbf{B}_{ext} denotes external

* Corresponding author.

E-mail addresses: chlan@mbox.troja.mff.cuni.cz, vojtech.chlan@mff.cuni.cz (V. Chlan).

magnetic field (if present). The hyperfine field originates due to Fermi contact interaction ($\mathbf{B}_{\text{hf}}^{\text{cont}}$) and interactions of nuclear spin with the on-site spin and orbital moments of electrons ($\mathbf{B}_{\text{hf}}^{\text{dip}}$, $\mathbf{B}_{\text{hf}}^{\text{orb}}$):

$$\mathbf{B}_{\text{hf}} = \mathbf{B}_{\text{hf}}^{\text{cont}} + \mathbf{B}_{\text{hf}}^{\text{dip}} + \mathbf{B}_{\text{hf}}^{\text{orb}}. \quad (3)$$

A detailed discussion of how these fields are calculated using the DFT and how they are connected to the interaction between the electron and the nuclei was given by Blügel et al. [3].

The local magnetic field may be considered as a sum of isotropic and anisotropic parts where only the latter is subject to further analysis. The Fermi contact term $\mathbf{B}_{\text{hf}}^{\text{cont}}$ is purely isotropic, i.e. its magnitude does not depend on the direction of electron magnetization. For ^{57}Fe nuclei $\mathbf{B}_{\text{hf}}^{\text{cont}}$ is oriented antiparallel to the direction of electron magnetization.

The terms $\mathbf{B}_{\text{hf}}^{\text{dip}}$, $\mathbf{B}_{\text{hf}}^{\text{orb}}$ and $\mathbf{B}_{\text{la}}^{\text{dip}}$ may be anisotropic (dependent on the direction of electron magnetization). In case of Fe^{3+} the contact term is the dominant contribution to the local field, and therefore, the anisotropic terms may be considered as projections on the direction of electron magnetization.

The anisotropy of hyperfine interaction reflects the local symmetry of the crystal site [14]. Note, however, that nuclei on the crystallographically equivalent sites may possess different resonant frequencies due to the anisotropy of hyperfine interaction. As a consequence, one crystallographic site may be connected with several spectral lines. Such pattern is a fingerprint of particular crystal site, and therefore, it helps to interpret the NMR spectra.

3. ^{57}Fe NMR in lithium ferrite

Lithium ferrite $\text{Fe}_{2.5}\text{Li}_{0.5}\text{O}_4$ is well studied experimentally, including extensive ^{57}Fe NMR data [5]. It has a spinel structure with two types of cation sites: tetrahedral A sites occupied by iron and octahedral B sites containing both lithium and iron ions. If Li and Fe ions on the B sites are disordered, the crystal lattice symmetry is cubic. Ordering of these ions leads to lowering of the cubic symmetry to rhombohedral $P4_332$. Local symmetry of the A-sites is then D_3 , while the local symmetry of the B sites occupied by iron is C_2 ; each Fe(B) having two Li and four Fe atoms as the nearest neighbors on the B-sites. In the presence of the magnetization \vec{M} the symmetry is lowered further. If \vec{M} is confined to the $(0\bar{1}1)$ plane the tetrahedral sites split into four subgroups (each with multiplicity 2:2:2:2 in the cell containing eight $\text{Fe}_{2.5}\text{Li}_{0.5}\text{O}_4$ formula units), while the Fe(B) sites split into seven subgroups (1:2:1:2:2:2:2). For $\vec{M} \parallel \langle 111 \rangle$ the symmetry analysis shows that there are two Fe(A) subgroups with multiplicity 6:2 and three Fe(B) subgroups (ratio 3:3:6).

We used single crystal of ordered lithium ferrite, grown by the spontaneous crystallization method from a solution of the molten salt [12] of volume approximately 0.2 cm^3 . Fig. 1 displays ^{57}Fe NMR spectrum of lithium ferrite single crystal that was measured at 4.2 K in zero magnetic field by the spin-echo method using phase-coherent pulse spectrometer Bruker Avance and home-made broadband probehead. The signal-to-noise ratio was significantly improved by using the Carr–Purcell–Meiboom–Gill pulse sequence. Amplitude of rf field was carefully set to obtain NMR signal from nuclei in the magnetic domains only. At given excitation frequency the echoes 1–100 were summed up within the sequence and the sum was Fourier transformed. The length of the sequence (26 ms) and repetition time (25 s) were set carefully not to influence the spectral shape by spin–spin and spin–lattice relaxations. The resulting frequency swept spectrum was evaluated as an envelope of Fourier transforms at individual excitation frequencies (changed with step of 25 kHz).

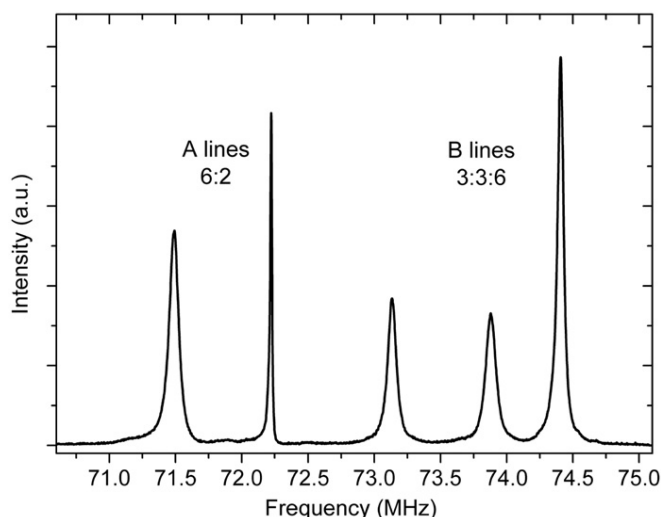


Fig. 1. ^{57}Fe NMR spectrum of lithium ferrite measured at 4.2 K in zero magnetic field.

The easy direction of the magnetization of the Li ferrite is $\langle 111 \rangle$. The symmetry then predicts that the NMR spectrum will consist of two lines with the ratio 6:2 that originate from the tetrahedral irons and three lines (ratio 3:3:6) arising from the octahedral irons. As shown in Fig. 1, this pattern was indeed observed experimentally.

Already from the NMR spectrum in the zero field the tetrahedral subspectrum may be unambiguously interpreted: two of the eight A sites in unit cell have their local C_3 -axis parallel to the direction of magnetization (e.g. $[111]$) and produce the weaker, sharp line at 72.224 MHz, while the axes of remaining six A sites lie in $[\bar{1}11]$, $[1\bar{1}1]$ and $[11\bar{1}]$ directions and generate the broader line at 71.49 MHz. One should note that all Fe(A) are crystallographically equivalent: the differences in resonance frequencies arise due to anisotropy of hyperfine interaction. If the experiment is done with external magnetic field in $(0\bar{1}1)$ plane (see Fig. 2), lines of those A sites with axis in $[\bar{1}11]$ direction would be additionally separated.

Similar analysis can be done for the 12 octahedral sites and $\vec{M} \parallel \langle 111 \rangle$. There are then two different angles between the local C_2 -axis and magnetization: (i) for a group of six sites C_2 -axis is of type $\langle 110 \rangle$ and it makes an angle 35.26° with the direction of magnetization, producing the line at 74.407 MHz, (ii) for remaining six Fe(B) sites the magnetization is perpendicular to the C_2 -axis (in these cases C_2 -axis is of type $\langle 110 \rangle$). The later six sites are further subdivided into two magnetically non-equivalent subgroups, each comprising three sites. These subgroups differ in the angle that \vec{M} makes with the line joining the resonating iron nuclei with the nearest Li ions. In the first case \vec{M} is perpendicular to both Fe–Li bonds, while in the second case corresponding angles are 61.42° and 118.58° . The nuclei in these two subgroups give rise to the lines at 73.134 and 73.879 MHz. However, based solely on the experiment, it is not possible to decide, which spectral line corresponds to which of the subgroups.

4. Calculation of hyperfine field anisotropy

The calculations of electronic structure were performed using the augmented plane waves+local orbital method based on density functional theory as implemented in the WIEN2k program package [2]. To improve the description of electron

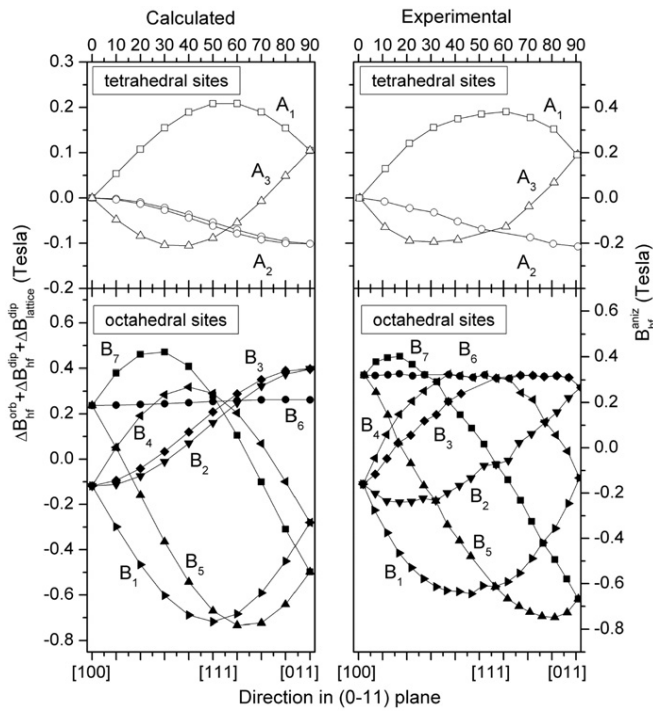


Fig. 2. Comparison of calculated and experimental [5] hyperfine fields for tetrahedral and octahedral irons in lithium ferrite. Both experimental and calculated fields were adjusted by subtracting their isotropic parts. The curves A_2 , B_1 – B_4 and B_6 are double degenerate.

Table 1

Assignment of the individual curves with the corresponding positions of the resonating nucleus in the crystal structure with respect to direction of magnetization [1 1 1]. Structural parameters $x=0.49816$ and $y=0.63195$ were calculated by optimizing the crystal structure.

Line	Multiplicity	Crystal coordinates
A_1	2	(x, x, x)
A_2	4	$(-x + \frac{1}{2}, -x, x + \frac{1}{2})$
A_3	2	$(x + \frac{1}{2}, -x + \frac{1}{2}, -x)$
B_1	2	$(-y + \frac{1}{4}, \frac{1}{8}, y)$
B_2	2	$(y + \frac{3}{4}, \frac{5}{8}, -y + \frac{1}{2})$
B_3	2	$(y + \frac{1}{4}, \frac{7}{8}, y + \frac{1}{2})$
B_4	2	$(-y + \frac{3}{4}, \frac{3}{8}, -y)$
B_5	1	$(\frac{1}{8}, y, -y + \frac{1}{4})$
B_6	2	$(\frac{3}{8}, y + \frac{1}{2}, y + \frac{1}{4})$
B_7	1	$(\frac{5}{8}, -y + \frac{1}{2}, y + \frac{3}{4})$

correlation we used rotationally invariant version of LDA+U method as described by Liechtenstein et al. [7], but with the GGA-PBE [11] as the exchange correlation potential and with single parameter $U_{\text{eff}}=U-J$, for which the value $U_{\text{eff}}=4.5$ eV was adopted. The atomic sphere radii were set to 1.8 a.u. for iron, 1.7 a.u. for lithium and 1.6 a.u. for oxygen. The equilibrium values of the internal parameters $x=0.49816$ and $y=0.63195$, characterizing the crystal structure (Table 1), were found by minimizing the forces acting on the atoms.

In order to calculate the anisotropic contributions to the hyperfine field the spin–orbit (s–o) interaction was included using the second variational treatment [13]. Using the equilibrium crystal structure, the self-consistent s–o calculations were

performed in 40k-points in the irreducible part of the Brillouin zone, number of the basis functions was 4048 ($RK_{\text{max}}=6.0$), and the charge density was Fourier expanded to $G_{\text{max}}=14 \text{ Ry}^{1/2}$.

The calculations were designed to correspond to the NMR experiment of Doroshev et al. [5] who measured the angular dependence of the NMR spectra with the electron magnetization in the $(0 \bar{1} 1)$ plane. For each direction of magnetization, changed within the $(0 \bar{1} 1)$ plane with steps of 10° , the calculation that includes the s–o was converged and projections of $B_{\text{hf}}^{\text{dip}}$ and $B_{\text{hf}}^{\text{orb}}$ to the direction of magnetization ($B_{\text{hf}}^{\text{dip}}$ and $B_{\text{hf}}^{\text{orb}}$) were then calculated. For the same directions the off-site dipolar contribution $B_{\text{lat}}^{\text{dip}}$ was obtained by direct summation over the magnetic moments of all sites in a sphere with radius of 128 atomic units. Since we were interested in anisotropy of the hyperfine field, the isotropic parts of the calculated fields were subtracted to obtain $\Delta B_{\text{hf}}^{\text{dip}}$, $\Delta B_{\text{hf}}^{\text{orb}}$ and $\Delta B_{\text{lat}}^{\text{dip}}$ ($B_{\text{lat}}^{\text{dip}}$ has zero isotropic part).

5. Results

Angular dependence of ^{57}Fe NMR spectra at both tetrahedral and octahedral sites of ordered lithium ferrite was acquired experimentally by Doroshev et al. [5] using a sphere shaped sample. Spectra were measured in external magnetic field 0.266 T, which was applied in $(0 \bar{1} 1)$ plane. For the sake of comparison of experimental anisotropic field $B_{\text{hf}}^{\text{anis}}$ with the calculated anisotropy (see Fig. 2), we rescaled the experimental data into units of Tesla and subtracted the isotropic parts (52.15 T for A sites and 53.57 T for B sites). With the direction of magnetization confined to the $(0 \bar{1} 1)$ plane, two of the A lines should coincide due to symmetry reasons. This is not fully reproduced in our calculated dependences and the small splitting of the curve A_2 in Fig. 2 thus provides an estimation of the calculation accuracy.

For the octahedral sites the calculated dependences of hyperfine field on the direction of magnetization fall within the interval $(-0.75, 0.48)$ in units of Tesla, which matches with the interval $(-0.75, 0.41)$ of the experimental data. For the tetrahedral sites the calculated curves are found within a range of ~ 0.32 T, while the experimental ones span somewhat larger interval of ~ 0.59 T. The discrepancy is most likely connected with an underestimation of the orbital moment and thus $B_{\text{hf}}^{\text{dip}}$ and $B_{\text{hf}}^{\text{orb}}$, which is often encountered in the density functional based calculations. As seen in Fig. 2, however, the character of the dependences is similar to the extent that the assignment of calculated and experimental curves is clear. This allows to establish an unambiguous connection between the observed NMR lines and the positions of resonating Fe nuclei in the crystal.

6. Conclusions

The anisotropic part of ^{57}Fe hyperfine field in lithium ferrite was calculated from the first principles. Comparison of calculated results with experimental dependence of NMR spectra on the direction of external magnetic field allowed an unambiguous assignment of the experimentally observed NMR lines to individual sites occupied by iron ions. An important point of our approach is subtraction of the isotropic part from the experimental as well as calculated hyperfine field. In this way we eliminated the influence of the contact term, calculation of which is problematic. We believe that an analogous approach might be applicable for spectral line assignment also in more complicated compounds.

Acknowledgments

We thank to Prof. V.D. Doroshev for supplying the single crystal of ordered lithium ferrite. This work was supported by the Grant Agency of Czech Republic under Project no. 202/08/0541 and by the Project MS0021620834 of the Ministry of Education of the Czech Republic. R.Ř. also acknowledges support of GAUK Project no. 392111.

References

- [1] H. Akai, T. Kotani, *Hyperfine Interact.* 120–121 (1999) 3.
- [2] P. Blaha, K. Schwarz, G.K.H. Madsen, D. Kvasnicka, J. Luitz, WIEN2k, An augmented plane wave+local orbitals program for calculating crystal properties, Technischen Universität Wien, 2001. ISBN 3-9501031-1-2.
- [3] S. Blügel, H. Akai, R. Zeller, P.H. Dederichs, *Phys. Rev. B* 35 (1987) 3271.
- [4] R. Coehoorn, *J. Magn. Magn. Mater.* 159 (1996) 55.
- [5] V.D. Doroshev, V.A. Klochan, N.M. Kovtun, V.N. Selesnev, *Phys. Status Solidi A* 9 (1972) 679.
- [6] H. Ebert, H. Winter, B.L. Gyorffy, D.D. Johnson, F.J. Pinski, *J. Phys. F: Met. Phys.* 18 (1988) 719.
- [7] A.I. Liechtenstein, V.I. Anisimov, J. Zaanen, *Phys. Rev. B* 52 (1995) R5467.
- [8] U. Lundin, O. Eriksson, *Int. J. Quantum Chem.* 81 (2001) 247.
- [9] P. Novák, V. Chlan, *Phys. Rev. B* 81 (2010) 174412.
- [10] P. Novák, J. Kuneš, W.E. Pickett, W. Ku, F.R. Wagner, *Phys. Rev. B* 67 (2003) 140403(R).
- [11] J.P. Perdew, S. Burke, M. Ernzerhof, *Phys. Rev. Lett.* 77 (1996) 3865.
- [12] V.N. Selesnev, K. Pukhov, A.I. Drokin, V.A. Shapovalov, *Fiz. Tverd. Tela* 12 (1970) 885.
- [13] D.J. Singh, *Planewaves, Pseudopotentials and the LAPW Method*, Kluwer Academic, Boston, 1994.
- [14] H. Štěpánková, J. Kohout, J. Englich, P. Novák, *Hyperfine Interact.* 131 (2000) 2.



Hexagonal ferrites of X-, W-, and M-type in the system Sr–Fe–O: A comparative study

Jörg Töpfer^{a,*}, Daniela Seifert^a, Jean-Marie Le Breton^b, Falko Langenhorst^c,
Vojtech Chlan^d, Karel Kouřil^d, Helena Štěpánková^d

^a University of Applied Sciences Jena, Department of SciTec, Carl-Zeiss-Promenade 2, 07745 Jena, Germany

^b Groupe de Physique des Matériaux UMR 6634 CNRS Université de Rouen, Faculté des Sciences, BP12, 76801 Saint Etienne du Rouvray, France

^c Institute of Geosciences, University of Jena, Carl-Zeiss-Promenade 10, 07745 Jena, Germany

^d Faculty of Mathematics Physics, Charles University in Prague, V Holešovičkách 2, 18000 Prague, Czech Republic

ARTICLE INFO

Article history:

Received 17 November 2014

Received in revised form

4 February 2015

Accepted 9 February 2015

Available online 19 February 2015

Keywords:

Hexagonal ferrites

X-type ferrite

Magnetization

Mössbauer spectroscopy

NMR spectroscopy

ABSTRACT

Three hexagonal ferrites from the Fe-rich part of the pseudo-binary system SrO–Fe₂O₃ were investigated. Besides the well-known M-type SrFe₁₂O₁₉ two other ferrites were found to exist at high temperatures: W-type SrFe₂²⁺Fe₁₆³⁺O₂₇ and X-type Sr₂Fe₂²⁺Fe₂₈³⁺O₄₆ ferrites. A detailed characterization of the X-type Sr-ferrite is reported here for the first time using XRD, HRTEM, magnetization measurements, Mössbauer and ⁵⁷Fe NMR spectroscopies and ab initio calculations of the electronic structure. The results are compared to those of W- and M-type Sr ferrites. Mössbauer spectra were analyzed with six Fe contributions in the case of the X-type, seven Fe-sites for the W-type and five Fe sites for the M-type in agreement with crystal structure arrangements. Based on a detailed analysis of the NMR spectra in comparison with ab initio calculations the NMR lines were assigned to individual crystal sites. A preferential occupation of ferrous ions in the S blocks of the X- and W-type ferrites was elucidated from Mössbauer and NMR data as well as ab initio calculations.

© 2015 Elsevier Inc. All rights reserved.

1. Introduction

The hexagonal ferrites are an important family of magnetic materials with M-type SrFe₁₂O₁₉ as the dominating composition in the Fe-rich part of the pseudo-binary system SrO–Fe₂O₃. It was reported that M-type Sr ferrite (Sr-M) is stable up to 1448 °C [1], a fact that enables the straightforward industrial-scale fabrication of this material via the mixed-oxide route and high temperature sintering. Goto et al. [2] reported a second phase diagram including a W-type hexagonal ferrite SrFe₂Fe₁₆O₂₇ (SrFe₂-W) which was found to be stable in a small temperature region between 1390 and 1420 °C only. Recently, a reinvestigation of the Fe-rich part of the Sr–Fe–O system has revealed the existence of another hexagonal ferrite Sr₂Fe₂Fe₂₈O₄₆ (Sr₂Fe₂-X) with X-type structure [3]. In the Ba–Fe–O system, an X-type ferrite of composition Ba₂Fe₂Fe₂₈O₄₆ (Ba₂Fe₂-X) was already reported by van Hook [4]. Preliminary magnetic characterization of Ba₂Fe₂-X revealed a saturation magnetization $M_s = 98$ emu/g at 0 K and a $T_c = 522$ °C [5]. Substituted Ba₂Me₂-X and Sr₂Zn₂-X ferrites were synthesized and a remarkable

$M_s = 120$ emu/g was reported for the latter one [6,7]. On the other hand, reports on the preparation and characterization of the non-substituted hexagonal X-type Sr ferrite Sr₂Fe₂-X are very scarce. Dey and Valenzuela measured some magnetic data (M vs. T curve) with a $M_s = 100$ emu/g at low temperature [8]. Another study reports on the disaccommodation behavior of that ferrite [9]. Magnetic properties of W-type hexagonal ferrite SrFe₂Fe₁₆O₂₇ (SrFe₂-W) were already reported in the literature [10,11]. The saturation magnetization of SrFe₂-W was found to be larger than that of M-type ferrite [10]; hence X- and W-type Sr-ferrites show some potential as alternative permanent magnetic materials. However, due to their limited stability at high temperatures [3], the preparation of these materials is not straightforward.

The crystal structures of the M-, W-, and X-type hexagonal strontium ferrites are characterized by stacking sequences of R- and S-blocks along the hexagonal c -axis, where S is a two-layer building unit (Fe₆O₈)²⁺ and R is a three layer block of composition (SrFe₆O₁₁)²⁻. Iron cations are localized in various crystallographic sites (formed by close-packed oxygen/strontium layers) that differ by coordination, site symmetry and arrangement of surrounding atoms (for details see Table 1). Combination of RS gives the structure of the M-type ferrite SrFe₁₂O₁₉ which is equivalent to the magnetoplumbite structure of PbFe₁₂O₁₉ described by Adelskjöld [12]. A stacking

* Corresponding author. Tel.: +49 3641 205350; fax: +49 3641 205451.
E-mail address: joerg.toepfer@fh-jena.de (J. Töpfer).

Table 1
Crystallographic sites of the Fe ions in the M-, W-, and X-type hexagonal ferrites Sr-M, SrFe₂-W and Sr₂Fe₂-X.

M-type (<i>P6₃/mmc</i>)				W-type (<i>P6₃/mmc</i>)				X-type (<i>R-3m</i>) (site notation in <i>P6₃/mmc</i>)				All (simplified description)
Site	Coord.	Block	Spin	Site	Coord.	Block	Spin	Site	Coord.	Block	Spin	Magnetic sublattices
12k _{VI}	Octa	R-S	↑	12k _{VI}	Octa	R-SS	↑	18h _{VI}	Octa	R-S	↑	<i>k</i>
								18h' _{VI}	Octa	R-SS	↑	
4f _{IV} (4f ₁)	Tetra	S	↓	4e _{IV}	Tetra	SS	↓	6c _{IV}	Tetra	S	↓	<i>f_{IV}</i>
				4f _{IV} (4f ₁)	Tetra	SS	↓	6c' _{IV}	Tetra	SS	↓	
								6c'' _{IV}	Tetra	SS	↓	
4f _{VI} (4f ₂)	Octa	R	↓	4f _{VI} (4f ₂)	Octa	R	↓	6c' _{VI}	Octa	R	↓	<i>f_{VI}</i>
								6c'' _{VI}	Octa	R	↓	
2b _V	Five	R	↑	2d _V	Five	R	↑	6c _V	Five	R	↑	<i>b</i>
2a _{VI}	Octa	S	↑					3b _{VI}	Octa	S	↑	<i>a</i>
				6g _{VI}	Octa	S-S	↑	9e _{VI}	Octa	S-S	↑	
				4f _{VI} (4f ₃)	Octa	SS	↑	6c _{VI}	Octa	SS	↑	

Block notation:

S inside S block

R inside R block

SS inside S block in SS stacking

S-S between two S blocks

R-S between R and S blocks

R-SS between R block and S block in SS stacking

sequence RSS (or MS) results in the W-type hexagonal variant SrMe₂Fe₁₆O₂₇ and that of RSRSS (or M₂S) in the X-type hexagonal ferrite Sr₂Me₂Fe₂₈O₄₆ [13,14].

The M-type ferrite (SG *P6₃/mmc*) is formed by a stacking sequence of R- and S-blocks SRS*R* where * denotes a 180° rotation around the *c*-axis. The unit cell contains two formulae SrFe₁₂O₁₉ (*z*=2), ferric ions occupy 12*k* sites (octahedral sites between R- and S-blocks), tetrahedral 4*f_{IV}* (or *f₁*) sites (in S-block), octahedral 4*f_{VI}* (or *f₂*) sites (in R-block), bipyramidal 2*b* sites (in R-block) and octahedral 2*a* sites in S-block (Table 1) [15]. The magnetic moments of the Fe ions in the 12*k*, 2*b* and 2*a* sites are parallel to the *c*-axis. The magnetic moments of the 4*f_{IV}* and 4*f_{VI}* sites are antiparallel to the *c*-axis. Thus, the unit cell of the M-phase contains 12*k* sites, 4*f_{IV}* sites, 4*f_{VI}* sites, 2*b* sites and 2*a* sites.

The stacking sequence of the W-type phase SrFe₁₈O₂₇ is SSRS*S*R*, the space group is *P6₃/mmc*. The unit cell (*z*=2) contains 4 Fe²⁺ and 32 Fe³⁺ cations in 12*k* sites (octahedral sites between R- and S-blocks, similar to the 12*k* sites in the M-type phase), 6*g* sites (octahedral sites between two S-blocks), 4*e* and 4*f_{IV}* (or 4*f₁*) tetrahedral sites (in the S-blocks), 4*f_{VI}* (or 4*f₂*) octahedral sites (in the R-blocks), 4*f_{VI}* (or 4*f₃*) octahedral sites (in the S-blocks) and 2*d* bipyramidal sites in R-block, similar to the 2*b* sites in the R-blocks of the M-type structure. The magnetic moments of the Fe ions in the 12*k*, 6*g*, 4*f_{VI}* (*f₃*) and 2*d* sites are parallel to the *c*-axis. The magnetic moments of the 4*e*, 4*f_{IV}* (*f₁*) and 4*f_{VI}* (*f₂*) sites are antiparallel to the *c*-axis [13,14].

The stacking sequence of the X-type ferrite Sr₂Fe₃₀O₄₆ is SRSRSS*S*S*R*S*. The rhombohedral unit cell (*z*=1) has space group *R-3m* and contains 11 Fe positions, it is however more conveniently described in hexagonal axes (Table 1) [13,7]. The crystal structure of the X-type phase can be interpreted as the superposition of the M and W structures [7]. The hexagonal unit cell (*z*=3) contains 6 Fe²⁺ and 84 Fe³⁺ in 18*h* and 18*h'* octahedral sites between R- and S-blocks respectively, 6*c_{IV}*, 6*c'_{IV}*, and 6*c''_{IV}* tetrahedral sites in S-blocks, 6*c'_{VI}* and 6*c''_{VI}* octahedral sites in R-blocks, 6*c_V* octahedral sites in R-blocks, and 3*b_{VI}*, 9*e_{VI}* and 6*c_{VI}* octahedral sites in S-blocks.

To simplify the discussion and comparison of the three hexagonal ferrites, Fe ion sublattices with similar magnetic characteristics were

categorized into five magnetic sublattices (*k*, *f_{IV}*, *f_{VI}*, *b*, *a*); a concept already proposed by Leccabue et al. [7]. This simplified description is displayed in Table 1; in this context, e.g., Fe ions on the 18*h* and 18*h'* positions of X-type are classified as sublattice *k*. According to the Gorter scheme, the magnetic moments of the Fe ions in the *k*, *a* and *b* sublattices are parallel to the *c*-axis, while the magnetic moments of the *f_{IV}* and *f_{VI}* are antiparallel [7]. The relations between Fe ions in different crystallographic sites and crystal structures are summarized in Table 1.

This contribution reports for the first time a detailed analysis of the hexagonal X-type Sr ferrite Sr₂Fe₂Fe₂₈O₄₆ (Sr₂Fe₂-X). Mössbauer and NMR spectroscopic studies and ab initio electronic structure calculations were performed in order to analyze the occupation of metal sites in the ferrite structures. We will compare the results obtained on the Sr₂Fe₂-X ferrite with those for the well-known hexagonal Sr ferrites with M-type (SrFe₁₂O₁₉) and W-type (SrFe₂Fe₁₆O₂₇) structure.

2. Methods

2.1. Sample preparation

All ferrite samples were prepared using the standard mixed-oxide route. After mixing SrCO₃ (Aldrich) and Fe₂O₃ (Thyssen-Krupp-Steel TKS-HP) in a polyethylene container with 2-propanol and zirconia beads (diameter 1 mm) for 3 h, the dried mixture was calcined at 1200 °C for 6 h. The samples were ground with a planetary mill (Pulverisette 5; Fritsch GmbH, Germany) for 8 h in a WC container with 2-propanol and WC grinding beads (3 mm diameter). The resulting powders exhibit a mean particle size of about 1 μm and specific surface of 1.2 m²/g. The powders were pressed into pellets 10 mm in diameter and sintered for 24 h at 1200 °C (M-type), 1370 °C (X-type), and 1400 °C (W-type) in air. Samples of X- and W-type ferrites were quenched in water.

2.2. Measurements

The samples were studied using powder X-ray diffraction (Siemens D5000 with CuKα radiation; step time 8 s; step size 0.02°; 10–70(140) °2θ). Lattice parameters were refined using the TOPAS R software

package (Bruker AXS, Karlsruhe, Germany). The microstructure of polished samples was monitored by Scanning Electron Microscopy SEM (DSM 940A, Zeiss, Germany). High-resolution Transmission Electron Microscopy (HRTEM) and selected area electron diffraction (SAED) were performed with a Philips CM20 Field Emission Gun TEM, operated at 200 kV. Prior to TEM inspection, samples were Ar ion-thinned in a Gatan Duomill ion at 4.5 kV and 1 mA.

The specific surface area of the powders A_s was determined by the BET method (Nova 2000, Quantachrome Instruments, Boynton Beach, U.S.A.). Thermal analysis (TG, DTA) was carried out with a SETARAM TGA92 system, the samples were heated in air to 1500 °C with a rate of 10 K/min. Magnetic properties were measured with a Quantum design MPMS SQUID magnetometer. Hysteresis loops were measured at 5 and 298 K. The saturation magnetization was estimated from M vs. $1/H$ plots and the $M(H)$ intercept was taken as M_s .

The Fe^{2+} -concentration was determined by chemical titration after dissolution of the powdered sample in hydrochloric acid under argon. The Fe^{2+} ions were titrated with potentiometric end point detection with a 0.05 N Ce^{4+} solution under a flow of argon. The detection limit of the titration is given by the first drop of Ce^{4+} solution ($V \approx 0.03$ ml) which corresponds to 0.08 wt% Fe^{2+} for 100 mg of a ferrite sample.

^{57}Fe Mössbauer spectrometry measurements were performed on powdered samples at room temperature in transmission geometry, using a ^{57}Co source in a rhodium matrix. The isomer shift δ (relative to metallic $\alpha\text{-Fe}$ at room temperature), quadrupolar shift ε and hyperfine field B are given with statistical errors from the MOSFIT fitting program [16].

^{57}Fe NMR spectra were recorded by spin-echo technique using a coherent pulse spectrometer Bruker Avance with data accumulation and Fourier transform (FT). All spectra were measured in zero external magnetic field at $T=4.2$ K. The radiofrequency pulse parameters were set in order to excite signal from nuclei in magnetic domains. The signal-to-noise ratio was improved by applying the Carr–Purcell–Meiboom–Gill (CPMG) multi-pulse excitation sequence where spin echoes, formed between the pulses in the sequence, were monitored and coherently summed. The nuclear spin–spin relaxation was slow enough to use first 10 spin echoes for spectra evaluations, the remaining echoes in the train were used to estimate the rate of spin–spin relaxation. To cover the required spectral range, excitation frequency was swept with steps of ~ 25 kHz and the spectra were evaluated as an envelope of FTs of signals at individual excitation frequencies.

2.3. Ab initio calculations

The electronic structures of Sr hexaferrites were calculated using the augmented plane waves+local orbital method based on the density functional theory as implemented in the WIEN2k program [17]. The calculations were started from experimental unit cells [18–20] and optimized by minimizing the atomic forces.

To improve the description of iron 3d electron correlations we used the rotationally invariant version of the LDA+U method as described by Liechtenstein et al. [21], with the PBE-GGA [22] instead of LSDA exchange–correlation potential and with a single parameter $U_{\text{eff}}=U-J$ only; the value of parameter $U_{\text{eff}}=4.5$ eV was adopted for 3d orbitals of Fe atoms. The number of the basic functions used was $\sim 90/\text{atom}$ ($RK_{\text{max}}=6.0$), and the number of k-points in irreducible part of Brillouin zone was 10. The charge density was Fourier expanded to $G_{\text{max}}=16 \text{ Ry}^{1/2}$.

The hyperfine fields were calculated using correction procedure as described in Novák et al. [23]. Atomic valences (in units of electron charge) and magnetic moments were determined using the Atoms in Molecules (AIM) method [24]. To obtain the valence states of irons the valence charges calculated from AIM were

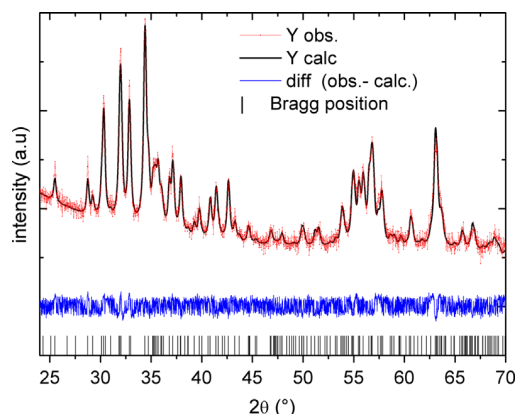


Fig. 1. X-ray diffraction pattern of X-type $\text{Sr}_2\text{Fe}_{30}\text{O}_{46}$ ferrite sintered at 1370 °C (measured, calculated, and difference data).

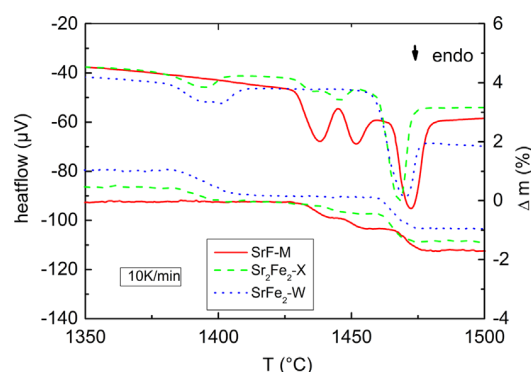


Fig. 2. DTA and TG curves of M-, X-, and W-type hexagonal Sr ferrites.

rescaled by such a factor (~ 1.6) that produces oxygen atoms with formal average valence -2 .

3. Results

3.1. Powder X-ray diffraction

The XRD patterns of the synthesized hexagonal ferrites confirm their single-phase character. X-type ferrite $\text{Sr}_2\text{Fe}_{30}\text{O}_{46}$ crystallizes within the rhombohedral crystal structure (SG: $R\bar{3}m$; $z=1$), commonly described in hexagonal axes ($z=3$). The XRD pattern (Fig. 1) was refined to give the lattice parameters $a_0=5.8940(5)$ Å and $c_0=83.808(8)$ Å. For M-type $\text{SrFe}_{12}\text{O}_{19}$ ferrite, all reflections were indexed within the magnetoplumbite-type structure (SG: $P6_3/mmc$; $z=2$). Unit cell dimensions were refined to $a_0=5.8847(2)$ Å and $c_0=23.0511(9)$ Å in good agreement with data from other studies [15,25]. The X-ray pattern of W-type $\text{SrFe}_{18}\text{O}_{27}$ was also refined within the space group $P6_3/mmc$ to unit cell parameters of $a_0=5.8969(5)$ Å and $c_0=32.799(3)$ Å ($z=2$). The single-phase character of all three samples was further confirmed by scanning electron microscopy [3].

3.2. Thermal stability and ferrous concentration

The thermal stability of the hexagonal ferrites was monitored using thermal analysis; details are reported in Ref. [3]. The TG curve of the $\text{SrFe}_{12}\text{O}_{19}$ shows a constant mass until at $T > 1350$ °C a series of mass losses accompanied by three endothermic DTA peaks signal a step-wise phase transformation sequence (Fig. 2). At $T=1418$ °C incongruent melting of $\text{SrFe}_{12}\text{O}_{19}$ and simultaneous formation of X-type ferrite occurs. At $T_{\text{on}}=1435$ °C melting of the $\text{Sr}_2\text{Fe}_2\text{-X}$ and formation of $\text{SrFe}_2\text{-W}$ set in and a third peak at $T_{\text{on}}=1452$ °C finally

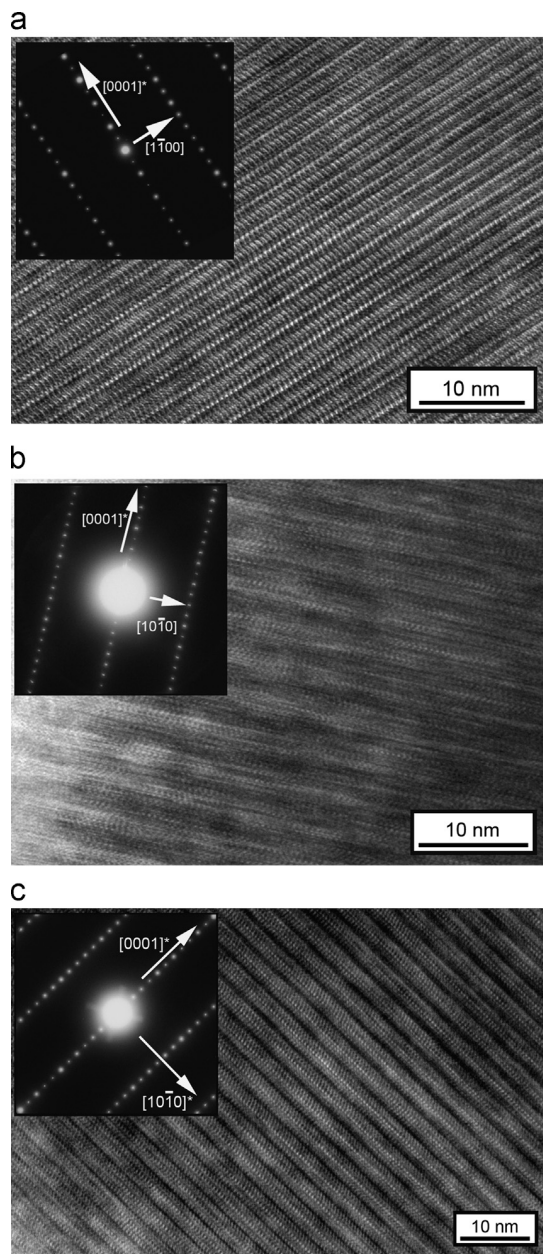


Fig. 3. HRTEM micrographs and SAED electron diffraction patterns of (a) M-type $\text{SrFe}_{12}\text{O}_{19}$, SAED along $[1\bar{1}-20]$ zone axis; (b) W-type $\text{SrFe}_{18}\text{O}_{27}$, SAED along $[0\bar{1}-10]$ zone axis, and (c) X-type $\text{Sr}_2\text{Fe}_{30}\text{O}_{46}$, SAED along $[0\bar{1}-10]$ zone axis.

signals the decomposition of W-type ferrite. The TG curves of both, W- and X-hexagonal ferrites exhibit a slow mass gain during heating (not shown here) as footprint of their thermodynamic instability at low temperature (decomposition into a mixture of M-type ferrite and magnetite [3]). In both cases, an endothermic DTA peak with onset at 1365°C and a corresponding mass loss indicates the re-formation of the hexagonal W- and X-type ferrites (Fig. 2). On further heating, two endothermic DTA peaks are observed for $\text{Sr}_2\text{Fe}_2\text{-X}$; one at $T_{\text{on}}=1423^\circ\text{C}$ signaling the incongruent melting of the X-type and W-type ferrite formation, and another one at $T_{\text{on}}=1443^\circ\text{C}$ for the incongruent melting of W-type ferrite. Accordingly, a two-step mass loss process is observed at $T > 1400^\circ\text{C}$. For $\text{SrFe}_{18}\text{O}_{27}$ (W-type) only one DTA peak with $T_{\text{on}}=1447^\circ\text{C}$ and one mass loss is observed indicating the incongruent melting of $\text{SrFe}_2\text{-W}$ and transformation into magnetite and liquid. In contrast to Sr-M which is stable from room temperature to 1418°C in air, $\text{Sr}_2\text{Fe}_2\text{-X}$ and $\text{SrFe}_2\text{-W}$ hexagonal

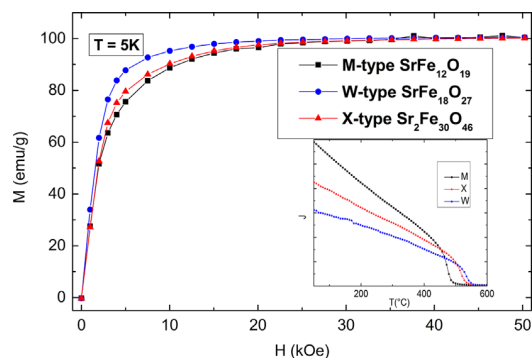


Fig. 4. Magnetization vs. field curves of M-, X-, and W-type hexagonal Sr ferrites (inset: M vs. T).

ferrites exhibit small stability ranges at high temperature only, i.e. approximately from 1365°C to 1425°C for X-type and from 1365°C to 1450°C for W-type ferrite.

The Fe^{2+} concentrations of the W- and X-type ferrites were determined by redox titration. For the X-type ferrite $\text{Sr}_2\text{Fe}_2^{2+}\text{Fe}_{38}^{3+}\text{O}_{46}$ (theoretical 4.32%) the Fe^{2+} -content was measured to be $3.42 \pm 0.02\text{ wt\%}$, whereas for W-type $\text{SrFe}_2^{2+}\text{Fe}_{16}^{3+}\text{O}_{27}$ a Fe^{2+} -concentration of $6.06 \pm 0.05\text{ wt\%}$ was found (theoretical: 7.32%). These data confirm a significant ferrous ion concentration in both ferrites; however, titration results differ somewhat from expectation possibly due to practical difficulties in dissolving the samples under protective atmospheres or due to substoichiometric Fe^{2+} -concentrations.

3.3. HRTEM

A high-resolution TEM image of the M-type ferrite $\text{SrFe}_{12}\text{O}_{19}$ is shown in Fig. 3a. The regular lattice repeats show that the sample is well crystallized with a periodicity of 23.05 \AA in the c -direction without any lattice defects or other stacking variants. Electron diffraction along the $[11\bar{2}0]$ zone-axis shows diffraction spots (Fig. 3a, inset) in agreement with space group $P6_3/mmc$ typical of the M-type structure. For $\text{SrFe}_{18}\text{O}_{27}$ (W-type) the HRTEM micrograph (Fig. 3b) displays a lattice periodicity in the c -direction of 32.8 \AA resembling two MS blocks alternating by a 180° rotation. A HRTEM image of the newly synthesized X-type $\text{Sr}_2\text{Fe}_{30}\text{O}_{46}$ ferrite (Fig. 3c) demonstrates the regular lattice; one block in the c -direction corresponds to a M_2S unit. The unit cell has three M_2S blocks in the c -direction and amounts to 83.81 \AA which is in good agreement to XRD data. All observed electron diffraction spots are in agreement with space group $R\bar{3}m$.

3.4. Magnetic properties

The M vs. H curves at 5 K for the three hexagonal Sr ferrites are shown in Fig. 4. The magnetization of all samples is almost saturated at $20\text{--}40\text{ kOe}$. Slight differences between the magnetization behavior of the three ferrites are present: Sr-M ferrite becomes saturated at relatively high fields, whereas for the W-type smaller fields are sufficient for complete saturation. This can be understood as a signature of the large magneto-crystalline anisotropy of $\text{SrFe}_{12}\text{O}_{19}$ ferrite at 5 K . The saturation magnetizations at $T=5\text{ K}$ of the samples were deduced from M vs. $1/H$ plots and the values of M_s for M-, X- and W-type hexagonal ferrites are $101.9(5)\text{ emu/g}$, $101.5(5)\text{ emu/g}$, and $101.4(5)\text{ emu/g}$, respectively. The $M(T)$ curves of all three samples are displayed in the inset of Fig. 4. The Curie temperature of the M-type Sr ferrite is found at $T_c=475^\circ\text{C}$ in good agreement with Refs. [8,15]. The T_c of $\text{SrFe}_2\text{-W}$ and $\text{Sr}_2\text{Fe}_2\text{-X}$ ferrites is at 550°C and 530°C , respectively, which are somewhat larger compared to results reported by Dey et al. [8].

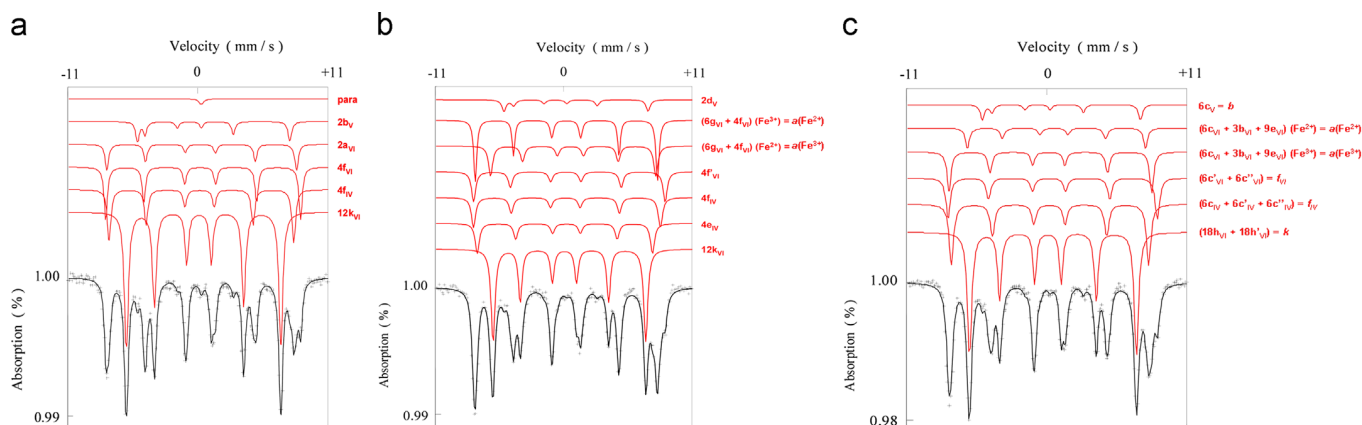


Fig. 5. Room-temperature Mössbauer spectra of (a) M-type $\text{SrFe}_{12}\text{O}_{19}$, (b) W-type $\text{SrFe}_{18}\text{O}_{27}$, and (c) X-type $\text{Sr}_2\text{Fe}_{30}\text{O}_{46}$; (the different Fe contributions used to fit the spectra are displayed).

3.5. Mössbauer spectroscopy

The room-temperature Mössbauer spectra of the three samples are shown in Fig. 5a–c. In agreement with the crystal structures, the Mössbauer spectrum of $\text{SrFe}_{12}\text{O}_{19}$ (Fig. 5a) is fitted with five components, that correspond to the five different sites of the M-type crystal structure, i.e. the 12k, 4f_{IV}, 4f_{VI}, 2a and 2b sites. Preliminary fittings revealed that the relative intensities deviate from the crystallographic occupancy, and the proportions 12:4:4:2:1.5 for the 12k, 4f_{IV}, 4f_{VI}, 2a and 2b sites, respectively, were used. Such a deviation is generally observed in the M-type hexaferrites, and can be attributed to the pronounced anisotropy of the 2b site coordination which leads to an anisotropic f-factor, considerably lower along the hexagonal axis. In the spectrum of the M-type phase, one paramagnetic contribution has been fitted to account for extra absorption at the center of the spectrum. This contribution, whose relative intensity is less than 1%, is attributed to Fe atoms in paramagnetic Sr–Fe–O impurities.

According to their nominal compositions, W-type and X-type ferrites contain two Fe^{2+} ions per formula unit. It is well established that in the M-type $\text{LaFe}_{12}\text{O}_{19}$ phase, the complete substitution of Sr^{2+} for La^{3+} leads to a change of the valence state of iron ions in the 2a site from Fe^{3+} to Fe^{2+} due to the introduction of La^{3+} ion instead of Sr^{2+} ion to compensate for the excess of positive charges [26–28]; analogous conclusions arise from the analysis of NMR measurements in M-type hexaferrites with partial or full substitution of La^{3+} in the heavy cations sites [29]. Fe^{2+} ions being thus located in the 2a octahedral sites of the S-blocks in the M-type ferrite, we assumed by comparing the crystal structure of the three phases, that the Fe^{2+} ions occupy four magnetic a sites corresponding to the 4f_{VI} (or 4f₃) and 6g octahedral sites in the SS and S–S blocks of the W unit cell and six magnetic a sites corresponding to the 3b_{VI}, 9e_{VI} and 6c_{VI} octahedral sites in the S-, S–S- and SS-blocks of the X-unit cell, respectively.

In agreement with the literature [30,31], the spectrum of the W-type ferrite $\text{SrFe}_2\text{Fe}_{16}\text{O}_{27}$ (Fig. 5b) was fitted with seven contributions with proportions 12:6:4:4:4:4:1.5 corresponding to the 12k, 6a(Fe^{3+}), 4e, 4f_{IV}, 4f_{VI}, 4a(Fe^{2+}) and 2d sites, respectively, where a denotes both 6g and 4f_{VI} sites. The split of a sublattices into a(Fe^{3+}), and a(Fe^{2+}) was chosen with relative proportions corresponding to the occupation of four of the ten magnetic a sites (corresponding to the 6g and 4f_{VI} octahedral sites) by Fe^{2+} ions, the six other magnetic a sites being occupied by Fe^{3+} ions. It has to be mentioned that Van Diepen and Lotgering concluded from their Mössbauer data that ferrous ions reside on 6g sites [30]. However, they attributed the whole 6g contribution to Fe^{2+} ions, thus overestimating the Fe^{2+} amount in the W-unit cell that can

contain at most 4 Fe^{2+} ions, not 6. Our assumption is in agreement with a previous investigation of the localization of Fe^{2+} ions in the BaFe_2W hexaferrite by NMR, which concluded on the possible presence of Fe^{2+} ions on both 4f_{VI} and 6g octahedral sites [32].

According to the concept that the X-type can be understood as mixture of M- and W-type structural elements it follows that combining the numbers of 24 and 36 Fe ions in the M- and W-type unit cells, respectively, one obtains $(24 + 36)/2 = 30$ Fe ions for one third of the X-type hexagonal unit cell. In agreement with Leccabue et al. [7], we considered the five magnetic sublattices to fit the Mössbauer spectrum of the X-phase. However, we considered only one contribution for the magnetic k sublattice. The spectrum of the X-phase $\text{Sr}_2\text{Fe}_2\text{Fe}_{28}\text{O}_{46}$ (Fig. 5c) was thus fitted with six contributions: five contributions from Fe^{3+} ions (one for each magnetic sublattice) and one contribution for Fe^{2+} ions, on the magnetic a site. The proportions 12:6:4:4:2:1.5 were used for the magnetic sublattices k, f_{IV}, f_{VI}, a(Fe^{3+}), a(Fe^{2+}) and b, respectively. The split of a sublattices into a(Fe^{3+}) and a(Fe^{2+}) was chosen with relative proportions corresponding to the occupation of six of the eighteen magnetic a sites (corresponding to the 3b_{VI}, 9e_{VI} and 6c_{VI} octahedral sites) by Fe^{2+} ions, the twelve other magnetic a sites being occupied by Fe^{3+} ions. The detailed fitted Mössbauer spectra of the M-, X- and W-phases are shown in Fig. 5a–c, respectively. The fitted hyperfine parameters are reported in Table 2.

3.6. NMR spectroscopy

The ^{57}Fe NMR spectra of Sr-M, SrFe_2W and $\text{Sr}_2\text{Fe}_2\text{X}$ ferrites recorded at 4.2 K are shown in Fig. 6. Five narrow and well separated resonance lines are observed for M-type and assigned to the five different Fe^{3+} positions. The spectra of W- and X-type are more complex; however, the spectral lines are quite narrow, which indicates high quality of the powder samples. A brief survey shows that spectrum of $\text{Sr}_2\text{Fe}_2\text{X}$ corresponds approximately to a superposition of M- and W-type hexagonal ferrite spectra.

3.7. Ab initio calculations

The calculated valences and magnetic moments of Fe atoms displayed in Table 3 allow us to estimate the distribution of Fe^{2+} and Fe^{3+} in the studied structures. Magnetic moment $\sim 4 \mu_B$ corresponds to Fe^{3+} while somewhat lowered values indicate the presence of Fe^{2+} . One should note that the theoretical value of $5 \mu_B$ corresponding to free Fe^{3+} ions is reduced in a crystal environment, as part of the magnetic moment is transferred to neighboring oxygen ions.

The magnetic field 'calc B' (in Table 3) was obtained as a sum of the contact (Fermi), orbital and dipolar contributions to the

Table 2

Mössbauer hyperfine parameters of (a) M-type $\text{SrFe}_{12}\text{O}_{19}$, (b) W-type $\text{SrFe}_{18}\text{O}_{27}$, and (c) X-type $\text{Sr}_2\text{Fe}_{30}\text{O}_{46}$ from experiment and calculations. The 2ϵ values were obtained from calculated V_{zz} and η (see Table 3) as $2\epsilon = \Delta$, $\Delta = \frac{eQV_{zz}}{2I_0} \left(1 + \frac{1}{3}\eta^2\right)^{1/2}$.

Site, coordination	Experiment				Calculation	
	B (T)	δ (mm/s)	2ϵ (mm/s)	Relative intensity (fixed)	2ϵ (mm/s)	
Sr-M						
$12k_{VI}$	41.5 ± 0.1	0.35 ± 0.01	0.40 ± 0.01	12	0.40	
$4f_{IV}$	49.5 ± 0.1	0.28 ± 0.02	0.16 ± 0.04	4	0.14	
$4f_{VI}$	52.3 ± 0.1	0.38 ± 0.02	0.25 ± 0.04	4	0.27	
$2b_V$	40.9 ± 0.3	0.36 ± 0.04	2.12 ± 0.09	1.5	1.96	
$2a_{VI}$	50.8 ± 0.3	0.32 ± 0.04	0.10 ± 0.08	2	−0.05	
SrFe₂W						
$12k_{VI}$	41.5 ± 0.1	0.36 ± 0.01	0.44 ± 0.02	12	0.44	
$4e_{IV}$	47.7 ± 0.2	0.25 ± 0.04	-0.14 ± 0.08	4	−0.30	
$4f_{IV}$	50.9 ± 1.0	0.29 ± 0.12	0.14 ± 0.18	4	0.52	
$4f_{VI}$	52.1 ± 1.0	0.41 ± 0.12	0.31 ± 0.16	4	0.27	
$2d_V$	39.2 ± 0.8	0.25 ± 0.10	1.81 ± 0.20	1.5	2.00	
$6g_{VI}$, $4f_{VI}$ (Fe ³⁺)	49.6 ± 0.1	0.30 ± 0.02	0.01 ± 0.04	6	0.60	
$6g_{VI}$, $4f_{VI}$ (Fe ²⁺)	45.0 ± 0.4	0.79 ± 0.04	0.25 ± 0.08	4	−1.31	
Sr₂Fe₂X						
Site, coordination	Simplified magnetic sublattice	Experiment				Calculation
		B (T)	δ (mm/s)	2ϵ (mm/s)	Relative intensity (fixed)	2ϵ (mm/s)
$18h_{VI}$ $18h'_{VI}$	k	41.6 ± 0.1	0.36 ± 0.01	0.41 ± 0.02	12	0.40 0.40
$6c_{IV}$ $6c'_{IV}$ $6c''_{IV}$	f_{IV}	49.3 ± 0.1	0.30 ± 0.02	0.04 ± 0.04	6	0.10 −0.06 −0.11
$6c'_{VI}$ $6c''_{VI}$	f_{VI}	52.2 ± 0.2	0.39 ± 0.03	0.29 ± 0.06	4	0.31 0.31
$6c_V$	b	39.4 ± 0.4	0.27 ± 0.06	1.91 ± 0.12	1.5	1.99
$3b_{VI}$ $9e_{VI}$ $6c_{VI}$ (Fe ²⁺)	$a(\text{Fe}^{3+})$ $a(\text{Fe}^{2+})$	50.6 ± 0.2 44.4 ± 0.3	0.29 ± 0.03 0.74 ± 0.05	0.13 ± 0.06 0.20 ± 0.10	4 2	−0.02 1.74 0.07

hyperfine magnetic field and also the dipolar field of surrounding atomic moments. It is directly comparable to observed local magnetic fields in NMR experiment, and thus can help with interpretation of NMR spectra. Besides the magnetic fields we also present calculated parameters of EFG tensors that are compared to Mössbauer parameter 2ϵ (Table 2).

4. Discussion

The synthesis of a single-phase $\text{Sr}_2\text{Fe}_2\text{-X}$ hexagonal ferrite is reported here for the first time and revealed by XRD (Fig. 1) and HRTEM measurements (Fig. 3). Thermal analysis (Fig. 2) has shown that X-type Sr-ferrite is stable in a small temperature range only (1365–1425 °C). For discussion, the magnetic and spectroscopic properties of the $\text{Sr}_2\text{Fe}_2\text{-X}$ ferrite are compared to Sr-M and $\text{SrFe}_2\text{-W}$ type hexagonal ferrites.

The saturation magnetization of the samples can be estimated following the collinear Gorter model. Assuming the orientation of the magnetic moments of the ferric ions in M-type $\text{SrFe}_{12}\text{O}_{19}$ (Sr-M) as reported above (see Table 1), a magnetic moment of $20 \mu_B$ ($M_s = 105 \text{ emu/g}$) is expected at low temperature. The measured value of 101.9 emu/g is somewhat smaller which might be explained by a small fraction of an impurity phase as detected by Mössbauer spectroscopy. For the W- and X-type ferrites the formation of ferrous ions has to be taken into account, resulting in Fe mixed valency, i.e.: $\text{SrFe}_2^{2+}\text{Fe}_{16}^{3+}\text{O}_{27}$ ($\text{SrFe}_2\text{-W}$) and $\text{Sr}_2\text{Fe}_2^{2+}\text{Fe}_{28}^{3+}\text{O}_{46}$ ($\text{Sr}_2\text{Fe}_2\text{-X}$). This was

confirmed by chemical titrations. It has been concluded from spectroscopic studies that in La-substituted M-type ferrites Fe^{2+} ions are formed for charge compensation which tend to occupy octahedral $2a$ positions [26–28]. If it is assumed that the ferrous ions in the W- and X-type ferrites also favor to occupy these octahedral sites in the S-blocks (spin-up magnetic sublattice a), then a magnetic net moment of $28 \mu_B$ (corresponding to a saturation magnetization of $M_s = 102.5 \text{ emu/g}$) and $\mu = 48 \mu_B$ ($M_s = 103.6 \text{ emu/g}$), respectively, is expected using the collinear Gorter model. If the Fe^{2+} ions would be positioned on spin-down sites, larger magnetic moments of $32 \mu_B$ and $52 \mu_B$ would be expected for $\text{SrFe}_2\text{-W}$ and $\text{Sr}_2\text{Fe}_2\text{-X}$, respectively. The measured data of $M_s = 101.4 \text{ emu/g}$ (equivalent to $27.7 \mu_B$) for $\text{SrFe}_2\text{-W}$ and of $M_s = 101.5 \text{ emu/g}$ (equivalent to $47.0 \mu_B$) for $\text{Sr}_2\text{Fe}_2\text{-X}$ strongly support the assumption that the Fe^{2+} ions with $S=2$ occupy spin-up sites in the a magnetic sublattices. Our data very well agree with $M_s = 27.9 \mu_B$ for SrFe_2W reported by Lotgering et al. [10] and with a $M_s = 100 \text{ emu/g}$ for $\text{Sr}_2\text{Fe}_2\text{X}$ reported in Ref. [8].

According to the Mössbauer analysis of the $\text{SrFe}_{12}\text{O}_{19}$ M-type phase, the isomer shifts (Table 2) indicate that all Fe ions are in the Fe^{3+} state. The fitted hyperfine parameters are in very good agreement with the literature [33]. Also excellent agreement of EFG parameters with our calculations was reached (Table 2). The room temperature Mössbauer parameter 2ϵ can be compared to calculations corresponding to 0 K, since EFG parameters are only weakly dependent on temperature. On the other hand, the hyperfine magnetic fields decrease non-uniformly with increasing temperature, and therefore, cannot be simply compared.

The analysis of the Mössbauer spectrum of the $\text{SrFe}_{12}\text{O}_{19}$ W-type ferrite yields fitted hyperfine fields which are in fair agreement with the values reported in Ref. [30]. Experimental and calculated EFG parameters agree well for the sites in R blocks ($2d$, $4f_{VI}$) and $12k$, while the agreement for sites in S block is

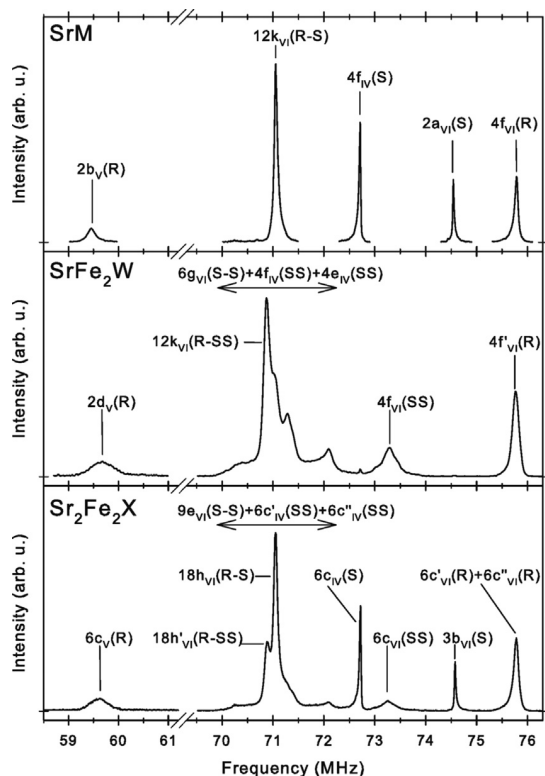


Fig. 6. ^{57}Fe NMR spectra of M-type $\text{SrFe}_{12}\text{O}_{19}$, W-type $\text{SrFe}_{18}\text{O}_{27}$, and X-type $\text{Sr}_2\text{Fe}_{30}\text{O}_{46}$; measured at 4.2 K in zero magnetic field.

worse, mainly due to different approach: the Mössbauer experiment resolves the Fe^{2+} and Fe^{3+} contributions separately, while calculations give averaged results for the whole site (Table 2).

In the Mössbauer spectrum of the $\text{Sr}_2\text{Fe}_{28}^{2+}\text{Fe}_{16}^{3+}\text{O}_{46}$ X-type ferrite (Fig. 5c), the sextet assigned to the $a(\text{Fe}^{2+})$ sublattice exhibits an isomer shift of 0.74 mm/s which implies that the ferrous ions are located in one of the three possible Wyckoff sites ($3b_{VI}$, $9e_{VI}$, and $6c_{VI}$) grouped together in this simplified sublattice a ; however, detailed assignment is not possible. Some years ago, Leccabue et al. [7] reported Mössbauer data on the Zn-substituted X-type ferrite ($\text{Sr}_2\text{Zn}_2\text{-X}$), which has no Fe^{2+} ions. The room-temperature spectrum was assigned to six subspectra, i.e. the k , f_{IV} , f_{VI} , b and a sublattices; two distinct sextets for Fe^{3+} in the k magnetic sublattice were detected (k_1 , k_2). Our study of the $\text{Sr}_2\text{Fe}_2\text{-X}$ material has revealed the location of ferrous ions and supports the general interpretation of Ref. [7]; however, two different k sextets were not observed. Very probably, the fact that Leccabue et al. distinguished two sextets for the k contribution has to be related to the presence of nonmagnetic Zn^{2+} ions located in tetrahedral sites close to k sites, thus leading to a distribution of environments around k sites, as observed for the M-phase [34].

Table 2 shows good agreement between the calculated and experimental EFG parameters with exception of the sites $3b_{VI}$, $9e_{VI}$, and $6c_{VI}$ which cannot be compared directly because the Mössbauer spectra were decomposed into two contributions with: $a(\text{Fe}^{2+})$ and $a(\text{Fe}^{3+})$ with ratio 2:4.

In the ^{57}Fe NMR spectrum of M-type hexaferrite $\text{SrFe}_{12}\text{O}_{19}$ five narrow and well separated resonance lines are observed (Fig. 6). According to previous works [35,36] they are assigned to the five Fe^{3+} sites $2a$, $2b$, $4f_{IV}$, $4f_{VI}$ and $12k$. The integral intensities of the spectral lines in the interval 69–76 MHz are proportional to the nominal occupancy of the crystal sites with precision better than 8%. As the interpretation is well known, the ^{57}Fe NMR spectrum of the M-type hexaferrite was used to estimate the accuracy of our ab initio calculations. The calculated hyperfine fields agree well with the NMR experiment: the succession of hf field values of individual lines is the same, the hyperfine fields match the experiment with standard deviation $\sigma \sim 1$ T and the calculated formal valences are close

Table 3

Results of ab initio calculations (formal AIM valences, ionic magnetic moments, hyperfine fields B, EFG tensor components V_{zz} and asymmetry parameters η) for iron sites and experimental values of hyperfine fields B from NMR spectroscopy. Signs of the ionic magnetic moments indicate their orientation.

Site, coordination	Block	Formal AIM valence	Magnetic moment (μ_B)	Calc B (T)	Exp B (T)	V_{zz} (10^{21} V m $^{-2}$)	η
SrM							
$12k_{VI}$	R-S	2.96	4.20	50.63	51.426	2.24	0.68
$4f_{IV}$	S	2.88	−4.11	54.18	52.626	0.85	0
$4f_{VI}$	R	3.01	−4.14	55.89	54.855	1.59	0
$2b_V$	R	2.86	4.12	43.66	43.029	11.8	0
$2a_{VI}$	S	2.99	4.20	53.51	52.025	−0.28	0
SrFe₂W							
$12k_{VI}$	R-SS	2.94	4.20	50.99	51.30	2.48	0.64
$4e_{IV}$	SS	2.86	−4.10	52.12	50.67–52.48	−1.78	0
$4f_{IV}$	SS	2.85	−4.10	50.68	50.67–52.48	3.14	0
$4f_{VI}$	R	2.99	−4.14	56.07	54.84	1.65	0
$2d_V$	R	2.85	4.11	43.56	43.20	12.01	0
$6g_{VI}$	S-S	2.79	4.10	46.53	50.67–52.48	3.25	0.81
$4f_{VI}$	SS	2.55	3.87	57.13	53.05	−7.89	0
Sr₂Fe₂X							
$18h_{VI}$	R-S	2.95	4.25	49.92	52.64	2.25	0.640
$18h'_{VI}$	R-SS	2.94	4.24	49.86	51.31	2.26	0.619
$6c_{IV}$	S	2.89	−4.16	53.68	51.43	0.63	0
$6c'_{IV}$	SS	2.87	−4.16	52.85	50.67–52.49	−0.38	0
$6c''_{IV}$	SS	2.88	−4.16	53.93	50.67–52.49	−0.66	0
$6c'_{VI}$	R	3.00	−4.19	55.07	54.86	1.87	0
$6c''_{VI}$	R	3.00	−4.19	55.07	54.86	1.86	0
$6c_V$	R	2.87	4.16	43.14	43.15	11.98	0
$3b_{VI}$	S	2.97	4.24	53.53	53.98	−0.10	0
$9e_{VI}$	S-S	2.53	3.91	33.71	50.67–52.48	10.47	0.004
$6c_{VI}$	SS	2.94	4.23	52.72	53.02	0.43	0

to 3+ for all iron sites; the magnetic moments are within the range 4.0–4.1 μ_B .

Analysis of the ^{57}Fe NMR spectrum of the $\text{SrFe}_2\text{-W}$ ferrite (Fig. 6) was performed taking into account integral intensities of the spectral lines, detailed site symmetry, similarity of nearest neighborhood with M-type ferrite and by analogy with the NMR spectrum of Ba W-type ferrite [32] – the lines were assigned as shown in Fig. 6. Small traces of $4f_{IV}$ and $2a$ lines of M-type structure were also detected, which corresponds to concentration of stacking faults less than 1.5%.

Regarding the presence of Fe^{2+} in the W-type ferrite, the NMR signal from nuclei in Fe^{2+} is shifted to lower frequencies and is not detected (probably due to fast spin–spin relaxations and large linewidth). Since the number of resonating nuclei is proportional to the integral intensity of corresponding spectral line, we analysed the integral intensities in the spectral range 69–76 MHz to evaluate the Fe^{2+} preferences. We estimated that $\sim 0.9 \text{ Fe}^{2+}$ occupies $4f_{VI}$ sites. The band in the range 70.0–72.5 MHz composed of overlapped Fe^{3+} resonance lines 12k, 6g, 4e, and $4f_{IV}$ has lowered the integral intensity. Therefore, the remaining $\sim 3.1 \text{ Fe}^{2+}$ occupy one or more of the sites 12k, 6g, 4e, or $4f_{IV}$; however the detailed distribution of Fe^{2+} among them cannot be evaluated. These results are consistent with the situation in BaFe_2W where from NMR measurements of single crystal in external magnetic field the distribution of Fe^{2+} was found as approximately 1.3 Fe^{2+} in $4f_{VI}$ and about 2.7 Fe^{2+} in 6g [32]. Besides, these results are in accordance with Pauling valence rules as applied in [32].

In the calculations, the cations Fe^{2+} can be distinguished from Fe^{3+} by lower magnetic moment and/or large dipolar and orbital contributions to hyperfine field. In the W-type hexaferrite that is the case of Fe in $4f_{VI}$ with magnetic moment of 3.87 μ_B and dipolar hf field 6 T, and Fe in $6g_{VI}$ with magnetic moment of 4.10 μ_B and orbital hf field 7.8 T. The Fe^{2+} localization into these two sites is also supported by formal valences obtained from AIM. The differences between the calculated parameters of sites with Fe^{2+} ($4f_{VI}$ and $6g_{VI}$) and parameters of the other sites in SrFe_2W are subtle. This is due to the $4f_{VI}$ and $6g_{VI}$ sites being only partially occupied by Fe^{2+} , which cannot be considered in the calculations performed for a given space symmetry group. When these two sites with Fe^{2+} are omitted from comparison, the calculated hyperfine fields agree well with the NMR experiment with standard deviation $\sigma \sim 0.7$ T.

An analogous approach was applied for the interpretation of the NMR spectrum of the $\text{Sr}_2\text{Fe}_2\text{-X}$ ferrite. Due to high complexity of X-type structure the assignment relied on the calculations and on comparison of local symmetries of sites in X-type structure with respect to M- and W-types. The line assignment is displayed in Fig. 6.

We again analysed the integral intensities in the spectral range 69–76 MHz and found that similarly to $\text{SrFe}_2\text{-W}$ case approximately 25% Fe^{2+} occupies $6c_{VI}$ sites and the remaining 75% reduces the intensity of band of lines 18h, 18h', $9e_{VI}$, $6c'_{IV}$, and $6c''_{IV}$. The calculations yielded a strong preference for $9e_{VI}$ with magnetic moment of 3.91 μ_B and large (~ 16 T) orbital and dipolar contributions to hyperfine field compared to all other Fe atoms (~ 1 T); the formal valence of $9e_{VI}$ is 2.53 also indicating Fe^{2+} . Excluding the $9e_{VI}$ site from comparison, the agreement of calculated hyperfine fields with NMR experiment is good ($\sigma \sim 1.3$ T).

5. Conclusions

Hexagonal X-type Sr-ferrite was prepared as single-phase material and thoroughly characterized and discussed in relation to the hexagonal Sr-M and $\text{SrFe}_2\text{-W}$ ferrites as follows:

- (i) $\text{Sr}_2\text{Fe}_2\text{-X}$ ferrite is stable at high temperature between 1365 and 1425 °C only. Since the material is metastable at room

temperature it needs to be quenched from the high-temperature stability window.

- (ii) XRD and HR-TEM confirm a structural building motif with a unit cell length in the *c*-direction of 83.81 Å.
- (iii) Magnetization measurements indicate that the Fe^{2+} ions are located on spin-up sites.
- (iv) The room-temperature Mössbauer spectrum was decomposed into six subspectra and the location of ferrous ions was assigned to the magnetic *a* spin-up sublattice.
- (v) ^{57}Fe NMR revealed a complex spectrum which was interpreted by comparison with spectra of M- and W-type spectra and on the basis of ab initio calculations of electronic structure. Ferrous ions are preferentially located in spin-up $9e_{VI}$ sites and partially also in $6c_{VI}$ (both located in the magnetic *a* sublattice in the S blocks of the X- and W-type ferrites.)

Based on results of magnetic moment measurements, Mössbauer spectroscopy, ^{57}Fe NMR, and ab initio calculations it can thus be concluded that the Fe^{2+} ions in W- and X-type are located in spin up octahedral sites within the pair of two S blocks (between two S blocks or inside S block in SS stacking).

Acknowledgments

This work was supported by a Grant (To165-3-2) from the Deutsche Forschungsgemeinschaft (DFG), Germany. V.Ch. acknowledges support by the Project P204-12-P352 of the Grant Agency of the Czech Republic. K.K. and V.Ch. thank the support of UNCE 204023/2014.

References

- [1] P. Batti, *Ceramurgia* 6 (1976) 11–16.
- [2] Y. Goto, K. Takahashi, *J. Jpn. Soc. Powder Metall.* 17 (1971) 193–197.
- [3] N. Langhof, D. Seifert, M. Goebbels, J. Töpfer, *J. Solid State Chem.* 182 (2009) 2409–2416.
- [4] H.J. Van Hook, *J. Am. Ceram. Soc.* 47 (1964) 579–581.
- [5] B. Gu, H.X. Huai, Y.W. Du, *J. Magn. Magn. Mater.* 31–34 (1983) 803–804.
- [6] B.X. Gu, *J. Appl. Phys.* 71 (1992) 5103–5106.
- [7] F. Leccabue, G. Albanese, O. Ares Muzio, *J. Appl. Phys.* 61 (1987) 2600–2605.
- [8] S. Dey, R. Valenzuela, *J. Appl. Phys.* 55 (1984) 2340–2342.
- [9] P. Hernandez-Gomez, P.G. Bercoff, O. Alejos, C. Torres, J.M. Munoz, C. DeFrancesco, J.I. Iniguez, H.R. Bertorello, *Physica B* 320 (2002) 267–269.
- [10] F.K. Lotgering, P.R. Locher, R.P. van Staple, *J. Phys. Chem. Solids* 41 (1980) 481–487.
- [11] H. Kojima, C. Miyakawa, T. Sato, *Jpn. J. Appl. Phys.* 24 (1985) 51–56.
- [12] V. Adelsjöld, *Ark. Kemi. Min. Geol.* 12 (a) (1938) 1–9.
- [13] P.B. Braun, *Philips Res. Rep.* 12 (1957) 491–548.
- [14] M. Sugimoto, *Ferromagnetic Materials*, in: E.P. Wohlfahrt (Ed.), North-Holland Publ., 1982, pp. 393–439.
- [15] H. Kojima, *Ferromagnetic Materials*, in: E.P. Wohlfahrt (Ed.), North-Holland Publ., Amsterdam, 1982, pp. 305–391.
- [16] F. Varret, J. Teillet, Unpublished MOSFIT Program, 1983.
- [17] P. Blaha, K.-H. Schwarz, G.K.H. Madsen, D. Kvasnicka, J. Luitz, WIEN2k, an augmented plane wave+local orbitals program for calculating crystal properties, In: K.-H. Schwarz, Technische Universität, Wien, Austria, 2001, ISBN 3-9501031-1-2.
- [18] J. Muller, A. Collomb, *J. Magn. Magn. Mater.* 103 (1992) 194–203.
- [19] A. Collomb, P. Wolfers, X. Obradors, *J. Magn. Magn. Mater.* 62 (1986) 57–67.
- [20] F. Leccabue, R. Panizzieri, G. Bocelli, G. Calestani, C. Rizzoli, *J. Magn. Magn. Mater.* 68 (1987) 365–373.
- [21] A.I. Liechtenstein, V.I. Anisimov, J. Zaanen, *Phys. Rev. B* 52 (1995) R5467–R5471.
- [22] J.P. Perdew, K. Burke, M. Ernzerhof, *Phys. Rev. Lett.* 77 (1996) 3865–3868.
- [23] P. Novák, V. Chlan, *Phys. Rev. B* 81 (2010) 174412.
- [24] R.F.W. Bader, *Atoms in Molecules: A Quantum Theory*, Oxford University Press, 1990.
- [25] X. Obradors, X. Solans, A. Collomb, D. Samaras, J. Rodriguez, M. Pernet, M. Font-Alaba, *J. Solid State Chem.* 72 (1988) 218–224.
- [26] F.K. Lotgering, *J. Phys. Chem. Solids* 35 (1974) 1633–1639.
- [27] C. Sauer, U. Köbler, W. Zinn, H. Stäblein, *J. Phys. Chem. Solids* 39 (1978) 1197–1201.
- [28] D. Seifert, J. Töpfer, F. Langenhorst, J.-M. Le Breton, H. Chiron, L. Lechevallier, *J. Magn. Magn. Mater.* 321 (2009) 4045–4051.
- [29] H. Štěpánková, J. Englich, P. Novák, H. Lütgemeier, *J. Magn. Magn. Mater.* 104–107 (1992) 409–410.

- [30] A.M. van Diepen, F.K. Lotgering, *Solid State Commun.* 27 (1978) 255–258.
- [31] G. Albanese, J.L. Sanchez Ll, G. Lopez, S. Diaz, F. Leccabue, B.E. Watts, *J. Magn. Magn. Mater.* 137 (1994) 313–321.
- [32] H. Stepankova, J. Englich, J. Kohout, H. Lutgemeier, *J. Magn. Magn. Mater.* 140–144 (1995) 2099–2100.
- [33] O.A. Pringle, G.J. Long, *Mössbauer spectroscopy Applied to Inorganic Chemistry*, in: G.J. Long, F. Grandjean (Eds.), Plenum Press, New York, 1989, pp. 13–57.
- [34] L. Lechevallier, J.M. Le Breton, J.F. Wang, I.R. Harris, *J. Phys.: Condens. Matter* 16 (2004) 5359–5376.
- [35] R.L. Streever, *Phys. Rev.* 186 (1969) 285–290.
- [36] H. Stepankova, J. Englich, P. Novak, B. Sedlak, M. Pfeffer, *Hyperfine Interact.* 50 (1989) 639–644.

Charge localization and magnetocrystalline anisotropy in La, Pr, and Nd substituted Sr hexaferritesVojtěch Chlan,^{*} Karel Kouřil, Kateřina Uličná, and Helena Štěpánková*Faculty of Mathematics and Physics, Charles University in Prague, V Holešovičkách 2, 18000 Prague 8, Czech Republic*

Jörg Töpfer and Daniela Seifert

University of Applied Sciences Jena, Dept. SciTec, Carl-Zeiss-Promenade 2, 07745 Jena, Germany

(Received 27 February 2015; published 14 September 2015)

Charge compensation in strontium M-type hexaferrites $A_x^{3+}\text{Sr}_{1-x}\text{Fe}_{12}\text{O}_{19}$ ($A = \text{La, Nd, or Pr}$) is studied by means of calculations of electronic structure and ^{57}Fe nuclear magnetic resonance (NMR) experiments. Two different states are realized in the calculations: a localized scenario as a ground state with the extra valence charge preferentially in the octahedral 2a sites and a delocalized scenario with the charge delocalized over multiple sites. From the calculations and NMR experiments, it is deduced that the localized state $\text{Fe}^{2+}(2a)$ occurs at low temperatures regardless of the type of used substitution and that the distribution of ferric and ferrous ions within the 2a sublattice is static at low temperatures. The magnetocrystalline anisotropy energy of Sr and La hexaferrites is calculated and the contributions of individual Fe sublattices are evaluated. The temperature dependence of the anisotropy for La hexaferrite is explained as a transition between localized and delocalized states causing changes in the single ion contributions of Fe in 2a and also 12k sites.

DOI: [10.1103/PhysRevB.92.125125](https://doi.org/10.1103/PhysRevB.92.125125)

PACS number(s): 32.10.-f, 76.60.-k, 75.30.Gw

I. INTRODUCTION

Hexagonal ferrites [1–3] are well established ferrimagnetic materials with many uses: they can be found in cost-effective hard magnets as well as in components for high-frequency applications. Interest in hexaferrites has been rekindled by the discovery of intrinsic magnetoelectrics with strong coupling of magnetic and electric order as well as by the emergence of various low-dimensional hexaferrite systems, e.g., nanoparticles, fibres, thin layers, or composites [4]. Finally, there is still effort devoted to classical hexaferrite systems aimed on improving their performance in applications and unveiling related physics.

One of the important properties of strontium M-type hexaferrite $\text{SrFe}_{12}\text{O}_{19}$ (SrM) is the magnetocrystalline anisotropy. The anisotropy arises mainly from contributions of ferric cations. In the hexaferrite structure (space group $P6_3/mmc$), Fe atoms occupy sites 2a, 2b, 4f_{IV}, 4f_{VI}, and 12k, which form five magnetic sublattices (see Fig. 1). The magnetocrystalline anisotropy of SrM is uniaxial with the easy axis of magnetization parallel to the hexagonal axis, but the way how the individual Fe sublattices add up to the total anisotropy is less clear, as the contributions of individual sublattices are difficult to obtain experimentally. These contributions have thus been estimated indirectly, e.g., from changes of the measured anisotropy in substituted hexaferrites [5–7], or calculated as single-ion contributions using appropriate spin Hamiltonians and considering the symmetry of the crystal field [8–10]. It became generally accepted that mainly Fe^{3+} in 2b sites are responsible for the uniaxial character of anisotropy in Sr (and Ba) M-type hexaferrites [11] and that the contributions of other ferric cations, especially the 12k, are also important [8–10].

The magnetocrystalline anisotropy due to ferric ions can be altered by replacing the Fe with suitable substitutions [12–15] as well as by substituting the Sr by a trivalent cation [16–18]. Particularly, in La^{3+} M-type hexaferrites

(LaM), the observed magnetocrystalline anisotropy increases with decreasing temperature, in contrast to almost a constant character of the temperature dependence for Sr or Ba M-type hexaferrites [19,20]. At low temperatures, the anisotropy of La hexaferrites was found two times higher than the value for Sr or Ba hexaferrites. Based on measurements of the anisotropy field and total magnetic moment, it was proposed by Lotgering [19] that the increased anisotropy at low temperatures is due to the formation of Fe^{2+} in octahedral 2a sites.

Although the $\text{Fe}^{2+}(2a)$ localization was supported by local hyperfine methods [16,20–24], the mechanism of increased magnetic anisotropy proposed by Lotgering is still an open question. In published calculations of the electronic structure of these hexaferrites [25,26], the localized state was not reached—the calculations resulted in a delocalized solution with excess charge contained in the interstitial space or smeared over all iron sites, which is not in accord with the conclusions of the experiments. Since the explanation of how the charge compensation and anisotropy are connected is lacking, this issue is addressed in the present paper.

The aim of this work is to understand the increase of magnetocrystalline anisotropy in La hexaferrite at low temperatures, and to explain the relation of this increase to the presence of Fe^{2+} . For this purpose, we studied M-type hexaferrites $A_x^{3+}\text{Sr}_{1-x}\text{Fe}_{12}\text{O}_{19}$ ($A = \text{La, Nd, or Pr}$) by means of electronic structure calculations and nuclear magnetic resonance experiments. Contrary to previous calculations [25,26], we found the ground state with Fe^{2+} in 2a sites for all studied systems with A^{3+} . Such localization was also confirmed by our NMR experiments. Based on calculations, we present a mechanism of increased (decreased) magnetocrystalline anisotropy in La hexaferrites at low (high) temperatures.

II. METHODS**A. Electronic structure calculations**

Our calculations used the augmented plane waves + local orbital method based on the density functional theory (DFT)

^{*}vojtech.chlan@mff.cuni.cz

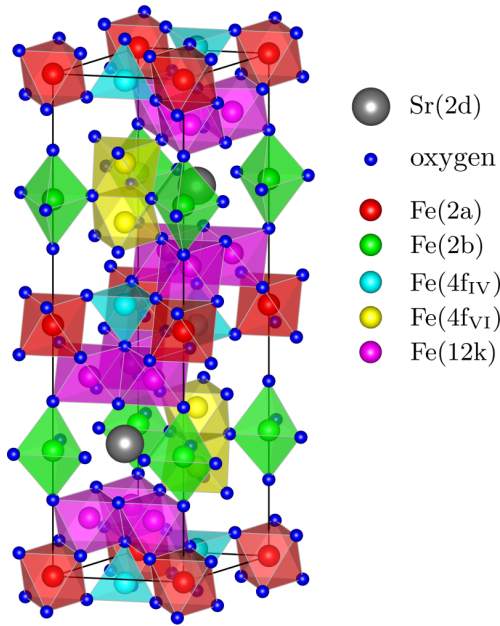


FIG. 1. (Color online) Unit cell of hexaferrite $\text{SrFe}_{12}\text{O}_{19}$. The five nonequivalent Fe sites are octahedral 2a (site symmetry $\bar{3}m$), bipyramidal 2b ($\bar{6}m2$), tetrahedral $4f_{\text{IV}}$, octahedral $4f_{\text{VI}}$ (both $3m$), and 12k (site symmetry m). The three- and sixfold local axes are parallel to the hexagonal axis c of the crystal (vertical direction in the picture), which is also the easy axis of magnetization.

as implemented in WIEN2K [27]. For the exchange-correlation functional, the PBE-GGA form was adopted [28]. To improve the description of iron $3d$ electron correlations, we used the rotationally invariant version of the LDA+ U method [29] with the GGA instead of LSDA exchange-correlation potential and with a single parameter $U_{\text{eff}} = U - J$.

The electronic structure of hexaferrites, with unit cells containing two formula units $A\text{Fe}_{12}\text{O}_{19}$ ($A = \text{Sr}, \text{La}, \text{Nd}$, and Pr), were calculated within space group $P6_3/mmc$; the lattice constants that were used are displayed in Table I. There are eleven nonequivalent atomic sites in the structure including the five Fe sites. The magnetic structure was considered as collinear, with the moments of Fe atoms in 2a, 2b, and 12k sites being antiparallel to the moments of Fe in $4f_{\text{IV}}$ and $4f_{\text{VI}}$ sites.

The calculation of the electronic structure of mixed LaSr hexaferrite $\text{La}_{0.5}\text{Sr}_{0.5}\text{Fe}_{12}\text{O}_{19}$ was performed within space group $P\bar{6}m2$, where the number of nonequivalent atoms increased to 21, as only the 2a octahedra retained their multiplicity 2; all other sites split 1:1. As a comparison,

TABLE I. Lattice parameters in angstroms used by the presented calculations.

Structure	a	b	c
SrM	5.9618	5.9618	23.3533
LaSrM	5.9373	5.9373	23.1962
LaM, PrM, NdM	5.9128	5.9128	23.0391
LaM (orthorhombic) [24]	5.9025	10.1593	22.7883

calculations were performed for a low-temperature structure of $\text{LaFe}_{12}\text{O}_{19}$ with the orthorhombic $Cmcm$ space group proposed by Küpferling *et al.* [24]. This structure loses hexagonal symmetry due to orthorhombic distortion: the 12k site of the original hexagonal structure splits into 16h and $8f_3$, otherwise there is one-to-one correspondence between hexagonal (2a, 2b, $4f_{\text{IV}}$, $4f_{\text{VI}}$) and orthorhombic sites (4a, 4b, $8f_1$, $8f_2$).

The atomic positions of all calculated structures were optimized within their space groups by minimization of the total energy and atomic forces. The lattice parameters (Table I) of Sr and La hexaferrites were optimized with $\text{RK}_{\text{max}} = 7.0$. The lattice parameters of La hexaferrite were then used also for Nd and Pr hexaferrites (NdM, PrM), while those of the mixed LaSr hexaferrite (LaSrM) were interpolated from Sr and La structures. The lattice parameters of the orthorhombic structure were not optimized, we used the parameters acquired by Küpferling *et al.* [24].

The radii of the atomic spheres were chosen as 1.45 a.u. for oxygen, 2.0 a.u. for iron, and 2.5 a.u. for large cations (La, Sr, Nd, or Pr). The dependence on the size of the basis, the number of k points, and the high-energy cutoff was tested on the Sr hexaferrite where the energy of magnetocrystalline anisotropy was satisfactorily converged already for $\text{RK}_{\text{max}} = 6.0$ (APW+lo method), k -mesh $7 \times 7 \times 1$, and $E_{\text{max}} = 5.0 \text{ Ry}$. The charge density was Fourier expanded to $G_{\text{max}} = 16\sqrt{\text{Ry}}$ and the value of parameter $U_{\text{eff}} = 4.5 \text{ eV}$ was adopted for the $3d$ orbitals of iron atoms; its influence on the calculated quantities is discussed in the text.

The self-consistent calculation of the magnetocrystalline anisotropy is a difficult task as the corresponding energy differences of the order of $1\text{--}10 \mu\text{Ry/atom}$ are comparable to the energetic resolution of available full potential calculations. The results obtained in a self-consistent calculation are thus overly sensitive to various calculational parameters (size of the basis set, number of k points). Since in case of these hexaferrites the spin-orbit coupling is small compared to $3d$ bandwidth or the exchange splitting, the anisotropies of the studied compounds can be studied using the force theorem approach, where the spin-orbit coupling is introduced non-self-consistently (for details and further references see Ref. [30]). Our practice was as follows: the spin-polarized calculation was converged self-consistently without spin-orbit coupling, using such a set of symmetry operations that satisfied all intended $[hkl]$ directions of magnetization. Then, starting from the converged potential, the eigenvalue problem was solved for each direction with the spin-orbit coupling switched on non-self-consistently, i.e., within one iteration only. The difference in total energies was then evaluated for different $[hkl]$ directions to determine the magnetocrystalline anisotropy. This spin-orbit interaction was applied within the atomic spheres using the second variational method, which allowed us to resolve the contributions of individual Fe sublattices to anisotropy.

B. Hexaferrite samples

The studied powder samples of hexaferrites with a substitution of the large cation were prepared by the standard ceramic process (for details see Refs. [16,31]). In the case of the $\text{La}_x\text{Sr}_{1-x}\text{Fe}_{12}\text{O}_{19}$ system, the samples covered the whole

concentration range—five samples with $x = 0, 0.25, 0.5, 0.75$, and 1 . For Nd and Pr substitutions, the single phase limits are 0.375 for Pr and below 0.37 for Nd; we studied the samples $\text{Nd}_x\text{Sr}_{1-x}\text{Fe}_{12}\text{O}_{19}$ ($x = 0.125, 0.250$, and 0.300) and $\text{Pr}_x\text{Sr}_{1-x}\text{Fe}_{12}\text{O}_{19}$ ($x = 0.125, 0.250$, and 0.375). The single-phase samples were characterized by powder XRD, microscopy, electron-probe microanalysis, thermal analysis, magnetic measurements, and Mössbauer spectroscopy [31].

C. ^{57}Fe nuclear magnetic resonance experiments

Frequency-swept ^{57}Fe NMR spectra were recorded in zero external field at 4.2 K using spectrometer console Bruker Avance and a home-made probe. The nuclear spin of ^{57}Fe is $\frac{1}{2}$ and the magnetogyric ratio $\gamma = 1.38\text{ MHz T}^{-1}$, so that the resonance frequency corresponds directly to the local magnetic field. A tuned and well matched resonance circuit in the probe was used and special care was given to ensure reliable intensities of NMR spectra in the whole frequency range. The Carr-Purcell-Meiboom-Gill (CPMG) pulse sequence was applied and the pulse lengths and amplitudes were set to excite the signal of nuclei in the magnetic domains. Depending on the sample composition, the required lengths of $\frac{\pi}{2}$ pulses were $1.5\text{--}10\text{ }\mu\text{s}$, the frequency step in spectra $10\text{--}50\text{ kHz}$, and the delay between scans $1\text{--}150\text{ s}$. Spin echoes formed within the CPMG sequence were detected and coherently summed in the time domain. The signals obtained at individual excitation frequencies were then Fourier transformed to the frequency domain. To minimize the modulation of spectra by T_2 relaxation, only the first five recorded echoes were used for evaluation. The final spectrum was constructed as an envelope of the particular FT lines and a frequency correction $1/f^3$ of spectral intensity was applied.

III. RESULTS AND DISCUSSION

In the first part of this section, we describe how the state with Fe^{2+} localized in 2a was reached in DFT calculations. Then the results of calculations and experiments regarding the localization are presented. The last part concerns magnetocrystalline anisotropy: its calculation, comparison with available experimental data, and also discussion of the results.

A. Charge localization from DFT calculations

The GGA+ U method improves the description of iron $3d$ electron correlations and in the case of hexaferrites provides correctly the insulating ground state, while with GGA, the ground state would be almost metallic [25]. However, one has to be careful when using the GGA+ U method on complex structures as there is a danger that an incorrect electron density is stabilized by the applied orbital potential. The calculation then becomes trapped in some local energy minimum, which may depend on the starting conditions, the process of including the orbital potential, or various parameters of the calculation (e.g., mixing scheme). On the other hand, the fact that GGA+ U stabilizes (and amplifies) inequivalency and leads to a charge disproportionation can be exploited in order to search for energetic minima that a pure GGA calculation would not reach. When more than one stable self-consistent solutions are obtained, apparently, it is justified to choose the

one with the lowest total energy as the correct solution. Our approach to obtain and evaluate such energy minima is thus similar to the common practice for the calculation of magnetic exchange interactions from the differences of the total energies of states with different atomic spin configurations [32–35]. Instead of starting the self-consistent calculations with various orientations of atomic spins, our procedure is more subtle: calculations start with the same spin structure but we modify the initial occupations of electronic states.

Local energy minima for La M-type hexaferrite (LaM) $\text{LaFe}_{12}\text{O}_{19}$ were searched by arranging several different occupations of valence electrons of Fe atoms in the initial electron density. The calculation for each of these density templates was then carried out without any further interventions in the population matrices until it self-consistently converged using GGA+ U with $U_{\text{eff}} = 4.5\text{ eV}$. All calculations reached either a solution corresponding to a delocalized scenario with all iron atoms being Fe^{3+} -like, or a solution having Fe^{2+} localized in the 2a site, as was indicated by the lowered magnetic moment of Fe(2a) in Table II. The latter, localized solution had the total energy lower by $\approx 0.64\text{ eV}$ and thus was declared as the ground state. Between two calculations with different starting conditions but reaching the same type of solution only slight variations of calculated quantities were observed ($\approx 0.001\text{ }\mu_B$ in atomic moments and below 0.1 meV in total energy). Such differences were not attributed to additional solutions since they are close to the precision threshold of our DFT calculations, which was estimated as $\approx 0.01\text{ meV}$.

Analogous calculations were carried out for pure Sr, Nd, and Pr hexaferrites, the mixed La/Sr hexaferrite, and also for the La hexaferrite with the orthorhombic structure proposed by Küpferling *et al.* [24]. For structures with a trivalent large atom, we again found a delocalized and a localized solution, the latter being energetically favorable. As expected, for Sr hexaferrites, such calculations found only a single solution with all Fe ions in a ferric state (Table II). Similarly to the situation in La hexaferrites, for all structures with a trivalent large cation, the localized solution was assigned to the ground

TABLE II. Magnetic moments (in μ_B units) and valences of atoms in La and Sr M-type hexaferrites. The moments were calculated inside generalized atomic volumes using the atoms-in-molecules (AIM) method. The valence was obtained as the difference of the integrated electronic charge inside the AIM volume and the atomic number Z .

atom	magnetic moment (μ_B)			valence		
	SrM	LaM deloc.	LaM loc.	SrM	LaM deloc.	LaM loc.
Fe(2a)	4.20	4.12	3.63	1.84	1.76	1.42
Fe(2b)	4.11	4.11	4.11	1.77	1.76	1.76
Fe(4f _{IV})	−4.11	−4.11	−4.10	1.79	1.78	1.77
Fe(4f _{VI})	−4.15	−4.17	−4.17	1.86	1.85	1.85
Fe(12k)	4.20	4.16	4.22	1.82	1.77	1.82
O(4e)	0.42	0.40	0.42	−1.23	−1.24	−1.23
O(4f)	0.10	0.08	0.14	−1.24	−1.25	−1.25
O(6h)	0.03	0.04	0.04	−1.24	−1.23	−1.22
O(12k ₁)	0.10	0.08	0.06	−1.24	−1.25	−1.25
O(12k ₂)	0.21	0.14	0.15	−1.22	−1.23	−1.23
La/Sr(2d)	0.00	−0.02	0.00	1.65	2.15	2.15

TABLE III. The formal valence states for all studied hexaferrite structures. The values were obtained by normalizing the valences (extracted from AIM method) by a factor ≈ 0.62 , which scaled the average charge of oxygen atoms to the value of -2 , representing the oxidation state O^{2-} . Label of cation A stands for Sr, La, Nd, or Pr.

atom	SrM	LaM		PrM		NdM		atom	deloc.	loc.
		deloc.	loc.	deloc.	loc.	deloc.	loc.			
Fe(2a)	2.99	2.84	2.30	2.87	2.35	2.91	2.58	Fe(2a)	2.92	2.70
Fe(2b)	2.87	2.84	2.85	2.84	2.86	2.84	2.86	Fe(2b')	2.84	2.85
								Fe(2b'')	2.86	2.86
Fe(4f _{IV})	2.89	2.87	2.86	2.88	2.86	2.88	2.87	Fe(4f' _{IV})	2.88	2.88
								Fe(4f'' _{IV})	2.89	2.88
Fe(4f _{VI})	3.01	2.98	2.99	2.99	2.99	2.99	2.99	Fe(4f' _{VI})	2.99	2.99
								Fe(4f'' _{VI})	2.99	3.00
Fe(12k)	2.95	2.86	2.95	2.88	2.95	2.90	2.94	Fe(12k')	2.94	2.94
								Fe(12k'')	2.87	2.93
A(2d)	2.67	3.47	3.49	3.28	3.38	3.13	3.21	Sr(2d)	2.67	2.67
								La(2d)	3.49	3.50

state, while the delocalized solution was found approximately 0.5 eV higher in energy.

The valence states of Fe cations in hexaferrites can be estimated from their calculated magnetic moments, since all Fe cations are expected to be in high spin states, i.e., free iron ion possessing a magnetic moment of $5 \mu_B$ or $4 \mu_B$ is nominally Fe^{3+} or Fe^{2+} , respectively. In a crystal, the calculated moments are lower, because of the hybridization effect of iron $3d$ orbitals with oxygen orbitals, which is a physically correct picture. However, a fraction of the magnetic moment leaks out of the atomic spheres, and thus is not attributed to any specific atom. We avoid this undesired effect by using the AIM approach [36], where for the purpose of evaluating the atomic valences or magnetic moments, generalized atomic volumes are calculated and used instead of the original atomic spheres. The valences from the AIM analysis are presented in Table III. For easier differentiation between Fe^{2+} and Fe^{3+} states we introduce formal valence states obtained by normalizing the calculated atomic charges by such a factor (≈ 0.62) that would bring the average charge of oxygen ions to the value of -2 , representing the oxidation state O^{2-} . These formal valence states for Fe atoms in all calculated hexaferrites are displayed in Tables III and IV.

From a survey of Table III, one finds the Fe cations in the Sr hexaferrite on average to possess a formal valence state 2.95,

TABLE IV. The formal valence states extracted from AIM method are displayed for the orthorhombic structure of La hexaferrite proposed by Küpferling *et al.* [24]. The values were obtained by normalizing the valences (extracted from AIM method) by a factor ≈ 0.62 , which scaled the average charge of oxygen atoms to the value of -2 , representing the oxidation state O^{2-} .

atom	deloc.	loc.
Fe(4a)	2.72	2.39
Fe(4b)	2.81	2.84
Fe(8f ₁)	2.94	2.94
Fe(8f ₂)	2.97	2.97
Fe(8f ₃)	2.83	2.88
Fe(16h)	2.89	2.94
La(4c)	3.44	3.46

i.e., essentially Fe^{3+} states. As expected due to the presence of an extra valence charge, the averaged formal valence state of Fe in the La hexaferrite (2.88) is somewhat lower than in the Sr hexaferrite and is practically the same for both localized and delocalized solutions of the La hexaferrite. Roughly, half of the extra charge is localized at lanthanum for both types of solutions. In the case of the delocalized solution, the remaining charge is distributed among Fe cations (especially in 2a and 12k sites) and oxygens. For the localized solution, however, the excess charge is almost exclusively at the 2a sites, as indicated by its reduced valence state. This behavior can be observed also in data for NdM and PrM (Table III) and analogous charge compensation is found also in the orthorhombic LaM structure (Table IV). Furthermore, the localization, albeit a weak one, can be observed also in the mixed $(LaSr)_{0.5}Fe_{12}O_{19}$ (LaSrM) hexaferrite (Table III). All these results indicate that the Fe^{2+} appears in the octahedral 2a sites regardless of the choice of the trivalent large cation (La, Nd, or Pr). Moreover, this localization effect is not inherent to the hexagonal structure: Fe^{2+} is present (in 4a sites) also in the orthorhombic structure.

Besides the abrupt change of valence of Fe in 2a sites (respectively, 4a in the orthorhombic structure) for all localized solutions, we can notice differences also in delocalized solutions. Compared to SrM, the valence states of Fe cations in 2a and 12k sites of LaM are lower, while the other Fe cations remain relatively intact. In the mixed structure LaSrM, where the 12k sublattice splits into two, only the six $Fe(12k'')$ cations, which are near the La^{3+} sites display such a difference. In the delocalized state, the extra minority charge thus slightly prefers the 2a sites and those 12k sites that are close to the trivalent large cation.

B. Charge localization from ^{57}Fe NMR experiments

Zero field ^{57}Fe NMR spectra of the Sr hexaferrite, La, Nd, and Pr substituted Sr hexaferrites, and the La hexaferrite measured at 4.2 K are displayed in Fig. 2. The Sr hexaferrite spectrum contains five lines corresponding to five sublattices 2b, 12k, 4f_{IV}, 2a, and 4f_{VI} (listed by increasing frequency). With increasing concentration of La, Nd, or Pr, the local environment of ^{57}Fe nuclei is perturbed: the local symmetry

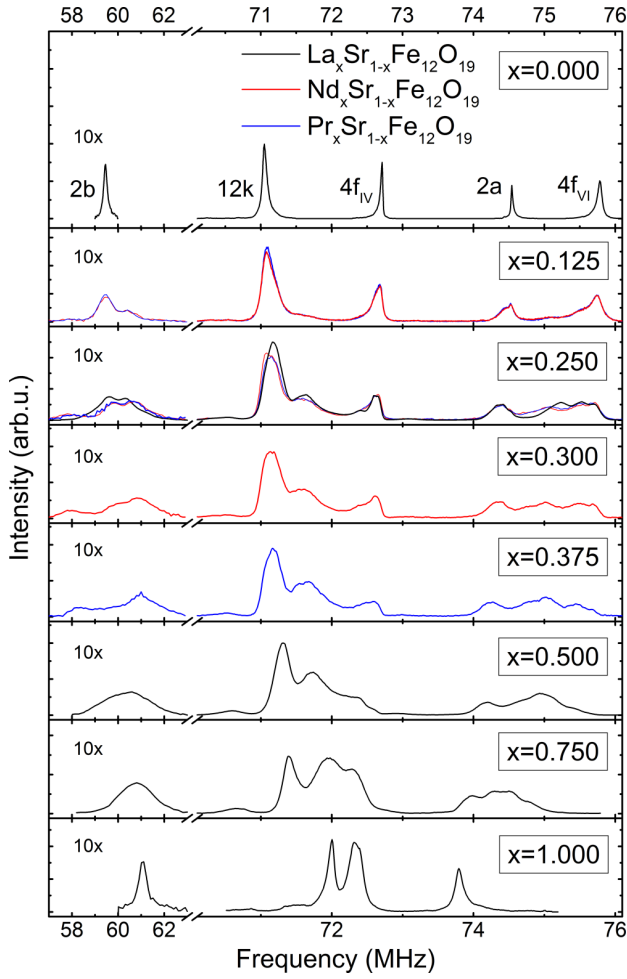


FIG. 2. (Color online) ^{57}Fe NMR spectra of the Sr hexaferrite ($x = 0$), La, Nd, and Pr substituted Sr hexaferrites ($x \in (0.125, 0.75)$), and the La hexaferrite ($x = 1$) measured at 4.2 K in zero external field. Spectra are sorted with increasing concentration x of the trivalent large cation from top to bottom; the weak resonance of 2b at lower frequencies is scaled 10x.

of Fe sites is reduced by the substituent, which causes visible line splitting for the neighboring Fe sites or line broadening when the sites are further away. Additionally, these changes manifest also as gradual shifts in resonance frequency; see the shift of center of mass of 2b line in Fig. 3.

The spectra in the frequency range of 71–76 MHz noticeably follow a common trend regardless of the type of substituting atom. On the other hand, the Fe(2b) subspectrum at lower frequencies differs for Nd and Pr substituted samples from that of La substituted hexaferrite. This is attributed to the fact that Nd and Pr both possess a magnetic moment. Since 2b are the nearest iron sites to the large cation site (see Fig. 1), the Fe(2b) resonance is visibly affected by an additional field due to the interaction with the magnetic moment of Nd or Pr. Analogous yet smaller differences can be observed in Fig. 2 (panel $x = 0.25$) for 12k and $4f_{\text{VI}}$ spectral lines, as the 12k and $4f_{\text{VI}}$ sites are the next nearest neighbors to the large cation site. And finally, the effect on $4f_{\text{IV}}$ and 2a lines is negligible as these sites are the most distant to the large cation in 2d site.

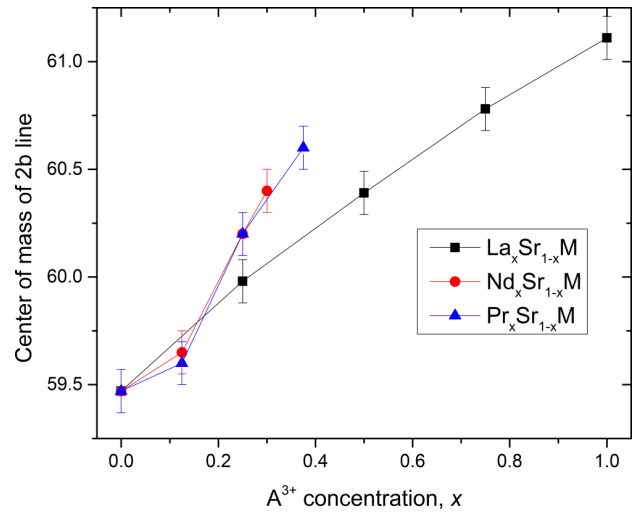


FIG. 3. (Color online) Shift of 2b line resonance frequency (evaluated as a center of mass) in dependence on the concentration of trivalent large cation. Lines are only a guide for the eye.

The resonance line of ^{57}Fe in 2a sites is interesting, its intensity diminishes with increasing concentration of La, Nd, or Pr, while the resonance frequency remains rather constant. The loss of 2a line intensity is attributed to the change of the valence state of some of the Fe(2a) ions towards Fe^{2+} state. Such a change is accompanied by a decrease of Fe 3d magnetic moment, which in turn decreases the local hyperfine magnetic field, i.e., the resonance frequency of ^{57}Fe in Fe^{2+} (2a) is significantly shifted to lower frequencies with respect to the position of ^{57}Fe in Fe^{3+} (2a). This is in accord with the results of Mössbauer spectroscopy by Seifert *et al.* [31] who found the hyperfine field of ^{57}Fe in Fe^{2+} (2a) approximately 10 T lower than the field of ^{57}Fe in Fe^{3+} (2a) in Sr hexaferrites partially substituted by La, Nd, Pr, or Sm at room temperature. At lower temperatures, this difference increases to more than 20 T as was observed by Grössinger *et al.* in a La hexaferrite [20].

Direct measurement of Fe^{2+} by ^{57}Fe NMR is difficult, probably due to the rapid spin-spin relaxations and line broadening; the formation of Fe^{2+} (2a) is thus observed indirectly as a decrease of the Fe^{3+} (2a) intensity. Due to the overlap of some of the spectral lines, the intensities were evaluated for groups: (12k + $4f_{\text{IV}}$) and (2a + $4f_{\text{VI}}$). The intensity of (2a + $4f_{\text{VI}}$) lines decreases linearly with increasing concentration of the trivalent large ion while the intensity of (12k + $4f_{\text{IV}}$) remains constant for all concentrations (Fig. 4).

Because of the La-Sr disorder, the $4f_{\text{VI}}$ line is split into four overlapping components with unknown asymmetric profiles, therefore, a quantitatively reliable decomposition of the (2a + $4f_{\text{VI}}$) profile into contributions of the 2a and $4f_{\text{VI}}$ sublattices is not possible. From a qualitative comparison of spectral profiles, it is evident that the observed decrease of the (2a + $4f_{\text{VI}}$) intensity is due to the decrease of the 2a line intensity. From the dependence of NMR line intensities, we thus confirm that at low temperatures, the Fe^{2+} cations form in 2a sites to compensate the addition of trivalent substitution.

Apparently, the character of the changes is uniform regardless of the type of used substitution, which is in a very

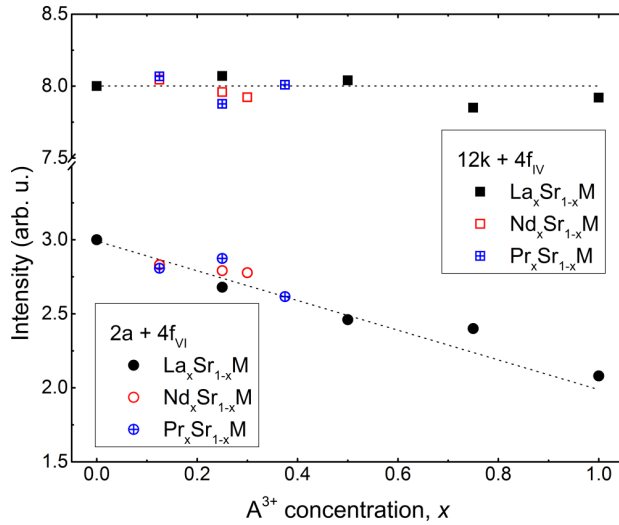


FIG. 4. (Color online) Integral intensities of $12k + 4f_{IV}$ and $2a + 4f_{VI}$ resonance lines depending on the concentration of the trivalent large cation. Lines correspond to nominal numbers of Fe^{3+} atoms per formula unit $A_x^{3+}Sr_{1-x}Fe_{12}O_{19}$ for the scenario with the Fe^{2+} cation occupying the 2a sites, i.e., eight atoms for $12k + 4f_{IV}$ and $3 - x$ atoms for $2a + 4f_{VI}$. The total integral intensities of the four considered spectral lines were normalized to $11 - x$.

good agreement with our calculations for structures with a trivalent A^{3+} large cation. The calculated La, Nd, and Pr hexaferrites exhibit a ground state with localized Fe^{2+} , while the other Fe ions remain ferric. The NMR and DFT results are also consistent in finding that the number of ferric ions in the 2a sublattice changes gradually with concentration x . Although only one structure with a mixed content of La and Sr is available from calculations (see Table III), the formal valence state of its Fe(2a) is between the values of $Fe^{3+}(2a)$ in SrM and $Fe^{2+}(2a)$ in LaM.

The linear decrease of $Fe^{3+}(2a)$ intensity in our NMR spectra also indicates that the distribution of Fe^{2+} in the 2a sublattice is rather static at low temperatures. Significant fast electron hopping within the 2a sublattice would induce a gradual decrease of resonance frequency with increasing concentration of substitution because of the decrease of the local field—the observed field would have been the weighted average of Fe^{2+} and Fe^{3+} fields. Such a rapid shift of the 2a line frequency with increasing concentration of substitution is not observed in our NMR spectra. Furthermore, the NMR relaxation times would be shortened due to the increasingly ferrous character of ions, which is again not the case as the relaxation times of the 2a line do not significantly differ from the values of other resonance lines. Therefore we can conclude that there are well defined ferric and ferrous ions in the 2a sublattice and their arrangement at low temperatures does not change significantly on the time scale of at least $100 \mu s$ (typical duration of performed NMR experiments at $T = 4.2$ K). While these findings are in agreement with the Mössbauer measurements of Seifert *et al.* [31] performed on the same set of samples, they are in contrast with the ^{57}Fe NMR results by Küpferling *et al.* [24] who reported no loss of 2a intensity (up to $x_{La} = 0.3$).

C. Calculation of magnetocrystalline anisotropy

The magnetocrystalline anisotropy of La and Sr hexaferrites was calculated within the force theorem approach as described in Sec. II. The energy of magnetocrystalline anisotropy was evaluated as $E_{MA} = E_{\perp} - E_{\parallel}$, where E_{\parallel} stands for the total energy with the direction of the magnetization in the hexagonal axis, while E_{\perp} denotes the averaged energy of calculations with the magnetization in the hexagonal plane. In our calculations, the variations of such in-plane total energies were more than two orders of magnitude lower than E_{MA} , in agreement with the uniaxial character of anisotropy in M-type hexaferrites.

In practice, E_{MA} consists of two parts: a contribution arising due to the presence of spin-orbit coupling and a contribution resulting from the interaction of an atomic moment with the dipolar magnetic field of atoms in the whole crystal. The first contribution was calculated using a second-variational method (as implemented in WIEN2K), which included the spin-orbit interaction within the atomic spheres. In calculations of unit cells with periodic boundary conditions, the evaluation of the latter (dipole-dipole) contribution reduced to the summation of atomic contributions within a Lorentz sphere—in our case, the value of this dipolar contribution was well converged for a sphere with a radius of 256 atomic units. The total magnetic anisotropy energies as sums of both contributions in units of meV/unit cell are displayed in the bottom row of Table V. In all studied cases, the dipolar anisotropies were of the order of $1\text{--}10 \mu eV/\text{unit cell}$, i.e., two or more orders of magnitude smaller than the contribution due to spin-orbit interactions.

The calculated energy of the magnetocrystalline anisotropy of the Sr hexaferrite, $E_{MA} = 0.78$ meV/unit cell (Table V), corresponds to an anisotropy constant $K_1 = 0.18$ MJ/m³ (roughly half of the experimental value 0.33 MJ/m³, Refs. [37,38]) and is in a good agreement with the value 0.84 meV/unit cell calculated by Liyanage *et al.* using DFT with PAW potentials [15]. The anisotropy calculated for the localized solution of La hexaferrite is two times higher than that of the Sr hexaferrite, while the delocalized solution of the La hexaferrite has an anisotropy two times weaker than SrM. The localized solution of the La hexaferrite has thus more than four times higher calculated anisotropy than the delocalized

TABLE V. The contributions of individual iron sublattices to the magnetocrystalline anisotropy energy E_{MA} were calculated for the studied La and Sr hexaferrites. Due to the reduced symmetry when the magnetization is along [100], the 12k sites split with ratio 4:8 into two species $12k_1$ and $12k_2$.

atom	E_{MA} of sublattice (meV/cell)			E_{MA} per atom (meV)		
	SrM	LaM loc.	LaM deloc.	SrM	LaM loc.	LaM deloc.
Fe(2a)	−0.01	1.11	0.66	−0.01	0.56	0.33
Fe(2b)	0.48	0.24	0.42	0.24	0.12	0.21
Fe(4f _{IV})	0.04	−0.02	0.00	0.01	0.00	0.00
Fe(4f _{VI})	−0.02	0.02	0.00	−0.01	0.01	0.00
Fe(12k ₁)	0.09	0.17	0.03	0.02	0.04	0.01
Fe(12k ₂)	0.20	0.03	−0.75	0.02	0.00	−0.09
total	0.78	1.55	0.37			

solution. This result can be confronted with the experimental estimation of magnetocrystalline anisotropy by Grössinger *et al.* [20] who measured the temperature dependence of the anisotropy field of La and Sr hexaferrite powders. While for the Sr hexaferrite the authors found an anisotropy field of around 2 T which is almost constant up to 500 K, the La hexaferrite displayed a relatively monotonous decrease of the field from ~ 4 T at low temperatures to ~ 1.2 T at 500 K. Similar results were obtained already by Lotgering [19] for Ba and La hexaferrites. Despite the fact that our calculations correspond to temperature 0 K and a proper description would go beyond DFT, we draw a simple picture of the localization process with temperature. At low temperatures, the scenario corresponding to the localized $\text{Fe}^{2+}(2a)$ solution calculated as the ground state is realized with a well established arrangement of $\text{Fe}^{2+}(2a)$ ions—in accordance with the observation of no dynamics of the extra valence electron by our NMR experiments. With increasing temperature, the state corresponding to the delocalized solution appears and dominates at high temperatures, which in effect substantially reduces the anisotropy of the La hexaferrite. In the Sr hexaferrite, there is no such transition and the anisotropy remains relatively temperature independent.

The calculated magnetocrystalline anisotropies can be analyzed further by a decomposition into contributions of individual Fe sublattices—since the spin-orbit interaction is enabled only within an atomic sphere, the decomposition can be achieved by including the spin-orbit interaction selectively on sets of atoms. We adopt an approach where the anisotropy energy due to the presence of spin-orbit coupling consists of “on site” (single ion), which is determined by the interaction of the orbital moment with the surrounding crystal field and is usually a dominant term, and “off site” contributions, which comprise the pairwise (e.g., pseudodipolar) interactions of orbital moments of neighboring atoms. We can thus evaluate the contribution of a given Fe sublattice from energies calculated with spin-orbit enabled on all atoms, including the particular Fe, and on all but the particular Fe atom (for details see Appendix).

The calculated contributions of Fe sublattices to E_{MA} are displayed in Table V. In the Sr hexaferrite, the largest contribution arises from the single-ion contribution of Fe(2b). The anisotropic character of 2b bipyramidal site is expected from the geometry of the oxygen hexahedron—strong elongation along its local axis (parallel to hexagonal axis of the unit cell) imposes large single-ion contribution to the uniaxial anisotropy. When considering E_{MA} per atom, the anisotropies of other Fe sublattices in SrM are almost an order of magnitude weaker than the anisotropy of Fe(2b), however, their total contribution is not negligible due to the larger number of atoms in the respective sublattices, especially in the case of Fe(12k). These outcomes are in accord with the generally accepted notion that the anisotropy in Sr and Ba hexaferrites is mainly due to the Fe(2b) contributions but also due to contributions of other Fe ions [8–10], although our results differ in the sign of 12k anisotropy from those obtained by means of a point charge model for the crystal field [9].

Despite the substitution of La for Sr in close vicinity to 2b sites, the contribution of Fe(2b) to the anisotropy remains large also for both La solutions. A considerable increase of anisotropy is, however, observed in the La hexaferrite due to

the contribution of localized $\text{Fe}^{2+}(2a)$ ions, whose calculated single-ion anisotropy is 1.19 meV (the contribution from the pair term is -0.08 meV).

In the delocalized solution for LaM, the extra valence charge is distributed among several sites, mainly Fe(2a) and Fe(12k), as is evidenced by the reduced (formal) valences compared to SrM (in Table III). As a consequence, the Fe(2a) and Fe(12k) contributions to anisotropy are substantially reduced. The single-ion contribution of Fe(2a) reduces to 0.87 meV (the pair-interaction term is -0.21 meV) and for Fe(12k) the single-ion term even becomes negative, -0.68 meV (the pair-interaction term is -0.07 meV).

The following text qualitatively explains the values of $\text{Fe}^{2+}(2a)$ and Fe(12k) contributions from considerations of the site symmetry and charge density plots. In case of $\text{Fe}^{2+}(2a)$, the single-ion contribution to anisotropy can be understood within the crystal-field theory [39]. The orbital moments of Fe are largely quenched and the orientation of 3d orbitals is governed by the crystal field, to which the spin-orbit interaction is only a small correction in iron oxides. For the 2a site, the 3d energy levels of Fe^{2+} are split by the octahedral crystal field into lower a lying triplet and a doublet. The triplet is further split by the trigonal component of the crystal field to a singlet and a doublet—their position in energy depends on the character of the trigonal distortion. The decomposition of charge within the atomic sphere of Fe(2a) reveals that in our case it is the singlet: the extra electron is contained predominately within the d_{z^2} orbital. This can be depicted by plotting the difference of charge density between the localized and the delocalized solutions [Fig. 5(b)]. Contrary to the typical setting of local axes in octahedron, here, the axes do not point toward the oxygen ligands: the distorted octahedron of the 2a site possesses trigonal symmetry with the z axis parallel to the global hexagonal axis of the crystal. The ground state of $\text{Fe}^{2+}(2a)$ is the d_{z^2} singlet and its orbital moment (as well as orbital moments of other Fe) remains nearly quenched by the crystal field—all the calculated Fe orbital moments are of the order of $0.01 \mu_B$. For the orbital singlet d_{z^2} , even a weak spin-orbit coupling will act against the deviation of the atomic moment of the 2a iron from the trigonal axis induced by the crystal field, and as a consequence, the ion significantly increases its single-ion contribution to the anisotropy [39].

For the delocalized solution of LaM, however, the excess minority charge is smeared over various sites—notably the occupation of Fe(2a) minority band is reduced while the occupation of Fe(12k) minority band increases. This in turn decreases the large anisotropy contribution of Fe(2a) and also strongly affects the anisotropy of Fe in the 12k sites. Compared to 2a, the octahedron of the 12k site has low symmetry and an analysis analogous to the 2a case would be complicated. We thus refer only to the density plots in Fig. 5. The partial electronic charge at the 12k sites forms irregular and quite generally oriented clouds [see dark blue structures in Fig. 5(c)] with one dimension noticeably shorter than the other two. When the magnetization is set in the [100] direction, the 12k sites split into two groups 4:8. For the first group of four sites, $12k_1$, the charge clouds are favorably oriented with respect to both considered directions of magnetization [100] and [001], thus the single-ion contribution to anisotropy is almost zero. While for the eight $12k_2$ sites the clouds are slightly

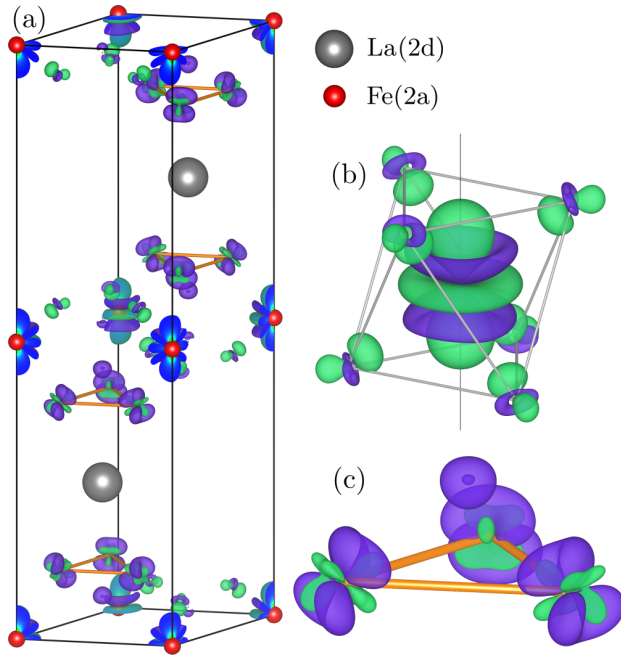


FIG. 5. (Color online) The area of the greatest difference between the localized and the delocalized solution of La hexaferrite. To construct the isosurface plot, the charge density of the delocalized solution was subtracted from that of the localized solution. Light green corresponds to areas where the charge density of the localized state is higher than the density of the delocalized state, while dark blue color corresponds to areas where the density of the delocalized state prevails. The isosurface level is $0.004 a_0^{-3}$ (a_0 is Bohr radius). (a) View of the hexagonal unit cell in perspective corresponding to Fig. 1. (b) The detail of the 2a site with a neighboring oxygen octahedron and (c) the detail of three of the 12k sites with one neighboring oxygen. These sites are the only sites in the unit cell where any significant difference between localized and delocalized solutions is visible.

more prolate towards the [100] direction, which implies a negative contribution to E_{MA} . The total contribution due to the minority charge on the 12k is thus negative, which is responsible (together with decrease of positive 2a contribution) for the reduction of overall anisotropy in the delocalized La hexaferrite.

We make a note concerning the accuracy of the presented anisotropy results with respect to the used k mesh and U_{eff} . Quite surprisingly, a relatively small number of k points was needed for sufficient convergence of the calculated anisotropy, however, the k mesh used in this work ($7 \times 7 \times 1$) is consistent with other calculations of anisotropy in Sr hexaferrites [15,40]. Liyange *et al.* [15] used a $7 \times 7 \times 1$ mesh for the calculation of anisotropy in Zn- and Sb-doped Sr hexaferrites, and Feng *et al.* [40] used an $8 \times 8 \times 1$ mesh for the case of Ti- and Co-doped Sr hexaferrite. This is due to the fact that the studied hexaferrites are relatively insulating (calculated gap ~ 2 eV) and the occupied Fe 3d states are quite localized.

Also, we point out that our calculated anisotropy is sensitive to the value of U_{eff} . With increasing U_{eff} , the occupied 3d states become more localized and the orbital moments are reduced, which in turn reduces the anisotropy. Varying the value of

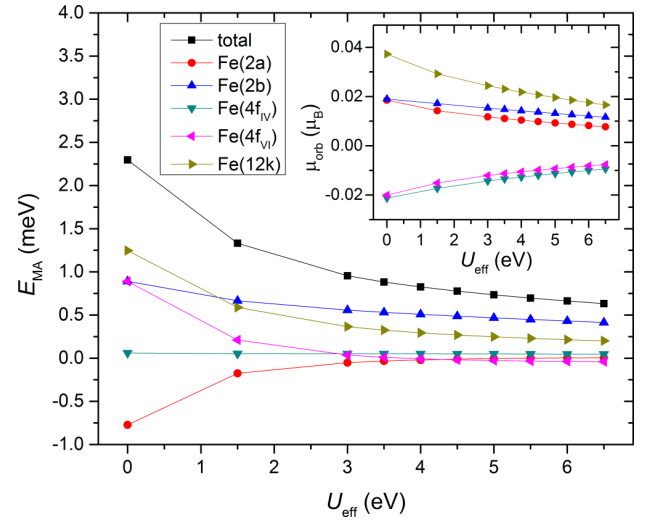


FIG. 6. (Color online) Dependence of calculated E_{MA} of Sr hexaferrite on applied U_{eff} . The inset displays an analogous dependence for the calculated orbital moments.

U_{eff} in the range 3–6 eV, which are reasonable values for iron oxides, induces monotonous changes to the orbital moments and anisotropies by $\approx 20\%$ (see Fig. 6). The trend scales in the same way for all Fe ions, therefore, we believe this dependence on U_{eff} does not impair our conclusions, at least in a qualitative level.

IV. CONCLUSIONS

The ground state with Fe^{2+} localized in 2a sites and an excited state with the charge delocalized were realized in calculations of the electronic structure of La, Nd, and Pr hexaferrites, and the localized state was observed in the spectra of ^{57}Fe nuclear magnetic resonance at 4.2 K. The preference of the extra valence charge for 2a sites was found independent on the type of the trivalent cation A^{3+} ($A = La, Nd, \text{ and } Pr$). Apparently, the fraction of $Fe^{3+}(2a)$ ions increases with increasing concentration of A^{3+} in the Sr hexaferrite, and at low temperatures the arrangement of ferric and ferrous ions within the 2a sublattice is static.

The magnetocrystalline anisotropy of Sr and La hexaferrites was calculated within the force theorem approach. For La hexaferrite with localized $Fe^{2+}(2a)$, the calculated anisotropy is twice the value of the Sr hexaferrite, while the La hexaferrite with delocalized electrons has half the value of the Sr hexaferrite, which is in agreement with the temperature dependence of anisotropy fields obtained in experiment [20]. From calculations of the individual Fe sites contributions to the anisotropy, we conclude that the increased anisotropy of the La hexaferrite at low temperatures is due to the single-ion contribution of 2a sites; the contributions of Fe in 2b remain appreciable in all cases. The Fe ions in 2a and 12k sites are the most affected by delocalization and are thus responsible for the decrease of anisotropy in La hexaferrites with increasing temperature.

ACKNOWLEDGMENTS

We thank to Pavel Novák from Institute of Physics ASCR for valuable discussions regarding the calculations of magnetocrystalline anisotropy. Support by the project P204-12-P352 of the Grant Agency of the Czech Republic is acknowledged. Computational resources were provided by the MetaCentrum under the program LM2010005 and the CERIT-SC under the program Centre CERIT Scientific Cloud, part of the Operational Program Research and Development for Innovations, Reg. No. CZ.1.05/3.2.00/08.0144.

APPENDIX: CALCULATION OF ATOMIC CONTRIBUTIONS TO MAGNETOCRYSTALLINE ANISOTROPY

The energy relevant for the anisotropy due to the presence of spin-orbit coupling can be expressed as (\mathbf{n} is the direction of magnetization)

$$E(\mathbf{n}) = E^{\text{ion}}(\mathbf{n}) + E^{\text{pair}}(\mathbf{n}), \quad (\text{A1})$$

where $E^{\text{ion}}(\mathbf{n})$ represents the “on-site” contribution to anisotropy (single-ion contribution), and $E^{\text{pair}}(\mathbf{n})$ denotes all “off-site” contributions appearing due to spin-orbit interaction (all pair interactions that may contribute to anisotropy, e.g., pseudodipolar interaction).

The single-ion contribution is a simple sum of all N individual atomic contributions e_i ,

$$E^{\text{ion}}(\mathbf{n}) = \sum_{i=1}^N E_i^{\text{ion}}(\mathbf{n}), \quad (\text{A2})$$

while the pair interactions take the form

$$E^{\text{pair}}(\mathbf{n}) = \frac{1}{2} \sum_{i \neq j}^N P_{ij} \mu_i(\mathbf{n}) \mu_j(\mathbf{n}), \quad (\text{A3})$$

where P is a tensor describing these pair interactions and μ_i and μ_j are the magnetic moments of i th and j th atoms. The spin component of μ_i and μ_j is virtually unaffected by enabling of the spin-orbit interaction non-self-consistently, while the orbital momentum at a given atom emerges in the calculations only when the spin-orbit interaction is enabled for the atom. As a consequence, the vast majority of $E^{\text{pair}}(\mathbf{n})$ is in fact isotropic and the anisotropy is due to orbital moments emerging when the spin-orbit interaction is present at a given atom. Therefore in calculations, when the spin-orbit is disabled for a particular atom, such an atom does not contribute to anisotropy through the pair interactions. Here, by “atom” we mean one particular sort of equivalent atoms; any contribution from pair interactions within such a sort of atoms cannot be further distinguished from the on-site (“single-ion”) contribution to anisotropy. (However, such a contribution cancels out if the pair of equivalent atoms possesses a center of inversion.)

The magnetocrystalline anisotropy energy (due to spin-orbit interaction) for the whole hexaferrite cell is thus the difference of $E(\mathbf{n})$ for \mathbf{n} along and perpendicular to the

hexagonal axis:

$$E_{\text{MA}} = E^{\perp} - E^{\parallel} = \sum_i^N (E_i^{\text{ion},\perp} - E_i^{\text{ion},\parallel}) + \frac{1}{2} \sum_{i \neq j}^N (P_{ij} \mu_i^{\perp} \mu_j^{\perp} - P_{ij} \mu_i^{\parallel} \mu_j^{\parallel}) = E_{\text{MA}}^{\text{ion}} + E_{\text{MA}}^{\text{pair}}. \quad (\text{A4})$$

Such quantity is calculated when the spin-orbit interaction is enabled for all atoms. In order to evaluate the individual contributions, one has to disable the spin-orbit interaction on some of the atoms and compare the results.

When the spin-orbit interaction is enabled only for k th atomic sphere and disabled for the rest, we obtain the energy

$$E_{\text{MA},k}^{(1)} = (E_k^{\text{ion},\perp} - E_k^{\text{ion},\parallel}) = E_{\text{MA},k}^{\text{ion}}; \quad (\text{A5})$$

the pair-interaction term vanishes, since only the k th orbital moment is nonzero; thus we calculate only the single-ion contribution.

To obtain the pair-interaction contribution, the setting can be inverted, i.e., we can calculate the energy for the situation with spin-orbit interaction disabled for the k th atomic sphere and enabled for the rest. Then, we get the contribution of k th atom by subtracting this energy from the energy E_{MA} where the spin-orbit interaction was enabled for all atoms:

$$\begin{aligned} E_{\text{MA},k}^{(2)} &= E_{\text{MA}} - \left(\sum_{i \neq k}^N (E_i^{\text{ion},\perp} - E_i^{\text{ion},\parallel}) + \frac{1}{2} \sum_{i \neq j, i, j \neq k}^N (P_{ij} \mu_i^{\perp} \mu_j^{\perp} - P_{ij} \mu_i^{\parallel} \mu_j^{\parallel}) \right) \\ &= E_k^{\text{ion},\perp} - E_k^{\text{ion},\parallel} + \frac{1}{2} \sum_{i \neq k}^N (P_{ik} \mu_i^{\perp} \mu_k^{\perp} - P_{ik} \mu_i^{\parallel} \mu_k^{\parallel}) \\ &\quad + \frac{1}{2} \sum_{j \neq k}^N (P_{kj} \mu_k^{\perp} \mu_j^{\perp} - P_{kj} \mu_k^{\parallel} \mu_j^{\parallel}) \\ &= E_{\text{MA},k}^{\text{ion}} + 2E_{\text{MA},k}^{\text{pair}}. \end{aligned} \quad (\text{A6})$$

While the $E_k^{(1)}$ was lacking the pair-interaction contribution, $E_k^{(2)}$ contains it twice.

The pair-interaction contribution to anisotropy can now be expressed as

$$\frac{1}{2} (E_k^{(2)} - E_k^{(1)}). \quad (\text{A7})$$

Eventually, the contribution of k th atom to the magnetocrystalline anisotropy (arising due to spin-orbit interaction) is calculated as

$$E_k = \frac{1}{2} (E_k^{(1)} + E_k^{(2)}). \quad (\text{A8})$$

- [1] H. Kojima, *Ferromagnetic Materials. A Handbook of the Properties of Magnetically Ordered Substances*, edited by E. P. Wohlfarth (North Holland, Amsterdam, 1982), Vol. 3, Chap. 5.
- [2] M. Sugimoto, *Ferromagnetic Materials. A Handbook of the Properties of Magnetically Ordered Substances*, edited by E. P. Wohlfarth (North Holland, Amsterdam, 1982), Vol. 3, Chap. 6.
- [3] E. Pollert, *Prog. Cryst. Growth Charact. Mater.* **11**, 155 (1985).
- [4] R. C. Pullar, *Prog. Mater. Sci.* **57**, 1191 (2012).
- [5] D. H. Han, Z. Yang, H. X. Zeng, X. Z. Zhou, and A. H. Morrish, *J. Magn. Magn. Mater.* **137**, 191 (1994).
- [6] X. Battle, X. Obradors, J. Rodríguez-Carvajal, M. Pernet, M. V. Cabañas, and M. Vallet, *J. Appl. Phys.* **70**, 1614 (1991).
- [7] Z. W. Li, C. K. Ong, Z. Yang, F. L. Wei, X. Z. Zhou, J. H. Zhao, and A. H. Morrish, *Phys. Rev. B* **62**, 6530 (2000).
- [8] G. Asti and S. Rinaldi, *AIP Conf. Proc.* **34**, 214 (1976).
- [9] Y. Xu, G.-L. Yang, D.-P. Chu, and H.-R. Zhai, *Phys. Status Solidi B* **157**, 685 (1990).
- [10] P. Novák, *Czech. J. Phys.* **44**, 603 (1994).
- [11] M. I. Darby and E. D. Isaac, *IEEE Trans. Magn.* **10**, 259 (1974).
- [12] D. J. D. Bitetto, *J. Appl. Phys.* **35**, 3482 (1964).
- [13] J. Kreisel, H. Vincent, F. Tasset, M. Paté, and J. P. Ganne, *J. Magn. Magn. Mater.* **224**, 17 (2001).
- [14] Q. Fang, H. Bao, D. Fang, and J. Wang, *J. Appl. Phys.* **95**, 6360 (2004).
- [15] L. S. I. Liyanage, S. Kim, Y.-K. Hong, J.-H. Park, S. C. Erwin, and S.-G. Kim, *J. Magn. Magn. Mater.* **348**, 75 (2013).
- [16] D. Seifert, J. Töpfer, F. Langenhorst, J.-M. Le Breton, H. Chiron, and L. Lechevallier, *J. Magn. Magn. Mater.* **321**, 4045 (2009).
- [17] J. Wang, C. Ponton, and I. Harris, *J. Magn. Magn. Mater.* **234**, 233 (2001).
- [18] J. Wang, C. Ponton, and I. Harris, *J. Alloys Compd.* **403**, 104 (2005).
- [19] F. K. Lotgering, *J. Phys. Chem. Solids* **35**, 1633 (1974).
- [20] R. Grössinger, M. Küpferling, M. Haas, H. Müller, G. Wiesinger, and C. Ritter, *J. Magn. Magn. Mater.* **310**, 2587 (2007).
- [21] C. Sauer, U. Köbler, W. Zinn, and H. Stäblein, *J. Phys. Chem. Solids* **39**, 1197 (1978).
- [22] H. Štěpánková, J. Englich, P. Novák, and H. Lütgemeier, *J. Magn. Magn. Mater.* **104–107**, 409 (1992).
- [23] R. Grössinger, C. T. Blanco, M. Küpferling, H. Müller, and G. Wiesinger, *Physica B* **327**, 202 (2003).
- [24] M. Küpferling, R. Grössinger, M. W. Pieper, G. Wiesinger, H. Michor, C. Ritter, and F. Kubel, *Phys. Rev. B* **73**, 144408 (2006).
- [25] P. Novák, K. Knížek, M. Küpferling, R. Grössinger, and M. W. Pieper, *Eur. Phys. J.* **43**, 509 (2005).
- [26] M. Küpferling, P. Novák, K. Knížek, M. W. Pieper, R. Grössinger, G. Wiesinger, and M. Reissner, *J. Appl. Phys.* **97**, 10F309 (2005).
- [27] P. Blaha, K. Schwarz, G. K. H. Madsen, D. Kvasnicka, and J. Luitz, *WIEN2k, An Augmented Plane Wave + Local Orbitals Program for Calculating Crystal Properties* (Techn. Universität Wien, Vienna, 2001).
- [28] J. P. Perdew, K. Burke, and M. Ernzerhof, *Phys. Rev. Lett.* **77**, 3865 (1996).
- [29] A. I. Liechtenstein, V. I. Anisimov, and J. Zaanen, *Phys. Rev. B* **52**, R5467 (1995).
- [30] S. Abdelouahed and M. Alouani, *Phys. Rev. B* **79**, 054406 (2009).
- [31] D. Seifert, J. Töpfer, M. Stadelbauer, R. Grössinger, and J.-M. Le Breton, *J. Am. Ceram. Soc.* **94**, 2109 (2011).
- [32] P. Novák and J. Rusz, *Phys. Rev. B* **71**, 184433 (2005).
- [33] C. M. Fang, F. Kools, R. Metselaar, G. de With, and R. A. de Groot, *J. Phys.: Condens. Mat.* **15**, 6229 (2003).
- [34] M. Feng, B. Shao, Y. Lu, and X. Zuo, *J. Appl. Phys.* **115**, 17D908 (2014).
- [35] P. Novák, I. Chaplygin, G. Seifert, S. Gemming, and R. Laskowski, *Comput. Mater. Sci.* **44**, 79 (2008).
- [36] R. F. W. Bader, *Atoms in Molecules. A Quantum Theory* (Oxford University Press, Oxford, 1990).
- [37] L. Jahn and H. G. Muller, *Phys. Status Solidi* **35**, 723 (1969).
- [38] B. T. Shirk and W. R. Buessem, *J. Appl. Phys.* **40**, 1294 (1969).
- [39] J. C. Slonczewski, *J. Appl. Phys.* **32**, S253 (1961).
- [40] M. Feng, B. Shao, J. Wu, and X. Zuo, *J. Appl. Phys.* **113**, 17D909 (2013).

Hyperfine Fields and Lattice Deformations in Ba and Sr Hexaferrites

V. CHLAN*, K. KOUŘIL, H. ŠTĚPÁNKOVÁ

Faculty of Mathematics and Physics, Charles University in Prague, V Holešovičkách 2, Prague, Czech Republic

Hyperfine magnetic fields on ^{57}Fe nuclei in Sr and Ba hexagonal ferrites are calculated in dependence on unit cell volume and c/a ratio. By analysing the local deformations of Fe–O–Fe triads the results are explained as changes to contact hyperfine field due to Fe–O covalency effects and supertransferred hyperfine fields. Most pronounced effect is found for bipyramidal iron Fe(b) where the total contact field is reduced due to noticeable shortening of Fe(b)–O bonds.

DOI: [10.12693/APhysPolA.127.594](https://doi.org/10.12693/APhysPolA.127.594)

PACS: 31.15.aj, 75.30.Et, 76.60.Jx

1. Introduction

Hyperfine interactions are highly sensitive to local crystal and magnetic structure, and therefore, significant changes of hyperfine fields are expected under lattice deformations. Current electronic structure calculations are well suited for studying how the structural changes and crystal properties are linked, and thus can serve as a tool for interpretation and better understanding of experimental results. Nuclear magnetic resonance experiments in thin films of Sr hexagonal ferrite with lattice mismatch [1] have shown that additional mechanisms other than macroscopic demagnetization field contribute to the resulting spectrum. In this work we employ density functional theory calculations to study the changes of hyperfine interactions with lattice deformations of Sr and Ba M-type hexaferrites.

The hyperfine field is the sum of fields created by interactions of the nucleus with dipolar and orbital moments of on-site electrons and by Fermi contact interaction of s electrons with the nucleus, which is usually the dominant term for iron. The s electrons of iron are polarised by the on-site unpaired $3d$ electrons, and especially $4s$ are also strongly influenced by the neighbouring oxygens and irons.

2. Method

Density functional theory calculations of Sr and Ba hexaferrites were performed using the full-potential, augmented plane waves with local orbital method as implemented in the WIEN2k code [2]. The radii of atomic spheres were chosen as 2.0 a.u. for Fe, 2.5 a.u. for Sr and Ba atoms and 1.45 a.u. for oxygens (1 a.u. ≈ 0.529 Å). In the wave function expansion maximum value of L was set to $L_{\text{max}} = 10$ inside the atomic spheres, while for plane wave cut off in the interstitial space $R_{\text{MT}} \times K_{\text{max}} = 6.0$ was used. The charge density Fourier series was truncated at $G_{\text{max}} = 16\sqrt{\text{Ry}}$ and the k -point sampling of

the irreducible Brillouin zone was $7 \times 7 \times 1$. For the exchange-correlation functional we employed the GGA variant of Perdew, Burke and Ernzerhof [3], and the rotationally invariant version of the LDA+ U method of Liechtenstein et al. [4] with the GGA instead of LSDA exchange-correlation potential and with single parameter $U_{\text{eff}} = U - J = 4.5$ eV applied to iron $3d$ orbitals.

For Sr and Ba hexaferrites we calculated structures with various volumes and c/a ratios near the equilibrium values. In each structure with given volume and c/a ratio the coordinates of atomic positions were relaxed with respect to minimizing the total energy and atomic forces. Subsequently, the spin-orbit coupling was introduced with magnetization parallel to the hexagonal axis in order to calculate the orbital and dipolar contributions to the hyperfine field on irons. The contact hyperfine fields on iron nuclei were evaluated using a semi-empirical method [5] based on calculated magnetic moments of $3d$ and $4s$ electrons of the Fe atoms. In addition to hyperfine fields, the dipolar fields on iron nuclei due to dipole-dipole interaction with the off-site atomic moments were calculated by direct summation within a sphere of radius 256 a.u.

Space group of M-type hexaferrite, $\text{LFe}_{12}\text{O}_{19}$, is $P6_3/mmc$. Large cations ($L = \text{Ba}$ or Sr) are in 2d sites, ferric cations occupy five different crystallographic sites: octahedral 2a, 4f₂ and 12k, tetrahedral 4f₁ and bipyramidal 2b. Oxygens occupy five non-equivalent sites 4e, 4f, 6h, 12k₁, and 12k₂. The magnetic structure is collinear ferrimagnetic with easy direction of magnetization along the hexagonal axis. The magnetic moments of Fe(f₁) and Fe(f₂) are oriented opposite to those of Fe(k), Fe(a) and Fe(b).

3. Results and discussion

The dependences of total energy on c/a ratio and on volume (Fig. 1) were studied in the range of 5% change of volume and 15% of c/a , while the symmetry of the structure was kept unchanged. The calculated equilibrium lattice parameters, i.e., parameters of structure with the minimum total energy, are displayed in Table I together with experimental values. Difference between the experimental [6, 7] and the calculated unit cell volume (4.7% for

*corresponding author; e-mail: vojtech.chlan@mff.cuni.cz

SrM and 6.0% for BaM) is expectable since the gradient correction acts as an isotropic negative pressure, and thus GGA overestimates the volume by several percent [8]. Very good agreement of c/a ratio was reached for SrM, while the difference is larger yet below 1% for BaM.

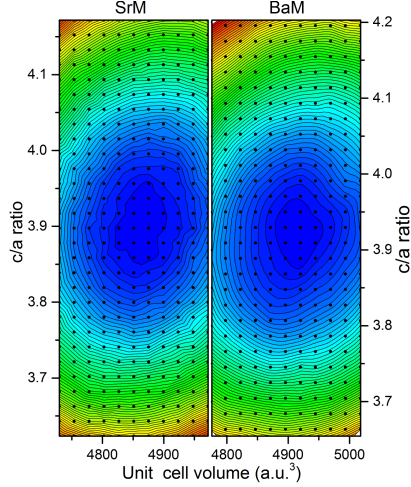


Fig. 1. Plot of total energy in dependence on unit cell volume and c/a ratio for Sr and Ba hexaferrites. Black dots represent structural parameters of the actual calculations. The step in energy, represented by lines and colour change, is 25 meV.

TABLE I

Calculated and experimental (at 4.2 K) lattice parameters, volumes and c/a ratios.

Structure	a [Å]	c [Å]	V [Å ³]	c/a
SrM (calc.)	5.9618	23.3533	718.85	3.9171
SrM (exp.) [6]	5.8758	22.958	686.43	3.9072
BaM (calc.)	5.9941	23.4315	729.09	3.9091
BaM (exp.) [7]	5.865	23.099	688.11	3.9385

Of interest are dependences of hyperfine fields on either volume or c/a ratio. Since these are not entirely independent (e.g., for high c/a deformation the most favourable volume is slightly different from the equilibrium value), we constructed the dependences as paths with minimum energy: in each point of dependence on volume we used the c/a ratio with minimum total energy and vice versa. How the hyperfine fields on iron nuclei react to changes of volume or c/a ratio is plotted in Fig. 2. The hyperfine fields on ^{57}Fe nuclei show varying dependences on c/a ratio, while the volume dependences are weak — only Fe(b) field displays mild decrease with increasing volume.

By analysing separately the dependences of individual contributions to hyperfine field on performed deformations, we found that the contribution of core $1s$, $2s$ and $3s$ electrons to contact field, orbital and dipolar terms and lattice dipolar field exhibited variations below 1%. On the other hand, the contact field due to the valence $4s$ electrons varied dramatically and was almost solely responsible for all observed changes. For explanation we analysed the impact of deformation on the local structure in more detail.

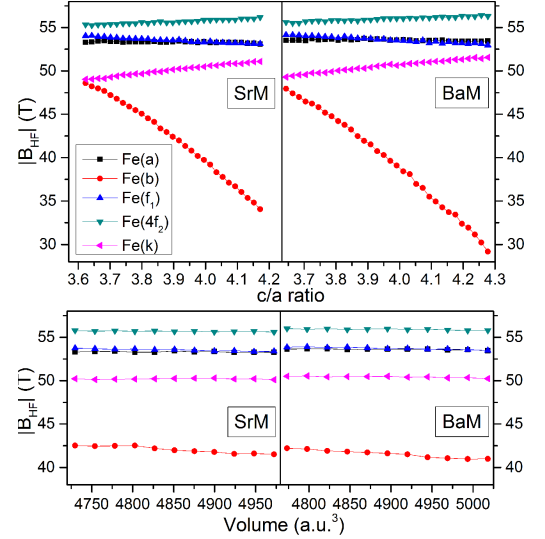


Fig. 2. Absolute values of the total hyperfine fields on iron nuclei are displayed in dependence on volume and c/a ratio of the unit cell for Ba and Sr hexaferrites.

The contribution of $4s$ electrons to the contact field arises due to supertransferred hyperfine field (STHF) and polarisation effects originating in Fe–O covalence [9, 10]. The STHF is produced by overlap of the Fe s states with oxygen orbitals (polarised by the transfer to unoccupied $3d$ states of neighbouring Fe) and by the electron transfer from $3d$ shell of the neighbouring Fe via shared oxygen ligand. Both transfers enhance the density of spins antiparallel to the $3d$ spins, and therefore, the STHF increases the total hyperfine field. The oxygen influence manifests also by two transfers: from oxygen neighbour to empty Fe $3d$ orbital and from oxygen to Fe $4s$ orbital. The first transfer must be weak in our case since the core contributions are almost intact. The latter one, however, produces strong polarisation directed opposite to the core contributions, thus effectively reducing the total hyperfine field.

In order to evaluate the impact of these contributions on hyperfine fields we have to analyse the geometry of the surroundings of the particular iron. The strong effect of Fe–O covalency on the hyperfine field is governed by the interatomic distance, while the STHF is influenced by the local geometry in a more subtle way, but in analogy with superexchange interaction. This allows us to limit our analysis to such Fe–O–Fe triads, where there is some substantial exchange interaction present. The triads in question are Fe(a)–O(k_1)–Fe(f_1), Fe(b)–O(h)–Fe(f_2), and Fe(f_2)–O(k_2)–Fe(k) where the exchange is very strong, Fe(f_1)–O(k_1)–Fe(k) and Fe(f_1)–O(f_2)–Fe(k) with intermediate strengths and perhaps also Fe(b)–O(e)–Fe(k) with rather a weak exchange interaction [11]. Table II lists how geometric properties of these triads develop throughout the full range of applied c/a deformation and in the following text we discuss how these changes affect the hyperfine fields. The analysis is done for SrM since the results for BaM are the same in essence.

TABLE II

Nearest neighbours and their numbers are displayed, together with percentage changes to bond lengths and angles in Fe–O_{NN}–Fe_{NN} triads due to 15% increase of c/a ratio of Sr hexaferrite. Triads with intermediate or weak superexchange interaction are in parenthesis. *) denotes equilibrium Fe–O distances.

Fe	# O _{NN}	Fe–O _{NN} dist. *) [Å]	Fe–O _{NN} change [%]	# Fe _{NN}	O _{NN} –Fe _{NN} change [%]	Triad angle change [%]
a	6 O(k ₁)	2.0315	+0.5	6 f ₁	–1.1	–6.9
b	3 O(h)	1.8808	–3.2	6 f ₂	+1.5	–3.0
	2 O(e)	2.2875	+14.3	(6 k)	–2.0	+6.5
f ₁	1 O(f)	1.9200	+3.1	(3 k)	–0.8	+3.4
	3 O(k ₁)	1.9264	–1.1	3 a	+0.5	–6.9
f ₂	3 O(h)	2.0828	+1.5	(6 k)	+1.2	+3.7
	3 O(k ₂)	1.9937	–1.4	3 b	–3.2	–3.0
k	1 O(e)	2.0079	–2.0	6 k	+0.3	+2.3
	1 O(f)	2.1140	–0.8	(1 b)	+14.3	+6.5
	2 O(k ₁)	2.1414	+1.2	(1 f ₁)	+3.1	+3.4
	2 O(k ₂)	1.9533	+0.3	(3 f ₁)	–1.1	+3.7
				2 f ₂	–1.4	+2.3

Small expansion of Fe(a) oxygen octahedron weakens slightly the covalence of the Fe–O bond and increases the total hyperfine field. This is however compensated by reducing of the STHF: lowering of the angle and increase of its bond-length asymmetry weakens the exchange polarization from neighbouring Fe(f₁). The resulting change of the contact field thus should be small, which is in agreement with constant dependence in Fig. 2.

In case of Fe(b) the three already very short Fe(b)–O(h) bonds become even shorter and more covalent, while the influence of distant O(e) can be neglected. The STHF from Fe(b)–O(h)–Fe(f₂) triad is reduced due to lower angle and increase of the asymmetry, and additionally, the weak negative effect to STHF from Fe(k) diminishes. All these effects add up and reduce strongly the total field of Fe(b).

Polyhedra of f₁ and f₂ irons deform substantially, however, the effects of Fe–O covalence quite precisely compensate. The change of the total field is thus determined by STHF, which is lowered for f₁ due to weakening of Fe(f₁)–O(k₁)–Fe(a) polarisation and raised for f₂ since the polarisation from Fe(k) is enhanced whereas the polarisation from Fe(b) is diminished only slightly.

For Fe(k) the influences of oxygen transfer again compensate and the prevailing STHF is increased due to improved interactions with f₁ and f₂ — in agreement with increase of the total hyperfine field on Fe(k) in Fig. 2.

Analogous discussion for volume deformation is more straightforward. The oxygen polyhedra are inflated and Fe–O distances increase by 1.7% on average, which decreases the covalence character of the bond and thus decreases the polarization of 4s electrons. However, this is

quite well compensated by lower STHF due to stretching of the Fe–O–Fe triads, with exception of Fe(b) where the bipyramid also elongates with increasing volume, and thus the hyperfine field slightly decreases, similarly as for c/a deformation.

Our qualitative analysis can also explain why in NMR experiment the hyperfine field of Fe(b) in BaM is by 0.9 T lower than field in SrM at 4.2 K [12]. The bipyramid in BaM is more expanded than in SrM: the key distance Fe(b)–O(h) is 1.8904 Å (1.8807 Å for SrM). In SrM structure such value would correspond to c/a ratio lower by –1.5% which would have the hyperfine field lower by about 1.4 T.

4. Conclusions

Lattice deformations of Sr and Ba hexaferrites lead to changes in valence part of the contact hyperfine field, which were explained by analysing the connection between geometry of the Fe–O–Fe triads and polarisation effects originating in Fe–O–Fe supertransfer and Fe–O covalence.

Acknowledgments

V.Ch. acknowledges support by the project P204-12-P352 of the Grant Agency of the Czech Republic. Access to computing and storage facilities owned by parties and projects contributing to the National Grid Infrastructure MetaCentrum, provided under the programme “Projects of Large Infrastructure for Research, Development, and Innovations” (LM2010005), is greatly appreciated.

References

- [1] J. Buršík, I. Drbohlav, Z. Frait, K. Knížek, R. Kužel, K. Kouřil, *J. Solid State Chem.* **184**, 3085 (2011).
- [2] P. Blaha, K. Schwarz, G.K.H. Madsen, D. Kvasnicka, J. Luitz, *WIEN2k, An Augmented Plane Wave Local Orbitals Program for Calculating Crystal Properties*, Karlheinz Schwarz, Techn. Universität Wien, Austria 2001.
- [3] J.P. Perdew, S. Burke, M. Ernzerhof, *Phys. Rev. Lett.* **77**, 3865L (1996).
- [4] A.I. Liechtenstein, V.I. Anisimov, J. Zaanen, *Phys. Rev. B* **52**, R5467 (1995).
- [5] P. Novák, V. Chlan, *Phys. Rev. B* **81**, 174412 (2010).
- [6] J. Muller, A. Collomb, *J. Magn. Magn. Mater.* **103**, 194 (1992).
- [7] A. Collomb, P. Wolfers, X. Obradors, *J. Magn. Magn. Mater.* **62**, 57 (1986).
- [8] J. Goniakowski, J.M. Holender, L.N. Kantorovich, M.J. Gillan, *Phys. Rev. B* **53**, 957 (1996).
- [9] Nai Li Huang, R. Orbach, E. Šimánek, *Phys. Rev. Lett.* **17**, 134 (1966).
- [10] F. van der Woude, G.A. Sawatzky, *Phys. Rev. B* **4**, 3159 (1971).
- [11] V. Procházka, H. Štěpánková, J. Štěpánek, A. Snezhko, V. Chlan, K. Kouřil, *Acta Phys. Slov.* **56**, 165 (2006).
- [12] H. Štěpánková, J. Englich, P. Novák, D. Sedlák, M. Pfeffer, *Hyperfine Interact.* **50**, 639 (1989).



Hyperfine interactions in magnetoelectric hexaferrite system

Karel Kouřil^a, Vojtěch Chlan^a, Helena Štěpánková^a, Pavel Novák^{b,*}, Karel Knížek^b, Jiří Hybler^b, Tsuyoshi Kimura^c, Yuji Hiraoka^c, Josef Buršík^d

^a Charles University in Prague, Faculty of Mathematics and Physics, V Holešovičkách 2, 180 00 Prague 8, Czech Republic

^b Institute of Physics ASCR, Cukrovarnická 10, 162 53 Prague 6, Czech Republic

^c Graduate School of Engineering Science, Osaka University, Toyonaka, Osaka 560-8531, Japan

^d Institute of Inorganic Chemistry ASCR, 250 68 Řež, Czech Republic

ARTICLE INFO

Available online 16 March 2009

Keywords:

Multiferroics

Hexaferrites

Nuclear magnetic resonance

ABSTRACT

Nuclear magnetic resonance (NMR) in Y-hexaferrite system $(\text{Ba}_{1-x}\text{Sr}_x)_2\text{Zn}_2\text{Fe}_{12}\text{O}_{22}$ was measured on both monocrystalline and polycrystalline samples at liquid helium temperature. Corresponding *ab-initio* calculation of the hyperfine parameters was also performed. The signal from ^{57}Fe was detected in the frequency interval 65–76 MHz, while NMR spectrum of ^{67}Zn nuclei occurs between 15 and 30 MHz. Due to the disorder in two tetrahedral sublattices occupied partly by Zn and partly by Fe, the NMR lines are broad and the spectra are poorly resolved. Comparison between the experimentally observed ^{67}Zn spectra and the spectra modelled using the calculated hyperfine parameters was made. It indicates that the spectra of ^{67}Zn can be used to determine the distribution of Zn and Fe between the two tetrahedral sublattices.

© 2009 Elsevier B.V. All rights reserved.

1. Introduction

Discovery of ferroelectricity in a Y-type hexaferrite system $(\text{Ba}_{1-x}\text{Sr}_x)_2\text{Zn}_2\text{Fe}_{12}\text{O}_{22}$ for $x = 0.75$ was reported in [1]. In the zero magnetic field $\text{Ba}_{0.5}\text{Sr}_{1.5}\text{Zn}_2\text{Fe}_{12}\text{O}_{22}$ is a nonferroelectric insulator with noncollinear spin arrangement. In the applied field it undergoes several phase transitions and some of the phases exhibit ferroelectricity. The magnetic transition temperature is ~ 326 K and the phases that exhibit the ferroelectricity persist up to the room temperature. Thus in principle, the system may possess both magnetism and ferroelectricity above the room temperature. This promises important applications, but two problems hinder them. First, the electrical conductivity that increases with increasing temperature prevents the ferroelectricity above ≈ 130 K. Second, the occurrence of the ferroelectricity is rather susceptible to the composition and details of the preparation.

The crystal structure of the Y-type hexaferrite consists of the spinel (S) and T blocks alternating along the hexagonal axis (Fig. 1). The iron occupies fully four octahedral sublattices, tetrahedral sublattice in the S block contains fraction γ of Zn and $1-\gamma$ of Fe, while the opposite holds for the tetrahedral sublattice of the T block. Neutron diffraction carried out recently on a number of single crystals with $0 < x < 0.8$ [2] yielded γ between 0.65 and 0.82, though other values of γ were reported earlier (see [3] for a list).

Our recent calculations [3,4] of the electronic structure indicated that the occurrence of ferroelectricity, and to a smaller extent also the electrical conductivity, are sensitive to the value of γ . Theoretical prediction is that for multiferroicity to occur γ should be close to $\frac{1}{2}$. The distribution may be, at least in principle, changed by a thermal treatment, but a reliable experimental method is needed to determine the change of γ . Nuclear magnetic resonance (NMR) is well suited for this purpose, as the NMR lines originating from nuclei in different sublattices will have different resonance frequency and the integrated signal is proportional to the number of resonating nuclei. The purpose of this work is to study NMR in the $(\text{Ba}_{1-x}\text{Sr}_x)_2\text{Zn}_2\text{Fe}_{12}\text{O}_{22}$ in order to find out whether NMR could be used to determine γ . In this paper our attention is focused on the $x = 0$ compound, though the compositions close to Sr concentration for which the multiferroic behavior occur were also studied. The $\text{Ba}_2\text{Zn}_2\text{Fe}_{12}\text{O}_{22}$ compound was chosen because there is no disorder in the sublattice of the large cations and the spin arrangement is collinear, making the analysis of the NMR spectra simpler.

2. Experimental

Powder samples have been prepared by the Pecchini process: using solution of metal ions prepared by decomposition of $\text{Fe}(\text{NO}_3)_3 \cdot 9\text{H}_2\text{O}$, BaCO_3 , SrCO_3 and ZnO , mixed with citric acid–diethylenglycol solution clear and transparent gel has been obtained. This polymeric gel has been converted into crystalline

* Corresponding author. Tel.: +420 220 318 532.

E-mail address: novakp@fzu.cz (P. Novák).

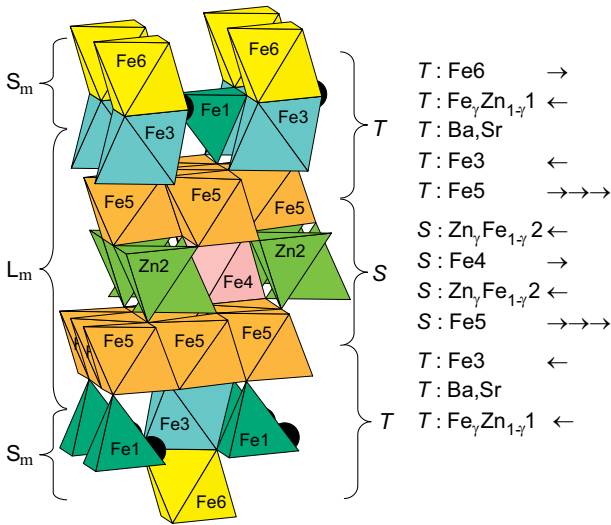


Fig. 1. One formula unit of $(\text{Ba}_{1-x}\text{Sr}_x)_2\text{Zn}_2\text{Fe}_{12}\text{O}_{22}$ structure. Shown are Fe and Zn polyhedra and the sites of the large cations (black bullets). The arrows indicate directions of spins corresponding to the $x = 0$ collinear ferrimagnetic structure.

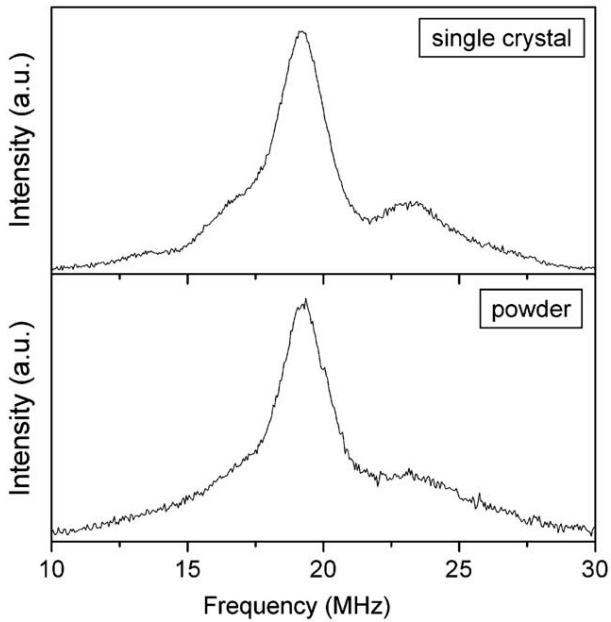


Fig. 2. NMR spectrum of ^{67}Zn in single crystal and powder samples of $\text{Ba}_2\text{Zn}_2\text{Fe}_{12}\text{O}_{22}$ in zero external magnetic field at 4.2 K.

powder by proper heat treatment. Single-crystal samples have been prepared by a $\text{Na}_2\text{O}-\text{Fe}_2\text{O}_3$ flux technique in Pt crucibles [5].

The NMR spectra were measured by the spin-echo method using the phase-coherent pulse spectrometer with averaging technique and Fourier transform. The signal-to-noise ratio was significantly improved by using the Carr–Purcell pulse sequence.

A strong NMR signal was detected at 4.2 K and zero external field for frequencies between 65 and 78 MHz. It consists of several unresolved spectral lines and comparison with NMR in other hexaferrites [6] shows that it originates from the ^{57}Fe nuclei. Much weaker signal corresponding to ^{67}Zn was found between 10 and 30 MHz. For a single crystal and polycrystalline sample this NMR spectrum is shown in Fig. 2.

Table 1

Hyperfine field and electric field gradient for Zn in tetrahedral sublattice of block T and S.

Block	γ	n_T	n_S	B_{hf} (T)	EFG (10^{21} V/m ²)
T	0	0	3	11.65	3.38
T	$\frac{1}{2}$	3	3	10.17	2.83
S	$\frac{1}{2}$	3	3	9.73	1.77
S	1	3	0	9.64	2.22

n_T , (n_S) is number of iron neighbors in the nearest sites belonging to tetrahedral sublattices in T and S block.

3. Modelling NMR spectra of ^{67}Zn

To calculate the electronic structure of $\text{Ba}_2\text{Zn}_2\text{Fe}_{12}\text{O}_{22}$ we employed the density functional theory as implemented in the WIEN2k program [7]. All computational parameters were the same as in our previous paper [3]. Sites in both tetrahedral sublattices have an axial symmetry with the axis parallel to c . The contact contribution to the hyperfine field, as well as the electric field gradient, is calculated routinely by the WIEN2k program and the results for the Zn ions are given in Table 1.

Neglecting the anisotropy of the hyperfine field, the Hamiltonian that describes the nuclear energy levels is

$$H = \gamma_n \hbar B I + C_q [3I_z^2 - I(I+1)], \quad (1)$$

where $\gamma_n = 1.677 \text{ rad T}^{-1} \text{ s}^{-1}$ is the nuclear gyromagnetic factor of the ^{67}Zn nuclei, $I = \frac{5}{2}$ is the nuclear spin of ^{67}Zn , B is the magnetic field on the nucleus consisting of the external and hyperfine field, the parameter C_q is given by

$$C_q = eQV_{zz}/[4I(2I-1)], \quad (2)$$

where V_{zz} is the electric field gradient (Table 1) and $Q = 15.10^{-26} \text{ m}^2$ is the electric quadrupole moment of ^{67}Zn .

In $(\text{Ba}_{1-x}\text{Sr}_x)_2\text{Zn}_2\text{Fe}_{12}\text{O}_{22}$ the magnetization is in the c plane. The Hamiltonian (1) is diagonalized, from the differences of eigenenergies the resonance frequencies are determined and, using the eigenvectors, relative amplitudes of the transitions are computed. The remaining problem is that while the distribution of Fe and Zn in the tetrahedral sublattices is random, hyperfine field and V_{zz} were calculated for two configurations only: 3 nearest neighbor sites occupied by Zn ($V_{zz}^{(0)}$) or by Fe ($V_{zz}^{(3)}$). To obtain V_{zz} for the remaining configurations we use a ‘superposition model’ approximation

$$V_{zz}^{(1)} = (2V_{zz}^{(0)} + V_{zz}^{(3)})/3, \quad V_{zz}^{(2)} = (V_{zz}^{(0)} + 2V_{zz}^{(3)})/3, \quad (3)$$

for configurations of neighbors (2 Zn, 1 Fe) and (2 Fe, 1 Zn), respectively. Analogously the hyperfine field is treated. Finally, the amplitudes are multiplied by binomical coefficients corresponding to random distribution of Fe and Zn and the lines are broadened using the Gaussian distribution (the linewidth assumed to be the same for all transitions).

4. Discussion and conclusions

The ^{57}Fe signals from the six sublattices overlap strongly, and it would be difficult to separate the contributions from the two tetrahedral sublattices, i.e. determination of γ from ^{57}Fe NMR would hardly be possible. The situation with NMR of ^{67}Zn is more promising. To this signal contribute the nuclei from two sublattices only and the spectrum has a clear structure (Fig. 2). In Fig. 3 the spectrum, calculated as described above for $\gamma = \frac{1}{2}$ is displayed. It is seen that the form of observed and calculated spectra are similar, but the calculated spectrum is shifted to

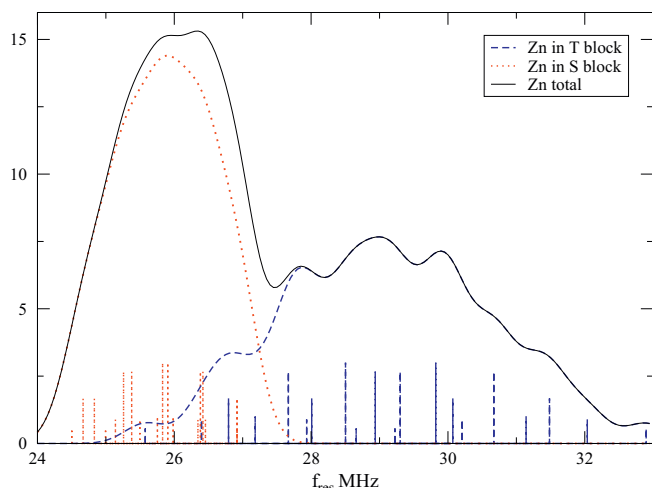


Fig. 3. NMR spectrum of ^{67}Zn in $\text{Ba}_2\text{Zn}_2\text{Fe}_{12}\text{O}_{22}$ with $\gamma = \frac{1}{2}$ modelled using the *ab-initio* calculated parameters (full curve). Dashed and dotted curves are the contributions of Zn in the *T* and *S* blocks, respectively. Vertical lines depict individual transitions.

higher frequencies. The reason may be that the crystal structures used in calculation were not relaxed, i.e. the local environments of tetrahedral Zn^{2+} and Fe^{3+} were assumed to be the same. Ionic radius of Zn^{2+} (0.083 nm) is considerably bigger than the one of Fe^{3+} (0.067 nm). Thus the Zn–O distances will be larger than those assumed and, as a consequence, the transferred field will be

smaller. The spectrum of Zn in the *T* block is at higher frequencies and it is broader than the one of Zn in the *S* block.

Both experimental and calculated spectra of ^{67}Zn display similar features and enable to distinguish two contributions arising from the tetrahedral sites in the *T* and *S* block. Therefore, the changes of the parameter γ in dependence on sample preparation conditions or thermal treatment will lead to measurable effects in the ^{67}Zn NMR spectra. In conclusion we showed that NMR of ^{67}Zn can be used to determine the distribution of Fe and Zn in the studied system.

Acknowledgements

This work was supported by the Project IAA100100803 of the Grant Agency of the AS CR and Program Kontakt ME08059. The authors acknowledge the support by project LUNA with the help of which the calculations were performed.

References

- [1] T. Kimura, G. Laves, A.P. Ramirez, *Phys. Rev. Lett.* 94 (2005) 137201.
- [2] S. Utsumi, D. Yoshida, N. Momozawa, *J. Phys. Soc. Jpn.* 76 (2007) 034704.
- [3] P. Novák, K. Knížek, J. Ruzs, *Phys. Rev. B* 76 (2007) 024432.
- [4] K. Knížek, P. Novák, M. Kűpferling, *Phys. Rev. B* 73 (2006) 153103.
- [5] N. Momozawa, M. Mita, H. Takei, *J. Cryst. Growth* 83 (1987) 403.
- [6] H. Štěpánková, J. Englich, M. Nejezchleba, J. Kohout, H. Lűtgemeier, *J. Magn. Mater.* 157/158 (1996) 393.
- [7] P. Blaha, K. Schwarz, G. K. H. Madsen, D. Kvasnicka, J. Luitz, *WIEN2k, An Augmented Plane Wave+Local Orbitals Program for Calculating Crystal Properties*, Karlheinz Schwarz, Techn. Universität Wien Austria, 2001.

Distribution of Zn in Magnetoelectric Y-Type Hexaferrite

K. KOUŘIL^{a,*}, V. CHLAN^a, H. ŠTĚPÁNKOVÁ^a, A. TELFAH^a, P. NOVÁK^b, K. KNÍŽEK^b,
Y. HIRAOKA^c AND T. KIMURA^c

^aCharles University in Prague, Faculty of Mathematics and Physics

V Holešovičkách 2, 18000, Praha 8, Czech Republic

^bInstitute of Physics ASCR, Cukrovarnická 10, 162 53 Praha, Czech Republic

^cDivision of Materials Physics, Graduate School of Engineering Science, Osaka University

Toyonaka, Osaka 560–8531, Japan

We employ ^{67}Zn NMR to study distribution of Zn^{2+} in cationic sites of magnetoelectric Y-type hexaferrite single crystal, $\text{Ba}_{0.5}\text{Sr}_{1.5}\text{Zn}_2\text{Fe}_{12}\text{O}_{22}$. The experimental data are interpreted by comparison with NMR spectra simulated from *ab initio* calculated hyperfine parameters.

PACS numbers: 61.05.Qr, 75.85.+t, 75.50.Gg, 31.15.E–

1. Introduction

Y-type hexaferrite $\text{Ba}_{0.5}\text{Sr}_{1.5}\text{Zn}_2\text{Fe}_{12}\text{O}_{22}$ is a non-collinear insulating ferrimagnet, which in external magnetic field undergoes several phase transitions. One of the phases is known to exhibit magnetoelectricity at low temperatures [1]. It is promising that this phase persists up to room temperature [2], however, electrical conductivity increases rapidly with temperature, soon concealing the ferroelectric order.

Y-type hexaferrite structure contains four octahedral and two tetrahedral sites occupied by small cations. The octahedral sites are fully occupied by Fe^{3+} , while the tetrahedral sites contain both Fe^{3+} and Zn^{2+} . The crystal structure can also be viewed as built of alternating spinel (S) and T blocks stacked along the hexagonal axis [3]. Each block contains one type of the tetrahedral site. The distribution of Zn^{2+} and Fe^{3+} between the blocks is described by parameter γ : S block contains γ of Zn^{2+} and $(1 - \gamma)$ of Fe^{3+} , while the opposite holds for the T block.

Magnetoelectricity is sensitive to fine alterations of the system, e.g. changes of composition (Ba:Sr ratio), stoichiometry (oxygen content) and cation distribution (γ). It is desirable to explore possibilities of determination and control of these parameters. In this work we focus on the determination of the γ parameter, which is expected to have a strong influence on electrical conductivity of the system [4]. We employed nuclear magnetic resonance of ^{67}Zn nuclei in order to estimate γ and its changes induced by thermal treatment. Further we performed

ab initio calculations of $\text{Ba}_2\text{Zn}_2\text{Fe}_{12}\text{O}_{22}$ electronic structure, which provided us with insight into the experimental data.

2. Experimental

Single crystal of $\text{Ba}_{0.5}\text{Sr}_{1.5}\text{Zn}_2\text{Fe}_{12}\text{O}_{22}$ was prepared using $\text{Na}_2\text{O}-\text{Fe}_2\text{O}_3$ flux technique in Pt crucibles [5] and cut into two parts of approximately same size. One part was annealed for 7 days in oxygen atmosphere at 900 °C and then slowly cooled (1 °C per minute), while the other part was left as grown for reference. Finally plane parallel plates (≈ 0.5 mm thick and with areas of ≈ 5 mm²) were prepared from each part. Both plates were characterized by NMR.

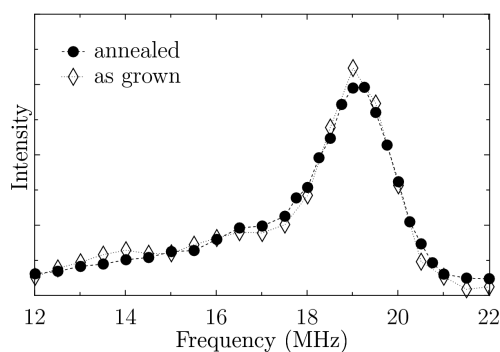


Fig. 1. Experimental NMR spectra of ^{67}Zn . The spectra have been normalized to unit area.

We used pulse coherent NMR spectrometer with the Fourier transform (Bruker Avance) and a homemade tunable NMR probe to measure frequency-swept spectra of

* corresponding author; e-mail: karel.kouril@mff.cuni.cz

^{67}Zn resonance. The spectra were recorded at 4.2 K in zero static external field, rf field was perpendicular to the hexagonal plane of the sample. Experimental NMR spectra of ^{67}Zn resonance are shown in Fig. 1.

3. Simulation of ^{67}Zn NMR spectra

In order to extract the parameter γ from experiment we simulated NMR spectra for various values of γ . The simulations were based on *ab initio* calculations of electron structure of $\text{Ba}_2\text{Zn}_2\text{Fe}_{12}\text{O}_{22}$ using WIEN2k [6]. In contrast to our previous paper [7] the crystal structure was fully relaxed — both lattice parameters (c/a and unit cell volume) and internal structural parameters were optimized. The hyperfine magnetic fields and electric field gradients on Zn nuclei were calculated for $\gamma = 0, 1/2, 1$ and linearly interpolated in between. The NMR spectra were simulated from energies and relative intensities of ^{67}Zn nuclear magnetic transitions with suitable line broadening. Simulated NMR ^{67}Zn spectra for varying γ are shown in Fig. 2 with contributions of S and T blocks denoted.

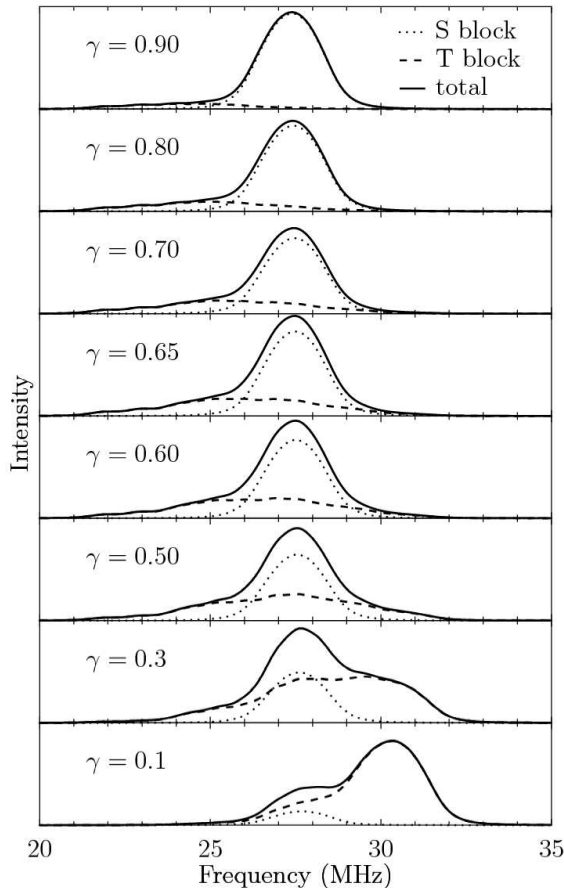


Fig. 2. Simulated ^{67}Zn NMR spectra for various values of γ parameter.

4. Results

The experimental ^{67}Zn NMR spectra (Fig. 1) resemble the shape of simulated NMR profiles (Fig. 2), allowing direct comparison despite the shifted frequency scale. The calculations have shown that resulting ^{67}Zn NMR lineshapes consist of two overlapping components: a narrow one, originating from resonance of the nuclei in the S block, and a broad one, from the nuclei in the T block. Further one can see that the position and width of the S block contribution is nearly insensitive to the value of γ , while the T block contribution varies significantly. The dependence of the spectral shape on γ can be used to determine its value from an experimental lineshape. The experimental data can thus be assigned to the simulated spectrum of $\gamma \approx 0.65$.

5. Conclusions

Comparison of measured NMR spectra and simulated lineshapes based on *ab initio* calculated hyperfine parameters enabled us to estimate the value of the γ parameter. The differences in experimental spectra induced by the performed thermal treatment are subtle and the change of γ probably does not exceed 10%.

Acknowledgments

This work was supported by the project IAA100100803 of the Grant Agency of the AS CR and by the project MS0021620834 of the Ministry of Education of the Czech Republic. The calculations were performed using *dorje* cluster at Institute of Physics of the AS CR.

References

- [1] T. Kimura, G. Lawes, A.P. Ramirez, *Phys. Rev. Lett.* **94**, 137201 (2005).
- [2] Y.S. Chai, S.H. Chun, S.H. Haam, Y.S. Oh, I. Kim, K.H. Kim, *New J. Phys.* **11**, 073030 (2009).
- [3] M. Sugimoto, in: *Ferromagnetic Materials*, Ed. E.P. Wolfarth, Vol. 3, North-Holland, Amsterdam 1982, p. 397.
- [4] K. Knížek, P. Novák, M. Küpferling, *Phys. Rev. B* **73**, 153103 (2006).
- [5] N. Momozawa, M. Mita, H. Takei, *J. Cryst. Growth* **83**, 403 (1983).
- [6] P. Blaha, K. Schwarz, G.K.H. Madsen, D. Kvasnicka, J. Luitz, *WIEN2k, An Augmented Plane Wave+Local Orbitals Program for Calculating Crystal Properties*, Karlheinz Schwarz, Techn. Universität Wien, Austria 2001.
- [7] K. Kouřil, V. Chlan, H. Štěpánková, P. Novák, K. Knížek, J. Hybler, T. Kimura, Y. Hiraoka, J. Buršík, *J. Magn. Magn. Mater.* **322**, 1243 (2010).

Study of Y-type Hexaferrite by Means of ^{57}Fe NMR and Electronic Structure Calculations

V. CHLAN*, K. KOUŘIL, H. ŠTĚPÁNKOVÁ, R. ŘEZNÍČEK, J. ENGLISH

Faculty of Mathematics and Physics, Charles University in Prague, V Holešovičkách 2, Prague, Czech Republic

The electron structure and site preferences of Zn and Fe cations in Y hexaferrite system were calculated. The hyperfine magnetic fields on ^{57}Fe nuclei were determined using WIEN2k and corrections for hyperfine contact interaction. The calculated fields were compared to ^{57}Fe nuclear magnetic resonance (NMR) experiment in $\text{Ba}_2\text{Zn}_2\text{Fe}_{12}\text{O}_{22}$ single crystal with an aim of interpretation of experimental NMR spectrum.

DOI: [10.12693/APhysPolA.126.42](https://doi.org/10.12693/APhysPolA.126.42)

PACS: 61.05.Qr, 75.85.+t, 75.50.Gg, 31.15.E–

1. Introduction

Observation of magnetoelectric coupling in Y type hexaferrite system $\text{Ba}_{0.5}\text{Sr}_{1.5}\text{Zn}_2\text{Fe}_{12}\text{O}_{22}$ reported by [1] rekindled interest in these hexaferrite systems. Electronic structure calculations of band gap [2] have indicated that distribution of zinc in hexaferrite structure could play an important role in emergence of magnetoelectricity. We present a study performed mainly on related Y type compound $\text{Ba}_2\text{Zn}_2\text{Fe}_{12}\text{O}_{22}$ with identical crystal structure, but without Ba-Sr disorder in large cation sublattice. Such a simplification allows us to calculate the hyperfine fields on ^{57}Fe nuclei. Comparison of calculated and measured ^{67}Zn NMR spectra was accomplished recently [3, 4].

Crystal structure of Y type hexaferrite is formed by stacking of two types of structural blocks (S and T) along hexagonal axis, one unit cell contains three formula units. Ferric ions occupy six positions, four octahedral ($3b_{VI}$ and $6c_{VI}$ in T block, $3a_{VI}$ in S block and $18h_{VI}$ shared by adjacent S and T blocks) and partially with zinc two tetrahedral ($6c_{IV}$ in S block and $6c_{IV}^*$ in T block). The Fe/Zn distribution in tetrahedral sites can be described by parameter γ : fraction γ of Zn is in S blocks, and $1-\gamma$ is in T blocks. Magnetic structure of studied Y-type hexaferrite is collinear, the moments of ferric ions in $3a_{VI}$, $18h_{VI}$ and $3b_{VI}$ sites are parallel with total magnetization (spin up), while those in $6c_{IV}$, $6c_{IV}^*$ and $6c_{VI}$ are antiparallel (spin down). Magnetocrystalline anisotropy is of easy plane type, magnetization is perpendicular to hexagonal c-axis.

2. Methods

The electronic structures of Ba and Sr hexaferrites were calculated using the augmented plane waves and local orbital method, based on the density functional theory (DFT) as implemented in the WIEN2k program [5]. For the exchange-correlation functional the generalized gradient approximation (GGA) form [6] was adopted. To improve the description of iron 3d electron correlations

we used the rotationally invariant version of the LDA+U method as described by Liechtenstein et al. [7], with the GGA instead of LSDA exchange-correlation potential and with a single parameter $U_{\text{eff}} = U - J$. The radii of the atomic spheres were chosen as 2.5 a.u. for large cations (Ba, Sr), 2.0 a.u. for small cations (Fe, Zn) and 1.5 a.u. for oxygens. The number of the basis functions was 95/atom ($RK_{\text{max}} = 6.0$), and the charge density was Fourier expanded to $G_{\text{max}} = 16 \sqrt{Ry}$. The number of k-points in irreducible part of Brillouine zone was 10 (20 for BaSrY case). $U_{\text{eff}} = 4.5$ eV was used for Fe and 6 eV for Zn. The atomic positions were optimized by minimizing the total energy and the atomic forces.

Single crystal sample of $\text{Ba}_2\text{Zn}_2\text{Fe}_{12}\text{O}_{22}$ was grown using $\text{Na}_2\text{O}-\text{Fe}_2\text{O}_3$ flux technique in Pt crucibles [8]. Frequency swept ^{57}Fe NMR spectra were recorded at 4.2 K in external magnetic fields from zero up to 1.5 T parallel with hexagonal axis of sample.

3. Results and discussion

It is well known that the DFT significantly underestimates the Fermi contact term of the hyperfine magnetic field at magnetic atoms. To correct for this error we obtained the NMR frequencies for Ba_2Y structures with $\gamma = 0$, $\gamma = 0.5$, and $\gamma = 1$ by applying procedure described in [9]. In this procedure the spin-orbit coupling was introduced which lowered the symmetry and some equivalent atoms became non-equivalent. Corrected contact field was summed with orbital and dipolar contributions to the hyperfine field and with dipolar magnetic field from the neighboring atoms (in sphere with 256 a.u. radius).

The calculated frequencies are summarized in Table I, together with frequencies for $\gamma = 0.65$ obtained from $\gamma = 0.5$ and $\gamma = 1$ by linear interpolation. One should note from Table I that the crystal sites are influenced differently by γ ; the resonance frequency of $3a_{VI}$ and $3b_{VI}$ lines depends strongly on γ while e.g., $18h_{IV}$ is practically unaffected. The value $\gamma = 0.65$ is taken from our previous ^{67}Zn NMR study [4] and matches well with a value of $\gamma = 0.62$ that would yield the best agreement for our current ^{57}Fe NMR data.

*corresponding author; e-mail: vojtech.chlan@mff.cuni.cz

TABLE I
Calculated resonance frequencies (in MHz, gyromagnetic ratio of ^{57}Fe is $1.38 \text{ MHz}\cdot\text{T}^{-1}$) for several values of γ and assigned resonance frequencies in experimental ^{57}Fe NMR spectra

Fe site	$\gamma = 0$	$\gamma = 0.5$	$\gamma = 1$	$\gamma = 0.65$	NMR
$6c_{IV}(1)$	(zinc)	70.37	72.65	71.05	69–70
$6c_{IV}(2)$	74.08	74.44	(zinc)	74.44	71–73
$6c_{VI}(1)$	74.07	74.38	71.41	73.49	71–73
$6c_{VI}(2)$		72.49		72.17	71–73
$3a_{VI}$	76.13	71.62	66.76	70.16	74.5
$18h_{VI}(1)$	68.80	67.72	68.87	68.07	69 ± 2
$18h_{VI}(2)$		68.72		68.76	
$18h_{VI}(3)$	69.72	69.46	69.62	69.51	69 ± 2
$18h_{VI}(4)$		70.87		70.49	
$18h_{VI}(5)$	68.65	69.92	68.09	69.37	69 ± 2
$18h_{VI}(6)$		69.61		69.15	
$3b_{VI}$	68.90	73.70	80.92	75.87	77.0

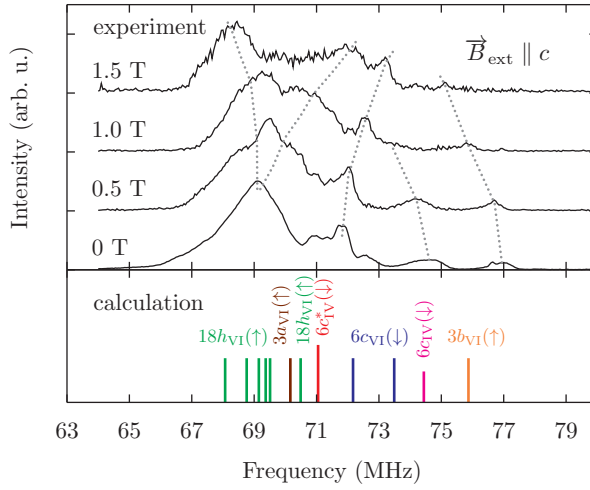


Fig. 1. Top: experimental ^{57}Fe NMR spectra of $\text{Ba}_2\text{Zn}_2\text{Y}$ in external magnetic fields up to 1.5 T at 4.2 K, dotted gray lines indicate shifts of resonance frequencies. Bottom: calculated resonance frequencies for $\gamma = 0.65$, height of the lines is proportional to NMR intensity. (See text for details).

The calculated frequencies for $\gamma = 0.65$ are displayed in Fig. 1 together with the experimental ^{57}Fe NMR spectra. By comparison of calculated frequencies with the NMR experiment we are able to assign all spectral lines to crystallographic positions. For the assignment we also used information on the spin orientation of individual sublattices from the shifts of spectral lines in applied external magnetic field. Shift to higher frequencies with increasing field indicates spin down sublattice and vice versa. We interpret the strong and broad signal centered at 69 MHz as overlapped resonances from $18h_{VI}$, $6c_{IV}$ and $6c_{VI}$ sublattices, peak at 71.8 MHz to $6c_{IV}^*$ sublattice, line at 74.5 MHz to $3a_{VI}$ and the line at 77 MHz to $3b_{VI}$.

In Table II we report the calculated total energies for nine hexaferrite structures with three Ba/Sr compositions and three different values of γ . The zinc preference for $6c_{IV}$ sites is relatively independent of the large cations.

TABLE II
Calculated difference ΔE in total energy per unit cell (in eV) is displayed as a function of γ for three Ba/Sr compositions. (For a given composition, ΔE are presented relative to the value for $\gamma = 1$)

	$\gamma = 0$	$\gamma = 0.5$	$\gamma = 1$
Ba_2Y	0.40	0.17	0.00
BaSrY	0.54	0.22	0.00
Sr_2Y	0.69	0.35	0.00

4. Conclusions

We calculated the electronic structure of $\text{Ba}_2\text{Zn}_2\text{Y}$ with various distributions of zinc between the tetrahedral sites, which allowed us to interpret the experimental ^{57}Fe NMR spectrum. The observed value of γ agreed with value obtained in previous ^{67}Zn NMR study [4].

Acknowledgments

V. Ch. acknowledges support by the project P204-12-P352 of the Grant Agency of the Czech Republic. R. Ř. thanks to SVV-2013-267303 and project GAUK no. 392111. We thank to prof. T. Kimura (Osaka University) for the hexaferrite sample. The access to computing and storage facilities owned by parties and projects contributing to the National Grid Infrastructure MetaCentrum, provided under the programme "Projects of Large Infrastructure for Research, Development, and Innovations" (LM2010005), is highly acknowledged.

References

- [1] T. Kimura, G. Lawes, A.P. Ramirez, *Phys. Rev. Lett.* **94**, 137201 (2005).
- [2] K. Knížek, P. Novák, and M. Küpferling, *Phys. Rev. B* **73**, 153103 (2006).
- [3] K. Kouřil, V. Chlan, H. Štěpánková, P. Novák, K. Knížek, J. Hybler, T. Kimura, Y. Hiraoka, J. Buršík, *J. Mag. Magn. Mater.* **322**, 1243 (2010).
- [4] K. Kouřil, V. Chlan, H. Štěpánková, A. Telfah, P. Novák, K. Knížek, Y. Hiraoka, T. Kimura, *Acta Phys. Pol. A* **118**, 732 (2010).
- [5] P. Blaha, K. Schwarz, G. K. H. Madsen, D. Kvasnicka, J. Luitz, *WIEN2k, An Augmented Plane Wave + Local Orbitals Program for Calculating Crystal Properties* Techn. Universität Wien, 2001 ISBN 3-9501031-1-2.
- [6] J.P. Perdew, K. Burke, M. Ernzerhof, *Phys. Rev. Lett.* **77**, 3865 (1996).
- [7] A.I. Liechtenstein, V.I. Anisimov, J. Zaanen, *Phys. Rev.* **52**, R5467 (1995).
- [8] N. Momozawa, M. Mita, H. Takei, *J. Cryst. Growth* **83**, 403 (1987).
- [9] P. Novák, V. Chlan, *Phys. Rev. B* **81**, 174412 (2010).

Hyperfine field and electronic structure of magnetite below the Verwey transition

R. Řezníček,* V. Chlan, and H. Štěpánková

Faculty of Mathematics and Physics, Charles University in Prague, V Holešovičkách 2, 180 00 Prague 8, Czech Republic

P. Novák

Institute of Physics, ASCR, Cukrovarnická 10, 162 00 Prague 6, Czech Republic

(Received 17 September 2014; revised manuscript received 12 January 2015; published 23 March 2015)

Magnetite represents a prototype compound with a mixed valence of iron cations. Its structure and electron ordering below the Verwey transition have been studied for decades. A recently published precise crystallographic structure [Senn *et al.*, *Nature (London)* **481**, 173 (2012)] accompanied by a suggestion of a “trimeron” model has given a new impulse to magnetite research. Here we investigate hyperfine field anisotropy in the *Cc* phase of magnetite by quantitative reanalysis of published measurements of the dependences of the ^{57}Fe nuclear magnetic resonance frequencies on the external magnetic field direction. Further, *ab initio* density-functional-theory-based calculations of hyperfine field depending on the magnetization direction using the recently reported crystal structure are carried out, and analogous hyperfine anisotropy data linked to particular crystallographic sites are determined. These two sets of data are compared, and mutually matching groups of the iron B sites in the 8:5:3 ratio are found. Moreover, information on electronic structure is obtained from the *ab initio* calculations. Our results are compared with the trimeron model and with an alternative analysis [Patterson, *Phys. Rev. B* **90**, 075134 (2014)] as well.

DOI: [10.1103/PhysRevB.91.125134](https://doi.org/10.1103/PhysRevB.91.125134)

PACS number(s): 31.30.Gs, 71.15.Mb, 76.60.-k

I. INTRODUCTION

Magnetite is a prototype compound with a mixed cation valence. Its formal valence composition is $(\text{Fe}^{3+})_A(\text{Fe}^{3+}\text{Fe}^{2+})_B\text{O}_4$, where A and B refer to tetrahedrally and octahedrally coordinated sites, respectively. It crystallizes in the inverse cubic spinel structure (*Fd $\bar{3}m$*), which undergoes a first-order phase transition to the monoclinic *Cc* structure at the Verwey temperature $T_V \sim 120$ K. The mechanism of the transition, the character of the low-temperature structure, the ordering of cations, and their orbitals below T_V have been studied for several decades (as reviewed, e.g., in Refs. [1–3]) and still present intensively investigated topics [4–9]. Recently, using high-energy x-ray diffraction, Senn *et al.* [10] found that to a first approximation the original Verwey hypothesis [11] is adequate, although there are important deviations. To explain them, Senn *et al.* introduced “trimerons,” which may be important quasiparticles not only in magnetite above T_V [12] but also in other transition metal oxides. Moreover, trimerons seem to play a crucial role in the mechanism of the Verwey transition [13].

In magnetite all iron ions are in a high-spin state. Fe(A) on the tetrahedral sublattice are trivalent with the half-filled $3d$ shell. In the B sublattice, the octahedral crystal field splits the d states into a higher e_g doublet and a lower t_{2g} triplet. The five $3d$ electrons fill the e_g and t_{2g} majority-spin states, and the remaining electrons (one electron per two B sites) enter the minority-spin t_{2g} levels.

Trimerons are linear objects consisting of three Fe(B) ions. Bonds between these ions are typically shorter than the average Fe(B)-Fe(B) distances. The central ion is Fe^{2+} -like, and it donates part of its minority-spin t_{2g} electron to the remaining two Fe^{3+} -like ions. The charge distribution is described and

qualitatively analyzed in Ref. [10]. Trimerons are linked together and form a complex network. There are two B sites which are not included in any trimeron. More information on electronic structure is provided by *ab initio* calculations in Ref. [14].

Another *ab initio* calculation of electronic structure (using the hybrid Becke, three-parameter, Lee-Yang-Parr (B3LYP) exchange-correlation potential) was recently published by Patterson [15] together with an alternative description of Fe(B) charge ordering: Patterson focused on the ten shortest Fe(B)-Fe(B) bonds of bimodal distribution of Fe(B)-Fe(B) distances; part of these bonds forms a branched broken zigzag chain with delocalized minority-spin $3d$ electrons, while the rest presents one-electron bonds between pairs of Fe(B). Note that in the context of the trimeron model, these ten Fe(B)-Fe(B) bonds are parts of trimerons.

Nuclear magnetic resonance (NMR) is an efficient tool to study the inhomogeneous electron distribution locally. The analysis of the temperature dependence of ^{57}Fe NMR frequency in magnetite [16,17] evidenced the *Cc* space group of the Fe_3O_4 low-temperature crystal structure. The spectra acquired without an external magnetic field consisted of 16 Fe(B) and 8 Fe(A) resonance lines.

More than 10 years ago, Mizoguchi [18] succeeded in measuring the dependence of NMR frequencies on the direction of the external magnetic field. The data contain important information on the orbital state of individual Fe ions. However, the interpretation of such an experiment, in which magnetization lies in a general direction, is extremely difficult: the resonance lines are split due to the nature of *ac*-glide symmetry and also due to the presence of different elastic domains. At that time, the knowledge of the magnetite low-temperature crystal structure was far from complete, and the analysis of the results did not match the uniqueness of the experimental results.

Our work comprises a rigorous quantitative reanalysis of the experimental data of Mizoguchi. Although Patterson [15]

*reznicek@mbbox.troja.mff.cuni.cz

also compared the calculated hyperfine field of iron ions to the data of Mizoguchi, there are important differences between his study and ours, which are explained in Secs. IV and V. We treat the presence of monoclinic twins and noncolinearity of the external magnetic field and magnetization properly, and our fits yield hyperfine anisotropy tensors and isotropic parts. Further, we calculate the electronic structure using the density functional theory (DFT) based WIEN2K program, with the main goal to determine the hyperfine field on the ^{57}Fe nuclei, including its anisotropy. We include the spin-orbit coupling in the calculation and focus on a proper calculation of the hyperfine field. The benefits of comparing experimental and calculated hyperfine field anisotropies were already clearly demonstrated in Ref. [19]. The results then allow us to assess the trimeron model validity.

II. TWINNING BELOW THE VERWEY TEMPERATURE

During cooling through the Verwey transition, the main deformation of magnetite structure is orthorhombic with orthogonal coordinates \vec{a} , \vec{b} , \vec{c}_0 . The \vec{c}_0 axis would be the easy magnetization direction, while \vec{a} is the hard direction. The lowering of symmetry from cubic to orthorhombic is accompanied by “orthorhombic” twinning; that is, below T_V , the crystal would consist of six types of orthorhombic domains. Mizoguchi applied an external magnetic field in a suitable direction during cooling to prevent orthorhombic twinning [18].

Simultaneously with orthorhombic deformation, a small monoclinic deformation occurs: the monoclinic axis \vec{c} is tilted from \vec{c}_0 by an angle 0.23° towards the $-\vec{a}$ axis. This small crystallographic deformation has a significant impact on magnetic anisotropy: the easy axis is not \vec{c}_0 , but it is canted by $\simeq 2^\circ$ towards $-\vec{a}$ [20]. There are two equivalent cantings, and accordingly, a monoclinic twinning exists. More details about the twinning are provided in the Supplemental Material [21].

III. ANGULAR DEPENDENCE OF THE NMR FREQUENCY

The frequency of the ^{57}Fe NMR resonance is proportional to the hyperfine magnetic field on the site of the resonating nucleus by a gyromagnetic factor $\gamma = 1.38156 \text{ MHz T}^{-1}$ [22]. The dependence of the NMR frequency f on the direction of \vec{M} is expressed using the direction cosines ϑ_α , $\alpha = a, b, c$ with respect to the orthorhombic \vec{a} , \vec{b} , \vec{c}_0 axes as

$$f = f_{\text{iso}} + \begin{pmatrix} \vartheta_a \\ \vartheta_b \\ \vartheta_c \end{pmatrix} \begin{pmatrix} f_{aa} & f_{ab} & f_{ac} \\ f_{ab} & f_{bb} & f_{bc} \\ f_{ac} & f_{bc} & f_{cc} \end{pmatrix} \begin{pmatrix} \vartheta_a \\ \vartheta_b \\ \vartheta_c \end{pmatrix} \\ = f_{\text{iso}} + \begin{pmatrix} \vartheta_a \\ \vartheta_b \\ \vartheta_c \end{pmatrix} \hat{F}_{\text{ani}} \begin{pmatrix} \vartheta_a \\ \vartheta_b \\ \vartheta_c \end{pmatrix}, \quad (1)$$

which explicitly contains a constant isotropic term f_{iso} and anisotropy tensor \hat{F}_{ani} ($\text{Tr}[\hat{F}_{\text{ani}}] = 0$). (The fourth- and higher-order terms in the direction cosines are neglected.) The tensor of anisotropy can be brought to the canonical form

$$\hat{F}'_{\text{ani}} = \begin{pmatrix} f'_a & 0 & 0 \\ 0 & f'_b & 0 \\ 0 & 0 & f'_c \end{pmatrix}, \quad (2)$$

while at the same time obtaining principal axes \vec{p}_a , \vec{p}_b , and \vec{p}_c of the tensor. The following parameter can be defined as a measure of hyperfine anisotropy:

$$f_{\text{ani}} = \sqrt{f_a'^2 + f_b'^2 + f_c'^2} \quad (3)$$

In Cc symmetry, 16 sites from 32 Fe(B) are crystallographically inequivalent, and 8 sites from 16 Fe(A) are inequivalent. The symmetry operation that connects B_i, B'_i (A_i, A'_i) is represented by a glide along the \vec{c} axis with the ac -glide plane. Due to the symmetry, the parameter f_{ac} is the same for the two crystallographically equivalent sites, while the parameters f_{ab} , f_{bc} have opposite signs.

IV. REEVALUATION OF THE NMR DATA OF MIZOGUCHI

Mizoguchi measured the angular dependence of the NMR frequency of all inequivalent Fe nuclei in the low-symmetry phase of magnetite [18]. At 4.2 K, an external field $B_{\text{ext}} = 1.3 \text{ T}$ was rotated in the planes perpendicular to the orthorhombic \vec{a} , \vec{b} , \vec{c}_0 axes of a spherical sample in 10° steps. Thus 48 $f(B_{\text{ext}})$ curves were obtained: 16 for Fe on the A sites and 32 for Fe on the B sites. The splitting of the curves for magnetic field in the ac plane is due to monoclinic twinning, while the splitting for magnetization in the ab and bc planes is caused by the nature of the ac -glide symmetry (see Sec. III).

In order to analyze the experimental data, the noncolinearity of \vec{M} and \vec{B}_{ext} must be accounted for. To this end, we employed a procedure similar to the one used by Mizoguchi [23]: the direction of the magnetization in \vec{B}_{ext} was numerically determined using the magnetic anisotropy reported originally by Abe *et al.* [20] (see the Supplemental Material [21]). (Note that in the analysis in Ref. [15], the presence of monoclinic twins and noncolinearity of the external magnetic field and magnetization in the sample were neglected; their effect was mentioned only in discussion.)

The frequency shift induced by the external field was compensated for by subtracting a projection of \vec{B}_{ext} onto the \vec{M} direction (multiplied by γ) from the data. Next, the data were fitted with the dependence (1) while taking into account the splitting of the curves for each Fe site. Typical errors of the fitted parameters were below or around 0.01 MHz for the A sites and 0.02–0.7 MHz for the B sites. Finally, the canonical form of the \hat{F}_{ani} tensor was found. The results are listed in Table S1 in the Supplemental Material [21], and fitted curves are plotted in Fig. 1. The fitted frequency dependences match the experimental data well, showing that the truncation of the fourth-order terms in Eq. (1) is well founded. Unfortunately, a comparison of these results with the work of Patterson [15] is not feasible since the isotropic parts and anisotropy tensors of the hyperfine field were not extracted from the calculated and experimental data in his work.

V. CALCULATION OF THE ELECTRONIC STRUCTURE AND HYPERFINE FIELD

To calculate the hyperfine field as well as the electronic structure, the WIEN2K program [24] based on the density functional theory was used. The number of basis functions used was 9500 ($\text{RK}_{\text{max}} = 6.0$), and the number of k points in

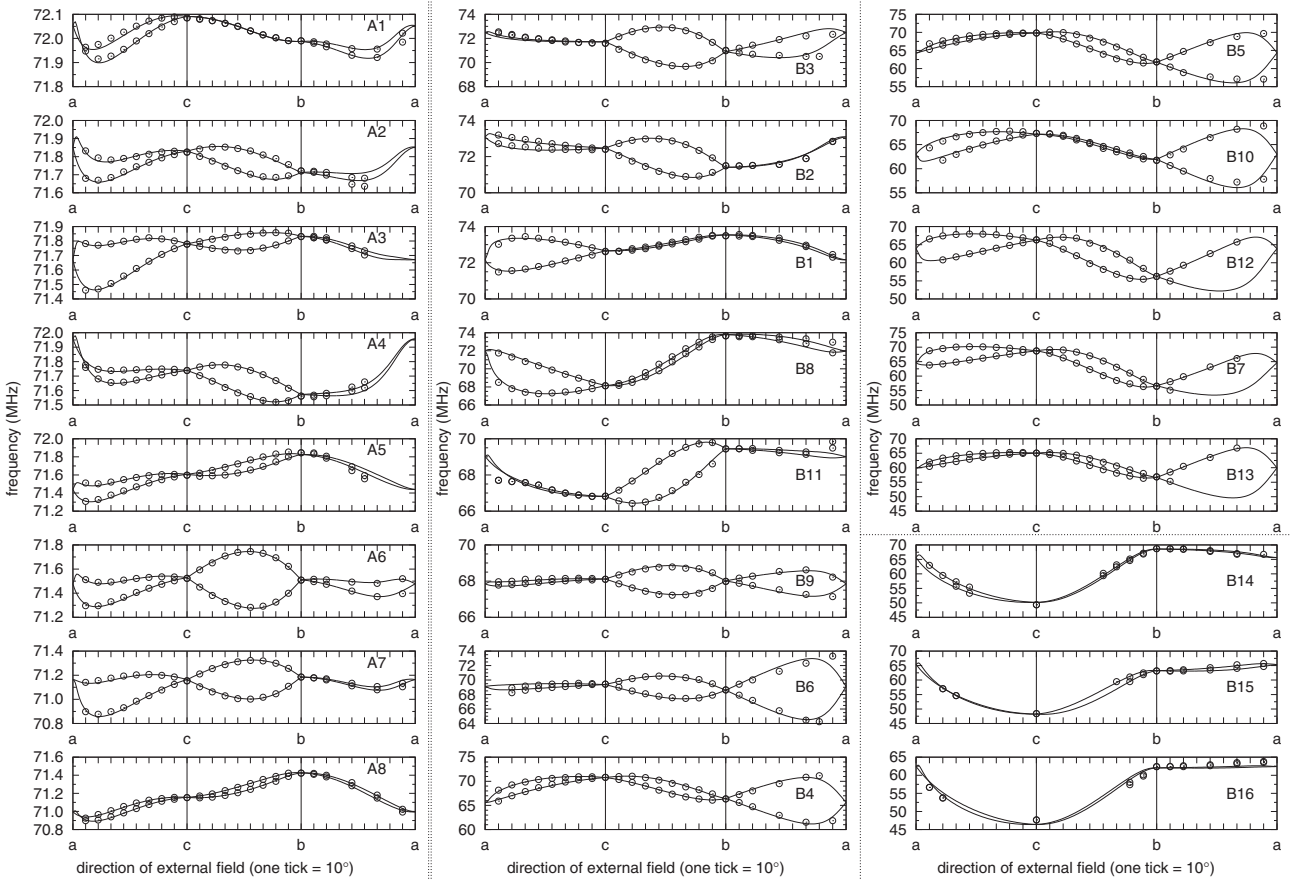


FIG. 1. Angular dependence of ^{57}Fe NMR frequencies with $H_{\text{ext}} = 1.3$ T applied in the ac , bc , and ab planes. Circles correspond to the experimental data [18], and curves represent the best fit of Eq. (1) to these data. The labels of the sites follow the convention in Ref. [18]. Ordering of the B sites corresponds to the ordering in Table S3 and Fig. S4 in the Supplemental Material [21].

the irreducible part of the Brillouin zone was 9. The charge density was Fourier expanded to $G_{\text{max}} = 16 \text{ Ry}^{\frac{1}{2}}$.

The crystal structure parameters used were those published by Senn *et al.* [10] for the low-temperature phase of magnetite. While Patterson [15] optimized the structure, we decided to avoid the optimization process because the structure is complicated and a number of crystal-structure parameters would change during the optimization. Necessarily, multiple total-energy minima exist, and there is no guarantee that the correct minimum would be reached. Moreover, the situation is complicated by magnetostriction, which is not taken into account in the optimization procedure. Therefore we decided to use the unoptimized experimental structure, in which the average force acting on the ions was $9.8 \text{ mRy a.u.}^{-1}$ and the maximum force was $19.3 \text{ mRy a.u.}^{-1}$.

The contact part of the hyperfine field was calculated using a semiempirical method suggested recently by Novák and Chlan [25], which is better than the approach used in Ref. [15] as the corresponding Eq. (3) in Ref. [15] is a poor approximation of the contact term [26]. To this end, the spin magnetic moments m_{3d} and m_{4s} of the $3d$ and $4s$ electrons of Fe are needed. These were calculated using $R_{\text{MT}}(\text{Fe}) = 2 \text{ a.u.}$ and the generalized gradient approximation $+U$ (GGA $+U$) method, with $U_{\text{eff}} = 4.5 \text{ eV}$. Unlike in Ref. [14], spin-orbit coupling was not omitted. The on-site contributions to the hyperfine

field from the interaction of nuclear spin with the electron spin (B_{dip}) and orbital moment (B_{orb}) were calculated as described in Ref. [25], and the contribution of other magnetic moments in the lattice B_{lat} was also calculated. For the iron ions at the B sites, $|B_{\text{dip}}|$ ranges up to 13.7 T , $|B_{\text{orb}}|$ ranges up to 4.6 T , $|B_{\text{lat}}|$ ranges up to 1.1 T , and the anisotropy of all of these terms is significant. (In Ref. [15], the terms corresponding to the interaction of nuclear spin with orbital moments and with electron magnetic moments on other sites are missing.) The total hyperfine field was then obtained by summing up all components.

A. Valence-electron density in trimeron planes

One of the ways in which the DFT calculations may contribute to the understanding of the trimeron concept [10] is maps of minority-spin valence-electron density in selected planes of the trimerons (see Fig. 2; see also Fig. S2 in the Supplemental Material [21], which is limited to minority-spin iron $3d$ valence electrons). The electron density is calculated for the magnetization set in the \vec{c} axis, and the maps are plotted as averages of the ac -glide-connected sites to remove possible (although minor) artifacts arising from switching off this symmetry operation in order to be consistent with calculations of the angular dependences. The main finding is that the electron cloud around the central Fe^{2+} -like ion of each

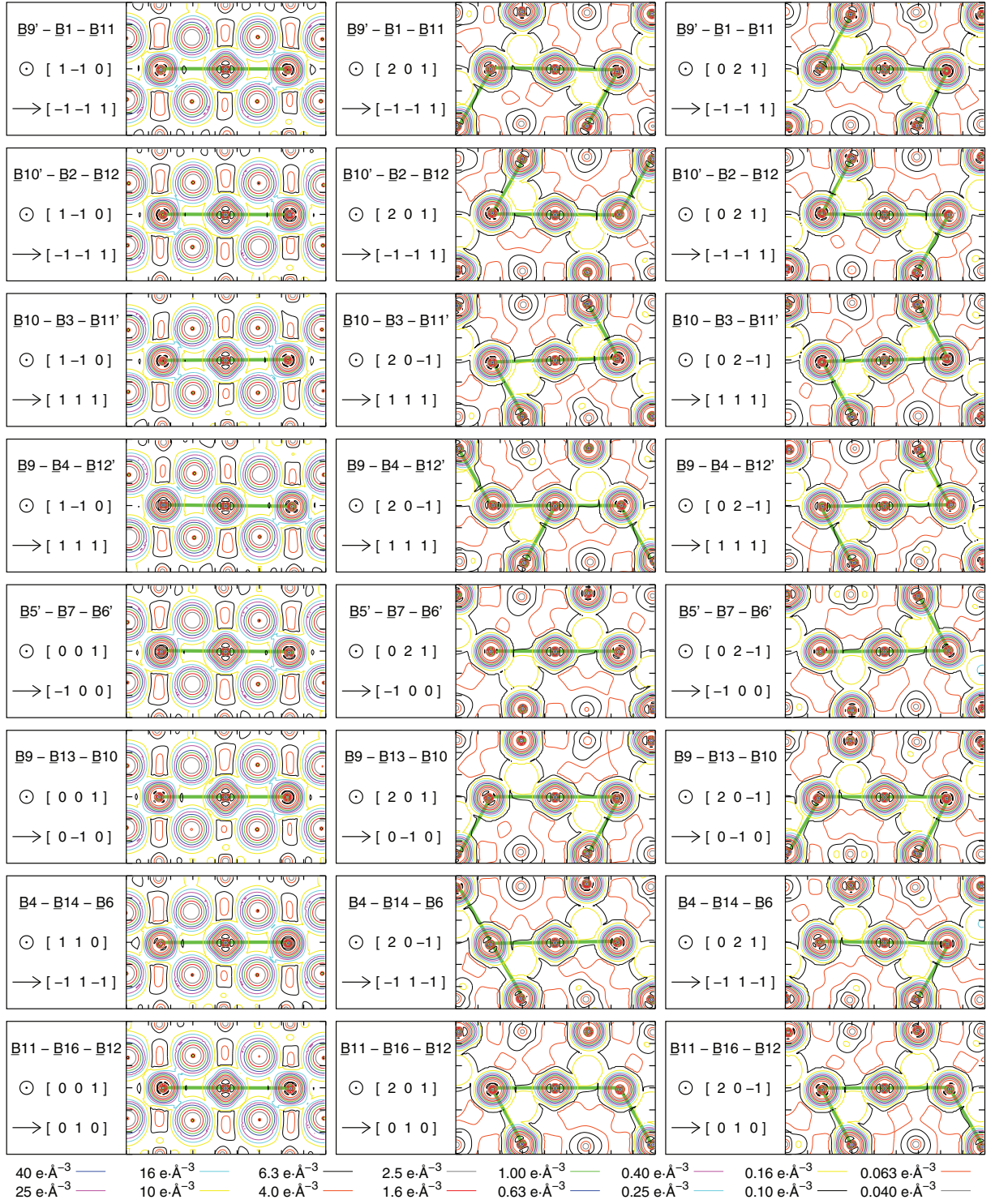


FIG. 2. (Color) Minority-spin valence-electron-density maps plotted in trimeron planes. The size of each plot is $9 \times 6 \text{ \AA}$. Trimerons [10] are highlighted with green lines. The sites of iron ions forming the trimeron lying on a horizontal axis of a particular plot are written on each plot; the center of the image plane coincides with the position of the central ion of the trimeron. Since the \tilde{c} axis tilt in the monoclinic Cc cell of magnetite renders the standard crystallographic plane notation inconvenient for selected planes, the orientation of the planes is indicated by the normal vector of the plane (pointing out of the image) written at the circled dot symbol and by an in-plane vector drawn by an arrow; indices of these vectors refer to Cc coordinates. The planes in the first column form with the other two planes in a corresponding row an angle of $\approx 55^\circ$, while the latter planes make together an angle of $\approx 70.5^\circ$. Sites are numbered in the order in which they are listed in Ref. [10]; primes denote sites generated by the ac -glide symmetry operation.

TABLE I. Minority-spin electron populations relative to Fe^{3+} , as derived from [10] (first line) and from the DFT calculations (second line), accompanied by formal valence and oxidation states (in units of electron charge) and magnetic moments (in Bohr magnetons) from the AIM method. The n_{3d} populations taken from [15] correspond to 16 bands just below the valence-band maximum. Sites are numbered in the order in which they are listed in Ref. [10]. Populations are taken with respect to local coordinates with the \bar{z} axis parallel to the \bar{c} axis of the Cc system and the \bar{x} axis set to the [110] direction with respect to the Cc coordinates. For the A sites, the AIM yielded valences of 1.77 (i.e., oxidation states of 2.82) and magnetic moments in the range from -4.079 to -4.095 .

DFT site	Nominal valence state	n_{xy}	n_{xz}	n_{yz}	$n_{t_{2g}}$	n_{z^2}	$n_{x^2-y^2}$	n_{e_g}	$n_{t_{2g}} + n_{e_g}$	n_{3d} [15]	AIM valence	AIM oxidation state	AIM spin magnetic moment
<u>B1</u>	2+	0.00	0.60	0.00	0.60	0.00	0.00	0.00	0.60				
		0.03	0.73	0.04	0.80	0.10	0.11	0.21	1.01	0.63	1.47	2.34	3.691
<u>B2</u>	2+	0.00	0.60	0.00	0.60	0.00	0.00	0.00	0.60				
		0.03	0.74	0.04	0.80	0.09	0.11	0.20	1.01	0.61	1.46	2.33	3.696
<u>B3</u>	2+	0.00	0.60	0.00	0.60	0.00	0.00	0.00	0.60				
		0.03	0.70	0.05	0.78	0.10	0.11	0.21	0.99	0.65	1.47	2.35	3.708
<u>B4</u>	2+	0.00	0.60	0.20	0.80	0.00	0.00	0.00	0.80				
		0.03	0.55	0.05	0.63	0.12	0.13	0.25	0.88	0.48	1.57	2.51	3.858
<u>B5</u>	3+	0.20	0.00	0.00	0.20	0.00	0.00	0.00	0.20				
		0.12	0.07	0.06	0.25	0.21	0.19	0.40	0.65	0.29	1.79	2.85	4.153
<u>B6</u>	3+	0.20	0.00	0.20	0.40	0.00	0.00	0.00	0.40				
		0.09	0.05	0.19	0.33	0.18	0.18	0.36	0.69	0.39	1.74	2.78	4.095
<u>B7</u>	2+	0.60	0.00	0.00	0.60	0.00	0.00	0.00	0.60				
		0.72	0.03	0.03	0.78	0.12	0.09	0.21	0.99	0.53	1.48	2.36	3.722
<u>B8</u>	3+	0.00	0.00	0.00	0.00	0.00	0.00	0.00	0.00				
		0.07	0.06	0.06	0.20	0.22	0.21	0.43	0.62	0.07	1.83	2.92	4.192
<u>B9</u>	3+	0.20	0.20	0.20	0.60	0.00	0.00	0.00	0.60				
		0.05	0.31	0.07	0.43	0.15	0.17	0.32	0.75	0.44	1.68	2.68	4.021
<u>B10</u>	3+	0.20	0.20	0.20	0.60	0.00	0.00	0.00	0.60				
		0.13	0.11	0.11	0.34	0.18	0.18	0.36	0.70	0.45	1.73	2.76	4.081
<u>B11</u>	3+	0.20	0.20	0.20	0.60	0.00	0.00	0.00	0.60				
		0.11	0.13	0.12	0.36	0.18	0.18	0.35	0.71	0.45	1.72	2.74	4.066
<u>B12</u>	3+	0.20	0.20	0.20	0.60	0.00	0.00	0.00	0.60				
		0.08	0.09	0.07	0.25	0.20	0.20	0.41	0.65	0.26	1.79	2.86	4.146
<u>B13</u>	2+	0.60	0.00	0.00	0.60	0.00	0.00	0.00	0.60				
		0.76	0.03	0.03	0.81	0.12	0.09	0.20	1.01	0.60	1.46	2.33	3.692
<u>B14</u>	2+	0.00	0.00	0.60	0.60	0.00	0.00	0.00	0.60				
		0.03	0.03	0.69	0.76	0.10	0.12	0.22	0.97	0.52	1.50	2.39	3.736
<u>B15</u>	3+	0.00	0.00	0.00	0.00	0.00	0.00	0.00	0.00				
		0.07	0.06	0.06	0.19	0.21	0.21	0.42	0.62	0.07	1.83	2.92	4.195
<u>B16</u>	2+	0.60	0.00	0.00	0.60	0.00	0.00	0.00	0.60				
		0.75	0.03	0.03	0.80	0.12	0.08	0.20	1.00	0.64	1.46	2.32	3.703

trimeron is notably prolate along the trimeron axis. Moreover, the asymmetry of the electron density around the end ions of trimers is smaller and, in some cases, negligible.

The observations correspond well to the picture of trimers: a significant fraction of minority-spin $3d$ electron is located in that central ion's t_{2g} orbital which corresponds to the trimeron axis direction, while the rest of the electron is donated to the same orbitals of the end ions. Therefore the electron density around the central ion is considerably anisotropic. The symmetry of the electron clouds around the end ions is affected much less even if the ion belongs to more than one trimeron as the donated fractional charges enter different orbitals in such a case.

The comparison of the data with the model of Patterson [15] is less plausible: While the description above might fulfill the expectations for inner ions of the zigzag chain, a shift of the electron cloud towards the chain would be intuitively presumed

in the case of the chain end or branch ions (e.g., B1, B13), which is not observed. The expected situation for the Fe(B) pairs not included in the chain (e.g., B5'–B7) also differs from the maps.

B. Electron populations and valence states of iron on the B sites

The description of trimers in Ref. [10] allows us to determine qualitatively the populations of the iron minority-spin $3d$ states; that is, assuming maximum donor-to-acceptor transfer, $0.6e$ (e stands for elementary charge) remains in the central ion's t_{2g} orbital which corresponds to the trimeron axis direction, while $0.2e$ is donated to the same orbital of each of the end ions. These populations are compared with the results of the DFT calculation in Table I. [These populations are taken with respect to orthogonal coordinates reflecting local (pseudo)symmetry: the \bar{z} axis parallel to \bar{c} , the \bar{x} axis

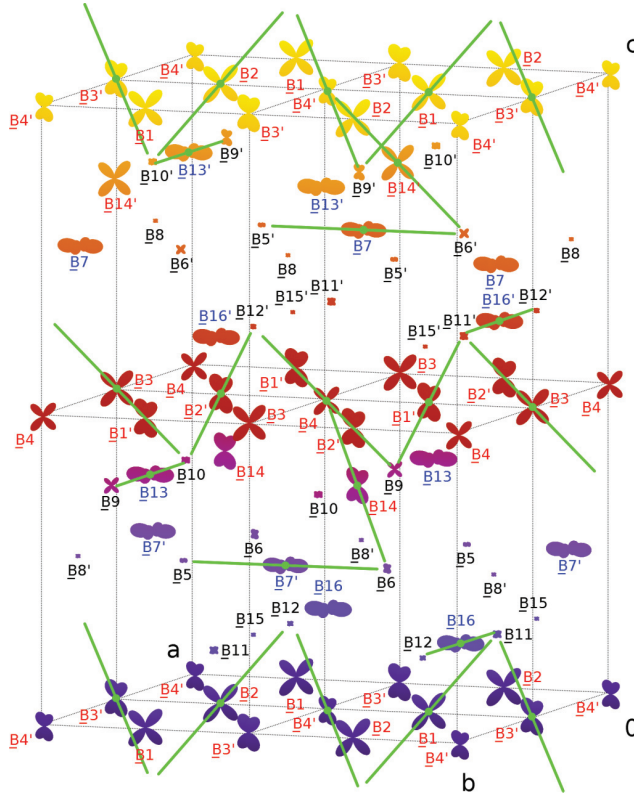


FIG. 3. (Color) Minority-spin t_{2g} electron populations of iron ions at the B sites plotted as an angular variation of the electron density; that is, the surface distance from a particular site represents the density at the corresponding angle multiplied by a scaling coefficient of 3 \AA^{-1} . Green lines denote trimerons introduced in Ref. [10]. Sites are numbered in the order in which they are listed in Ref. [10]; primes denote sites generated by the ac -glide symmetry operation. Sites in the same group in Fig. S4 in the Supplemental Material [21] share the same label color. (Surface color corresponds to the z coordinate and is used just for clarity.)

along the $[110] Cc$ direction.] The populations obtained from the DFT calculation are visualized in Fig. 3 [27], and it is seen that the calculation results correlate well with the expected t_{2g} populations. Mulliken populations of minority-spin $3d$ electrons from Ref. [15] were added to Table I for a comparison (note that these populations correspond to 16 bands just below the valence-band maximum, whereas there was no additional energy or band restriction of the $3d$ orbitals applied in our data); the apparent correlation to our data and trimeron model predictions is interesting. Concerning the valence of the B irons, the sums of t_{2g} and e_g spin-down electron densities of Fe^{2+} -like ions are close to 1, while they are systematically lower for Fe^{3+} -like ions, although still significantly higher than zero. The total number of these electrons yields 13.25 electrons at the 16 B sites, while only 8.00 electrons are expected if, formally, eight divalent and eight trivalent iron ions occupy these sites. The surplus 5.25 electrons are transferred from oxygen ligands. In order to reliably quantify the valence states of the B sites, atomic valences, oxidation states, and also magnetic moments were determined using the atoms in molecules (AIM) method [28] (see the last three columns in

Table I). In order to obtain oxidation states, the valence charges calculated from AIM were rescaled by a factor of 1.6, which brings the average valence charge of oxygen ions to -2 , thus representing the oxidation state O^{2-} . The resulting B iron valence states correlate very well with the bond valence sum (BVS) values reported in Ref. [10].

C. Hyperfine field anisotropy

Complementary to Mizoguchi's experiments [18], the DFT calculations of the hyperfine field at iron sites were carried out for various directions of magnetization and subsequently fitted with Eq. (1). Typical uncertainty of the fitted parameters was smaller than 0.03 MHz for the A sites and 0.03–0.6 MHz for the B sites. The results are collected in Table S2 in the Supplemental Material [21], and fitted curves are drawn in Fig. 4. Note the difference that Mizoguchi rotated the external magnetic field in the ac , cb , and ab planes, while in our calculations it was the magnetization that was rotated in these planes.

The DFT calculations performed for magnetization not parallel to the easy axis have two limitations. First, for a general specified magnetization direction, the spin and orbital magnetization tends to incline towards the easy magnetization axis due to the spin-orbit coupling. In the case of our calculations, the resulting direction of total magnetization (which entered then into the fit) deflected from the specified direction for not more than 10° , and the magnetic moments of individual iron ions were collinear, as expected (deviations from the total magnetization direction were less than 0.5°). Second, the complex dependence of the total energy on the magnetization direction is likely to possess multiple local minima. Therefore, the self-consistent iteration procedure for neighboring (or even the same) magnetization directions may be prone to converge to unrelated minima depending on the population matrices with which the GGA+ U calculation was started. In order to estimate the impact of this effect, the calculations for the specified magnetization direction $[30\bar{1}]$ were carried out independently twice, and the determined error of the hyperfine field was up to 0.3 T (i.e., 0.4 MHz error of the ^{57}Fe NMR frequency).

The hyperfine anisotropy tensors \hat{F}_{ani} of $\text{Fe}(\text{B})$ ions are visualized in Fig. 5 as objects drawn in the elementary cell; the following formula defines the distance r of the object surface from the particular iron position:

$$r = C[f_{aa}\vartheta_a^2 + f_{bb}\vartheta_b^2 + f_{cc}\vartheta_c^2 + 2(f_{ab}\vartheta_a\vartheta_b + f_{ac}\vartheta_a\vartheta_c + f_{bc}\vartheta_b\vartheta_c)], \quad (4)$$

where ϑ_α , $\alpha = a, b, c$, are direction cosines taken relative to the iron site in question and C is a scaling coefficient common for all B sites, allowing for a clear drawing. Figure 5 provides an overview of mutual orientation of principal axes of hyperfine anisotropy tensors of neighboring $\text{Fe}(\text{B})$ ions, which can be compared to the concept of trimerons suggested by Senn *et al.* [10]. The trimerons are depicted in Fig. 5 by the line segments in the center of which the Fe^{2+} -like ions are situated. Apparently, the trimeron central ions exhibit considerably larger anisotropy than the end ions, while the principal axis linked with the smallest eigenvalue of the

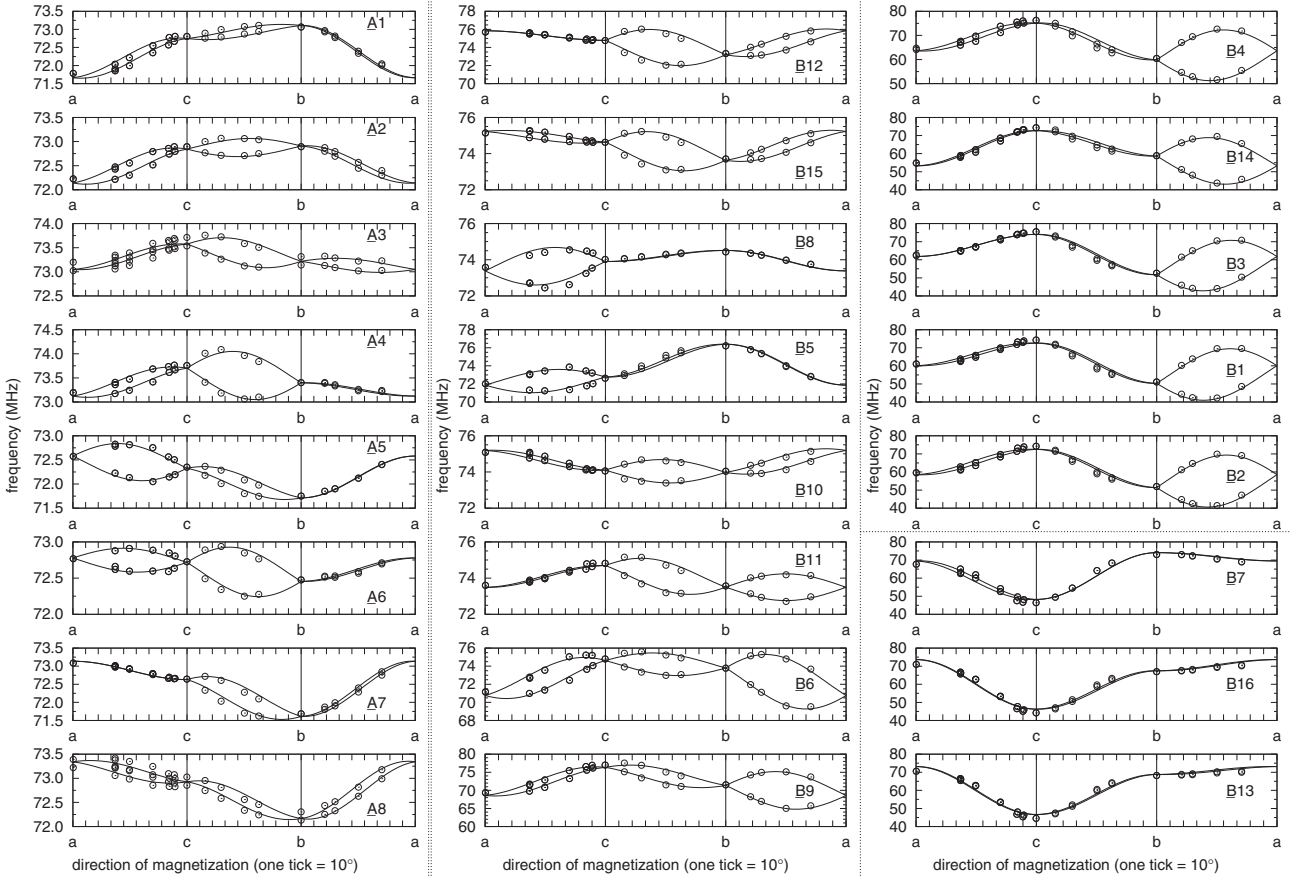


FIG. 4. Angular dependence of ^{57}Fe NMR frequencies with magnetization in the ac , bc , and ab planes. Circles correspond to the data from the DFT calculations, and curves represent the best fit of Eq. (1) to these data. Sites are numbered in the order in which they are listed in Ref. [10]. Ordering of the B sites corresponds to the ordering in Table S3 and Fig. S4 in the Supplemental Material [21].

corresponding anisotropy tensor of the central ion is the closest to the trimeron axis. These findings are in agreement with the expectations deduced from the electronic structure of trimerons: The minority-spin charge density around the central Fe^{2+} -like ions is significantly anisotropic as the charge is located in a t_{2g} orbital corresponding to the trimeron axis. On the other hand, the roughly spherical symmetry of the Fe^{3+} -like end ions is affected only by the partial charge donated by the central ions. (If the end ion is a member of multiple trimerons, the central ions donate the charge into different orbitals; thus the impact on the end-ion symmetry remains small.) In the case of Fe^{3+} -like ions $\underline{\text{B8}}$ and $\underline{\text{B15}}$, which do not belong to any trimeron, the anisotropy is small as their symmetry is not significantly perturbed. We note that the model proposed by Patterson [15] implies a similar charge configuration of the two iron ions in the pairs that are not in the zigzag chain (e. g. $\underline{\text{B5'}}$ – $\underline{\text{B7}}$). This is not corroborated by our calculations as their anisotropies are apparently different. For a visualization of the significantly smaller anisotropy tensors of $\text{Fe}(\text{A})$ ions, see Fig. S3 in the Supplemental Material [21]. The small anisotropy of the Fe^{3+} ions at the A sites corresponds to nearly spherical symmetry of their electronic configuration.

VI. COMPARISON OF THE HYPERFINE PARAMETERS EXTRACTED FROM THE NMR DATA AND FROM THE DFT CALCULATIONS

A simple way to compare experimental and calculated NMR frequencies of $\text{Fe}(\text{B})$ ions is displayed in Fig. 6. In this figure, the frequencies are ordered according to their decreasing isotropic part f_{iso} , and it is seen that both data sets can be divided into two groups. Fe ions in the left part of the plot possess smaller anisotropy f_{ani} and higher f_{iso} compared to Fe in the right part. This is understandable: The iron ions in the first group are Fe^{3+} -like (see Table I), and as a consequence, they have a small orbital moment, and thus anisotropy is also small. At the same time, the occupation of the minority-spin $3d$ states is small, leading to higher spin moment and, consequently, also a higher isotropic part of the NMR frequency. The interpretation of the experimental hyperfine parameters in the context of the trimeron electronic structure is essentially the same as that provided in Sec. VC.

Closer correlation of experimental and calculated NMR frequencies may be obtained by considering both f_{iso} and the anisotropy tensor \hat{F}_{ani} . To this end, we calculate the mean

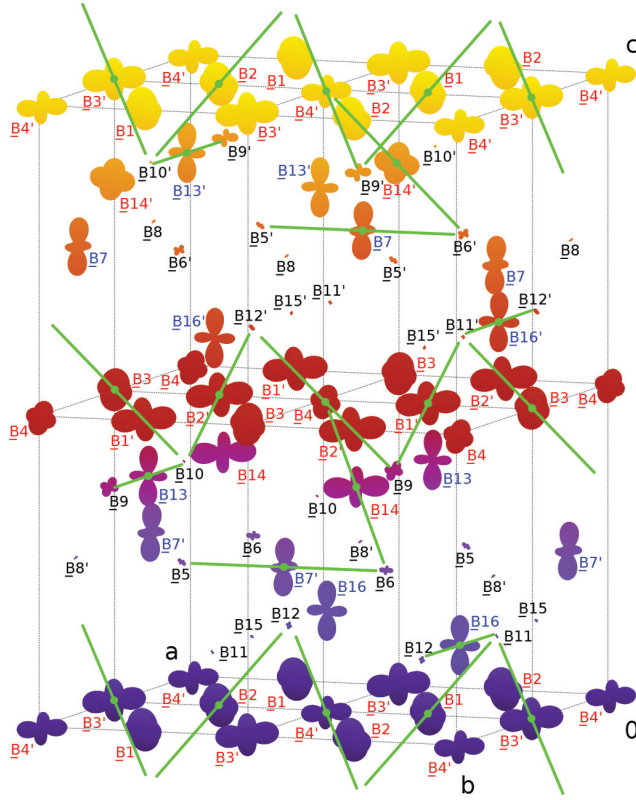


FIG. 5. (Color) Tensors of hyperfine anisotropy of iron B sites from the DFT calculations drawn in the elementary cell (scaling coefficient $C = 0.05 \text{ \AA MHz}^{-1}$). Green line segments correspond to trimerons suggested in Ref. [10]. Sites are numbered in the order in which they are listed in Ref. [10]; primes denote sites generated by the ac -glide symmetry operation. Sites in the same group in Fig. S4 in the Supplemental Material [21] share the same label color. (Surface color corresponds to the z coordinate and is used just for clarity.)

square deviation $\sigma(i, j)$:

$$\sigma(i, j) = \left(\sum_{\alpha=aa, bb, cc} \{ [f_{\text{iso}}^{\text{calc}}(i) + f_{\alpha}^{\text{calc}}(i)] - [f_{\text{iso}}^{\text{exp}}(j) + f_{\alpha}^{\text{exp}}(j)] \}^2 + 2 \sum_{\alpha=ab, ac, bc} [f_{\alpha}^{\text{calc}}(i) - f_{\alpha}^{\text{exp}}(j)]^2 \right)^{1/2}. \quad (5)$$

The index i of the calculated data corresponds to a specific B site in the unit cell, while for the experimental data the index j corresponds to a particular pair of branches of angular dependence of the NMR frequency. (The f_{ab} and f_{bc} elements obtained from experimental data have an arbitrary sign, whereas the sign of their product is known. Considering this, the variants of the signs resulting in the smallest $\sigma(i, j)$ were chosen for the calculation.) The $\sigma(i, j)$ then helps us to associate the B sites and the hyperfine field experimentally observed. The values of $\sigma(i, j)$ determined using the above equation are collected in Table S3 in the Supplemental Material [21]. Total mean-square deviation

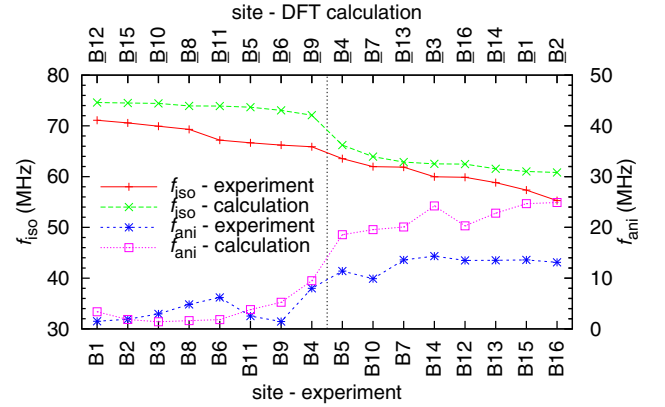


FIG. 6. (Color online) Comparison of the anisotropic and isotropic parts of the NMR frequencies extracted from the experimental data of Mizoguchi and from the DFT calculations. The B sites are ordered by decreasing f_{iso} . For experimental data, the labels of the sites follow the convention in Ref. [18]. For the DFT results, the sites are numbered in the order in which they are listed in Ref. [10].

for each assignment of calculated and experimental data is obtained by summing $\sigma(i, j)$:

$$\sigma = \frac{1}{16} \sum_{K=1}^{16} \sigma(i_K, j_K). \quad (6)$$

The 16 pairs (i_K, j_K) of indices are fixed by selecting the assignment. The minimal value of σ is $\sigma_{\min} = 11 \text{ MHz}$. One of the best assignments (the diagonal of Fig. S4 in the Supplemental Material [21]) is plotted in Fig. 7 in the same way as for Fig. 5. We note, however, that there exist several assignments with σ close to σ_{\min} .

Inspection of the results revealed three groups (in 8:5:3 ratio) of B sites in which the parameters of experimental and DFT data correlate. These groups are marked by label colors in Figs. 3, 5, and 7. The first group contains eight Fe^{3+} -like ions exhibiting lower anisotropy, confirming the observation from Fig. 6. Moreover, the procedure successfully identified the three NMR signals which are separated at low frequencies from the rest of a zero-field spectrum [16,17] with a group of three crystallographic sites with similar tensors of anisotropy; the longest principal axis of the tensors points along the \vec{c}_0 axis, while the other two principal axes are close to the \vec{a} and \vec{b} directions. The five Fe^{2+} -like ions in the remaining group are located approximately in $\{002\}$ planes of the Cc cell, with the exception of the B14 iron ion, and the principal axis of the anisotropy tensor corresponding to the largest (in absolute value) eigenvalue is not far from either the $[110]$ or $[1\bar{1}0]$ direction (with respect to Cc coordinates).

Hyperfine anisotropy of Fe^{3+} at the A sites is small, and also the isotropic terms differ only slightly. For these reasons we did not attempt to correlate the calculated and experimental data.

VII. CONCLUSIONS

We succeeded in quantitatively reanalyzing Mizoguchi's measurements of the angular dependences of the ^{57}Fe NMR

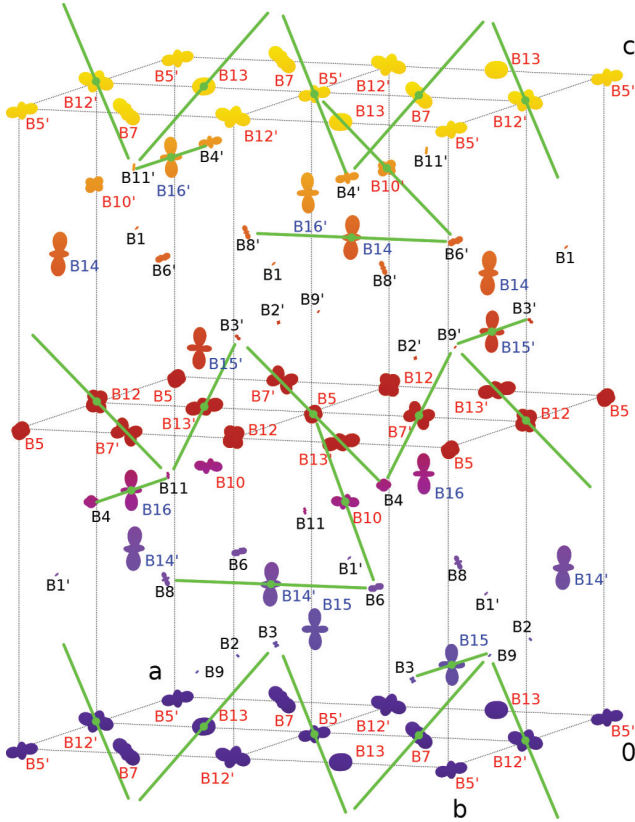


FIG. 7. (Color) Tensors of the anisotropy of iron B sites from the NMR data drawn in the elementary cell (scaling coefficient $C = 0.05 \text{ \AA MHz}^{-1}$). The assignment with one of the minimal total mean-square deviations σ (6) is plotted. Green lines denote trimers as suggested in Ref. [10]. The labels of the sites follow the convention in Ref. [18]; primes denote sites generated by the ac -glide symmetry operation. Sites in the same group in Fig. S4 in the Supplemental Material [21] share the same label color. (Surface color corresponds to the z coordinate and is used just for clarity.)

frequencies [18] in the low-temperature phase of magnetite and extracted the isotropic parts and anisotropy tensors of the NMR frequency. These data are directly proportional to the isotropic parts and anisotropy tensors of the hyperfine field. Moreover, we performed the DFT calculations of the hyperfine field dependence on the magnetization direction using the crystal structure reported by Senn *et al.* [10] and evaluated the results in order to obtain analogous anisotropy data linked to particular crystallographic sites. These two sets of data were compared, and although a reliable unique assignment of NMR lines to crystallographic sites was not feasible, three mutually

matching groups of B sites in a ratio of 8:5:3 were found. The first group is occupied by the Fe^{3+} -like ions; the other ones are occupied by the Fe^{2+} -like ions. This grouping allows one to narrow down the range of B sites a particular NMR signal may originate from and also supports the validity of the calculations and the underlying crystal structure as the B-site data sets from the DFT calculations share the same grouping ratio as the ones from the experiment.

Further, the hyperfine anisotropy data obtained from the DFT calculations support the trimeron concept [10] as the central Fe^{2+} -like ions of the suggested trimers exhibit significantly larger anisotropy than the end ions and the principal axis linked with the smallest eigenvalue of the corresponding anisotropy tensor of the central ions is the closest to the trimeron axis, which is in agreement with expectations deduced from the description of the electron distribution in the trimers. Even more direct insight into the electronic ordering of the trimers can be found in the calculated maps of minority-spin valence-electron density, which indicate that the electron cloud around the central ion of each trimeron is prolate along the trimeron axis.

Moreover, the minority-spin valence-electron populations at the B sites were acquired from the DFT calculations, and the AIM method was used to determine iron valences and magnetic moments. The populations were compared to the trimeron model, and the valences correlated to the BVS data [10], both showing good agreement.

Despite the discrepancies found between the approach of Patterson [15] and our results, we understand Patterson's model and the model of trimers as alternative views on the same physical reality: Patterson's concept of the broken branched zigzag chain and pairs of Fe(B) ions with one-electron bonds coincides with the trimeron network without longer bonds. The $\text{Fe(B)}\text{-Fe(B)}$ distances present important information on which both models are based. However, imposing a strict limit on bond length between Fe(B) pairs to qualify for a charge transfer in Patterson's model does not seem appropriate as the bond length distribution is not wide, so the overlap of t_{2g} orbitals of neighboring Fe(B) ions is significant even if their distance is not so short. Therefore the trimeron model provides a more precise description of the electronic structure of magnetite, as was shown by our results.

ACKNOWLEDGMENTS

This study was supported by project SVV-2014-260091. The work is part of the activities of the Charles University Research Center UNCE 204023 "Physics of Condensed Matter and Functional Materials." Last but not least, the authors are grateful to J. Šváb and K. Uličná for extraction of the data points from the plots in Ref. [18].

- [1] V. A. M. Brabers, Progress in spinel ferrite research, in *Handbook of Magnetic Materials*, edited by K. H. J. Buschow, Vol. 8 (Elsevier, Amsterdam, 1995), pp. 189–234.
- [2] J. M. Honig, Analysis of the Verwey transition in magnetite, *J. Alloys Compd.* **229**, 24 (1995).

- [3] F. Walz, The Verwey transition—A topical review, *J. Phys. Condens. Matter* **14**, R285 (2002).
- [4] J. P. Wright, J. P. Attfield, and P. G. Radaelli, Charge ordered structure of magnetite Fe_3O_4 below the Verwey transition, *Phys. Rev. B* **66**, 214422 (2002).

- [5] J. García and G. Subías, The Verwey transition—A new perspective, *J. Phys. Condens. Matter* **16**, R145 (2004).
- [6] M. S. Senn, J. P. Wright, and J. P. Attfield, The Verwey Phase of Magnetite—A Long-Running Mystery in Magnetism, *J. Korean Phys. Soc.* **62**, 1372 (2013).
- [7] G. Subías, J. García, J. Blasco, J. Herrero-Martín, M. C. Sánchez, J. Orna, and L. Morellón, Structural distortion, charge modulation and local anisotropies in magnetite below the Verwey transition using resonant X-ray scattering, *J. Synchrotron Rad.* **19**, 159 (2012).
- [8] S.-Ch. Weng, Y.-R. Lee, Ch.-G. Chen, Ch.-H. Chu, Y.-L. Soo, and S.-L. Chang, Direct observation of charge ordering in magnetite using resonant multiwave X-Ray diffraction, *Phys. Rev. Lett.* **108**, 146404 (2012).
- [9] A. Tanaka *et al.*, Symmetry of Orbital Order in Fe₃O₄ Studied by Fe L_{2,3} Resonant X-Ray Diffraction, *Phys. Rev. Lett.* **108**, 227203 (2012).
- [10] M. S. Senn, J. P. Wright, and J. P. Attfield, Charge order and three-site distortions in the Verwey structure of magnetite, *Nature (London)* **481**, 173 (2012).
- [11] E. J. W. Verwey, Electronic Conduction of Magnetite (Fe₃O₄) and its Transition Point at Low Temperatures, *Nature (London)* **144**, 327 (1939).
- [12] A. Bosak, D. Chernyshov, M. Hoesch, P. Piekarczyk, M. Le Tacon, M. Krisch, A. Kozłowski, A. M. Oleś, and K. Parlinski, Short-range correlations in magnetite above the Verwey temperature, *Phys. Rev. X* **4**, 011040 (2014).
- [13] S. de Jong, R. Kukreja *et al.*, Speed limit of the insulator-metal transition in magnetite, *Nat. Mater.* **12**, 882 (2013).
- [14] M. S. Senn, I. Loa, J. P. Wright, and J. P. Attfield, Electronic orders in the Verwey structure of magnetite, *Phys. Rev. B* **85**, 125119 (2012).
- [15] C. H. Patterson, Hybrid DFT calculation of ⁵⁷Fe NMR resonances and orbital order in magnetite, *Phys. Rev. B* **90**, 075134 (2014).
- [16] P. Novák, H. Štěpánková, J. Englich, J. Kohout, and V. A. M. Brabers, NMR in magnetite below and around the Verwey transition, *Phys. Rev. B* **61**, 1256 (2000).
- [17] P. Novák, H. Štěpánková, J. Englich, J. Kohout, and V. A. M. Brabers, Temperature Dependence of NMR in Magnetite, in *Ferrites: proceedings of ICF 8, Kyoto and Tokyo, Japan 2000*, edited by M. Abe and Y. Yamazaki (Japan Society of Powder and Powder Metallurgy, Kyoto and Tokyo, Japan, 2000), p. 131.
- [18] M. Mizoguchi, Charge and Orbital Ordering Structure of Fe₃O₄ in the Low-Temperature Phase as Deduced from NMR Study, *J. Phys. Soc. Jpn.* **70**, 2333 (2001).
- [19] V. Chlan, H. Štěpánková, R. Řezníček, and P. Novák, Anisotropy of hyperfine interactions as a tool for interpretation of NMR spectra in magnetic materials, *Solid State Nucl. Mag.* **40**, 27 (2011).
- [20] K. Abe, Y. Miyamoto, and S. Chikazumi, Magnetocrystalline anisotropy of low-temperature phase of magnetite, *J. Phys. Soc. Jpn.* **41**, 1894 (1976).
- [21] See Supplemental Material at <http://link.aps.org/supplemental/10.1103/PhysRevB.91.125134> for additional notes, figures, and tables.
- [22] S. Berger and S. Braun, *200 and More NMR Experiments* (Wiley-VCH, Weinheim, 2004).
- [23] M. Mizoguchi, NMR Study of the Low Temperature Phase of Fe₃O₄. I. Experiments, *J. Phys. Soc. Jpn.* **44**, 1501 (1978).
- [24] P. Blaha, K. Schwarz, G. K. H. Madsen, D. Kvasnicka, and J. Luitz, *WIEN2k, An Augmented Plane Wave + Local Orbitals Program for Calculating Crystal Properties* (Karlheinz Schwarz, Technische Universität Wien, Vienna, 2001).
- [25] P. Novák and V. Chlan, Contact hyperfine field at Fe nuclei from density functional calculations, *Phys. Rev. B* **81**, 174412 (2010).
- [26] S. Blügel, H. Akai, R. Zeller, and P. H. Dederichs, Hyperfine fields of 3d and 4d impurities in nickel, *Phys. Rev. B* **35**, 3271 (1987).
- [27] For clarity, Figs. 3, 5, and 7 in this work show the same trimers as those plotted in Fig. 4 d in Ref. [10], and the coordinates of iron ions also follow those in Ref. [10]. On the other hand, Fig. 3 in Ref. [14] is offset (e.g., B1B2, which corresponds to B4 in our work, is not in the cell center), and a partly different set of trimers is displayed, but it represents the same trimeron network. Unfortunately, there is no similar figure suitable for a straightforward comparison provided in Ref. [15].
- [28] R. F. W. Bader, *Atoms in Molecules: A Quantum Theory* (Oxford University Press, Oxford, 1990).

Hyperfine field and electronic structure of magnetite below the Verwey transition

Supplemental Material

R. Řezníček,* V. Chlan, and H. Štěpánková
*Faculty of Mathematics and Physics, Charles University in Prague,
 V Holešovičkách 2, 180 00 Prague 8, Czech Republic*

P. Novák
Institute of Physics of ASCR, Cukrovarnická 10, 162 00 Prague 6, Czech Republic
 (Dated: September 16, 2014; Revised: January 12, 2015)

Note: Twinning below the Verwey temperature

Orthorhombic twinning

At the Verwey temperature T_V symmetry of magnetite is lowered from cubic to monoclinic Cc symmetry. Main deformation is orthorhombic, with orthogonal coordination system defined by axes \vec{a} , \vec{b} , \vec{c}_0 . As a rule, \vec{c}_0 is chosen to be parallel to cubic [001] direction, $\vec{a} \parallel [\bar{1}\bar{1}0]$, $\vec{b} \parallel [1\bar{1}0]$. Magnetically, \vec{c}_0 would be the easy direction in orthorhombic symmetry, \vec{a} is the hard direction. To the cubic \rightarrow orthorhombic symmetry lowering corresponds 'orthorhombic' twinning, i.e. below T_V , the crystal would consist of six orthorhombic domain types:

$$\begin{aligned} O_1 &\equiv \vec{a} \parallel [\bar{1}\bar{1}0], \vec{b} \parallel [1\bar{1}0], \vec{c}_0 \parallel [001] \\ O_2 &\equiv \vec{a} \parallel [1\bar{1}0], \vec{b} \parallel [110], \vec{c}_0 \parallel [001] \\ O_3 &\text{ to } O_6 \text{ obtained by cyclic} \\ &\text{permutations of Miller indices} \end{aligned} \quad (S1)$$

Orthorhombic twinning can be prevented by applying the external magnetic field when the temperature crosses T_V . Mizoguchi used $B_{\text{ext}}=1.5$ T parallel to $[113]$ or $[\bar{1}23]$ [1] and $\vec{B}_{\text{ext}} \parallel [\bar{1}12]$ [2]. Abe et al. [3] used field making an angle 40° with $[001]$ in $(1\bar{1}0)$ plane to prevent orthorhombic twinning. In all these cases, \vec{c}_0 was parallel to $[001]$ and \vec{a} , \vec{b} were unambiguously determined.

Monoclinic twinning

Together with orthorhombic deformation, small monoclinic deformation happens: axis \vec{c} is tilted by an angle 0.23° towards the $-\vec{a}$ axis. This small crystallographic deformation has a relatively large effect on the magnetic anisotropy: the easy axis is not $[001]$, but it is canted by $\simeq 2^\circ$ from $[001]$ towards the longer cube diagonal (i.e. to $[111]$ direction if $\vec{a} \parallel [\bar{1}\bar{1}0]$) [4]. There are two equivalent cantings, and therefore a monoclinic twinning exists. This was not removed by application of $B_{\text{ext}}=1.5$ T parallel to $[\bar{1}23]$ [1] nor $\vec{B}_{\text{ext}} \parallel [\bar{1}12]$ [2]. To prevent it, Abe et al. [4] used $B_{\text{ext}}=1.35$ T parallel to $[001]$ and simultaneously squeezed the crystal along the $[111]$.

If monoclinic twinning is not prevented, usually an assumption is made that two possible monoclinic twins occur with the same probability [1, 2, 4].

Note: Calculation of magnetization direction

Due to the magnetocrystalline anisotropy, direction of \vec{M} in general differs from the direction of \vec{B}_{ext} . In the case of a spherical sample, direction of \vec{M} is found for a given \vec{B}_{ext} by minimizing the energy

$$E = -\vec{B}_{\text{ext}}\vec{M} + E_a, \quad (S2)$$

*Electronic address: reznicek@mbox.troja.mff.cuni.cz

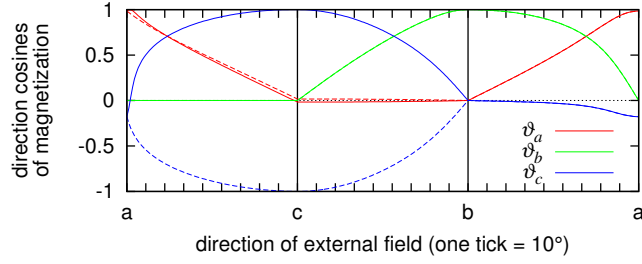


FIG. S1: Calculated direction of magnetization in dependence on the direction of the external magnetic field $B_{\text{ext}} = 1.3$ T. Dashed lines correspond to magnetization trajectory in the monoclinic twin. The tilt of the \vec{c} axis was not considered, i.e. the dependence was determined with respect to the orthorhombic coordinates.

where E_a represents the magnetocrystalline anisotropy. Magnetocrystalline anisotropy of Fe_3O_4 at $T=4.2$ K was measured by Abe et al. [4]. Taking the symmetry into account and neglecting terms of 6th and higher order in direction cosines $\vartheta_a, \vartheta_b, \vartheta_{111}$ (taken with respect to the monoclinic \vec{a}, \vec{b} axes and cubic [111] direction) of magnetization \vec{M} , it can be expressed as

$$E_a = K_a \vartheta_a^2 + K_b \vartheta_b^2 + K_{aa} \vartheta_a^4 + K_{bb} \vartheta_b^4 + K_{ab} \vartheta_a^2 \vartheta_b^2 - K_u \vartheta_{111}^2. \quad (\text{S3})$$

The values of the anisotropy constants in $10^4 \text{ J} \cdot \text{m}^{-3}$, as determined by Abe et al. [4] are

$$\begin{aligned} K_a &= 25.5, \quad K_b = 3.7, \quad K_{aa} = 1.8, \\ K_{bb} &= 2.4, \quad K_{ab} = 7.0, \quad K_u = 2.1, \end{aligned} \quad (\text{S4})$$

while Mizoguchi [1, 2] used more precise values

$$\begin{aligned} K_a &= 25.52, \quad K_b = 3.66, \quad K_{aa} = 1.76, \\ K_{bb} &= 2.42, \quad K_{ab} = 7.0, \quad K_u = 2.13. \end{aligned} \quad (\text{S5})$$

Measuring the torque in the $(1\bar{1}0)$ plane and taking

$$M = 5.104 \cdot 10^5 \text{ A} \cdot \text{m}^{-1}, B_{\text{ext}} = 1.45 \text{ T} \quad (\text{S6})$$

Abe et al. [4] give an example of the correction for \vec{B}_{ext} and \vec{M} noncollinearity. In case of the NMR experiments of Mizoguchi [1, 2], the following values of the external field and magnetization apply:

$$M = 5.09 \cdot 10^5 \text{ A} \cdot \text{m}^{-1}, B_{\text{ext}} = 1.3 \text{ T}. \quad (\text{S7})$$

For the analysis of Mizoguchi's NMR data [2] acquired using the spherical sample, the values (S5) and (S7) were used and the resulting $\vec{M}(\vec{B}_{\text{ext}})$ dependence is plotted in Fig. S1. It turns out that for \vec{B}_{ext} in bc and ac planes \vec{M} remains almost perfectly in these planes, while in the ab plane this is not the case. Moreover, any small misorientation of \vec{B}_{ext} near the hard \vec{a} direction magnifies the error when determining the direction of \vec{M} .

The presence of monoclinic twins in the sample leads to a situation when a demagnetizing field of one monoclinic domain contributes to the magnetic field in other domain(s) and vice versa. Since there is probably no way to determine the actual structure of monoclinic domains in the sample during the experiment (i.e. post facto), we confined ourselves only to a test of a simple model assuming a homogeneous distribution of both domain types (in 1:1 ratio) in a volume of the spherical sample. This model indeed produced slightly different dependences of the magnetization direction on the external field and resulted in small changes of the fitted frequency dependences (equation (1) in the main paper). However, the quality of the fit with and without this model was more or less the same, and since the model is too simple to describe actual reality, we decided not to consider the demagnetizing field of the domains at all.

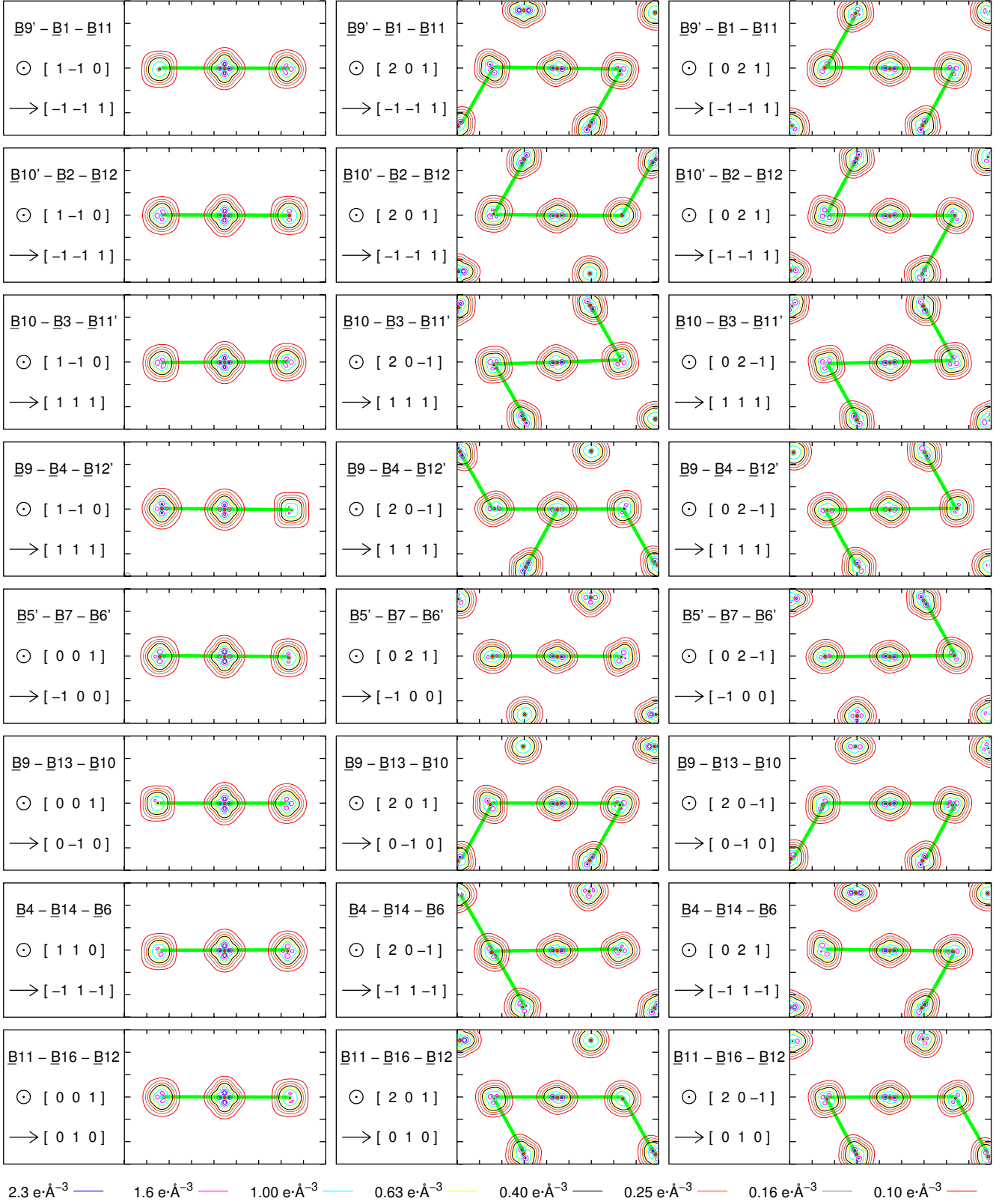


FIG. S2: Minority spin iron 3d valence electron density maps plotted in trimeron planes. Size of each plot is $9 \text{ \AA} \times 6 \text{ \AA}$. Trimerons [5] are highlighted with green lines. Sites of iron ions forming the trimeron lying on a horizontal axis of a particular plot are written at each plot; the centre of the image plane coincides with the position of the central ion of the trimeron. Since the \vec{c} axis tilt in monoclinic Cc cell of magnetite renders the standard crystallographic plane notation inconvenient for selected planes, orientation of the planes is indicated by normal vector of the plane (pointing out of the paper) written at the \odot symbol and by an in-plane vector drawn by an arrow – indices of these vectors refer to Cc coordinates. The planes in the first column form with the other two planes in a corresponding row an angle of $\approx 55^\circ$, while the latter planes make together an angle of $\approx 70.5^\circ$. Sites are numbered in the order in which they are listed in [5]; primes denote sites generated by the ac -glide symmetry operation.

Data obtained by decomposition of the angular dependence of the NMR frequency

TABLE S1: Parameters in equations (1), (2) in the main paper obtained by applying linear regression to experimental data of Mizoguchi. Column labeled "error" contains typical error of the fitted parameters. Note that the sign of f_{ab} , f_{bc} (provided their product does not change) and of b -component of principal axes is arbitrary because the iron positions connected by the ac -glide symmetry are in principle indistinguishable from the data. Labels of the sites follow the convention in [2].

site	f_{iso} (MHz)	f_{ani} (MHz)	f_{aa} (MHz)	f_{bb} (MHz)	f_{cc} (MHz)	f_{ab} (MHz)	f_{ac} (MHz)	f_{bc} (MHz)	error (MHz)	f'_a (MHz)	f'_b (MHz)	f'_c (MHz)	principal axis \vec{p}_a	principal axis \vec{p}_b	principal axis \vec{p}_c
A1	70.253	0.092	0.021	-0.062	0.041	0.019	-0.030	-0.000	0.003	-0.067	0.064	0.003	(-0.236, 0.970, -0.065)	(0.601, 0.093, -0.794)	(0.763, 0.226, 0.605)
A2	70.020	0.188	0.087	-0.104	0.016	0.027	0.057	0.066	0.005	0.133	-0.133	-0.000	(0.810, 0.242, 0.534)	(0.009, -0.916, 0.401)	(0.586, -0.320, -0.744)
A3	69.994	0.236	-0.039	0.042	-0.004	0.018	0.151	0.056	0.003	-0.176	0.157	0.019	(-0.728, -0.114, 0.676)	(0.576, 0.432, 0.694)	(0.371, -0.895, 0.249)
A4	69.968	0.325	0.217	-0.191	-0.026	0.026	-0.036	0.095	0.004	-0.237	0.222	0.015	(0.086, -0.904, 0.419)	(0.991, 0.034, -0.130)	(0.104, 0.427, 0.898)
A5	69.848	0.280	-0.149	0.182	-0.033	0.027	0.085	0.055	0.010	0.202	-0.194	-0.008	(-0.139, -0.952, -0.273)	(0.883, 0.006, -0.470)	(-0.449, 0.307, -0.839)
A6	69.731	0.362	0.012	-0.016	0.005	0.041	0.094	-0.234	0.003	-0.272	0.236	0.036	(0.319, -0.667, -0.673)	(0.191, -0.651, 0.735)	(-0.928, -0.363, -0.080)
A7	69.366	0.305	-0.020	0.023	-0.003	0.001	-0.141	-0.161	0.004	0.217	-0.214	-0.003	(-0.419, -0.582, 0.697)	(0.513, 0.482, 0.710)	(0.749, -0.656, -0.097)
A8	69.400	0.308	-0.188	0.230	-0.041	0.023	-0.031	0.033	0.003	0.234	-0.197	-0.038	(0.045, 0.992, 0.115)	(0.975, -0.069, 0.212)	(-0.218, -0.103, 0.970)
B1	71.113	1.499	-0.407	0.628	-0.221	0.067	0.901	-0.052	0.019	-1.224	0.633	0.591	(0.742, -0.046, -0.669)	(-0.146, -0.985, -0.095)	(-0.654, 0.168, -0.737)
B2	70.576	1.889	0.854	-0.959	0.106	0.077	0.238	0.944	0.034	-1.512	1.020	0.492	(-0.023, -0.862, 0.506)	(0.829, 0.266, 0.491)	(0.559, -0.431, -0.709)
B3	69.933	2.957	0.833	-0.825	-0.008	1.049	0.066	1.607	0.069	-2.283	1.823	0.459	(-0.255, 0.793, -0.553)	(-0.636, -0.568, -0.522)	(-0.728, 0.219, 0.650)
B4	65.900	7.994	-1.846	-1.274	3.120	4.729	1.036	-1.060	0.098	-6.526	3.367	3.159	(0.719, -0.678, -0.152)	(-0.104, -0.320, 0.942)	(-0.687, -0.661, -0.301)
B5	63.55	11.39	-0.93	-3.59	4.52	6.70	0.62	-1.56	0.22	-9.28	5.15	4.13	(-0.63, 0.77, 0.12)	(0.46, 0.48, -0.75)	(-0.63, -0.42, -0.66)
B6	67.19	6.19	0.01	-0.39	0.38	4.10	-0.36	-1.45	0.15	-4.43	4.32	0.11	(0.66, -0.73, -0.17)	(-0.67, -0.68, 0.31)	(0.34, 0.09, 0.94)
B7	61.856	13.580	1.792	-6.964	5.172	6.261	2.684	2.566	0.095	-10.299	8.708	1.590	(-0.446, 0.892, -0.071)	(-0.601, -0.357, -0.715)	(-0.663, -0.277, 0.695)
B8	69.323	4.813	0.356	2.672	-3.028	0.333	-1.776	-0.316	0.068	-3.793	2.787	1.005	(0.392, 0.025, 0.920)	(0.220, 0.968, -0.120)	(-0.893, 0.249, 0.374)
B9	66.221	1.453	-0.103	-0.002	0.105	0.637	0.120	-0.790	0.026	-1.071	0.977	0.094	(0.515, -0.686, -0.513)	(-0.356, -0.716, 0.600)	(-0.780, -0.126, -0.613)
B10	61.96	9.90	-1.53	-1.80	3.33	6.10	-1.85	-0.14	0.22	-7.90	5.44	2.45	(-0.70, 0.70, -0.11)	(0.62, 0.53, -0.58)	(0.35, 0.47, 0.81)
B11	66.661	2.515	0.650	0.988	-1.638	0.027	-0.029	-1.058	0.082	-2.011	1.363	0.648	(0.007, 0.333, 0.943)	(-0.049, -0.942, 0.333)	(0.999, -0.048, 0.010)
B12	59.873	13.490	0.978	-5.437	4.459	6.742	-3.263	3.111	0.091	-10.943	6.552	4.392	(-0.529, 0.803, -0.274)	(0.639, 0.164, -0.752)	(0.559, 0.573, 0.600)
B13	58.83	13.51	-0.50	-3.96	4.46	8.43	0.94	-1.16	0.10	-10.99	6.38	4.61	(-0.63, 0.77, 0.10)	(0.77, 0.63, -0.00)	(0.06, -0.07, 1.00)
B14	59.97	14.33	4.77	6.80	-11.57	0.20	1.02	-0.37	0.26	-11.64	6.82	4.82	(-0.06, 0.02, 1.00)	(-0.09, -1.00, 0.02)	(0.99, -0.09, 0.06)
B15	57.34	13.60	6.80	4.09	-10.89	0.53	0.03	-1.16	0.14	-10.98	6.90	4.08	(-0.00, 0.08, 1.00)	(0.98, 0.19, -0.01)	(0.19, -0.98, 0.08)
B16	55.29	13.12	5.72	4.97	-10.68	0.16	-0.44	-0.39	0.70	-10.70	5.76	4.94	(-0.03, -0.02, -1.00)	(0.98, 0.21, -0.03)	(-0.21, 0.98, -0.02)

TABLE S2: Parameters in equations (1), (2) in the main paper obtained by applying linear regression to data from the DFT calculations. Column labeled "error" contains the typical error of the fitted parameters. Sites are numbered in the order in which they are listed in [5].

site	f_{iso} (MHz)	f_{ani} (MHz)	f_{aa} (MHz)	f_{bb} (MHz)	f_{cc} (MHz)	f_{ab} (MHz)	f_{ac} (MHz)	f_{bc} (MHz)	error (MHz)	f'_a (MHz)	f'_b (MHz)	f'_c (MHz)	principal axis \bar{p}_a	principal axis \bar{p}_b	principal axis \bar{p}_c
A1	72.506	1.088	-0.843	0.601	0.242	0.028	0.117	0.109	0.023	-0.856	0.634	0.222	(0.994, -0.011, -0.105)	(-0.041, -0.959, -0.279)	(-0.098, 0.282, -0.954)
A2	72.631	0.689	-0.490	0.278	0.213	-0.060	-0.133	0.185	0.016	-0.516	0.452	0.064	(0.985, 0.035, 0.172)	(0.140, -0.744, -0.654)	(-0.105, -0.668, 0.737)
A3	73.280	0.553	-0.230	-0.062	0.292	0.119	-0.051	-0.255	0.031	0.441	-0.305	-0.136	(-0.151, -0.475, 0.867)	(-0.796, 0.578, 0.178)	(0.586, 0.663, 0.466)
A4	73.408	0.808	-0.285	-0.009	0.294	0.013	-0.124	-0.476	0.017	0.654	-0.397	-0.258	(0.115, 0.580, -0.806)	(0.530, 0.650, 0.544)	(0.840, -0.490, -0.233)
A5	72.207	0.840	0.374	-0.493	0.120	-0.005	-0.363	-0.148	0.016	0.637	-0.537	-0.100	(0.806, 0.073, -0.587)	(-0.116, -0.953, -0.279)	(-0.580, 0.293, -0.760)
A6	72.650	0.557	0.128	-0.195	0.067	0.012	0.162	0.315	0.013	-0.418	0.365	0.053	(-0.152, -0.805, 0.574)	(0.526, 0.426, 0.736)	(0.837, -0.414, -0.358)
A7	72.460	1.181	0.677	-0.847	0.170	0.054	-0.001	-0.303	0.021	-0.932	0.679	0.253	(0.032, -0.964, -0.265)	(0.999, 0.041, -0.026)	(0.036, -0.264, 0.964)
A8	72.811	0.890	0.531	-0.646	0.115	0.112	-0.106	-0.129	0.031	-0.674	0.573	0.102	(-0.078, 0.986, 0.150)	(0.960, 0.115, -0.255)	(0.269, -0.124, 0.955)
B1	61.01	24.69	-0.92	-10.67	11.59	13.39	0.72	0.51	0.44	-20.05	11.83	8.22	(-0.57, 0.82, -0.00)	(0.21, 0.15, 0.97)	(0.79, 0.55, -0.25)
B2	60.81	24.90	-2.29	-9.40	11.69	13.92	1.01	0.53	0.44	-20.21	12.05	8.16	(0.61, -0.79, -0.01)	(0.24, 0.18, 0.95)	(-0.75, -0.59, 0.30)
B3	62.52	24.23	-0.71	-10.79	11.50	12.99	-0.01	-0.45	0.42	-19.69	11.52	8.17	(-0.56, 0.83, 0.01)	(-0.06, -0.05, 1.00)	(0.82, 0.56, 0.08)
B4	66.21	18.55	-2.58	-6.33	8.91	10.36	-1.04	-0.87	0.32	-14.98	9.45	5.52	(0.64, -0.77, -0.00)	(-0.29, -0.24, 0.93)	(-0.71, -0.60, -0.37)
B5	73.676	3.796	-1.806	2.715	-0.909	-0.036	-1.205	-0.150	0.087	2.721	-2.646	-0.075	(-0.003, -0.999, 0.042)	(0.821, 0.022, 0.571)	(0.572, -0.037, -0.820)
B6	73.063	5.235	-2.297	0.735	1.562	-2.599	-1.193	1.181	0.088	-3.830	3.558	0.272	(-0.875, -0.475, -0.090)	(-0.418, 0.650, 0.635)	(0.243, -0.593, 0.768)
B7	63.93	19.57	5.56	10.14	-15.70	-0.11	1.09	0.02	0.56	-15.76	10.14	5.62	(0.05, 0.00, -1.00)	(-0.02, 1.00, -0.00)	(1.00, 0.02, 0.05)
B8	73.934	1.629	-0.549	0.581	-0.032	-0.011	1.003	-0.018	0.058	-1.326	0.748	0.578	(0.790, -0.001, -0.612)	(0.608, -0.123, 0.785)	(0.076, 0.992, 0.097)
B9	72.11	9.50	-3.51	-0.74	4.25	5.01	-1.05	-1.86	0.17	-7.33	5.86	1.47	(0.79, -0.61, -0.03)	(-0.35, -0.49, 0.80)	(-0.50, -0.62, -0.60)
B10	74.422	1.409	0.766	-0.447	-0.319	-0.352	-0.118	-0.641	0.032	-1.090	0.864	0.227	(0.182, 0.742, 0.645)	(0.956, -0.286, 0.060)	(-0.229, -0.606, 0.762)
B11	73.897	1.825	-0.405	-0.393	0.798	0.739	0.047	0.800	0.038	1.292	-1.289	-0.004	(0.241, 0.500, 0.832)	(0.609, -0.745, 0.272)	(-0.756, -0.441, 0.484)
B12	74.608	3.383	1.236	-1.415	0.178	0.755	-0.008	1.837	0.055	-2.723	1.765	0.958	(-0.160, 0.834, -0.528)	(-0.680, -0.481, -0.554)	(-0.716, 0.270, 0.644)
B13	62.86	20.09	10.29	5.91	-16.20	0.33	0.27	0.38	0.61	-16.21	10.31	5.89	(-0.01, -0.02, 1.00)	(1.00, 0.08, 0.01)	(0.08, -1.00, -0.02)
B14	61.54	22.79	-8.27	-2.88	11.15	-12.59	-0.47	0.76	0.40	-18.45	11.34	7.10	(0.78, 0.63, -0.00)	(-0.13, 0.17, 0.98)	(0.61, -0.76, 0.21)
B15	74.498	1.849	0.730	-0.867	0.137	-0.322	-0.188	-0.958	0.031	-1.509	0.793	0.716	(0.164, 0.844, 0.510)	(0.983, -0.180, -0.018)	(-0.077, -0.505, 0.860)
B16	62.46	20.32	11.19	4.99	-16.18	-0.24	0.22	-0.50	0.61	-16.20	11.20	5.00	(-0.01, 0.02, 1.00)	(1.00, -0.04, 0.01)	(-0.04, -1.00, 0.02)

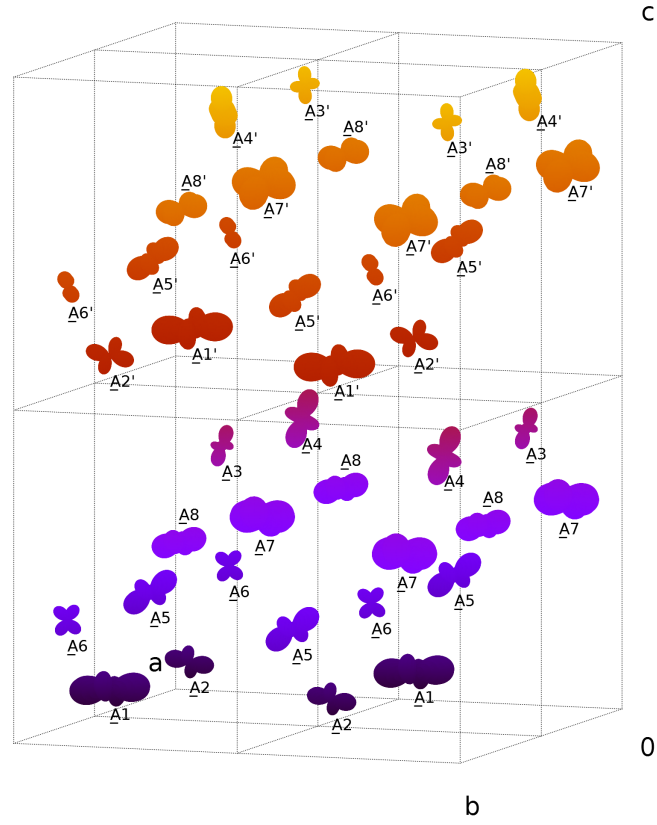


FIG. S3: Tensors of hyperfine anisotropy of particular iron A sites from the DFT calculations drawn in the elementary cell (scaling coefficient $C = 1.25 \text{ \AA} \cdot \text{MHz}^{-1}$). Sites are numbered in the order in which they are listed in [5]; primes denote sites generated by the *ac*-glide symmetry operation. (Surface colour corresponds to the *z*-coordinate and serves just for clarity.)

Correlation of experimental and calculated hyperfine parameters

TABLE S3: Mean square deviation $\sigma(i, j)$ (in MHz) according to equation (5) in the main paper (in bold face if $\sigma(i, j) < 18$ MHz) for all combinations of B site data obtained from the experiment and from the DFT results. Lower value indicates better correspondence. For experimental data, labels of the sites follow the convention in [2]. For the DFT results, the sites are numbered in the order in which they are listed in [5]. The sites were ordered to make the grouping (see the main paper text) clearly visible.

DFT site	experiment site															
	B3	B2	B1	B8	B11	B9	B6	B4	B5	B10	B12	B7	B13	B14	B15	B16
<u>B12</u>	8.15	7.20	7.28	11.17	14.19	14.86	14.56	17.21	22.13	23.87	27.97	24.90	30.21	29.47	32.90	36.12
<u>B15</u>	8.04	6.83	6.51	10.48	13.83	14.46	14.17	16.96	22.01	23.72	28.14	25.21	30.16	29.14	32.68	35.84
<u>B8</u>	7.80	6.41	4.89	9.68	12.93	13.51	13.39	15.99	21.37	23.21	28.25	24.98	29.50	28.02	31.87	34.92
<u>B5</u>	8.48	7.47	5.95	8.18	12.71	13.54	13.41	16.45	21.88	22.91	28.12	26.12	29.84	27.33	31.34	34.25
<u>B10</u>	7.98	6.74	6.21	10.09	13.61	14.32	13.96	16.85	21.96	23.66	28.22	25.30	30.10	28.72	32.35	35.51
<u>B11</u>	7.14	6.04	5.40	9.84	12.94	13.47	12.98	15.52	20.70	22.45	27.12	24.15	28.90	28.59	32.17	35.21
<u>B6</u>	8.22	7.21	6.50	9.29	12.57	12.62	10.84	13.40	18.47	20.19	25.67	23.47	26.81	28.21	31.66	34.56
<u>B9</u>	10.44	10.00	9.87	12.34	14.04	13.29	10.16	11.41	15.69	18.02	23.59	21.29	24.11	29.61	32.51	35.24
<u>B4</u>	18.74	19.91	20.72	21.54	19.78	17.76	14.06	11.48	9.16	12.07	14.88	13.24	14.44	31.27	31.94	33.88
<u>B14</u>	26.47	27.81	28.22	28.14	25.55	23.43	20.77	17.13	13.54	14.03	16.10	16.62	12.93	33.15	33.26	34.07
<u>B3</u>	26.32	27.59	28.73	29.31	26.49	24.36	21.41	18.32	13.64	15.85	15.06	13.62	13.47	34.93	34.22	35.61
<u>B1</u>	27.95	29.31	30.49	30.91	27.77	25.64	23.02	19.70	14.75	16.44	14.81	13.51	12.85	35.04	34.08	35.19
<u>B2</u>	28.37	29.76	30.80	31.19	28.08	25.94	23.26	19.78	14.92	16.48	15.30	14.12	12.75	35.12	34.30	35.32
<u>B7</u>	22.50	23.05	22.82	18.64	18.24	20.11	21.73	24.41	27.06	25.61	29.41	29.15	29.35	8.72	14.02	16.77
<u>B16</u>	23.96	24.61	25.19	21.12	19.81	21.50	23.10	25.77	27.30	25.84	27.96	27.96	28.70	9.27	11.35	14.69
<u>B13</u>	23.48	24.11	24.56	20.43	19.33	21.09	22.63	25.37	27.12	25.67	28.12	28.09	28.74	8.90	11.74	15.02

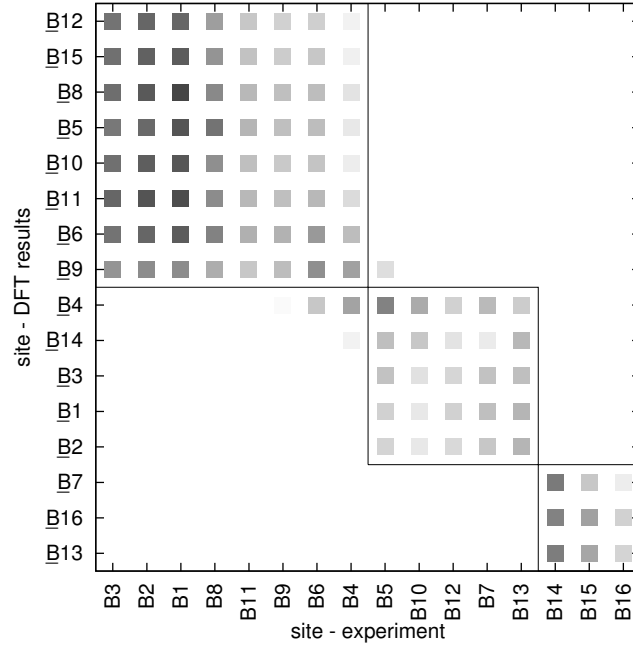


FIG. S4: Mean square deviation $\sigma(i, j)$ according to equation (5) in the main paper plotted for all combinations of B site data obtained from the experiment and from the DFT results. Brightness is proportional to $\sigma(i, j)$ value (black for $\sigma(i, j) = 0$ MHz; white for $\sigma(i, j) \geq 18$ MHz) – darker field indicates better correspondence. For experimental data, labels of the sites follow the convention in [2]. For the DFT results, the sites are numbered in the order in which they are listed in [5]. The sites were ordered to make the grouping (see the main paper text) clearly visible.

-
- [1] M. Mizoguchi, *NMR Study of the Low Temperature Phase of Fe_3O_4 . I. Experiments*, J. Phys. Soc. Jap. **44**, 1501-1511 (1978).
 - [2] M. Mizoguchi, *Charge and Orbital Ordering Structure of Fe_3O_4 in the Low-Temperature Phase as Deduced from NMR Study*, J. Phys. Soc. Jap. **70**, 2333-2344 (2001).
 - [3] K. Abe and S. Chikazumi, *Computer Controlled Torque Magnetometer for Automatic Determination of Crystal Orientation*, Japan. J. Appl. Phys. **15**, 619 (1976).
 - [4] K. Abe, Y. Miyamoto, and S. Chikazumi, *Magnetocrystalline anisotropy of low-temperature phase of magnetite*, J. Phys. Soc. Jap. **41**, 1894-1902 (1976).
 - [5] M. S. Senn, J. P. Wright and J. P. Attfield, *Charge order and three-site distortions in the Verwey structure of magnetite*, Nature **481**, 173-176 (2012).

Magnetocrystalline anisotropy of magnetite

R Řezníček¹, V Chlan¹, H Štěpánková¹, P Novák² and M Maryško²

¹ Faculty of Mathematics and Physics, Charles University in Prague, V Holešovičkách 2, CZ-180 00 Prague 8, Czech Republic

² Institute of Physics of ASCR, Cukrovarnická 10, CZ-162 53 Prague 6, Czech Republic

E-mail: reznicek@mbox.troja.mff.cuni.cz

Received 16 September 2011, in final form 28 November 2011

Published 6 January 2012

Online at stacks.iop.org/JPhysCM/24/055501

Abstract

The spin reorientation temperature T_{SR} of stoichiometric Fe_3O_4 , as well as of magnetite with a small number of vacancies and magnetite containing a low concentration of Ti, Zn, Al and Ga was measured on single-crystal samples using the ac susceptibility. In the same experiment the temperature T_V of the Verwey transition was also found. The results show that a correlation between T_{SR} and T_V exists. The electronic structure of the compounds studied was determined using the density-functional-based GGA + U method. For stoichiometric magnetite the first and second cubic anisotropy constants were calculated, while for magnetite with defects the distribution of electron density using the ‘atoms in molecules’ approach was determined. Based on a combination of experimental results with the electronic structure calculations an explanation of the temperature dependence of the magnetocrystalline anisotropy of magnetite is suggested.

(Some figures may appear in colour only in the online journal)

1. Introduction

Temperature dependence of the magnetocrystalline anisotropy of magnetite was the subject of numerous studies in the past (for a survey see [1]). In the cubic phase, above the Verwey transition, the anisotropic part E_{an} of the energy is well described by the first and second anisotropy constant K_1 and K_2 :

$$E_{an} = K_1 (\vartheta_x^2 \vartheta_y^2 + \vartheta_x^2 \vartheta_z^2 + \vartheta_y^2 \vartheta_z^2) + K_2 \vartheta_x^2 \vartheta_y^2 \vartheta_z^2, \quad (1)$$

where $\vartheta_x, \vartheta_y, \vartheta_z$ are direction cosines of the magnetization. Unlike the magnetization, the magnitude of which increases monotonically with decreasing temperature, the $K_1(T)$ and $K_2(T)$ dependences are nonmonotonic. K_1 is negative at ambient temperature; it first decreases with decreasing temperature, acquiring a minimum at $T \simeq 250$ K. It then increases and becomes positive at the spin reorientation temperature T_{SR} , which is slightly higher than the temperature T_V of the Verwey transition. The temperature dependence of K_2 is similar [2]. Abe *et al* [3] suggested to decompose $K_1(T)$ into a monotonically decreasing, negative, term K_1^0 and

a positive, anomalous, part ΔK_1 :

$$K_1 = K_1^0 + \Delta K_1. \quad (2)$$

Below T_V the crystal symmetry is monoclinic with the space group Cc and the anisotropy is described by

$$E_{an}^{Cc} = K_a \vartheta_a^2 + K_b \vartheta_b^2 - K_u \vartheta_{101}^2 + K_{aa} \vartheta_a^4 + K_{bb} \vartheta_b^4 + K_{ab} \vartheta_a^2 \vartheta_b^2, \quad (3)$$

where ϑ_a and ϑ_b are the direction cosines with respect to the monoclinic a and b axes, and ϑ_{101} with respect to the axis $[101]$ of the monoclinic system defined in [3] (i.e. the elongated body diagonal of cubic cell). The values of the anisotropy constants at 4.2 K, determined experimentally by Abe *et al* [3], are (in 10^4 J m^{-3})

$$\begin{aligned} K_a &= 25.5, & K_b &= 3.7, & K_u &= 2.1, \\ K_{aa} &= 1.8, & K_{bb} &= 2.4, & K_{ab} &= 7.0, \end{aligned} \quad (4)$$

and below T_V the anisotropy energy is thus dominated by the second-order term proportional to K_a . The fourth-order terms in E_{an}^{Cc} may be averaged [3] to obtain an analog of the cubic

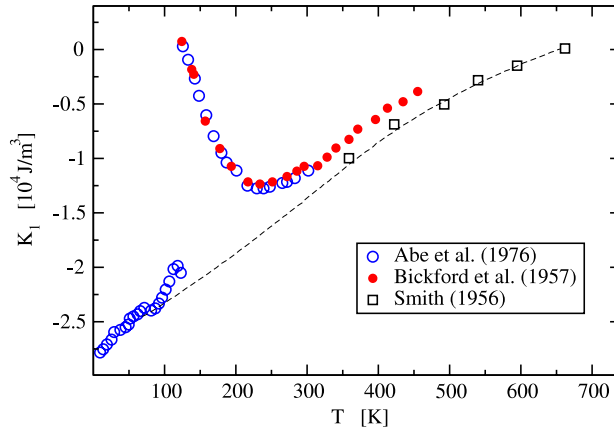


Figure 1. Temperature dependence of the magnetic anisotropy constant K_1 in magnetite. The dashed line is an estimation of the $K_1(T)$ dependence using the high temperature data of Smith [7] and low temperature K_1^{Cc} data of Abe *et al* [3]. Adapted from [1].

K_1 constant:

$$K_1^{Cc} = \frac{1}{45}(-20K_{aa} - 20K_{bb} - 6K_{ab}). \quad (5)$$

The K_1^{Cc} temperature dependence smoothly connects to $K_1^0(T)$ extrapolated from the cubic phase. The situation is shown in figure 1 adapted from [1].

There were several attempts to explain the increase of K_1 below 250 K. Abe *et al* [3] connected ΔK_1 with the possible presence of strongly anisotropic ions, the most probable candidate being Fe^{2+} . Siratori and Kino [4] proposed that ΔK_1 originates from a short range ordering of Fe^{2+} ions on the octahedral sublattice that presumably appears above T_V and becomes stronger as temperature decreases. As pointed out by Kąkol and Honig [2] both these suggestions are rather improbable. These authors showed that the deviation from ideal stoichiometry influences the anisotropy only slightly, despite the fact that the resulting increase of the mean valency of Fe(B) ions reduces the number of (hypothetical) ferrous ions on the octahedral sites. Also the nuclear magnetic resonance (NMR) results [6] showed that, if any short order exists, it must be dynamic, with a characteristic frequency larger than ~ 100 MHz.

Using thermodynamic considerations and the mean-field model Aragón [5] analyzed the temperature dependence of K_1 in stoichiometric and slightly non-stoichiometric magnetite. He concluded that the anomalous term $\Delta K_1(T)$ is caused by a degeneracy of the excited states, which should be twice the degeneracy of the ground state. The nature of the excited states was not specified by Aragón, however.

To achieve a deeper insight into the anisotropy of magnetite and magnetite containing defects we determined the spin reorientation temperature T_{SR} using the ac susceptibility. T_{SR} is very sensitive to the details of the temperature dependence of the anisotropy, yet its determination using ac susceptibility is relatively easy. In the same experiment the Verwey temperature is also determined. The systems studied comprise stoichiometric Fe_3O_4 , magnetite with a small number of vacancies

$\text{Fe}_{3(1-\delta)}\text{O}_4$ and magnetite $\text{Fe}_{3-x}\text{M}_x\text{O}_4$ containing a low concentration of $M = \text{Ti}, \text{Zn}, \text{Al}$ and Ga . These substitutions, as well as the vacancies, represent ‘charged’ defects, i.e. they change the nominal valency of iron ions on the octahedral sites. In stoichiometric magnetite all tetrahedral (A) sites are occupied by ferric ions, while the formal valency of iron on the octahedral (B) sublattice v_B is 2.5, so that formally its formula may be written as $\text{Fe}^{3+}(\text{A})[\text{Fe}^{3+}(\text{B})\text{Fe}^{2+}(\text{B})]\text{O}_4$. Cation vacancies occur in the B sublattice [2] and to maintain charge neutrality more electron holes should appear on the B sublattice, i.e. according to the above formula part of Fe^{2+} becomes Fe^{3+} . The stable valency of zinc is 2+ and it replaces trivalent iron on the A sites [9]. The presence of Zn thus again leads to an increase of Fe(B) valency. Another charged impurity is titanium, which is tetravalent and enters into the B sublattice [8]. In this case charge neutrality requires a decrease in the average valency of Fe(B) ions. Weaker influence on the charge distribution is from aluminum, which is trivalent and enters the B sublattice, providing its concentration is low [11]. The situation in magnetite containing Ga is more complex: Ga is trivalent and it preferentially occupies the A sites, though part may be found also in the B sublattice [12, 13]—the Fe(B) valency is therefore affected mostly by the Ga ions in the B sites.

We also calculate the anisotropy of stoichiometric cubic magnetite using the method based on the density functional theory. As such a calculation probes the energy of the system at absolute zero temperature, the calculated K_1 corresponds to $K_1^{Cc}(T = 0 \text{ K})$ of (5). Analogous determination of anisotropy in the defect-containing systems would be too demanding on the computing power. For these systems we calculate the electron and spin density distribution, which quantities are of considerable interest, especially when the defect is charged. In the gas of quasifree electrons the screening of a static point charge results in the Friedel oscillations. In the magnetite the situation is more complex. First, the extra charge is screened both by a local distortion of the crystal and by a redistribution of the electron density. Second, due to the half-metallic character of the compound, only the minority spin electrons are effective in screening the extra charge. Finally the 3d electrons of iron are correlated. An interesting question is whether the extra charge carriers induced by the charged defect remain localized on a single B sites close to the defect, or to which extent they become delocalized.

2. Experimental details

Chemical formulae of samples with cation substitution and non-stoichiometric samples are $\text{Fe}_{3-x}\text{M}_x\text{O}_4$ and $\text{Fe}_{3(1-\delta)}\text{O}_4$, where the x parameter stands for the concentration of substitution metal M and the δ parameter denotes the concentration of vacancies. Single-crystal samples were either prepared by the floating zone technique [8] or grown from the melt by using the cold crucible method [9]. The electron microprobe assisted in a determination of the concentration of the substitution. A list of studied samples is provided in table 1, where T_V and T_{SR} are also given.

Table 1. List of investigated compounds. Compounds denoted by an asterisk (*) were prepared by the floating zone method [8]; all other samples were grown from the melt by the cold crucible technique [9]. ν_B is a formal mean valency of Fe on the B sublattice. Spin reorientation T_{SR} and temperature of the Verwey transition T_V are in K. Although trivalent Ga ions preferentially occupy the A sites, part of them ($x_B \sim 0.01$ [13]) entering into the B sublattice was taken into account when calculating ν_B .

Compound notation	x or δ	ν_B	T_{SR}	T_V
Pure*	0.000	2.500	132.7	122.2
Ga*	0.050	2.497	126.7	117.5
Zn ₁	0.007	2.504	124.0	113.2
Zn ₂	0.009	2.505	122.5	110.0
Zn ₃	0.017	2.509	121.0	104.3
vac ₁	0.002	2.503	128.0	114.1
vac ₂	0.009	2.511	124.0	101.0
Ti ₁ *	0.008	2.494	128.0	116.4
Ti ₂	0.008	2.494	126.0	119.0
Ti ₃	0.020	2.485	110.0	79.1
Al ₁ *	0.005	2.499	128.3	119.7
Al ₂ *	0.030	2.492	126.5	97.3

As a suitable tool to determine T_V and T_{SR} we used the ac susceptibility at a zero applied static magnetic field (initial susceptibility). It was measured by a SQUID magnetometer MPMS-5S (Quantum Design) in ac magnetic field $h_e = 0.3$ Oe at frequency 1 Hz. Samples of approximately cylindrical form were used with the external driving ac magnetic field h_e directed along the longitudinal axis. The evaluated external complex susceptibility $\chi_e = \chi'_e - i\chi''_e = m/h_e$ was not corrected for demagnetizing effects depending on the sample dimensions. χ_e sensitively reflects the magnetic and electronic structure of the system, though the details of the underlying mechanism may be complex. In the past, temperature dependence of the susceptibility of stoichiometric Fe_3O_4 was studied by several authors. In particular Skumryev *et al* [10] showed that there is a clear anomaly in the $\chi'_e(T)$ and $\chi''_e(T)$ at T_V , while the spin reorientation transition manifests itself in a less pronounced maximum in $\chi'_e(T)$ accompanied by a minimum in $\chi''_e(T)$. These authors also discussed the possible origin of the observed $\chi_e(T)$ dependence.

We studied the temperature dependence of χ_e in the temperature region of the Verwey transition, i.e. between about 70 and 140 K, and found that in all samples its behavior is similar to the one of stoichiometric magnetite. A typical example is displayed in figure 2. The temperature of the Verwey transition T_V was determined as a point of maximum first derivative $d\chi'_e/dT$. This temperature corresponds approximately to a maximum of the imaginary part χ''_e . For low concentration of defects the increase of the susceptibility is abrupt which suggests the first-order character of the transition. Above a critical concentration the character of the $\chi'_e(T)$ becomes continuous, pointing to the second-order character of the phase transition [2]. Above the Verwey transition the real part of the susceptibility increases with increasing temperature and at $T = T_{SR}$ it passes through a maximum (at this temperature we also observed a less pronounced minimum of the $\chi''_e(T)$). This temperature was taken as a spin reorientation temperature.

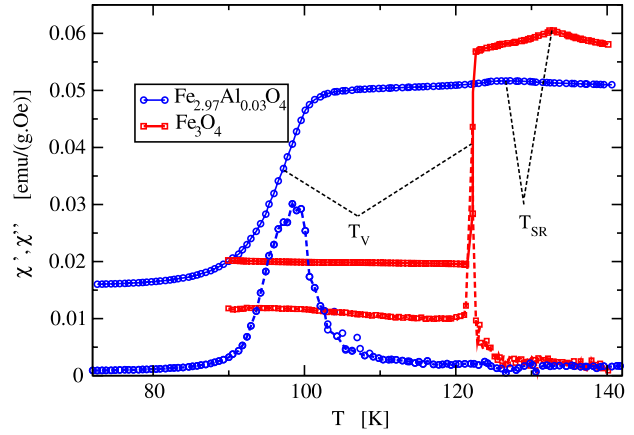


Figure 2. Temperature dependence of the real (full curves) and imaginary (dashed curves) parts of the external susceptibility for the pure magnetite and $\text{Fe}_{2.97}\text{Al}_{0.03}\text{O}_4$ (sample Al₂ in table 1). The imaginary part was multiplied by a factor of 50.

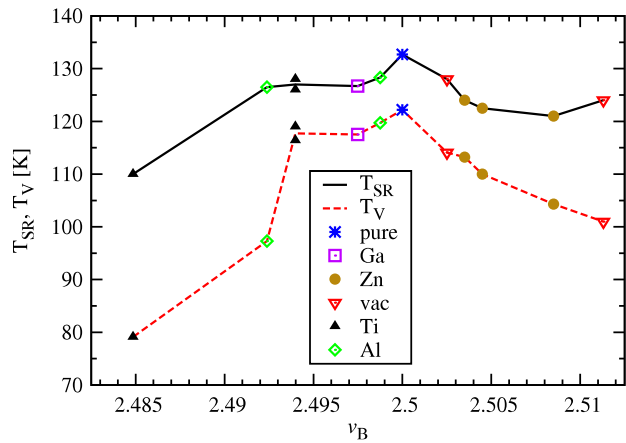


Figure 3. Dependence of spin reorientation temperature T_{SR} and temperature T_V of Verwey transition on the average valency ν_B of iron ions on the octahedral sites. The lines serve only as guides for the eyes.

Our measurements were performed during warming the samples after verifying that for pure magnetite the temperature hysteresis between T_V measured during warming and cooling seems to be finite but less than 0.1 K. This is in accord with the hysteresis 0.03 K obtained from the measurements of the specific heat [14]. In our experiments no hysteresis was found at the temperature T_{SR} .

The dependence of T_{SR} and T_V on the mean valency of Fe(B) ions is displayed in figure 3. We also studied in all 12 systems the temperature dependence of the ^{57}Fe NMR spectra. The results will be published elsewhere; here we only mention that T_V determined by NMR agrees well with the value obtained from the ac susceptibility.

3. Calculations

The electronic structure of the respective compounds was calculated using the augmented plane wave + local orbital method based on the density functional theory as implemented

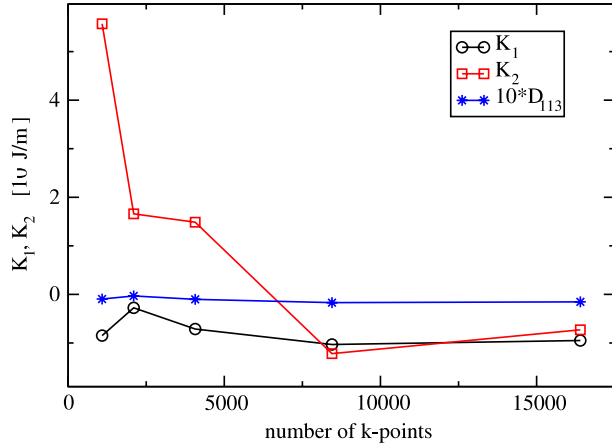


Figure 4. Calculated anisotropy constants of the stoichiometric Fe_3O_4 as functions of the number of k -points in the irreducible wedge of the Brillouin zone.

in the WIEN2k program [15]. For the exchange–correlation functional the generalized-gradient approximation form [16] was adopted. To improve the description of iron 3d electron correlations we used the rotationally invariant version of the LDA+ U method as described by Liechtenstein *et al* [17], with the GGA instead of LSDA exchange–correlation potential and with a single parameter $U_{\text{eff}} = U - J$ only. In most of the calculations described in what follows, $U_{\text{eff}} = 4.5$ eV, which value was successfully used to explain the contact hyperfine field in a number of iron oxides [18]. The radii of the atomic spheres were chosen as 1.6 au for oxygen and 1.8 au for the cations. The number of basis functions was $\sim 100/\text{atom}$ ($RK_{\text{max}} = 7.0$), and the charge density was Fourier-expanded to $G_{\text{max}} = 16 \sqrt{\text{Ryd}}$.

In all cases considered the band structure corresponds to a half-metal: the density of minority spin states is nonzero on the Fermi energy, while there is a gap in the density of the majority spin states. The magnitude of this gap increases with increasing U_{eff} and for $U_{\text{eff}} = 4.5$ eV it amounts to 2.28 eV in the stoichiometric magnetite. In the defect-containing Fe_3O_4 the value of the gap is reduced, being 2.02, 1.87, 1.76, 1.55 and 1.38 eV for Ga(A), vacancy(B), Zn(A), Al(B) and Ti(B), respectively. The magnitude of the gap is important for the eventual application of magnetite in spintronics.

3.1. Magnetocrystalline anisotropy

Calculation of the magnetocrystalline anisotropy of ferric compounds which possess cubic symmetry is a formidable problem—the anisotropy is small as a rule and calculated results are sensitive to the method used, as well as to the parameters of the calculation (number of the k -points, number of the basis functions, form of the exchange–correlation functional, etc). This concerns the first anisotropy constant K_1 and it presents an even more serious problem for the second and higher anisotropy constants. K_1 of the stoichiometric magnetite was calculated by Jeng and Huo [19], who used the local-spin-density approximation, as implemented in the linear muffin-tin orbital method [20]. No attempt was made

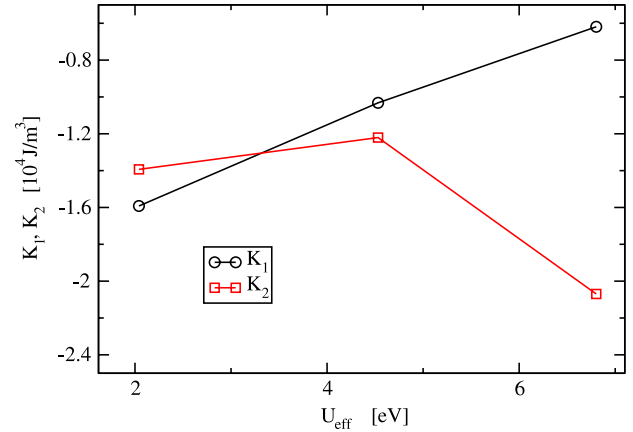


Figure 5. Calculated anisotropy constants of the stoichiometric Fe_3O_4 as functions of the parameter U_{eff} .

to improve the description of the electron correlation by employing the LDA + U method.

In view of the differences between our and [19] theoretical methods we recalculated the anisotropy of the cubic magnetite using the force theorem (for a recent discussion of the force theorem and further references see [21]). The spin-polarized calculation is first converged; then the magnetization direction $[hkl]$ is specified and the eigenvalue problem with a converged potential and the spin–orbit coupling switched on is solved. Finally the sum of eigenvalues E_{hkl} up to the Fermi energy is evaluated for different $[hkl]$ and used to determine the anisotropy. In cubic systems three calculations with magnetization along $[001]$, $[111]$ and $[110]$ symmetry directions are sufficient to determine the first and second anisotropy constant:

$$\begin{aligned} K_1 &= 4(E_{110} - E_{001}); \\ K_2 &= 9(3E_{111} + E_{001} - 4E_{110}). \end{aligned} \quad (6)$$

The key problem in calculating the magnetocrystalline anisotropy is its dependence on the number N_k of k -points in which the eigenvalue problem is solved. For $U_{\text{eff}} = 4.5$ eV this dependence is displayed in figure 4. To see the role of third- and higher-order anisotropy constants, the calculation was also performed for $\vec{M} \parallel [113]$ and the resulting E_{113} subtracted from the anisotropy energy \bar{E}_{113} calculated using K_1, K_2 of (6). The result

$$D_{113} = E_{113} - \bar{E}_{113} \quad (7)$$

is also displayed in figure 4. As seen from this figure K_1 is negative and reasonably converged for $N_k \gtrsim 7000$, which to a lesser extent holds also for K_2 . The energy difference D_{113} is small, indicating that the anisotropy is well approximated using only two anisotropy constants.

The dependence of K_1 and K_2 on the parameter U_{eff} is shown in figure 5. As the calculation with $N_k = 16400$ (corresponding to the division of the Brillouin zone 40, 40, 40) represented the upper limit of our computer possibilities, this dependence was determined by adopting $N_k = 8448$ (division 32, 32, 32). The value of the first anisotropy constant

Table 2. Stoichiometric Fe₃O₄. Atomic valence charges q determined by the AIM method (in units of electron charge) and spin magnetic moments m_s (in Bohr magnetons). q is calculated as the difference of the atom's atomic number and the charge contained in the AIM volume.

Atom					
Fe(B)		Fe(A)		Oxygen	
q	m_s	q	m_s	q	m_s
1.624	3.955	1.804	4.106	-1.261	0.049

extrapolated to $U_{\text{eff}} \rightarrow 0$ is $-2.1 \times 10^4 \text{ J m}^{-3}$, which is surprisingly close to $-2.7 \times 10^4 \text{ J m}^{-3}$ obtained by Jeng and Guo [19].

3.2. Magnetite with defects

The experimentally studied compounds were modeled by supercells $2 \times 2 \times 2$, where one iron atom was substituted by Zn, Ti, Al, Ga or removed. Denoting the defect as X, the formula is Fe₄₇XO₆₄, corresponding to the defect concentration 0.0625, which is not far from the situation in the studied samples. The unit cell contains 112 atoms (111 atoms for magnetite with the vacancy). Internal positions in all structures were optimized by minimizing the forces exerted on the atoms. The calculations were performed in 28 k -points in the irreducible part of the Brillouin zone. In all cases the value of the parameter $U_{\text{eff}} = 4.5 \text{ eV}$ was adopted.

Properties of interest is the distortion of crystal lattice around the defect as well as the change of charges and magnetic moments of neighboring atoms. In a standard FPLAPW calculation atomic charges and spin moments are evaluated in a simple way as a sum or difference of spin-up and spin-down electron density within the given atomic sphere. Then, however, the contribution of the density in the interstitial region is disregarded and the result depends to some extent on the atomic radii. More correctly, the atom can be considered as a generalized volume around the nucleus, in the sense of the *atoms in molecules* approach (AIM) [22], charge and magnetic moments are then evaluated within such a volume. The results are given in tables 2–4.

4. Discussion

The results of electronic structure calculations presented in section 3.2 are a convenient starting point for a discussion of the physics of defect-containing magnetite. The data in table 3 show that ferric ions on the tetrahedral sublattice are almost intact by the defect, the largest difference in their valence charge in the systems studied being $\sim 1\%$. As expected, the iron ions on the octahedral sites are much more affected, the difference in their valence charge, relative to the stoichiometric magnetite (see table 2), ranging from -12% to $+5\%$ for the defect's nearest Fe(B) neighbors. For the next-nearest Fe(B) neighbors of the defect this difference lies between -0.2% and $+11\%$. Note that there is also an appreciable change of the charge of the nearest oxygen

neighbors to the defect. Larger supercells will be necessary, however, in order to find whether an analog of the Friedel oscillations in magnetite exists.

Inspection of table 4 reveals that a considerable part of screening is due to the local distortion around the defect. Both Zn²⁺ and the vacancy on the B site carry negative charge relative to Fe(B) and thus the nearest oxygen ions are repelled. The distortion is particularly large around the vacancy, for which the distance to the nearest oxygen is increased by $\sim 7\%$. As expected the Ti⁴⁺ ion on the B site causes the contraction of the octahedron. A somewhat stronger contraction is associated with Al³⁺(B). In this case the attraction caused by the Coulomb interaction is upheld by the smaller ionic radius of Al³⁺ (0.0675 nm) compared with the ferrous and ferric ions (0.092 and 0.0785 nm [23]).

The above-described results show that in the ground state of the defect-containing cubic magnetite the modification of the charge density spreads over a considerable distance. As a consequence no localized, strongly anisotropic ions are present. It is thus understandable why the magnetocrystalline anisotropy and hence also the temperature of spin reorientation (table 1) is only weakly modified by the presence of defects. Figure 3 suggests strongly that the Verwey and spin reorientation transitions are correlated. The difference between T_{SR} and T_V is $\sim 10 \text{ K}$ for stoichiometric magnetite or low concentration x of the defects (namely for small deviation of average valency ν_B of iron in octahedral sites from the stoichiometric value 2.5) and it increases up to $\sim 30 \text{ K}$ when x (and thus also the difference $\nu_B - 2.5$) is larger.

The calculated first anisotropy constant has the same sign, but its magnitude is ~ 2 times smaller comparing to K_1^{Cc} (cf figures 1 and 5). As noted by Brabers [1] the magnitude of K_1^{Cc} may be too large because the high temperature data of Smith [7] were used in the extrapolation. Part of the discrepancy could also be connected with an underestimation of the orbital moment, which is often encountered in the density-functional-based calculations. In view of these uncertainties the agreement between calculated K_1 and K_1^{Cc} is reasonable.

Attention can now be turned to the anomalous part ΔK_1 of the cubic first anisotropy constant. The fact that both K_1^{Cc} obtained by the extrapolation of the experimental data and K_1 calculated by GGA + U are negative, while ΔK_1 is positive, shows that ΔK_1 is connected to the degeneracy of the excited state present in the cubic phase only. This agrees with the hypothesis of Aragón [5] who, however, avoids specifying the nature of this state. Figure 3 indicates a strong correlation between the spin reorientation transition (and thus anisotropy) and the Verwey transition. This leads us to suggest that the excited state corresponds to a local charge and orbital ordering that becomes long range and stable for $T < T_V$. It will be degenerate as several orderings are equivalent in the cubic symmetry. Assuming that there is a one-to-one correspondence between the Cc symmetry crystallographic domains that appear below T_V and the excited state in question, the degeneracy of the state will be 12, which is the number of different crystallographic domains. At the Verwey transition the symmetry is broken, the degeneracy is lifted

Table 3. Atomic valence charges and spin magnetic moments in defect-containing magnetite. X, Fe (B)_{nn}, Fe(A)_{nn}, O_{nn}, Fe (B)_{nnn} correspond to the defect, its nearest Fe(B) neighbor, Fe(A) neighbor, oxygen neighbor and the next-nearest Fe(B) neighbor. q and m_s have the same meaning as in table 2, in which the data for the pure magnetite are given.

Defect	X		Fe (B) _{nn}		Fe (A) _{nn}		O _{nn}		Fe (B) _{nnn}	
	q	m_s	q	m_s	q	m_s	q	m_s	q	m_s
Ga ³⁺ (A)	1.873	0.026	1.537	3.825	1.761	4.109	-1.293	0.175	1.633	3.953
Zn ²⁺ (A)	1.275	0.052	1.644	3.984	1.755	4.091	-1.277	0.266	1.791	4.153
vac(B)			1.712	4.033	1.772	4.097	-1.188	0.008	1.701	4.041
Ti ⁴⁺ (B)	2.252	0.087	1.423	3.634	1.770	4.111	-1.246	-0.051	1.797	4.155
Al ³⁺ (B)	2.561	0.009	1.445	3.642	1.767	4.114	-1.364	-0.071	1.624	3.939

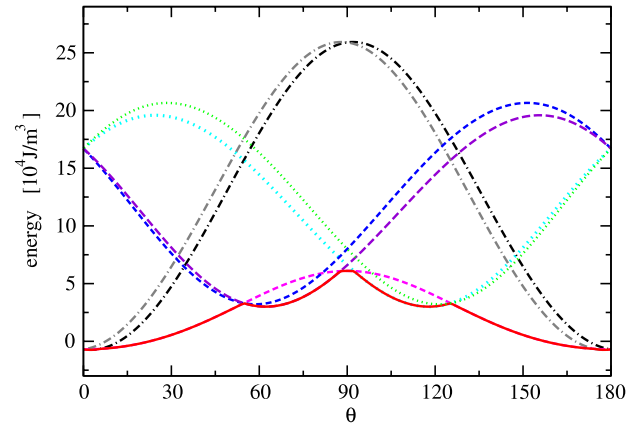
Table 4. Equilibrium distances in defect-containing (lines 2–5) and stoichiometric magnetite (lines 6–7) in nm.

	Fe (B) _{nn}	Fe (A) _{nn}	O _{nn}	O _{nnn}
Ga ³⁺ (A)	0.3454	0.3658	0.1848	0.3535
Zn ²⁺ (A)	0.3451	0.3647	0.1963	0.3534
vac(B)	0.2804	0.3506	0.2200	0.3564
Ti ⁴⁺ (B)	0.3025	0.3485	0.1976	0.3651
Al ³⁺ (B)	0.2947	0.3457	0.1939	0.3564
Fe(B)	0.2967	0.3480	0.2059	0.3565
Fe ³⁺ (A)	0.3480	0.3635	0.1887	0.3493

and, as a consequence, ΔK_1 disappears. The form of the anisotropy energy of each of the 12 components of the excited state will have the form (3), albeit written in the coordinate system of the corresponding Cc domain. To illustrate the situation, we calculated the dependence of the energy on the direction of magnetization \vec{M} in the (110) plane, assuming that the anisotropy constants of the excited state are as given in (4). The number of energy branches is smaller than 12 due to the fact that some of the components of the excited state are equivalent when the magnetization is kept in the (110) plane. The energy branches intersect and, as a consequence, the minimal energy E_0 (full curve in figure 6) has a discontinuous first derivative. The first anisotropy constant that corresponds to E_0 comes out large and positive $K_1^{\text{exc}} \sim 3 \times 10^5 \text{ J m}^{-3}$.

5. Conclusions

The discussion given above leads us to propose the following scenario for temperature dependence of the anisotropy of magnetite: above the Verwey temperature its ground state is half-metallic, possessing small magnetocrystalline anisotropy characterized by the negative K_1 anisotropy constant. An excited state at energy Δ above the ground state is degenerate and its anisotropy is large with positive K_1^{exc} . Δ depends on temperature, it is large for temperatures high above the room temperature and the excited state is almost empty. With decreasing temperature Δ is reduced and below RT the population of the excited state leads to a notable change in the temperature dependence of the anisotropy, resulting in the reversal of the sign of K_1 at the spin reorientation transition. At the Verwey transition Δ becomes zero, components of the degenerate state transform to Cc crystallographic domains with considerable macroscopic distortion, the degeneracy is

**Figure 6.** Anisotropy of the excited state components for magnetization in the (110) plane. The energies of individual components correspond to dotted, dashed and dashed-dotted curves, the lowest energy E_0 for a given angle is emphasized by a full curve. θ is the angle, which magnetization makes with the [001] direction.

lifted and the positive contribution to K_1^{Cc} (the analog ((5)) of the cubic K_1) disappears.

The strong temperature dependence of Δ may be reflected in the behavior of the elastic constants, the strong temperature variation of which was reported by Kąkol and Kozłowski [24].

We note that a similar mechanism to that described above should also influence the magnetostriction. Indeed Brabers and Hendriks found strongly temperature-dependent magnetostriction constants in the pure and Al-substituted magnetite [25].

In conclusion, based on the experimentally determined temperatures of spin reorientation and Verwey transitions and on calculations of the anisotropy from first principles, a model explaining the anomalous temperature dependence of the magnetocrystalline anisotropy in the cubic phase of magnetite was proposed. As a by-product of the electron structure calculations the gap in the band structure of the majority spin electrons in defect-containing magnetite was calculated. This quantity could be important for eventual application of magnetite in spintronics.

Acknowledgments

This work was supported by the Grant Agency of the Czech Republic under project no. 202/08/0541, project no. 392111

of the Grant Agency of the Charles University, project MS0021620834 of the Ministry of Education of the Czech Republic and project SVV-2011-263303. The authors are grateful to Professor V A M Brabers of Eindhoven University of Technology, The Netherlands, Professor J M Honig, Purdue University, USA and Professor A Kozłowski, AGH Kraków, Poland for supplying the single crystals of magnetites.

References

- [1] Brabers V A M 1995 Progress in spinel ferrite research *Handbook of Magnetic Materials* ed K H J Buschow (Amsterdam: Elsevier)
- [2] Kąkol Z and Honig J M 1989 *Phys. Rev. B* **40** 9090
- [3] Abe K, Miyamoto Y and Chikazumi S 1976 *J. Phys. Soc. Japan* **41** 1894
- [4] Siratori K and Abe Y 1980 *J. Magn. Magn. Mater.* **290** 87
- [5] Aragón R 1992 *Phys. Rev. B* **46** 5334
- [6] Novák P, Štěpánková H, Englich J, Kohout J and Brabers V A M 2000 *Phys. Rev. B* **61** 1256
- [7] Smith D O 1956 *Phys. Rev.* **102** 959
- [8] Brabers V A M 1992 *Proc. 6th Int. Conf. Ferrites, Tokyo-Kyoto* p 678
- [9] Bałanda M, Wiecheć A, Kim D, Kąkol Z, Kozłowski A, Niedziela P, Sabol J, Tarnawski Z and Honig J M 2005 *Eur. Phys. J. B* **43** 201–12
- [10] Skumryev V, Blythe H J, Cullen J and Coey J M D 1999 *J. Magn. Magn. Mater.* **196–197** 515–7
- [11] Dehe G, Seidel B, Melzer K and Michalk C 1975 *Phys. Status Solidi a* **31** 439
- [12] Dehe G, Suwalski J, Wiener E and Kabisch A 1981 *Phys. Status Solidi a* **65** 669
- [13] Chlan V, Gamaliy E, Štěpánková H, Kouřil K, Englich J, Kohout J and Brabers V 2007 *J. Magn. Magn. Mater.* **310** 2555–7
- [14] Tarnawski Z, Wiecheć A, Madei M, Nowak D, Owoc D, Król G, Kąkol Z, Kolwicz-Chodak L, Kozłowski A and Dawid T 2004 *Acta Phys. Polon. A* **106** 771
<http://przyrbwn.icm.edu.pl/APP/PDF/106/a106z531.pdf>
- [15] Blaha P, Schwarz K, Madsen G K H, Kvasnicka D and Luitz J 2001 *WIEN2k, An Augmented Plane Wave + Local Orbitals Program for Calculating Crystal Properties* ed K-H Schwarz (Wien: Technische Universität) ISBN 3-9501031-1-2 www.wien2k.at/reg_user/textbooks/usersguide.pdf
- [16] Perdew J P, Burke K and Ernzerhof M 1996 *Phys. Rev. Lett.* **77** 3865
- [17] Liechtenstein A I, Anisimov V I and Zaanen J 1995 *Phys. Rev. B* **52** R5467
- [18] Novák P and Chlan V 2010 *Phys. Rev. B* **81** 174412
- [19] Jeng H-T and Huo G Y 2002 *Phys. Rev. B* **65** 094429
- [20] Andersen O K 1975 *Phys. Rev. B* **12** 3060
- [21] Abdelouahed S and Alouani M 2009 *Phys. Rev. B* **79** 054406
- [22] Bader R F W 1990 Atoms in molecules *A Quantum Theory* (Oxford: Oxford University Press)
- [23] Shannon R D 1976 *Acta Crystallogr. A* **32** 751–67
- [24] Kąkol Z and Kozłowski A 2000 *Solid State Sci.* **2** 737
- [25] Brabers V A M and Hendriks J H 1982 *J. Magn. Magn. Mater.* **26** 300

Understanding the Mössbauer spectrum of magnetite below the Verwey transition: *Ab initio* calculations, simulation, and experiment

R. Řezníček,^{1,2,*} V. Chlan,¹ H. Štěpánková,¹ P. Novák,³ J. Żukrowski,⁴ A. Kozłowski,⁵ Z. Kałol,⁵ Z. Tarnawski,⁵ and J. M. Honig⁶

¹*Faculty of Mathematics and Physics, Charles University, V Holešovičkách 2, 180 00 Prague 8, Czech Republic*

²*Faculty of Physics and Earth Sciences, University of Leipzig, Linnéstrasse 5, D-04103 Leipzig, Germany*

³*Institute of Physics of ASCR, Cukrovarnická 10, 162 53 Prague 6, Czech Republic*

⁴*Academic Centre for Materials and Nanotechnology, AGH University of Science and Technology, aleja Mickiewicza 30, 30-059 Kraków, Poland*

⁵*Faculty of Physics and Applied Computer Science, AGH University of Science and Technology, aleja Mickiewicza 30, 30-059 Kraków, Poland*

⁶*Department of Chemistry, Purdue University, 560 Oval Drive, West Lafayette, Indiana 47907-2084, USA*

(Received 29 August 2017; revised manuscript received 10 October 2017; published 13 November 2017)

Magnetite is often the subject of Mössbauer spectroscopy experiments either as a part of fundamental research of this compound or during various geological studies. However, the complicated structure of the low-temperature phase of magnetite exhibits 24 crystallographic iron sites, which presents a considerable obstruction for spectrum interpretation. In this work, we carried out *ab initio* calculations to obtain a complete set of hyperfine parameters of all the sites, and we used these parameters to simulate the corresponding Mössbauer spectrum. Simulation analysis suggested an approximation of the spectrum by four sextets. Parameters of these four sextets were calculated, and the approximation was shown to be appropriate. Further, the Mössbauer spectrum of a high-quality synthetic single crystal of magnetite was measured at 4 K, allowing for a comparison of the theoretical results with the experimental data. Finally, the four-sextet approximation was successfully applied to fit the measured spectrum.

DOI: [10.1103/PhysRevB.96.195124](https://doi.org/10.1103/PhysRevB.96.195124)

I. INTRODUCTION

The formal composition of magnetite can be written as $[\text{Fe}^{3+}]_A[\text{Fe}^{2+}\text{Fe}^{3+}]_B\text{O}_4$, where A denotes iron sites surrounded by oxygen ions forming tetrahedra and B corresponds to the iron ions inside octahedra formed by the nearest oxygen ions. Apparently, the B sublattice exhibits mixed-valence character. Magnetite has been drawing the attention of physicists since 1939 when the Verwey phase transition was found [1]. This transition occurring at temperature $T_V \approx 120$ K is accompanied by a step change in electrical conductivity. When temperature drops below T_V , the inverse cubic ($Fd\bar{3}m$) spinel structure of magnetite reduces its symmetry and transforms into the monoclinic Cc structure. Accordingly, the cubic crystal splits into 12 magnetically nonequivalent monoclinic domains [2]. In the high-temperature cubic phase, all A sites are crystallographically equivalent, and the same holds for all B sites. On the other hand, there are 8 different groups of crystallographically equivalent A sites and 16 different groups of crystallographically equivalent B sites in the low-temperature monoclinic structure. Thus, one of the most interesting open questions concerns the charge ordering of the low-temperature phase [3–6], which has been probed by various means, including the hyperfine methods comprising the Mössbauer spectroscopy [7–11] as well as nuclear magnetic resonance (NMR) [2,12–14].

Recent progress comprises mainly the determination of the crystal-structure parameters of the Cc phase by Senn *et al.* [15]. Based on their data, Senn *et al.* suggested a trimeron model to describe the charge order of the B sublattice. The trimeron

consists of three nearest-neighbor Fe(B) ions in a line; the Fe^{2+} -like ion in the trimeron's center donates a part of its minority-spin t_{2g} electron to the two Fe^{3+} -like ions at the trimeron's ends. The trimers form a complex network, but there are also two groups of crystallographically equivalent Fe(B) sites which do not participate in any trimeron. The publication of Senn *et al.* was followed by several works which employed the structure data for *ab initio* calculations (see Refs. [2,16,17]). The work of Patterson [17] presented an alternative model consisting of Fe(B) ions incorporated either in a broken branched zigzag chain or in pairs with one-electron bonds. On the other hand, Ref. [2] supported the trimeron model as a more adequate description of the electronic structure and grouped the B sites in an 8:5:3 ratio. The first group contains Fe^{3+} -like ions, while the other groups are occupied by Fe^{2+} -like ions.

Despite a significant number of publications concerning the Mössbauer spectroscopy of the low-temperature Cc phase of magnetite, a reliable detailed interpretation of the structure of the spectra is still unavailable because of a significant overlap of the spectral components (sextets) originating from the 24 different groups of iron sites. In this situation, the authors of existing experimental studies of magnetite [7–11,18–21] usually have had to resort to various phenomenological assumptions to be able to decompose their spectra into several sextets. However, the choice of suitable assumptions is difficult from both fundamental and practical points of view since subsequent analysis of the results is bound within the limits determined by the assumptions and a comparison of different studies is complicated if different decomposition approaches are used. Thus, the aim of the present work is to understand the Mössbauer spectra in the context of current knowledge. The *ab initio* calculations based on the density functional theory (DFT) are employed as a primary source of hyperfine

*reznicek@mbbox.troja.mff.cuni.cz

parameters for spectrum simulation. The calculation outputs are supplemented with the hyperfine data extracted from ^{57}Fe NMR experiments [2,12,13]. Finally, the analysis of the simulation results allows for an appropriate fit of the experimental Mössbauer spectrum.

II. CALCULATIONS

In order to obtain the hyperfine parameters necessary for the simulation of the Mössbauer spectrum, the WIEN2K software [22] was utilized for the DFT calculations of the electronic structure of the Cc phase of magnetite. We used 9500 ($RK_{\text{max}} = 6.0$) basis functions and 9 k points in the irreducible part of the Brillouin zone. The density of charge was Fourier expanded to $G_{\text{max}} = 16 \text{ Ry}^{\frac{1}{2}}$. The generalized gradient approximation plus U method with $U_{\text{eff}} = 4.5 \text{ eV}$, $R_{\text{MT}}(\text{Fe}) = 2 \text{ a.u.}$, and $R_{\text{MT}}(\text{O}) = 1.5 \text{ a.u.}$ was employed. The spin-orbit coupling was included in the calculations.

The calculations used the crystal-structure parameters of the Cc phase of magnetite published by Senn *et al.* [15]. Structure optimization was not performed in order to avoid the risk of reaching an incorrect total energy minimum. Thus, consistency with the calculations in Ref. [2] was kept. The average force acting on the ions in the experimental structure was $9.8 \text{ mRy a.u.}^{-1}$, while the maximum force was $19.3 \text{ mRy a.u.}^{-1}$.

A. Charge density at iron nuclei and isomer shift

The electron charge density at the iron nuclei manifests itself in the Mössbauer spectra as an isomer shift relative to the reference (metallic bcc $\alpha\text{-Fe}$). The charge densities at the iron nuclei at 8 nonequivalent A sites and 16 nonequivalent B sites were determined from the DFT calculations as the density at the radial grid point R_0 closest to the nucleus position (this density is assumed to be constant over the corresponding sphere with radius R_0). The value of $R_0 = 5 \times 10^{-5} a_0$ ($a_0 \approx 5.292 \times 10^{-11} \text{ m}$ is the Bohr radius) was comparable to the nuclear radius. The resulting charge densities ρ_0 at iron nuclei (and corresponding isomer shifts) are provided in Table I.

Isomer shift δ (expressed in γ source-velocity units) is related to the charge density ρ_0 at the nucleus [23]:

$$\delta = \frac{c}{E_0} \frac{1}{10\epsilon_0} Z e [(R^*)^2 - R^2] (\rho_0 - \rho_{0,\text{Fe}}), \quad (1)$$

where $\rho_{0,\text{Fe}}$ is the electron charge density at the nuclei in $\alpha\text{-Fe}$, ϵ_0 denotes vacuum permittivity, E_0 represents the energy of the first excited state of the ^{57}Fe nucleus, c is the speed of light, Z stands for the proton number, and R and R^* are nuclear charge radii of the ^{57}Fe nucleus in the ground state and the first excited state, respectively. Unfortunately, this relation does not allow us to directly obtain the isomer shift from calculated charge densities due to the significant uncertainty of the ^{57}Fe nuclear charge radius R^* in the excited state [24]. Instead, the following expression has to be used:

$$\delta = \alpha (\rho_0 - \rho_{0,\text{Fe}}), \quad (2)$$

where the coefficient α is determined by a calibration procedure described, e.g., in Ref. [25]. Our calibration required a calculation of charge densities at iron nuclei in various

TABLE I. Electron charge density ρ_0 at iron nuclei in magnetite obtained from the DFT calculations together with isomer shift δ derived using Eq. (2) [the $\pm 4\%$ error of the isomer shift is determined by the calibration error of α (see text); $a_0 \approx 5.292 \times 10^{-11} \text{ m}$ denotes the Bohr radius]. The site numbering is the same as in Ref. [2] and corresponds to site listing order in Ref. [15].

DFT site	Nominal valence state [15]	$\rho_0 (e a_0^{-3})$	$\rho_0 - \rho_{0,\text{Fe}} (e a_0^{-3})$	$\delta (\text{mm s}^{-1})$
A1	3+	15308.964	-1.233	0.350
A2	3+	15308.964	-1.233	0.350
A3	3+	15308.951	-1.245	0.354
A4	3+	15308.982	-1.215	0.345
A5	3+	15308.975	-1.222	0.347
A6	3+	15308.991	-1.206	0.342
A7	3+	15308.994	-1.202	0.341
A8	3+	15308.985	-1.211	0.344
B1	2+	15306.875	-3.322	0.943
B2	2+	15306.844	-3.352	0.952
B3	2+	15306.924	-3.273	0.929
B4	2+	15307.382	-2.815	0.799
B5	3+	15308.316	-1.880	0.534
B6	3+	15308.095	-2.101	0.597
B7	2+	15306.885	-3.311	0.940
B8	3+	15308.513	-1.684	0.478
B9	3+	15307.812	-2.385	0.677
B10	3+	15308.095	-2.101	0.597
B11	3+	15308.063	-2.133	0.606
B12	3+	15308.347	-1.849	0.525
B13	2+	15306.805	-3.392	0.963
B14	2+	15307.029	-3.167	0.899
B15	3+	15308.499	-1.697	0.482
B16	2+	15306.790	-3.406	0.967

compounds (including iron oxides) in the same way as for the data in Table I. These values of charge density were then paired with published experimental isomer shifts (see Table II) and utilized for fitting the dependence (2) (see Fig. 1). The fit determined the coefficient value of $\alpha = -0.284 \pm 0.011 \text{ mm s}^{-1} e^{-1} a_0^3$ ($a_0 \approx 5.292 \times 10^{-11} \text{ m}$ is the Bohr radius), which is in agreement with the values obtained in Ref. [25] ($\alpha = -0.291 \pm 0.014 \text{ mm s}^{-1} e^{-1} a_0^3$ for halides and TiFe using the full-potential linearized augmented plane-wave and augmented plane-wave plus local-orbital methods implemented in the WIEN2K software) and Ref. [26] ($\alpha = -0.278 \pm 0.028 \text{ mm s}^{-1} e^{-1} a_0^3$ for iron complexes using quasirelativistic DFT within the zero-order regular approximation). It should be noted that despite the good agreement with the published coefficient values, it was necessary to perform the calibration with our particular DFT calculation method (including specific parameter settings) rather than just using some of published values because the resulting α value is influenced by the applied DFT calculation method [32,33].

The values of isomer shift obtained from Eq. (2) for particular iron sites in magnetite are included in Table I. The values exhibit a sensitivity to the configuration of $3d$ electrons [30]: $\delta = 0.34\text{--}0.35 \text{ mm s}^{-1}$ for Fe^{3+} ions at the A sites, while at the B sites $\delta = 0.48\text{--}0.68 \text{ mm s}^{-1}$ for Fe^{3+} -like ions and $\delta = 0.80\text{--}0.97 \text{ mm s}^{-1}$ for Fe^{2+} -like ions.

TABLE II. Calculated electron charge density ρ_0 at iron nuclei accompanied by experimental isomer shift δ_{exp} for various compounds of iron ($a_0 \approx 5.292 \times 10^{-11}$ m denotes the Bohr radius).

Compound	ρ_0 ($e a_0^{-3}$)	$\rho_0 - \rho_{0,\text{Fe}}$ ($e a_0^{-3}$)	δ_{exp} (mm s $^{-1}$)
TiFe	15310.829	0.632	-0.145 ± 0.007 [27]
α -Fe	15310.196	0	0
FeAl	15309.133	-1.064	0.272 ± 0.015 [28]
Fe ₂ O ₃	15308.139	-2.058	0.47 ± 0.03 [29]
FeF ₃	15307.628	-2.568	0.489 [23]
YIG (<i>a</i>)	15308.219	-1.978	0.57 ± 0.05 [30]
YIG (<i>d</i>)	15308.996	-1.200	0.26 ± 0.05 [30]
Fe ₃ O ₄ (A)	15308.866	-1.330	0.36 [7]
(above T_V)			0.34 [8]
			0.27 ± 0.03 [9]
Fe ₃ O ₄ (B)	15307.608	-2.589	0.78 [7]
(above T_V)			0.66 [8]
			0.67 ± 0.03 [9]
FeS	15307.176	-3.020	1.1 ± 0.1 [30]
FeF ₂	15305.414	-4.783	1.467 [31]
			1.40 ± 0.05 [30]

B. Electric field gradient at iron nuclei

Another characteristic of the electronic structure influencing the Mössbauer spectra is the electric field gradient (EFG) tensors at particular iron sites. The EFG tensors obtained from the DFT calculations are provided in Table III, expressed in the orthorhombic coordinate system [34] (as tensor elements $V_{\alpha\alpha'}$; $\alpha, \alpha' = a, b, c$) as well as in a canonical form (as diagonal elements V_{zz} , V_{yy} , and V_{xx}), together with the asymmetry parameters [$\eta = (V_{xx} - V_{yy})/V_{zz}$] and principal axes (\vec{v}_{zz} , \vec{v}_{yy} , and \vec{v}_{xx}) of the tensors. Visualization of the EFG tensors is shown in Fig. 2 for the B sites and in Fig. 1 of the Supplemental Material [35] for the A sites; the tensors are represented by objects drawn in the elementary cell; the following formula determines the distance r of the object surface from a particular

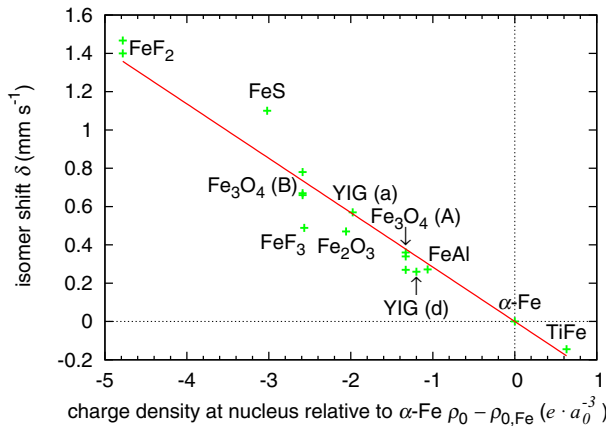


FIG. 1. Isomer shift calibration. The values from Table II are represented by the points; the line corresponds to a fit of expression (2). The *a* and *d* crystallographic sites of yttrium iron garnet (YIG) are distinguished. The labels Fe₃O₄ (A) and Fe₃O₄ (B) refer to the A and B sites of the high-temperature phase of magnetite, respectively. ($a_0 \approx 5.292 \times 10^{-11}$ m is the Bohr radius.)

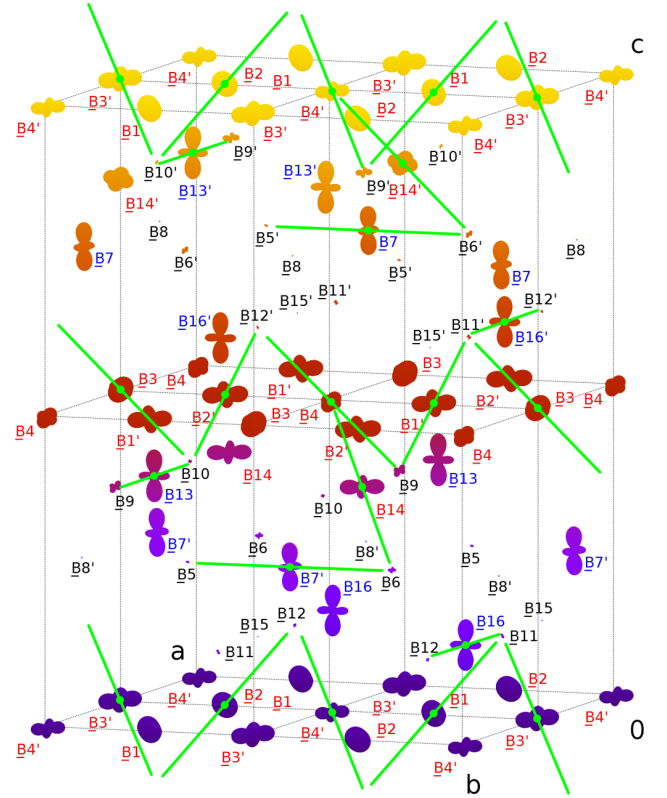


FIG. 2. Visualization of the EFG tensors at Fe(B) sites in the elementary cell (scaling coefficient $C = 0.05 \text{ \AA} \times 10^{-21} \text{ V}^{-1} \text{ m}^2$). Trimers [15] are highlighted by the green lines. The site numbering is the same as in Ref. [2] and corresponds to site listing order in Ref. [15]; primes denote the sites generated by the *ac*-glide symmetry. (Surface color corresponding to the *z* coordinate is to improve clarity.)

iron-ion site:

$$r = C[V_{aa}\vartheta_a^2 + V_{bb}\vartheta_b^2 + V_{cc}\vartheta_c^2 + 2(V_{ab}\vartheta_a\vartheta_b + V_{ac}\vartheta_a\vartheta_c + V_{bc}\vartheta_b\vartheta_c)], \quad (3)$$

where ϑ_α , $\alpha = a, b, c$, stands for direction cosines with respect to the orthorhombic axes and C is a scaling coefficient (common for all sites in the plot). The figures illustrate the size of the EFG at particular sites, as well as the orientation of the principal axes of the tensors. The EFG at the Fe³⁺(A) ions is small because of the nearly spherical symmetry of their electronic configuration. The complex situation concerning the B sites, which is depicted in Fig. 2, can be understood in the context of trimers. Obviously, the EFG at the trimeron central ions is much larger than at the end ions, and the principal axis related to the smallest eigenvalue of the corresponding EFG tensor of the central ion is roughly collinear with the axis of the trimeron. This conforms well with the assumptions based on the electronic structure of trimers: the minority-spin charge density encompassing the central Fe²⁺-like ions is significantly anisotropic as the charge is located in the t_{2g} orbital corresponding to the trimeron axis. Concerning the Fe³⁺-like end ions, the approximately spherical symmetry of the electron density is impacted only by the partial charge donated by the central ions. (When the

TABLE III. The EFG tensors at iron sites in *Cc* phase of magnetite determined by the DFT calculations. See the text for symbol definitions. The site numbering is the same as in Ref. [2] and corresponds to site listing order in Ref. [15].

Site	$V_{aa}(\times 10^{21} \text{ V m}^{-2})$	$V_{bb}(\times 10^{21} \text{ V m}^{-2})$	$V_{cc}(\times 10^{21} \text{ V m}^{-2})$	$V_{ab}(\times 10^{21} \text{ V m}^{-2})$	$V_{ac}(\times 10^{21} \text{ V m}^{-2})$	$V_{bc}(\times 10^{21} \text{ V m}^{-2})$	$V_{zz}(\times 10^{21} \text{ V m}^{-2})$	$V_{xy}(\times 10^{21} \text{ V m}^{-2})$	$V_{xx}(\times 10^{21} \text{ V m}^{-2})$	η	Principal axis \hat{v}_{zz}	Principal axis \hat{v}_{yy}	Principal axis \hat{v}_{xx}
A1	1.522	-1.294	-0.228	-0.298	-0.395	-0.439	1.621	-1.509	-0.112	0.862	(0.979, -0.071, -0.192)	(-0.137, -0.923, -0.359)	(0.152, -0.378, 0.913)
A2	0.739	-0.573	-0.166	0.404	0.211	-0.752	-1.250	0.853	0.397	0.365	(-0.221, 0.781, 0.585)	(0.962, 0.274, -0.004)	(0.163, -0.561, 0.811)
A3	0.286	0.344	-0.630	-0.367	0.256	0.508	-0.965	0.724	0.242	0.499	(0.298, 0.417, -0.859)	(0.561, -0.804, -0.196)	(-0.772, -0.423, -0.473)
A4	0.289	0.166	-0.455	-0.235	0.603	1.415	-1.778	1.344	0.433	0.512	(0.287, 0.586, -0.758)	(0.205, 0.735, 0.646)	(0.936, -0.341, 0.091)
A5	-0.839	0.568	0.272	-0.096	1.038	0.662	-1.550	1.298	0.252	0.675	(0.816, 0.206, -0.540)	(0.323, 0.612, 0.722)	(0.479, -0.764, 0.433)
A6	-0.472	-0.127	0.599	-0.259	-0.363	-0.711	1.055	-0.937	-0.118	0.776	(-0.122, -0.492, 0.862)	(0.673, 0.598, 0.436)	(0.729, -0.633, -0.258)
A7	-1.434	1.572	-0.138	-0.426	0.050	0.651	1.838	-1.509	-0.329	0.642	(0.118, -0.944, -0.308)	(0.981, 0.159, -0.111)	(0.154, -0.289, 0.945)
A8	-1.162	1.104	0.059	-0.035	0.237	-0.035	-1.207	1.106	0.101	0.832	(0.983, 0.012, -0.184)	(-0.019, 0.999, -0.038)	(0.183, 0.041, 0.982)
B1	0.223	6.949	-7.171	-9.551	-0.314	-0.832	13.723	-7.666	-6.058	0.117	(-0.577, 0.816, -0.024)	(0.436, 0.332, 0.836)	(0.691, 0.472, -0.548)
B2	0.622	6.221	-6.843	-10.170	-0.330	-0.857	13.980	-7.784	-6.196	0.114	(-0.605, 0.796, -0.023)	(-0.600, -0.475, -0.643)	(0.523, 0.375, -0.765)
B3	-0.485	7.224	-6.738	-9.466	0.389	0.849	13.601	-7.598	-6.003	0.117	(-0.557, 0.830, 0.024)	(0.596, 0.420, -0.684)	(0.578, 0.367, 0.729)
B4	0.841	4.201	-5.042	-7.589	0.845	0.953	10.297	-6.408	-3.889	0.245	(-0.625, 0.780, 0.014)	(0.568, 0.467, -0.677)	(0.535, 0.415, 0.735)
B5	0.897	-1.249	0.352	0.036	0.277	0.133	-1.260	1.016	0.243	0.614	(0.006, -0.997, 0.081)	(0.919, 0.038, 0.391)	(0.393, -0.072, -0.917)
B6	1.079	-0.092	-0.987	1.629	0.700	-1.053	-2.383	2.224	0.158	0.867	(0.422, -0.609, -0.671)	(-0.815, -0.579, 0.012)	(0.396, -0.542, 0.741)
B7	-4.473	-8.621	13.095	0.393	0.297	0.061	13.100	-8.658	-4.441	0.322	(0.017, 0.003, 1.000)	(0.093, -0.996, 0.002)	(0.995, 0.093, -0.017)
B8	-0.123	0.501	-0.379	0.279	-0.023	-0.191	0.642	-0.424	-0.219	0.319	(0.342, 0.922, -0.180)	(-0.155, 0.244, 0.957)	(0.927, -0.300, 0.226)
B9	1.936	0.174	-2.110	-3.495	0.892	1.376	4.662	-3.979	-0.683	0.707	(0.786, -0.618, -0.022)	(0.454, 0.600, -0.659)	(0.421, 0.507, 0.752)
B10	-1.012	0.640	0.372	-0.313	0.039	0.953	1.486	-1.113	-0.373	0.497	(-0.085, 0.759, 0.646)	(0.939, 0.278, -0.203)	(0.334, -0.589, 0.736)
B11	0.023	0.746	-0.769	-0.764	-0.130	-1.024	1.533	-1.445	-0.088	0.885	(0.398, -0.847, 0.354)	(-0.327, -0.491, -0.807)	(0.857, 0.205, -0.472)
B12	-0.571	0.839	-0.268	0.100	-0.312	-0.889	1.363	-0.918	-0.444	0.348	(0.124, 0.861, -0.493)	(0.571, 0.344, 0.745)	(0.812, -0.374, -0.449)
B13	-8.337	-5.836	14.173	-0.328	0.034	0.401	14.181	-8.380	-5.801	0.182	(0.001, 0.020, 1.000)	(0.992, 0.129, -0.004)	(0.129, -0.991, 0.020)
B14	5.018	1.274	-6.291	9.161	0.845	-0.507	12.502	-7.179	-5.323	0.148	(0.775, 0.632, 0.018)	(0.445, -0.526, -0.725)	(-0.448, 0.570, -0.689)
B15	0.160	-0.283	0.124	-0.179	-0.192	-0.139	-0.421	0.338	0.083	0.606	(-0.381, -0.855, -0.353)	(-0.766, 0.078, 0.638)	(0.518, -0.513, 0.685)
B16	-8.531	-5.295	13.826	-0.040	0.025	-0.397	13.835	-8.531	-5.303	0.233	(0.001, -0.021, 1.000)	(1.000, 0.012, -0.001)	(0.012, -1.000, -0.021)

end ion is a part of multiple trimeron, the donated charges from different central ions enter different orbitals; thus, the symmetry of the end ion is affected still only to a small extent.) In the case of Fe^{3+} -like ions B8 and B15, which do not participate in any trimeron, the EFG is the smallest among the B sites as no transferred charge perturbs the symmetry of their electronic configuration.

On the other hand, the results do not support the model of Patterson [17], as can be seen from the Fe(B) pairs not included in the zigzag chain (e.g., B5'–B7): one would expect a relatively similar charge configuration of these ions due to the one-electron bond, but the difference in the EFG at these sites is striking.

C. Hyperfine magnetic fields

The parameters of the hyperfine magnetic field obtained from the DFT calculations and from the ^{57}Fe NMR data [14] were published in our previous work [2] in the form of isotropic parts and anisotropy tensors of the hyperfine field. The present work has to rely on the parameters from the DFT results since they are assigned to particular iron sites with known coordinates in the elementary cell, unlike the data from the NMR experiment, where an attempt at such an assignment was successful only to a limited extent. However, the DFT calculations tend to systematically overestimate isotropic parts B_{iso} as well as the anisotropy characterized by the following parameter:

$$B_{\text{ani}} = \sqrt{B_a'^2 + B_b'^2 + B_c'^2}, \quad (4)$$

where B_a' , B_b' , and B_c' denote elements of the hyperfine field anisotropy tensor in a canonical form. This effect can be compensated for by a renormalization of these parameters in order to match their average with the average of parameters extracted from the experimental data ($i = 1, \dots, 8$ for the A sites, while $i = 1, \dots, 16$ for the B sites):

$$c_{\text{iso}} = \frac{\sum_i B_{\text{iso}}^{\text{exp}}(i)}{\sum_i B_{\text{iso}}^{\text{calc}}(i)},$$

$$c_{\text{ani}} = \frac{\sum_i B_{\text{ani}}^{\text{exp}}(i)}{\sum_i B_{\text{ani}}^{\text{calc}}(i)}.$$

The following values of the renormalization coefficients were found: $c_{\text{iso}} = 0.96$ and $c_{\text{ani}} = 0.32$ [36] in the case of the A sites; $c_{\text{iso}} = 0.94$ and $c_{\text{ani}} = 0.65$ for the B sites. Now, the hyperfine field B_{hf} for a particular magnetization direction (denoted by direction cosines ϑ_α , $\alpha = a, b, c$, with respect to the orthorhombic coordinates) can be calculated:

$$B_{\text{hf}} = c_{\text{iso}} B_{\text{iso}} + c_{\text{ani}} [B_{aa} \vartheta_a^2 + B_{bb} \vartheta_b^2 + B_{cc} \vartheta_c^2 + 2(B_{ab} \vartheta_a \vartheta_b + B_{ac} \vartheta_a \vartheta_c + B_{bc} \vartheta_b \vartheta_c)], \quad (5)$$

where $B_{\alpha\alpha'}$ ($\alpha, \alpha' = a, b, c$) are elements of the hyperfine field anisotropy tensor expressed in the orthorhombic coordinates.

D. Correlations of hyperfine parameters

Hyperfine properties of particular iron ions are closely related to their electronic configuration; thus, their comparison may illustrate how these parameters are mutually correlated in

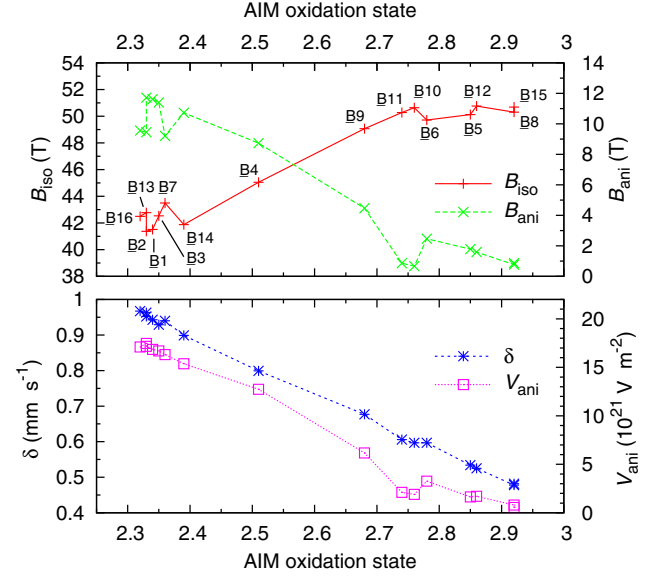


FIG. 3. Renormalized isotropic and anisotropic parts of the hyperfine magnetic field $V_{\text{ani}} = \sqrt{V_{zz}^2 + V_{yy}^2 + V_{xx}^2}$ parameter of EFG and isomer shift δ of the B-site iron ions plotted as a function of oxidation state determined by the AIM method in Ref. [2]. The site numbering is the same as in Ref. [2] and corresponds to site listing order in Ref. [15]. The lines serve only to guide the eye.

the context of the valence character of the iron ions (quantified in Ref. [2] using the atoms in molecules (AIM) method [37]). While the situation is fairly simple for the A sites, the case of B-site ions is much more interesting (see Fig. 3). The right part of Fig. 3 shows Fe^{3+} -like ions exhibiting a higher isotropic part B_{iso} , smaller anisotropy B_{ani} , lower EFG [represented by the parameter $V_{\text{ani}} = \sqrt{V_{zz}^2 + V_{yy}^2 + V_{xx}^2}$, where $V_{\beta\beta}$, $\beta = z, y, x$, are EFG tensor eigenvalues, in analogy to Eq. (4)], and smaller isomer shift than the Fe^{2+} -like ions in the left part. This is caused by low minority-spin $3d$ populations of Fe^{3+} -like ions leading to higher spin moment and, consequently, to higher B_{iso} . At the same time, orbital moments of these ions are small, resulting into a low hyperfine field anisotropy. The relatively high symmetry of the $3d$ electron distribution of Fe^{3+} -like ions is responsible for the low EFG. An opposite description can be used for the Fe^{2+} -like ions. The overall valence character of the iron ions is reflected by the isomer shift. Clearly, all parameters plotted in Fig. 3 exhibit roughly linear dependence on the valence state of a particular iron ion.

III. SIMULATION

The hyperfine parameters obtained in Sec. II allowed for a simulation of a zero-field ^{57}Fe Mössbauer spectrum of the Cc phase of magnetite using the FITSUITE 1.1.0.RC.11 software [38]. A single crystal consisting of a single domain (with the magnetization along the easy c axis) in an orientation with the $[201]$ direction parallel to the γ beam was considered. This special orientation results in sextet line-intensity ratio of 3:2:1:1:2:3 [39]. The line broadening was set equal to the natural linewidth Γ_N for the A sites and to twice the natural linewidth in the case of the B sites, where more significant

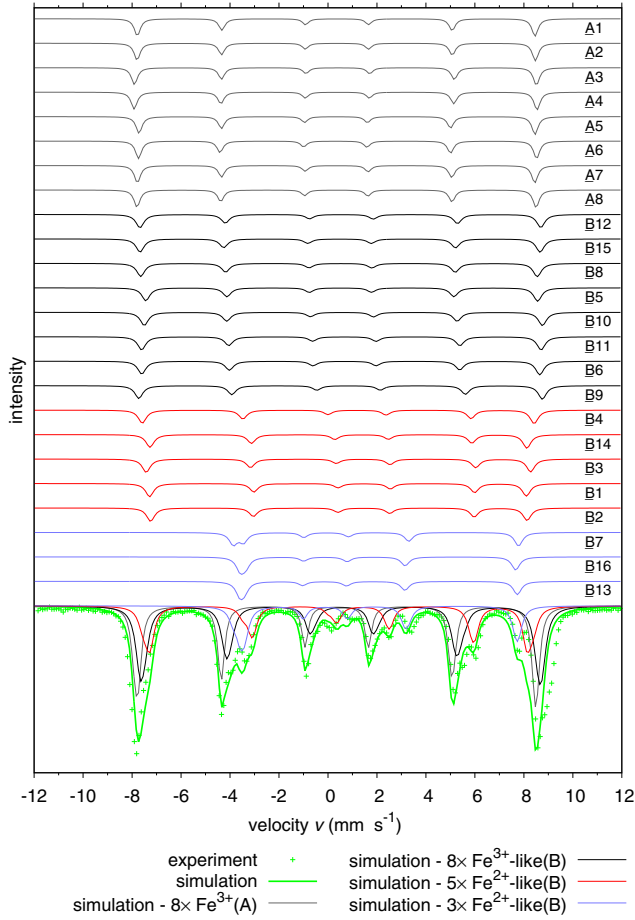


FIG. 4. Simulation of a zero-field ^{57}Fe Mössbauer spectrum (referenced to $\alpha\text{-Fe}$) of a single-domain single-crystal sample of magnetite (in the low-temperature phase) oriented in the [201] direction along the incident γ ray. The site numbering is the same as in Ref. [2] and corresponds to site listing order in Ref. [15]. Black, red, and blue indicate the three groups of Fe(B) subspectra corresponding to the three groups of Fe(B) ions identified in Ref. [2]. The experimental data (see Sec. IV) are given for comparison.

charge fluctuation can be expected. The result of the simulation shown in Fig. 4 can be compared to the experimental spectra of the single-domain crystal, as well as of a powder sample or a sample presented in Sec. IV because the configurations of these samples yield the same sextet line-intensity ratio [39].

The result reveals contributions of four groups of iron sites identified in Ref. [2] to the spectrum. Namely, the line near 3 mm s^{-1} described by Pasternak *et al.* [8] as a characteristic feature of the Cc phase spectrum can be attributed to the group of $\underline{\text{B7}}$, $\underline{\text{B13}}$, and $\underline{\text{B16}}$ Fe^{2+} -like ions. The apparent difference between the subspectra of this group of ions and subspectra of other Fe^{2+} -like(B) ions illustrates the differences between the electronic configurations of these two groups of ions (see Ref. [2] for details) [40].

The spectral contributions of Fe(B) sites from the same group are very similar. This suggests a decomposition of experimental ^{57}Fe Mössbauer spectra into four sextets [$8 \times \text{Fe}^{3+}(\text{A})$, $8 \times \text{Fe}^{3+}\text{-like}(\text{B})$, $5 \times \text{Fe}^{2+}\text{-like}(\text{B})$, and $3 \times \text{Fe}^{2+}\text{-like}(\text{B})$] as

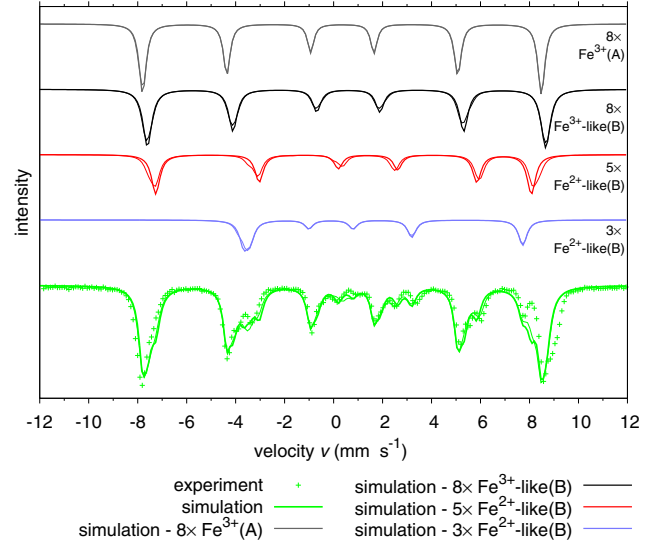


FIG. 5. Comparison of the four-sextet approximation (thick lines) with the subspectra calculated by considering individual sites in the groups (thin lines); see text for details. Black, red, and blue indicate the three groups of Fe(B) subspectra corresponding to the three groups of Fe(B) ions identified in Ref. [2]. The experimental data (see Sec. IV) are given for comparison. The spectra are referenced to $\alpha\text{-Fe}$.

a suitable approach, while indicating that identifying individual iron sites in experimental spectra is virtually impossible.

In a simple approximation, a subspectrum of each of the groups of iron ions can be replaced by a single sextet described by hyperfine parameters calculated as the average of the corresponding parameters [41] within the group (see Table IV; a detailed listing of the average EFG tensors is provided in Table V). A comparison of these four sextets with the subspectra calculated by considering individual sites in the groups is shown in Fig. 5. The correspondence is particularly good for the $8 \times \text{Fe}^{3+}(\text{A})$, $8 \times \text{Fe}^{3+}\text{-like}(\text{B})$, and $3 \times \text{Fe}^{2+}\text{-like}(\text{B})$ groups, while it is still acceptable for the group of five $\text{Fe}^{2+}\text{-like}(\text{B})$ ions, where the hyperfine parameters of the $\underline{\text{B3}}$ and $\underline{\text{B4}}$ sites make the subspectra of these sites slightly different from the rest of this group.

Even better agreement of the simulation with the experiment can be reached by calculating the average hyperfine magnetic fields directly from the zero-field NMR measurement at 4.2 K [12,13]; the result can be found in Fig. 6. The increased magnetic splitting of the four sextets leads to an apparent overall improvement of the match with the experimental data.

IV. EXPERIMENT

The measurement of the ^{57}Fe Mössbauer spectrum was carried out at 4 K using a thin-plate single-crystal magnetite sample. The single crystal was prepared using the skull-melting method [42] followed by subsolidus annealing in CO/CO_2 atmospheres in order to achieve the appropriate stoichiometry [43,44]. The quality of the sample was checked by the ac magnetic susceptibility measurement (the result is shown in Fig. 2 in the Supplemental Material [35]); the Verwey

TABLE IV. Average hyperfine parameters assigned to the four sextets representing the four groups of iron ions in the simulated Mössbauer spectrum (see text). See Table V for the details of the EFG tensors including principal-axis orientation.

Parameter	$8 \times \text{Fe}^{3+}(\text{A})$ (<u>A1</u> , <u>A2</u> , <u>A3</u> , <u>A4</u> , <u>A5</u> , <u>A6</u> , <u>A7</u> , <u>A8</u>)	$8 \times \text{Fe}^{3+}\text{-like}(\text{B})$ (<u>B12</u> , <u>B15</u> , <u>B8</u> , <u>B5</u> , <u>B10</u> , <u>B11</u> , <u>B6</u> , <u>B9</u>)	$5 \times \text{Fe}^{2+}\text{-like}(\text{B})$ (<u>B4</u> , <u>B14</u> , <u>B3</u> , <u>B1</u> , <u>B2</u>)	$3 \times \text{Fe}^{2+}\text{-like}(\text{B})$ (<u>B7</u> , <u>B16</u> , <u>B13</u>)
Isomer shift $\bar{\delta}$ (mm s^{-1})	0.347	0.562	0.905	0.957
Hyperfine magnetic field \bar{B}_{hf} (T)	50.59	50.53	47.62	35.39
Hyperfine magnetic field based on NMR $\bar{B}_{\text{hf}}^{\text{NMR}}$ (T)	50.74	51.72	49.87	36.06
EFG \bar{V}_{zz} ($\times 10^{21} \text{ V m}^{-2}$)	-0.316	-0.489	-6.428	13.699
EFG $\bar{\eta}$	0.392	0.348	0.610	0.039
Line broadening (Γ_{N})	1	2	2	2

transition was found at 123.1 K, indicating an almost perfect sample structure, close to the ideal stoichiometry.

The measurements of ^{57}Fe Mössbauer spectra were performed in the transmission geometry using a constant-acceleration-type spectrometer with a ^{57}Co in Rh source kept at room temperature. The spectrometer was calibrated at room temperature with a 10- μm -thick $\alpha\text{-Fe}$ foil. The thin plate (approximately 0.1 mm) of the magnetite crystal cut along the (001) plane (in cubic notation) was glued to the sapphire plate by wax and placed in a helium cryostat with the [001] direction (in cubic notation) parallel to the γ ray. (The Mössbauer spectrum measured above the Verwey transition temperature is presented in Fig. 3 of the Supplemental Material [35].) The sample was then cooled down to 4 K.

All possible structural domains originating from the orthorhombic and monoclinic twinings were present in the sample since no magnetic field was used during the cooling and spectrum measurement. Taking into account the magnetization directions (close to the local c axis) in these domains with respect to the direction of the γ ray, the ratio of total line intensities of particular sextets is expected to match the one found in the simulation [45]. Note, however, that since the sample was glued to the sapphire plate, the resulting strain might affect the domain structure to some extent.

The spectrum was analyzed by means of a least-squares fitting procedure which entailed calculations of the positions

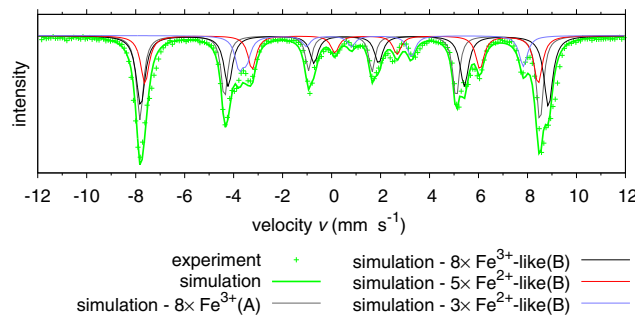


FIG. 6. The four-sextet approximation improved by taking the average hyperfine magnetic fields directly from the zero-field NMR measurement at 4.2 K [12]; see text for details. Black, red, and blue indicate the three groups of Fe(B) subspectra corresponding to the three groups of Fe(B) ions identified in Ref. [2]. The experimental data (see Sec. IV) are given for comparison. The spectra are referenced to $\alpha\text{-Fe}$.

and relative intensities of the absorption lines by numerical diagonalization of the full hyperfine interaction Hamiltonian [46]. The absorption line shape of the spectrum was described using a transmission integral formula [47]. The final fit was carried out in the same FITSUITE software as the simulation. The acquired spectrum is presented in Fig. 7 together with a decomposition into four components corresponding to the four groups of Fe ions. The hyperfine parameters in Table IV (using the NMR-based magnetic field values) were used as starting parameters for the decomposition fit. The fitted parameters comprised isomer shifts, hyperfine magnetic fields, EFG \bar{V}_{zz} values [48], line broadenings, and total absorption, while other parameters (namely, the EFG asymmetry parameters $\bar{\eta}$ and the orientations of the EFG principal axes, as well as the γ -ray direction and relative spectral contributions of the four sextets) remained intentionally fixed. The resulting output parameters of the fit are provided in Table VI. [The EFG \bar{V}_{zz} values corresponding to the groups of $8 \times \text{Fe}^{3+}(\text{A})$ and $8 \times \text{Fe}^{3+}\text{-like}(\text{B})$ ions were kept fixed because their variation within reasonable limits had a negligible impact.] Clearly, the fit reproduces all significant features of the experimental spectrum well. The small deviations from experimental peak intensities can be attributed to the influence of the strain (caused by gluing the sample) on the abundance of particular structural domain types.

Compared to the initial values, the fit yielded systematically larger isomer shifts (by up to 11%; the estimated error of isomer shift values obtained by the DFT calculations is $\pm 4\%$)

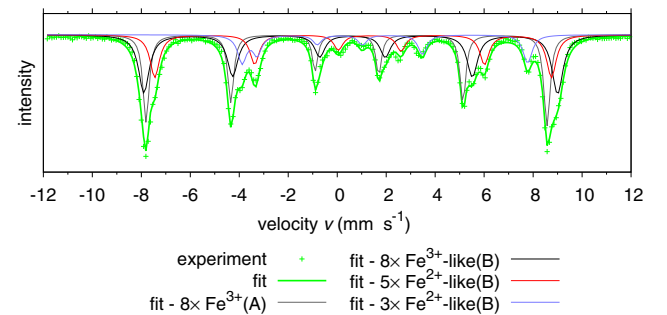


FIG. 7. Experimental Mössbauer spectrum (referenced to $\alpha\text{-Fe}$) of magnetite at 4 K decomposed into four sextets by the fit (see text). The gray line denotes the sextet corresponding to the group of Fe(A) ions, while the black, red, and blue lines indicate the three sextets representing the three groups of Fe(B) ions identified in Ref. [2].

TABLE V. Average EFG tensors assigned to the sextets representing particular groups of iron ions in simulated Mössbauer spectrum. See the text for symbol definitions.

Group	\bar{V}_{aa} ($\times 10^{21}$ V m $^{-2}$)	\bar{V}_{bb} ($\times 10^{21}$ V m $^{-2}$)	\bar{V}_{cc} ($\times 10^{21}$ V m $^{-2}$)	\bar{V}_{ab} ($\times 10^{21}$ V m $^{-2}$)	\bar{V}_{ac} ($\times 10^{21}$ V m $^{-2}$)	\bar{V}_{bc} ($\times 10^{21}$ V m $^{-2}$)	\bar{V}_{zz} ($\times 10^{21}$ V m $^{-2}$)	\bar{V}_{yy} ($\times 10^{21}$ V m $^{-2}$)	\bar{V}_{xx} ($\times 10^{21}$ V m $^{-2}$)	$\bar{\eta}$	Principal axis \bar{v}_{zz}	Principal axis \bar{v}_{yy}	Principal axis \bar{v}_{xx}
$8 \times \text{Fe}^{3+}(\text{A})$	-0.134	0.220	-0.086	0.000	0.205	0.000	-0.316	0.220	0.096	0.392	(0.747, 0, -0.665)	(0, -1, 0)	(-0.665, 0, -0.747)
$8 \times \text{Fe}^{3+}\text{-like(B)}$	0.299	0.160	-0.458	0.000	0.156	0.000	-0.489	0.330	0.160	0.348	(0.195, 0, -0.981)	(0.981, 0, 0.195)	(0, -1, 0)
$5 \times \text{Fe}^{2+}\text{-like(B)}$	1.244	5.174	-6.417	0.000	0.287	0.000	-6.428	5.174	1.255	0.610	(0.037, 0, -0.999)	(0, -1, 0)	(0.999, 0, 0.037)
$3 \times \text{Fe}^{2+}\text{-like(B)}$	-7.114	-6.584	13.698	0.000	0.119	0.000	13.699	-7.114	-6.584	0.039	(-0.006, 0, -1)	(1, 0, -0.006)	(0, -1, 0)

TABLE VI. Average hyperfine parameters assigned to the sextets representing the four groups of iron ions after a refinement by the fit of the experimental Mössbauer spectrum (see text). Free parameters of the fit are in bold, and the percentage in parentheses denotes the relative difference compared to the starting values in Table IV (hyperfine magnetic fields are related to the NMR-based values); all other parameters (except total absorption) were kept fixed. See Table V for the details of the orientation of principal axes of the EFG tensors.

Parameter	$8 \times \text{Fe}^{3+}(\text{A})$ (<u>A1</u> , <u>A2</u> , <u>A3</u> , <u>A4</u> , <u>A5</u> , <u>A6</u> , <u>A7</u> , <u>A8</u>)	$8 \times \text{Fe}^{3+}\text{-like}(\text{B})$ (<u>B12</u> , <u>B15</u> , <u>B8</u> , <u>B5</u> , <u>B10</u> , <u>B11</u> , <u>B6</u> , <u>B9</u>)	$5 \times \text{Fe}^{2+}\text{-like}(\text{B})$ (<u>B4</u> , <u>B14</u> , <u>B3</u> , <u>B1</u> , <u>B2</u>)	$3 \times \text{Fe}^{2+}\text{-like}(\text{B})$ (<u>B7</u> , <u>B16</u> , <u>B13</u>)
Isomer shift δ (mm s ⁻¹)	0.386 (+11%)	0.577 (+3%)	0.985 (+9%)	1.018 (+6%)
Hyperfine magnetic field \bar{B}_{hf} (T)	50.88 (+0.3%)	52.58 (+1.6%)	50.32 (+0.9%)	36.23 (+0.5%)
EFG \bar{V}_{zz} ($\times 10^{21}$ V m ⁻²)	-0.316	-0.489	-4.34 (-33%)	11.90 (-13%)
EFG $\bar{\eta}$	0.392	0.348	0.610	0.039
Line broadening (Γ_{N})	0.88 (-12%)	3.31 (+65%)	2.48 (+24%)	2.13 (+7%)

and hyperfine magnetic fields (by up to 1.6%). On the other hand, the fitted EFG \bar{V}_{zz} parameters are lower in absolute values than the starting ones. The significant difference of -33% in the case of the group of $5 \times \text{Fe}^{2+}\text{-like}(\text{B})$ ions can be caused by a wide range of hyperfine fields at iron sites in this group, which slightly complicates the approximation of the group subspectrum by the single sextet. Resulting line broadening values are relatively close to the initial estimation used for the simulations in the case of the groups of $8 \times \text{Fe}^{3+}(\text{A})$ and $3 \times \text{Fe}^{2+}\text{-like}(\text{B})$ ions, whereas they reach higher values for the groups of $8 \times \text{Fe}^{3+}\text{-like}(\text{B})$ and $5 \times \text{Fe}^{2+}\text{-like}(\text{B})$ ions, most likely due to the broader ranges of hyperfine fields at particular ions in these groups. The fitted total absorption is smaller than the value used for the simulation by just 3% of the value.

V. CONCLUSIONS

We have carried out DFT calculations of isomer shifts and EFG tensors for all 24 crystallographic iron sites in the low-temperature structure of magnetite. The results support the concept of trimerons [15]. The calculated data together with corresponding hyperfine magnetic fields derived from our previous work [2] form a complete set of hyperfine parameters, allowing for a simulation and deeper analysis of the Mössbauer spectrum of this compound. We have simulated Mössbauer sextets for each of the 24 iron positions and, comparing these results with the experimental spectrum, have found that the experimental line positions and all spectral subtleties are reproduced. Thus, every feature visible in the experimental Mössbauer spectrum is understood and can be explained by the *ab initio* calculated electronic structure.

Based on the 24 sextets, we have also verified our previous finding [2] that the 24 iron sites naturally break into four groups: $8 \times \text{Fe}^{3+}(\text{A})$, $8 \times \text{Fe}^{3+}\text{-like}(\text{B})$, $5 \times \text{Fe}^{2+}\text{-like}(\text{B})$, and $3 \times \text{Fe}^{2+}\text{-like}(\text{B})$ ions. The hyperfine parameters of the ions within each group share common characteristics, which means that any effort to identify individual iron sites in Mössbauer spectra is futile. On the other hand, it also allows us to approximate the spectrum by four sextets, as we demonstrated. The parameters of these four sextets, which we derived from

the hyperfine parameter sets of the 24 iron positions, were further improved by determining the corresponding hyperfine magnetic fields from zero-field NMR experiments [12,13]. We thus propose those parameters as starting values for a fit of the experimental Mössbauer spectrum of magnetite.

Trying to check how good our suggestion is, we performed a Mössbauer spectroscopy measurement of a high-quality single-crystalline synthetic sample of stoichiometric magnetite. When fitting the acquired spectrum, we paid special attention to keeping the number of free parameters low to demonstrate the suitability of the four-sextet approximation. The fit matched the experimental spectrum very well, and the final hyperfine parameters are not far from the initial ones. The only limitations concerning the usability of the fit results are the probable impact of the relatively broad range of hyperfine fields at particular ion sites in the $5 \times \text{Fe}^{2+}\text{-like}(\text{B})$ group on the EFG \bar{V}_{zz} value corresponding to this group and also the low sensitivity of the fit to the rather small EFG \bar{V}_{zz} values of the $8 \times \text{Fe}^{3+}(\text{A})$ and $8 \times \text{Fe}^{3+}\text{-like}(\text{B})$ groups, which was the reason for keeping them fixed.

We believe that our results will serve not only for a deeper understanding of the fundamental problem of the electronic structure of magnetite but also as a tool for experimentalists who usually work from a different side of the problem trying to fit the experimental data to get parameters that give the best possible description of the processes the sample undergoes. Indeed, there are numerous situations where Mössbauer spectroscopy was used not only to solve basic problems of magnetite but also just to check for the existence of this mineral, as in many geological studies, or to suggest how geological conditions changed magnetite structure.

ACKNOWLEDGMENTS

This work was supported by the Faculty of Physics and Applied Computer Science of the AGH University of Science and Technology in Krakow. Computational resources were provided by the CESNET LM2015042 and the CERIT Scientific Cloud LM2015085, provided under the program “Projects of Large Research, Development, and Innovations Infrastructures.”

- [1] E. J. W. Verwey, *Nature (London)* **144**, 327 (1939).
- [2] R. Řezníček, V. Chlan, H. Štěpánková, and P. Novák, *Phys. Rev. B* **91**, 125134 (2015); R. Řezníček, Ph.D. thesis, Charles University in Prague, 2015.
- [3] V. A. M. Brabers, in *Handbook of Magnetic Materials*, edited by K. H. J. Buschow (Elsevier, Amsterdam, 1995), p. 189.
- [4] J. M. Honig, *J. Alloys Compd.* **229**, 24 (1995).
- [5] F. Walz, *J. Phys. Condens. Matter* **14**, R285 (2002).
- [6] J. García and G. Subías, *J. Phys. Condens. Matter* **16**, R145 (2004).
- [7] J. Żukrowski, A. Wiecheć, R. Zach, W. Tabiś, Z. Tarnawski, N.-T. H. Kim-Ngan, Z. Kąkol, and A. Kozłowski, *J. Alloys Compd.* **442**, 219 (2007).
- [8] M. P. Pasternak, W. M. Xu, G. Kh. Rozenberg, R. D. Taylor, and R. Jeanloz, *J. Magn. Magn. Mater.* **265**, L107 (2003).
- [9] B. J. Evans and S. S. Hafner, *J. Appl. Phys.* **40**, 1411 (1969).
- [10] R. S. Hargrove and W. Kündig, *Solid State Commun.* **8**, 303 (1970).
- [11] F. J. Berry, S. Skinner, and M. F. Thomas, *J. Phys. Condens. Matter* **10**, 215 (1998).
- [12] P. Novák, H. Štěpánková, J. Englich, J. Kohout, and V. A. M. Brabers, *Phys. Rev. B* **61**, 1256 (2000).
- [13] P. Novák, H. Štěpánková, J. Englich, J. Kohout, and V. A. M. Brabers, in *Ferrites: Proceedings of the Eighth International Conference on Ferrites (ICF 8)*, edited by M. Abe and Y. Yamazaki (The Japan Society of Powder and Powder Metallurgy, Kyoto and Tokyo, Japan, 2000), p. 131.
- [14] M. Mizoguchi, *J. Phys. Soc. Jpn.* **70**, 2333 (2001).
- [15] M. S. Senn, J. P. Wright, and J. P. Attfield, *Nature (London)* **481**, 173 (2012).
- [16] M. S. Senn, I. Loa, J. P. Wright, and J. P. Attfield, *Phys. Rev. B* **85**, 125119 (2012).
- [17] C. H. Patterson, *Phys. Rev. B* **90**, 075134 (2014).
- [18] G. A. Sawatzky, J. M. D. Coey, and A. H. Morrish, *J. Appl. Phys.* **40**, 1402 (1969).
- [19] C. M. Srivastava, S. N. Shringi, and M. V. Babu, *Phys. Status Solidi A* **65**, 731 (1981).
- [20] M. Rubinstein and D. W. Forester, *Solid State Commun.* **9**, 1675 (1971).
- [21] I. Dézsi, Cs. Fetzter, Á. Gombkötő, I. Szűcs, J. Gubicza, and T. Ungár, *J. Appl. Phys.* **103**, 104312 (2008).
- [22] P. Blaha, K. Schwarz, G. Madsen, D. Kvasnicka, and J. Luitz, *WIEN2k, An Augmented Plane Wave + Local Orbitals Program for Calculating Crystal Properties* (Karlheinz Schwarz, Techn. Universität Wien, Austria, 2001).
- [23] G. K. Wertheim, H. J. Guggenheim, and D. N. E. Buchanan, *Phys. Rev.* **169**, 465 (1968).
- [24] M. Filatov, *Coordin. Chem. Rev.* **253**, 594 (2009).
- [25] U. D. Wdowik and K. Ruebenbauer, *Phys. Rev. B* **76**, 155118 (2007).
- [26] S. Sinnecker, L. D. Slep, E. Bill, and F. Neese, *Inorg. Chem.* **44**, 2245 (2005).
- [27] E. V. Mielczarek and W. P. Winfree, *Phys. Rev. B* **11**, 1026 (1975).
- [28] E. V. Mielczarek and D. A. Papaconstantopoulos, *Phys. Rev. B* **17**, 4223 (1978).
- [29] O. C. Kistner and A. W. Sunyar, *Phys. Rev. Lett.* **4**, 412 (1960).
- [30] L. R. Walker, G. K. Wertheim, and V. Jaccarino, *Phys. Rev. Lett.* **6**, 98 (1961).
- [31] G. K. Wertheim and D. N. E. Buchanan, *Phys. Rev.* **161**, 478 (1967).
- [32] K. J. Duff, *Phys. Rev. B* **9**, 66 (1974).
- [33] Y. Zhang, J. Mao, and E. Oldfield, *J. Am. Chem. Soc.* **124**, 7829 (2002).
- [34] The use of orthorhombic coordinates is convenient here since the symmetry lowering during cooling through T_V is dominated by orthorhombic deformation of the magnetite unit cell, whereas simultaneous monoclinic deformation is rather small; see Ref. [2] for details.
- [35] See Supplemental Material at <http://link.aps.org/supplemental/10.1103/PhysRevB.96.195124> for additional figures.
- [36] The $B_{\text{ani}}^{\text{calc}}$ values of all A sites are lower than 2% of their $B_{\text{iso}}^{\text{calc}}$. Thus, the significant reduction of the corresponding anisotropy tensors by the renormalization does not impact the simulated spectrum dramatically. The difference in c_{ani} for the A and B sites is related to generally different characters of electronic and structural configurations of the A and B sites.
- [37] R. F. W. Bader, *Atoms in Molecules: A Quantum Theory* (Oxford University Press, Oxford, 1990).
- [38] Sz. Sajti, L. Deák, and L. Bottyán, [arXiv:0907.2805](https://arxiv.org/abs/0907.2805).
- [39] J. M. Cadogan and D. H. Ryan, in *Handbook of Applied Solid State Spectroscopy*, edited by D. R. Vij (Springer, New York, 2006).
- [40] The specific shape of the B7, B13, and B16 subspectra is a result of a merging of the sextet lines near -3.5 mm s^{-1} caused by a special orientation of the principal axes of the EFG and hyperfine field anisotropy tensors along the crystallographic axes. The reason is that minority-spin electrons occupy the xy orbitals of these sites and the axes of the trimerons in which these sites participate are parallel to the a or b axes; see Ref. [2].
- [41] In the case of the EFG tensors, individual tensor elements $V_{\alpha\alpha'}$ ($\alpha, \alpha' = a, b, c$) are averaged. The ac -glide-generated sites are also taken into account, yielding average \bar{V}_{ab} and \bar{V}_{bc} values equal to zero.
- [42] H. R. Harrison and R. Aragón, *Mater. Res. Bull.* **13**, 1097 (1978).
- [43] R. Aragón, H. R. Harrison, R. H. McCallister, and C. J. Sandberg, *J. Cryst. Growth.* **61**, 221 (1983).
- [44] H. Flood and D. G. Hill, *Z. Elektrochem., Ber. Bunsen-Ges. Phys. Chem.* **61**, 18 (1957).
- [45] This can be simply illustrated by considering only the orthorhombic twinning: the domains with the c axis parallel to the γ -ray direction yield relative sextet line intensities 3:0:1:1:0:3, while the other two types of domains have the c axis perpendicular to the γ -ray direction, so they provide a sextet line-intensity ratio of 3:4:1:1:4:3. These three types of domains are present in the sample with the same probability, so together they give rise to sextets with a total relative line-intensity ratio of 3:2:1:1:2:3.
- [46] N. N. Greenwood and T. C. Gibb, *Mössbauer Spectroscopy* (Chapman and Hall, London, 1971); P. Gülich, R. Link, and A. Trautwein, *Mössbauer Spectroscopy and Transition Metal Chemistry* (Springer, Berlin, 1978).
- [47] S. Margulies and J. R. Ehrman, *Nucl. Instrum. Methods* **12**, 131 (1961); G. K. Shenoy, J. M. Friedt, H. Maletta, and S. L. Ruby, in *Mössbauer Effect Methodology*, edited by I. J. Gruverman, C. W. Seidel, and D. K. Dieterly (Plenum, New York, 1974), Vol. 10, p. 277.
- [48] In other words, all elements of a particular EFG tensor were scaled by the same fitted factor.

Understanding Mössbauer spectrum of magnetite below the Verwey transition: ab initio calculations, simulation and experiment

Supplemental Material

R. Řezníček,^{1,2,*} V. Chlan,¹ H. Štěpánková,¹ P. Novák,³ J. Żukrowski,⁴
A. Kozłowski,⁵ Z. Kąkol,⁵ Z. Tarnawski,⁵ and J. M. Honig⁶

¹*Faculty of Mathematics and Physics, Charles University,
V Holešovičkách 2, 180 00 Prague 8, Czech Republic*

²*Faculty of Physics and Earth Sciences, University of Leipzig, Linnéstrasse 5, D-04103 Leipzig, Germany*

³*Institute of Physics of ASCR, Cukrovarnická 10, 162 53 Prague 6, Czech Republic*

⁴*Academic Centre for Materials and Nanotechnology,
AGH University of Science and Technology, al. Mickiewicza 30, 30-059 Kraków, Poland*

⁵*Faculty of Physics and Applied Computer Science,
AGH University of Science and Technology, al. Mickiewicza 30, 30-059 Kraków, Poland*

⁶*Purdue University, Department of Chemistry, 560 Oval Drive, West Lafayette, Indiana 47907-2084, USA*

(Dated: August 28, 2017; Revised: October 10, 2017)

*Electronic address: reznicek@mbbox.troja.mff.cuni.cz

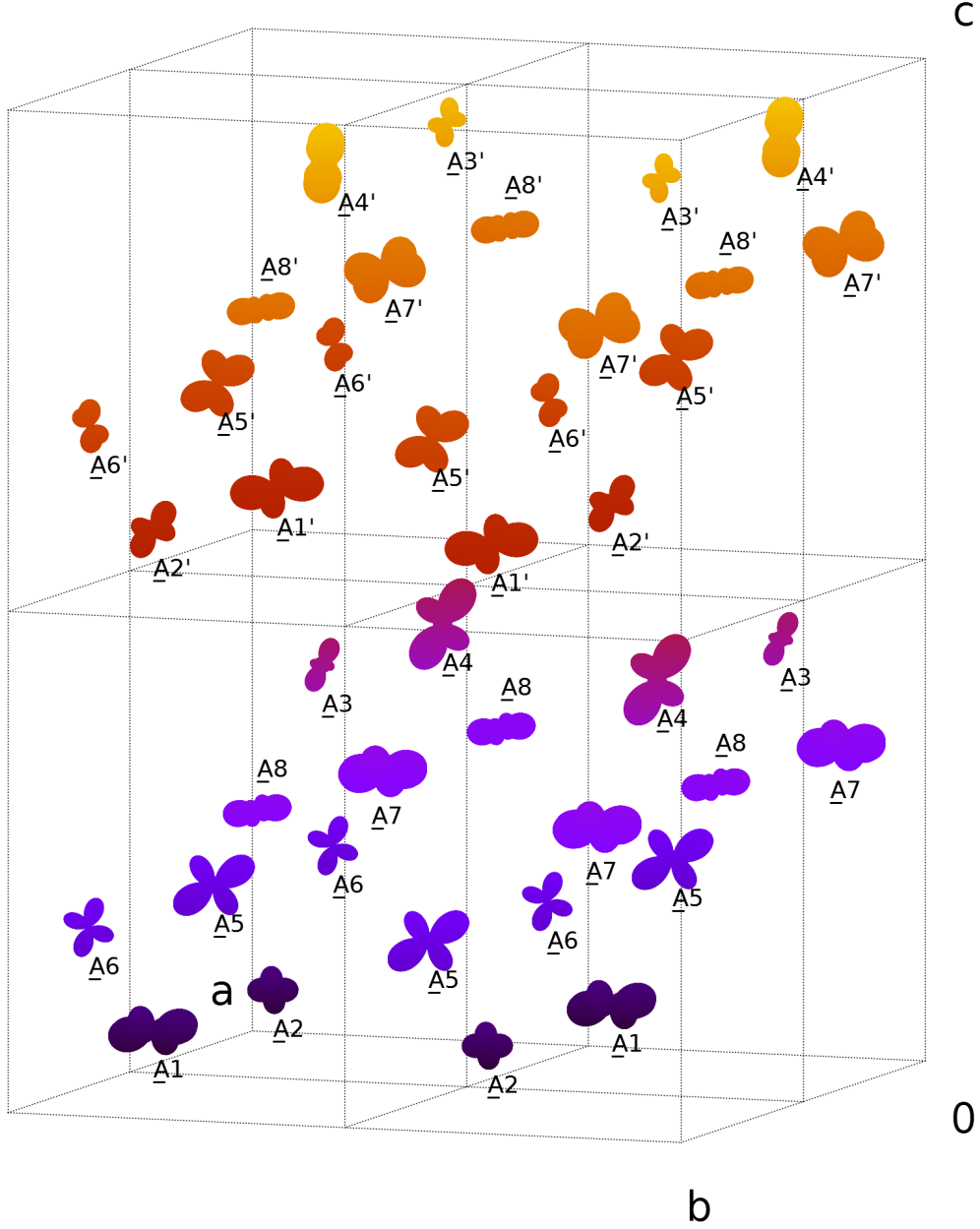


FIG. 1: Visualization of the EFG tensors at Fe(A) sites in the elementary cell (scaling coefficient $C = 0.5 \text{ \AA} \cdot 10^{-21} \text{ V}^{-1} \cdot \text{m}^2$). The site numbering is the same as in Ref. [1] and corresponds to site listing order in Ref. [2]; primes denote the sites generated by the ac -glide symmetry. (Surface colour corresponding to the z -coordinate serves for clarity improvement.)

Sample characterization

AC magnetic susceptibility of the studied sample was measured prior to the grinding to 0.1 mm thickness. The results are shown in Fig. 2, whereas the Mössbauer spectrum above the Verwey transition is presented in Fig. 3.

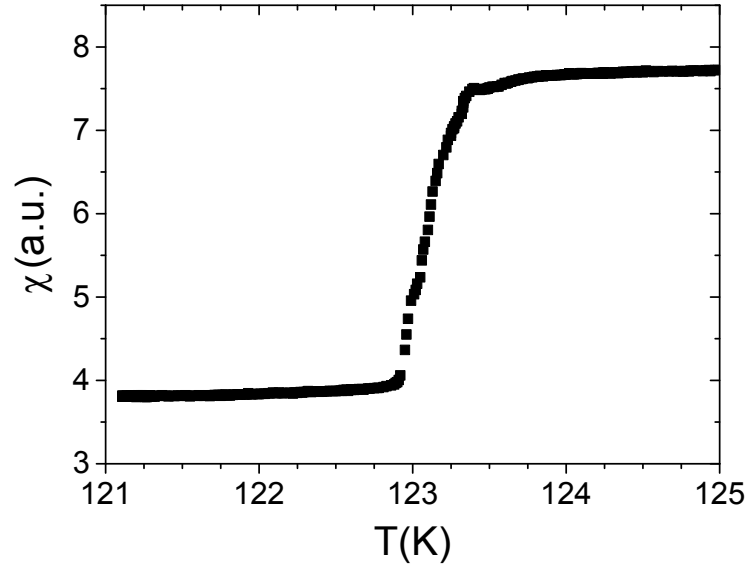


FIG. 2: The results of AC susceptibility measurement of the investigated sample proving its high quality.

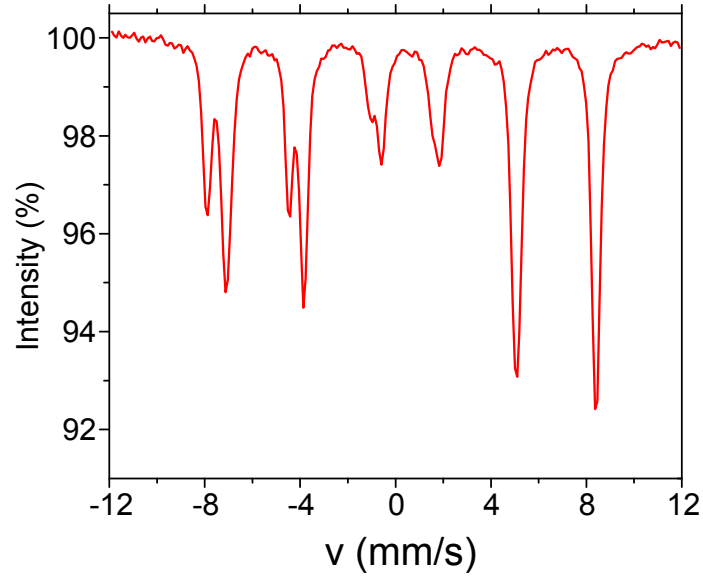


FIG. 3: Mössbauer spectrum of the investigated sample measured at 160 K referenced to the ^{57}Co in Rh source.

-
- [1] R. Řezníček, V. Chlan, H. Štěpánková, and P. Novák, Phys. Rev. B **91** 125134 (2015).
 - [2] M. S. Senn, J. P. Wright, and J. P. Attfield, Nature **481**, 173 (2012).

Hyperfine interactions in lutetium iron garnet

V. Chlan

Faculty of Mathematics and Physics, Charles University, 180 00 Prague 8, Czech Republic

P. Novák

Institute of Physics, Academy of Sciences of the Czech Republic, 162 53 Prague 6, Czech Republic

H. Štěpánková,^{a)} J. Englich, and J. Kuriplach

Faculty of Mathematics and Physics, Charles University, 180 00 Prague 8, Czech Republic

D. Nižňanský

Faculty of Science, Charles University, 128 40 Prague 2, Czech Republic

(Presented on 3 November 2005; published online 17 April 2006)

Nuclear Magnetic Resonance/Near Quadupole Resonance spectra of ^{175}Lu in lutetium iron garnet (LuIG) were measured in the range of 10–500 MHz in zero external magnetic field at a temperature of 4.2 K. Experimentally observed spectra had complicated structure and a theory was needed to interpret them. To this end we calculated the electronic structure of LuIG and from it the values of magnetic hyperfine fields and the components of electric-field-gradient tensor at the lutetium nuclei were determined. These parameters were used to simulate the theoretical spectra of ^{175}Lu in LuIG. Simulated spectral lines of ^{175}Lu at dodecahedral sublattice correspond reasonably well with the system of measured lines in the range of 10–200 MHz. Several spectral lines in the range of 300–500 MHz can be interpreted as the resonance of ^{175}Lu at the octahedral sites that are nominally occupied by the ferric cations. © 2006 American Institute of Physics.

[DOI: [10.1063/1.2158687](https://doi.org/10.1063/1.2158687)]

I. INTRODUCTION

Lutetium iron garnet ($\text{Lu}_3\text{Fe}_5\text{O}_{12}$, LuIG) is a collinear ferromagnetic oxide with a cubic crystal structure (space group $Ia\bar{3}d$),¹ and an easy magnetization axis along the $[111]$ direction. LuIG is a parent compound of promising magneto-optical systems.² In an ideal system the Fe^{3+} ions fully occupy tetrahedral d sites and octahedral a sites, while dodecahedral c sites are occupied by Lu^{3+} . For magnetization along $[111]$ there are two magnetically nonequivalent dodecahedral sites with the ratio 1:1 and two magnetically nonequivalent octahedral sites with the ratio 3:1. Due to a relatively small ionic radius of Lu^{3+} a fraction of these ions enter the octahedral sites in a real system, creating Lu antisite defect.

Besides precise measurement of hyperfine interactions, nuclear magnetic resonance (NMR) allows to study defects in garnet systems that could hardly be detected by other methods.^{3,4} Our previous results obtained by ^{57}Fe NMR in LuIG were published in Ref. 5

In addition to ^{57}Fe NMR two lutetium isotopes also contribute to the NMR signal: ^{175}Lu (nuclear spin $I=7/2$, natural abundance 97.41%) and ^{176}Lu ($I=7$, natural abundance 2.59%). The high nuclear spins of lutetium isotopes together with a low local symmetry of c sites lead to complicated NMR/nuclear quadrupole resonance (NQR) spectra. In this paper we report the measured NMR spectra and compare them with the spectra simulated using the *ab initio* calculated hyperfine parameters.

^{a)}Electronic mail: helena.stepankova@mff.cuni.cz

II. EXPERIMENT

The polycrystalline sample $\text{Lu}_3\text{Fe}_5\text{O}_{12}$ used in the present study was prepared by a liquid mix technique.^{5,6} NMR/NQR spectra were measured by the spin-echo method using the phase-coherent pulse spectrometer with an averaging technique and the Fourier transformation. The measurements were performed in zero external magnetic field at temperature $T=4.2$ K. The signal-to-noise ratio was significantly improved by using the Carr-Purcell pulse sequence.

The measured spectrum consisted of narrow resonance lines of ^{57}Fe from tetrahedral site at frequency 64.6 MHz and from octahedral sites at 74.6 and 75.7 MHz. In the vicinity of the ^{57}Fe lines a set of weak satellite lines was detected and interpreted as a resonance of ^{57}Fe close to Lu antisite defect.⁵ From the relative intensities in the ^{57}Fe spectra the concentration of this defect at a sites was determined as 1.6%.

Besides these lines a complicated structure of broad lines at frequency range of 30–200 MHz and additional spectral lines of much lower intensity at the range of 300–550 MHz were found (see Figs. 1 and 2), which could be assigned to the lutetium nuclei.

III. CALCULATION OF ELECTRONIC PROPERTIES

Ab initio calculation of the electronic structure was based on the density-functional theory (DFT). It used the full-potential augmented-plane-wave method as implemented in the WIEN2K program.⁷ The calculations were performed using a structural cell of LuIG containing four formulae of $\text{Lu}_3\text{Fe}_5\text{O}_{12}$. To obtain the properties of Lu^{3+} ion on both a and c sites for the structure containing the antisite defects, one $\text{Fe}(a)$ atom was replaced by Lu. All calculations

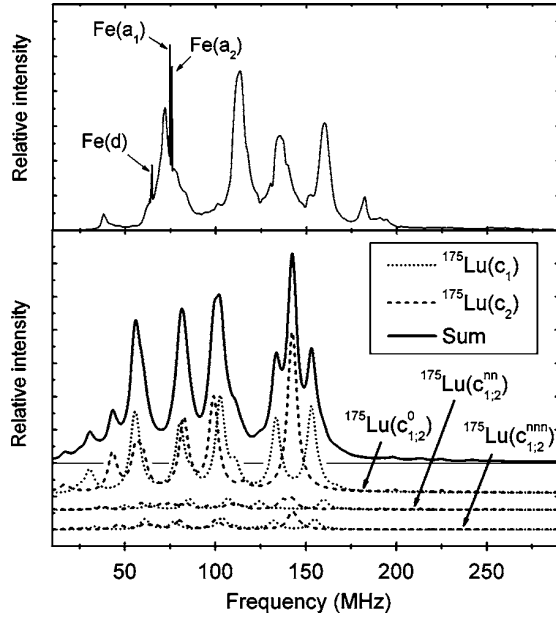


FIG. 1. Experimental ^{175}Lu NMR spectrum of lutetium at dodecahedral c sites (top) and spectrum simulated independently from parameters calculated *ab initio* (bottom) in the frequency range of 10–290 MHz. Contributions to the simulated spectrum from ^{175}Lu having no lutetium antisite defect in its vicinity [denoted as $^{175}\text{Lu}(c_1^0)$], one defect in its nearest a neighborhood [$^{175}\text{Lu}(c_{1,2}^{nn})$], and one defect in its next nearest a neighborhood [$^{175}\text{Lu}(c_{1,2}^{nnn})$] are displayed. Relative intensities of these contributions are calculated using the concentration of the defect in the measured sample.

were spin polarized, with local spin-density approximation⁸ for the exchange-correlation potential. Band-structure calculations were performed in four points in the irreducible part of the Brillouin zone; the number of the basis functions was ~ 5000 .

Dominant part of the Lu hyperfine field B_{hf} arises from the Fermi contact term that is due to the transfer of spin density from the $3d$ states of Fe to the outer s states of Lu.

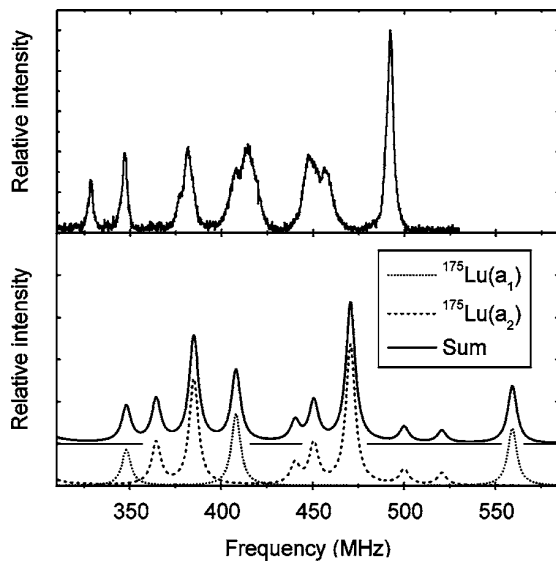


FIG. 2. Experimental ^{175}Lu NMR spectrum of lutetium at octahedral a sites (top) and spectrum simulated independently from parameters calculated *ab initio* (bottom) in the frequency range of 310–585 MHz.

TABLE I. Values of hyperfine parameters at the lutetium nuclei calculated *ab initio*. Angles ϑ and φ determine the direction of magnetization in the system of local axes. Notations (c_1^0) , (c_2^0) , (c_1^{nn}) , (c_2^{nn}) , (c_1^{nnn}) , and (c_2^{nnn}) mean c_1 and c_2 sites with no lutetium antisite defect in its vicinity, one defect in its nearest a neighborhood, and one defect in its next nearest a neighborhood, respectively.

	V_{zz} (10^{-21} V m $^{-2}$)	η	B_{hf} (T)	ϑ (deg)	φ (deg)
$\text{Lu}(c_1^0)$	8.00	0.130	3.40	54.7	90
$\text{Lu}(c_2^0)$	8.00	0.130	3.40	90	54.7
$\text{Lu}(c_1^{nnn})$	8.03	0.133	3.89	54.7	90
$\text{Lu}(c_2^{nnn})$	8.03	0.133	3.89	90	54.7
$\text{Lu}(c_1^{nn})$	8.08	0.231	5.88	54.7	90
$\text{Lu}(c_2^{nn})$	8.08	0.231	5.88	90	54.7
$\text{Lu}(a_1)$	−25.1	0	21.73	0	
$\text{Lu}(a_2)$	−25.1	0	21.73	70.5	0

The calculation that involved the spin-orbit coupling showed that the orbital and spin dipolar contributions to B_{hf} are small and were neglected. Calculated magnetic hyperfine fields and the parameters V_{zz} and η of electric quadrupolar interactions of lutetium at two magnetically nonequivalent c and a sites are given in Table I.

IV. SIMULATION OF THEORETICAL SPECTRA

The Hamiltonian that determines the NMR/NQR spectra consists of electric quadrupolar interaction \hat{H}_Q and magnetic dipolar interaction \hat{H}_M :

$$\hat{H} = \hat{H}_Q + \hat{H}_M, \quad (1)$$

$$\hat{H}_Q = \frac{eQV_{zz}}{4I(2I-1)} \left[3\hat{I}_z^2 - \hat{I}^2 + \frac{\eta}{2}(\hat{I}_+^2 + \hat{I}_-^2) \right], \quad (2)$$

$$\begin{aligned} \hat{H}_M = & -\gamma \mathbf{B}_{\text{hf}} \cdot \hat{\mathbf{I}} = -\gamma B_{\text{hf}} (\hat{I}_+ e^{-i\varphi} \sin \vartheta \\ & + \hat{I}_- e^{i\varphi} \sin \vartheta + \hat{I}_z \cos \vartheta), \end{aligned} \quad (3)$$

where the component V_{zz} and the asymmetry parameter η determine the electric-field-gradient tensor V_{ij} , \mathbf{B}_{hf} is the hyperfine magnetic-field vector, eQ is the nuclear quadrupolar momentum, γ is the nuclear magnetogyric ratio, and \hat{I}_+ , \hat{I}_- , \hat{I}_z , and \hat{I}^2 are the nuclear-spin operators. The Hamiltonian is expressed in the system of main axes of the V_{ij} tensor that coincides with the local symmetry axes of Lu sites. Angles ϑ and φ are the spherical coordinates of the direction of \mathbf{B}_{hf} in the system.

Both electric and magnetic hyperfine interactions were of comparable magnitude, which makes necessary to solve the eigenvalue problem of the total interaction Hamiltonian. The diagonalization had to be carried out separately for c_1 , c_2 , a_1 , and a_2 sites and it provided the eigenvalues which gave us resonance frequencies of transitions between various energy levels and wave functions corresponding to the energy levels. The comparability of both electric and magnetic hyperfine interactions allows 28 transitions for isotope ^{175}Lu and 105 transitions for isotope ^{176}Lu for each nonequivalent site. Probability of each transition was calculated using the first-order perturbation theory.

Resulting simulated spectra were obtained as a superposition of the Lorentz curves at calculated frequencies with the amplitude proportional to the transition probability. We did not try to best fit the theory to the experiment. Instead, to illustrate the connection, a Lorentzian broadening of the calculated lines with the half-width of 6 MHz was used. To take into account the differences in energy-level populations, linear scaling of the amplitudes with increased frequency was applied.

V. RESULTS AND DISCUSSION

Density-functional-based calculations of electric-field gradient (EFG) are usually in a fair agreement with the experiment (see, e.g., Ref. 9). The situation is worse with the hyperfine field, as the contact contribution is often underestimated by tens of percent.¹⁰ This discrepancy is connected with the failure of the present DFT approximations to describe precisely the inner s electron states. If \mathbf{B}_{hf} arises from the transferred hyperfine interaction to the outer s states, better agreement with the experiment is achieved.¹¹ Our simulated spectra are very sensitive to the input parameters and a full agreement of their structure with the experiment cannot be expected. The center of gravity of the resonance lines and the width of frequency interval give better information on the adequacy of the theory. Comparison of the simulated spectrum with experiment in Fig. 1 shows unambiguously that the group of broad lines in the range of 30–200 MHz arises from ^{175}Lu at c sites.

Weaker lines found in the range of 300–530 MHz were compared to the simulated spectrum of ^{175}Lu at a sites (see Fig. 2) and to the simulated spectrum of isotope ^{176}Lu at c sites. Intensities of experimental lines at this frequency range were approximately 50 times lower than the intensities of lines of ^{175}Lu at c sites. This ratio could therefore correspond to the concentration of Lu antisite defect as well as to natural abundance of isotope ^{176}Lu at c sites. Ten lines of simulated

spectrum of ^{175}Lu at a sites lied in the 330–570 MHz range, while the others at lower frequencies contributed to the background of the spectrum of ^{175}Lu at c sites. The whole simulated spectrum of ^{176}Lu at c sites occurred below 150 MHz and it is thus hidden in the $^{175}\text{Lu}(c)$ spectrum of much higher intensity. This allowed us to interpret the lines in the 300–530 MHz range as a resonance of ^{175}Lu at the a sites.

In conclusion, the comparison of experimental NMR/NQR spectra with the simulation based on *ab initio* calculations of hyperfine parameters enabled to test the accuracy of the calculations for a complex garnet structure and allowed us to assign the spectral lines to the resonance of ^{175}Lu in c and a sites.

ACKNOWLEDGMENT

This work is a part of the research plan MS0021620834 that is financed by the Ministry of Education of the Czech Republic.

¹G. Winkler, *Magnetic Garnets* (Vieweg, Braunschweig, 1981).

²I. M. Syvortoka, S. B. Ubizskii, M. Kučera, M. Kuhn, and Z. Vertesy, J. Phys. D **34**, 1178 (2001).

³P. Novák, J. Englich, H. Štěpánková, J. Kohout, H. Lütgemeier, K. Wagner, and W. Tolksdorf, Phys. Rev. Lett. **75**, 545 (1995).

⁴H. Štěpánková, P. Novák, J. Englich, J. Kohout, E. G. Caspary, M. Kučera, K. Nitsch, and H. de Gronckel, J. Magn. Magn. Mater. **196–197**, 412 (1999).

⁵V. Chlan, H. Štěpánková, V. Procházka, J. Englich, J. Kohout, D. Nižňanský, and J. Buršík, J. Magn. Magn. Mater. **290–291**, 993 (2005).

⁶L. W. Tai and P. A. Lessing, J. Mater. Res. **7**, 502 (1992).

⁷P. Blaha, K. Schwarz, G. K. Madsen, D. Kvasnicka, and J. Luitz, WIEN2K, *An Augmented Plane Wave + Local Orbitals Program for Calculating Crystal Properties* (Karlheinz Schwarz, Technische Universität Wien, Vienna, Austria, 2001).

⁸J. P. Perdew and Y. Wang, Phys. Rev. B **45**, 13244 (1992).

⁹P. Blaha, K. Schwarz, W. Faber, and J. Luitz, Hyperfine Interact. **126**, 389 (2000).

¹⁰P. Novák, J. Kuneš, W. E. Pickett, Wei Ku, and F. R. Wagner, Phys. Rev. B **67**, 140403R (2003).

¹¹S. Blügel, H. Akai, R. Zeller, and P. H. Dederichs, Phys. Rev. B **35**, 3271 (1987).

Electric field gradient in FeTiO₃ by nuclear magnetic resonance and *ab initio* calculations

V Procházka¹, H Štěpánková², V Chlan², J Tuček^{1,3}, J Čuda^{1,3},
K Kouřil², J Filip^{1,3} and R Zbořil^{1,3}

¹ Centre for Nanomaterial Research, Faculty of Science, Palacky University, Svobody 26, CZ-771 46 Olomouc, Czech Republic

² Faculty of Mathematics and Physics, Charles University in Prague, V Holešovičkách 2, CZ-180 00 Praha 8, Czech Republic

³ Regional Centre of Advanced Technologies and Materials, Departments of Physical Chemistry and Experimental Physics, Faculty of Science, Palacky University, Šlechtitelů 11, CZ-783 71 Olomouc, Czech Republic

E-mail: prochavi@upol.cz

Received 8 March 2011, in final form 31 March 2011

Published 4 May 2011

Online at stacks.iop.org/JPhysCM/23/205503

Abstract

Temperature dependence of nuclear magnetic resonance (NMR) spectra of ⁴⁷Ti and ⁴⁹Ti in polycrystalline ilmenite FeTiO₃ was measured in the range from 5 to 300 K under an external magnetic field of 9.401 T. NMR spectra collected between 300 and 77 K exhibit a resolved quadrupole splitting. The electric field gradient (EFG) tensor was evaluated for Ti nuclei and the ratio of ⁴⁷Ti and ⁴⁹Ti nuclear quadrupole moments was refined during the fitting procedure. Below 77 K, the fine structure of quadrupole splitting disappears due to the enormous increase of anisotropy.

As a counterpart, *ab initio* calculations were performed using full potential augmented plane waves + local orbitals. The calculated EFG tensors for Ti and Fe were compared to the experimental ones evaluated from NMR and the Mössbauer spectroscopy experiments.

(Some figures in this article are in colour only in the electronic version)

1. Introduction

Ilmenite is a titanium iron oxide with a chemical formula of FeTiO₃. Its solid solution with hematite (α -Fe₂O₃) exhibits an anomalously high thermoremanent magnetization [1]. This anomalous behavior can be understood as a Martial anomaly analog [2]. An intensive research interest in ilmenite and hemato-ilmenite is devoted to understanding the processes and conditions of growth of ilmenite and its solid solution with hematite (hemato-ilmenite) and the observed physical phenomena. Investigation of structural details of pure ilmenite is an important contribution to the widely discussed exchange bias mechanism [3, 4] in the hemato-ilmenite solid solutions. As far as we know, the hemato-ilmenite solid solutions exhibit the highest ever observed exchange bias in natural systems.

Ilmenite crystallizes in rhombohedral crystal structure with space group $R\bar{3}$. Fe and Ti planes alternate in the

material along the z direction [5, 6]. Ti⁴⁺–Fe²⁺ and Ti³⁺–Fe³⁺ arrangements are discussed in the literature. According to Fujii *et al.*, the Ti⁴⁺–Fe²⁺ arrangement is preferred, but the presence of a small amount (less than 10%) of Ti³⁺–Fe³⁺ was also reported [7].

FeTiO₃ is an antiferromagnet with a Néel temperature (T_N) of 56 K. Magnetic moments of Fe are ferromagnetically ordered within the xy planes and the planes with an antiparallel orientation of magnetic moments alternate along the z axis, [8, 9]. FeTiO₃ exhibits a metamagnetic transition with a critical field of 7.99 T [10] applied along the z direction, [9, 11]. Neutron diffraction studies suggested that the magnetic moments of irons are slightly deviated from the z direction [12–14].

This paper focuses on investigating the hyperfine interactions of titanium nuclei in a pure ilmenite. The experimental approach employing nuclear magnetic resonance

(NMR) and Mössbauer spectroscopy is complemented by calculations of electronic structure based on density functional theory (DFT).

Titanium has two stable isotopes with a nonzero dipolar magnetic moment: ^{47}Ti (spin 5/2, natural abundance of 7.3%) and ^{49}Ti (spin 7/2, natural abundance of 5.5%). NMR experiments and mainly the analysis of NMR spectra on titanium are rather complicated due to the very close values of nuclear gyromagnetic ratio of the isotopes, $-2.404\,035\text{ MHz T}^{-1}$ and $-2.404\,752\text{ MHz T}^{-1}$ [15]. The quadrupole moments of ^{47}Ti and ^{49}Ti are relatively large and moreover the values of quadrupole moments (especially for ^{47}Ti) reported by various authors [16–22] differ; the ratio of the quadrupole moments ranges from 0.818 to 0.741 in the literature.

Regardless of the complications mentioned above, several works on titanium oxide systems were published (rutile [17, 23], brookite [24], perovskite-type titanates, e.g. [25, 26]). NMR measurements of FeTiO_3 at room temperature under 9.4 T were published in [27]. Padro *et al* [28] estimated the electric field gradient (EFG) tensor at Ti nuclei from the NMR experiment of Bastow *et al* [27] and confronted them with their DFT calculations. However, these studies were restricted only to the central transition in the titanium spectra.

2. Sample and methods

2.1. Sample

We measured a commercial polycrystalline sample of FeTiO_3 purchased from Sigma Aldrich Company. From the x-ray powder diffraction, we confirmed that the structure is rhombohedral and the sample is well crystalline, with a small amount of TiO_2 impurities (less than 0.5%). According to the x-ray fluorescence, the ratio of iron and titanium amount is approximately 1.03.

2.2. Mössbauer spectroscopy

Mössbauer spectra were recorded in zero external magnetic field using a constant acceleration spectrometer with a 50 mCi ^{57}Co (Rh) source moving at room temperature. For low-temperature measurement the sample was placed in a variable-temperature cryostat. Isomer shift values are reported with respect to $\alpha\text{-Fe}$. The collected Mössbauer spectra were fitted by the MossWinn software package employing the least-squares method.

2.3. NMR

The pulse spectrometer used for our NMR experiments is a system based on a Bruker Avance high-resolution console of special customer configuration. The sample was fixed in the excitation coil of a parallel resonant circuit and the probe head was inserted into the helium continuous-flow cryostat. The measurements were performed under an external magnetic field of 9.401 T. In order to reach a sufficiently high signal-to-noise ratio (S/N), 4096 scans were acquired at each frequency.

To further increase the S/N ratio, we used the Carr–Purcell multi-echo pulse sequence with 51 echoes in the train where all echoes were recorded and coherently summed.

The values of the nuclear gyromagnetic factor of titanium isotopes ^{47}Ti and ^{49}Ti are very close; as a consequence, their NMR spectra overlap. Furthermore, relatively large quadrupole moments lead to a broad spectral range, therefore, we employed a frequency swept regime with a step of 50 kHz in the excitation frequency. At each frequency step, the resonant circuit of the probe was tuned and well matched and the optimal excitation conditions were found. The delay between the scans was set long enough to allow a relaxation of nuclear magnetization to its equilibrium. Fast Fourier transformation (FFT) of the time domain data was performed at each excitation frequency and the final spectrum was constructed as an envelope of the individual FFT.

2.4. Calculations

The electronic structure was calculated with the full potential augmented plane waves + local orbital (APW + lo) method, as implemented in the WIEN2k package [29]. To improve the description of electron correlation, we used a rotationally invariant version of the LDA + U method as described by Liechtenstein *et al* [30], but with the GGA-PBE (generalized gradient approximation of Perdew–Burke–Ernzerhof) [31] exchange correlation potential and single parameter $U_{\text{eff}} = U - J$ ($J = 0$). The values of applied U_{eff} on Fe and Ti were chosen (in agreement with [32]) as 4.5 eV and 3 eV, respectively. The radii of the atomic spheres were 2 au for Fe and Ti, 1.5 au for oxygen. We checked the sensitivity of the results to the parameters of the APW + lo: the calculations were performed in 32 k -points in the irreducible part of the Brillouin zone, the number of basis functions was 1453 ($RK_{\text{max}} = 7.8$) and the charge density was Fourier-expanded to $G_{\text{max}} = 16\text{ (Ryd)}^{1/2}$.

3. Results and their analysis

3.1. Mössbauer experiments

Zero-field Mössbauer spectra of FeTiO_3 were measured at 300 and 5 K; those evaluated are summarized in table 1. At 300 K, the mathematical deconvolution of the respective Mössbauer spectrum leads to two components: a doublet and a singlet (see figure 1(a)). From the isomer shift we deduce that the doublet corresponds to the Fe^{2+} ion in the

Table 1. Mössbauer hyperfine parameters of FeTiO_3 derived from zero-field Mössbauer spectra, recorded at a temperature of 5 and 300 K, where δ is the isomer shift, ΔE_Q denotes the quadrupole splitting, B_{hf} represents the hyperfine magnetic field and RA is the relative spectral area of individual spectral components.

T (K)	Component	$\delta \pm 0.01$ (mm s $^{-1}$)	$\Delta E_Q \pm 0.01$ (mm s $^{-1}$)	$B_{\text{hf}} \pm 0.3$ (T)	RA \pm (%)
5	Sextet	1.19	1.45	4.5	100
300	Doublet	1.08	0.66	—	96
	Singlet	0.28	—	—	4

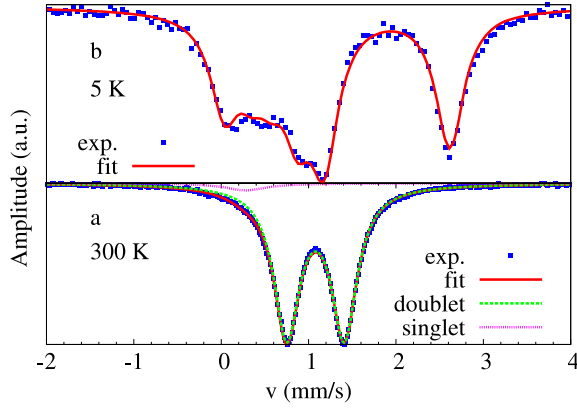


Figure 1. Mössbauer spectra of FeTiO₃ at 300 and 5 K; experimental data together with the fit.

high spin state (i.e. $S = 2$), whereas the singlet reflects the presence of the Fe³⁺ ion in the high spin state (i.e. $S = 5/2$) [33]. Fe³⁺ acts as an impurity; its presence is very low in the sample as demonstrated by the relative spectral area of the singlet component. For temperatures below ~ 55 K, FeTiO₃ magnetically orders as indicated by the magnetically split profile of the low-temperature Mössbauer spectra. At 5 K (see figure 1(b)) only one component is observed. The Mössbauer spectrum has an isomer shift typical for Fe²⁺. Fe³⁺ was not detected since its signal is hidden in the much more intense Fe²⁺ spectrum. From figure 1(b), one can see that the individual peaks of the sextet are strongly overlapped, which is a consequence of the relatively low value of hyperfine magnetic field. Electric quadrupole interaction and magnetic dipolar interaction are thus of comparable strength and in the fitting neither of them can be treated as a perturbation with respect to the other one. Having this in mind, the relative spectral intensities of individual sextet lines were fixed to 2:1:1:2:3:3, which applies for a randomly oriented powdered non-magnetized sample (see [34]).

3.2. NMR experiments

Spectra of titanium isotopes measured in a broad frequency range are plotted in figure 2 for temperatures 300, 77, 35 and 5 K. The spectra shift to the higher frequencies with decreasing temperature down to 77 K, while below 77 K the position of the maximum remains constant. Besides the shift, the spectra gradually broaden with decreasing temperature: at 150 K, the fine structure of the quadrupole splitting is still resolved, but in the spectra measured at 35 and 5 K, it completely disappears. Below T_N , the spectra are composed of a broad line of triangular shape.

Further analysis focused on the well-resolved ^{47,49}Ti NMR spectrum at room temperature (see figure 3), since, besides the central transitions, other significant transitions were also detected for both titanium isotopes. The analysis was aimed at determining the parameters involved in Hamiltonians of magnetic dipolar (\hat{H}_m) and electric quadrupolar (\hat{H}_q) interactions. The magnetic part of the interaction is $\hat{H}_m = -\gamma \hat{\mathbf{I}} \cdot \mathbf{B}_{\text{loc}}$, where the local magnetic field \mathbf{B}_{loc} is given by

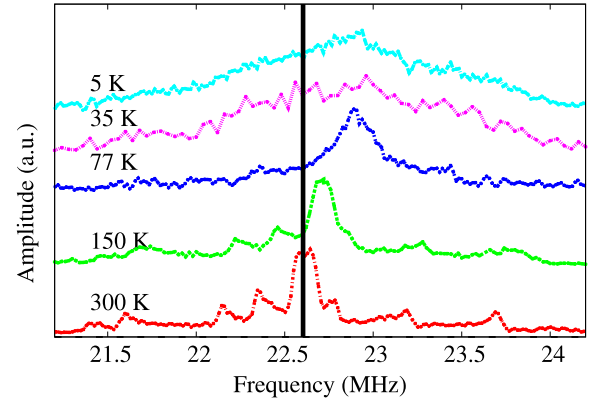


Figure 2. ⁴⁷Ti, ⁴⁹Ti NMR spectra of ilmenite FeTiO₃ depending on temperature. The vertical line corresponds to the resonant frequency of Ti nuclei given by γB_{ext} where the external field is $B_{\text{ext}} = 9.401$ T.

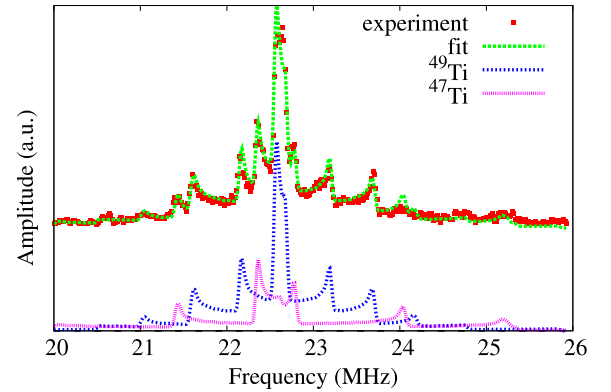


Figure 3. NMR spectrum of FeTiO₃ measured at a temperature of 300 K. Experimental data, fit and spectral decomposition to the contributions belonging to isotopes ⁴⁷Ti and ⁴⁹Ti are plotted.

the chemical shielding tensor σ and external magnetic field, $\mathbf{B}_{\text{loc}} = (1 - \sigma) \cdot \mathbf{B}_{\text{ext}}$. The Hamiltonian of the quadrupole interaction \hat{H}_q is expressed in a system of the main axes of the EFG tensor V_{ii} as

$$\hat{W}_Q = \frac{eQV_{zz}}{4I(2I-1)}(3\hat{I}_z^2 - \hat{I}^2 + \eta(\hat{I}_x^2 - \hat{I}_y^2)), \quad (1)$$

where Q is the quadrupole moment of the nucleus, e denotes the elementary electric charge, $\hat{\mathbf{I}}$ represents the operator of nuclear spin vector, \hat{I}_i , $i = x, y, z$, denote the operators of the nuclear spin components, $\eta = \frac{V_{xx} - V_{yy}}{V_{zz}}$ is the parameter of asymmetry, and V_{xx} , V_{yy} and V_{zz} stand for components (eigenvalues) of the diagonalized EFG tensor ($|V_{xx}| \leq |V_{yy}| \leq |V_{zz}|$).

The tensor of the chemical shielding σ and EFG tensor reflect the local symmetry of the crystallographic site. Crystallographic data [35] suppose that local symmetry of titanium (and iron) sites possess a trigonal axis parallel to the z direction of the unit cell. In such a case, the EFG tensor is defined solely by V_{zz} , ($\eta = 0$). On the other hand, if the local trigonal axis was not present, the parameter η would be nonzero. In further analysis, we did not constrain

Table 2. Calculated and experimental EFG parameters. The calculated values were obtained on experimental structures, except nonzero η denoted by * which was acquired from the optimized structure. Experimental values for Fe are from the Mössbauer experiment at a temperature of 5 K.

Atom	Experiment		Calculation	
	EFG (10^{21} V m $^{-2}$)	η	EFG (10^{21} V m $^{-2}$)	η
Ti	2.58	0.03	2.24	0 (0.17)*
Fe	8.61	—	6.95	0
O	—	—	−2.53	0.64

axial symmetry, allowing it to take nonzero values. Similar consequences are valid for σ : however, in our analysis, we neglected the influence of chemical shielding anisotropy.

To obtain the EFG tensor, we constructed the spectral function and fitted it to the experimental NMR spectrum. For the spectral function in polycrystalline samples, one has to take into account various orientations of EFG tensor main axes with respect to the external magnetic field and also with respect to the radio frequency field. For a particular configuration, the eigenproblem of Hamiltonian \hat{H} was solved, resonance frequencies were derived from the eigenvalues and transition intensities were evaluated according to the Fermi golden rule [36]. Such particular spectra were summed up (assuming a random orientation of grains) and the fitting function was composed as a convolution with a Gaussian broadening function (with a half-width as one of the fitting parameters). The fitting function comprised ^{47}Ti and ^{49}Ti signals in the ratio of their natural abundances.

For the quality of the fit, proper setting of the nuclear parameters turned out to be an important issue. As the value of the quadrupolar moment of ^{47}Ti isotope (Q_{47}) reported in the literature varies considerably, we included it as an additional fitting parameter, while gyromagnetic ratios of both isotopes and quadrupolar moment of ^{49}Ti (Q_{49}) were kept constant, $Q_{49} = 0.24$ barn [17]. The quadrupolar moment (Q_{47}) was refined during the fit to a value of 0.291 ± 0.002 barn; the obtained ratio of $Q_{49}/Q_{47} = 0.8245$ agrees with [16–18, 22].

The fitting function and its decomposition to contributions of both isotopes is displayed in figure 3 and the EFG tensor parameters were evaluated as $V_{zz} = (2.578 \pm 0.040) \times 10^{21}$ V m $^{-2}$ and $\eta = 0.029 \pm 0.003$, see also table 2. The fitting function agrees well in positions of the critical points of non-central transitions. The lineshape of the central transition differs slightly, probably due to a neglected contribution of the chemical shift anisotropy, a possible amount of other titanium oxide phases or non-stoichiometry.

3.3. Results of calculations

EFG tensors on titanium and iron sites were calculated for the structure based on experimental data in [35]; the orientation of iron spins was considered as being antiparallel. The calculated value of the largest component of the EFG tensor on the Ti nucleus was $V_{zz} = 2.24 \times 10^{21}$ V m $^{-2}$. Symmetry of the structure in [35] implied the value of $\eta = 0$. To estimate a possible asymmetry, the symmetry constraints were

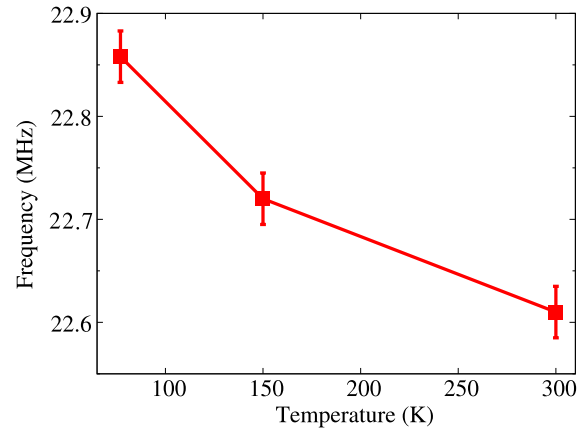


Figure 4. The position of central transition depending on temperature for spectra collected above T_N . The line is a guide for the eyes only.

released and the structure was optimized, i.e. lattice parameters (unit cell volume and c/a ratio) and internal parameters were optimized with respect to the total energy and atomic forces. This process led to a nonzero but low value of η at Ti sites. The results of calculations, including EFG at the Fe nuclei, are displayed in table 2.

4. Discussion

Values of our experimental and calculated V_{zz} parameter for Ti in ilmenite differ by less than 15% (see table 2). The evaluated value for asymmetry (both from experiment and calculations) is close to zero. Padro *et al* [28] determined $V_{zz} = 2.1 \times 10^{21}$ V m $^{-2}$ and a rather higher value of $\eta = 0.35(10)$, but their analysis considered the central transition only, and moreover its lineshape was not well defined. Our analysis relies on the critical points (peaks and steps) of non-central transitions, which naturally increases the accuracy. Since the EFG tensor at the Fe nuclei cannot be obtained by NMR, we compared our calculated values with Mössbauer data.

The shape of NMR spectra at 150 and 77 K resemble that of a 300 K spectrum, but shifted to higher frequencies. The quadrupolar splitting does not seem to change substantially with the temperature and the shift can be assigned to a change in the local magnetic field. The position of the central transition depending on temperature is plotted in figure 4. The shift is probably connected with a change in susceptibility (magnetization) with temperature, not only directly (due to the demagnetization field) but also indirectly, via an average value of the transferred magnetic hyperfine field that is proportional to the magnetization of irons. NMR spectra at lower temperatures (35 and 5 K) are highly broadened and all features are smeared out. An important aspect that influences the behavior of ilmenite in an external magnetic field is the anisotropy of magnetic susceptibility [11]. While the material is magnetically isotropic at room temperature, the anisotropy increases with decreasing temperature. The broadening may have several possible explanations.

- (i) Distribution of grain orientation leads to different magnetic states of the grains. The external field

used (9 T) was sufficient to induce a transition from antiferromagnetic to ferromagnetic state for those grains that have the hexagonal axis approximately parallel to the magnetic field, while for a large portion of grains, their orientation would lead only to a canted antiferromagnetic state [10].

- (ii) Distribution of grain orientation and also distribution of their shapes lead to a distribution of demagnetization fields.
- (iii) Similarly, a distribution of dipolar magnetic fields within the Lorentz sphere can be expected.

5. Conclusions

The spectra of $^{47,49}\text{Ti}$ NMR were measured in the temperature range 5–300 K, including non-central transitions. The NMR spectra shift to higher frequencies with decreasing temperature. The experimental data allowed us to evaluate accurately the parameters of the EFG tensor of Ti nuclei at room temperature. The experimental values agree well with the results of our *ab initio* calculations and confirmed a slight axial asymmetry predicted by *ab initio* calculations.

Acknowledgments

This study was supported by project MS00213620834 of the Ministry of Education of the Czech Republic, the Operational Programme Research and Development for Innovations—European Social Fund (CZ.1.05/2.1.00/03.0058), the projects of the Ministry of Education of the Czech Republic (1M6198959201 and MSM6198959218) and the project of the Academy of Sciences of the Czech Republic (KAN115600801).

References

- [1] Kletetchka G, Wasilewski P J and Taylor P T 2002 *Technophys* **347** 167
- [2] McEnroe S A, Brown L L and Robinson P 2004 *J. Appl. Geophys.* **56** 195–212
- [3] McEnroe S A, Carter-Stiglitz B, Harrison R J, Robinson P, Fabian K and McCammon C 2007 *Nature Nanotechnol.* **2** 633
- [4] Harrison R J, McEnroe S A, Robinson P, Carter-Stiglitz B, Palin E J and Kasama T 2007 *Phys. Rev. B* **76** 174436
- [5] Shirane G, Pickart S J, Nathans R and Ishikawa Y 1959 *J. Phys. Chem. Solids* **10** 35
- [6] Wilson N C, Muscat J, Mkhonto D, Ngoepe P E and Harrison N M 2005 *Phys. Rev. B* **71** 075202
- [7] Fujii T, Yamashita M, Fujimori S, Saitoh Y, Nakamura T, Kobayashi K and Takada J 2007 *J. Magn. Magn. Mater.* **310** e555
- [8] Stickler J J, Kern S, Wold A and Heller G S 1967 *Phys. Rev.* **164** 765
- [9] McDonald P F, Parasiris A, Pandey R K, Gries B L and Kirk W P 1991 *J. Appl. Phys.* **69** 1104
- [10] Kato H and Nakagawa Y 1994 *Physica B* **201** 80–3
- [11] Kato H, Yamada M, Yamaguchi H, Hiroyoshi H, Takei H and Watanabe H 1982 *J. Phys. Soc. Japan* **51** 1769
- [12] Kato H, Ohashi Y Y M, Yamada M, Takei H and Funahashi S 1983 *Solid State Commun.* **45** 669
- [13] Kato H, Yamaguchi Y, Yamada M, Funahashi S, Nakagawa Y and Takei H 1986 *J. Phys. C: Solid State Phys.* **19** 6993
- [14] Yamaguchi Y, Kato H, Takei H, Golgman A I and Shirane G 1986 *Solid State Commun.* **59** 865
- [15] Grant D M and Harris R K 1996 *Encyclopedia of Nuclear Magnetic Resonance* vol 5 (Chichester: Wiley)
- [16] Channappa K H and Pendlebury J M 1965 *Proc. Phys. Soc.* **86** 1145–6
- [17] Kanert O and Kolem H 1988 *J. Phys. C: Solid State Phys.* **21** 3909
- [18] Raghavan P 1989 *At. Data Nucl. Data Tables* **42** 189
- [19] Pyykko P 2001 *Mol. Phys.* **99** 1617
- [20] Pyykko P 2008 *Mol. Phys.* **106** 1965
- [21] Bieron J, Fischer C F and Grant I P 1999 *Phys. Rev. A* **59** 4295
- [22] Kiyama T and Itoh M 2003 *Phys. Rev. Lett.* **91** 167202
- [23] Labouriau A and Earl W L 1997 *Chem. Phys. Lett.* **270** 278
- [24] Bastow T J, Doran G and Whitfield H J 2000 *Chem. Mater.* **12** 436
- [25] Dec S F, Davis M F, Maciel G E, Bronnimann C E, Fitzgerald J J and Han S 1993 *Inorg. Chem.* **32** 955
- [26] Zalar B, Lebar A, Seliger J, Blinc R, Laguta V V and Itoh M 1999 *Phys. Rev. B* **71** 064107
- [27] Bastow T J, Gibson M A and Forwood C T 1998 *Solid State Nucl. Magn. Reson.* **12** 201
- [28] Padro D, Jennings V, Smith M E, Hoppe R, Thomas A and Dupree R 2002 *J. Phys. Chem. B* **106** 13176
- [29] Blaha P, Schwarz K, Madsen G K H, Kvasnicka D and Luitz J 2001 *WIEN2k, An Augmented Plane Wave+Local Orbitals Program for Calculating Crystal Properties* (Wien: TU Wien)
- [30] Liechtenstein A I, Anisimov V I and Zaanen J 1995 *Phys. Rev. B* **52** R5467
- [31] Perdew J P, Burke S and Ernzerhof M 1996 *Phys. Rev. Lett.* **77** 3865
- [32] Aryasetiawan F, Karlsson K, Jepsen O and Schönberger U 2006 *Phys. Rev. B* **74** 125106
- [33] Greenwood N N and Gibb T C 1971 *Mössbauer Spectroscopy* (London: Chapman and Hall) pp 294–6
- [34] Cuda J, Zboril R, Schneeweiss O, Tucek J, Procházka V, Maslan M and Tucek P 2010 *AIP Conf. Proc.* **1258** 55–66
- [35] Wechsler B A and Prewitt C T 1984 *Am. Mineral.* **69** 176–85
- [36] Egorov A V, Mukhamedshin I R and Suzuki H 2003 *Physica B* **329** 1397–8

NMR and *ab initio* study of gallium metal under pressureR. Řezníček,^{1,*} V. Chlan,² and J. Haase¹¹*Faculty of Physics and Earth Sciences, University of Leipzig, Linnéstrasse 5, D-04103 Leipzig, Germany*²*Faculty of Mathematics and Physics, Charles University, V Holešovičkách 2, 180 00 Prague 8, Czech Republic*

(Received 28 June 2018; revised manuscript received 27 February 2019; published 15 March 2019)

Gallium metal possesses a complex phase diagram and it has been the subject of many experimental and theoretical studies. Nevertheless, hyperfine properties of its phases requiring higher pressure beyond the liquid-I-II triple point were seldom examined. In this work, hyperfine parameters of liquid and solid gallium metal under pressure are investigated by nuclear magnetic resonance (NMR) measurements and *ab initio* calculations. The electric field gradient and NMR shift of the Ga-III phase are both measured and calculated and their relation to electronic structure is interpreted. Further, calculations of pressure dependencies of the hyperfine parameters of several other solid gallium phases are presented.

DOI: [10.1103/PhysRevB.99.125121](https://doi.org/10.1103/PhysRevB.99.125121)

I. INTRODUCTION

Gallium exhibits a complex phase-temperature (P-T) diagram comprising a variety of metastable phases [1,2]. Thus, it generally presents a great opportunity to explore the effects of pressure, temperature, and crystal structure for the physical properties of different phases of the same metallic element. Many experimental results concerning structure determination and phase transition identification [1–10] were published. Various studies focused on other properties including, e.g., elastic properties, phonon dispersion, or the behavior of Ga clusters and superconductivity of gallium [11–22]. The Ga element was also the subject of numerous theoretical investigations [23–40].

The chemical and electronic properties of gallium metal under pressure are rather complex and nuclear magnetic resonance (NMR) may significantly help to understand both. Indeed, there were several NMR or nuclear quadrupole resonance (NQR) studies of liquid gallium [41–49] and of the α -Ga (i.e. Ga-I) [50–58] and β -Ga [58–61] solid phases carried out. However, with the only exception of Ref. [62], the papers on hyperfine properties of gallium metal do not cover phases requiring higher pressure (i.e., well above 1.25 GPa to get beyond the liquid-I-II triple point). Thus, this work takes advantage of the anvil-cell-based high-pressure NMR technique and focuses on NMR experiments on liquid and solid gallium under a pressure up to about 2 GPa at room temperature. The measurements are complemented with *ab initio* calculations of electronic and hyperfine structure of solid gallium, allowing for a corroboration of experimental results and a deeper insight into electronic structure.

II. EXPERIMENT

A. Experimental method

The high-sensitivity NMR anvil pressure cell [63] consisting of a piston and a cylinder made of titanium was fitted

with moissanite anvils with a culet diameter of 1.0 mm. A beryllium copper gasket with a 0.5 mm hole contained an RF microcoil of about 300 μm (inner) diameter and 5 turns wound from 25 μm copper wire with 5 μm insulation. A drop of approximately 200 μm of liquid gallium (6N purity level, supplied by ESPI Metals) was placed in the coil together with a ruby chip (coated with cryogenic varnish to avoid any undesired reaction with the gallium sample) serving as a pressure gauge. The cell was then filled with paraffine oil used as a pressure medium and external pressure was applied. Care was taken to ensure hydrostatic conditions in the pressure cell by the appropriate choice of the pressure medium and by minimizing the risk of squeezing the gallium sample directly by the culets of the anvils. The pressure was monitored using a laser spectrometer by observing a shift of the R_1 ruby luminescence line [64–66].

At first, only small pressure was applied, so the first experiments were performed under nearly ambient pressure. Next, the pressure in the sample space was increased to 1.15(5) GPa. In the final step, the pressure on the sample reached 2.15(5) GPa and the gallium sample became solid. Most probably (see below) the sample crystallized into the Ga-III phase with body-centered-tetragonal $tI2$ structure [1], which is metastable in this region and can be typically obtained by this approach [1,8]. The stable phase in this P-T region is Ga-II with a complex orthorhombic structure [8] (earlier described as body-centered-cubic [1]), but it requires a different procedure to prepare. One should also consider the metastable monoclinic β -Ga phase [5], although its existence is relatively unlikely under these conditions. The location of the investigated pressure-temperature points in the phase diagram is illustrated in the Supplemental Material [67].

The pressure cell with the sample was installed in a home-made wide-bore NMR probe. The NMR experiments were carried out in a 9.4 T cryomagnet using a phase-coherent spectrometer. The ^{69}Ga and ^{71}Ga isotopes (both with 3/2 spin) were observed. Resonance frequencies of ^{69}Ga and ^{71}Ga nuclei in a reference $\text{Ga}(\text{NO}_3)_3/\text{D}_2\text{O}$ solution were

*Richard.Reznicek@physik.uni-leipzig.de

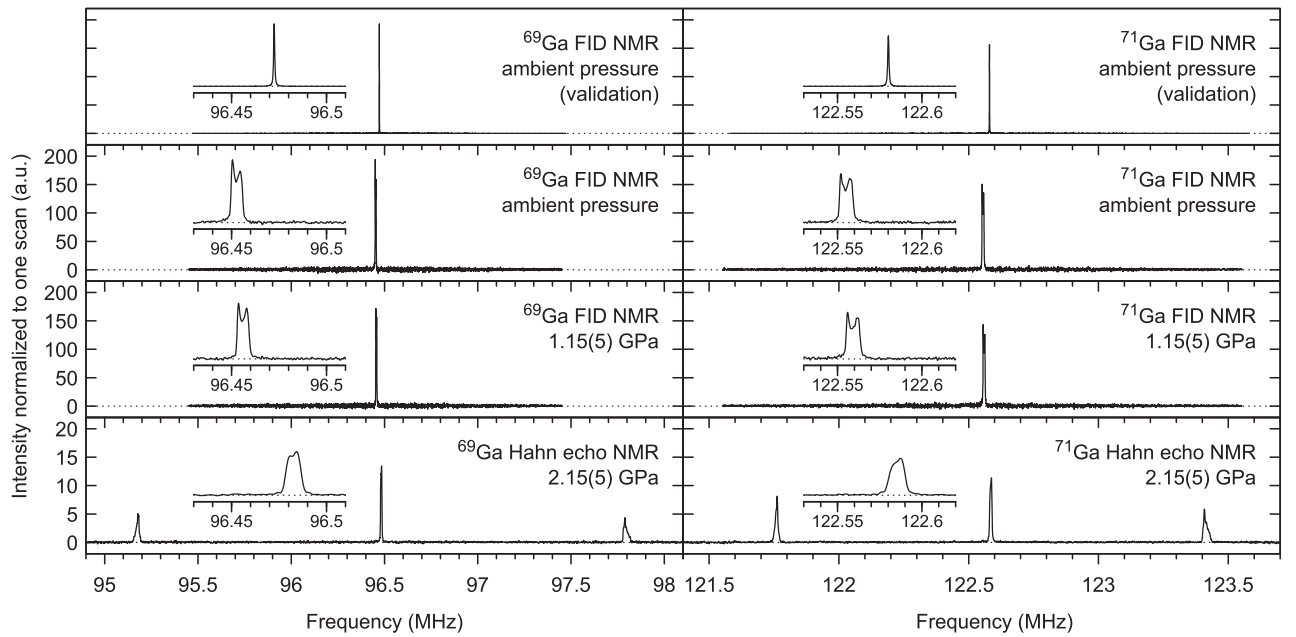


FIG. 1. The NMR spectra of both isotopes of gallium recorded at room temperature for three different pressures. The insets show details of central parts of the spectra.

$^{69}f_{\text{ref}} = 96.04159$ MHz and $^{71}f_{\text{ref}} = 122.03277$ MHz, respectively. The quadrupole moments of the gallium nuclei are $^{69}Q = 17.1(2)$ fm² for ^{69}Ga and $^{71}Q = 10.7(1)$ fm² for ^{71}Ga [68]. Single-pulse (FID) and Hahn echo pulse sequences were employed for spectra measurements. The relaxation times were determined using the inversion recovery and Hahn echo experiments. The population transfer sequence for detecting shared Zeeman levels consisted of an inversion pulse at satellite frequency immediately followed by the Hahn echo pulse sequence at the central transition frequency. Pulse power of up to 1 W was in most cases sufficient for the microcoil and the pulse duration was adjusted to avoid undesired excitation of neighboring transitions whenever possible, resulting in pulse lengths of several μs . The typical number of scans was on the order of 10^3 to 10^4 for the liquid phase and on the order of 10^5 to 10^6 for the solid phase.

For validation experiments under ambient conditions, a plastic foam (approximately $14 \times 3 \times 1.5$ mm) soaked with gallium metal (the same as above) and wrapped in polyethylene foil was used as a sample. The coil of 10 turns was wound from insulated 0.3 mm copper wire around the sample. The coil with the sample was then installed in the NMR probe instead of the pressure cell and its holder. The pulse sequence consisted of a single pulse (110 W, 5 μs for ^{71}Ga , 7 μs for ^{69}Ga) with a repetition time of 1 s (to avoid heating of the sample) and 512 scans.

B. Experimental results

The NMR spectra of both isotopes in liquid and solid gallium are provided in Fig. 1. Each of the liquid phase spectra (the second and third row in Fig. 1) consists of a single resonance signal [full width at half maximum of ≈ 67 ppm (≈ 8.2 kHz) for ^{71}Ga and ≈ 65 ppm (≈ 6.2 kHz) for ^{69}Ga] exhibiting a small splitting [≈ 47 ppm (≈ 5.7 kHz)

for ^{71}Ga and ≈ 43 ppm (≈ 4.2 kHz) for ^{69}Ga]. Once the pressure was increased to 2.15(5) GPa, the sample turned into a solid crystalline phase manifested by a quadrupole split spectrum typical for single crystals; see the lowest panels of Fig. 1. The linewidth of the central transition became a bit bigger than (while still comparable with) the width of the signal observed in the liquid. The central transition splitting was similar to the one of the resonance line in the liquid. The integral intensity of each of the satellites was about 80% of the central transition integral intensity, which can be explained by slightly suboptimal excitation and detection conditions at the satellite frequencies as the probe was tuned to the central transition frequency. In order to verify that the side peaks are indeed satellite signals, a population transfer experiment was performed: an inversion pulse applied at satellite frequency resulted in a significant increase of signal detected by subsequent Hahn echo sequence at the central transition frequency, which meets the expectations following from the considered 4-level system [69].

Since even contemporary works (not limited by available resolution as early experiments) comprising NMR measurements on liquid gallium [70–72] do not mention such splitting as observed here, validation measurements on the gallium sample without the pressure cell were carried out under ambient conditions. The validation experiments (the topmost panels of Fig. 1) yielded much narrower resonance lines (full width at half maximum of 7.2 ppm, no splitting) at frequencies higher by 207 ppm. This indicates an unexpected presence of local magnetic field inhomogeneity in the pressure cell. The mechanism of line splitting by field inhomogeneity is illustrated in a note in the Supplemental Material [67]. Nevertheless, the comparison of the data from the validation experiments allowed for correction of the NMR shifts measured on the liquid and solid phases of the sample in the pressure cell (see below).

TABLE I. Experimental NMR frequencies and (corrected) shifts Δ^{exp} [isotropic parts of frequency and shift $\Delta_{\text{iso}}^{\text{exp}}$ at 2.15(5) GPa].

Pressure	Isotope	Observed frequency (MHz)	Corrected frequency (MHz)	Shift Δ^{exp} ($\Delta_{\text{iso}}^{\text{exp}}$) (ppm)
Ambient (validation)	^{69}Ga	96.47241(1)		4486
	^{71}Ga	122.58012(1)		4485
Nearly ambient	^{69}Ga	96.453(1)		
	^{71}Ga	122.555(1)		
1.15(5) GPa	^{69}Ga	96.456(1)	96.475(10)	4517(80)
	^{71}Ga	122.559(1)	122.584(10)	4518(80)
2.15(5) GPa	^{71}Ga	122.605(2)	122.612(10)	4746(80)

The NMR shifts Δ^{exp} are summarized in Table I, while the spin-lattice (T_1) and spin-spin (T_2) relaxation times can be found in Table II. The spin-lattice relaxation is assumed to be composed of magnetic and quadrupole contributions, characterized by T_{1m} and T_{1q} times, respectively:

$$\begin{aligned} 1/T_1 &= 1/T_{1m} + 1/T_{1q}, \\ 1/T_{1m} &= C_m \gamma^2, \\ 1/T_{1q} &= C_q Q^2, \end{aligned} \quad (1)$$

where γ denotes the gyromagnetic ratio of resonating nuclei, Q stands for the quadrupole moment, while C_m and C_q are corresponding proportionality coefficients. Thus, the T_1 relaxation times of both gallium isotopes can be expressed by these relations:

$$\begin{aligned} 1/^{69}T_1 &= C_m {}^{69}\gamma^2 + C_q {}^{69}Q^2, \\ 1/^{71}T_1 &= C_m {}^{71}\gamma^2 + C_q {}^{71}Q^2. \end{aligned} \quad (2)$$

Solving the set of equations (2) allows for a separation of the magnetic and quadrupole contributions (Table II). Apparently, the magnetic part of relaxation is dominant in the liquid phase and is virtually the only relaxation mechanism in the solid phase [at 2.15(5) GPa, $^{71}T_1/^{69}T_1$ is equal within experimental error to $^{69}\gamma^2/^{71}\gamma^2$]. Under the assumption that Δ^{exp} is composed solely of the Knight shift K , the fulfillment of the Korringa relation [73] can be checked by comparing $T_{1m}K^2T$ to

$$S_0 = \frac{\hbar}{4\pi k_B} \frac{\gamma_e^2}{\gamma^2}, \quad (3)$$

where k_B is the Boltzmann constant and γ_e denotes the gyromagnetic ratio of electron (see the last column of Table II).

The most valuable information was obtained from a measurement of the dependence of the spectra on the orientation

of the sample with respect to the magnetic field direction; see Fig. 2. The dependencies of the central transition frequency and frequency splitting between the satellites on the angle ϕ (Fig. 3) was fitted with this expression [74,75]:

$$f(\phi_i) = A_i + B_i \cos(2\phi_i) + C_i \sin(2\phi_i), \quad i = x, y, z. \quad (4)$$

The coefficients A_i , B_i , and C_i found by the fit were then used to construct the following tensor \mathbf{T} expressed in the pressure cell axis system:

$$\begin{aligned} T_{xx} &= (A_y - B_y + A_z + B_z)/2, \\ T_{yy} &= (A_z - B_z + A_x + B_x)/2, \\ T_{zz} &= (A_x - B_x + A_y + B_y)/2, \\ T_{xy} &= T_{yx} = -C_z, \\ T_{xz} &= T_{zx} = -C_y, \\ T_{yz} &= T_{zy} = -C_x. \end{aligned} \quad (5)$$

In the case of the central transition, the tensor \mathbf{T} is usually related to the isotropic NMR shift Δ_{iso} and the traceless shift anisotropy tensor Δ'_{ani} in the pressure cell frame of reference:

$$\frac{\mathbf{T}^{\text{CT}}}{\gamma_1 f_{\text{ref}}} = \Delta_{\text{iso}} + \Delta'_{\text{ani}}. \quad (6)$$

However, the impact of the field inhomogeneity in the pressure cell exceeded the expected shift anisotropy (see below) by two orders of magnitude, so the resulting tensor \mathbf{T}^{CT} was treated as

$$\frac{\mathbf{T}^{\text{CT}}}{\gamma_1 f_{\text{ref}}} = \Delta_{\text{iso}} + X_{\text{iso}} + \mathbf{X}'_{\text{ani}}, \quad (7)$$

where X_{iso} and \mathbf{X}'_{ani} describe the isotropic and anisotropic effects of the field inhomogeneity, respectively. Although the NMR shift anisotropy was neglected, this approach in

TABLE II. Spin-lattice (T_1) and spin-spin (T_2) relaxation times, decomposition of T_1 into magnetic (T_{1m}) and quadrupole (T_{1q}) parts, and check of Korringa relation fulfillment.

Pressure	Isotope	T_1 (ms)	T_2 (ms)	T_{1m} (ms)	T_{1q} (ms)	$T_{1m}K^2T/S_0$
Nearly ambient	^{69}Ga	0.696(10)	0.660(9)	0.943(14)	2.65(22)	1.24(2)
	^{71}Ga	0.538(5)	0.512(8)	0.584(9)	6.78(55)	
1.15(5) GPa	^{69}Ga	0.673(10)	0.630(28)	0.947(17)	2.32(18)	1.26(5)
	^{71}Ga	0.534(6)	0.503(16)	0.587(10)	5.94(47)	
2.15(5) GPa	^{69}Ga	0.825(30)	0.358(10)	$= T_1$		1.21(6)
	^{71}Ga	0.514(8)	0.122(3)	$= T_1$		1.22(5)

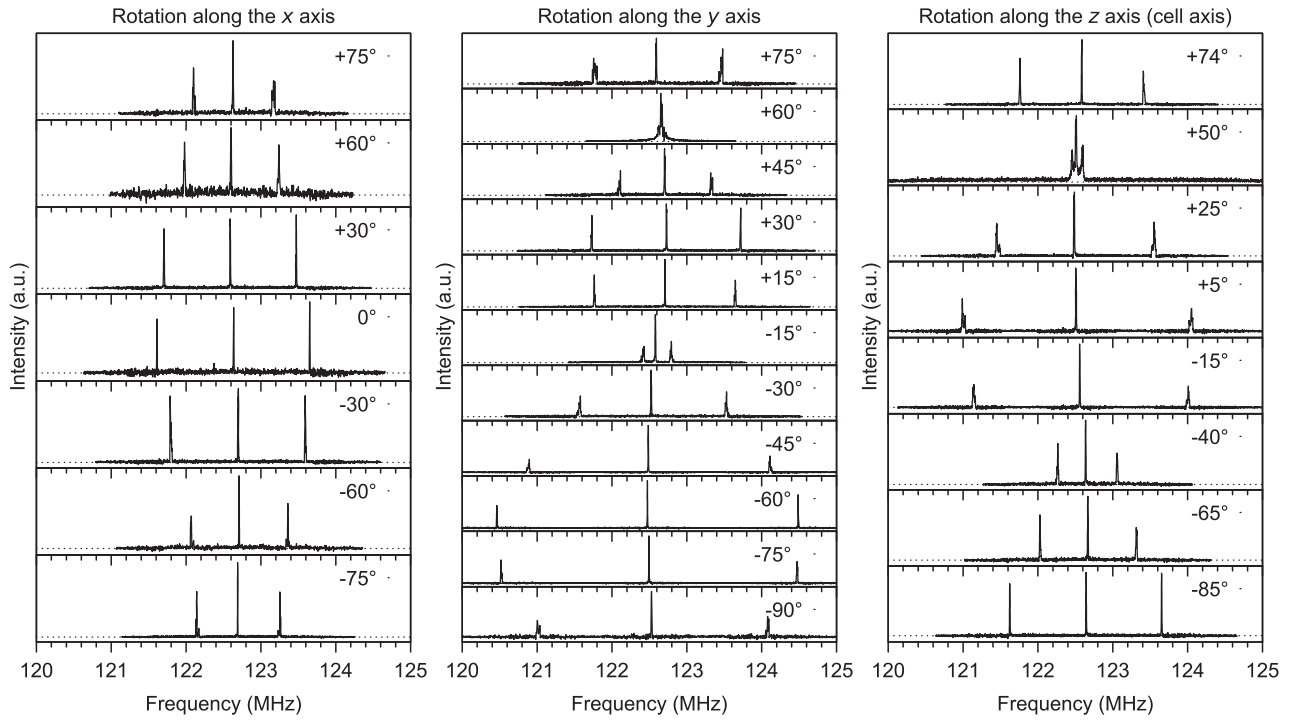


FIG. 2. The dependence of ^{71}Ga NMR spectra on the orientation of the sample with respect to the magnetic field direction measured at 2.15(5) GPa pressure. The rotation axis was perpendicular to the field direction.

combination with the validation measurements allowed for the determination of the isotropic NMR shift. The fit of the experimental data for 2.15(5) GPa yielded the tensor \mathbf{X}'_{ani} and the sum $\Delta_{\text{iso}} + X_{\text{iso}}$. Since the X_{iso} and \mathbf{X}'_{ani} parameters are the same for all the measurements in the cell (and the cell orientations \vec{u} are known), comparison of the shift $\Delta_{\text{ambient}}^{\text{cell}}(\vec{u})$ at ambient pressure in the cell (NMR shift plus the shift due to the field inhomogeneity) with the NMR shift $\Delta_{\text{ambient}}^{\text{validation}}$ observed in the validation experiment provided the value of $X_{\text{iso}} = \Delta_{\text{ambient}}^{\text{cell}}(\vec{u}) - \Delta_{\text{ambient}}^{\text{validation}} - \vec{u}^T \mathbf{X}'_{\text{ani}} \vec{u}$. Then it was straightforward to obtain the isotropic NMR shift for the 2.15(5) GPa measurement, as well as to correct the NMR shift from the measurement at 1.15(5) GPa.

For the satellite transitions, the tensor \mathbf{T} can be converted into the electric field gradient (EFG) tensor \mathbf{V}' in the pressure cell coordinates:

$$\frac{h\mathbf{T}^{\text{sat}}}{e^{71}Q} = \mathbf{V}'. \quad (8)$$

The EFG tensor \mathbf{V}' was brought to its canonical form \mathbf{V} , yielding $V_{zz} = 1.584 \times 10^{21} \text{ V m}^{-2}$ and almost negligible asymmetry parameter $\eta = 0.011$.

III. CALCULATIONS

A. Calculation method

In order to better understand the experimental data and to confirm the particular phase of the obtained solid gallium, we carried out the *ab initio* calculations of the electronic structure of the Ga-III, Ga-II, and β -Ga phases, with the aim of extracting the hyperfine parameters as well as electronic populations. Density functional theory (DFT) calculations were performed

using the full-potential augmented plane wave method as implemented in WIEN2k [76]. In all calculated structures (see Supplemental Material [67] for structural details) the radii of the gallium atomic spheres were 2.4 a.u. and the size of the basis $RK_{\text{MAX}} \sim 11$; the charge was Fourier-expanded up to $G_{\text{MAX}} = 14 \text{ Ry}^{1/2}$ and PBE-GGA [77] was used as the exchange-correlation potential. For calculation of the spin-dipolar contribution to the hyperfine field, the spin-orbit coupling was considered within the atomic spheres using a second-variational method with the scalar-relativistic orbitals.

While the electric field gradient is readily available from the charge density, the NMR shift requires additional calculations to obtain the values of the diamagnetic and, in the case of metals, also paramagnetic shielding of the studied compounds, as well as of an appropriate reference compound. The method of calculating the NMR shielding, implemented in WIEN2k [78–80], is based on linear response theory. In the case of a diamagnetic contribution due to orbital moments of electrons, eigenvectors of the original and six slightly shifted (in the $\pm x$, $\pm y$, $\pm z$ directions) k meshes are used to compute the induced current and magnetic susceptibility, and the diamagnetic shielding is then calculated by integrating the induced current. In metallic systems a very dense k -point mesh and a suitable Fermi level smearing are needed. For the presented gallium structures the diamagnetic shieldings were well converged with 2.2×10^5 k points and Fermi broadening 5 mRy. The macroscopic magnetic susceptibility was impossible to converge even with mesh of 10^6 k points; however, its contribution to the shielding is on the order of a few ppm, and was thus neglected. To obtain the paramagnetic shielding is even more intricate and requires spin-polarized calculation to allow for interaction of electronic spins with

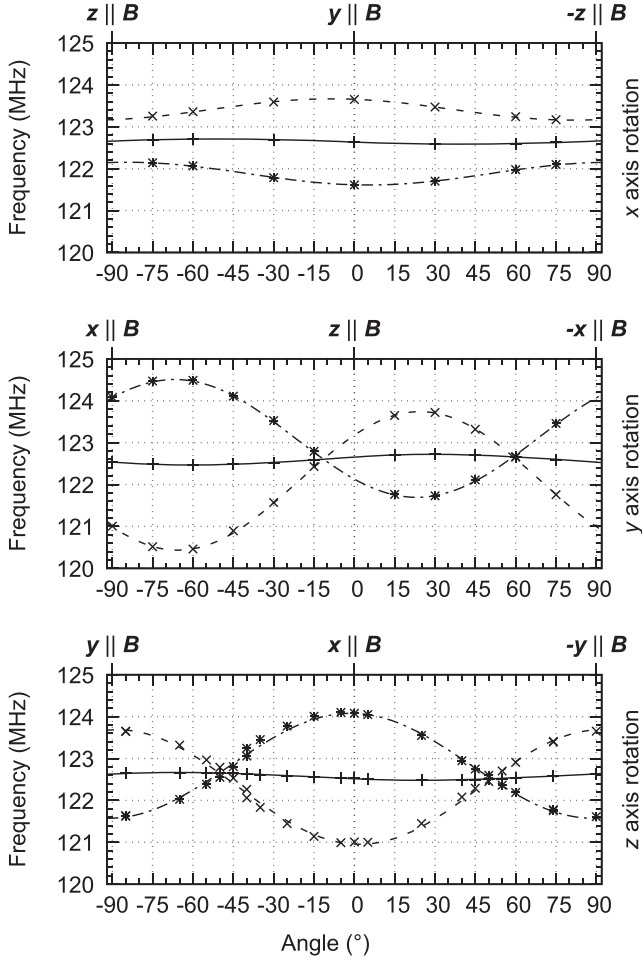


FIG. 3. The fit of the dependence of ^{71}Ga NMR resonance frequencies of the central (solid line) and satellite (dashed lines) transitions on the orientation of the sample with respect to the magnetic field direction measured at 2.15(5) GPa pressure. The rotation axes were perpendicular to the field direction \mathbf{B} .

explicitly applied magnetic field [81]. In order to estimate the contact field and spin dipolar field, we applied an interaction with external magnetic field of 100 T in the form of an appropriate energy shift $\pm\mu_B B_{\text{ext}}$ of the spin up/down exchange correlation potentials. The paramagnetic shielding was then evaluated from the contact and spin dipolar hyperfine fields as a response to the polarization by the external field. Again, the Fermi broadening of 5 mRy and very fine k -point meshes (10^6 k points) were required to provide a good convergence of the shielding in these metallic structures.

As an NMR reference, paramagnetic and diamagnetic shielding of cubic GaAs at 0 GPa was calculated analogously with the same parameters as for the metallic Ga compounds and assigned to the experimental shift 216(1) ppm [82]. Since the response to the external field was too small in the case of semiconducting GaAs, the applied field was increased to 1000 T to improve the precision.

Influence of various calculational parameters on calculated NMR shielding was tested and reasonable convergence (~ 1 ppm) was achieved: especially the number of k points and Fermi level smearing but also other parameters related

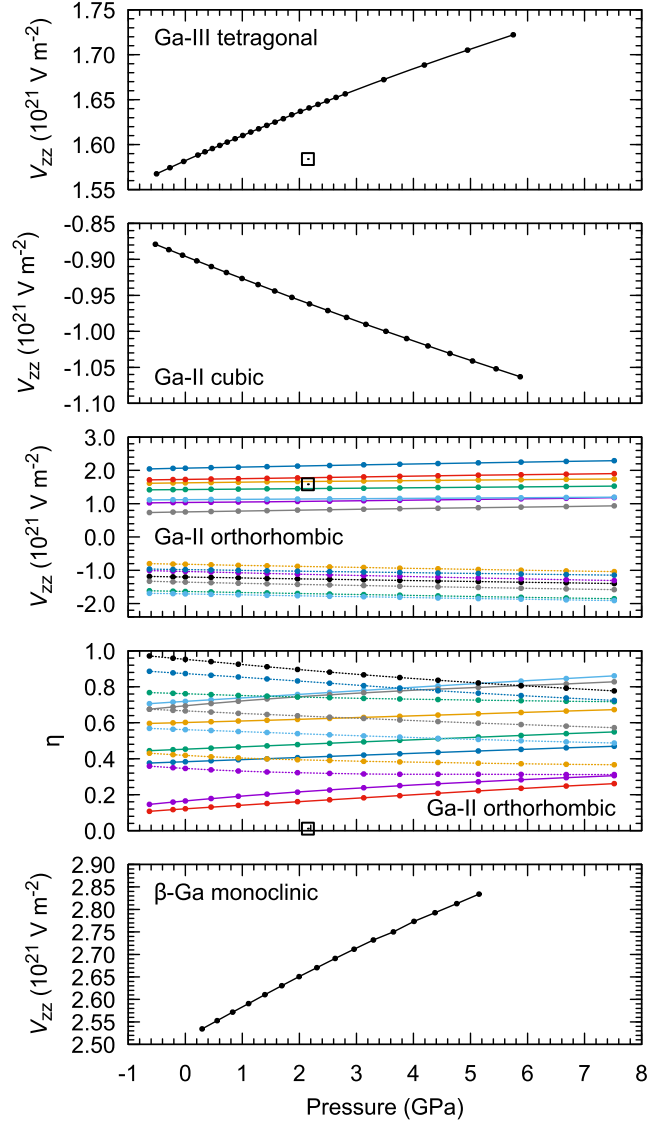


FIG. 4. Calculated pressure dependencies of EFG V_{zz} at Ga sites in the four considered Ga structures. Asymmetry parameter in the case of Ga-III and cubic Ga-II is $\eta = 0$, while it is $\eta = 0.37$ for β -Ga in the whole calculated range. For comparison, the square symbols denote the values measured on the investigated solid Ga phase. (The lines serve just as eye guides.)

to NMR calculations were checked, such as the number of additional NMR local orbitals. The linearity of the response to the external field was found to be well assured in the range of about 30–2000 T. Higher fields already perturb the electronic structure, while calculations with lower values of external field suffer from insufficient numerical precision of the hyperfine field.

As a model to our NMR experiments under pressure, volume dependencies of the total energy were calculated and transformed to pressure dependencies via fitting by the Birch-Murnaghan equation of state [83]. The DFT calculations correspond to zero temperature while the experiments were performed at room temperature; therefore, we expect all calculated pressure dependencies to display a systematic

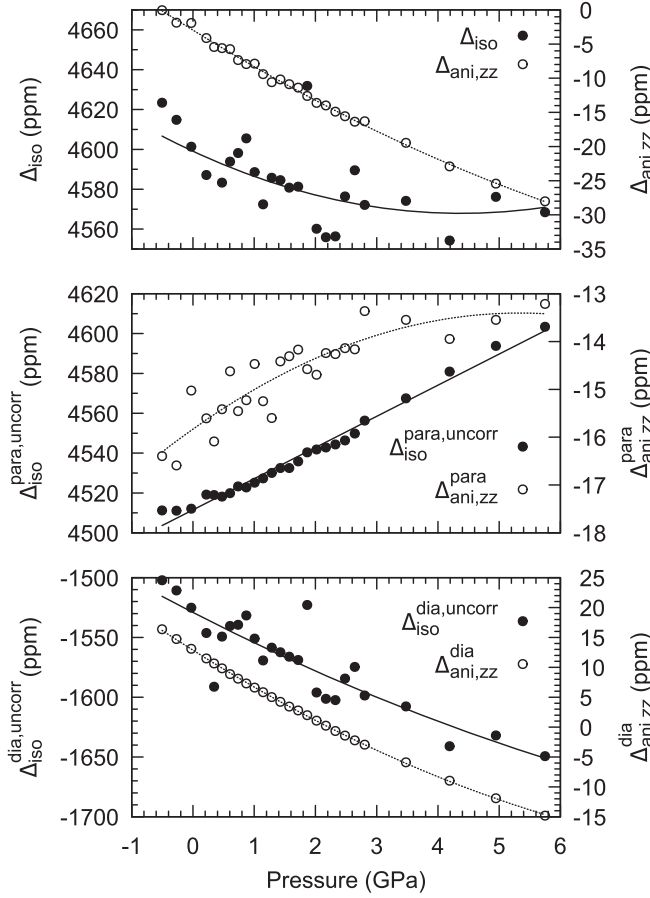


FIG. 5. Calculated pressure dependencies of isotropic and anisotropic parts of NMR shift in Ga-III structure; the total values corrected with respect to the GaAs reference, as well as uncorrected paramagnetic and diamagnetic contributions are shown. (The lines serve just as eye guides.)

shift due to thermal expansion, which roughly corresponds to negative pressure of about -0.3 GPa.

B. Calculation results

We focused mainly on the tetragonal Ga-III phase; however, the pressure dependencies of EFGs were calculated also for cubic Ga-II and monoclinic β -Ga; orthorhombic Ga-II was calculated with reduced size of the basis set and number of k points; see Fig. 4. In the case of cubic Ga-II and monoclinic β -Ga, the demanding calculations of NMR shieldings were performed for only one value of pressure (2.2 GPa; lower part

TABLE III. Calculated isotropic Δ_{iso} and anisotropic $\Delta_{\text{ani,zz}}$ parts of NMR shift of Ga-III phase at several pressures and their decomposition into diamagnetic (index $^{\text{dia}}$) and paramagnetic (index $^{\text{para}}$) contributions. The index $^{\text{uncorr}}$ denotes values not corrected with respect to the GaAs reference. The experimental value in the last row is provided for comparison.

Pressure	$\Delta_{\text{iso}}^{\text{dia,uncorr}}$ (ppm)	$\Delta_{\text{iso}}^{\text{para,uncorr}}$ (ppm)	$\Delta_{\text{iso}}^{\text{uncorr}}$ (ppm)	Δ_{iso} (ppm)	$\Delta_{\text{ani,zz}}^{\text{dia}}$ (ppm)	$\Delta_{\text{ani,zz}}^{\text{para}}$ (ppm)	$\Delta_{\text{ani,zz}}$ (ppm)
0 GPa	-1525	4512	2987	4601	13	-15	-2
2.2 GPa	-1601	4543	2942	4556	0	-14	-14
4.2 GPa	-1641	4581	2940	4554	-9	-14	-23
2.15(5) GPa experiment				4746(80)			

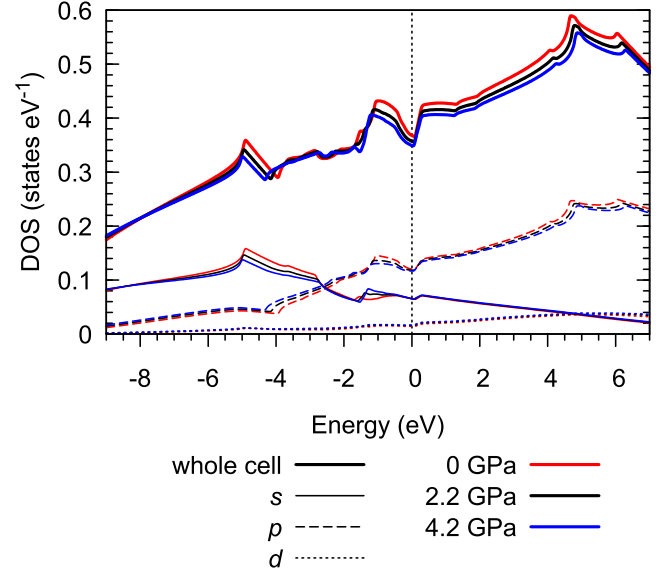


FIG. 6. Calculated total and partial densities of states in Ga-III structure at several pressures.

of Table VI). For each particular pressure, the atomic positions and remaining degrees of freedom in lattice parameters were optimized, with the exceptions of complex orthorhombic Ga-II structure and of monoclinic angle in β -Ga. In tetragonal Ga-III, special attention was paid to careful optimization of the c/a ratio, to which the values of EFG were sensitive. Detailed information about the calculated structures and changes during their optimization is provided in the Supplemental Material [67].

In all studied Ga structures, the dominant source of the EFG tensor originates from the pp contribution, which is slightly reduced by the dd contribution. As expected, with increasing pressure the interatomic distances shrink proportionally. The Ga $4p$ states thus become more populated and the corresponding elements of EFG increase in absolute value. The pressure dependence of the NMR shift in the Ga-III structure can be found in Fig. 5 and Table III. The anisotropy of the NMR shift was estimated by applying the interaction with external magnetic field in various crystallographic directions. Concerning the pressure variation of general electronic properties of the Ga-III phase, the plots of the density of states for several pressures can be found in Fig. 6, while the relation between electronic populations (Table IV) and hyperfine parameters can be assessed from Tables V and VI.

TABLE IV. Calculated electronic populations of Ga-III phase at several pressures (corrected for pressure-induced changes of interstitial volume).

Pressure	<i>s</i>	<i>p</i>	<i>d</i>	<i>f</i>	<i>p_z</i>	<i>p_x + p_y</i>	<i>d_{z²}</i>	<i>d_{xy}</i>	<i>d_{x²-y²}</i>	<i>d_{xz} + d_{yz}</i>
0 GPa	1.030	0.566	9.954	0.007	0.177	0.389	1.989	1.987	1.994	3.984
2.2 GPa	1.024	0.593	9.949	0.008	0.186	0.408	1.988	1.986	1.993	3.982
4.2 GPa	1.019	0.616	9.946	0.009	0.193	0.423	1.987	1.984	1.993	3.981

IV. DISCUSSION

The experimental NMR shifts of liquid gallium at ambient conditions reported in this work are comparable to the shifts published in older works: 4528 ppm [48] and 4490 ppm [41]. The relaxation times under the same conditions match very well the spin-lattice relaxation data in Ref. [48] and they are also comparable to the spin-lattice and spin-spin relaxation times of the sample with the longest relaxations in Ref. [41], while they are about 5% shorter compared with the spin-lattice relaxations reported in Ref. [44]. The spin-lattice relaxation times in the liquid and solid phases exceed the expectations based on the Korringa relation by 21% to 26%, indicating the presence of electronic correlations.

The verification of the gallium solid phase obtained in the experiment takes advantage of the quadrupole splitting. The calculated EFG parameters of the metastable monoclinic β -Ga phase are in reasonable agreement with published experimental data [$V_{zz} = 2.400(2) \times 10^{21} \text{ V m}^{-2}$, $\eta = 0.312(5)$ at 242 K] [60] and they clearly differ from the values measured in this work. Calculations of the cubic Ga-II structure also yielded V_{zz} noticeably different from our measurement, whereas the complex orthorhombic Ga-II phase with 14 independent crystal sites of Ga ions would apparently give rise to a complicated structure of spectra which is not the case ¹. On the other hand, the axially symmetric EFG tensor found in our experiment corresponds well to a symmetry of the tetragonal Ga-III phase and comparison of the measured value of $V_{zz} = 1.584 \times 10^{21} \text{ V m}^{-2}$ at 2.15(5) GPa with the EFG calculated for this structure ($V_{zz} = 1.641 \times 10^{21} \text{ V m}^{-2}$ at 2.2 GPa) clearly yields Ga-III as the best match.

The experimentally observed isotropic part of the NMR shift in the solid phase $\Delta_{\text{iso}}^{\text{exp}} = 4746(80) \text{ ppm}$ at 2.15(5) GPa

reasonably matches the value calculated for the Ga-III structure ($\Delta_{\text{iso}} = 4556 \text{ ppm}$ at 2.2 GPa). The local perturbation of field homogeneity in the pressure cell, which led to the line splitting, reduced the precision ² of the measured isotropic NMR shifts and completely hindered the determination of the NMR shift anisotropy. It was caused probably by the presence of some tiny magnetic impurity introduced perhaps in the cell chassis during machining or in the gasket when carving the channels for the RF coil leads; alternatively, a small content of magnetic impurities in the three set screws for fine alignment of the anvils could be also a possible explanation. We should also note that due to the field inhomogeneity, closer examination of satellite signals of the solid phase revealed in some orientations rather complex line patterns.

The DFT calculations identified the *p* electrons as the primary source of the EFG in all calculated gallium metal phases. The differences in calculated EFGs between the Ga structures correspond to a character of the local structure. The gallium site with the highest local symmetry (-4) is in the cubic Ga-II structure and possesses the lowest value of EFG. Similarly, in the Ga-III structure, which also lacks any free internal structural parameters, the EFG appears due to tetragonal deformation that makes the local symmetry $4/mmm$; otherwise, for $c/a = \sqrt{2}$, the structure would be cubic $Fm\bar{3}m$ with local symmetry of Ga site $m\bar{3}m$ and zero EFG. Gallium in β -Ga has the highest EFG values among the studied compounds, which corresponds to low local symmetry (point group 2).

Concerning the origin of the NMR shift in Ga-III, as well as in cubic Ga-II and β -Ga, Table VI reveals that the Fermi contact contribution presents a dominant part of the shift, while the dipolar contributions of the *p* shell are much smaller and those of the *d* shell are even weaker. The diamagnetic shift

¹Unfortunately, comparison with the NMR experiments on the Ga-II phase in Ref. [62] is not possible since only central line data are reported therein.

²Since the pressure cell had to be removed from the holder for every pressure increase, the orientation uncertainty of $\pm 3^\circ$ had to be taken into account in the compensation for the field inhomogeneity impact on the resulting NMR shifts.

TABLE V. The decomposition of calculated EFG of Ga-III phase at several pressures. The experimental value in the last row is provided for comparison.

Pressure	<i>pp</i> (10^{21} V m^{-2})	<i>sd</i> (10^{21} V m^{-2})	<i>dd</i> (10^{21} V m^{-2})	<i>pf</i> (10^{21} V m^{-2})	<i>ff</i> (10^{21} V m^{-2})	total (10^{21} V m^{-2})	V_{zz} (including interstitial) (10^{21} V m^{-2})
0 GPa	1.673	0.005	-0.087	0.005	0.000	1.596	1.581
2.2 GPa	1.746	0.007	-0.099	0.005	0.000	1.658	1.641
4.2 GPa	1.806	0.007	-0.107	0.005	0.000	1.710	1.689
2.15(5) GPa experiment							1.584

TABLE VI. The decomposition of calculated NMR shifts Δ of Ga-III phase for magnetic field along the c and a axes at several pressures and of GaAs used as a reference compound. The calculated data for cubic Ga-II and β -Ga phases for magnetic field along the c axis are provided for comparison. ($\Delta^{\text{dia,uncorr}}$ corresponds to diamagnetic part obtained as chemical shielding and the other columns form together paramagnetic part $\Delta^{\text{para,uncorr}}$: contact stands for Fermi contact contribution, while dip denotes spin-dipolar contribution of particular shell.) (The index uncorr denotes values not corrected with respect to the GaAs reference.)

Structure	Pressure	$\Delta^{\text{dia,uncorr}}$ (ppm)	$\Delta^{\text{para,uncorr}}$				Total shift		Field direction
			contact (ppm)	dip s (ppm)	dip p (ppm)	dip d (ppm)	Δ^{uncorr} (ppm)	Δ (ppm)	
Ga-III	0 GPa	−1512	4517	0	−20	1	2987	4601	c axis
	2.2 GPa	−1601	4547	0	−18	1	2929	4543	c axis
	4.2 GPa	−1650	4584	0	−18	1	2917	4532	c axis
Ga-III	0 GPa	−1532	4511	0	8	−1	2987	4602	a axis
	2.2 GPa	−1601	4543	0	8	−1	2949	4563	a axis
	4.2 GPa	−1637	4580	0	8	−1	2950	4565	a axis
GaAs	0 GPa	−1344	−55	0	0	0	−1398	216	
Ga-II cubic	2.2 GPa	−1537	4135	0	5	0	2603	4217	c axis
β -Ga	2.2 GPa	−1367	3748	0	33	−3	2412	4026	c axis

contribution is to a large extent canceled by the correction using the GaAs reference. The dipolar moments of p electrons are a major source of the paramagnetic shift anisotropy.

Calculated total and partial densities of states in the Ga-III structure (Fig. 6) correspond to the metallic, free-electron character of the Ga-III electronic structure. The shape of the displayed DOS does not change much within the considered pressure range and is in good agreement with calculated data published in Ref. [26].

V. CONCLUSION

We carried out ^{69}Ga and ^{71}Ga NMR measurements on liquid and solid gallium metal under pressure. The *ab initio* calculations were employed as a complement of the measurements, allowing for verification of the particular phase of solid gallium obtained in the experiment and for deeper insight into the hyperfine and electronic properties. While our experimental data (NMR shift and relaxation times) on the liquid phase fit the current picture of this metal, the investigation of the solid phase presents an experimental and theoretical study of the hyperfine parameters of the Ga-III phase. The EFG and NMR shift of Ga-III were both measured and calculated,

yielding reasonable agreement of the EFG parameters and of the isotropic components of the NMR shifts. The experimentally observed line splitting was ascribed to magnetic field inhomogeneities in the pressure cell, while the additional shift caused by these inhomogeneities was subtracted from the resulting NMR shift parameters. The hyperfine parameters were interpreted in terms of electronic structure, revealing the dominant contribution of Fermi contact interaction to the NMR shift and the significant role of p electrons in the shift anisotropy and EFG. Further, the calculations of the pressure dependence of the EFG parameters of complex orthorhombic Ga-II structure prepare the ground for prospective experimental study.

ACKNOWLEDGMENTS

The experimental part of this work was supported by Deutsche Forschungsgemeinschaft within Project No. 252360796 (HA 1893/12-1), “Metals under extreme conditions.” Computational resources were provided by CESNET LM2015042 and CERIT Scientific Cloud LM2015085, provided under the program “Projects of Large Research, Development, and Innovations Infrastructures.”

- [1] L. Bosio, *J. Chem. Phys.* **68**, 1221 (1978).
- [2] L. Comez, A. Di Cicco, J. P. Itié, and A. Polian, *Phys. Rev. B* **65**, 014114 (2001).
- [3] P. W. Bridgman, *Phys. Rev.* **48**, 893 (1935).
- [4] C. E. Weir, G. J. Piermarini, and S. Block, *J. Chem. Phys.* **54**, 2768 (1971).
- [5] L. Bosio, A. Defrain, H. Curien, and A. Rimsky, *Acta Crystallogr. B* **25**, 995 (1969).
- [6] A. Jayaraman, W. Klement, Jr., R. C. Newton, and G. C. Kennedy, *J. Phys. Chem. Solids* **24**, 7 (1963).
- [7] O. Schulte and W. B. Holzapfel, *Phys. Rev. B* **55**, 8122 (1997).
- [8] O. Degtyareva, M. I. McMahon, D. R. Allan, and R. J. Nelmes, *Phys. Rev. Lett.* **93**, 205502 (2004).
- [9] K. Takemura, K. Kobayashi, and M. Arai, *Phys. Rev. B* **58**, 2482 (1998).
- [10] O. Schulte, A. Nikolaenko, and W. B. Holzapfel, *High Pressure Res.* **6**, 169 (1991).
- [11] A. G. Lyapin, E. L. Gromnitskaya, O. F. Yagafarov, O. V. Stal’gorova, and V. V. Brazhkin, *J. Exp. Theor. Phys.* **107**, 818 (2008).
- [12] E. L. Gromnitskaya, O. F. Yagafarov, O. V. Stalgorova, V. V. Brazhkin, and A. G. Lyapin, *Phys. Rev. Lett.* **98**, 165503 (2007).
- [13] L. Bosio, R. Cortes, J. R. D. Copley, W. D. Teuchert, and J. Lefebvre, *J. Phys. F: Metal Phys.* **11**, 2261 (1981).
- [14] V. M. Nield, R. L. McGreevy, and M. G. Tucker, *J. Phys.: Condens. Matter* **10**, 3293 (1998).

- [15] D. A. Jackson, *Phys. Rev.* **103**, 1738 (1956).
- [16] R. H. Hammond and W. D. Knight, *Phys. Rev.* **120**, 762 (1960).
- [17] E. J. Unterhorst, V. Müller, and G. Schanz, *Phys. Status Solidi B* **84**, K53 (1977).
- [18] B. P. Panda and N. C. Mohapatra, *Pramana J. Phys.* **61**, 1151 (2003).
- [19] O. N. Bakharev, D. Bono, H. B. Brom, A. Schnepf, H. Schnöckel, and L. J. de Jongh, *Phys. Rev. Lett.* **96**, 117002 (2006).
- [20] F. Greuter and P. Oelhafen, *Z. Phys. B* **34**, 123 (1979).
- [21] Ch. Splx-sol-plxondergaard, Ch. Schultz, S. Agergaard, H. Li, Z. Li, S. V. Hoffmann, Ch. Grütter, J. H. Bilgram, and Ph. Hofmann, *Phys. Rev. B* **67**, 205105 (2003).
- [22] H. Schnöckel, *Chem. Rev.* **110**, 4125 (2010).
- [23] J. E. Inglesfield, *J. Phys. C (Proc. Phys. Soc.)* **1**, 1337 (1968).
- [24] M. Bernasconi, G. L. Chiarotti, and E. Tosatti, *Phys. Rev. B* **52**, 9988 (1995).
- [25] M. I. Baskes, S. P. Chen, and F. J. Cherne, *Phys. Rev. B* **66**, 104107 (2002).
- [26] E. Voloshina, K. Rosciszewski, and B. Paulus, *Phys. Rev. B* **79**, 045113 (2009).
- [27] Z. Li and J. S. Tse, *Phys. Rev. B* **62**, 9900 (2000).
- [28] M. de Koning, A. Antonelli, and D. A. C. Jara, *Phys. Rev. B* **80**, 045209 (2009).
- [29] M. Bernasconi, G. L. Chiarotti, and E. Tosatti, *Phys. Rev. Lett.* **70**, 3295 (1993).
- [30] B. K. Acharya and N. C. Mohapatra, *Hyperfine Interact.* **116**, 179 (1998).
- [31] B. P. Panda and N. C. Mohapatra, *Physica B* **344**, 108 (2004).
- [32] B. K. Acharya and N. C. Mohapatra, *Pramana J. Phys.* **43**, 391 (1994).
- [33] K. W. Lodge, *J. Phys. F* **8**, 447 (1978).
- [34] J. D. Stroudt and M. J. Stott, *J. Phys. F* **5**, 1667 (1975).
- [35] S. Chacko, K. Joshi, D. G. Kanhere, and S. A. Blundell, *Phys. Rev. Lett.* **92**, 135506 (2004).
- [36] X. G. Gong, G. L. Chiarotti, M. Parrinello, and E. Tosatti, *Phys. Rev. B* **43**, 14277 (1991).
- [37] Z. Y. Zhu, Y. C. Cheng, and U. Schwingenschlögl, *J. Phys.: Condens. Matter* **23**, 475502 (2011).
- [38] Z. Zhu, X. Wang, and U. Schwingenschlögl, *Appl. Phys. Lett.* **98**, 241902 (2011).
- [39] A. S. Mikhaylushkin, S. I. Simak, B. Johansson, and U. Häussermann, *J. Phys. Chem. Solids* **67**, 2132 (2006).
- [40] I. Spagnolatti and M. Bernasconi, *Eur. Phys. J. B* **36**, 87 (2003).
- [41] D. A. Cornell, *Phys. Rev.* **153**, 208 (1967).
- [42] K. Suzuki and O. Uemura, *J. Phys. Chem. Solids* **32**, 1801 (1971).
- [43] D. Hechtfisher, R. Karcher, and K. Lüders, *J. Phys. F* **3**, 2021 (1973).
- [44] G. Cartledge, R. L. Havill, and J. M. Titman, *J. Phys. F* **3**, 213 (1973).
- [45] W. W. Warren, Jr., *Phys. Rev. A* **10**, 657 (1974).
- [46] N. C. Halder, *J. Magn. Reson.* **15**, 339 (1974).
- [47] N. C. Halder, *Phys. Rev. B* **10**, 2333 (1974).
- [48] A. L. Kerlin and W. G. Clark, *Phys. Rev. B* **12**, 3533 (1975).
- [49] N. C. Halder, *J. Magn. Reson.* **22**, 33 (1976).
- [50] R. H. Hammond, E. G. Wiener, and G. M. Kelly, *Phys. Rev.* **143**, 275 (1966).
- [51] J. Y. Hwang, P. C. Canepa, and T. A. Scott, *J. Phys. Chem. Solids* **38**, 1403 (1977).
- [52] M. I. Valič and D. Llewelyn Williams, *J. Phys. Chem. Solids* **30**, 2337 (1969).
- [53] M. I. Valič and D. Llewelyn Williams, *J. Phys. Chem. Solids* **33**, 1583 (1972).
- [54] M. I. Valič, S. N. Sharma, and D. Llewelyn Williams, *Phys. Lett. A* **26**, 528 (1968).
- [55] M. I. Valič and D. Llewelyn Williams, *Solid State Commun.* **8**, 1455 (1970).
- [56] M. I. Valič, Ph.D. thesis, University of British Columbia, 1970.
- [57] M. Huebner, Th. Wagner, S. Götz, and G. Eska, *Physica B* **210**, 484 (1995).
- [58] S. L. Segel and J. D. Stroud, *J. Phys. F* **5**, 1986 (1975).
- [59] R. J. C. Brown and S. Segel, *J. Phys. F* **5**, 1073 (1975).
- [60] J. D. Stroud and S. L. Segel, *J. Phys. F* **5**, 1981 (1975).
- [61] S. L. Segel, R. D. Heyding, and E. F. W. Seymour, *Phys. Rev. Lett.* **28**, 970 (1972).
- [62] T. Meier, *Annu. Rep. NMR Spectrosc.* **93**, 1 (2018); Ph.D. thesis, University of Leipzig, 2016.
- [63] T. Meier, T. Herzig, and J. Haase, *Rev. Sci. Instrum.* **85**, 043903 (2014).
- [64] H. K. Mao, P. M. Bell, J. W. Shaner, and D. J. Steinberg, *J. Appl. Phys.* **49**, 3276 (1978).
- [65] P. M. Bell, J. A. Xu, and H. K. Mao, in *Shock Waves in Condensed Matter* (Springer US, Boston, MA, 1986), pp. 125–130.
- [66] R. J. Hemley, C. S. Zha, A. P. Jephcoat, H. K. Mao, L. W. Finger, and D. E. Cox, *Phys. Rev. B* **39**, 11820 (1989).
- [67] See Supplemental Material at <http://link.aps.org/supplemental/10.1103/PhysRevB.99.125121> for additional notes, table, figures, and files.
- [68] P. Pykkö, *Mol. Phys.* **99**, 1617 (2001).
- [69] J. Haase, N. J. Curro, R. Stern, and C. P. Slichter, *Phys. Rev. Lett.* **81**, 1489 (1998).
- [70] E. Shabanova, E. V. Charnaya, K. Schaumburg, and Yu. A. Kumzerov, *Physica B* **229**, 268 (1997).
- [71] E. V. Charnaya, T. Loeser, D. Michel, C. Tien, D. Yaskov, and Yu. A. Kumzerov, *Phys. Rev. Lett.* **88**, 097602 (2002).
- [72] E. V. Charnaya, D. Michel, C. Tien, Yu. A. Kumzerov, and D. Yaskov, *J. Phys.: Condens. Matter* **15**, 5469 (2003).
- [73] J. Korringa, *Physica* **16**, 601 (1950).
- [74] M. A. Kennedy and P. D. Ellis, *Concept. Magnetic Res.* **1**, 109 (1989).
- [75] A. J. Woo, *Bull. Korean Chem. Soc.* **20**, 1205 (1999).
- [76] P. Blaha, K. Schwarz, G. K. H. Madsen, D. Kvasnicka, and J. Luitz, *WIEN2k, An Augmented Plane Wave + Local Orbitals Program for Calculating Crystal Properties* (Karlheinz Schwarz, Techn. Universität Wien, Austria, 2001).
- [77] J. P. Perdew, K. Burke, and M. Ernzerhof, *Phys. Rev. Lett.* **77**, 3865 (1996).
- [78] R. Laskowski and P. Blaha, *Phys. Rev. B* **85**, 035132 (2012).
- [79] R. Laskowski and P. Blaha, *Phys. Rev. B* **85**, 245117 (2012).
- [80] R. Laskowski and P. Blaha, *Phys. Rev. B* **89**, 014402 (2014).
- [81] R. Laskowski, K. Khoo, F. Haarmann, and P. Blaha, *J. Phys. Chem. C* **121**, 753 (2017).
- [82] O. H. Han, H. K. C. Timken, and E. Oldfield, *J. Chem. Phys.* **89**, 6046 (1988).
- [83] F. Birch, *Phys. Rev.* **71**, 809 (1947).

NMR and ab initio study of gallium metal under pressure

Supplemental Material

R. Řezníček,^{1,*} V. Chlan,² and J. Haase¹

¹*Faculty of Physics and Earth Sciences, University of Leipzig, Linnéstrasse 5, D-04103 Leipzig, Germany*

²*Faculty of Mathematics and Physics, Charles University,
V Holešovičkách 2, 180 00 Prague 8, Czech Republic*

Investigated points in phase diagram

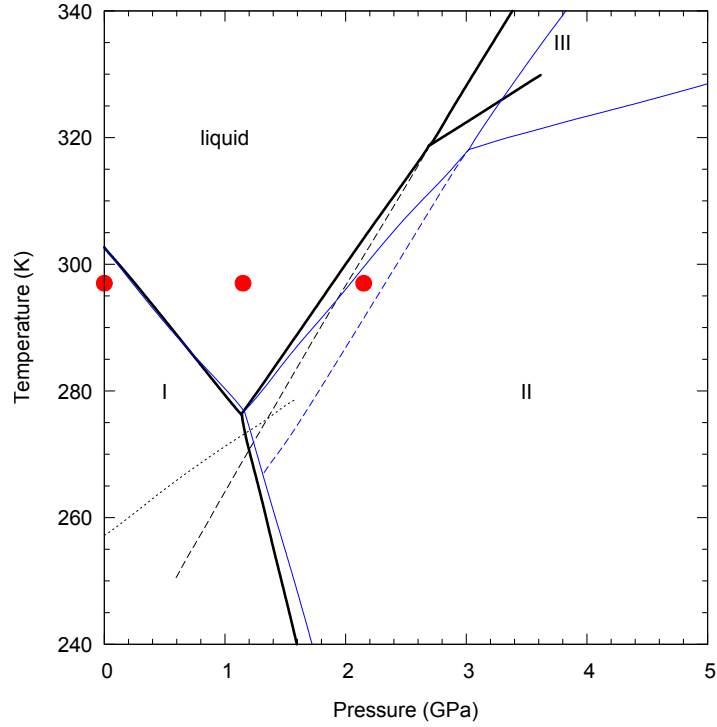


FIG. S1: Investigated pressure-temperature points (red symbols) marked in the phase diagram of gallium (replotted after Ref. [1] (black lines) and Ref. [2] (blue lines)). The dashed and dotted lines represent the metastable liquid-Ga-III and liquid- β -Ga phase boundaries, respectively. The measured sample was undercooled liquid under ambient conditions.

*Electronic address: Richard.Reznicek@physik.uni-leipzig.de

Note on line splitting

The line splitting observed in our experiments is explained in the main paper by a local perturbation of field homogeneity in the pressure cell. We are aware that such explanation can be perceived as counterintuitive by the reader: taking into account the spherical shape of the sample, simple linear or quadratic gradients do not result in line splitting, even if skin effect is considered – see Fig. S2a-d. However, the most likely scenario of a presence of tiny magnetic impurities relatively close to the sample should be understood in terms of dipole moments. The field of these dipole moments cannot be easily approximated by few simple low-order gradients due to their proximity to the sample. Since any attempt to determine the actual spatial distribution of magnetic field in the cell corresponding to the observed lineshape would be far beyond the scope of the this work, we limit this note to a demonstration that even just slightly more complicated situations can yield line splitting. Therefore, we analyzed a combination of z and $x^2 - y^2$ gradients (Fig. S2e), as well as a simple configuration of two dipole moments (see Fig. S2f). The dipole configuration in Fig. S2f corresponds to one of the simplest realistic scenarios: magnetic impurities present at the inner ends of the channels (for NMR coil leads) curved in the gasket. Monte Carlo simulations were performed for all the investigated cases. In addition to the simulations taking into account the whole volume of the sample, simulations considering only a $25\ \mu\text{m}$ shell of the spherical sample were carried out to mimic the skin effect [13]. The shift of the field at particular point of the sample was evaluated as a projection of the sum of the gradients or dipolar fields onto the direction of the external static magnetic field \mathbf{B} .

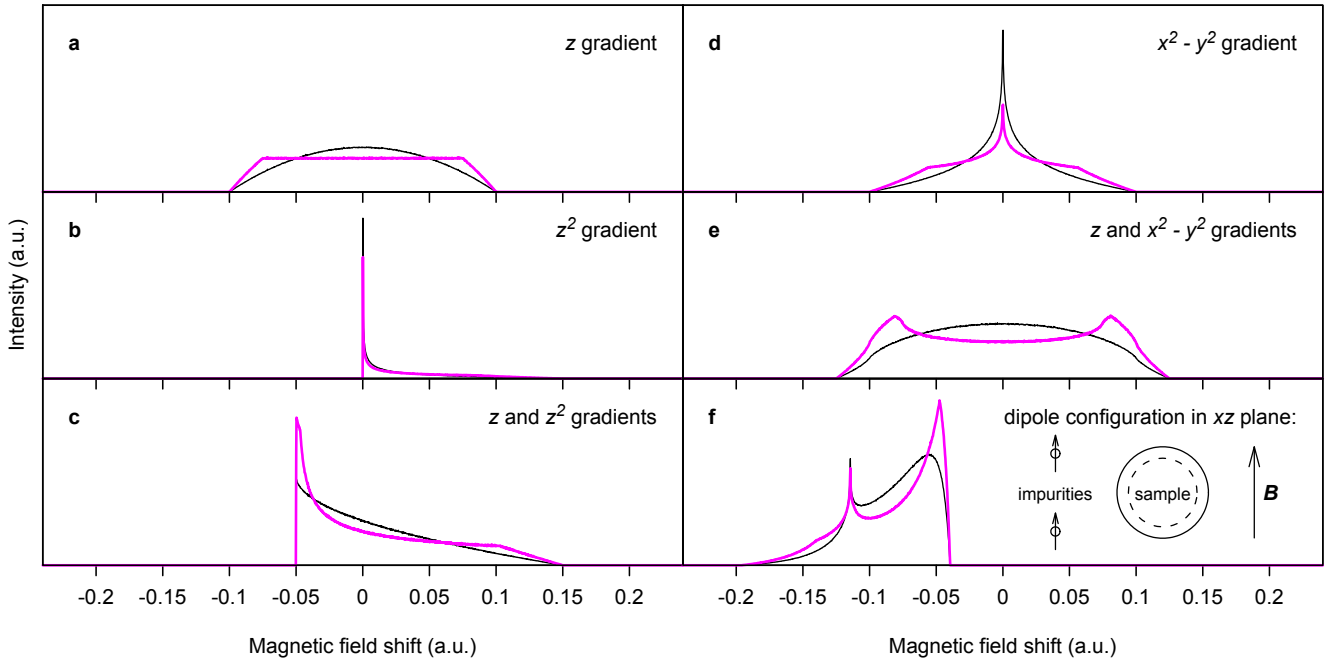


FIG. S2: Monte Carlo simulations of lineshape for several spatial distributions of magnetic field. The results of simulations taking into account the whole volume of the sample are in black, while those of simulations considering only a $25\ \mu\text{m}$ shell (denoted by dashed line in the drawing in panel f) of the spherical sample are in magenta.

Calculated structures

An overview of selected structures used for the DFT calculations is provided in Tab. S1. The monoclinic angle of β -Ga was not optimized since the value of V_{zz} depends on the angle only slightly (see Fig. S3) – it does not approach the value observed in our experiment, so it would not influence our interpretation. Due to that, and also because 4-dimensional lattice optimization would be quite demanding, we chose not to vary the value of the angle at all.

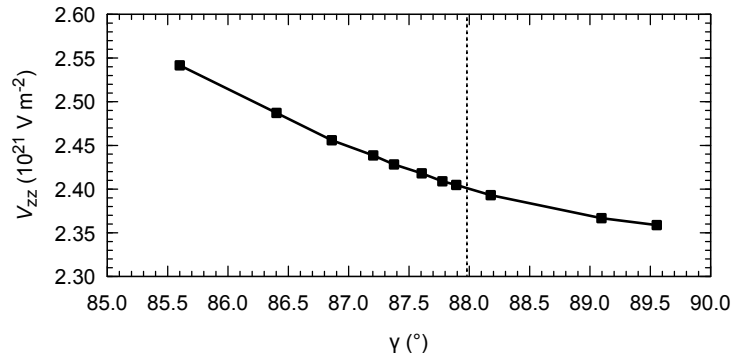


FIG. S3: The dependence of EFG V_{zz} on the monoclinic angle γ of the β -Ga structure at 0 GPa.

We note also two technical points: First, the y and z axes were swapped for the β -Ga structure – this is for technical (or rather historical) reasons: the WIEN2k [3] supports only the CXZ setting for centered monoclinic lattices (and the monoclinic angle must be γ). Second, the equilibrium volumes (0 GPa) obtained from calculations are higher than the experimental ones because the used exchange correlation potential (GGA-PBE [4]) is known to overestimate the volume by a few % (compared to experiments).

-
- [1] L. Bosio, J. Chem. Phys. **68**, 1221 (1978).
 - [2] A. Jayaraman, W. Klement JR., R. C. Newton, and G. C. Kennedy, J. Phys. Chem. Solids **24**, 7 (1963).
 - [3] P. Blaha, K. Schwarz, G. K. H. Madsen, D. Kvasnicka, and J. Luitz, WIEN2k, *An Augmented Plane Wave + Local Orbitals Program for Calculating Crystal Properties* (Karlheinz Schwarz, Techn. Universität Wien, Austria, 2001).
 - [4] J. P. Perdew, K. Burke, and M. Ernzerhof, Phys. Rev. Lett. **77**, 3865 (1996).
 - [5] Crystallography Open Database (COD), <http://www.crystallography.net/> [Online]. 2014.
svn://www.crystallography.net/cod/cif/9/01/24/9012483.cif [16 Apr. 2017]
 - [6] Crystallography Open Database (COD), <http://www.crystallography.net/> [Online]. 2014.
svn://www.crystallography.net/cod/cif/9/01/24/9012484.cif [15 Apr. 2017]
 - [7] Crystallography Open Database (COD), <http://www.crystallography.net/> [Online]. 2014.
svn://www.crystallography.net/cod/cif/9/01/10/9011089.cif [15 Apr. 2017]
 - [8] L. Bosio, A. Defrain, H. Curien, and A. Rimsky, Acta Cryst. **B25**, 995 (1969).
 - [9] O. Degtyareva, M. I. McMahon, D. R. Allan, and R. J. Nelmes, Phys. Rev. Lett. **93**, 205502 (2004).
 - [10] J. W. Carlson, J. Magn. Reson. **78**, 563 (1988).
 - [11] A. J. Illott, S. Chandrashekar, A. Klckner, H. Jung Chang, N. M. Trease, C. P. Grey, L. Greengard, A. Jerschow, J. Magn. Reson. **245**, 143 (2014).
 - [12] A. J. Illott, A. Jerschow, arXiv:1806.01390v2 (2018).
 - [13] Taking into account the demonstration purpose of the simulations, this simple approach was chosen instead of more complicated precise treatment of the skin effect [10–12].

TABLE S1: The overview of selected structures used for the DFT calculations

phase	structure	CIF file	space group	lattice parameters (Å, °)	atomic parameters	source
Ga-III tetra- gonal	original (experimental)	Ref. [5]	I4/mmm (139)	$a = 2.813$, $c = 4.452$	Ga(2a): (0, 0, 0)	[1]
	optimized (0 GPa)	Ga_III.0GPa.cif	I4/mmm (139)	$a = 2.89798$, $c = 4.51787$	Ga(2a): (0, 0, 0)	
	optimized (2.2 GPa)	Ga_III.2.2GPa.cif	I4/mmm (139)	$a = 2.85993$, $c = 4.45334$	Ga(2a): (0, 0, 0)	
Ga-II cubic	original (experimental)	Ref. [6]	I-43d (220)	$a = 5.951$	Ga(12a): (3/8, 0, 1/4)	[1]
	optimized (0 GPa)	Ga_IIcubic.0GPa.cif	I-43d (220)	$a = 6.10671$	Ga(12a): (3/8, 0, 1/4)	
	optimized (2.2 GPa)	Ga_IIcubic.2.2GPa.cif	I-43d (220)	$a = 6.02333$	Ga(12a): (3/8, 0, 1/4)	
β -Ga mono- clinic	original (experimental)	Ref. [7]	I-43d (220)	$a = 2.766$, $b = 3.332$, $c = 8.053$, $\gamma = 87.98$	Ga(4e): (0, 3/4, 0.131)	[8]
	optimized (0 GPa)	Ga_beta.0GPa.cif	I-43d (220)	$a = 2.80364$, $b = 3.36046$, $c = 8.16240$, $\gamma = 87.98^*$	Ga(4e): (0, 3/4, 0.13399)	
	optimized (2.2 GPa)	Ga_beta.2.2GPa.cif	I-43d (220)	$a = 2.76729$, $b = 3.31688$, $c = 8.05655$, $\gamma = 87.98^*$	Ga(4e): (0, 3/4, 0.13399)	
				*) monoclinic angle γ not optimized		
Ga-II ortho- rhom- bic	original (experimental) (structure not optimized)	Ga_IIortho.orig.cif	C222 ₁ (20)	$a = 5.976$, $b = 8.576$, $c = 35.000$	Ga(4b): (1/2, 0.1802, 1/4)	[9]
					Ga(8c): (0.6965, 0.4684, 0.2716)	
					Ga(8c): (0.5804, 0.7858, 0.2861)	
					Ga(8c): (0.2772, 0.5622, 0.3081)	
					Ga(8c): (0.9659, 0.7809, 0.3292)	
					Ga(8c): (0.8482, 0.4567, 0.3430)	
					Ga(8c): (0.5632, 0.6919, 0.3666)	
					Ga(8c): (0.2324, 0.4838, 0.3851)	
					Ga(8c): (0.6129, 0.2914, 0.4003)	
					Ga(8c): (0.8276, 0.5660, 0.4250)	
					Ga(8c): (0.9970, 0.2613, 0.4435)	
					Ga(4a): (0.2460, 0, 1/2)	
					Ga(8c): (0.1052, 0.3090, 0.5170)	
					Ga(8c): (0.3574, 0.5518, 0.5409)	

Local atomic arrangement in LaCuAl_3 and LaAuAl_3 by NMR and density functional theory

Vojtěch Chlan¹, Petr Doležal², Ráchel Sgallová¹, Milan Klicpera², Christian Franz^{3,4} and Pavel Javorský²

¹ Faculty of Mathematics and Physics, Department of Low Temperature Physics, Charles University, V Holešovičkách 2, 180 00 Prague 8, Czech Republic

² Faculty of Mathematics and Physics, Department of Condensed Matter Physics, Charles University, Ke Karlovu 5, 121 16 Prague 2, Czech Republic

³ Physik Department, Technische Universität München, D-85747, Garching, Germany

⁴ Heinz Maier-Leibnitz Zentrum (MLZ), Technische Universität München, D-85748 Garching, Germany

E-mail: vojtech.chlan@mff.cuni.cz

Received 7 January 2019, revised 15 May 2019

Accepted for publication 6 June 2019


Published 2 July 2019



Abstract

CeCuAl_3 and CeAuAl_3 , crystallizing in the non-centrosymmetric BaNiSn_3 tetragonal structure, are known mainly for their unusual neutron scattering spectra involving additional excitations ascribed to vibron quasi-bound quantum state in CeCuAl_3 and anti-crossing of phonon and crystal field excitations in CeAuAl_3 . In this work, we present results of nuclear magnetic resonance (NMR) experiments on their lanthanum analogues— LaCuAl_3 and LaAuAl_3 . The character of NMR spectra of ^{139}La , ^{27}Al , and ^{65}Cu measured in LaAuAl_3 and LaCuAl_3 is dominated by electric quadrupole interaction. The spectral parameters acquired from experimental data are confronted with values obtained from the electronic structure calculations. The results show remarkable differences for the two compounds. The ^{139}La spectrum in LaAuAl_3 can be interpreted by a single spectral component corresponding to uniform environment of La atoms in the crystal structure, whereas for LaCuAl_3 the spectrum decomposition yields a wide distribution of spectral parameters, which is not possible to explain by a single La environment, and multiple non-equivalent La positions in the crystal structure are required to interpret the spectrum.

Keywords: LaCuAl_3 , LaAuAl_3 , nuclear magnetic resonance, density functional theory

 Supplementary material for this article is available [online](#)

(Some figures may appear in colour only in the online journal)

1. Introduction

LaCuAl_3 and LaAuAl_3 belong to a large group of RTX_3 (R stands for rare earth atoms, T for transition metal, and X for a p-metal) compounds crystallizing in the tetragonal BaNiSn_3 -type structure. The structure is non-centrosymmetric and the lack of inversion symmetry affects physical properties of these materials. The most intriguing properties exhibit

the Ce-based ones. Remarkable is the observation [3] of the pressure-induced superconductivity in CeTSi_3 ($T = \text{Co, Rh, Ir}$) which classifies these materials among superconductors where the properties are dictated by an antisymmetric spin-orbit coupling as a consequence of the lack of inversion symmetry. In compounds with $X = \text{Al}$, the superconductivity was not found until now. Concerning compounds of our present study, LaCuAl_3 and LaAuAl_3 remain paramagnetic down to

0.4 K and their Ce-based counterparts CeCuAl_3 and CeAuAl_3 order antiferromagnetically at low temperatures ($T_N = 2.5$ K for CeCuAl_3 , see [1], and $T_N = 1.1$ K for CeAuAl_3 , see [2]).

The main interest in CeCuAl_3 and CeAuAl_3 lies in experimental observations which were ascribed to electron–phonon interaction. The interaction between the crystal electric field (CEF) and lattice degrees of freedom, usually considered as a weak effect in intermetallic compounds, is believed to be responsible for unusual phenomena experimentally observed in these two compounds by inelastic neutron scattering. The anti-crossing of the CEF level and the phonon states was recently reported in CeAuAl_3 [27]. CeCuAl_3 then belongs to the few compounds showing an additional peak in the neutron energy spectra [4] which cannot be explained on the basis of standard CEF theory. This effect, first observed in the cubic CeAl_2 [5, 6], was theoretically described on the basis of a strong magnetoelastic interaction between the CEF excitations and lattice vibrations which leads to a formation of a new quantum state—vibron quasi-bound state [7].

The alternative view on the existence of the additional excitation in the neutron spectra of CeCuAl_3 was discussed on the basis of certain Cu–Al atomic site disorder which would lead to existence of different local surroundings of the Ce ions [8]. Although the x-ray single crystal study [9] concluded the BaNiSn_3 -type of structure to be the most reliable one for CeCuAl_3 , the crystal structure is apparently not perfectly ordered one, but there is indeed a certain, relatively low Cu–Al atomic site disorder as reported in several studies [10, 11]. Such disorder occurs also in other members of this family of materials and has a huge impact on their electronic properties. For example, the type of magnetic order in CeCuGa_3 was discussed to be dependent on the Cu–Ga atomic site disorder [12]: the ordered non-centrosymmetric BaNiSn_3 -type variant tends to be antiferromagnetic, while a ferromagnetic order is reported for the disordered BaAl_4 -type structure. On the other hand, no such disorder was found for CeAuAl_3 or LaAuAl_3 [11].

As the atomic site disorder might substantially influence the electronic properties of CeTAl_3 compounds, it is important to study it more deeply by microscopic techniques. The nuclear magnetic resonance (NMR) spectroscopy is the most powerful technique sensitive to the local atomic surroundings. The direct investigation of the Ce-based compounds by NMR is, however, complicated by lack of cerium isotopes with nuclear spin, and additionally, the resonance lines would presumably be significantly broadened by interaction with the atomic magnetic moments. Therefore, we have performed a comparative NMR study of the LaCuAl_3 and LaAuAl_3 compounds. The structural properties of the CeTAl_3 and LaTAl_3 are very similar (see, e.g. [13]), so we assume that the main observations found for the lanthanum compounds are valid also for their cerium analogs.

2. Methods

Polycrystalline samples of LaCuAl_3 and LaAuAl_3 were prepared by arc-melting stoichiometric mixtures of pure elements (Solid State Electrotransport purified La, 6N Cu, 5N Au and

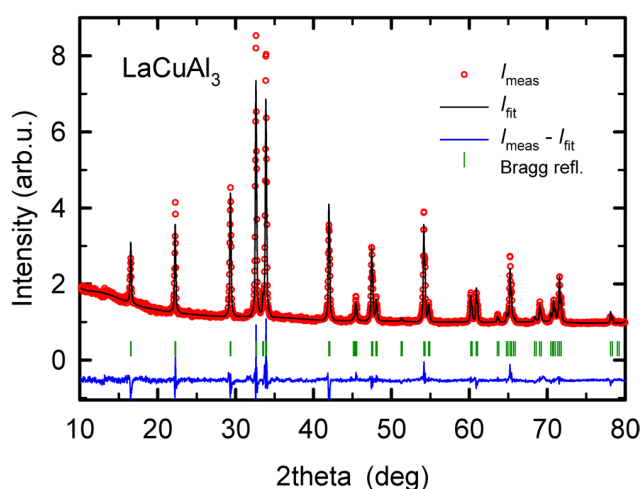


Figure 1. Powder x-ray (Cu radiation) diffraction pattern of LaCuAl_3 taken at the room temperature and fitted to the BaNiSn_3 structure mode.

6N Al) in mono-arc furnace under protection of argon atmosphere. The samples were turned and re-melted several times to achieve better homogeneity. Additionally, the samples were sealed under vacuum in a quartz glass and annealed for 10 d at 850 °C—they were heated up to 850 °C with the rate of 3 °C per minute and cooled down with the rate of 1 °C per minute. The powder x-ray diffractometer Bruker and the scanning electron microscope TESCAN equipped with back-scattering electron detector and energy dispersive x-ray analyzer (EDX) were used to check the structure, chemical composition and phase purity of the studied samples. The analysis of the EDX spectra, taken at several points of the sample surface, yielded the values that agree with the expected 1:1:3 stoichiometry within the experimental error of two atomic percent. No foreign phases were observed. The powder samples for the NMR experiments were sieved by 50 μm sieve.

Nuclear magnetic resonance spectra of ^{139}La , ^{27}Al , and ^{65}Cu nuclei were measured by Bruker Avance II spectrometer at room temperature in 9.4 T static magnetic field. The frequency-swept spectra were acquired by a modified Carr–Purcell–Meiboom–Gill (CPMG) pulse sequence where all (up to 50) induced spin echoes were coherently summed and their sum Fourier transformed. The frequency steps were varied (10–250 kHz) in order to cover all spectral features properly, the NMR probe was well tuned and matched at each excitation frequency, and the rf pulse lengths were set to induce maximum intensity of the signal. Typical rf pulse lengths were 3–6 μs , the delays between pulses in the CPMG train were 70–150 μs , and 1000–2000 scans were accumulated at each excitation frequency with delays between the scans 50–300 ms depending on spin-lattice relaxation.

In the presence of a strong electric quadrupole interaction its influence cannot be neglected within duration of the excitation rf pulse and a mixing of populations during the pulse occurs—in contrast to situation with only a magnetic Zeeman interaction of nuclear spin I with static magnetic field, when each energy level corresponds to a well-defined quantum number $m \in \langle -I, I \rangle$. Different transitions between the quadrupolarly split nuclear energy levels then possess different

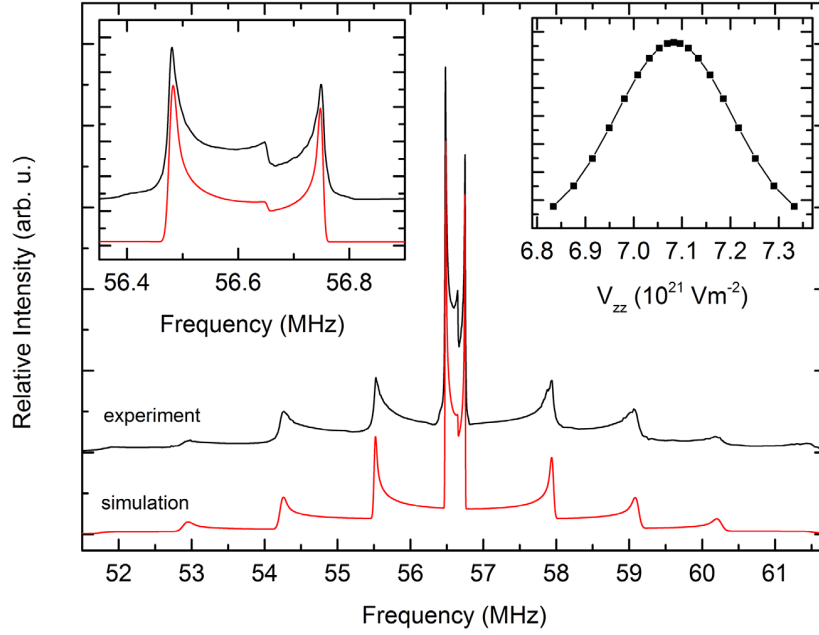


Figure 2. ^{139}La NMR spectrum of LaAuAl_3 in comparison with simulated spectrum. The inset on the left side details the central transition, inset on the right side shows distribution of V_{zz} parameter used in the simulation.

nutations frequencies, and therefore, also different lengths of the optimal rf pulse [14]. The excitation by a CPMG sequence with fixed rf pulse lengths thus fails to accomplish optimal excitation, and as a consequence, the relative contributions of individual transition to the overall intensity may differ from the ratios expected from theory. We also note that our approach in addition neglects phase in the evaluation of spectral intensity, i.e. plotting magnitude $\sqrt{(\chi')^2 + (\chi'')^2}$ versus frequency, which results in a small perturbation of the powder pattern shape compared to the case where the absorption component of the susceptibility χ' is used. This approach, however, had to be chosen due to extreme breadths of the NMR spectra and in order to obtain reasonable signal-to-noise ratio.

The electronic structures of LaAuAl_3 and LaCuAl_3 with various atomic arrangements were calculated within the density functional theory (DFT) by means of full-potential all-electrons augmented plane wave + local orbitals method implemented in WIEN2k code [20]. The radii of atomic spheres were 2.5 a.u. for La and Au, 2.1 a.u. for Cu, and 2.0 a.u. for Al. The lattice parameters as well as the atomic coordinates were optimized (within the space group symmetry of each calculated structure) by minimizing the total energy and atomic forces. Space group symmetries and lattice parameters of all calculated structures are listed in the supplemental material (available online at stacks.iop.org/JPhysCM/31/385601/mmedia). The size of the basis set and the density of the k -point mesh were well converged with respect to the structure geometry (lattice parameters) and the calculated quantities of interest (electric field gradients). The value for the RK_{max} parameter was 8.0, yielding the matrix size about 1600 basis functions (half the size for the structures with I -centration). 3000 k -points were used, leading to 220–400 k -points in the irreducible part of the Brillouin zone.

The charge density and potentials were Fourier expanded up to the largest k -vector $G_{\text{max}} = 14 \sqrt{\text{Ry}}$ and as the exchange-correlation potential Perdew–Burke–Ernzerhof variant [21] of generalized gradient approximation was used.

3. Results and discussion

The powder x-ray diffraction pattern of LaCuAl_3 is shown in figure 1. All the diffraction lines can be indexed considering the tetragonal structure of LaCuAl_3 . No additional intensities that would indicate presence of impurity phase(s) were detected, in agreement with the results of EDX analysis.

Measured ^{139}La NMR spectrum of LaAuAl_3 (see figure 2) shows features which are characteristic for a powder spectrum in presence of a strong electric quadrupole interaction of the nuclear quadrupole momentum Q with electric field gradient (EFG). For ^{139}La nucleus (spin $I = 7/2$) there are seven nuclear transitions expected: one central transition located approximately at the Larmor frequency $\nu_L \sim 56.53$ MHz and six satellite transitions spread in frequency range ~ 50 – 64 MHz. Due to a random orientation of the powder grains, each nuclear transition contributes with all possible mutual orientations of the static magnetic field vector and the EFG tensor. The quadrupole interaction is often considered as a perturbation to the Zeeman interaction with static magnetic field, in the first-order expansion (‘first-order quadrupole correction’) the frequencies of the transitions $m \leftrightarrow m + 1$ can be expressed as [15]:

$$\omega_{m,m+1} = \frac{\omega_Q}{2}(1 - 2m)(3 \cos^2 \vartheta - 1 + \eta \sin^2 \vartheta \cos 2\phi),$$

$$\omega_Q = \frac{3eQV_{zz}}{2I(2I - 1)\hbar}, \quad (1)$$

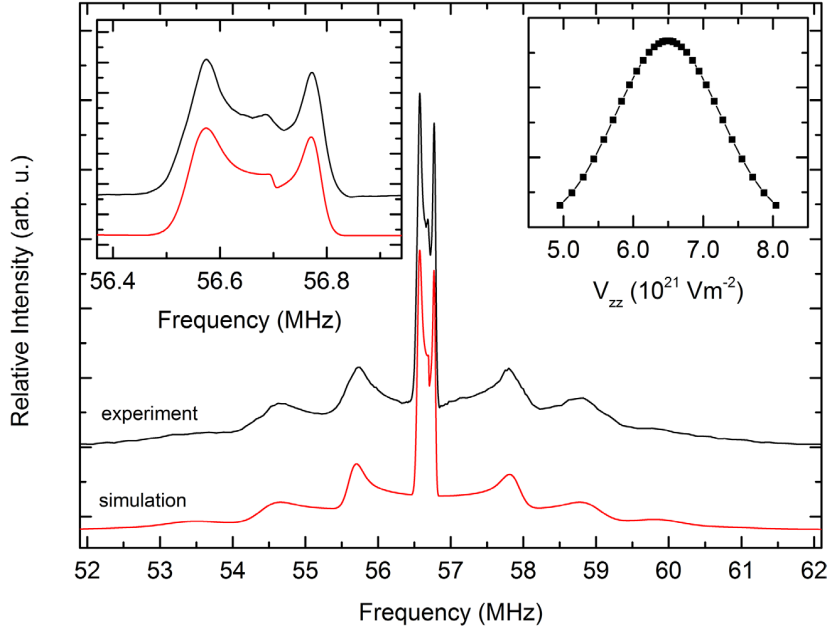


Figure 3. ^{139}La NMR spectrum of LaCuAl_3 in comparison with simulated spectrum. The inset on the left side details the central transition, inset on the right side shows distribution of V_{zz} parameter used in the simulation.

where ω_Q is the quadrupole frequency, V_{zz} is the zz component of the EFG tensor, η is the parameter of asymmetry $\eta = \frac{V_{xx} - V_{yy}}{V_{zz}}$, and ϑ and φ are the Euler angles of the external magnetic field within the principal axis system of the EFG tensor. Since $\omega_{-\frac{1}{2}, \frac{1}{2}} = 0$, the central transition $-\frac{1}{2} \leftrightarrow \frac{1}{2}$ is not affected by the first-order quadrupole correction. In order to describe the effect of strong quadrupole interaction on the central transition, one has to expand up to the second-order ('second-order quadrupole correction') [15]:

$$\omega_{-\frac{1}{2}, \frac{1}{2}} = -\frac{\omega_Q^2}{6\omega_L} \left(I(I+1) - \frac{3}{4} \right) (A(\varphi, \eta) \cos^4 \vartheta + B(\varphi, \eta) \cos^2 \vartheta + C(\varphi, \eta)), \quad (2)$$

where A, B , and C terms possess the dependence on angle φ and asymmetry η (their expressions can be found in [15]).

The experimental spectrum of LaAuAl_3 in figure 2 clearly has a single dominant 7/2-spin powder pattern, which corresponds to one prevailing value of V_{zz} . This is evident from comparison with ^{139}La spectrum simulated using a narrow distribution of V_{zz} around value $7.1 \times 10^{21} \text{ Vm}^{-2}$, with $\eta = 0$, and convoluted with a Gaussian peak shape of width 6 kHz. Such simulation sufficiently describes all the spectral features of the experiment. The need for a distribution of V_{zz} rather than a single value is dictated by the fact that the quadrupole splitting for the satellite transitions is much more sensitive to V_{zz} (first-order effect), unlike for the central transition (second-order effect). A mere convolution with Gaussian shape would not capture the breadths of the central and satellite transitions all at once.

In the experimental ^{139}La NMR spectrum of LaCuAl_3 (see figure 3) the powder pattern spectral features are smeared-out in contrast to LaAuAl_3 , as is documented by an order of magnitude broader distribution of V_{zz} in the respective simulation

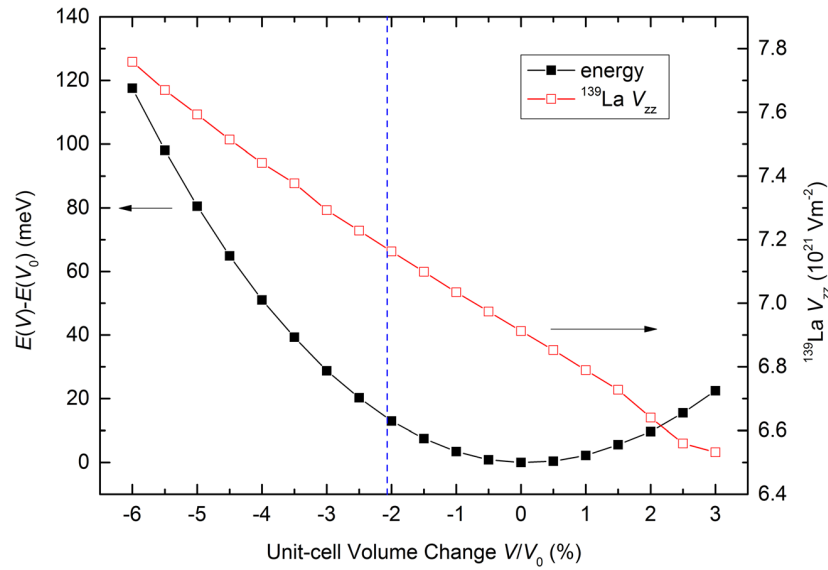
(note the different scales of the V_{zz} -axes in the insets of figures 2 and 3). Qualitatively, based solely on the experimental data, we can thus interpret the ^{139}La spectra in the following way: lanthanum in the LaAuAl_3 experiences very homogeneous environment with axial symmetry (asymmetry $\eta = 0$). On the contrary, in LaCuAl_3 the broad range of V_{zz} indicates a mixture of different lanthanum sites.

In order to assess our interpretation it is required to show that (i) different values of V_{zz} can be attributed to different arrangements of Au/Al or Cu/Al atoms in the structure and that (ii) there are no other effects that could possibly explain the smeared-out shape of ^{139}La NMR spectrum in LaCuAl_3 . Therefore, we compare the experiment with results of DFT calculations where the ordering of Au and Al atoms (or Cu and Al, respectively) was modeled within one tetragonal unit cell containing ten atoms, i.e. $\text{La}_2\text{Au}_2\text{Al}_6$ and $\text{La}_2\text{Cu}_2\text{Al}_6$. The starting point was the $I4mm$ BaAl_4 -type structure with La in the $2a$ sites and with Au (Cu) and Al atoms to be arbitrarily allocated within all the remaining $2a$ and $4b$ sites. Such model allows for eight crystallographically nonequivalent structures (listed in table 1), which differ by symmetry, atomic arrangement, and most importantly also by the calculated EFG parameters at La sites.

The calculated values of V_{zz} in table 1 vary substantially for different atomic configurations; likewise the value of η corresponds to presence of local symmetry axis. For the calculated values to be directly comparable with room temperature experiments, one should increase the calculated values by a few percent, in order to reflect the difference between unit cell volume in calculation and in experiment. This volume discrepancy is expected and caused by two sources: first, the calculation relates to temperature 0 K and as such corresponds to approximately 1%–2% smaller unit cell volume due to thermal expansion. Second, the

Table 1. Symmetries of modeled crystal structures of LaAuAl₃ and LaCuAl₃, and calculated EFG parameters of ¹³⁹La.

Structure	Space group	La-site point group	LaAuAl ₃		LaCuAl ₃	
			V_{zz}	η	V_{zz}	η
str01	<i>I4mm</i>	<i>4mm</i>	6.91	0	6.36	0
str02	<i>P4/mmm</i>	<i>4/mmm</i>	5.65	0	4.80	0
		<i>4/mmm</i>	7.98	0	8.28	0
str03	<i>P4/nmm</i>	<i>4mm</i>	7.47	0	6.95	0
str04	<i>P/mmm</i>	<i>mm2</i>	−3.29	0.97	4.25	0.93
		<i>mm2</i>	7.57	0.21	6.02	0.02
str05	<i>P/mmm</i>	<i>mm2</i>	4.25	0.44	4.32	0.72
		<i>mm2</i>	6.17	0.32	6.49	0.48
str06	<i>P42/mmc</i>	<i>mmm</i>	−3.06	0.76	−4.90	0.59
str07	<i>I4m2</i>	<i>42m</i>	2.68	0	3.80	0
str08	<i>P4/nmm</i>	<i>4mm</i>	1.25	0	2.65	0

**Figure 4.** Volume dependence of the total energy and V_{zz} on La nucleus in LaAuAl₃ str01 structure. Blue dashed line denotes unit cell volume corresponding to the room temperature experiment [19].

exchange-correlation potential [21] used in the calculations overestimates [16–18] the equilibrium volume by additional approximately 0%–2%. The value of V_{zz} on La nucleus is dominated by p–p and to some extent also d–d contributions which increase in value with decreasing volume as the La 5p and 4d orbitals become compressed towards the nucleus (see the volume dependence in figure 4). The calculated equilibrium volume is about 2% larger and one should thus increase the calculated V_{zz} by roughly 5% for comparison with experiment.

Confronting the calculated V_{zz} values for LaAuAl₃ in table 1 with the V_{zz} distribution acquired from the NMR experiment (figure 2), clearly only the str01 *I4mm* structure is possible: the V_{zz} values of all the other LaAuAl₃ configurations are too different to suit the experiment. On the other hand, in case of LaCuAl₃ the broad distribution of V_{zz} (figure 3) allows to include in addition to str01 also structure str03, and to some smaller extent also str02, str04, str05, and str06 can contribute to the spectrum.

There are additional interactions, besides the electric quadrupole interaction, which could, in principle, contribute to the observed smearing-out of the features in ¹³⁹La spectrum of LaCuAl₃: the chemical shielding (including Knight contribution in metals), nuclear dipole–dipole interaction, and indirect nuclear spin–spin interaction. However, we show in the following paragraph that these interactions are too weak to be responsible for the observed effects.

The nucleus is shielded from the external static magnetic field by the surrounding electrons, as described by the chemical shielding σ and Knight shielding K in case of conduction electrons in metals. The total shielding has isotropic part $\sigma_0 + K_0$, which in case of ¹³⁹La here is responsible for a uniform shift of the spectrum by approximately +200 kHz from the Larmor frequency, and anisotropic part $\Delta\sigma + \Delta K$, which we can estimate by employing our DFT calculations. Calculated anisotropic shieldings (evaluated as difference between shieldings for field in directions [001] and [100]), $\Delta\sigma = 70$ ppm and $\Delta K = -600$ ppm, which cause broadening of ~30 kHz

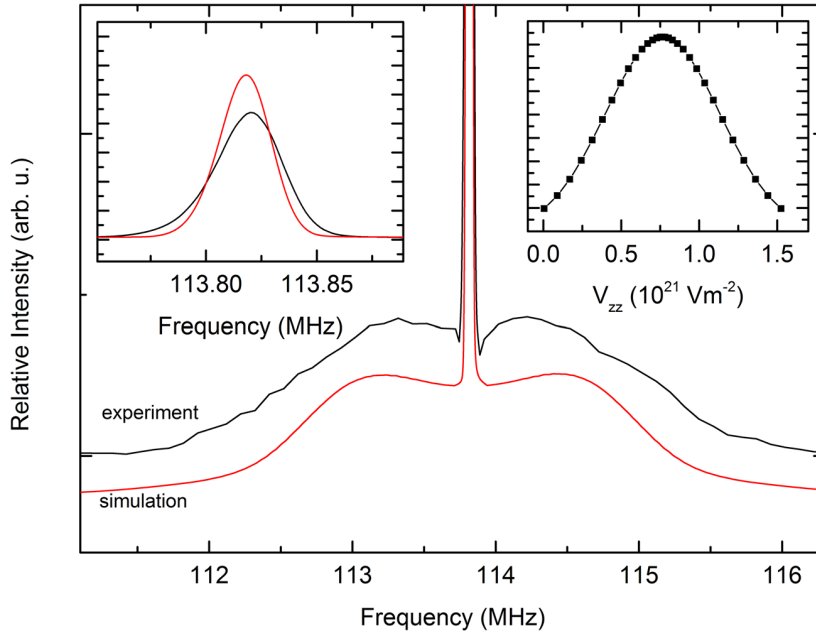


Figure 5. ^{65}Cu NMR spectrum of LaCuAl_3 in comparison with simulated spectrum. The inset on the left side details the central transition, inset on the right side shows distribution of V_{zz} parameter used in the simulation.

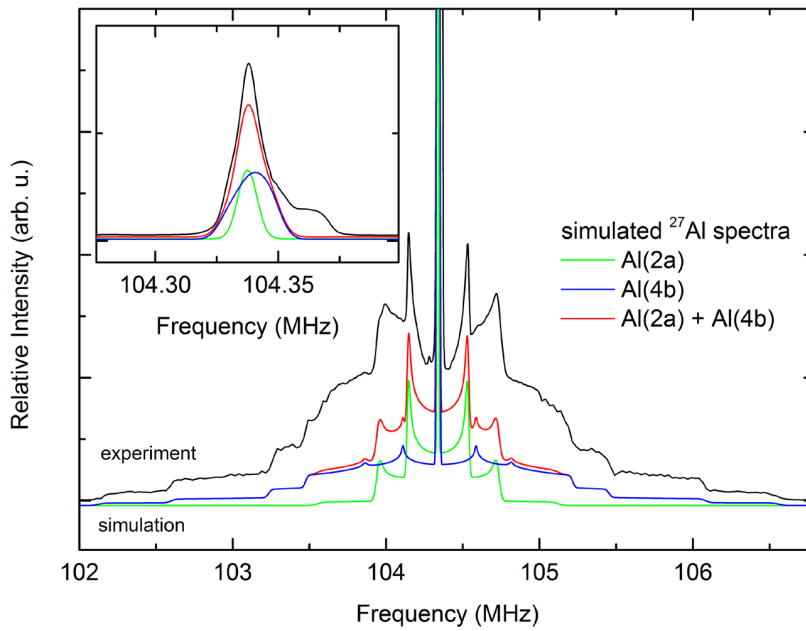


Figure 6. ^{27}Al NMR spectrum of LaAuAl_3 in comparison with simulated spectrum. The inset shows the central transition.

in addition to effect of quadrupole interaction. Values, $\Delta\sigma = 230$ ppm and $\Delta K = 260$ ppm, calculated for LaAuAl_3 structure yield similar value ~ 28 kHz. The broadening effect due to the anisotropy of chemical and Knight shielding is thus relatively small compared to the quadrupole interaction for our ^{139}La spectra, and moreover, it is present in spectra of both samples, therefore, it cannot be responsible for broadening of smearing-out of spectral features for LaCuAl_3 only. Next, the effect of dipolar interaction with surrounding nuclear moments can be calculated by direct summation within a sphere of radius 100 \AA , yielding estimate of < 1.8 kHz for LaCuAl_3 and < 2.0 kHz for LaAuAl_3 . Indirect nuclear spin–spin interaction, mediated

by conduction electrons (Rudermann–Kittel interaction), cannot usually be observed directly, however, its value rarely exceeds a few kHz [22, 23]. The effects of these interactions on smearing-out the ^{139}La spectrum are thus negligible compared to the effect of electric quadrupole interaction and its distribution of V_{zz} . Therefore, the only possible interpretation of the smeared-out shape of ^{139}La spectra in LaCuAl_3 is a presence of several different lanthanum sites with different V_{zz} .

Supplementary information concerning atomic ordering can be obtained from the other nuclei in the structure. ^{65}Cu NMR spectrum in LaCuAl_3 displays powder pattern, which is similarly unresolved as in case of LaCuAl_3 ^{139}La spectrum (figure 5):

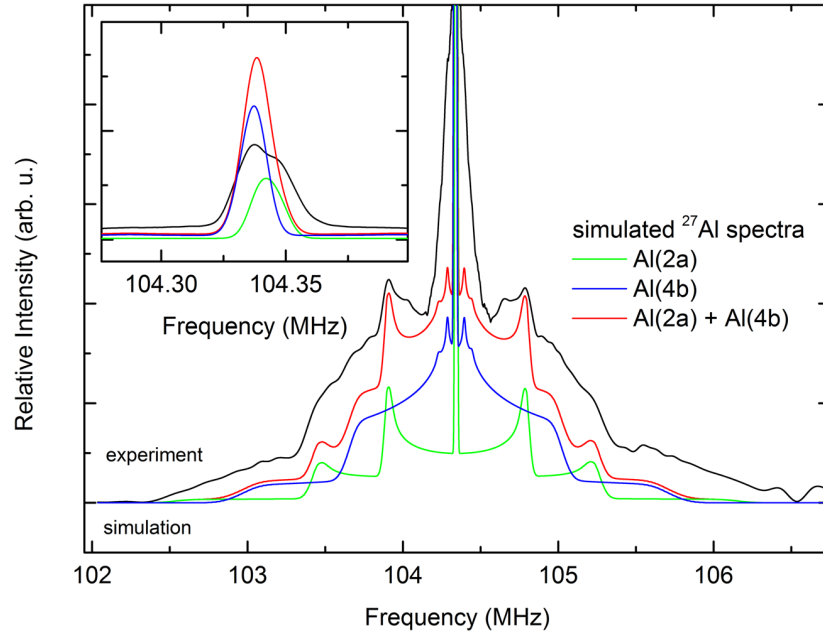


Figure 7. ^{27}Al NMR spectrum of LaCuAl_3 in comparison with simulated spectrum. The inset shows the central transition.

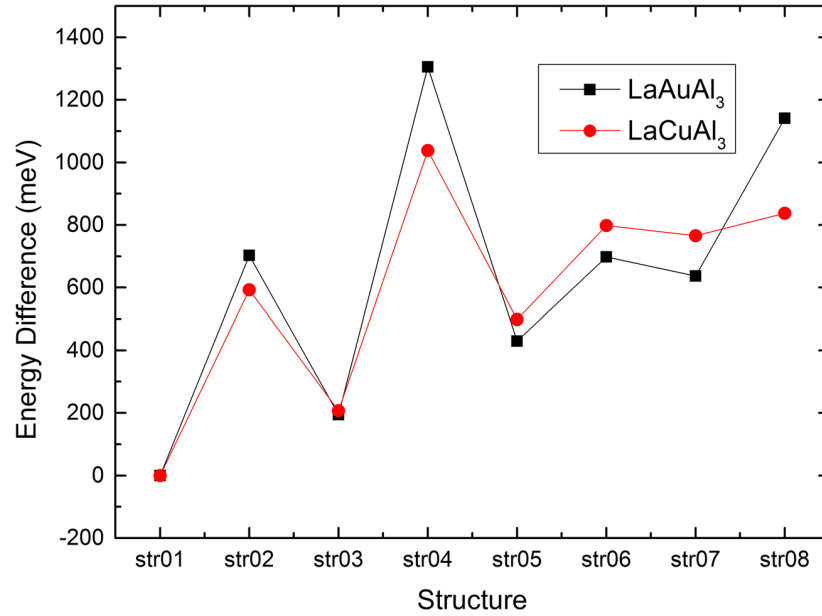


Figure 8. Differences in calculated total energies for eight possible configurations in the stoichiometric structures of LaAuAl_3 and LaCuAl_3 .

measured featureless powder pattern allows to match the spectrum with simulation using a very broad distribution of V_{zz} parameter. If the LaCuAl_3 structure was well ordered, there would be a single Cu(2a) site expected with a relatively sharp distribution of V_{zz} . Our calculations yield for such structure (str01) $V_{zz} = 0.40 \times 10^{21} \text{ V/m}^{-2}$, which is a value apparently contributing to the experimental spectrum but clearly has to be accompanied by several other components with larger values of V_{zz} . The analogous spectrum for LaAuAl_3 sample was not acquired due to a very low magnetogyric ratio of ^{197}Au isotope.

The notion about LaCuAl_3 being disordered can be further supported by ^{27}Al NMR spectra of both samples (see

figures 6 and 7). Al enters at least two nonequivalent sites even in the ‘ordered’ $I4mm$ structure str01, and above that, the Al(4b) sites lack local axial symmetry, i.e. η can be non-zero and acts as another free parameter. Therefore, the approach of independently simulating the NMR spectra as applied for ^{139}La is more difficult to implement for ^{27}Al . For LaAuAl_3 the most of the spectral features can still be captured by simulation using two ^{27}Al subspectra with ratio 1:2, which reflects the site occupancies Al(2a) and Al(4b), and relatively narrow distributions of V_{zz} around values $V_{zz}(2a) = -0.74$ and $V_{zz}(4b) = 2.09$ (in units 10^{21} V/m^{-2}), $\eta(2a) = 0$ due to symmetry and $\eta(4b) = 0.57$. Despite the fact that the simulation

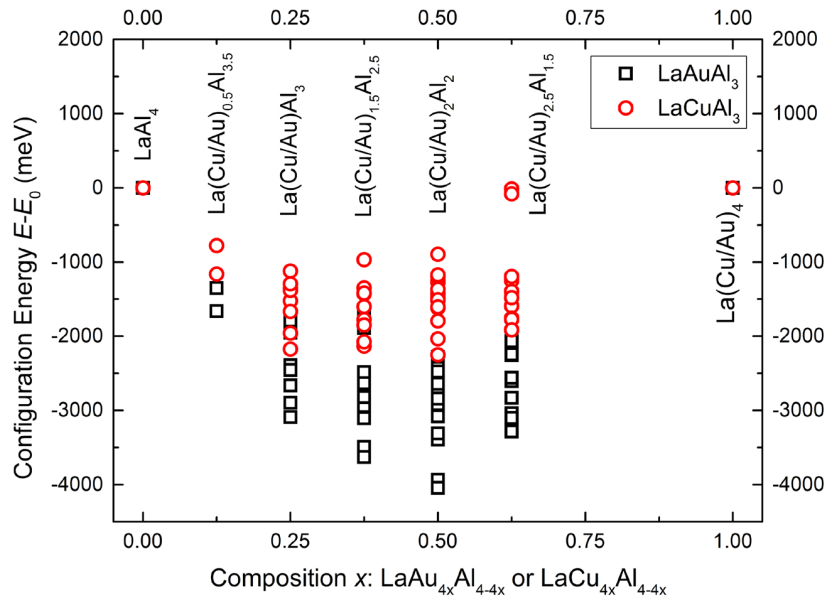


Figure 9. Dependence of the difference between the total energy of structure with composition $\text{LaAu}_{4x}\text{Al}_{4-4x}$ (or $\text{LaCu}_{4x}\text{Al}_{4-4x}$) and the total energy of its constituents LaAl_4 and LaAu_4 (or LaCu_4 , respectively).

did not consider distribution of $\eta(4b)$, these values correspond relatively well to $V_{zz}(2a) = -0.51$, $V_{zz}(4b) = 1.91$, $\eta(2a) = 0$ and $\eta(4b) = 0.83$ from *str01* LaAuAl_3 calculation. In case of LaCuAl_3 the smeared-out features make an analogous simulation impractical and allow ambiguous results. Our attempt to capture the experimental spectrum of LaCuAl_3 with two 1:2 Al subspectra (see figure 7) apparently leaves space for additional spectral components and/or wide distributions of EFG parameters, thus pointing to presence of more than two nonequivalent Al sites in LaCuAl_3 structure and again supporting our deduction that LaCuAl_3 is at least partially disordered.

Experimental NMR spectra of all isotopes thus lead us to conclusion that a single atomic arrangement occurs in LaAuAl_3 while at least two different configurations are present in LaCuAl_3 compound. Situation in La compounds is thus corroborating the scheme used to describe the specific heat data of $\text{Ce}(\text{Cu},\text{Al})_4$ series [8].

Natural question then arises why the behavior of LaCuAl_3 and LaAuAl_3 is so different, i.e. why LaCuAl_3 is more disordered than LaAuAl_3 . In stoichiometric 1:1:3 cases for both LaAuAl_3 and LaCuAl_3 , *str01* is the preferred arrangement of Au/Al and Cu/Al atoms, and the energies of the remaining structures *str02*–*str08* are very similar (figure 8). Apparently, to explore in more detail the differences in ordering, our model consisting of a single unit cell is too limiting. A supercell approach going beyond one cell would be very cumbersome, therefore, we instead calculated and fully optimized unit cells with varying stoichiometries: unit cells with several contents x of Au (or Cu) between 0 and 1, i.e. from LaAl_4 to LaAu_4 (LaCu_4). We can now evaluate the stability of a given structure $\text{LaAu}_{4x}\text{Al}_{4-4x}$ by confronting its calculated total energy E with the sum of calculated total energies of its constituents $E_0(x) = xE(\text{LaAu}_4) + (1-x)E(\text{LaAl}_4)$. Since there are again more possible arrangements of Au/Al for x (especially for x near 0.5) we observe a spread of energies

for each value of x , see figure 9. For $x < 0.5$ the most energetically favorable structure is always the one of the BaNiSn_3 type. Both LaAuAl_3 and LaCuAl_3 apparently are stable, however the minimum of the dependence in figure 9 is deeper for Au containing compounds. In general, for such mixtures the larger is the negative difference of $E - E_0$, the higher is the tendency of such mixture for ordering—in order to maximize the number of interactions between different atoms.

This behavior of LaAuAl_3 and LaCuAl_3 can be explained by difference of atomic sizes and electronegativities between Au and Cu atoms. We evaluated both properties by ‘Atoms in Molecules’ approach (Bader analysis [24]), where the atom is defined as a volume delimited by critical points (local minima or saddle points) in the charge density. Calculated volume 24.4 \AA^3 of Cu atom in LaCuAl_3 is rather close to 19.2 and 16.0 \AA^3 of aluminum in $\text{Al}(2a)$ and $\text{Al}(4b)$, respectively, and thus the mixing on individual atomic sites is relatively easy. On the other hand, gold atoms are somewhat larger (35.0 \AA^3) which prevents site mixing with smaller aluminum atoms (18.1 and 14.4 \AA^3) in the LaAuAl_3 structure. Another point is higher difference between the electronegativity of Au and Al compared to such difference between Cu and Al, which can be best demonstrated using calculated valences (evaluated as the difference between atomic number Z and the charge integrated within the atomic volume). In LaAuAl_3 gold has valence -2.86 and aluminium sites $\text{Al}(2a)$ and $\text{Al}(4b)$ possess $+0.01$ and $+0.75$, whereas in LaCuAl_3 copper has valence -1.91 and both Al have -0.22 and $+0.44$. Larger difference between Au and Al valences thus again increases tendency for ordered arrangement.

It is worthwhile to mention certain analogy which can be seen when inspecting the binary phase diagrams. One can find several compounds with defined exact stoichiometry in the Au–Al binary phase diagram [25]. On the other hand, Cu–Al phase diagram [26] does not contain any line stoichiometric

compound but rather regions of stability of several Cu–Al phases which allow for varying Cu–Al fractions. This observation reminds closely our case when comparing LaCuAl₃ and LaAuAl₃.

4. Conclusions

The character of NMR spectra of ¹³⁹La, ²⁷Al, and ⁶⁵Cu measured in LaAuAl₃ and LaCuAl₃ powder samples is dominated by electric quadrupole interaction. By simulating the NMR spectra and comparing to experiment, the spectral parameters were extracted and confronted with values obtained from the electronic structure calculations. In case of LaAuAl₃ the ¹³⁹La spectrum can be interpreted by a single spectral component corresponding to uniform environment of La atoms in the structure, whereas in case of LaCuAl₃ the spectrum decomposition yields a wide distribution of spectral parameters, and thus corresponds to multiple non-equivalent La positions in the structure. This scenario is also reflected in ⁶⁵Cu NMR spectrum of LaCuAl₃ and in ²⁷Al spectra of both samples, and together with analysis of our calculations leads to conclusion that LaCuAl₃ is somewhat disordered compared to ordered LaAuAl₃.

Acknowledgments

This work was supported by the Czech Science Foundation under Grant No. 17-04925J, and by the project SVV-260442. Sample preparation was performed in MGML (<http://mgml.eu/>), which was supported within the program of Czech Research Infrastructures (Project No. LM2018096). The NMR experiments used equipment of the Project CZ.2.16/3.1.00/21566 funded by the Operational Programme Prague Competitiveness. Computational resources were provided by the CESNET LM2015042 and the CERIT Scientific Cloud LM2015085, under the programme ‘Projects of Large Research, Development, and Innovations Infrastructures’.

ORCID iDs

Vojtěch Chlan  <https://orcid.org/0000-0001-6963-9273>

References

- [1] Klicpera M, Javorský P, Čermák P, Schneidewind A, Ouladdiaf B and Diviš M 2015 *Phys. Rev. B* **91** 224419
- [2] Adroja D T *et al* 2015 *Phys. Rev. B* **91** 134425
- [3] Mukuda H, Fujii T, Ohara T, Harada A, Yashima M, Kitaoka Y, Okuda Y, Settai R and Onuki Y 2008 *Phys. Rev. Lett.* **100** 107003
- [4] Adroja D T, del Moral A, de la Fuente C, Fraile A, Goremychkin E A, Taylor J W, Hillier A D and Fernandez-Alonso F 2012 *Phys. Rev. Lett.* **108** 216402
- [5] Klicpera M, Adroja D T, Vlášková K, Boehm M, Mutka H, Ouladdiaf B, Guidi T and Javorský P 2017 *Inorg. Chem.* **56** 12839–47
- [6] Steglich F, Bredl C D, Loewenhaupt M and Schotte K D 1979 *J. Phys. Colloques* **40** 301–7
- [7] Loewenhaupt M, Rainford B D and Steglich F 1979 *Phys. Rev. Lett.* **42** 1709–12
- [8] Thalmeier P and Fulde P 1982 *Phys. Rev. Lett.* **49** 1588–91
- [9] Vlášková K, Javorský P and Prokleška J 2018 *Intermetallics* **100** 52–6
- [10] Klicpera M, Javorský P, Čermák P, Rudajevová A, Daniš S, Brunátová T, and Císařová I 2014 *Intermetallics* **46** 126–30
- [11] Matsumura M, Kawamura Y, Yoshina M, Nishioka T and Kato H 2009 *J. Phys.: Conf. Ser.* **150** 042122
- [12] Franz C *et al* 2016 *J. Alloys Compd.* **688** 978–86
- [13] Joshi D A, Burger P, Adelmann P, Ernst D, Wolf T, Sparta K, Roth G, Grube K, Meingast C and Löhneysen H V 2012 *Phys. Rev. B* **86** 035144
- [14] Klicpera M and Javorský P 2014 *J. Magn. Magn. Mater.* **363** 88–94
- [15] Klicpera M and Javorský P 2015 *J. Alloys Compd.* **621** 78–85
- [16] Freude D 2006 Quadrupolar nuclei in solid-state nuclear magnetic resonance *Encyclopedia of Analytical Chemistry* ed R A Meyers and C Dybowski (Wiley: Chichester) (<https://doi.org/10.1002/9780470027318.a6112>)
- [17] Man P P 2011 Quadrupolar interactions *Encyclopedia of Magnetic Resonance* ed R K Harris and R E Wasylishen (Wiley: Chichester) (<https://doi.org/10.1002/9780470034590.emrstm0429.pub2>)
- [18] Mo Y, Car R, Staroverov V N, Scuseria G E and Tao J 2017 *Phys. Rev. B* **95** 035118
- [19] Csonka G I, Perdew J P, Ruzsinszky A, Philipsen P H T, Lebègue S, Paier J, Vydrov O A and Ángyán J G 2009 *Phys. Rev. B* **79** 155107
- [20] Zhang G-X, Reilly A M, Tkatchenko A and Scheffler M 2018 *New J. Phys.* **20** 063020
- [21] Hulliger F 1995 *J. Alloys Compd.* **218** 255–8
- [22] Blaha P, Schwarz K, Madsen G K H, Kvasnicka D, Luitz J, Laskowski R, Tran F and Marks L D 2018 *WIEN2k, an Augmented Plane Wave + Local Orbitals Program for Calculating Crystal Properties* ed K Schwarz (Austria: Technical Universität Wien)
- [23] Perdew J P, Burke K and Ernzerhof M 1996 *Phys. Rev. Lett.* **77** 3865–8
- [24] Ruderman M A and Kittel C 1953 *Phys. Rev.* **96** 99–102
- [25] Pennington C H and Slichter C P 1991 *Phys. Rev. Lett.* **66** 381–4
- [26] Bader R 1994 *Atoms in Molecules: a Quantum Theory* (Oxford: Oxford University Press)
- [27] Li M, Li C, Wang F, Luo D and Zhang W 2004 *J. Alloys Compd.* **385** 199–206
- [28] Ponweiser N, Lengauer C L and Richter K W 2011 *Intermetallics* **19** 1737–46
- [29] Liu B-Q, Čermák P, Franz C, Pfeleiderer C and Schneidewind A 2018 *Phys. Rev. B* **98** 174306
- [30] Čermák P, Schneidewind A, Liu B-Q, Koza M M, Franz C, Schönmann R, Sobolev O and Pfeleiderer C 2019 *Proc. Natl Acad. Sci.* **116** 6695–700

Local atomic arrangement in LaCuAl_3 and LaAuAl_3 by NMR and density functional theory

Vojtěch Chlan,¹ Petr Doležal,² Ráchel Sgallová,¹ Milan Klicpera,² Christian Franz,^{3,4} and Pavel Javorský²

¹*Charles University, Faculty of Mathematics and Physics,
Department of Low Temperature Physics,
V Holešovičkách 2, 180 00 Prague 8, Czech Republic*

²*Charles University, Faculty of Mathematics and Physics,
Department of Condensed Matter Physics,
Ke Karlovu 5, 121 16 Prague 2, Czech Republic.*

³*Physik Department, Technische Universität München, D-85747, Garching, Germany*

⁴*Heinz Maier-Leibnitz Zentrum (MLZ),
Technische Universität München, D-85748 Garching, Germany*

TABLE I. Lattice parameters of all modeled crystal structures.

compound	structure	SG	a (Å)	c (Å)	compound	a (Å)	c (Å)
La ₂ Al ₈	<i>str01</i>	$I4/mmm$	4.35136	11.25048			
La ₂ AuAl ₇	<i>str01</i>	$P4mm$	4.37907	11.04964	La ₂ CuAl ₇	4.33262	10.92985
	<i>str02</i>	$P\bar{4}m2$	4.36804	11.07376		4.33245	10.98352
La ₂ Au ₂ Al ₆	<i>str01</i>	$I4mm$	4.38423	10.98340	La ₂ Cu ₂ Al ₆	4.29745	10.73379
	<i>str02</i>	$P4/mmm$	4.32438	11.41571		4.23455	11.10975
	<i>str03</i>	$P4/nmm$	4.41804	10.87002		4.31908	10.62654
	<i>str04</i>	$Pmm2$	4.36119	11.25034		4.32598	10.75049
	<i>str05</i>	$Pmm2$	4.35236	11.14350		4.29038	10.82249
	<i>str06</i>	$P42/mmc$	4.33063	11.19959		4.26904	10.93099
	<i>str07</i>	$I\bar{4}m2$	4.32186	11.20992		4.27614	10.94864
	<i>str08</i>	$P4/nmm$	4.47021	10.72343		4.37005	10.53582
La ₂ Au ₃ Al ₅	<i>str01</i>	$P4mm$	4.37721	11.12182	La ₂ Cu ₃ Al ₅	4.24024	10.74975
	<i>str02</i>	$P\bar{4}m2$	4.34544	11.48400		4.35625	10.39321
	<i>str03</i>	$Pmm2$	4.30627	11.61105		4.23424	10.94607
	<i>str04</i>	$Pmm2$	4.37466	11.14655		4.29006	10.60817
	<i>str05</i>	$P\bar{4}m2$	4.41131	10.84676		4.29017	10.55486
	<i>str06</i>	$P4mm$	4.41931	11.11555		4.35656	10.39176
	<i>str07</i>	$Pmm2$	4.36436	11.20277		4.29755	10.62592
	<i>str08</i>	$Pmm2$	4.33851	11.32325		4.29024	10.66220
	<i>str09</i>	$P4mm$	4.44108	10.77932		4.31982	10.46409
	<i>str10</i>	$P\bar{4}m2$	4.45343	10.74393		4.34898	10.42800
La ₂ Au ₄ Al ₄	<i>str01</i>	$I4/mmm$	4.36481	11.27542	La ₂ Cu ₄ Al ₄	4.16402	10.92054
	<i>str02</i>	$Pmm2$	4.26571	11.92752		4.25043	10.58086
	<i>str03</i>	$Pmm2$	4.35647	11.35647		4.22685	10.64597
	<i>str04</i>	$P4/nmm$	4.36901	11.48300		4.33460	10.28525
	<i>str05</i>	$P4mm$	4.35964	11.46098		4.27027	10.53791
	<i>str06</i>	$Pmmm$	4.28544	11.79995		4.23401	10.72173
	<i>str07</i>	$P\bar{4}m2$	4.24934	11.93865		4.21988	10.84984
	<i>str08</i>	$P4mm$	4.40707	11.12097		4.31248	10.28392
	<i>str09</i>	$P\bar{4}m2$	4.33833	11.44998		4.30460	10.32158
	<i>str10</i>	$P\bar{4}m2$	4.30485	11.59093		4.31248	10.28392
	<i>str11</i>	$P42mc$	4.37203	11.28086		4.32740	10.26816
	<i>str12</i>	$Imm2$	4.33945	11.43969		4.32740	10.37084
	<i>str13</i>	$P4/nmm$	4.48781	10.53660		4.32663	10.11506
	<i>str14</i>	$Pmm2$	4.39623	11.14713		4.34992	10.21294
	<i>str15</i>	$Pmm2$	4.46510	10.78785		4.34995	10.16196
	<i>str16</i>	$I4/mmm$	4.56255	10.32345		4.41519	9.86388
La ₂ Au ₅ Al ₃	<i>str01</i>	$P4mm$	4.54344	10.55751	La ₂ Cu ₅ Al ₃	4.45977	9.42099
	<i>str02</i>	$P\bar{4}m2$	4.35233	11.52064		4.29654	10.19495
	<i>str03</i>	$Pmm2$	4.32194	11.74965		4.34366	9.98128
	<i>str04</i>	$Pmm2$	4.39538	11.25247		4.41712	9.55045
	<i>str05</i>	$P\bar{4}m2$	4.49991	10.75687		4.36919	9.76112
	<i>str06</i>	$P4mm$	4.30130	11.87058		4.22384	10.49667
	<i>str07</i>	$Pmm2$	4.21332	12.27289		4.18902	10.61886
	<i>str08</i>	$Pmm2$	4.18888	12.40442		4.27453	10.19824
	<i>str09</i>	$P4mm$	4.40111	11.22547		4.32837	9.89640
	<i>str10</i>	$P\bar{4}m2$	4.22607	12.23548		4.12803	10.88029
La ₂ Au ₈	<i>str01</i>	$I4/mmm$	4.11104	13.32528	La ₂ Cu ₈	4.13993	10.11804



ELSEVIER

Contents lists available at ScienceDirect

Journal of Magnetic Resonance

journal homepage: www.elsevier.com/locate/jmrUnusual ^{209}Bi NMR quadrupole effects in topological insulator Bi_2Se_3 Robin Guehne^{a,b,c}, Vojtěch Chlan^d, Grant V.M. Williams^b, Shen V. Chong^{b,c}, Kazuo Kadowaki^e, Andreas Pöpl^a, Jürgen Haase^{a,*}^a Felix Bloch Institute for Solid State Physics, University of Leipzig, Linnstrasse 5, 04103 Leipzig, Germany^b The MacDiarmid Institute for Advanced Materials and Nanotechnology, SCPS, Victoria University of Wellington, PO Box 600, Wellington 6140, New Zealand^c Robinson Research Institute, Victoria University of Wellington, PO Box 33436, Lower Hutt 5046, New Zealand^d Charles University in Prague, Faculty of Mathematics and Physics, V Holešových 2, 180 00 Prague 8, Czech Republic^e Division of Materials Science, Faculty of Pure and Applied Sciences, University of Tsukuba, 1-1-1, Tennodai, Tsukuba, Ibaraki 305-8573, Japan

ARTICLE INFO

Article history:

Received 21 February 2019

Revised 27 March 2019

Accepted 27 March 2019

Available online 29 March 2019

Keywords:

Energy band inversion

Spin-orbit coupling

Quadrupole interaction

Topological insulator

ABSTRACT

Three-dimensional topological insulators are an important class of modern materials, and a strong spin-orbit coupling is involved in making the bulk electronic states very different from those near the surface. Bi_2Se_3 is a model compound, and ^{209}Bi NMR is employed here to investigate the bulk properties of the material with focus on the quadrupole splitting. It will be shown that this splitting measures the energy band inversion induced by spin-orbit coupling in quantitative agreement with first-principle calculations. Furthermore, this quadrupole interaction is very unusual as it can show essentially no angular dependence, e.g., even at the magic angle the first-order splitting remains. Therefore, it is proposed that the magnetic field direction is involved in setting the quantization axis for the electrons, and that their life time leads to a new electronically driven relaxation mechanism, in particular for quadrupolar nuclei like ^{209}Bi . While a quantitative understanding of these effects cannot be given, the results implicate that NMR can become a powerful tool for the investigation of such systems.

© 2019 Published by Elsevier Inc.

1. Introduction

Ten years ago, it was predicted that Bi_2Se_3 is a topological insulator [1], i.e., in addition to the conventional insulating bulk it has a conducting surface. The corresponding metallic surface states are a consequence of strong spin-orbit coupling that leads to an inversion of bands (and atomic states) with different symmetries [1]. There is nothing new in terms of chemistry about Bi_2Se_3 , but these new electronic states are special since they are protected by topology. This may not only be of interest in physics, but also chemistry, e.g., if one thinks of heterogeneous catalysis.

For those familiar with reciprocal space and general symmetry arguments, the understanding of the concept of topological insulators is perhaps simple. However, NMR practitioners or those who are used to local thinking may experience difficulties in imagining real space consequences for these materials. In fact, it is not evident whether a bulk, local probe like NMR has something important to say about topological insulators. The characterization of the few nuclei near the material's surface, which must be affected by the special surface electrons, is a different challenge.

Nanometer-size grains with large surface to volume ratio, required for such investigations, may have different bulk properties, as well. Therefore, the bulk NMR properties of larger crystals should be understood first, an effort we pursue.

Before we address the very few NMR papers (with controversial observations), we would like to introduce a simple chemical example with consequences in topology, which we found helpful in thinking about such systems.

We believe that simple water molecules can offer some clues. Without any interference as a free gas, individual water molecules will be found in particular total angular momentum states ($J = 0, 1, 2, \dots$, with consequences for its nuclear spins according to the Pauli principle). In astrophysics, those differences, detected at great distances, prove facts about the universe [2]. However, in condensed matter systems water molecules lose some of their free gas identity due to interactions. Nevertheless, they can still have different reactivities, as recently reported [3], so that there might be even more surprises in some systems. NMR knows about this [4], but related effects are better studied for other small molecules, e.g., para and ortho molecular hydrogen [5,6]. This special quantum behavior of small molecules also affects nuclear relaxation, e.g., the famous spin-rotation interaction between nuclei and the molecular magnetic moment related to J was well studied

* Corresponding author.

E-mail address: j.haase@physik.uni-leipzig.de (J. Haase).

[7] (and it may have its analogue in topological systems, as we argue below).

If one thinks of ideal liquid water, it can only exist if enclosed in a container where it will be in equilibrium with its free gas molecules. This co-existence of liquid and gas can be looked upon in terms of topology in the sense that the water molecules are different objects if in liquid versus gas (with some appropriate time and length scales). Then, a closed container with walls that favor the liquid state has some resemblance with a topological insulator. For the latter, surface electrons have different topological properties compared to those in the bulk. Note that such scenarios are independent of the shape of the surface, cf. Fig. 1. And if there is another – appropriate – surface within the container (e.g., aerosol particles in a water atmosphere) it could be covered by a liquid film, as well. This may help comprehend why modifications of outside or inside surfaces of topological insulators are so interesting, and why a local probe like NMR can be of great help in the study of those effects.

In Bi_2Se_3 it is the strong spin-orbit coupling that disappears on the surface and changes the topology. Of course, any chemical (and subsequent electronic) surface reconstruction can complicate this simple scenario. Nevertheless, it appears from experimental surface probes that the predicted states are indeed present in this material [8].

Most of the reports on NMR of topological insulators, i.e., Bi_2Se_3 and Bi_2Te_3 , focussed on the spin $1/2$ nuclei ^{77}Se and ^{125}Te . They concerned the investigation of single crystals [9–13], powders [14–16], or nano-powders [17–19], and addressed relaxation, shifts, and the influence of surface states, but also the presence of a strong indirect nuclear spin coupling that gives rise to extensive NMR line broadening in Bi_2Se_3 [10]. The understanding of NMR in strongly spin-orbit coupled systems is not well developed. For example, as was shown very recently, Knight shift and orbital shift in spin-orbit coupled metals have rather different phenomenology compared to conventional systems [20].

There have been only a few accounts of ^{209}Bi NMR of Bi_2Se_3 [21–24]. As a spin $9/2$ system, ^{209}Bi appears to be affected by a smaller than expected quadrupole interaction of ~ 150 kHz [21]. The overall lineshape was found to be unusual, i.e., the intensity pattern of the individual transitions shows the lowest intensity for the central transition, and the intensity grows towards the outermost satellites. Young et al. [21] pointed to rapid transverse relaxation (T_2)

to be the origin of this intensity anomaly. Nisson et al. [23] measured the angular dependent spectra and found a significant loss of signal intensity when rotating the single crystal away from $c \parallel B_0$ (the magnetic field B_0 parallel to the crystal c -axis). They found discrepancies when comparing averaged orientation dependent single crystal spectra with those obtained from microscopic and nanoscopic powders. It was suggested [10] that the indirect nuclear spin coupling in these systems is behind the rapid T_2 .

Here we will address the ^{209}Bi NMR quadrupole splitting in more detail, and we will see that it can be highly unusual in these materials. We will show that the small quadrupole interaction is a consequence of the inverted band structure that affects the relative occupation of Se and Bi atomic levels. Thus, the electronic properties bear direct consequences for NMR, and there is even quantitative agreement with first-principle calculations. Even more stunning is the angular dependence of the Bi quadrupole splitting. It does *not* follow the lattice symmetry – as is usually the case in NMR. Here we find that the magnetic field appears to set the quantization axes of nuclei and electrons involved in the quadrupole interaction, not the lattice. This leads to very unusual angular dependences and new relaxation phenomena. While a theoretical understanding of the latter effects is still missing, we believe that our results prove that the quadrupole interaction can be used to gain unprecedented local insight into these fascinating materials.

2. Methods

2.1. Synthesis and characterization

Single crystals of Bi_2Se_3 (S1, S2, S4) were grown using the self-flux method. Elemental Se (99.999%, Sigma Aldrich) and Bi (99.999%, Sigma Aldrich) in three different molar ratios (S1 – $\text{Bi}_{1.95}\text{Se}_3$; S2 – $\text{Bi}_{2.00}\text{Se}_3$; S4 – $\text{Bi}_{2.05}\text{Se}_3$) were filled into quartz tubes under Ar atmosphere. The ampoules were then evacuated and sealed before they underwent heat treatment. The heating scheme reads as follows: melting and reaction at 800°C for 10 h followed by a slow cooling and crystal growth period of 100 h at a cooling rate of 2.5 K/h , finished by liquid-nitrogen quenching. Large single crystals with a few millimeters in size can easily be cleaved off the ingot. Note that the molar balance between Bi and Se as given in the chemical formulas above denotes the initial molar composition of the melt from which the crystals were grown, rather than the stoichiometry of the final product. Single crystal S3 (with dimensions $4 \times 3 \times 1\text{ mm}^3$) is the same as reported in [10] (details about the synthesis can be found there, as well). Microscopic powder of Bi_2Se_3 was obtained from grinding commercial Bi_2Se_3 flakes (Sigma Aldrich) using mortar and pestle.

We performed X-ray diffraction (XRD) of powders from each sample to confirm phase purity. Lattice constants are found to be stable across the samples with $a = 4.142(1)\text{ \AA}$ and $c = 28.640(4)\text{ \AA}$. In order to determine residual carrier concentrations in these small band-gap systems, the temperature dependent Hall effect was measured of pieces obtained from pressed and sintered powders as well as of single crystals using a Physical Properties Measurement System (PPMS) from Quantum Design Inc., USA. The carrier concentration n was found to be widely temperature independent with values between $n = 6.7(5) \times 10^{18}\text{ cm}^{-3}$ for the Se-rich material (S1) and $n = 1.7(1) \times 10^{19}\text{ cm}^{-3}$ for the Se-deficiency sample (S4).

2.2. Experimental techniques

Magnetic fields for the NMR experiments ranged from 9.4 to 11.74 T, and commercial consoles (Bruker, Tecmag) were used for excitation and detection. The home-built probes were equipped

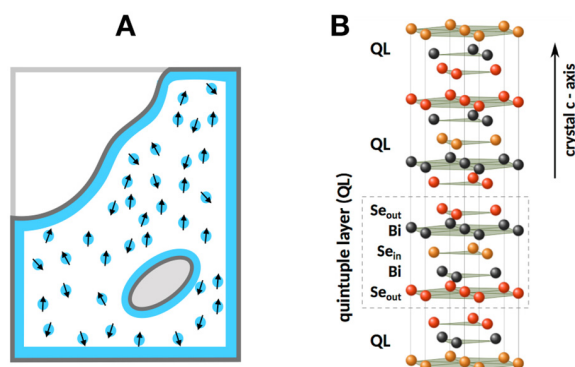


Fig. 1. A, water in a closed container at given temperature can hold two different types of molecules those in the liquid (blue full lines), or in the gas (blue circles with arrows) in particular total angular momentum (J) states. This scenario is robust and independent of the shape of inner or outer surfaces. B, schematic crystal structure of Bi_2Se_3 ; parallel planes (with Bi or Se atoms) stacked in crystal c -direction are of fcc type so that three quintuple layers ($\text{Se}_{\text{out}}\text{-Bi-Se}_{\text{in}}\text{-Bi-Se}_{\text{out}}$ planes) are needed before the stacking repeats. The unit cell consists of two chemically equivalent Bi, one Se_{in} , and two Se_{out} atoms. Any Bi_2Se_3 surface (i.e., an interface to vacuum or another regular insulator) carries topologically protected metallic states. (For interpretation of the references to colour in this figure legend, the reader is referred to the web version of this article.)

with single axis goniometers for sample rotation with an accuracy of about $\pm 2^\circ$. Single crystals of millimeter dimension were arranged within the NMR coils inside the goniometer with filling factors close to 1 to ensure maximum signal to noise. The effect on the resonance circuit's quality factor, Q , by the insertion of a single crystal into the NMR coil is significant, yielding typical Q s of 20–30. It is well established that the material shows residual bulk conductivity, but the skin effect can nearly be neglected [10].

High power solid echo sequences ($\pi/2 - \tau - \pi/2$) with typical pulse lengths of $0.75 \mu\text{s}$ were used to record the complete quadrupolar split spectra. The circuit's low quality factor ensures sufficient bandwidths for excitation and detection. Spin echo pulse sequences ($\pi/2 - \tau - \pi$) with a $\pi/2$ -pulse duration of $10 \mu\text{s}$ were employed for the selective excitation of individual transitions. Free induction decays (FIDs) were recorded of narrow resonance lines as in case of $^2\text{H}_2\text{O}$. The spin lattice relaxation ($1/T_1$) was measured with inversion or saturation recovery of parts of the spectrum (see discussion below). Nutation spectroscopy was used to distinguish different transitions in broad spectra. Here, the pulse power levels were changed rather than the pulse widths in order to keep excitation widths constant.

2.3. First principle calculations

Electric field gradients were obtained from electronic structure calculation within density functional theory (DFT) – using the all-electron full-potential WIEN2k code [25]. The sizes of atomic spheres were chosen as 2.50 and 2.42 a.u. for Bi and Se, respectively. All relevant parameters, especially the number of k-points ($18 \times 18 \times 18$ mesh) and the size of the basis set ($RK_{\text{max}}=14$), were properly converged with respect to the value of the electric field gradient of Bi. The spin-orbit interaction was included as second variational method using the scalar-relativistic approximation [26]. The exchange-correlation term was approximated by Perdew-Burke-Ernzenhof variant [27] of the generalized gradient approximation (PBE-GGA).

3. Results

3.1. Magnetic field parallel to the crystal c-axis and powder spectra

Given the single Bi site in the unit cell and its local symmetry, cf. Fig. 1B, we expect a single NMR line with a symmetric electric field gradient (EFG) that has its largest principle component (V_{zz}) along the crystal c-axis ($c \parallel Z$), thus $V_{xx} = V_{yy} = -V_{zz}/2$.

Then, if the magnetic field is along the crystal c-axis one expects the ^{209}Bi NMR resonance to be split into $2I = 9$ lines, i.e., a central transition with 4 pairs of satellite lines. This is indeed the case, as shown in Fig. 2A. We measure a quadrupole splitting of $141(3)$ kHz between the neighboring transitions (which is found to be slightly sample dependent, see below). Since the splitting is much smaller than the Larmor frequency even at the lowest employed field of 9.4 T (i.e. $\sim 64 \text{ MHz}$), the quadrupole interaction needs to be considered only in leading order.

In this very good approximation, the quadrupole Hamiltonian is typically written as,

$$\mathcal{H}_Q = \frac{3I_z^2 - I(I+1)}{4I(2I-1)} eQ \cdot V_{zz} \left\{ \frac{3 \cos^2 \beta - 1}{2} + \frac{\eta}{2} \sin^2 \beta \cos 2\alpha \right\}, \quad (1)$$

if one allows the laboratory frame (x, y, z) to be different from that of the principle axes system (X, Y, Z) of the EFG tensor. As usual, β is the polar angle between the z and Z axes, α is the azimuthal Euler angle, and $\eta = (V_{xx} - V_{yy})/V_{zz}$ is the asymmetry parameter. The nuclear spin is denoted by I , and the nuclear quadrupole moment by eQ . We adopt the usual definition of the quadrupole frequency,

$$\nu_Q \equiv \omega_Q/2\pi = \frac{3eQV_{zz}}{2I(2I-1)\hbar} \equiv \frac{3e^2qQ}{2I(2I-1)\hbar}, \quad (2)$$

and we measure from Fig. 2A, with $\beta = 0$ that $\nu_Q \approx 141(3) \text{ MHz}$. The frequency difference from the central transition for each satellite is given by,

$$\Delta\nu_\sigma = (\sigma + 1/2) \tilde{\nu}_Q(\beta, \alpha), \quad (3)$$

where $\sigma = -1/2$ denotes the central transition ($\sigma = -9/2, -7/2, \dots, +7/2$), and $\tilde{\nu}_Q$ the angular dependent quadrupole frequency,

$$\tilde{\nu}_Q(\beta, \alpha) = \nu_Q \left\{ \frac{3 \cos^2 \beta - 1}{2} + \frac{\eta}{2} \sin^2 \beta \cos 2\alpha \right\}. \quad (4)$$

Note that a spatial variation of the quadrupole frequency results in a rather typical set of linewidths of the 9 resonances: the central transition would have no broadening, but the outermost satellites would see an amplified broadening by a factor of 4 compared to the innermost satellites. Here, we find the central transition nearly as broad as the outermost satellite transitions, cf. Fig. 2A. We conclude that the principle components of the (traceless) EFG are rather well defined, and we estimate the variation of V_{zz} to be less than 5%, indicating a very homogeneous crystal. This is indeed a surprising finding since for NMR in systems where quadrupole interaction dominates, quadrupole broadened spectra are the rule. In particular for Bi_2Se_3 a material known to show considerable deviations from the average stoichiometry, e.g. as evidenced by self-doping [28], one would expect quadrupolar broadened spectra, which is clearly not the case.

Also shown, in Fig. 2B, is a typical powder spectrum. One sees immediately – we used the same frequency scale as for the single crystal spectra in Fig. 2A – that the powder spectrum has a similar width compared to the single crystal. This is *not* expected since the angular dependence in a powder does not favour crystallites with directions $\beta \approx 0$ (from near poles of the unit sphere), rather those near the equator ($\beta \approx 90^\circ$) determine the spectrum. So we expect for the powder spectrum roughly half the width in view of (4). This fact points to an unusual angular dependence, already.

To be certain that the observed resonances are due to first-order quadrupole effects, we performed nutation experiments on the individual ^{209}Bi lines, and compared the results with those obtained for ^2H NMR of deuterated water (the ^2H resonance is about 2.9 MHz below that of ^{209}Bi at 9.4 T and can thus serve as a reference – after correction for Q – for the non-selective radio frequency amplitude that is difficult to measure for the broad Bi spectrum). The results are shown in Fig. 3A. Excellent agreement with the expected effective radio frequency amplitudes for selective excitation is found for not too large power (the pulses for the selective spin echo experiments were $10 \mu\text{s}$ and $20 \mu\text{s}$ for the $\pi/2$ and π pulse, respectively, and the nutation was recorded as a function of the power level). Deviations at larger power levels are expected, given the narrowly spaced resonances and the excitation of the accompanied forbidden transitions [29].

In Fig. 3B we present the changes of the spectrum as a function of the pulse separation for the non-selective echo sequence used in Fig. 2. We observe a rather rapid decay with a $T_2 \sim 35 \mu\text{s}$, accompanied by significant spectral changes. Most notably, the central region of the spectrum decays more rapidly than the outer satellites. This leads to the pronounced dip in the center of the spectra.

In a next experiment we measured the spin echo decay of the selectively excited transitions with a $\pi/2 - \tau - \pi$ echo, cf. Fig. 4A. We observe nearly exponential decays and the selective T_2 's vary by about a factor of 5, i.e., the central transition decay is about 5 times as fast as that of the outermost lines. The overall non-selective T_2 is not very different, and for small τ similar to that

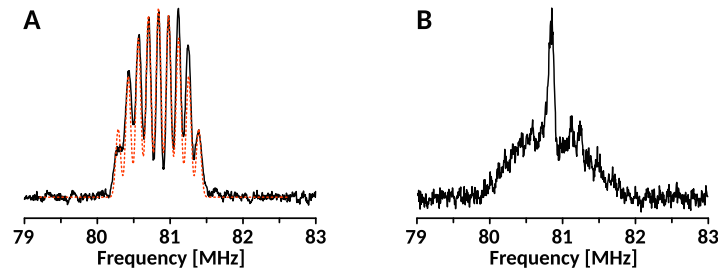


Fig. 2. ^{209}Bi NMR spectra at 11.74 T from Fourier transform of a solid echo with $\pi/2$ -pulse widths of $0.75\ \mu\text{s}$ and a pulse separation $\tau = 15.5\ \mu\text{s}$, obtained from, A, the Bi_2Se_3 single crystal S3 at $c||B_0$ (the red line is a fit to a $l = 9/2$ first-order quadrupole pattern with a magnetic broadening of about 70 kHz) and, B, a powder (see *Methods* for details). (For interpretation of the references to colour in this figure legend, the reader is referred to the web version of this article.)

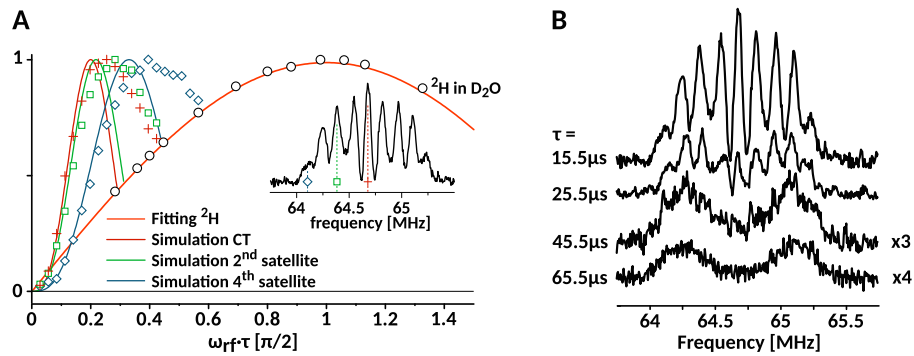


Fig. 3. A, selective spin echo nutation ($\pi/2$ -pulse width $10\ \mu\text{s}$; performed for all transitions, but shown here only for the central transition, CT, the 2nd, and the 4th lower satellite as indicated with the symbols in the inset) and the comparison with a rescaled ^2H nutation in $^2\text{H}_2\text{O}$ (open circles). Note, the deuterium nutation was fitted with a $\sin(x)$ function (red solid line) and from this result the ideal selective nutation of individually excited transitions of a quadrupolar split spin $9/2$ were simulated (colored lines). Intensities were normalized for the sake of clarity. The inset shows the spectrum with the 3 carrier frequencies used for nutation. B, the ^{209}Bi spectrum (Fig. 2A) obtained from solid echo measurements with increasing pulse separation τ as indicated. The lower two spectra ($\tau = 45.5\ \mu\text{s}$ and $\tau = 65.5\ \mu\text{s}$) have been magnified by a factor of 3 and 4, respectively. (For interpretation of the references to colour in this figure legend, the reader is referred to the web version of this article.)

of the selectively excited central region. This shows that the decay is rather independent on the number of flipped neighbors.

Also shown, in Fig. 4B, is a spectrum recorded with frequency stepped selective spin echoes. Clearly, the spectral features are lost and the faster decay in the central region leads to the double-horn spectrum that was reported earlier [21,23].

Due to the rapid spin echo decays and broad spectral features, the precise measurement of nuclear relaxation is difficult. In Fig. 5 we show the results of a selectively measured saturation recovery for $c||B_0$, as well as a nearly non-selective inversion recovery

ery near the magic angle for a single crystal (S3). One expects that the recovery after a nearly full saturation (or inversion) is considerably slower for a spin $9/2$ nucleus (since all spins are out of equilibrium) than the recovery of a selectively saturated (or inverted) central transition. This is what we observe, but we cannot exclude spectral diffusion for the selectively excited transitions. Also, we cannot say whether the observed, fast relaxation is magnetic or quadrupolar in origin.

We turn to the investigation of the angular dependences of the spectra, now.

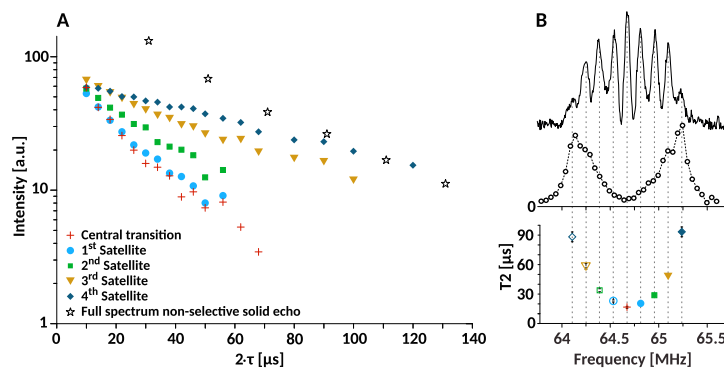


Fig. 4. A, spin echo decays (colored symbols) of the selectively excited transitions. The black open stars are data points from the full spectral intensity of the solid echo, cf. Fig. 3B. B, the upper panel shows a spectrum obtained with a nonselective solid echo with $\tau = 15.5\ \mu\text{s}$. B, middle panel shows the spin echo intensities from frequency stepped selective spin echoes (with $\tau = 45\ \mu\text{s}$). B, lower panel shows the T_2 values obtained from fits to the spin echo decays shown in A (simple exponential fits).

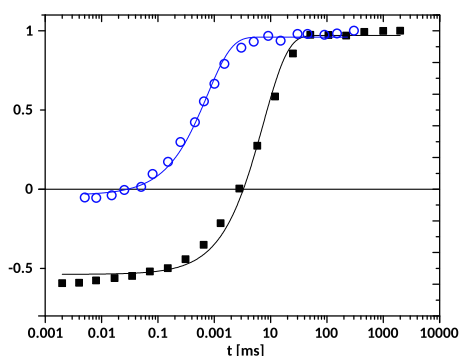


Fig. 5. Saturation recovery of the selectively excited central transition (open, blue) for $c \parallel B_0$, and inversion recovery (solid, black) near the magic angle for a broader non-selectively excited region, both obtained with sample S3. Solid lines represent simple, single exponential fits to $M(t) = (1 - f \exp(-t/T_1))$ resulting in apparent $T_1^{\text{eff}} = 0.75(5)$ ms and a non-selective $T_1 = 7.5(5)$ ms. (For interpretation of the references to colour in this figure legend, the reader is referred to the web version of this article.)

3.2. Angular dependences of single crystal spectra

Spectra for the four different samples (S1, S2, S3, S4) are shown in Fig. 6, recorded at three different angles β : first, for $\beta = 0$, i.e. with the field parallel to the crystal c -axis ($c \parallel B_0$); second, near the magic angle ($\beta \approx 54.7^\circ$); and third, for $\beta = 90^\circ$, i.e. with the field in the plane ($c \perp B_0$). While the spectra for $c \parallel B_0$ agree with the expected behavior, the spectra near the magic angle show the largest inconsistencies.

Sample S1, while similar to what one expects from (4), shows unexpected broadening at the magic angle and a missing intensity of about 30% (about 35% of the intensity are missing for $c \perp B_0$).

For sample S2 the deviations from the expected behavior are more obvious. There is substantial intensity in form of a broad resonance even at the magic angle (of up to ± 500 kHz away from the center). A somewhat larger amount of intensity is missing. Note also that there is an increased discrepancy for $c \perp B_0$, as the observed width is much larger than what is expected (about 1/2 of that for $c \parallel B_0$). Similar observations are made for samples S3

and S4, i.e., while the spectra for $c \parallel B_0$ appear to fit the symmetric quadrupole pattern, the lineshapes at the magic angle, as well as for $c \perp B_0$ are in stark disagreement with such an explanation (changes in T_2 cannot explain the discrepancies).

A more detailed angular dependence for sample S3 is presented in Fig. 7. Here it becomes obvious that the splittings as a function of β do not agree with (4). Rather, one is inclined to conclude, based on the positions of peaks and valleys, that the broad intensity – irrespective of the angle of rotation – represents the same satellite transitions. This, however, would be in striking disagreement with what one expects from angular dependent quadrupole spectra.

In order to learn more about these broad resonances, we performed NMR nutation experiments – similar to what is presented in Fig. 3, but now recorded near the magic angle (as far away in frequency as ± 600 kHz from the center). Selected results are shown in Fig. 8. Indeed, the intensity outside the central region appears to belong to satellite transitions, similar to what one finds for $c \parallel B_0$. Note that given the lattice symmetry, one demands that the asymmetry parameter is vanishingly small ($\eta \approx 0$) so that the spectra must narrow considerably near the magic angle. If this is true ($\eta \approx 0$), a rotation of the sample about the crystal c -axis for different β should leave the spectra largely unchanged (a change of α in (3)). The results are shown in Fig. 9. Since there are only minor changes to the spectra (some of them cannot be avoided since we change the orientation of the sample in the coil), we conclude on the rotational symmetry of the in-plane EFG components, i.e. we have indeed a nearly symmetric tensor independent on the orientation of the crystal with respect to the field.

The above experiments showed that the usual understanding of the spectra in terms of a quadrupole Hamiltonian (1) cannot explain the data, i.e., both coordinate systems (x, y, z and X, Y, Z) do not seem to rotate with respect to each other by changing the direction of the magnetic field with respect to the crystal axes.

4. Discussion

We begin the discussion with the spectrum for $c \parallel B_0$ in Fig. 2A. As mentioned above, in reference to the chemical structure we expect such a quadrupolar split set of lines. We find a systematic change of the quadrupole splitting from 164(2) kHz to 128(3)

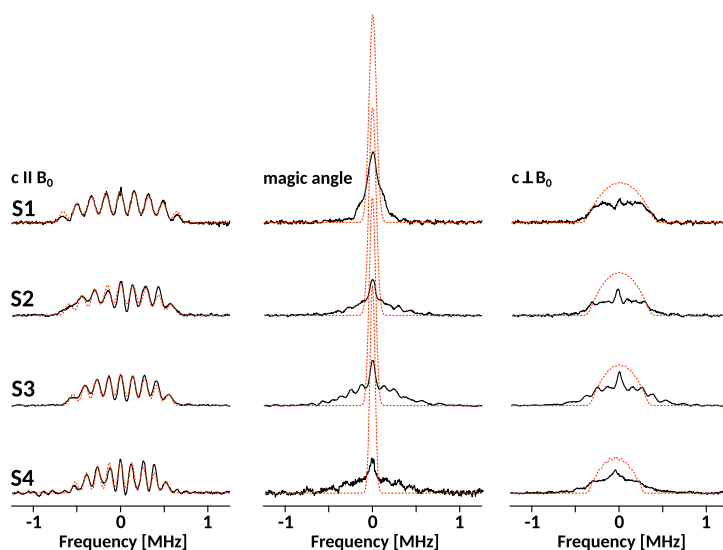


Fig. 6. Spectra (black) for the four single crystals (S1, S2, S3, S4) for three different orientations: $c \parallel B_0$ (left), the magic angle (middle), $c \perp B_0$ (right). The magnetic shifts have been subtracted, and the relative intensities are as measured (carrier concentration increases from top to bottom, see *Methods*). Red lines represent first-order quadrupole patterns fitted at $c \parallel B_0$. Apparently, the angular dependent fitted spectra that follow from (4) do not agree with the experimental data (black). (For interpretation of the references to colour in this figure legend, the reader is referred to the web version of this article.)

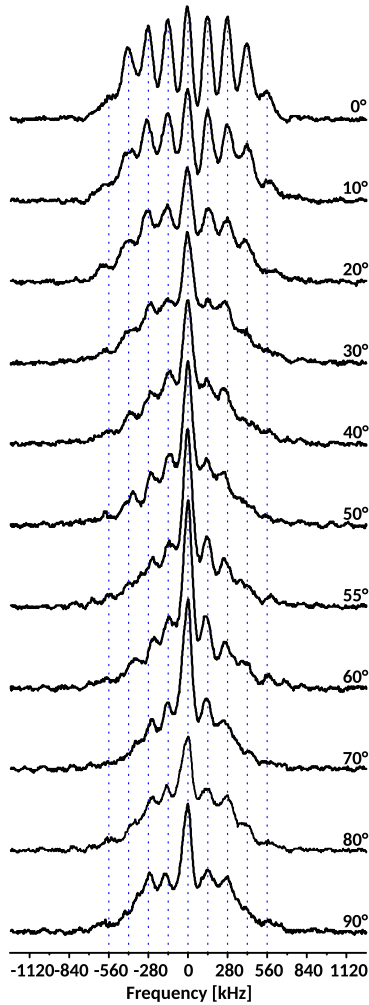


Fig. 7. Angular dependent spectra for the single crystal S3, recorded with a solid echo sequence (the pulse length and separation was 0.75 μ s and 15.5 μ s, respectively). 0° denotes $c \parallel B_0$, while 90° represents the $c \perp B_0$ orientation (the magnetic shift was subtracted). Measurements were performed at 9.4 T.

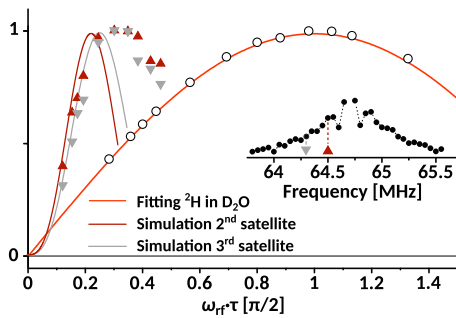


Fig. 8. Examples of selective nutation experiments at the magic angle at offset frequencies of -200 kHz (brown) and -400 kHz (gray), recorded with fixed, selective spin echo sequences ($\tau_{\pi/2} = 10 \mu$ s) as a function of the RF amplitude ($\omega_H \tau$). Intensities are normalized for the sake of clarity, also to compare with the (non-selective) ^2H nutation of $^2\text{H}_2\text{O}$ (open circles). The solid lines (brown, gray) are simulations for individual transitions (2nd and 3rd satellites) similar to those in Fig. 3. The spectral positions of the carrier are indicated in the inset compared to a spectrum recorded with frequency stepped spin echoes at the magic angle. This proves that the broad spectrum – even at the magic angle – is due to first-order quadrupole splitting. (For interpretation of the references to colour in this figure legend, the reader is referred to the web version of this article.)

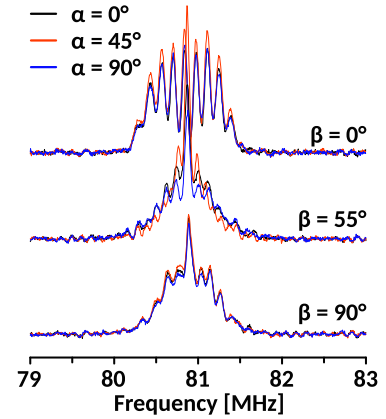


Fig. 9. Angular dependent spectra of single crystal S3. For three different values of the polar angle β , i.e., angles of the crystal c -axis with respect to the magnetic field, the crystal was rotated about the respective, new c -axis. This corresponds to a change of α in Eq. (4). Here, $\alpha = 0^\circ$ is arbitrarily chosen and does not correspond to the crystal a or b -axis (recorded at 11.74 T). This proves that the EFG is essentially axially symmetric with respect to the crystal c -axis independent of the direction of the magnetic field.

kHz, while the crystal lattice parameters obtained from XRD do not change across the different samples. And since samples S1, S2, and S4 were prepared with different molar ratios of Bi and Se atoms in order to drive self-doping effects, yielding samples with increasing excess carrier concentration n , we conclude that the EFG at ^{209}Bi in Bi_2Se_3 is related to n , as well.

These two facts and the absence of a significant inhomogeneity, we believe, point to the special band structure of topological insulators. It is known that the energy band structure near the Γ -point in the Brillouin zone is inverted due to spin-orbit coupling [1]. As a direct consequence for Bi_2Se_3 , Bi and Se states are being exchanged to some extent, which must reduce the EFG at the Bi site. Furthermore, extra electrons brought into the system by self-doping do inevitably emerge on the energetically lower most edges of the conduction band, namely in the vicinity of the Γ -point [1]. Thus, free carriers in this system must change the quadrupole splitting while reflecting the real-space characteristics of the energy band inversion.

In order to investigate this quantitatively, first-principle calculations with the Wien2k code [25] were performed. Some results are summarized in Fig. 10 and show, indeed, the role of spin-orbit coupling on the EFG. The carrier concentrations were modeled by adding small amounts of electronic charge into the rhombohedral Bi_2Se_3 unit cell: extra charges up to $0.005e$ cover the range of carrier densities in the studied samples. In order to preserve the neutrality of the unit cell, this additional charge was compensated by the same amount of positive background charge. Without spin-orbit interaction the extra charge visibly decreases the calculated Bi EFG: the extra charge occupies predominantly the $6p_z$ -states of Bi and the p - p term is the dominant contribution to the EFG for Bi. Since the Bi p_z -states are initially less occupied than the p_x - and p_y -states, the p -anisotropy decreases and we observe a monotonous decrease of the EFG tensor on Bi.

When the spin-orbit interaction is enabled, band inversion occurs – accompanied by charge transfer from p -states of Se to Bi. The occupation of Se p_z -states for both crystal sites is considerably reduced while the $6p_z$ -states of Bi are now more populated. As a consequence, the EFG on Bi abruptly decreases. The extra charge is then added also to p_x - and p_y -states, which leads to a less pronounced decrease of the EFG.

This explains our experimental results (note, that in the experiments we can only determine the absolute value of V_{zz} through v_Q , not its sign). The calculated EFG is slightly larger than the

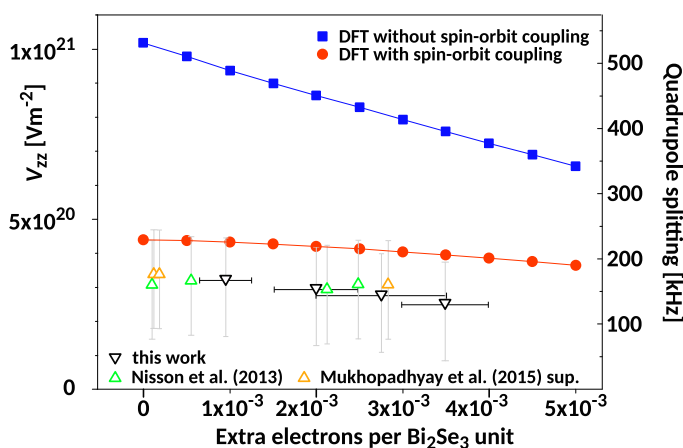


Fig. 10. Results of DFT calculations of the local EFG (V_{zz}) with (red) and without (blue) spin-orbit coupling (SOC) as a function of carrier concentration. Colored triangles give V_{zz} as obtained from measured quadrupole splittings (including literature data [22], also from the supplementary of [24]) using Eq. (2) and a quadrupole moment of $|Q_{Bi}| = 516 \text{ mb}$ [30]. The grey error bars indicate the variation of V_{zz} when assuming different $|Q_{Bi}|$, from 370 mb to 710 mb [30]. The black data points display the results of this work according to Hall-effect and shift measurements (supplementary Fig. S6 of [24]). Error bars indicate the expected variation of the carrier concentration among the samples. (For interpretation of the references to colour in this figure legend, the reader is referred to the web version of this article.)

experimentally observed one. Most likely, this discrepancy is due to imperfect optimization of the crystal lattice because of the presence of van der Waals bonds (GGA neglects dispersion interactions, only the volume was optimized, while the c/a ratio in hexagonal unit cell representation was kept fixed at value from the experiment). We estimate other sources of errors to be of the order of 0.01 (in units of 10^{21} Vm^{-2}). We conclude that the ^{209}Bi NMR quadrupole spectrum for $c\parallel B_0$ is well understood in terms of the electronic structure.

The rapid changes in the lineshapes with pulse separation (spin echo decay) were observed in earlier publications [21,23], but not fully acknowledged ([23] assumed a Redfield term). The large spectral width from the quadrupole interaction together with the rapid T_2 demand a high time resolution for NMR measurements, which is not readily available or limits signal to noise. In our experiments, by resorting to small sample volumes of $5\text{--}10 \text{ mm}^3$, we could separate the rapid T_2 from the changes in the lineshapes due to the angular dependence, sufficiently. On a qualitative level, we believe that the recently discovered large indirect spin-spin coupling between nuclei [10] is responsible for the rapid T_2 of Bi, in particular that it affects the central levels of the spectrum much more than the outer ones (a factor of almost 5 in Fig. 4). Such behavior is expected if the quadrupole interaction is not large compared to the indirect coupling, so that spin flips in the central levels are not fully suppressed [31].

We now turn to the conundrum of the angular dependence of the ^{209}Bi NMR spectra. Most surprising is the observation that the quadrupole pattern observed for $c\parallel B_0$ does not collapse near the magic angle, which is most obvious for the crystals with higher carrier concentrations ($n > 10^{19} \text{ cm}^{-3}$). We find that this effect is in agreement with hitherto published data [21–23], however, the problem was not addressed in detail, before.

One may seek an explanation for the unusual behavior in local imperfections that often cause quadrupolar broadening. In fact, the coordination of Se neighbors from a Bi atom point of view encloses an angle of $50\text{--}60^\circ$ with the crystal c -axis, i.e. close to the magic angle. Thus, the inhomogeneities arising from Se vacancies would not be very effective for $c\parallel B_0$ (when investigating Bi nuclei). However, one key problem with such attempts is that due to the measured intensities, the inhomogeneities must affect large numbers of Bi atoms, which appears highly unlikely since each Se vacancy adds 2 electrons, hence, from Fig. 10, only about 1 out of 1000 Se

atoms is missing. Only extended charge density waves scenarios could affect more nuclei, but these would certainly cause quadrupole broadened spectra also for $c\parallel B_0$, which are not observed. In addition, the various samples show very similar high quality patterns for $c\parallel B_0$, but not at other angles. Finally, the broad signal – even at the magic angle – appears to be single crystal like, similar to what one has for $c\parallel B_0$. The detailed angular dependence in Fig. 7 suggests that the spectra do not change very much at all if one turns the sample with respect to the magnetic field.

The fact that a random powder spectrum, cf. Fig. 2B, has a much larger width than what follows from the $c\parallel B_0$ spectra clearly prohibits an explanation in terms of a regular orientational dependence, already.

One might then be tempted to assume that the EFG consists of two terms. One term is caused by the chemical structure, e.g. from neighboring ionic charges, and shows the usual angular dependence given by (4). This background splitting, one would assume, should follow in the limit of zero carrier concentration, cf. Fig. 10. Then, the second part would be due to itinerant carriers and has a negative sign. For $c\parallel B_0$ the splitting is given by the sum of the two terms thus one could explain the observed shape. As one rotates the sample the second term should lead to the deviation from the regular angular dependence. However, we were not able to fit the data with such a scenario. The difficulty arises from the fact that the background term is large to begin with, and it should always disappear at the magic angle. This is not what is observed. Rather as the component with an unusual angular dependence grows, it also appears to affect the background EFG. These findings point to a single, dominant process from electrons near the Fermi surface also for the first term and there is essentially no lattice EFG (in agreement with the nearly cubic coordination of the six nearest Se atoms forming an octahedron, or the fact that we do not observe quadrupolar broadening in these inhomogeneous materials).

Therefore, all these observations led us to discard the usual picture and propose a very different scenario: an axially symmetric EFG tensor that follows the external field B_0 rather than the crystal c -axis. A possible line of (qualitative) arguments for this scenario is presented now.

The electric quadrupole interaction involves the nuclear spin. Therefore, it is written conveniently in terms of spherical tensors [32], i.e.,

$$\mathcal{H}_Q = \sum_{q=-2}^{+2} (-1)^q Q_{-q}^{(2)} V_q^{(2)}. \quad (5)$$

In this notation, one defines the nuclear quadrupole moment eQ by,

$$eQ = 2 \langle I m_I = I | Q_0^{(2)} | I m_I = I \rangle, \quad (6)$$

where $|I m_I = I\rangle$ is the eigenket of the nuclear spin (I) with the largest magnetic quantum number $m = I$. Similarly, the electric field gradient, eq , created by an electron in the state $|J, m_J\rangle$ is defined by,

$$eq = 2 \langle J m_J = J | V_0^{(2)} | J m_J = J \rangle, \quad (7)$$

where J is its total angular momentum of the electron. In terms of the spherical electronic coordinates (r_e, θ_e, ϕ_e) one has,

$$V_0^{(2)} = \sqrt{\frac{4\pi}{5}} \int \frac{\rho_e}{r_e^3} Y_{20}(\theta_e, \phi_e) d\tau_e. \quad (8)$$

In a solid, one imagines an effective electronic wave function, $|\psi_e\rangle$, since the state of the electrons is not known precisely, and one writes,

$$\langle I, m_I, \psi_e | H_Q | I, m_I, \psi_e \rangle = \sum_{q=-2}^{+2} (-1)^q \langle I, m_I | Q_{-q}^{(2)} | I, m_I \rangle \langle \psi_e | V_q^{(2)} | \psi_e \rangle. \quad (9)$$

Only the term with $q = 0$ contributes [32], i.e.,

$$\langle I, m_I, \psi_e | H_Q | I, m_I, \psi_e \rangle = \frac{3m^2 - I(I+1)}{2I(2I-1)} eQ \cdot \langle \psi_e | V_0^{(2)} | \psi_e \rangle. \quad (10)$$

In a strong magnetic field B_0 in z -direction the nuclear spin is quantized along the field axis (z -axis), and we can write,

$$\mathcal{H}_{Q_{\text{eff}}} = \frac{3I_z^2 - I(I+1)}{2I(2I-1)} eQ \cdot \langle \psi_e | V_0^{(2)} | \psi_e \rangle. \quad (11)$$

In systems without significant spin-orbit coupling one can neglect the electronic spin (that does align with the field) and consider only the resulting electronic orbital angular momentum. Then, for a given shell, it can be factorized into a radial and an angular part. The latter is tied to the chemical bonding and thus typically fixed in the crystal's unit cell. This makes the quadrupole coupling dependent on the local crystal symmetry, and yields the typical treatment of quadrupole coupling in solids, cf. (1).

We argue that in strongly spin-orbit coupled systems the situation might be different. Here, the electron has the total electron angular momentum \mathbf{J} as a good quantum number, and it may follow the field, loosely speaking. This must have consequences also for the electric field gradient $eq = 2 \langle J m_J = J | V_0^{(2)} | J m_J = J \rangle$, and such electrons should contribute to the EFG differently (in a simple molecule one can use the Wigner-Eckart theorem to relate the actual EFG to other quantum numbers). In particular, such an EFG should depend on the field axis, as well.

We think that this kind of behavior must be behind the observations for the angular dependences shown above. Bi_2Se_3 has certainly strong spin-orbit coupling with a g -factor of about 32 for $c \parallel B_0$ and 23 for $c \perp B_0$ [33]. While our explanation is lacking quantitative theory, we believe that the quadrupole interaction in these spin-orbit coupled systems must be fundamentally different. To our knowledge, this has never been proposed. Unfortunately, due to the design of the DFT calculations that limits the spin-orbit interaction to be accounted for only within the atomic spheres, we cannot model these electrons with large g -factors, or an angular dependence.

Corroborating evidence, we believe, is given by a recent report on electron paramagnetic resonance (EPR) in Bi_2Se_3 that shows spin-1/2 resonances with similar g -factors [34]. In a sense this

shows the Larmor precession of a large g -factor electron (with consequences for the quadrupole coupling).

Finally, if our conjecture is true, a finite life time of the involved electronic states should lead to a new relaxation mechanism in particular for quadrupolar nuclei, in analogy to (magnetic) spin-rotation interaction. Since the quadrupole interaction exceeds the magnetic coupling, the nuclear relaxation of Bi should then be fast and quadrupolar. Indeed, while the nuclear relaxation of Se spin-1/2 nuclei in Bi_2Se_3 is rather long (various seconds) [10], the Bi relaxation is rather short, cf. Fig. 5, and it was reported to show unusual temperature dependences, earlier [21,22]. Typically, quadrupolar relaxation is assumed to be due to phonons, but one needs Raman processes to account (qualitatively) for large rates that do not follow from single phonon scattering. The process suggested here is expected to be more effective since it couples directly to the electronic density of states, and a comparably long life time of the involved electrons can be much closer to the Larmor precession rate than in the case of phonons, and thus be more effective.

5. Conclusion

We investigated ^{209}Bi NMR quadrupole splittings for a number of Bi_2Se_3 samples with different carrier concentrations. If the magnetic field B_0 is parallel to the crystal c -axis ($c \parallel B_0$) we observe 9 equally broadened resonance lines as for an axially symmetric electric field gradient (EFG) with its largest Z -axis parallel to c for this $I = 9/2$ nucleus. Despite an expected chemical inhomogeneity the lines are only magnetically broadened. The quadrupole splittings decrease slightly with increasing carrier concentration. The data are in quantitative agreement with first-principle calculations when the magnetic field is along the crystal c -axis (for which calculations are possible), and comparison shows that the band inversion (near the Γ -point) due to the spin-orbit coupling decreases the quadrupole splitting as the inversion changes the occupation between Bi and Se orbitals.

As already the comparison of powder spectra with single crystal data for $c \parallel B_0$ shows, we discovered a non-trivial angular dependence of the quadrupole splitting if the B_0 is rotated with respect to c . While the spectra appear to maintain axial symmetry around c , the EFG's Z -axis appears to follow B_0 , i.e. it does not remain parallel to the crystal c -axis, as is typically the case for NMR of quadrupolar nuclei.

We propose that the special properties of the strongly spin-orbit coupled electrons in these topological materials must be behind this effect, and that the field leads to a non-trivial change of their quantization axis. Furthermore, since the electronic life time of these electrons leads to a time-dependent EFG, a new source of nuclear relaxation is proposed, which appears to be in agreement with the observations.

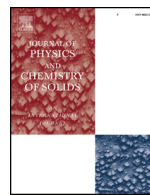
While a more detailed quantitative theory is missing, the results show that NMR can provide a quantitative measure of the band inversion, and quite possibly it holds further important information about these new class of materials.

Acknowledgement

We acknowledge stimulating discussions with I. Garate (Sherbrooke), U. Zuelicke (Wellington), O. Sushkov (Sydney), B. Fine (Moscow), M. Geilhufe (Stockholm), B. Buckley (Wellington), B. Mallet (Auckland), N. Georgieva, M. Jurkutat, and J. Nachtigal (Leipzig) and for help with XRD M. Ryan (Wellington) and H. Auer (Leipzig). R.G. acknowledges the funding by the MacDiarmid Institute. We thank the Universität Leipzig and the Deutsche Forschungsgemeinschaft for financial support.

References

- [1] Haijun Zhang, Chao-Xing Liu, Xiao-Liang Qi, Xi Dai, Zhong Fang, Shou-Cheng Zhang, Topological insulators in Bi_2Se_3 , Bi_2Te_3 and Sb_2Te_3 with a single Dirac cone on the surface, *Nat. Phys.* 5 (6) (2009) 438–442.
- [2] M. Emprechtinger, D.C. Lis, R. Rolfs, P. Schilke, R.R. Monje, C. Comito, C. Ceccarelli, D.A. Neufeld, F.F.S. van der Tak, The abundance, ortho/para ratio, and deuteration of water in the high-mass star-forming region NGC 6334 I, *Astrophys. J.* 765 (1) (2013) 61.
- [3] Ardit Kilaj, Hong Gao, Daniel Rösch, Uxia Rivero, Jochen Küpper, Stefan Willitsch, Observation of different reactivities of para and ortho-water towards trapped diazenylium ions, *Nat. Commun.* (2018) 1–7.
- [4] Benno Meier, Karel Kouřil, Christian Bengs, Hana Kouřilová, Timothy C. Barker, Stuart J. Elliott, Shamim Alom, Richard J. Whitby, Malcolm H. Levitt, Spin-isomer conversion of water at room temperature and quantum-rotor-induced nuclear polarization in the water-endofullerene $\text{H}_2\text{O}@\text{C}_{60}$, *Phys. Rev. Lett.* 120 (26) (2018) 266001.
- [5] M. Lipsicas, M. Bloom, Nuclear magnetic resonance measurements in hydrogen gas, *Can. J. Phys.* 39 (6) (1961) 881–907, <https://doi.org/10.1139/p61-095>.
- [6] Anatoly Abragam, *Principles of Nuclear Magnetism*, Oxford University Press, 1961.
- [7] Irwin Oppenheim, Myer Bloom, Nuclear spin relaxation in gases and liquids: I. Correlation functions, *Can. J. Phys.* 39 (6) (1961) 845–869, <https://doi.org/10.1139/p61-093>.
- [8] Y. Xia, D. Qian, D. Hsieh, L. Wray, A. Pal, H. Lin, A. Bansil, D. Grauer, Y.S. Hor, R.J. Cava, M.Z. Hasan, Observation of a large-gap topological-insulator class with a single Dirac cone on the surface, *Nat. Phys.* 5 (6) (2009) 398, <https://doi.org/10.1038/nphys1274>.
- [9] D. Yu. Podorozhkin, E.V. Charnaya, A. Antonenko, R. Mukhamad'yarov, V.V. Marchenkov, S.V. Naumov, J.C.A. Huang, H.W. Weber, A.S. Bugaev, Nuclear magnetic resonance study of a Bi_2Te_3 topological insulator, *Phys. Solid State* 57 (9) (2015) 1741–1745.
- [10] Nataliya M. Georgieva, Damian Rybicki, Robin Guehne, Grant V.M. Williams, Shen V. Chong, Kazuo Kadowaki, Ion Garate, Jürgen Haase, ^{77}Se nuclear magnetic resonance of topological insulator Bi_2Se_3 , *Phys. Rev. B* 93 (19) (2016) 195120.
- [11] K. Matano, M. Kriener, K. Segawa, Y. Ando, Guo-qing Zheng, Spin-rotation symmetry breaking in the superconducting state of $\text{Cu}_x\text{Bi}_2\text{Se}_3$, *Nat. Phys.* 12 (9) (2016) 852.
- [12] A.O. Antonenko, E.V. Charnaya, D. Yu. Nefedov, D. Yu. Podorozhkin, A.V. Uskov, A.S. Bugaev, M.K. Lee, L.J. Chang, S.V. Naumov, Yu. A. Perevozchikova, et al., NMR studies of single crystals of the topological insulator Bi_2Te_3 at low temperatures, *Phys. Solid State* 59 (5) (2017) 855–859.
- [13] A.O. Antonenko, E.V. Charnaya, D. Yu. Nefedov, D. Yu. Podorozhkin, A.V. Uskov, A.S. Bugaev, M.K. Lee, L.J. Chang, S.V. Naumov, Yu. A. Perevozchikova, et al., NMR study of topological insulator Bi_2Te_3 in a wide temperature range, *Phys. Solid State* 59 (12) (2017) 2331–2339.
- [14] Robert E. Taylor, Belinda Leung, Michael P. Lake, Louis-S Bouchard, Spin-lattice relaxation in bismuth chalcogenides, *J. Phys. Chem. C* 116 (32) (2012) 17300–17305.
- [15] Dimitrios Koumoulis, Belinda Leung, Thomas C. Chasapis, Robert Taylor, Daniel King Jr., Mercouri G. Kanatzidis, Louis-S. Bouchard, Understanding bulk defects in topological insulators from nuclear-spin interactions, *Adv. Funct. Mater.* 24 (11) (2014) 1519–1528.
- [16] E.M. Levin, Trevor M. Riedemann, A. Howard, Na H. Jo, Sergey L. Bud'ko, Paul C. Canfield, Thomas A. Lograsso, ^{125}Te NMR and Seebeck effect in Bi_2Te_3 synthesized from stoichiometric and Te-rich melts, *J. Phys. Chem. C* 120 (44) (2016) 25196–25202.
- [17] Dimitrios Koumoulis, Thomas C. Chasapis, Robert E. Taylor, Michael P. Lake, Danny King, Nanette N. Jarenwattananon, Gregory A. Fiete, Mercouri G. Kanatzidis, Louis-S. Bouchard, NMR probe of metallic states in nanoscale topological insulators, *Phys. Rev. Lett.* 110 (2) (2013) 026602.
- [18] Dong Min Choi, Cheol Eui Lee, ^{77}Se nuclear magnetic resonance study of the surface effect in topological insulator Bi_2Se_3 nanoparticles, *J. Korean Phys. Soc.* 72 (7) (2018) 835–837.
- [19] Dong Min Choi, Kyu Won Lee, Cheol Eui Lee, ^{125}Te nuclear magnetic resonance and impedance spectroscopy study of topological insulator Bi_2Te_3 nanoparticles mixed with insulating Al_2O_3 nanoparticles, *Mater. Res. Exp.* (2018), <http://iopscience.iop.org/10.1088/2053-1591/aaf524>.
- [20] S. Boutin, J. Ramírez-Ruiz, I. Garate, Tight-binding theory of NMR shifts in topological insulators and, *Phys. Rev. B* 94 (2016) 115204.
- [21] Ben-Li Young, Zong-Yo Lai, Zhijun Xu, Alina Yang, G.D. Gu, Z.-H. Pan, T. Valla, G. J. Shu, R. Sankar, F.C. Chou, Probing the bulk electronic states of Bi_2Se_3 using nuclear magnetic resonance, *Phys. Rev. B* 86 (7) (2012) 075137.
- [22] D.M. Nisson, A.P. Dioguardi, P. Klavins, C.H. Lin, K. Shirer, A.C. Shockley, J. Crocker, N.J. Curro, Nuclear magnetic resonance as a probe of electronic states of Bi_2Se_3 , *Phys. Rev. B* 87 (19) (2013) 195202.
- [23] D.M. Nisson, A.P. Dioguardi, X. Peng, D. Yu, N.J. Curro, Anomalous nuclear magnetic resonance spectra in Bi_2Se_3 nanowires, *Phys. Rev. B* 90 (12) (2014) 125121.
- [24] S. Mukhopadhyay, S. Krämer, H. Mayaffre, H.F. Legg, M. Orlita, C. Berthier, M. Horvatić, G. Martínez, M. Potemski, B.A. Piot, et al., Hyperfine coupling and spin polarization in the bulk of the topological insulator Bi_2Se_3 , *Phys. Rev. B* 91 (8) (2015) 081105.
- [25] P. Blaha, K. Schwarz, G.K.H. Madsen, D. Kvasnicka, J. Luitz, R. Laskowski, F. Tran, L.D. Marks, WIEN2k, An Augmented Plane Wave + Local Orbitals Program for Calculating Crystal Properties (Karlheinz Schwarz, Techn. Universität Wien, Austria), 2018.
- [26] A.H. MacDonald, W.E. Pickett, D.D. Koelling, A linearised relativistic augmented-plane-wave method utilising approximate pure spin basis functions, *J. Phys. C: Solid State Phys.* 13 (14) (1980) 2675, <http://stacks.iop.org/0022-3719/13/i=14/a=009>.
- [27] John P. Perdew, Kieron Burke, Matthias Ernzerhof, Generalized gradient approximation made simple, *Phys. Rev. Lett.* 77 (1996) 3865–3868, <https://doi.org/10.1103/PhysRevLett.77.3865>.
- [28] F.-T. Huang, M.-W. Chu, H.H. Kung, W.L. Lee, R. Sankar, S.-C. Liou, K.K. Wu, Y.K. Kuo, F.C. Chou, Nonstoichiometric doping and Bi antisite defect in single crystal Bi_2Se_3 , *Phys. Rev. B* 86 (2012) 081104, <https://doi.org/10.1103/PhysRevB.86.081104>.
- [29] J. Haase, M.S. Conradi, C. Grey, A. Vega, Population transfers for NMR of quadrupolar spins in solids, *J. Magn. Reson. Ser. A* 109 (1994) 90–97.
- [30] Jacek Bieroń, Pekka Pyykkö, Nuclear quadrupole moments of bismuth, *Phys. Rev. Lett.* 87 (13) (2001) 189–194.
- [31] J. Haase, E. Oldfield, Spin-echo behavior of nonintegral-spin quadrupolar nuclei in inorganic solids, *J. Magn. Reson. Ser. A* 101 (1) (1993) 30–40.
- [32] Igor I. Sobelman, *Atomic Spectra and Radiative Transitions*, Springer Science & Business Media, Berlin, Heidelberg, 2012.
- [33] H. Köhler, E. Wöchner, The g-factor of the conduction electrons in Bi_2Se_3 , *Phys. Stat. Solidi (b)* 67 (2) (1975) 665–675.
- [34] A. Wolos, S. Szyszko, A. Drabinska, M. Kaminska, S.G. Strzelecka, A. Hruban, A. Materna, M. Piersa, J. Borysiuk, K. Sobczak, M. Konczykowski, g-factors of conduction electrons and holes in Bi_2Se_3 three-dimensional topological insulator, *Phys. Rev. B* 93 (1) (2016) 155114.



Gallium preference for the occupation of tetrahedral sites in $\text{Lu}_3(\text{Al}_{5-x}\text{Ga}_x)\text{O}_{12}$ multicomponent garnet scintillators according to solid-state nuclear magnetic resonance and density functional theory calculations

Yu.O. Zagorodniy^{a,b,*}, V. Chlan^a, H. Štěpánková^a, Y. Fomichov^{a,b}, J. Pejchal^c, V.V. Laguta^{c,d}, M. Nikl^c

^a Charles University in Prague, Faculty of Mathematics and Physics, V Holešovičkách 2, 180 00, Prague 8, Czech Republic

^b Institute for Problems of Materials Science NAS Ukraine, Krjijanovsky 3, 03142, Kyiv, Ukraine

^c Institute of Physics, Academy of Sciences of the Czech Republic, Cukrovarnická 10, 162 00 Prague 6, Czech Republic

^d Institute of Physics, Opole University, Kopernika 11a, Opole, 45-052, Poland

ARTICLE INFO

Keywords:

Density functional theory calculation
 $\text{Lu}_3\text{Al}_{5-x}\text{Ga}_x\text{O}_{12}$
 Solid-state nuclear magnetic resonance spectroscopy

ABSTRACT

In this study, the distributions of aluminum and gallium atoms over the tetrahedral and octahedral sites in the garnet structure were investigated in mixed $\text{Lu}_3\text{Al}_{5-x}\text{Ga}_x\text{O}_{12}$ crystals by using ^{27}Al and ^{71}Ga magic angle spinning nuclear magnetic resonance (NMR) and single crystal ^{71}Ga NMR. The experimental study was supported by theoretical calculations based on density functional theory (DFT) in order to predict the trends in terms of the substitutions of Al by Ga in the mixed garnets. Both the experimental and theoretical results indicated the non-uniform distribution of Al and Ga over the tetrahedral and octahedral sites in the garnet structure, with a strong preference for Ga occupying the tetrahedral sites in the garnet structure at all Ga concentrations, despite Ga having a larger ionic radius than Al and tetrahedrons being smaller than octahedrons. The Ga occupation preference is primarily related to the involvement of Ga $3d^{10}$ electrons in interactions, and due to the different nature of the chemical bonds formed by Al and Ga when located in the tetrahedral and octahedral environments. The quadrupole coupling constants and chemical shift parameters for Al and Ga nuclei were determined for all of the compounds considered, and the electric field gradients at the Al and Ga nuclei were calculated in the DFT framework. Our results also showed that the structural relaxation after Al substitution with the larger Ga mainly occurs via deformation of the octahedrons, while leaving the tetrahedrons relatively undeformed.

1. Introduction

$\text{Lu}_3\text{Al}_{5-x}\text{Ga}_x\text{O}_{12}$ multicomponent garnets doped with rare earth ions belong to the group of functional materials with the general formula $(\text{A}_1\text{A}_2)_3(\text{B}_1\text{B}_2)_5\text{O}_{12}$ (where $\text{A}_1, \text{A}_2 = \text{Y}, \text{Lu}, \text{Gd}, \text{La}$; and $\text{B}_1, \text{B}_2 = \text{Al}, \text{Ga}, \text{Sc}$). These garnets are used widely as infrared laser media [1], blue-to-yellow downconverter phosphors in white light-emitting diodes [2,3], and very rapid and efficient scintillators with high light yields above 50000 photon/MeV [4–7], thereby approaching the theoretical limit expected for the garnet host [8].

In recent years, many studies have aimed to further improve the scintillation performance of $\text{Lu}_3\text{Al}_5\text{O}_{12}$ -based crystals via band gap engineering and by changing the energy position of the localized Ce^{3+} electronic levels within the host band gap by using multicomponent compounds with appropriate compositions (e.g., see Refs. [9–12]). In

particular, it was shown that Ga substituting for Al in garnet crystals leads to a shift of the conduction band edge to lower energies, while leaving the top of the valence band almost unchanged, thereby eliminating shallow electron traps (which arise predominantly from cation antisite defects, e.g., Lu^{3+} on Al^{3+} sites and vice versa) due to the location of their electronic levels within the conduction band. This has been demonstrated both experimentally [12,13] and theoretically [14]. The decrease in the band gap in mixed crystals is expected according to the increase in the unit cell volume when the larger Ga atoms substitute for smaller Al atoms (0.535 Å and 0.62 Å for VI-fold Al^{3+} and Ga^{3+} , respectively, and 0.39 Å and 0.47 Å for IV-fold Al^{3+} and Ga^{3+}) [15]. However, the selective shift of the conduction band edge is an exclusive property of the Ga ion and it is associated with its electronic structure.

The second effect expected due to the substitution of Al by Ga in mixed crystals of $\text{Lu}_3\text{Al}_{5-x}\text{Ga}_x\text{O}_{12}$ is a change in the distribution of Al

* Corresponding author. Institute for Problems of Materials Science NAS Ukraine, Krjijanovsky 3, 03142, Kyiv, Ukraine.

E-mail address: zagorodniy@ipms.kiev.ua (Y.O. Zagorodniy).

<https://doi.org/10.1016/j.jpcs.2018.10.027>

Received 24 May 2018; Received in revised form 26 October 2018; Accepted 29 October 2018

Available online 30 October 2018

0022-3697/ © 2018 Elsevier Ltd. All rights reserved.

over the tetrahedral and octahedral sites in the O_h^{10} – Ia3d garnet lattice [16]. Some previous studies of the classical $\text{Y}_3\text{Al}_5\text{O}_{12}$ garnet material (e.g., [17–20]) showed that Ga ions prefer to occupy the tetrahedral positions so the occupation numbers $\text{Al(IV)}/\text{Al(VI)}$ and $\text{Ga(IV)}/\text{Ga(VI)}$, which are equal to 3/2 in both $\text{Y}_3\text{Al}_5\text{O}_{12}$ and $\text{Y}_3\text{Ga}_5\text{O}_{12}$, can deviate significantly from 3/2 in the case of $\text{Y}_3\text{Al}_{5-x}\text{Ga}_x\text{O}_{12}$ solid solutions [17,20]. However, not all experimental data support the assumed preferable occupation of tetrahedral positions by Ga atoms. Thus, some results obtained using different experimental techniques suggest that Ga preferably occupies octahedral positions with a larger volume (e.g., see Refs. [21–23]). It has also been indicated that the ionic radius or differences in the electronegativity of the cations do not necessarily play key roles in the distribution of cations over the tetrahedral or octahedral positions.

Moreover, different theoretical calculations performed for some $\text{Y}_3\text{Al}_{5-x}\text{Ga}_x\text{O}_{12}$ compounds with different substitution degrees did not yield consistent results. Thus, calculations performed for the 80- and 160-atoms in the $\text{Y}_3\text{Al}_5\text{O}_{12}$ supercell showed that moving one Ga atom from a tetrahedral site to an octahedral site had an energy cost of 0.21 eV in both supercells, but it decreased to 0.17 eV for some higher Ga doping levels [24]. However, calculations of the formation energies for $\text{Y}_3\text{Al}_{2-y}^{\text{tet}}\text{Ga}_y^{\text{oct}}\text{Al}_3^{\text{tet}}\text{O}_{12}$ and $\text{Y}_3\text{Al}_{3-y}^{\text{oct}}\text{Al}_3^{\text{tet}}\text{Ga}_y^{\text{tet}}\text{O}_{12}$ compounds, where $y = 0.125$, showed that substituting Al^{oct} by Ga was slightly more favorable than substituting Al^{tet} , with an energy difference of 50 meV [23].

The substitutions of Al for Ga and vice versa in the octahedral or tetrahedral positions also cause different changes in the lattice parameters [24], and they obviously have different effects on the electronic band structure of the garnet host material. Therefore, understanding the cation distribution over the tetrahedral and octahedral sites is important for engineering mixed garnet crystals with predictable optical and scintillation properties. In particular, we studied the influence of the Ga content on the luminescence properties of $(\text{Y,Lu})_3\text{Al}_{5-x}\text{Ga}_x\text{O}_{12}$ garnets [25], where nuclear magnetic resonance (NMR) was used to determine the cation distributions in these crystals.

In the present study, we systematically investigated the Al and Ga occupancies of the tetrahedral and octahedral sites in the garnet structure to facilitate important applications of Ce-doped $\text{Lu}_3\text{Al}_{5-x}\text{Ga}_x\text{O}_{12}$ mixed garnet crystals ($x = 0, 1, 2, 3, 4, 5$) by using the ^{27}Al and ^{71}Ga solid-state NMR technique. We found that the actual Al and Ga site occupations could be determined from NMR spectra with high precision. NMR is a unique approach for quantifying the site occupancy in a material (in both liquid and solid states) [26] and the optimal tool for this task. In $\text{Lu}_3\text{Al}_{5-x}\text{Ga}_x\text{O}_{12}$, both the Al and Ga cations are suitable for NMR measurements, as demonstrated previously for $\text{Y}_3\text{Al}_{5-x}\text{Ga}_x\text{O}_{12}$ solid solutions [18,19,27]. The main advantage of NMR compared with other methods that are sensitive to ionic occupation in lattices, such as X-ray diffraction, is its universality, insensitivity to long-range atomic ordering, and the ability to provide information concerning local deformations that arise due to slightly different ion sizes. To the best of our knowledge, the determination of the Al and Ga distributions over the cation sites by X-ray diffraction has only been successfully achieved for high quality single crystals of $\text{Y}_3\text{Al}_{5-x}\text{Ga}_x\text{O}_{12}$ solid solutions [17,18].

Our experimental study was supported by theoretical calculations based on the density functional theory (DFT) in order to explain the trends in terms of the Al and Ga distributions over different positions in the garnet structure and to clarify unusual variations in the electric field gradients (EFGs) in the $\text{Lu}_3\text{Al}_{5-x}\text{Ga}_x\text{O}_{12}$ lattice. The theoretical calculations were performed for all of experimentally studied compositions, thereby facilitating direct comparisons of the experimental and theoretical results.

2. Methods

The crystals were grown using the micro-pulling down method with radiofrequency inductive heating [28]. An iridium crucible was used

with a die diameter of 3 mm. Growth occurred under an N_2 atmosphere using a $\langle 111 \rangle$ and $\langle 100 \rangle$ oriented $\text{Y}_3\text{Al}_5\text{O}_{12}$ single crystal as the seed. The starting materials were prepared by mixing 4 N purity Lu_2O_3 , Al_2O_3 , and Ga_2O_3 powders. Ce was added at a concentration of 0.2 at. %. The crystals were in the form of rods with a diameter of 3 mm and length of 2–3 cm.

^{27}Al and ^{71}Ga static NMR spectra were measured at room temperature using a Bruker Avance II spectrometer at Larmor frequencies of $\nu_L = 104.28$ and 122.06 MHz, respectively. Magic angle spinning (MAS) spectra were measured for both nuclei using a Bruker Avance III HD spectrometer equipped with a high speed MAS probe at Larmor frequencies of $\nu_L = 130.40$ and 152.62 MHz for ^{27}Al and ^{71}Ga , respectively. A single pulse sequence with a radio frequency field strength of 110 kHz and short pulses of 0.38 μs , which corresponded to rotation of the net magnetization by the angle $\pi/12$, was applied to ensure that quantitatively correct measurements of the ^{27}Al MAS NMR spectra were obtained, even for aluminum located in lattice positions with very different values for the quadrupole coupling constant. For each sample, 512 to 3072 scans were accumulated with a recycle delay of 80 s, depending on the Al concentration. A spectral width of 312 kHz and spinning speed of 22 kHz were used to observe the undistorted central transition of ^{27}Al in both the tetrahedral and octahedral positions. ^{27}Al NMR spectra were referenced to an external standard comprising Al (NO_3)₃. The presence of paramagnetic Ce^{3+} ions did not affect the shape of the NMR spectral lines but they substantially shortened the relaxation time for ^{27}Al nuclei, thereby allowing the usage of relatively short relaxation delays.

^{71}Ga static NMR spectra were measured utilizing the $90^\circ x - \tau - 90^\circ y - \tau$ spin echo pulse sequence. The four phase (xx , xy , $x-x$, $x-y$) “exorcycle” phase sequence was used to form echoes with minimal distortions due to anti-echoes, ill-refocused signals, or piezo-resonances [29]. In the case of the ^{71}Ga NMR spectrum with a linewidth up to 300 kHz for the $1/2 \leftrightarrow -1/2$ central transition, only selective excitation was achievable. In order to exclude the influence of the angle dependence of quadrupolar interactions on the signal intensity, $\pi/8$ pulse lengths of 0.5 μs were still used with 5 s delays between the scans. The ^{71}Ga MAS NMR spectra were measured with a rotation speed of 20 kHz based on a single pulse sequence with pulse length of 0.8 μs and recycle delay of 15 s. The external standard was 1.0 M $\text{Ga}(\text{NO}_3)_3$.

The electronic structures of the studied garnets were calculated within the DFT using the full-potential all-electrons augmented plane wave + local orbitals method implemented in the WIEN2k code [30]. The radii of the atomic spheres in the atomic units for Lu, Al, Ga, and O were 2.35, 1.70, 1.75, and 1.61, respectively. The atomic coordinates and lattice parameters were optimized for each structure with respect to the total energy and within the set space group symmetry. Special care was taken to check how the geometry optimization (lattice parameters and atomic forces) and the key calculated quantities (EFGs and density of states) converged with the size of the basis set and with the number of k-points. The final appropriate value for the RK_{max} parameter was 7.0 and the matrix size was determined as about 9000 (double the size for structures without I-centration). The number of k-points in the irreducible part of the Brillouin zone was between 14 and 45, and thus a mesh of $6 \times 6 \times 6$ was provided for each structure. The charge density and potentials were Fourier expanded up to the largest k-vector $G_{\text{max}} = 14 \text{ Ry}^{1/2}$ ($\sim 190 \text{ eV}^{1/2}$). The Perdew-Burke-Ernzerhof variant [31] of the generalized gradient approximation was used to approximate the exchange-correlation potential.

3. Results and discussion

Al and Ga ions can occupy two different crystallographic positions in the $\text{Lu}_3\text{Al}_{5-x}\text{Ga}_x\text{O}_{12}$ garnets with tetrahedral (Al(IV), Ga(IV)) and octahedral (Al(VI), Ga(VI)) oxygen environments [16]. Both these cations are suitable for NMR measurements, but the ^{27}Al isotope, which has nuclear spin $I = 5/2$ and a natural abundance of 100%, is easiest to

measure. Ga has two isotopes, i.e., ^{69}Ga and ^{71}Ga , where both have spin = 3/2 and natural abundances of 60% and 40%, respectively. All of these nuclei possess a quadrupole moment eQ , which interacts with the EFG generated by the surrounding ionic charges. The quadrupole interaction is usually expressed by the quadrupole coupling constant: $C_q = e^2QV_{zz}/h$, and the asymmetry parameter of the EFG tensor by: $\eta = \frac{V_{xx} - V_{yy}}{V_{zz}}$, where e is the electron charge and V_{ii} are the components of the EFG tensor in its principal axes system with $|V_{zz}| \geq |V_{xx}| \geq |V_{yy}|$. In the $1a\bar{3}d$ unit cell of the garnet structure [16], there are 24 structurally equivalent tetrahedral positions and 16 structurally equivalent octahedral positions available for Al/Ga cations. For both types of sites, the EFG tensor has axial symmetry ($\eta = 0$) and the main axis of the EFG tensor is aligned along the $\langle 100 \rangle$ and $\langle 111 \rangle$ cubic directions for the tetrahedral and octahedral sites, respectively [32,33]. In the case of solid solutions, the axial symmetry of the EFG tensor can be broken because some of the Al ions are substituted for Ga ions.

Quantitatively, all of the spectra measured for the static samples were interpreted using the spin Hamiltonian [34,35], which results in the following frequencies for the satellite and central transitions:

$$\nu_m^{(1)} = \nu_L + \left(m - \frac{1}{2}\right) \nu_Q \left\{ \left[(3 \cos^2 \theta - 1)/2 \right] + \frac{1}{2} \eta \sin^2 \theta \cos 2\varphi \right\} \quad (1)$$

$$\nu_{1/2}^{(2)} = \nu_L - \frac{\nu_Q^2}{16\nu_L} \left(I(I+1) - \frac{3}{4} \right) f_\eta(\theta, \varphi) + \nu_L [1 + \delta_{\text{iso}} + \delta_{\text{ax}}(3 \cos^2 \theta - 1) + \delta_{\text{aniso}} \sin^2 \theta \cos 2\varphi], \quad (2)$$

where $\nu_Q = \frac{3C_q}{2I(2I-1)}$ is the quadrupole frequency, and θ, φ are the Euler angles of the external magnetic field referenced to the principal x, y, and z axes system of the EFG tensor. Eq. (1) describes the frequency locations of satellite transitions as first-order perturbations of the Larmor frequency ν_L . Consequently, the frequency shift related to magnetic field screening at nucleus (chemical shift) is small compared with the quadrupole frequency, and thus it is neglected. However, the shift of the central transition has only a second-order effect on the quadrupole frequency (Eq. (2)), so the chemical shift mechanism is essential. Its contribution to the central transition frequency is described by the last term in Eq. (2), where δ_{iso} , δ_{ax} , and δ_{aniso} are the isotropic, axial, and anisotropic components of the chemical shift tensor, respectively, for which the principal axis system is assumed to coincide with the coordinate system of the EFG tensor. The function $f_\eta(\theta, \varphi)$ has a cumbersome form and its actual expression was presented in a previous study [34]. The MAS spectra obtained under rotation conditions were interpreted using the time-dependent spin Hamiltonian, which includes all of the interactions mentioned above. Its full analytic representation was presented in a previous study [35].

3.1. ^{27}Al NMR

The ^{27}Al static NMR spectra for the $\text{Lu}_3\text{Al}_5\text{O}_{12}$ and $\text{Lu}_3\text{Al}_2\text{Ga}_3\text{O}_{12}$ ground single crystals are presented in Fig. 1 as examples. In addition to the narrow intense signal belonging to the central $1/2 \leftrightarrow -1/2$ transition (CT), the NMR spectrum for $\text{Lu}_3\text{Al}_5\text{O}_{12}$ has highly pronounced singularities corresponding to the $\pm 3/2 \leftrightarrow \pm 1/2$ satellite transitions (ST) of both Al(IV) and Al(VI), from which the quadrupole parameters can be calculated. In contrast to $\text{Lu}_3\text{Al}_5\text{O}_{12}$, the singularities obtained from the satellite transitions in the mixed $\text{Lu}_3\text{Al}_{5-x}\text{Ga}_x\text{O}_{12}$ compounds are broadened and completely smeared out (see the bottom spectrum in Fig. 1) due to the distribution of quadrupole parameters in these samples, where the local environment for Al varies among sites. On the other hand, the linewidth of the CT, which is essentially unaffected by this distribution, is only about 20 kHz for all of the samples.

The ^{27}Al MAS NMR spectra obtained for all of the samples with a spinning rate of 22 kHz are presented in Fig. 2. This rotation frequency exceeds the linewidth of the CT for the static spectrum, so all of the magnetization from the CT is concentrated within two narrow lines,

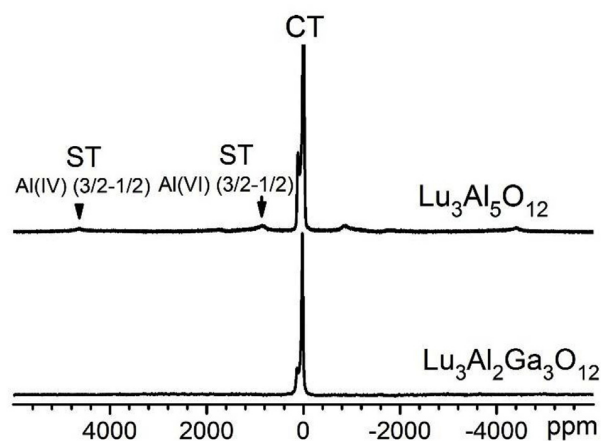


Fig. 1. ^{27}Al static nuclear magnetic resonance spectrum for $\text{Lu}_3\text{Al}_5\text{O}_{12}$ and $\text{Lu}_3\text{Al}_2\text{Ga}_3\text{O}_{12}$. (CT – the central transition). Arrows denote some of the singularities corresponding to the satellite transitions (ST).

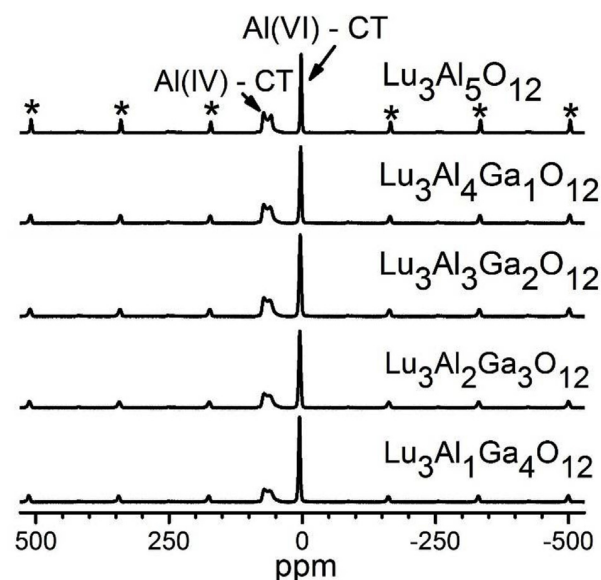


Fig. 2. ^{27}Al magic angle spinning nuclear magnetic resonance spectra for $\text{Lu}_3\text{Al}_{5-x}\text{Ga}_x\text{O}_{12}$ compounds obtained at a rotation speed of 22 kHz where the spinning side bands belonging to the Al(VI) satellite transitions are denoted by asterisks (CT – the central transition). The frequency region is cut at ± 530 ppm in order to show only a few of the first spinning side bands.

which are separated due to the difference in the chemical shifts at the Al(IV) and Al(VI) sites [32]. A set of spinning side bands (ssb) originating from the satellite transitions is also visible in the MAS NMR spectra.

The spectral line of the Al(IV) CT has a distinct shape due to strong quadrupole interactions (Fig. 2). Substituting Al by Ga in the mixed compounds leads to the distribution of the EFG values on Al nuclei, which results in some smearing of the spectral line edges. However, the spectral line corresponding to the central transition of Al(IV) still provides information concerning the quadrupole interactions. The quadrupole interaction parameters obtained after fitting the Al(IV) central transition line for all of the compounds are listed in Table 1, which shows that partial substitutions of Al by Ga generally do not change the mean EFG value, thereby indicating that the Al oxygen tetrahedrons remain mainly unchanged in the mixed compounds.

The EFG values at octahedral sites are almost six times smaller than those at tetrahedral sites (the determination of their actual values is described in the following), so the CT for Al(VI) is completely averaged

Table 1

Al(IV) NMR parameters determined for the mixed $\text{Lu}_3\text{Al}_{5-x}\text{Ga}_x\text{O}_{12}$ compounds from MAS NMR spectra.

Compound	δ_{iso} (ppm)	C_q (kHz)	η
$\text{Lu}_3\text{Al}_5\text{O}_{12}$	79.2	6330	0
$\text{Lu}_3\text{Al}_4\text{Ga}_1\text{O}_{12}$	79.2	6270	0.02
$\text{Lu}_3\text{Al}_3\text{Ga}_2\text{O}_{12}$	78.8	6200	0.03
$\text{Lu}_3\text{Al}_2\text{Ga}_3\text{O}_{12}$	78.5	6200	0.004
$\text{Lu}_3\text{AlGa}_4\text{O}_{12}$	78.2	6230	0.01

to one narrow line with a Gaussian shape. Its full width at half maximum (FWHM) changes from 2.9 ppm at $x = 0$ up to 4.6 ppm at $x = 2$ (Table 2), thereby indicating that the broadest distribution of the NMR parameters occurs for the $\text{Lu}_3\text{Al}_3\text{Ga}_2\text{O}_{12}$ solid solution. Clearly, the isotropic chemical shift determined directly from the MAS spectra increases gradually from 2.2 ppm in $\text{Lu}_3\text{Al}_5\text{O}_{12}$ up to 5.3 ppm in $\text{Lu}_3\text{AlGa}_4\text{O}_{12}$.

The Al(VI) quadrupole parameters were calculated based on the full fit of the ssb manifold that originated from the satellite transitions ($\pm 3/2 \leftrightarrow \pm 1/2$, $\pm 5/2 \leftrightarrow \pm 3/2$). In contrast to $\text{Lu}_3\text{Al}_5\text{O}_{12}$, the shape of the ssb manifold in the spectra for mixed $\text{Lu}_3\text{Al}_{5-x}\text{Ga}_x\text{O}_{12}$ compounds is smeared out due to the distribution of the EFG parameters. To increase the precision when determining the Al(VI) quadrupole parameters in mixed compounds, a larger number of ssbs were accumulated in the region of ± 0.55 MHz with a rotation speed of 5 kHz (Fig. 3). The intensities of the sidebands were also corrected for the Q-factor of the NMR probe by using a simple Lorentz function. Considering that the ssb envelope mimics the shape of the static spectrum to some extent (but not completely), the initial values of the quadrupole parameters were obtained by fitting the ssb envelope with the lineshape corresponding to the NMR spectrum of a static sample. As shown in a previous study [36] and according to our measurements for $\text{Lu}_3\text{Al}_5\text{O}_{12}$, the quadrupole parameters obtained from this fitting are lower than the real ones. However, the calculation of the static spectrum is rapid so they can be used as good starting values for further fitting of the sidebands manifold, and they indicate the correct trends in the behavior of the quadrupole parameters for various cation substitution degrees.

The spectrum of the satellite transitions for static samples was simulated using Eq. (1). The distribution of the quadrupole frequencies arising from EFG fluctuations was described by a Gaussian function. The satellite transitions spectrum was obtained by subsequently integrating over all the mutual orientations of the EFG tensor and magnetic field:

$$I(\nu) = \sum_m \int_0^{\pi/2} \int_0^{2\pi} \sqrt{\frac{\ln 2}{\pi}} \frac{\sin \theta}{\Delta} \exp \left[- \left(\frac{\nu - \nu_m^{(1)}(\theta, \varphi)}{\Delta} \right)^2 \right] d\theta d\varphi, \quad (3)$$

where the parameter Δ characterizes the width of the quadrupole frequency distribution and the frequency $\nu_m^{(1)}(\theta, \varphi)$ is defined by Eq. (1).

Subsequent simulation of the Al(VI) ssb manifold was performed by considering that the actual EFG distribution originates from the random distribution of Al and Ga atoms located in the nearest environment for Al(VI). Therefore, a finite number of different EFG values should be

Table 2

Al(VI) NMR spectral parameters determined for the mixed $\text{Lu}_3\text{Al}_{5-x}\text{Ga}_x\text{O}_{12}$ compounds from the MAS NMR spectra of the CT, simulation of the ssb envelope, and using the direct fit for all the ssbs.

Compound	δ_{iso} (ppm)	FWHM (ppm)	C_q (kHz)	η	δ_{iso} (ppm)	C_q (kHz)	η
	CT only		ssb envelope		all sidebands		
$\text{Lu}_3\text{Al}_5\text{O}_{12}$	2.2	2.9	1100	0	2.6	1230	0
$\text{Lu}_3\text{Al}_4\text{Ga}_1\text{O}_{12}$	2.9	3.9	1400	0.3	3.8	1560	0.4
$\text{Lu}_3\text{Al}_3\text{Ga}_2\text{O}_{12}$	3.8	4.6	1550	0.35	4.6	1690	0.4
$\text{Lu}_3\text{Al}_2\text{Ga}_3\text{O}_{12}$	4.7	4.4	1650	0.35	5.4	1820	0.4
$\text{Lu}_3\text{AlGa}_4\text{O}_{12}$	5.3	3.7	1750	0.3	6.3	1900	0.4

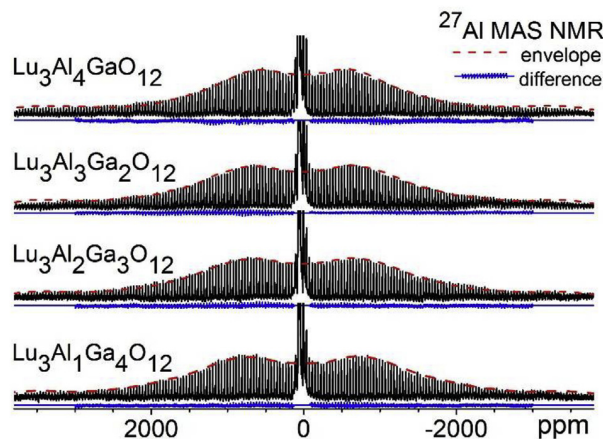


Fig. 3. ^{27}Al magic angle spinning nuclear magnetic resonance (MAS NMR) spectra obtained for $\text{Lu}_3\text{Al}_{5-x}\text{Ga}_x\text{O}_{12}$ at a rotation speed of 5 kHz as well as sidebands envelope simulation, the difference between the measured spectrum, and the best fit for all sideband manifolds (only the region corresponding to Al(VI) satellite transitions sidebands is presented in the difference curve). The sideband intensities were corrected by considering the Q-factor for the NMR probe.

used instead of a smooth EFG distribution during the simulation of the spectra. Furthermore, fixed parameters for Al(IV) were used in the simulation. The mean values of the quadrupole parameters obtained in this manner are listed in Table 2. To illustrate the precision of the simulation, the differences between the experimental spectra and simulated spectra are presented in Fig. 3 as blue solid lines for the region where the main signal from Al(VI) ST is located, where the Al(IV) ST and CT regions were excluded from the calculation.

In contrast to the Al(IV) tetrahedral sites (Table 1), the EFG parameters at Al(VI) octahedral sites essentially depend on Ga substitution, which indicates that oxygen octahedrons exhibit marked deformation after substituting Al by Ga. The extent of octahedron deformation increases steadily with the Ga content. The increase in the average value of the chemical shift for the line corresponding to Al(VI) with the gradual substitution of Al by Ga is in good agreement with the electronegativities of the Al and Ga atoms, which have Pauling values of 1.61 and 1.81, respectively. Substituting Al by more electronegative Ga atoms decreases the total charge on the oxygen framework, and additional transfer of the electron density occurs from Al to O atoms. This decreases the net charge on the Al atoms, thereby leading to lower shielding of the external magnetic field by the Al electronic shell. In addition, Ga prefers to occupy the tetrahedral positions (see below), so Al(VI) ions in the mixed structure are predominantly surrounded by Ga ions, which leads to essential changes in the EFG and chemical shift parameters compared with the $\text{Lu}_3\text{Al}_5\text{O}_{12}$ compound. Thus, in the case of disordered $\text{LuAl}_3\text{Ga}_2\text{O}_{12}$, a larger number of possible Al environments leads to a broader distribution of the chemical shifts.

The ^{27}Al MAS NMR spectral lines obtained from both Al structural positions are well separated by the chemical shift, so we can directly

Table 3

Occupation numbers (Al(IV)/Al(VI) ratio) determined directly for the mixed $\text{Lu}_3\text{Al}_{5-x}\text{Ga}_x\text{O}_{12}$ compounds from the ^{27}Al MAS spectra using the intensities ratio of the CTs and those obtained after simulating the full spectra.

Compound	Al(IV)/Al(VI) ratio	
	CT only	full simulation
$\text{Lu}_3\text{Al}_5\text{O}_{12}$	1.34	1.51
$\text{Lu}_3\text{Al}_4\text{GaO}_{12}$	1.08	1.19
$\text{Lu}_3\text{Al}_3\text{Ga}_2\text{O}_{12}$	0.92	1.01
$\text{Lu}_3\text{Al}_2\text{Ga}_3\text{O}_{12}$	0.78	0.84
$\text{Lu}_3\text{AlGa}_4\text{O}_{12}$	0.72	0.76

calculate the occupation numbers for Al located in the different positions, which should be simply given by the ratio of the integral intensities of the Al(IV) and Al(VI) spectral lines in principle. The ratios calculated for the CTs are presented in Table 3. However, the ratio of the Al(IV)/Al(VI) intensities obtained for pure $\text{Lu}_3\text{Al}_5\text{O}_{12}$ does not equal the value of 1.5 expected for the stoichiometric compound. This significant difference is caused by the overlap of the central transition line with lines originating from satellite transitions, which have sufficiently high intensity at this rotation speed (Fig. 2). The intensities of the ST lines are different for the Al(IV) and Al(VI) sites due to the difference in their quadrupole parameters, which determines the shape of the side bands manifold and their contribution to the overlap with the CT. In order to obtain the correct value of the Al(IV)/Al(VI) ratio from the intensity of the CTs, it is necessary to subtract part of the magnetization (spectral intensity) belonging to the ST from the CT region, or to obtain the full spectrum with all STs, where the total intensity of CT + STs belonging to tetrahedral (octahedral) Al is proportional to the number of Al atoms in tetrahedrons (octahedrons).

The full spectrum for the studied compounds exceeds the spectral width used in the experiment, so the quadrupolar parameters for both Al(IV) and Al(VI) sites were determined from the experimentally accumulated spectrum by fitting, and the entire spectrum was subsequently simulated in the range up to $4 \times \nu_Q$. This procedure considers all of the side bands from all the transitions that are not directly visible in the experimental spectrum, so the ratio of the integral intensities for the entire lines gives the correct Al occupation numbers. Using this algorithm, we first checked the Al occupation numbers for $\text{Lu}_3\text{Al}_5\text{O}_{12}$. The MAS spectrum can be well fitted with the following parameters [37]: $C_q = 1230$ and 6250 kHz for Al(VI) and Al(IV), respectively, and $\eta = 0$ for both sites. The Al(IV)/Al(VI) ratio calculated for $\text{Lu}_3\text{Al}_5\text{O}_{12}$ equals 1.51(1), which is within the error range and it agrees with the expected value of 1.5.

The quadrupole parameters obtained for the mixed compounds allowed us to calculate the actual Al(IV)/Al(VI) ratio from the MAS NMR spectra for all of the compounds. The Al(IV)/Al(VI) ratios obtained after simulating the spectra are listed in Table 3.

It should be noted that the envelope of the sidebands is very smooth in the case of mixed $\text{Lu}_3\text{Al}_{5-x}\text{Ga}_x\text{O}_{12}$ compounds, so almost the same correct Al(IV)/Al(VI) ratio can be obtained from MAS spectra simply by subtracting the intensity of the first sideband (measured at a rotation of 22 KHz) from the intensity of the central line.

3.2. ^{71}Ga NMR

The ^{71}Ga static NMR spectrum obtained for the $\text{Lu}_3\text{Ga}_5\text{O}_{12}$ sample from the ground single crystal is presented in Fig. 4 with its best fit. The spectrum was analyzed in a similar manner to that described in a previous study [27]. The central transition spectral line for Ga(VI) is approximately located between 200 and -200 ppm, and it was fitted using $C_q = 5300$ kHz and $\eta = 0$. The central transition spectrum for Ga(IV) spreads from 800 to -800 ppm and it yields $C_q = 13650$ kHz and η

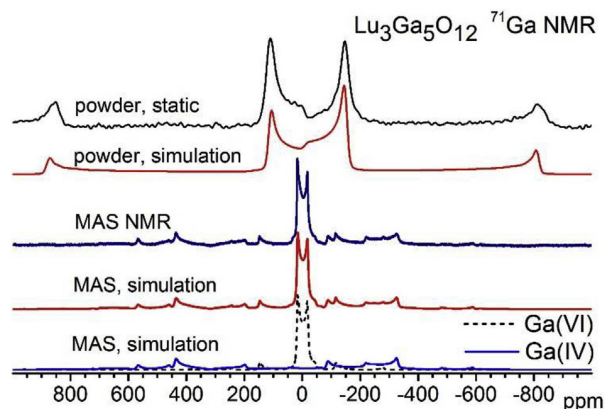


Fig. 4. ^{71}Ga nuclear magnetic resonance (NMR) static and magic angle spinning (MAS) spectra (rotation speed of 20 kHz) for the ground $\text{Lu}_3\text{Ga}_5\text{O}_{12}$ single crystal, and their best fit.

= 0.

The ^{71}Ga MAS NMR spectrum for $\text{Lu}_3\text{Ga}_5\text{O}_{12}$ is also presented in Fig. 4. The spectral line for the Ga(VI) central transition is clearly visible near 0 ppm. At this rotation speed, the Ga(VI) lineshape has distinct singularities related to quadrupole interactions, which allows the quadrupole parameters to be calculated. However, the Ga(IV) central transition cannot be resolved well at the available rotation speeds because it spreads over 200 kHz in the static spectrum. Nevertheless, all the features presented in the ^{71}Ga MAS NMR spectrum can be unambiguously fitted with good accuracy even for the spectrum obtained at a rotation of 20 kHz (Fig. 4). This contrasts with the fitting of the static spectrum, where different combinations of quadrupole interactions and chemical shift anisotropies could result in similar spectra. We note that quadrupole parameters obtained after simulating the MAS spectra yield an almost correct lineshape for the static spectrum, which validates the analysis of the MAS spectra for all of the samples.

The ^{71}Ga MAS NMR spectra for all of compounds are presented in Fig. 5. The quadrupole parameters obtained from the best fits of these spectra are summarized in Table 4.

As the gallium content increases, the quadrupole constant C_q exhibits analogous trends to ^{27}Al , where C_q increases for Ga located in an octahedral environment whereas it is almost unchanged in a tetrahedral environment. The very large differences between the C_q values for Ga and Al atoms located in similar environments are connected to the different values of the Sternheimer antishielding factors ("a measure of the magnification of the EFG at the nucleus due to distortion of the

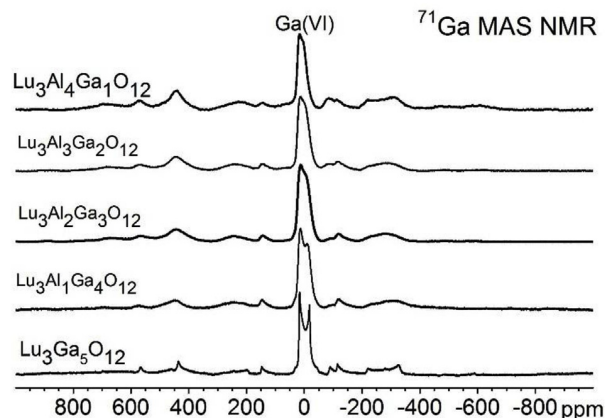
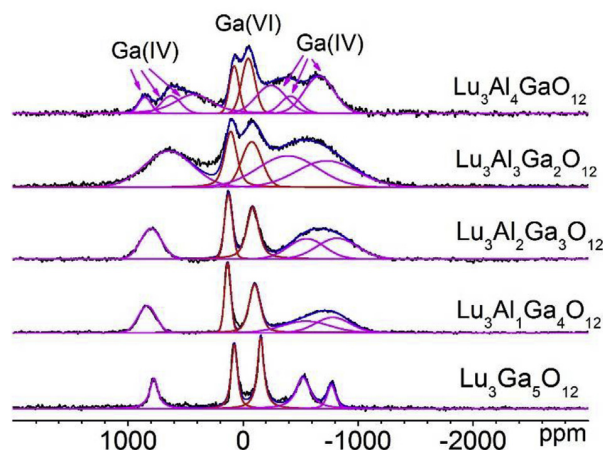


Fig. 5. ^{71}Ga magic angle spinning nuclear magnetic resonance (MAS NMR) spectra obtained for $\text{Lu}_3\text{Al}_{5-x}\text{Ga}_x\text{O}_{12}$ at a rotation speed of 20 kHz.

Table 4
⁷¹Ga NMR quadrupole parameters for the mixed Lu₃Al_{5-x}Ga_xO₁₂ compounds.

Compound	Ga(IV)			Ga(VI)		
	C _q (kHz)	η	δ _{iso} (ppm)	C _q (kHz)	η	δ _{iso} (ppm)
Lu ₃ Al ₄ GaO ₁₂	13500	0	250	4450	0	29
Lu ₃ Al ₃ Ga ₂ O ₁₂	13700	0	250	4950	0	29
Lu ₃ Al ₂ Ga ₃ O ₁₂	13800	0	260	5050	0	30
Lu ₃ AlGa ₄ O ₁₂	13900	0	270	5330	0	30
Lu ₃ Ga ₅ O ₁₂	13700	0	250	5310	0	28

**Fig. 6.** ⁷¹Ga nuclear magnetic resonance spectra obtained for Lu₃Al_{5-x}Ga_xO₁₂ single crystals. Solid lines with different colors indicate decomposition of the spectra into separate Gaussian contributions from the Ga(VI) and Ga(IV) sites (also see Ref. [25]).

inner electron shells close to the nucleus” [26]) for these atoms, i.e., −3.6 and −17 for Al and Ga, respectively.

In order to obtain the Ga(IV)/Ga(VI) occupation ratio and to consider the possible baseline distortions of the very broad Ga(IV) lines in the ⁷¹Ga MAS spectra, ⁷¹Ga static NMR spectra were measured for Lu₃Al_{5-x}Ga_xO₁₂ single crystals (Fig. 6). The spectral lines originating from the Ga(IV) and Ga(VI) sites were assigned based on the data obtained from MAS spectra while considering the essential differences between the Ga(IV) and Ga(VI) quadrupole parameters (Table 4). As a result, two groups of lines could be distinguished in the spectra for the single crystals: a group of lines shifting under crystal rotation in the range from approximately −200 to 200 ppm was assigned to Ga(VI), and another group of lines shifting with crystal rotation in the range from approximately −1000 to 1000 ppm was assigned to Ga(IV) due to its much larger quadrupole constant.

By selecting an appropriate crystal orientation, the ⁷¹Ga NMR lines of Ga(IV) can be resolved well from the Ga(VI) sites even for the broadened spectral lines of all the Lu₃Al_{5-x}Ga_xO₁₂ mixed compounds (x = 1–5; see Fig. 6). The Ga(IV)/Ga(VI) occupation ratios calculated from the single-crystal spectra are listed in Table 5 and they are compared with the values recalculated from the Al(IV)/Al(VI) ratio according to the following relationships:

$$(N_{\text{Al(IV)}} + N_{\text{Ga(IV)}})/(N_{\text{Al(VI)}} + N_{\text{Ga(VI)}}) = 3/2 \quad (4)$$

$$(N_{\text{Al(IV)}} + N_{\text{Al(VI)}})/(N_{\text{Ga(IV)}} + N_{\text{Ga(VI)}}) = (5-x)/x,$$

where $N_{\text{Al(IV)}}$ and $N_{\text{Al(VI)}}$, and $N_{\text{Ga(IV)}}$ and $N_{\text{Ga(VI)}}$ are the numbers of Al and Ga atoms in the tetrahedral and octahedral positions, respectively.

Due to the broad spectral lines in the ⁷¹Ga NMR spectra, the accuracy when determining the Ga(IV)/Ga(VI) ratio using the ⁷¹Ga NMR spectra is much lower than that recalculated from the ²⁷Al MAS NMR, and thus it can only be regarded as supplementary information.

Table 5

Ga(IV)/Ga(VI) occupation ratios in the mixed Lu₃Al_{5-x}Ga_xO₁₂ compounds determined from ⁷¹Ga and ²⁷Al NMR spectra (also see Ref. [25]).

Compound	Ga(IV)/Ga(VI)	
	Determined from ⁷¹ Ga NMR	Recalculated from ²⁷ Al MAS NMR
Lu ₃ Al ₅ O ₁₂	–	–
Lu ₃ Al ₄ GaO ₁₂	3.6	4.8
Lu ₃ Al ₃ Ga ₂ O ₁₂	3.01	2.9
Lu ₃ Al ₂ Ga ₃ O ₁₂	2.15	2.29
Lu ₃ AlGa ₄ O ₁₂	1.82	1.8
Lu ₃ Ga ₅ O ₁₂	1.49	–

Nevertheless, some additional information can be extracted from the single-crystal spectra. Considering the garnet structure with *Ia*3d symmetry, the main component of the EFG tensor of Ga(IV) should be oriented along the local $\bar{4}$ axis, which is aligned along one of the $\langle 100 \rangle$ cubic directions. This results in three magnetically inequivalent Ga(IV) sites in a single crystal, where $\eta = 0$ due to the symmetry of the tetrahedron (as also observed in MAS spectra), so only three lines should be present in the spectrum for Ga(IV). At least four distinct lines belonging to Ga(IV) are visible in the spectrum for Lu₃Al₄GaO₁₂ (Fig. 6), which indicates that the partial substitution of Al by Ga changes the orientation of the local axis for some tetrahedral sites, while leaving them otherwise undistorted. These findings together with the data obtained for Al suggest that the partial substitution of Al by Ga results in the rotation of oxygen tetrahedrons and the simultaneous deformation of oxygen octahedrons.

In order to characterize the Al and Ga ions occupations more precisely and to compare them with previously reported data for Y₃Ga_xAl_{5-x}O₁₂ crystals, the fractional occupation numbers defined as:

$$f_{\text{Al}}^{\text{tet}} = \text{Al(IV)} / (\text{Al(IV)} + \text{Al(VI)})$$

and

$$f_{\text{Al}}^{\text{oct}} = \text{Al(VI)} / (\text{Al(IV)} + \text{Al(VI)})$$

for the Al and Ga ions are shown in Fig. 7. Clearly, at x = 1, only 20% of the Ga ions occupy the octahedral sites whereas 80% occupy the tetrahedral sites. As the Ga concentration increases, both $f_{\text{Ga}}^{\text{tet}}$ and $f_{\text{Ga}}^{\text{oct}}$ tend to increase in a linear manner to values of 60% and 40%, which correspond to pure Ga garnet. Similar results were obtained for Y₃Ga_xAl_{5-x}O₁₂ by using X-ray diffraction [17] (filled and open squares in Fig. 7)

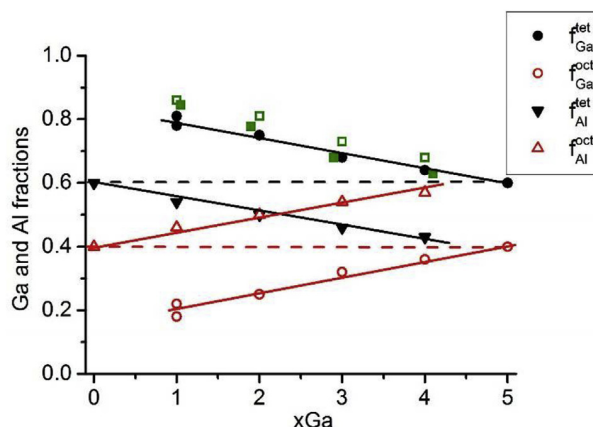
**Fig. 7.** Fractional occupations of Ga and Al ions in Lu₃Ga_xAl_{5-x}O₁₂ mixed crystals as a function of the total Ga content (also see Ref. [25]). Dashed lines correspond to the random distribution of Al and Ga over tetrahedral and octahedral sites. For comparison, the fractional occupation of Ga in Y₃Ga_xAl_{5-x}O₁₂ crystals measured by X-ray diffraction is shown by open [17] and filled [18] squares.

Table 6

List of the structures considered in the DFT calculations and the energy gained when swapping the Ga-Al pair between octahedral and tetrahedral positions.

Compound	Cation distribution over the sites, () = tetrahedral, [] = octahedral	Al(IV)/Al(VI) ratio	Space group	Energy difference per Ga-Al pair (meV)	Lattice (Å)
Lu ₃ Al ₅ O ₁₂	(Al ₂₄)[Al ₁₆]	1.5	Ia-3d	–	a = 12.02618
Lu ₃ Al ₄ GaO ₁₂	(Al ₁₆ Ga ₈)[Al ₁₆]	1.0	I4 ₁ /acd	0	a = 12.08551
	(Al ₂₄)[Al ₈ Ga ₈]	3.0	P-4	333	a = 12.08551 ^a
			Ia-3	212	a = 12.09840
			R32	535	a = 17.10972 ¹⁾ c = 20.95504
					γ = 120
Lu ₃ Al ₃ Ga ₂ O ₁₂	(Al ₈ Ga ₁₆)[Al ₁₆]	0.5	I4 ₁ /acd	0	a = 12.13917
	(Al ₁₆ Ga ₈)[Al ₈ Ga ₈]	2.0	Ibca	200	a = 12.15213
	(Al ₂₄)[Ga ₁₆]	∞	Ia-3d	195	a = 12.16265
Lu ₃ Al ₂ Ga ₃ O ₁₂	(Al ₁₆ Ga ₈)[Ga ₁₆]	∞	I4 ₁ /acd	183	a = 12.21798
	(Al ₈ Ga ₁₆)[Al ₈ Ga ₈]	1.0	Ibca	185	a = 12.21310
	(Ga ₂₄)[Al ₁₆]	0	Ia-3d	0	a = 12.19599
Lu ₃ AlGa ₄ O ₁₂	(Al ₈ Ga ₁₆)[Ga ₁₆]	∞	I4 ₁ /acd	179	a = 12.27570
			P-4	178	a = 12.27570 ¹⁾
	(Ga ₂₄)[Al ₈ Ga ₈]	0	Ia-3	9	a = 12.26098
			R32	0	a = 17.33964 ¹⁾
					c = 21.23664
					γ = 120
Lu ₃ Ga ₅ O ₁₂	(Ga ₂₄)[Ga ₁₆]	–	Ia-3d	–	a = 12.33093

^a For structures with lower symmetry, the lattice parameters were not fully optimized but instead they were taken from the corresponding structure with higher symmetry.

and NMR [20] methods, thereby indicating that the occupation of Al and Ga sites in garnets does not depend on rare earth dodecahedral cations.

3.3. DFT calculations

The electronic structures of the compounds with various gallium contents x were modeled using single garnet unit cells Lu₂₄Ga_{8x}Al_{40-8x}O₉₆ containing eight formula units. The number of possible arrangements of Al and Ga within one garnet unit cell increases rapidly when shifting away from the pure Lu₃Al₅O₁₂ or Lu₃Ga₅O₁₂ composition ($x = 0$ or 5). Therefore, in addition to designing different distributions of Ga and Al cations in the tetrahedral and octahedral sites, we also aimed to maintain reasonably high space group symmetry in order to make the calculations feasible. In addition to the two pure garnet structures Lu₃Al₅O₁₂ and Lu₃Ga₅O₁₂, we calculated mixed compounds with contents of Ga $x = 1, 2, 3$, and 4, where several symmetric configurations were tested for each x in order to consider possibly different but not necessarily random Ga distributions. All of the calculated structures and their structural data are listed in Table 6.

Different distributions of Ga over tetrahedral and octahedral sites affect the lattice parameters (Table 6), which then deviate slightly from the values predicted by Vegard's law (Fig. 8). In particular, the lattice constants for the configurations with the tetrahedral sites preferably occupied by Ga ions have somewhat lower values than those expected

according to Vegard's law. Moreover, the lattice constants for the model structures where we forced Ga to occupy the octahedral sites exhibited opposite deviations from Vegard's law (Fig. 8). The same qualitative deviation from Vegard's law was determined experimentally in a previous study [17] for Y₃Al_{5-x}Ga_xO₁₂ compounds, as well as theoretically [24] but only for two structures comprising Y₃Al_{5-x}Ga_xO₁₂, where $x = 0.6$ and Ga only occupied octahedral sites, and where $x = 0.4$ and Ga only occupied tetrahedral sites.

This deviation from Vegard's law implies changes in the cation–cation distances for different Ga distributions and effects on the repulsive forces between them [17]. We calculated the total energies for all of configurations considered, where their unit cell parameters and atomic coordinates were optimized correctly, and the remaining atomic forces were well below 0.05 eV/Å (2 mRy/a.u.). For every group of compounds with different distribution of Ga over tetrahedral and octahedral sites, the energy gains after swapping Ga(VI) + Al(IV) with Ga(IV) + Al(VI) are presented in Table 6. Our calculations clearly show that for any given composition (defined by the gallium content x), the Ga(IV) + Al(VI) scenario is more favorable than the opposite case comprising Ga(VI) + Al(IV). In all cases, the energy difference is about 0.2 eV per swapped Al + Ga pair, which implies that the occupation of the tetrahedral sites is favored more strongly for Ga regardless of the Ga concentration.

Despite Ga³⁺ having a larger ionic radius than Al³⁺, gallium clearly prefers to occupy tetrahedral sites, which have a smaller available volume than octahedral sites. Therefore, the differences in the formation of a chemical bond by Al and Ga should be considered in order to understand this apparent paradox. Analyses of the electronic structures obtained for our compounds based on the calculations demonstrate that both Al and Ga form a chemical bond in a different manner in a tetrahedral or octahedral environment, which can be clearly illustrated by considering the Lu₃Al₃Ga₂O₁₂ compound as an example. The density of states for this compound and the partial densities of states (PDOS) for selected atoms are shown in Fig. 9 (Lu 4f-states located near –2 eV are excluded from the partial densities of states because they do not participate in the formation of the chemical bond).

It is straightforward to observe that Lu d-states hybridized with Ga s-states dominate the conduction band bottom. The valence band states near the Fermi level are formed mainly by O p- and Lu d- and p-states, where a narrow band near –12 eV corresponds to the filled Ga 3d orbitals. The states near the bottom of the valence band represent semi-core O 2s-states that are slightly hybridized with Lu p- and Ga d-states.

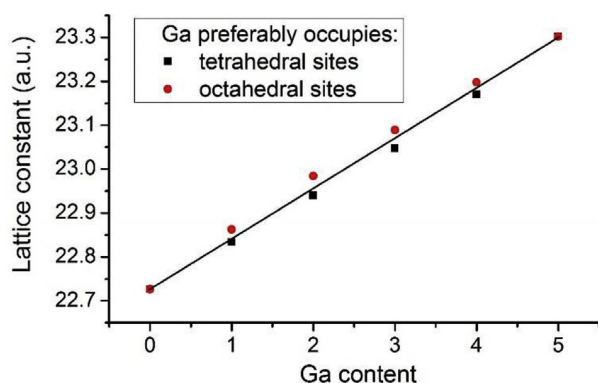


Fig. 8. Dependence of the lattice constant on the Ga content. The solid line shows the lattice constants expected according to Vegard's law.

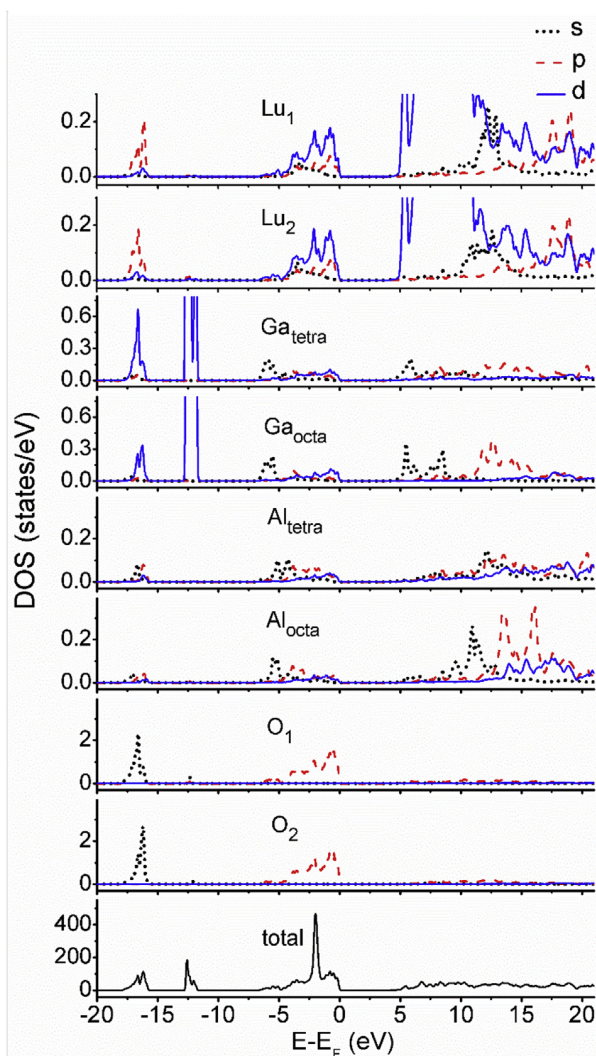


Fig. 9. Total density of states and partial densities of states for selected atoms in the $\text{Lu}_3\text{Al}_3\text{Ga}_2\text{O}_{12}$ compound.

Both the O 2s and Ga 3d orbitals are filled, so the formation of bonding and antibonding orbitals does not lead to a decrease in the total energy, and the involvement of empty Lu orbitals is necessary for the formation of the chemical bond. This results in an interaction between Lu and Ga cations, which influences the binding energy of the Ga 3d orbitals. The formation of these orbitals is shown in Fig. 10, where the spatial distribution of the Ga 3d electron density is represented. The involvement of Ga(IV) d orbitals in the formation of the chemical bond is more pronounced compared with those of Ga(VI) (see Fig. 9 and 10), apparently because of the shorter distances for Ga(IV)–O (1.86 Å compared with 2.01 Å for Ga (IV) and (VI)).

Bader charge analysis for this compound demonstrates that both Al and Ga have smaller positive charges in the tetrahedral environment than the octahedral environment (1.87 and 1.97 for Ga(IV) and Ga(VI), respectively and 2.53 and 2.57 for Al(IV) and Al(VI)), which indicates the formation of more covalent bonds by the cation located within the tetrahedron. This trend was also observed by Nakatsuka et al. [17] for $\text{Y}_3\text{Al}_{5-x}\text{Ga}_x\text{O}_{12}$ mixed compounds: “from an estimate of the proportion of covalent bonding based on bond strength.”

The tendency of Al and Ga to form more covalent bonds in a tetrahedral oxygen environment can be explained by their electronic structure. Both Al ($[\text{Ne}]3s^23p^1$) and Ga ($[\text{Ar}]3d^{10}4s^24p^1$) have ns^2np^1 valence electrons that can participate in the formation of sp^3 hybridized

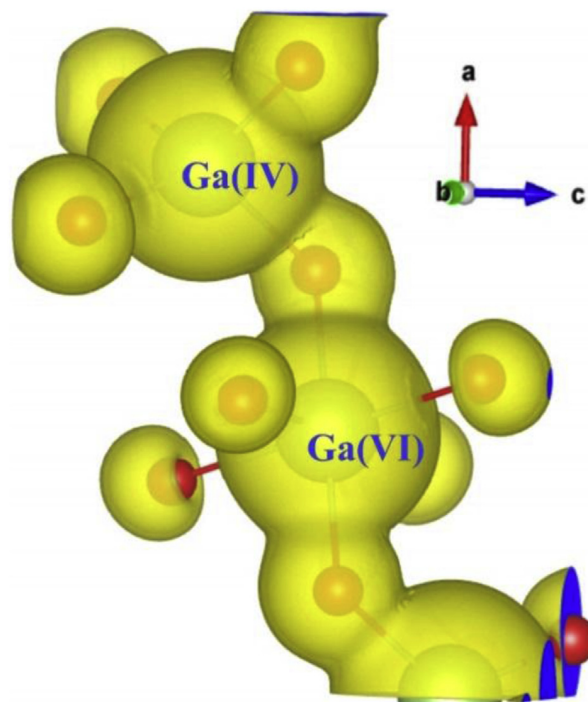


Fig. 10. Distribution of Ga 3d electron density around the Ga and O atoms in the range from -15 to -10 eV (at the isosurface level corresponding to a low charge density), showing the overlap between the electronic density of Ga and surrounding oxygen atoms (plotted using VESTA [38]).

orbitals. These hybridized orbitals have a directed character and they point to the oxygen atoms of the tetrahedron, which results in a better overlap of orbitals and leads to the formation of a more covalent bond. The formation of orbitals directed at the oxygen atoms in the octahedron (e.g., d^2sp^3 hybridization) is energetically unfavorable because of the necessary involvement of Al and Ga d- orbitals. Al 3d orbitals have substantially higher energy, whereas the Ga 3d orbitals are initially filled (they only participate weakly in the formation of the chemical bond) thus, the filled orbitals directed to oxygen exhibit Coulomb repulsion with a negative charge on it. This leads to the formation of orbitals with a delocalized character that is appropriate for an ionic bond.

Thus, both Al and Ga tend to occupy the tetrahedral environment in the garnet structure. The preference of Al for the tetrahedral sites was also deduced (e.g., see Ref. [39]) based on high pressure decomposition experiments and magnetic studies of Al- and Ga-substituted iron garnets, where it was suggested that the tetrahedral site preference “increases on going from Fe^{3+} to Al^{3+} to Ga^{3+} .” The higher electronegativity value for Ga compared with Al (1.81 vs. 1.61) results in formation of an even more covalent, stronger bond by Ga orbitals in the tetrahedron, and enhances the preference of Ga for the tetrahedral positions.

The interactions between Ga $3d^{10}$ electrons with the negative charges of the surrounding oxygen atoms also affect the energies of Ga (IV) and Ga(VI), as shown in Fig. 11, which focuses on the narrow 3d band near -12 eV. The Ga(VI) d states are shifted toward weaker binding energies compared with Ga(IV) (the opposite to the shift expected from a larger positive charge on Ga(VI)), where the “centers of gravity” are shifted by 0.34 eV. The role of Ga 3d electrons is clearly demonstrated by comparing our calculations with those performed for $\text{Y}_3\text{Al}_{2-y}\text{Ga}_y^{\text{tet}}\text{Al}_3^{\text{tet}}\text{O}_{12}$ and $\text{Y}_3\text{Al}_2^{\text{tet}}\text{Al}_{3-y}\text{Ga}_y^{\text{tet}}\text{O}_{12}$ compounds (see Ref. [23]), which were conducted using the “Ga pseudopotential generated for the reference configuration $\text{Ga}(4s^24p^1)$.” This pseudopotential considers Ga 3d electrons as core states, which effectively nullifies their

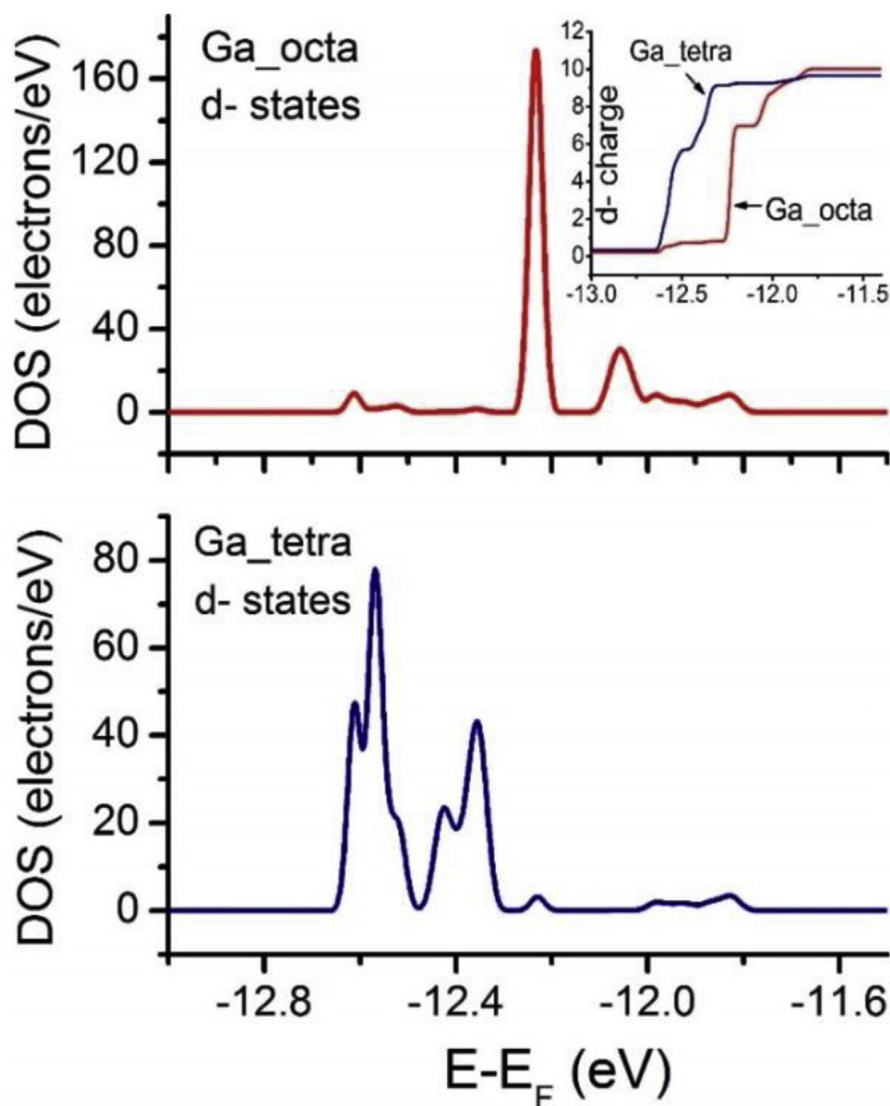


Fig. 11. Ga d local densities of states for Ga(VI) and Ga(IV) in $\text{Lu}_3\text{Al}_3\text{Ga}_2\text{O}_{12}$. The inset shows the integral charge on the d orbitals.

influence on Ga site preference. After calculating the difference in the formation energy, Munoz-Garcia and Seijo [23] concluded that at low Ga concentrations, the presence of Ga in octahedral positions is more favorable than that in tetrahedral positions, which is the opposite conclusion to that obtained based on our calculations where the 3d electrons were treated correctly.

Based on the results of both calculations and considering that the shift of the “centers of gravity” for Ga d electrons is comparable to the total energy gained for swapping a Ga–Al pair (0.2 eV for this compound), we may conclude that the interaction with Ga 3d electrons plays a decisive role in the high preference of Ga for occupying the tetrahedral positions in the garnet structure. We observe that the role of the Ga d orbitals decreases slightly as volume of all the polyhedrons increases because this leads to a decrease in the density of valence electrons. Thus, a higher concentration of Ga leads to an increase in the lattice constants and reduces the interactions with Ga d electrons, and thus the value of the energy gain is smaller for swapping the Ga–Al pair (Table 6).

The preference of Ga for occupying the tetrahedral positions at any Ga content according to our calculations and the discussion above was not fully reflected by the results of our NMR experiments where a small fraction of Ga atoms were also found in the octahedral sites and the Ga

(IV)/Ga(VI) ratio decreased as the Ga concentration increased. This discrepancy can be understood as follows. The DFT calculations correspond to the ground state at 0 K whereas in reality, the cation distribution arises during the synthesis of the crystal at high temperatures (~2000 K). The energy difference of about 0.2 eV per Ga–Al pair is comparable to the thermal energy $k_B T$ (where T is the temperature for garnet sample preparation or thermal treatment). Thus, the final cationic arrangement cannot be expected to correspond to equilibrium at 0 K, but instead it will be shifted toward a random distribution for the cations, which depends on the energy gains for the respective structures and the sample preparation conditions (thermal treatment). The effect of the treatment temperature on the distribution of cations over tetrahedral and octahedral sites in garnets was demonstrated in a previous study [40].

Our calculations show that the energy gain per one Ga(IV) + Al(VI) pair depends on the Ga concentration (Table 6) and it reflects the dependence of the Ga(IV)/Ga(VI) ratio on x according to experimental observations in $\text{Lu}_3\text{Al}_{5-x}\text{Ga}_x\text{O}_{12}$ solid solutions (Fig. 12).

We also computed the parameters for the EFG tensor: V_{zz} and asymmetry parameter η (Table 7, where V_{zz} is converted into C_q). The EFG parameters are usually in good agreement with the experimental values [41–43], and thus they can be compared directly with the NMR

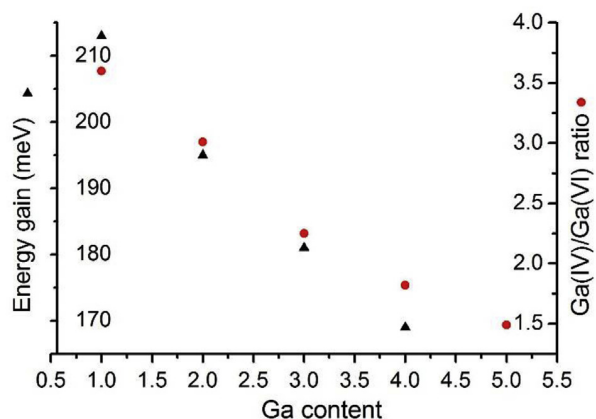


Fig. 12. Calculated energy difference for Ga occupying an octahedron instead of a tetrahedron (and vice versa for Al) according to the gallium content x (black squares), and the experimentally measured Ga(IV)/Ga(VI) ratios (red circles).

results.

Fig. 13 shows the C_q values calculated for the structures with the Al/Ga arrangement, which were set as close as possible to the real distribution observed by NMR, as well as the experimental values. The calculations slightly underestimate the C_q values but they general agree well with the NMR experimental values, thereby confirming our interpretation of the measured results.

According to our calculations and the experimental values, the partial substitution of Al by Ga leads to increases in the C_q values for both Al(VI) and Ga(VI), which indicates the distortion of oxygen octahedrons. However, X-ray diffraction data measured for $Y_3Al_{5-x}Ga_xO_{12}$ mixed compounds [17,18] and our calculations performed for mixed $Lu_3Al_{5-x}Ga_xO_{12}$ compounds indicate increases in the lattice constants, which are usually associated with decreased deformation.

The distortions of oxygen octahedrons as the Ga content increases can be explained by the non-uniformity of the octahedral environment due to the partial substitution of Al by Ga. Each oxygen atom in the garnet structure is shared by an octahedron, tetrahedron, and two Lu-dodecahedrons, so the Ga-O and Al-O distances in the octahedron depend on the type of central atom in the shared tetrahedron. For $Lu_3Al_5O_{12}$, all of the calculated Al(VI)-O distances are identical and equal to 1.93629 Å, whereas in the case of $Lu_3Al_4GaO_{12}$, the Al(VI)-O distances are elongated (1.94101 Å) for Al(VI)-O-Al(IV) and shortened (1.92392 Å) for Al(VI)-O-Ga(IV). Moreover, due to the higher Ga electronegativity (compared with Al), the oxygen atom connected to Ga receives a lower negative charge via the formation of a chemical bond, which results in a non-uniform charge distribution around the Al atom and adds to the EFG value.

However, in the case of Ga octahedrons, the observed changes in the C_q values cannot be explained in this manner for all compounds. In particular, the C_q value for Ga(VI) in $Lu_3Ga_5O_{12}$ is noticeably higher compared with that for Ga(VI) in $Lu_3Al_4GaO_{12}$ (Tables 4 and 7). At the same time, the $Lu_3Ga_5O_{12}$ compound has larger octahedral volumes and in contrast to $Lu_3Al_4GaO_{12}$, it has an absolutely uniform environment of Ga octahedrons. Therefore, other mechanisms must be responsible for the increased EFG in mixed crystals. In order to avoid the influence of the type of central atom (Al/Ga) on C_q , Table 8 shows the distortions in all of the polyhedrons in terms of the deviations between their bond angles and those in the regular polyhedron.

In general, Table 8 shows that Ga polyhedrons are more distorted than the Al polyhedrons, where the distortion of the octahedrons increases as the Ga content increases, whereas the tetrahedrons remain almost unchanged. Apparently, stronger covalent bonding formed due to sp^3 hybridization by the Al or Ga valence orbitals prevents any significant deformation of the tetrahedron, as shown by the unchanged C_q values in the tetrahedrons (Tables 2, 4 and 7) and the relatively constant bond angles (Table 8). Thus, we propose the following concept to explain the structural changes that accommodate the Al \leftrightarrow Ga substitution. The lengths of the Ga(IV)-O bonds are larger than those of Al(IV)-O, but the Lu-O distance and minimal O-O distance between the nearest oxygen atoms are limited only by the ionic radii of Lu and O. These radii do not change substantially after Al \leftrightarrow Ga substitution thus, the expansion of the structure is nonlinear. The Al \leftrightarrow Ga substitution changes the distance between the cation and oxygen atom, and distorts all of the remaining polyhedrons in order to preserve the shape of the Al/Ga tetrahedrons. However, a simple expansion of the tetrahedron in the Ga-O direction (see Fig. 14) would severely increase the trigonal distortion for a neighboring octahedron via the deformation of the oxygen triangle (denoted by the red dotted line in Fig. 14) positioned around the trigonal axis (blue arrow). Thus, it is more favorable to shift these three oxygen atoms (and their respective counterparts) in a perpendicular direction, i.e., along the trigonal axis, which increases the octahedral distortion only moderately while simultaneously causing rotation of the unperturbed tetrahedron. For a given octahedron, when more neighboring tetrahedrons are occupied by gallium, the forces that shift the oxygen triangles along the trigonal axis are higher, which enhances the trigonal deformation of the octahedron (Table 8) and C_q increases as a consequence, regardless of the type of the central atom (Al/Ga).

4. Summary

In this study, ^{27}Al and ^{71}Ga solid-state NMR data were obtained for mixed $Lu_3Al_{5-x}Ga_xO_{12}$ compounds in the form of bulk and ground single crystals. Single crystal, powder static, and MAS spectra were measured and analyzed, which allowed us to determine the full set of spectral

Table 7
Calculated EFG parameters C_q (in kHz) and η for Ga and Al nuclei in all of the structures considered.

Compound	Cation distribution over () = tetrahedral, [] = octahedral sites	Al(IV)/Al(VI)	Al(IV)		Al(VI)		Ga(IV)		Ga(VI)	
			C_q	η	C_q	η	C_q	η	C_q	η
$Lu_3Al_5O_{12}$	(Al ₂₄)[Al ₁₆]	1.5	5993	0	1045	0	–	–	–	–
$Lu_3Al_4GaO_{12}$	(Al ₁₆ Ga ₈)[Al ₁₆]	1.0	5766	0.1	1662	0.49	12568	0	–	–
$Lu_3Al_4GaO_{12}$	(Al ₂₄)[Al ₈ Ga ₈]	3.0	6183	0.46	907	0	–	–	2976	0
$Lu_3Al_3Ga_2O_{12}$	(Al ₈ Ga ₁₆)[Al ₁₆]	0.5	5608	0	1966	0.43	12195	0.1	–	–
$Lu_3Al_3Ga_2O_{12}$	(Al ₁₆ Ga ₈)[Al ₈ Ga ₈]	2.0	6040	0.58	1555	0.59	12897	0.37	3984	0.31
$Lu_3Al_3Ga_2O_{12}$	(Al ₂₄)[Ga ₁₆]	–	6326	0	–	–	–	–	2622	0
$Lu_3Al_2Ga_3O_{12}$	(Al ₁₆ Ga ₈)[Ga ₁₆]	–	6182	0.11	–	–	13022	0	3847	0.38
$Lu_3Al_2Ga_3O_{12}$	(Al ₈ Ga ₁₆)[Al ₈ Ga ₈]	1.0	5772	0.5	1785	0.47	12504	0.47	4474	0.32
$Lu_3Al_2Ga_3O_{12}$	(Ga ₂₄)[Al ₁₆]	–	–	–	2031	0	11803	0	–	–
$Lu_3AlGa_4O_{12}$	(Al ₈ Ga ₁₆)[Ga ₁₆]	–	5991	0	–	–	12686	0.09	4228	0.43
$Lu_3AlGa_4O_{12}$	(Ga ₂₄)[Al ₈ Ga ₈]	0	–	–	1797	0	12138	0.41	4692	0
$Lu_3Ga_5O_{12}$	(Ga ₂₄)[Ga ₁₆]	–	–	–	–	–	11514	0	4129	0

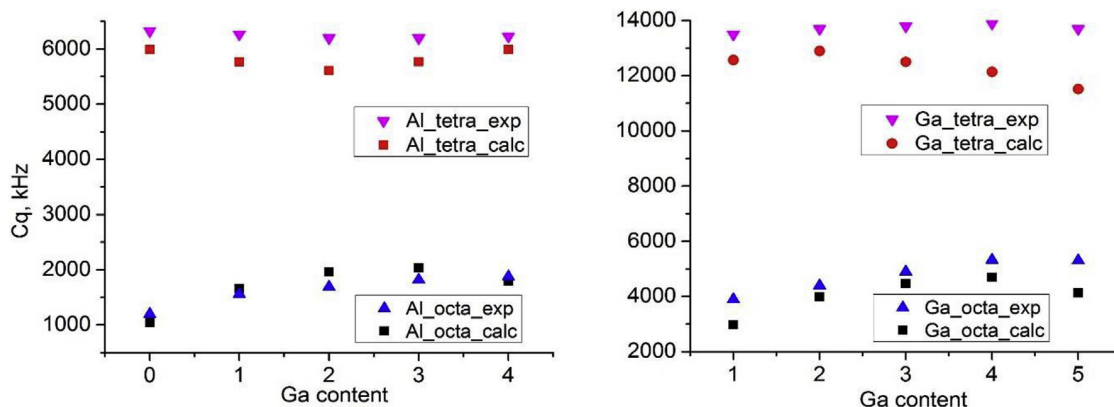


Fig. 13. Calculated quadrupole constants C_q obtained from nuclear magnetic resonance experiments and density functional theory calculations according to the gallium content x .

Table 8

Bond angle variance (represented as the sum of the squares of the differences between the angles in the computed and regular polyhedron) calculated for all of the structures considered.

Compound	Cation distribution over tetrahedral (), and octahedral [] sites	Bond angle variance (deg ²)			
		Al(IV)	Al(VI)	Ga(IV)	Ga(VI)
Lu ₃ Al ₅ O ₁₂	(Al24)[Al16]	59.14	17.73	–	–
Lu ₃ Al ₄ GaO ₁₂	(Al16Ga8)[Al16]	56.17	24.75	74.08	–
	(Al24)[Al8Ga8]	66.63	17.33	–	25.83
Lu ₃ Al ₃ Ga ₂ O ₁₂	(Al8Ga16)[Al16]	53.93	32.68	71.03	–
	(Al16Ga8)[Al8Ga8]	62.94	24.34	82.51	33.99
	(Al24)[Ga16]	68.06	–	–	24.80
Lu ₃ Al ₂ Ga ₃ O ₁₂	(Al16Ga8)[Ga16]	66.07	–	84.93	32.74
	(Al8Ga16)[Al8Ga8]	60.60	31.01	78.02	43.25
	(Ga24)[Al16]	–	41.00	67.62	–
Lu ₃ AlGa ₄ O ₁₂	(Al8Ga16)[Ga16]	63.00	–	82.17	41.47
	(Ga24)[Al8Ga8]	–	38.86	76.14	53.48
Lu ₃ Ga ₅ O ₁₂	(Ga24)[Ga16]	–	–	78.80	51.35

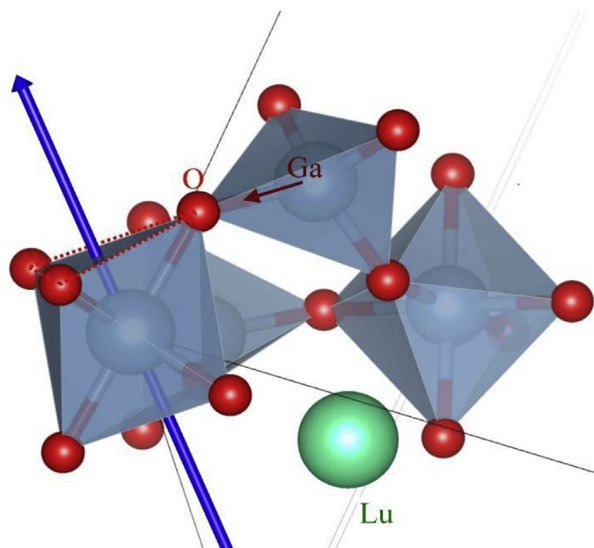


Fig. 14. Fragment of the Lu₃Ga₅O₁₂ structure showing the trigonal distortion of the oxygen octahedron (plotted using VESTA [38]).

parameters (chemical shifts and quadrupole frequencies) to describe the NMR spectra, including the distribution of the Al and Ga ions over the tetrahedral and octahedral sites in the garnet lattice as a function of the Ga content. In particular, we found that quadrupole interactions of

both ²⁷Al and ⁷¹Ga in a tetrahedral environment do not vary with the Ga content in the solid solutions, thereby suggesting that the tetrahedrons do not undergo additional marked distortion, but instead they can be rotated. By contrast, the quadrupole parameters of both nuclei in an octahedral environment increase substantially as the Ga content increases despite the growth of the octahedral volumes, which is associated with trigonal deformation of the octahedrons. Thus, most of the structural relaxation after Al is substituted by Ga occurs via deformations of the octahedrons and the simultaneous rotation of undeformed tetrahedrons. The observed behavior was well reproduced by our DFT calculations for the EFG tensor.

The Al and Ga site occupancies were calculated precisely from the ⁷¹Ga and ²⁷Al NMR spectra. We found that the partial substitution of Al by Ga results in a heterogeneous distribution of Ga atoms over the tetrahedral and octahedral sites in the garnet structure. In all of compounds considered, despite its larger ionic radius, gallium tends to occupy the tetrahedral positions, which have a smaller volume than the octahedral positions. This was also supported by the DFT calculations performed for all of the compounds, which showed that the allocation of Ga to the tetrahedral sites is energetically more favorable for any Ga content. The energy difference between the Ga(IV) + Al(VI) and Ga(VI) + Al(IV) scenarios is about 0.2 eV for one Ga + Al pair, and this value decreases slightly as the Ga content increases.

Both Al and Ga have a larger covalent component in the chemical bond in a tetrahedral environment compared with an octahedral environment. The higher electronegativity value of Ga compared with Al exacerbates this difference for Ga atoms and makes its replacement of Al in the tetrahedral sites energetically more favorable. Nevertheless, the differences in the electronic structure of Al and Ga atoms need to be considered in order to explain the Ga occupancy preferences. Both Al and Ga have ns²np¹ valence electrons, but Ga possesses a filled 3d shell, which must be considered when investigating substitutions in different environment. The involvement of Ga 3d electrons in the interaction leads to a significant shift of Ga-tetra d electron energies toward stronger binding energies in comparison with Ga-octa d electrons, which determines the tendency of Ga to occupy the tetrahedral positions in the garnet structure.

Acknowledgments

Financial support provided under Czech Science Foundation grant 17-09933S is gratefully acknowledged. Computational resources were provided by CESNET LM2015042 and the CERIT Scientific Cloud LM2015085 under the “Projects of Large Research, Development, and Innovations Infrastructures” program.

References

- [1] R.C. Powell, *Physics of Solid State Laser Materials*, AIP, New York, 1998.
- [2] V. Bachmann, C.R. Ronda, A. Meijerink, *Chem. Mater.* 21 (2009) 2077.
- [3] L. Havlák, J. Bárta, M. Buryi, V. Jarý, E. Mihóková, V. Laguta, M. Nikl, *J. Phys. Chem. C* 120 (2016) 21751.
- [4] M. Nikl, A. Yoshikawa, K. Kamada, K. Nejezchleb, C.R. Stanek, J.A. Mares, K. Blazek, *Prog. Cryst. Growth Char. Mater.* 59 (2013) 47–72.
- [5] Z. Xia, A. Meijerink, *Chem. Soc. Rev.* 46 (2017) 275.
- [6] K. Kamada, S. Kurosawa, P. Prusa, M. Nikl, V.V. Kochurikhin, T. Endo, K. Tsutumi, H. Sato, Y. Yokota, K. Sugiyama, A. Yoshikawa, *Opt. Mater.* 36 (2014) 1942–1945.
- [7] O. Sidletskiy, V. Kononets, K. Lebbou, S. Neicheva, O. Voloshina, V. Bondar, V. Baumer, K. Belikov, A. Gektin, B. Grinyov, M.-F. Joubert, *Mater. Res. Bull.* 47 (2012) 3249–3252.
- [8] P. Dorenbos, *IEEE Trans. Nucl. Sci.* 57 (2010) 1162–1167.
- [9] K. Kamada, T. Yanagida, T. Endo, K. Tsutumi, Y. Fujimoto, A. Fukabori, A. Yoshikawa, J. Pejchal, M. Nikl, *Cryst. Growth Des.* 11 (2011) 4484–4490.
- [10] P. Sibczynski, J. Iwanowska-Hanke, M. Moszyński, L. Swiderski, M. Szawłowski, M. Grodzicka, T. Szczesniak, K. Kamada, A. Yoshikawa, *Nucl. Instrum. Methods Phys. Res., Sect. A* 772 (2015) 112–117.
- [11] Y. Wu, J. Luo, M. Nikl, G. Ren, *Appl. Mater.* 2 (2014) 012101.
- [12] M. Fasoli, A. Vedda, M. Nikl, C. Jiang, B.P. Uberuaga, D.A. Andersson, K.J. McClellan, C.R. Stanek, *Phys. Rev. B* 84 (2011) 081102(R).
- [13] M. Nikl, A. Vedda, V.V. Laguta, *Radiat. Meas.* 42 (2007) 509–514.
- [14] S.K. Yadav, B.P. Uberuaga, M. Nikl, C. Jiang, C.R. Stanek, *Phys. Rev. Appl.* 4 (2015) 054012.
- [15] R.D. Shannon, *Acta Crystallogr. A: Found. Adv.* 32 (1976) 751–767.
- [16] F. Euler, J.A. Bruce, *Acta Crystallogr.* 19 (1965) 971.
- [17] A. Nakatsuka, A. Yoshiasa, T. Yamanaka, *Acta Crystallogr. B: Struct. Sci., Cryst. Eng. Mater. B* 55 (1999) 266–272.
- [18] M. Marezio, J.P. Remeika, P.D. Dernier, *Acta Crystallogr. B: Struct. Sci., Cryst. Eng. Mater. B* 24 (1968) 1670–1674.
- [19] N. Gautier, M. Gervais, C. Landron, D. Massiot, J.-P. Coutures, *Phys. Status Solidi* 165 (1998) 329–336.
- [20] V. Laguta, Yu. Zorenko, V. Gorbenko, A. Iskaliyeva, Yu. Zagorodniy, O. Sidletskiy, P. Bilski, A. Twardak, M. Nikl, *J. Phys. Chem. C* 120 (2016) 24400–24408.
- [21] T.Y. Tien, E.F. Gibbons, R.G. DeLosh, P.J. Zacmanidis, D.E. Smith, H.L. Stadler, *J. Electrochem. Soc.* 120 (1973) 278–281.
- [22] J.M. Robertson, M.W. van Tol, W.A. Smits, J.P.H. Heynen, *Philips J. Res.* 36 (1981) 15–30.
- [23] A.B. Munoz-Garcia, L. Seijo, *Phys. Rev. B* 82 (2010) 184118.
- [24] C.R. Stanek, C. Jiang, S.K. Yadav, K.J. McClellan, B.P. Uberuaga, D.A. Andersson, M. Nikl, *Phys. Status Solidi B* 250 (2013) 244–248.
- [25] V. Babin, M. Buryi, V. Chlan, Y. Fomichov, K. Kamada, V.V. Laguta, M. Nikl, J. Pejchal, H. Štěpánková, A. Yoshikawa, Yu. Zagorodniy, S. Zazubovich, *J. Lumin.* 200 (2018) 141–150.
- [26] K.J.D. Mackenzie, M.E. Smith, *Multinuclear Solid-state NMR of Inorganic Materials* vol. 6, Pergamon Materials Series, an Imprint of Elsevier Science, Amsterdam, 2002.
- [27] N. Gautier, D. Massiot, I. Farnan, J.P. Coutures, *J. Chem. Phys.* 92 (1995) 1843–1846.
- [28] A. Yoshikawa, M. Nikl, G. Boulon, T. Fukuda, *Opt. Mater.* 30 (2007) 6.
- [29] R. Ernst, S. Bodenhausen, A. Wokaun, *Principles of NMR in One and Two Dimensions*, Oxford University Press, New York, 1987.
- [30] P. Blaha, K. Schwarz, G. Madsen, D. Kvasnicka, J. Luitz, *WIEN2k, an Augmented Plane Wave + Local Orbitals Program for Calculating Crystal Properties*, vol. 28, Technische Universität Wien, Wien, 2001.
- [31] J.P. Perdew, K. Burke, M. Ernzerhof, *Phys. Rev. Lett.* 77 (1996) 3865L.
- [32] Th. Vosegaard, I.P. Byriel, D.A. Pawlak, K. Wozniak, H.J. Jakobsen, *J. Am. Chem. Soc.* 120 (1998) 7900–7904.
- [33] Th. Vosegaard, D. Massiot, N. Gautier, H.J. Jakobsen, *Inorg. Chem.* 36 (1997) 2446–2450.
- [34] J.F. Bangher, P.C. Taylor, T. Oja, P.J. Bray, *J. Chem. Phys.* 50 (1969) 4914–4925.
- [35] Pascal P. Man, Roderick E. Wasylshen, Sharon E. Ashbrook, Stephen Wimperis (Eds.), *NMR of Quadrupolar Nuclei in Solid Materials*, John Wiley & Sons, 2012, pp. 3–16 Part A: Basic Principles, (Chapter 1), Quadrupolar Interactions.
- [36] Jørgen Skibsted, Niels Chr. Nielsen, Henrik Bildsoe, Hans J. Jakobsen, *J. Magn. Reson.* 95 (1991) 88–117.
- [37] E.V. Charnaya, C. Tien, J.J. Lu, R.R. Wu, S.N. Ivanov, E.N. Khazanov, *J. Phys. Condens. Matter* 13 (2001) 8775–8782.
- [38] K. Momma, F. Izumi, *J. Appl. Crystallogr.* 44 (2011) 1272–1276.
- [39] M. Marezio, J.P. Remeika, A. Jayaraman, *J. Chem. Phys.* 45 (1966) 1821.
- [40] P. Roschmann, *J. Phys. Chem. Solid.* 41 (1980) 569–581.
- [41] Frédéric A. Perras, David L. Bryce, *J. Phys. Chem. C* 116 (2012) 19472–19482.
- [42] V. Chlan, P. Novák, H. Štěpánková, J. Englich, J. Kuriplach, D. Nižňanský, *J. Appl. Phys.* 99 (2006) 08M903.
- [43] R.E. Alonso, L. Errico, M. Taylor, A. Svane, N.E. Christensen, *Phys. Rev. B* 91 (2015) 085129.